Title

Symmetrically and Non-symmetrically Substituted 1,1’-ferrocenes as Supporting Ligands for Divalent Metals in Catalysis

Author

Abubekerov, Mark

Publication Date

2017

Peer reviewed|Thesis/dissertation

UNIVERSITY OF CALIFORNIA

Los Angeles

Symmetrically and Non-symmetrically Substituted 1,1'-ferrocenes as Supporting Ligands for Divalent Metals in Catalysis

A dissertation submitted in partial satisfaction of the

requirements for the degree Doctor of Philosophy

in Chemistry

by

Mark Abubekerov

2017

ABSTRACT OF THE DISSERTATION

Symmetrically and Non-symmetrically Substituted 1,1'-ferrocenes

as Supporting Ligands for Divalent Metals in Catalysis

by

Mark Abubekerov

Doctor of Philosophy in Chemistry

University of California, Los Angeles, 2017

Professor Paula Loredana Diaconescu, Chair

The synthesis of new polymers is motivated by the limitations of current materials. Recently, interest in copolymers containing blocks that display different or complementary properties has been increasing since these materials have potential for further performance enhancements. Inspired by recent developments in olefin polymerization catalysts, and based on the interest of the Diaconescu group in the reactivity of complexes supported by ferrocene-based chelating ligands, we developed a new ferrocene-chelating heteroscorpionate supporting ligand and investigated its applications in combination with late transition metals to redox-switchable catalysis for the production of multiblock copolymers. Additionally, we began investigations into the influence of the iron-secondary metal interactions on redox-switchable catalysis in complexes supported by symmetrically substituted, neutral ferrocene-based ligands.

The dissertation of Mark Abubekerov is approved.

Jeffrey I Zink

Andrea M Kasko

Paula Loredana Diaconescu, Committee Chair

University of California, Los Angeles

2017

This thesis is dedicated to my family.

TABLE OF CONTENTS

LIST OF FIGURES, EQUATIONS, SCHEMES AND TABLES

Chapter 1

Chapter 2

Chapter 3

ACKNOWLEDGMENTS

I would like to start by thanking my family. First of all, my endless gratitude goes to my wife Lucy without whom the last five years would have been intolerable. Your love and support allowed me to make it through the worst of days and continue through with my goals to the end. My parents and sister, you've always supported my educational endeavors and without you I would not have aspired to attend UC Berkeley for an undergraduate degree in chemistry, and thus make my way to graduate school.

As the beginning of my research endeavors, I would like to mention a few very important people who, during my undergraduate years, helped build the foundation of my scientific career. Thomas Gianetti and Henry (Pete) La Pierre, without your guidance I would have been lost as an undergraduate, and worse yet, completely unprepared for graduate school. Of course, all of this would not be possible without Prof. John Arnold who allowed me to pursue my scientific curiosity and pursue my choice of projects even after my graduation from UC Berkeley.

Over the last 5 years at UCLA I had the pleasure to work with some exceptional people. First, I'd like to mention two very capable and bright undergraduate students in particular, Scott Shepard and Kevin Swartz. Thank you for all your hard work during our collaborations and I wish you the best in your own graduate studies. To my fellow graduate students, Jon Brosmer and Stephanie Quan, thank you for all your help. Graduate school would not have been the same without you. To my good friend Ben Lesel, our gym days were indispensible for making it through this sanely and I will truly miss them. Finally, my sincerest and deepest gratitude goes to my advisor, Paula Diaconescu. Without your continual support and interest in my education and

development as a scientist I would not have been able to accomplish what I did or become who I am today.

Specific acknowledgements for this work:

Chapter 2 is a version of [Abubekerov, M.; Diaconescu, P. L. *Inorg. Chem.* **2015**, *54*, 1778-1784. DOI: 10.1021/ic502691b].

Chapter 3 is a version of [Abubekerov, M.; Shepard, S.; Diaconescu, P. L. *Eur. J. Inorg. Chem.* **2016**, 2634-2640. DOI: 10.1002/ejic.201501295].

Chapter 4 is a revised version of a submitted manuscript [Abubekerov, M.; Wei, J.; Swartz, K. R.; Xie, Z.; Pei, Q.; Diaconescu, P. L. *ACS Catalysis,* **2017**].

Chapter 5 is a version of a manuscript in the final stages of preparation prior to submission [Abubekerov, M.; Vlček, V.; Wei, J.; Miehlich, M. E.; Quan, S. M.; Meyer, K.; Neuhauser, D.; Diaconescu, P. L.]

Chapter 6 is a version of a submitted manuscript [Abubekerov, M.; Khan, S. I.; Diaconescu, P. L. *Organometallics,* **2017**].

Scott Shepard accomplished the preparation and characterization of substituted norbornenes for chapter 3.

Kevin Swartz's determination of the thermal and, along with Zhixin Xie with support from Prof. Qibing Pei, mechanical properties of the lactide/trimethylene carbonate block copolymer was an invaluable contribution to chapter 4.

Dr. Junnian Wei contributed computational work, which helped to explain the catalytic activity observed in zinc mediated ring-opening polymerizations described in chapters 4 and 5.

The determination of magnetic properties of the oxidized zinc complex described in chapter 5 would not have been possible without Matthias Miehlich and Prof. Karsten Meyer.

Dr. Vojtěch Vlček performed computational assessment of the electronic structure of the oxidized zinc complex in chapter 5 with the support from Prof. Daniel Neuhauser.

Dr. Saeed Khan was responsible for the acquisition of solid state molecular structures presented in chapter 6.

This work was financially supported by the NSF (CAREER Grant 0847735 and 1362999 to PLD and CHE-1048804 for NMR spectroscopy) and the John Simon Guggenheim Memorial Foundation.

VITA

EDUCATION

B.S., Chemistry, University of California – Berkeley, CA 2011

AWARDS

Inorganic Chemistry Award, UCLA Chemistry and Biochemistry Department 2017

Dissertation Year Fellowship, UCLA Graduate Division 2016

Travel Award, Division of Inorganic Chemistry of American Chemical Society 2016

Faculty Award for Innovation in Inorganic Chemistry, UCLA Chemistry and Biochemistry Department 2015

Excellence in Second Year Academics and Research, UCLA Chemistry and Biochemistry Department 2014

PUBLICATIONS

1. *Influence of the oxidation state of ferrocene heteroscorpionate zinc(II) complexes on the polymerization of cyclic esters and carbonates.* Abubekerov, M.; Vlček, V.; Wei, J.; Miehlich, M. E.; Quan, S. M.; Meyer, K.; Neuhauser, D.; Diaconescu, P. L. *manuscript in preparation.*
2. *Ferrocene-phosphinimine nickel(II) and palladium(II) alkyl complexes: influence of the Fe-M (M = Ni, Pd) interaction on redox activity and olefin coordination.* Abubekerov, M.; Khan, S. I.; Diaconescu, P. L. *Organometallics*, *manuscript submitted.*
3. *Preparation of multiblock copolymers via step-wise addition polymerization of L-lactide and trimethylene carbonate.* Abubekerov, M.; Wei, J.; Swartz, K. R.; Xie, Z.; Pei, Q.;

Diaconescu, P. L. *ACS Catalysis*, *under review*.

4. *Activation of heteroallenes by coordinatively unsaturated nickel(II) alkyl complexes supported by the hydrotris(3-phenyl-5-methyl)pyrazolyl borate ($Tp^{Ph,Me}$) ligand.* Abubekerov, M.; Eymann, L. Y. M.; Gianetti, T. L.; Arnold, J. *Dalton Trans.* **2016**, *45*, 14581-14590.
5. *Switchable polymerization of norbornene derivatives by a palladium(II) ferrocene heteroscorpionate complex.* Abubekerov, M.; Shepard, S.; Diaconescu, P. L. *Eur. J. Inorg. Chem.* **2016**, 2634-2640.
6. *Synthesis and characterization of ferrocene-chelating heteroscorpionate complexes of nickel(II) and zinc(II).* Abubekerov, M.; Diaconescu, P. L. *Inorg. Chem.* **2015**, *54*, 1778-1784.
7. *Synthesis and characterization of coordinatively unsaturated nickel(II) and manganese(II) alkyl complexes supported by the hydrotris(3-phenyl-5-methylpyrazolyl)borate ($Tp^{Ph,Me}$) ligand.* Abubekerov, M.; Gianetti, T. L.; Kunishita, A.; Arnold, J. *Dalton Trans.* **2013**, *42*, 10525-10530.
8. *Vanadium bisimide bonding investigated by x-ray crystallography, ^{51}V and ^{13}C nuclear magnetic resonance spectroscopy, and V $L_{3,2}$-edge x-ray absorption near-edge structure spectroscopy.* La Pierre, H. S.; Minasian, S. G.; Abubekerov, M.; Kozimor, S. A.; Shuh, D. K.; Tyliszczak, T.; Arnold, J.; Bergman, R. G.; Toste, F. D. *Inorg. Chem.* **2013**, *52*, 11650–11660.

CHAPTER 1: INTRODUCTION

1.1 Developing redox-switchable polymerization systems by utilizing divalent metals supported by ferrocene-based ligands

The synthesis of new polymers is motivated by the limitations of current materials. Recently, interest in copolymers containing blocks that display different or complementary properties has been increasing since it is thought that these materials have potential for further performance enhancements. A convenient method for the preparation of polymeric materials with complex microstructure is via switchable catalysis.[1] In such systems, the activity towards a select monomer depends on the distinct state of the catalyst that is induced by external stimuli (i.e. thermal, photo, chemical, or redox). Early examples of switchable catalysts showed polymerization rate dependence on the state of the catalyst towards a single monomer, i.e., it could be switched between two states with different activity, mostly on/off. In later examples, each state of the catalyst displayed reactivity towards a specific monomer, thus allowing for the single pot preparation of block copolymers.[1] Inspired by recent developments in olefin polymerization catalysts,[2] and based on the interest of the Diaconescu group in the reactivity of complexes supported by ferrocene-based chelating ligands, we began an investigation into redox-switchable catalysis in combination with earth abundant metals for the synthesis of olefinic copolymers and ring-opening polymerization of cyclic esters and carbonates for the formation of biodegradable copolymers.

Redox-switchable catalysis is an atom-economical method that generates multiple catalytically active species.[3] Because both species originate from a single precursor, the cost of chemical synthesis is greatly reduced. The attraction of redox-switchable catalysis is enhanced

by the possibility that a complex may show a difference in reactivity or selectivity during catalysis by switching between the oxidized and reduced forms.[4] One way to modulate reactivity and selectivity is through the redox control of the supporting ligand in a metal complex. Ferrocene is an ideal choice as a redox active handle in supporting ligands due to the typically reversible nature of its redox processes. For this reason, examples of ferrocene-based ligands in redox-switchable polymerizations are numerous and span ring-opening metathesis polymerization,[5,6] olefin polymerizations,[7,8] and ring-opening polymerizations.[9-11] In the majority of these cases, the ferrocene derivatives are symmetrically 1,1'-disubstituted, due to the ease of such modification, and display an "on" activity in one oxidation state of ferrocene and "off" in the other. Currently, there are only two examples of monomer-selective catalysts that are controlled by the identity of the redox state of ferrocene-based ligands; these examples were reported by our group and contain zirconium and titanium, early transition metals in high oxidation states. [10,11]

Due to the lack of suitable ferrocene-based, monoanionic supporting ligands for divalent metals, we decided to develop a new class of ligands. Our initial efforts in this regard began with a look at a versatile class, poly(pyrazolyl)borates, which made their first appearance in the 1960s and were initially described by Trofimenko as a "new and fertile" area of research.[12] Since then, poly(pyrazolyl)borates have found widespread applications in fields spanning from inorganic to bioinorganic chemistry.[13] Of these, tris(pyrazolyl)borates (Tp, Figure 1-1) typically coordinate in a κ^3 fashion and are synthetically easy to modify via substitutions at the 3, 4, and 5 positions of the pyrazole groups to produce specific steric and electronic properties. Despite their stereoelectronic versatility and widespread applications, poly(pyrazolyl)borates lack the potential for redox activity.[14] In order to address this dilemma, several examples of ferrocene substituted

poly(pyrazolyl)borates have been synthesized (Figure 1-1),[15,16] but no applications to catalysis have been reported.

Ferrocene-based chelating ligands are particularly interesting since they impart special steric and electronic properties to the resulting metal complexes and show better selectivity in redox-switchable catalysis than their non-chelating variants.[3,17] Based on this, we developed a class of novel bis(pyrazolyl)borates with a ferrocene moiety to be involved in the chelating process (Figure 1-1) as supporting ligands for earth abundant metals (nickel and zinc). The presence of a phosphine allows further tuning of the steric and electronic properties of the metal centers of interest. The resulting metal complexes were investigated as potential systems for redox-switchable catalysis for the formation of block copolymers (Chapters 2-5).

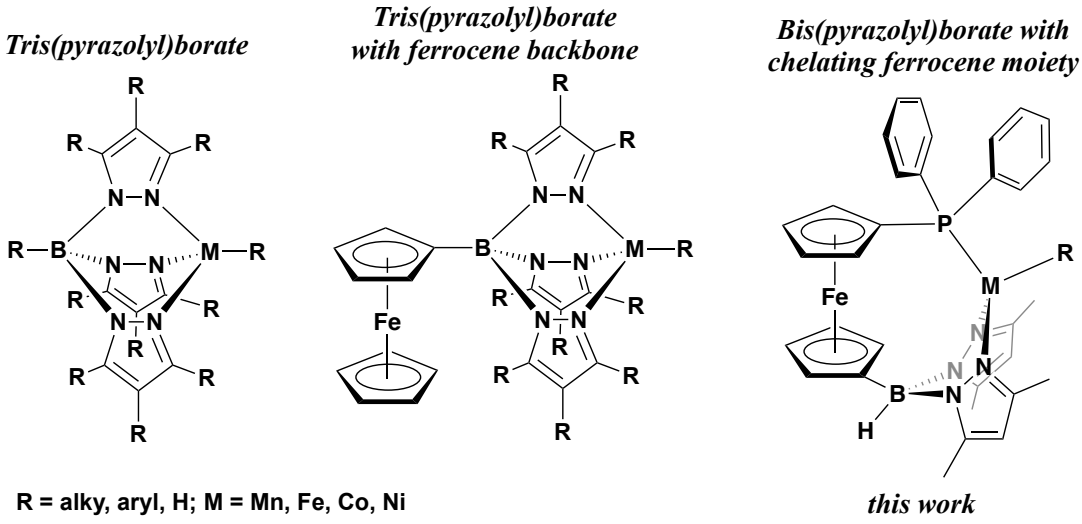

Figure 1-1. Variations in poly(pyrazolyl)borates.

In order to expand the scope of competent catalytic systems for redox-switchable olefin polymerization, we also focused on symmetrical and neutral bidentate ferrocene-based supporting ligands. Taking note of other prominent groups of neutral, bidentate ligands often

utilized with late transition metals for efficient olefin polymerization, such as the Brookhart diimine systems,[18] we began our investigations with a related, previously reported, but largely underexplored group of ligands such as the ferrocene-bis(phosphinimines). Initial findings for these complexes are reported in Chapter 6.

1.2 Redox-switchable ring-opening polymerization

We and others have been investigating redox-switchable systems concerning the ring-opening polymerization of cyclic esters and, recently, cyclic ethers. An initial report by Long et al.[19] described a ferrocene-derived system capable of influencing the rate of lactide polymerization based on the oxidation state of the ferrocene moieties. Next, our group reported the first examples of on/off switches in lactide polymerization using indium, yttrium,[17] and cerium[20] phosfen (phosfen = 1,1'-di(2-*tert*-butyl-6-diphenylphosphiniminophenoxy) ferrocene) complexes. Finally, our efforts culminated in the first cases of orthogonal monomer reactivity based on the oxidation state of the ferrocene-based supporting ligands. First, with the copolymerization of lactide and ε-caprolactone by the titanium thiolfan complex, (thiolfan*)Ti(O^iPr)$_2$ (thiolfan* = 1,1'-di(2,4-di-*tert*-butyl-6-thiophenoxy)ferrocene),[10] and then with the copolymerization of lactide and cyclohexene oxide utilizing a zirconium salfan complex, (salfan)Zr(O^tBu)$_2$ (salfan = 1,1'-di(2-*tert*-butyl-6-*N*-methylmethylenephenoxy)ferrocene).[11] Concurrently, a similar report of lactide/cyclohexene oxide copolymerization was published by Byers and coworkers utilizing an iron bis(imino)pyridine system.[21] Due to the success of the early transition metals in combination with ferrocene-based ligands and the iron bis(imino)pyridine system, we decided to investigate the use of ferrocene-based ligands to support late transition metals.

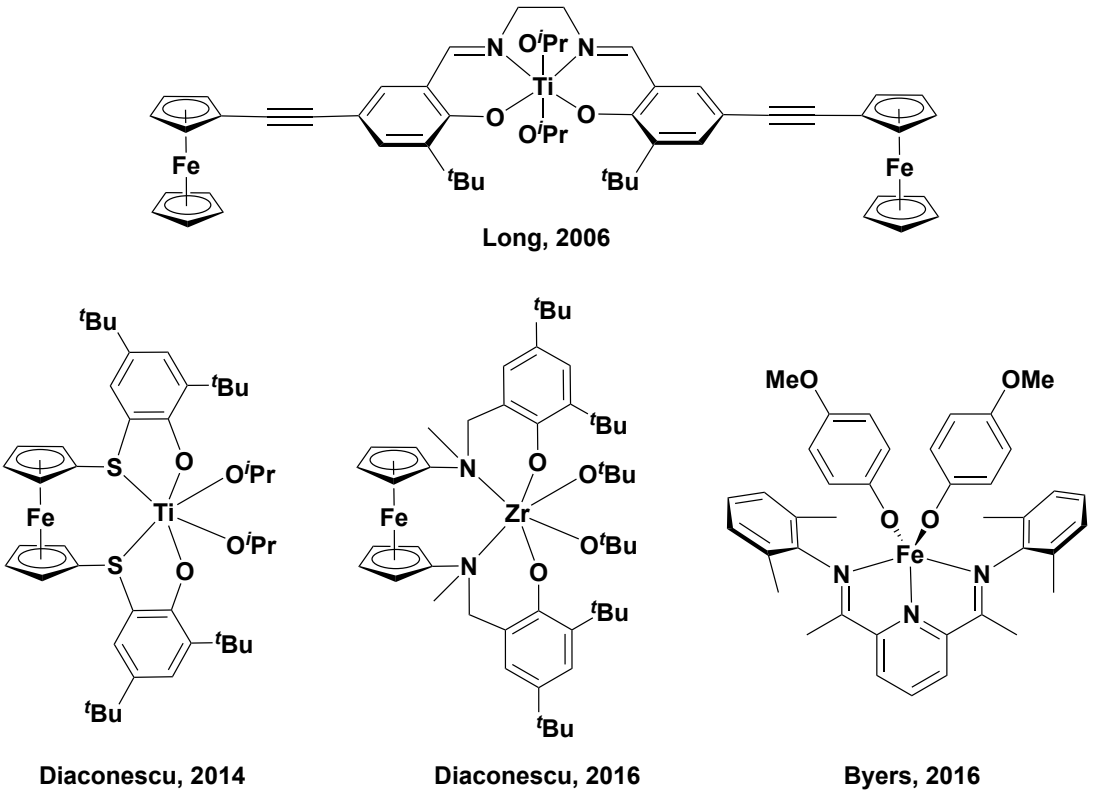

Figure 1-2. Examples of pre-catalysts used in redox-switchable ring-opening polymerization.

1.3 Redox-switchable olefin polymerization

Unlike the orthogonal reactivity based on the redox identity of the catalytically active species observed in several cases of redox switchable ring-opening polymerization of cyclic esters and ethers, the analogous reactivity concerning olefins is not known. Furthermore, only recently, reports by our group[8] and Chen et al.[7] described palladium complexes, supported by ferrocene-based ligands, capable of modulating the on/off activity of norbornene polymerization. Alternatively, Long et al.[22] have reported the influence of a redox active bis(arylimido)acenaphthene supporting ligand on the microstructure of polyethylene utilizing a nickel dibromide/methylalumoxane system. Based on these results, we investigated the use of

neutral ferrocene-bis(phosphinimine) ligands with nickel and palladium complexes. The close proximity of the iron metal center in ferrocene to the secondary metal, in these types of complexes, also permitted an investigation into the influence of a metal-metal interaction on redox and polymerization activity.

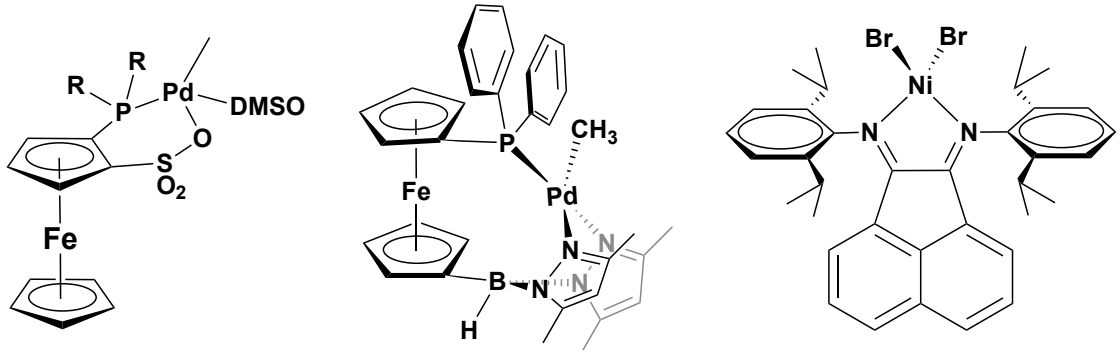

Chen, 2015 Diaconescu, 2016 Long, 2016

Figure 1-3. Examples of pre-catalysts used in redox-switchable olefin polymerization.

1.4 Thesis summary

In order to expand the class of catalysts that can be controlled by redox switches, we designed a new ferrocene ligand that would show suitable properties upon complexation to late transition metals. The heteroscorpionate ligand $fc(PPh_2)(BH[(3,5\text{-}Me)_2pz]_2)]$ ($fc^{P,B}$, fc = 1,1'-ferrocenediyl) was designed in order to combine the stereoelectronic versatility of poly(pyrazolyl)borates and the redox properties of a ferrocene-chelating moiety.[3,10]

My project started with the preparation of the first ferrocene-chelating heteroscorpionate complex, $(fc^{P,B})Li(THF)_2$, from a previously reported compound, $fcBr(PPh_2)$.[23] The redox properties of $fc^{P,B}$ were probed by characterizing the corresponding nickel(II) and zinc(II) complexes. The nickel complexes did not show a reversible, ligand based, redox process due to

the redox active nature of nickel. In contrast, the zinc complexes showed a single, ligand based, reversible redox process, consistent with the redox inactive nature of zinc. Because of the complicated redox events characteristic of ($fc^{P,B}$)NiMe, its application in redox switchable olefin polymerization was not possible (the redox switch has to function independently of the activity of the metal center performing the catalytic reactions of interest) (Chapter 2).

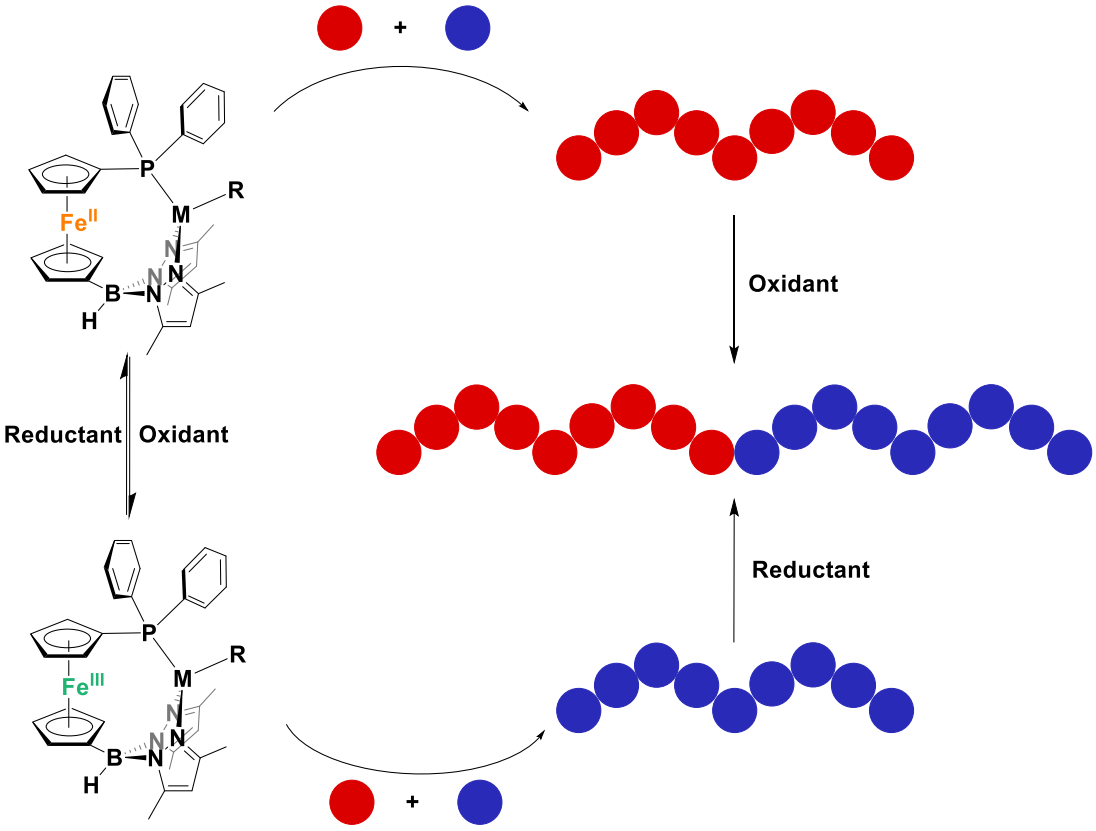

Figure 1-4. Selective monomer polymerization based on redox switchable catalysis.

To circumvent the redox issues affecting the nickel system, the palladium analogue ($fc^{P,B}$)PdMe was prepared and its application in palladium catalyzed norbornene polymerization was investigated. Compound ($fc^{P,B}$)PdMe shows a reversible on/off switch toward the polymerization of norbornene derivatives. While the reduced state of the catalyst, ($fc^{P,B}$)PdMe,

shows no activity, the oxidized complex, [($fc^{P,B}$)PdMe][BAr^F], exhibits activity toward norbornene polymerization. This activity was rationalized in terms of a different coordinating ability of the supporting ligand based on the oxidation state of iron in ferrocene. Ligands that display different coordinating abilities based on their oxidation state are known as redox-switchable hemilabile ligands and are capable of influencing both the electronic and steric properties of the transition metal.[24] Based on literature reports and our experimental results, we proposed that the oxidation of the ferrocene-chelating heteroscorpionate weakens the palladium-phosphine interaction allowing monomer coordination and migratory insertion into the metal-alkyl fragment, while the (pyrazolyl)borate portion remains unaffected. Since the displacement of the phosphine in the reduced complex by norbornene does not occur, the polymerization process is halted with this form of the catalyst (Chapter 3).

An initial investigation of the ferrocene-chelating heteroscorpionate zinc complexes revealed that no control over monomer polymerization, based on the oxidation state of the ligand, could be obtained (Chapter 5). However, despite the lack of redox-based selectivity, the preparation of multiblock copolymers was achieved via the ring-opening polymerization of cyclic esters and cyclic carbonates, in a step-wise addition, by the ferrocene-chelating heteroscorpionate zinc complex [($fc^{P,B}$)Zn(μ-OCH_2Ph)]$_2$. Up to pentablock copolymers could be obtained from combinations of lactide and trimethylene carbonate. The production of multiblock copolymers in such a fashion has not been previously reported due to reactivity limitations arising from the sequential addition of monomers.[25] The primary focus of this research project was the elucidation of the reaction mechanism by which these previously unreported multiblock copolymers are obtained. A combination of spectroscopic techniques, such as nuclear magnetic resonance, and computational methods (density functional theory) was utilized to determine the

key intermediate species during the polymerizations. In addition, the effects of the multiblock microstructure on the polymer properties were thoroughly investigated. The characterization of the basic composition, thermal, and mechanical properties of these materials was achieved via gel permeation chromatography (GPC), differential scanning calorimetry (DSC), and dynamic mechanical analysis (DMA, Chapter 4).

A further look into extending the methodology of the redox-switchable hemilabile behavior during olefin polymerization to symmetrically substituted 1,1'-bis(phosphinimino)ferrocenes was investigated. Halogen abstraction from mixed alkyl halide nickel(II) and palladium(II) complexes in the presence of ferrocene-bis(phosphinimine) resulted in the isolation of compounds with κ^3 bound supporting ligands featuring iron-nickel and iron-palladium interactions. The lability of the metal-metal interaction was investigated in the presence of weak nucleophiles and the redox properties of the metal complexes determined via cyclic voltammetry (Chapter 6).

Further modifications to the existing ferrocene heteroscorpionates have the potential to yield new redox-switchable systems, both in ring-opening and olefin polymerizations. Firstly, although the dimeric zinc compound shows no selective monomer polymerization based on the oxidation state of the heteroscorpionate supporting ligand, this is likely due to the lack of phosphine-zinc interaction in this compound. Increasing the steric bulk of the substituents at the 3-position of the pyrazoles could discourage dimerization and furnish the desired zinc-phosphine interaction. Thus, the influence of the oxidation state of ferrocene on the lability of the phosphine moiety could lead to unique monomer reactivity. Secondly, identifying an alternative metal to palladium for olefin polymerization is necessary. Due to the tridentate nature of the ferrocene heteroscorpionate ligand, a metal capable of higher coordination number than 4 should be

employed. The redox potential of the said metal must also differ from that of iron in ferrocene, if the metal is susceptible to one electron redox processes, or must undergo two electro redox processes similar to palladium. Preventing the heterolytic cleavage of the metal-carbon bonds in these metal complexes is the first step in developing redox-switchable olefin polymerization catalysts capable of producing multiblock copolymers.

1.5 References

1. Teator, A. J.; Lastovickova, D. N.; Bielawski, C. W. *Chem. Rev.* **2016**, *116* (4), 1969–1992.

2. Arriola, D. J. *Science* **2006**, *312* (5774), 714–719.

3. Lorkovic, I. M.; Duff, R. R., Jr; Wrighton, M. S. *J. Am. Chem. Soc.* **1995**, *117* (12), 3617–3618.

4. Gregson, C. K. A.; Gibson, V. C.; Long, N. J.; Marshall, E. L.; Oxford, P. J.; White, A. J. P. *J. Am. Chem. Soc.* **2006**, *128* (23), 7410–7411.

5. Savka, R.; Foro, S.; Gallei, M.; Rehahn, M.; Plenio, H. *Chem. Eur. J.* **2013**, *19* (32), 10655–10662.

6. Varnado, C. D.; Jr; Rosen, E. L.; Collins, M. S.; Lynch, V. M.; Bielawski, C. W. *Dalton Trans.* **2013**, *42* (36), 13251–14.

7. Chen, M.; Yang, B.; Chen, C. *Angew. Chem.* **2015**, *127* (51), 15740–15744.

8. Abubekerov, M.; Shepard, S. M.; Diaconescu, P. L. *Eur. J. Inorg. Chem.* **2016**, *2016* (15-16), 2634–2640.

9. Broderick, E. M.; Guo, N.; Vogel, C. S.; Xu, C.; Sutter, J.; Miller, J. T.; Meyer, K.; Mehrkhodavandi, P.; Diaconescu, P. L. *J. Am. Chem. Soc.* **2011**, *133* (24), 9278–9281.

10. Wang, X.; Thevenon, A.; Brosmer, J. L.; Yu, I.; Khan, S. I.; Mehrkhodavandi, P.; Diaconescu, P. L. *J. Am. Chem. Soc.* **2014**, *136* (32), 11264–11267.

11. Quan, S. M.; Wang, X.; Zhang, R.; Diaconescu, P. L. *Macromolecules* **2016**, *49* (18), 6768–6778.

12. Trofimenko, S. *J. Am. Chem. Soc.* **1966**, *88* (8), 1842–1844.

13. Trofimenko, S. *Chem Rev* **1993**, *93* (3), 943–980.

14. Luca, O. R.; Crabtree, R. H. *Chem. Soc. Rev.* **2013**, *42* (4), 1440.

15. Fabrizi de Biani, F.; Jäkle, F.; Spiegler, M.; Wagner, M.; Zanello, P. *Inorg. Chem.* **1997**, *36* (10), 2103–2111.

16. Sirianni, E. R.; Yap, G.; Theopold, K. H. *Inorg. Chem.* **2014**.

17. Broderick, E. M.; Guo, N.; Vogel, C. S.; Xu, C.; Sutter, J.; Miller, J. T.; Meyer, K.; Mehrkhodavandi, P.; Diaconescu, P. L. *J. Am. Chem. Soc.* **2011**, *133* (24), 9278–9281.

18. Johnson, L. K.; Killian, C. M.; Brookhart, M. *J. Am. Chem. Soc.* **1995**, *117* (23), 6414–6415.

19. Gregson, C. K. A.; Gibson, V. C.; Long, N. J.; Marshall, E. L.; Oxford, P. J.; White, A. J. P. *J. Am. Chem. Soc.* **2006**, *128* (23), 7410–7411.

20. Broderick, E. M.; Guo, N.; Wu, T.; Vogel, C. S.; Xu, C.; Sutter, J.; Miller, J. T.; Meyer, K.; Cantat, T.; Diaconescu, P. L. *Chem. Commun.* **2011**, *47* (35), 9897–3.

21. Biernesser, A. B.; Delle Chiaie, K. R.; Curley, J. B.; Byers, J. A. *Angew. Chem.* **2016**, *128* (17), 5337–5340.

22. Anderson, W. C., Jr.; Rhinehart, J. L.; Tennyson, A. G.; Long, B. K. *J. Am. Chem. Soc.* **2016**, *138* (3), 774–777.

23. Abubekerov, M.; Diaconescu, P. L. *Inorg. Chem.* **2015**, *54* (4), 1778–1784.

24. Allgeier, A. M.; Mirkin, C. A. *Angewandte Chemie International Edition* **1998**, *37* (7), 894–908.

25. Guerin, W.; Helou, M.; Carpentier, J.-F.; Slawinski, M.; Brusson, J.-M.; Guillaume, S. M. *Polym. Chem.* **2013**, *4* (4), 1095–1106.

CHAPTER 2: SYNTHESIS AND CHARACTERIZATION OF FERROCENE-CHELATING HETEROSCORPIONATE COMPLEXES OF NICKEL(II) AND ZINC(II)

2.1 Introduction

Poly(pyrazolyl)borates, also known as "scorpionates",[1-3] have versatile electronic and steric properties.[4-6] Due to the ease of introducing new substituents on the three carbon atoms of the pyrazolyl ring, such ligands have found widespread applications in coordination chemistry and catalysis.[2, 7-14] However, despite their advantages, poly(pyrazolyl)borates lack the potential for redox activity. Given the increasing interest in redox active ligands and their applications in catalysis,[15] several examples of ferrocene-substituted poly(pyrazolyl)borates have been synthesized,[16-21] but metal complexes containing chelating versions are unknown; these motifs are particularly interesting since they impart special steric and electronic properties to the resulting metal complexes.[22-25] Therefore, a new type of a heteroscorpionate ligand, $fc^{P,B}$ ($fc^{P,B}$ = $fc(PPh_2)(BH[(3,5\text{-}Me)_2pz]_2)$], fc = 1,1'-ferrocenediyl) was designed in order to combine the stereoelectronic versatility of poly(pyrazolyl)borates and the redox properties of a ferrocene-chelating moiety. Based on the interest of the Diaconescu group in redox active ferrocene-based chelating ligands,[23-24, 26] we set out to investigate the activity of the $fc^{P,B}$ ligand in combination with nickel for potential use in redox-switchable catalysis for the synthesis of olefinic copolymers. The redox properties of $fc^{P,B}$ were probed by characterizing two nickel(II) complexes. In order to provide an unambiguous interpretation of their redox properties, the analogous, redox inactive zinc(II) complexes were also prepared and characterized.

2.2 Synthesis and characterization of ferrocene derivatives

The addition of one equivalent of *n*-butyl lithium to fcBr(PPh_2) in THF followed by quenching with an excess of $B(OMe)_3$ resulted in the formation of fc(PPh_2)$B(Ome)_2$, which was isolated as a yellow powder in 91.1% yield from *n*-pentane at -40 °C (Scheme 2-1). The solid-state molecular structure of fc(PPh_2)$B(OMe)_2$ was determined using single-crystal X-ray diffraction (Figure 2-1). The carbon-phosphorus (P(1)-C(8), 1.8140(15) Å) and carbon-boron (C(3)-B(1), 1.552(2) Å) distances are similar to those in a related compound, fc(PPh_2)$Bmes_2$ (C(1)-P(1), 1.814(6) Å; C(6)-B(1), 1.565(9) Å).[32] The ^{1}H NMR spectrum (C_6D_6, 500 MHz, 298 K) displays a singlet at 3.61 ppm for the methoxy group in addition to proton resonance signals in the expected regions for the cyclopentadienyl (4-5 ppm) and phenyl protons (7.28-7.4 ppm).

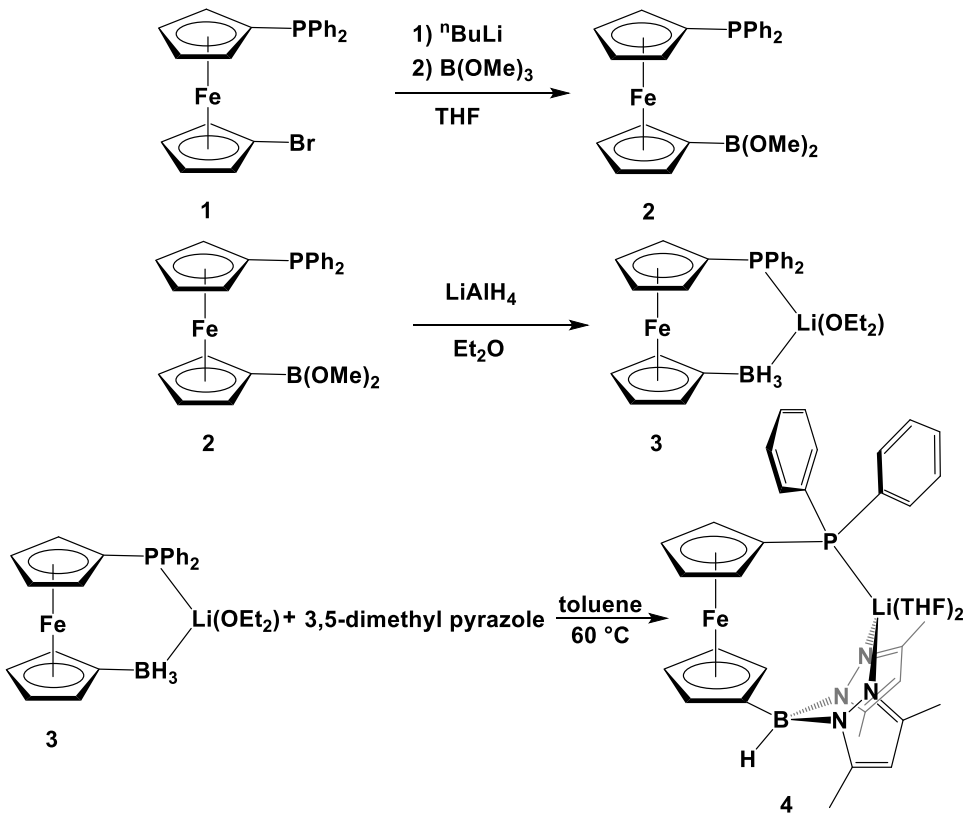

Scheme 2-1. Synthesis of compounds **1-4**.

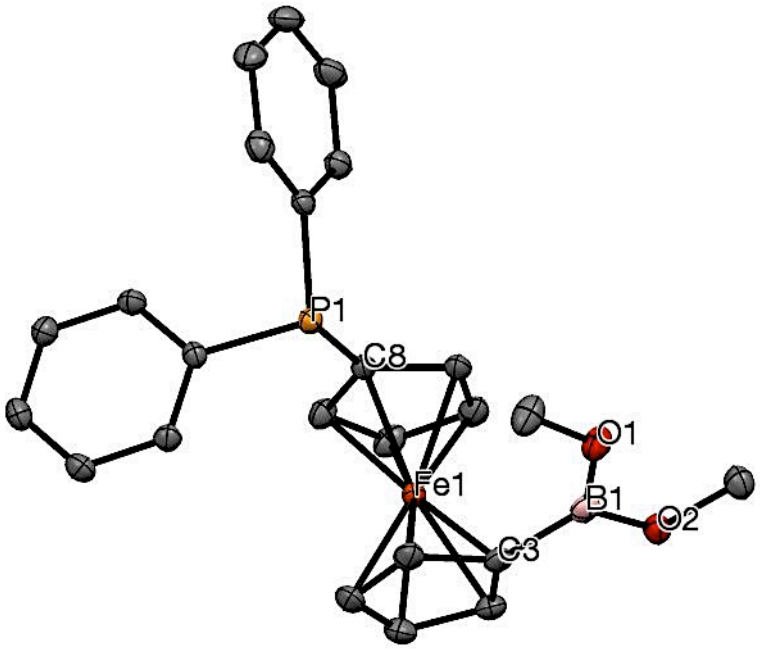

Figure 2-1. Molecular structure drawing of $fc(PPh_2)B(OMe)_2$ with thermal ellipsoids at 50% probability; hydrogen atoms are omitted for clarity. Selected distances (Å) and angles (°): P(1)-C(8), 1.8140(15); C(3)-B(1), 1.552(2); C(3)-B(1)-O(1), 128.50(14); O(1)-B(1)-O(2), 116.73(14); C(3)-B(1)-O(2), 114.61(14).

Reaction of $fc(PPh_2)B(OMe)_2$ with one equivalent of $LiAlH_4$ in diethyl ether resulted in the formation of $[Li(OEt_2)][fc(PPh_2)BH_3]$, isolated as orange crystals from diethyl ether at -40 °C in 84.6% yield (Scheme 2-1). The results of an X-ray diffraction study are displayed in Figure 2-2 along with selected distances and angles. The boron-lithium distances, B(1)-Li(1), 2.426(8) Å and 2.445(10) Å, are slightly shorter and the B(1)-Li(1)-B(1) angle of 102.0(3)° is slightly larger than those reported for similar complexes $[FcBH_3]Li\cdot(Et_2O)_2$ (B(1)-Li(1), 2.511(6) Å; B(1)-Li(1A), 2.455(6) Å; B(1)-Li(1)-B(1A), 97.5(2)°) and $[fc(BH_3)_2]Li\cdot(Et_2O)$ (B(1)-Li(2A), 2.553(5) Å; B(1)-Li(2), 2.579(6) Å; B(1)-Li(2)-B(1A), 92.7(2)°).[33] In the ^1H NMR spectrum

(C_6D_6, 300 MHz, 298 K), the protons of BH_3 give rise to a broad quartet at 1.90 ppm due to ^{11}B coupling.

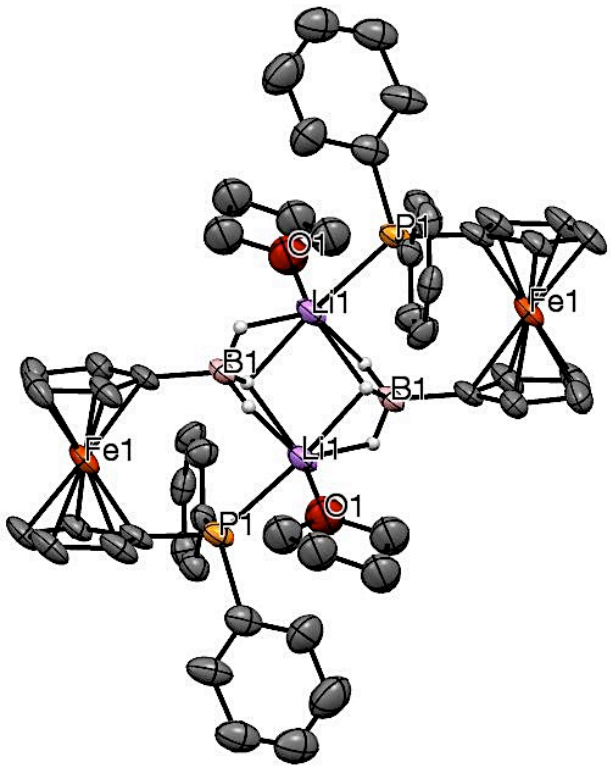

Figure 2-2. Molecular structure drawing of [Li(THF)][fc(PPh_2)BH_3] with thermal ellipsoids at 50% probability; most hydrogen atoms and disordered counterparts are omitted for clarity. Selected distances (Å) and angles (°): P(1)-Li(1), 2.640(7); B(1)-Li(1), 2.426(8), 2.445(10); B(1)-Li(1)-B(1), 102.0(3); P(1)-Li(1)-B(1), 94.4(3), 124.9(3); B(1)-Li(1)-O(1), 116.7(6), 119.6(7); O(1)-Li(1)-P(1), 98.6(8).

The reaction of two equivalents of 3,5-dimethylpyrazole with [fc(PPh_2)(BH_3)]Li·(Et_2O) in toluene at 60 °C resulted in the formation of [Li($THF)_2$][fc(PPh_2)(BH[(3,5-$Me)_2$pz]$_2$)], isolated in quantitative yield as an orange oil upon removal of volatiles (Scheme 2-1). Attempts to grow

X-ray quality crystals from saturated solutions of diethyl ether, toluene, and THF were unsuccessful. The ^{1}H NMR spectrum (C_6D_6, 300 MHz, 298 K) is reminiscent of those for other poly(3,5-dimethylpyrazolyl)borate ligands, displaying a singlet at 2.08 ppm and 2.57 ppm for the two sets of methyl groups and a singlet at 5.86 ppm for the proton at the 4-position of the pyrazolyl rings.

2.3 Preparation of nickel(II) and zinc(II) heteroscorpionate complexes

The addition of $[Li(THF)_2][fc(PPh_2)(BH[(3,5\text{-}Me)_2pz]_2)]$ to $(DME)NiCl_2$ in THF resulted in a color change of the solution from yellow to black. Following evaporation of the volatiles under reduced pressure, extraction in toluene and cooling to -40 °C led to the isolation of $(fc^{P,B})NiCl\cdot(C_7H_8)$ as black crystals in 92.1% yield (Scheme 2-2). The solid-state molecular structure of $(fc^{P,B})NiCl\cdot(C_7H_8)$ was determined using single-crystal X-ray diffraction (Figure 2-3). The coordination environment around the nickel center has a distorted tetrahedral geometry with a τ value of 0.83.[34] The metal-ligand distances (P(1)-Ni(1), 2.3257(5) Å; Cl(1)-Ni(1), 2.2142(5) Å; N(2)-Ni(1), 1.9560(15) Å; N(1)-Ni(1), 1.9615(15) Å) are similar to those in related $(Tp^{Ph,Me})NiCl$ complexes ($Tp^{Ph,Me}$ = hydrotris(3-phenyl-5-methylpyrazolyl)borate) (N(11)-Ni(1), 2.052(3) Å; N(12)-Ni(1), 2.052(2) Å; N(31)-Ni(1), 2.094(2) Å; Cl(1)-Ni(1), 2.237(1) Å)[35] and $(PPh_3)_2NiCl_2$ (Ni-P, 2.3180(2) Å).[36] The ^{1}H NMR spectrum (C_6D_6, 400 MHz, 298 K) showed only broadened, uninformative signals as expected for a paramagnetic species. The solution-state magnetic susceptibility of 3.12 μ_B is consistent with two unpaired electrons.

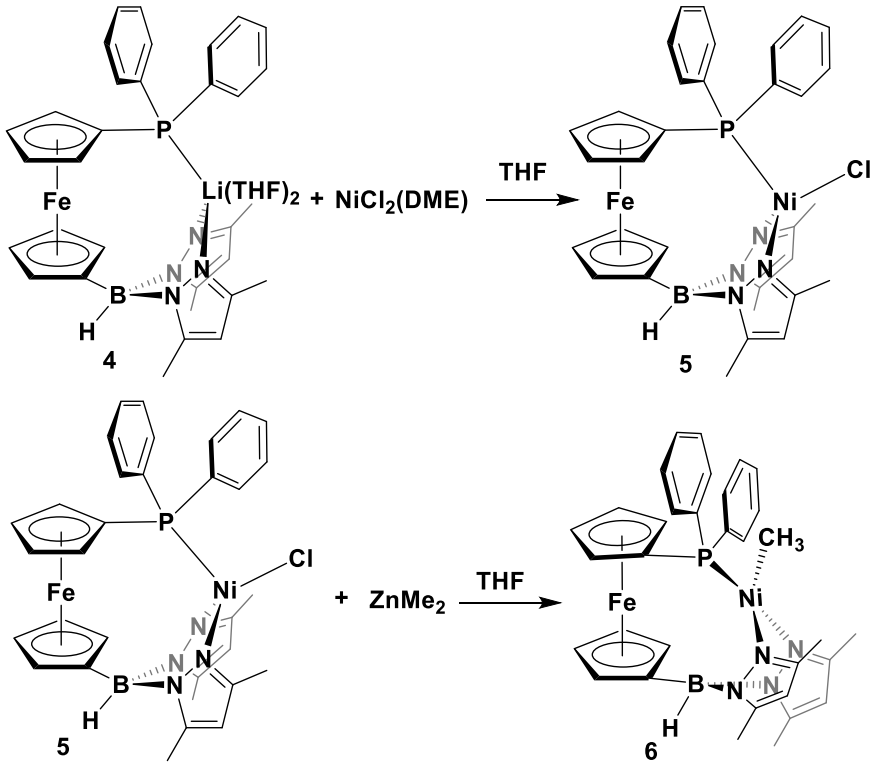

Scheme 2-2. Synthesis of nickel complexes.

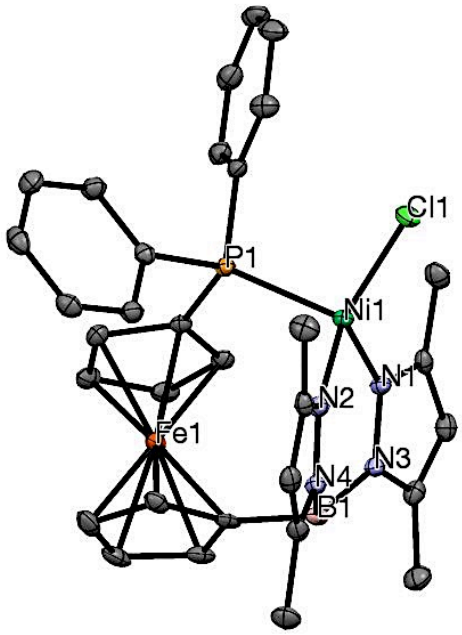

Figure 2-3. Molecular structure drawing of ($fc^{P,B}$)NiCl with thermal ellipsoids at 50% probability; hydrogen atoms and cocrystallized solvent are omitted for clarity. Selected distances

(Å) and angles (°): P(1)-Ni(1), 2.3257(5); Cl(1)-Ni(1), 2.2142(5); N(2)-Ni(1), 1.9560(15); N(1)-Ni(1), 1.9615(15); P(1)-Ni(1)-Cl(1), 105.584(19); P(1)-Ni(1)-N(1), 102.58(4); N(1)-Ni(1)-N(2), 95.79(6); Cl(1)-Ni(1)-N(1), 125.36(5); Cl(1)-Ni(1)-N(2), 117.12(5); P(1)-Ni(1)-N(2), 108.96(4).

The addition of $ZnMe_2$ to ($fc^{P,B}$)NiCl·(C_7H_8) in toluene resulted in an immediate color change from deep purple to orange. Removal of volatiles, extraction in *n*-pentane, and cooling to -40 °C led to the isolation of ($fc^{P,B}$)NiMe as orange crystals in 61.8% yield (Scheme 2-2). The results of an X-ray diffraction study are displayed in Figure 2-4 along with selected distances and angles. The coordination environment around the nickel center is in a distorted square planar geometry (τ = 0.17). The metal-ligand distances (P(1)-Ni(1), 2.1269(5) Å; C(1)-Ni(1), 1.9508(17) Å; N(3)-Ni(1), 1.9460(14) Å; N(1)-Ni(1), 1.9450(15) Å) are comparable with values reported for similar complexes NiCl(Ph)(PPh_3)$_2$ (P(1)-Ni(1), 2.2232(5) Å; P(2)-Ni(1), 2.2151(5) Å),[37] ($Tp^{Ph,Me}$)Ni[$CH_2Si(CH_3)_3$] ($Tp^{Ph,Me}$ = hydrotris(3-phenyl-5-methylpyrazolyl)borate) (C(1)-Ni(1), 1.999(2) Å; N(1)-Ni(1), 2.041(1) Å; N(2)-Ni(1), 2.040(2) Å; N(3)-Ni(1), 2.058(2) Å), and $Tp^{Ph,Me}$NiCH$_2$Ph (C(1)-Ni(1), 1.975(2) Å; N(1)-Ni(1), 1.912(1) Å; N(2)-Ni(1), 1.943(1) Å).[38] In the ^{1}H NMR spectrum (C_6D_6, 300 MHz, 298 K), the protons of the methyl ligand appear as a doublet at 0.02 ppm due to ^{31}P coupling. The rest of the signals are broadened, likely because of poor fluxionality of the $fc^{P,B}$ ligand in solution at 298 K. This supposition is supported by the results of a variable temperature ^{1}H NMR spectroscopic study (Figure A14), which shows the gradual coalescence and sharpening of the resonance signals, yielding identifiable signals for ($fc^{P,B}$)NiMe at 361 K (Figure A15).

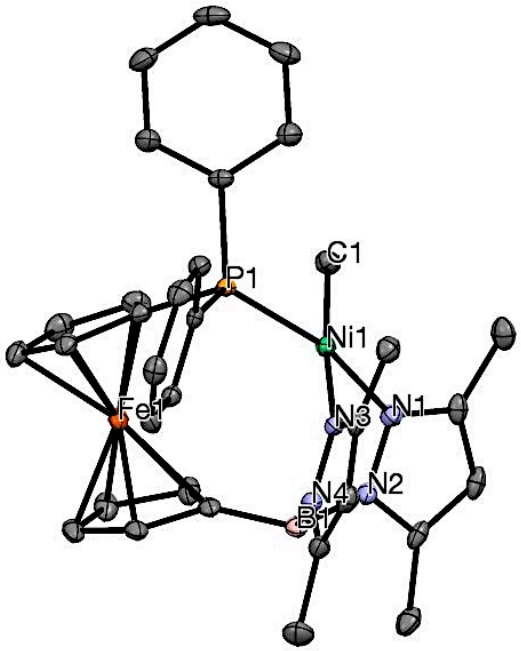

Figure 2-4. Molecular structure drawing of ($fc^{P,B}$)NiMe with thermal ellipsoids at 50% probability; hydrogen and solvent atoms are omitted for clarity. Selected distances (Å) and angles (°): P(1)-Ni(1), 2.1269(5); C(1)-Ni(1), 1.9508(17); N(1)-Ni(1), 1.9450(15); N(3)-Ni(1), 1.9460(14); P(1)-Ni(1)-C(1), 86.94(6); C(1)-Ni(1)-N(1) 91.51(7); P(1)-Ni(1)-N(3), 95.21(4); N(1)-Ni(1)-N(3), 88.13(6).

The reaction of $ZnCl_2$ with $(THF)_2$·Li[fc(PPh_2)(BH((3,5-Me)pz)$_2$)] in THF resulted in the formation of ($fc^{P,B}$)ZnCl, isolated as orange crystals from a 1:3 toluene/hexanes layering at -40 °C in 86.4% yield (Scheme 2-3). The solid-state molecular structure of ($fc^{P,B}$)ZnCl·(C_7H_8) was determined using single-crystal X-ray diffraction (Figure 2-5). The coordination environment around the zinc center is in a slightly distorted tetrahedral geometry with a τ value of 0.91. The metal-ligand distances (P(1)-Zn(1), 2.3986(5) Å; Cl(1)-Zn(1), 2.2293(5) Å; N(3)-Zn(1), 1.9771(14) Å; N(1)-Zn(1), 1.9891(14) Å) are similar to those in related complexes, (3,5-Me_2pz)$_2$CP(Ph)$_2$NphZnEt (N(2)-Zn(1), 2.045(2) Å; N(4)-Zn(1), 2.067(2) Å; Cl(1)-Zn(1),

2.1915(8) Å),[39] and $Tp^{Ms}ZnCl$ (Tp^{Ms} = hydrotris(3-(2,4,6-trimethylpheny)pyrazolyl)borate) (N(5)-Zn(1), 2.057(3) Å; N(10)-Zn(1), 2.021(3) Å; N(17)-Zn(1), 2.043(3) Å; Cl(1)-Zn(1), 2.1400(10).[40]

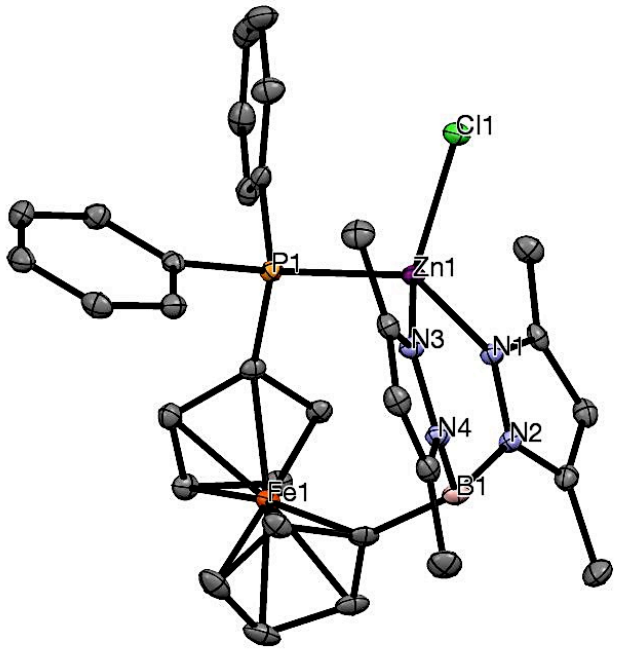

Figure 2-5. Molecular structure drawing of $(fc^{P,B})ZnCl$ with thermal ellipsoids at 50% probability; hydrogen and solvent atoms are omitted for clarity. Selected distances (Å) and angles (°): P(1)-Zn(1), 2.3986(5); Cl(1)-Zn(1), 2.2293(5); N(1)-Zn(1), 1.9891(14); N(3)-Zn(1), 1.9771(14); P(1)-Zn(1)-Cl(1), 107.583(17); P(1)-Zn(1)-N(1), 106.46(4); N(1)-Zn(1)-N(3), 97.98(6); Cl(1)-Zn(1)-N(1), 118.04(4); Cl(1)-Zn(1)-N(3), 113.28(4); P(1)-Zn(1)-N(3), 113.31(4).

The addition of MeLi to $(fc^{P,B})ZnCl\cdot(C_7H_8)$ in THF resulted in an immediate color change of the solution from orange to yellow. Removal of volatile substances under reduced pressure, extraction in hexanes, and cooling -40 °C resulted in the isolation of $(fc^{P,B})ZnMe$ as yellow crystals in 56.2% yield (Scheme 2-3). The results on an X-ray diffraction study are

displayed in Figure 2-6 along with selected distances and angles. The coordination environment around the zinc center is in a distorted tetrahedral geometry (τ = 0.79). The metal-ligand distances (P(1)-Zn(1), 2.5519(4) Å; C(1)-Zn(1), 1.9908(17) Å; N(3)-Zn(1), 2.0465(13) Å; N(1)-Zn(1), 2.0234(13) Å) are comparable with the values reported for similar complexes (3,5-$Me_2pz)_2CP(Ph)_2NphZnEt$ (N(2)-Zn(1), 2.1207(18) Å; N(4)-Zn(1), 2.1036(19) Å; C(30)-Zn(1), 1.994(2) Å),[39] (Tp^{Me2})ZnMe (C(1)-Zn(1), 1.981(8) Å; N(22)-Zn(1), 2.056(4) Å; N(12)-Zn(1), 2.048(6) Å),[41] and (Ph_3P)ZnEt(CCPh) (C(1)-Zn(1), 1.976(3) Å; P(1)-Zn(1), 2.5407(8) Å).[42] Similar to ($fc^{P,B}$)NiMe, the protons on the methyl ligand appear as a doublet at -0.03 ppm in the ^{1}H NMR spectrum (C_6D_6, 500 MHz, 298 K). However, the rest of the signals in the ^{1}H NMR spectrum are sharp and easily discernable.

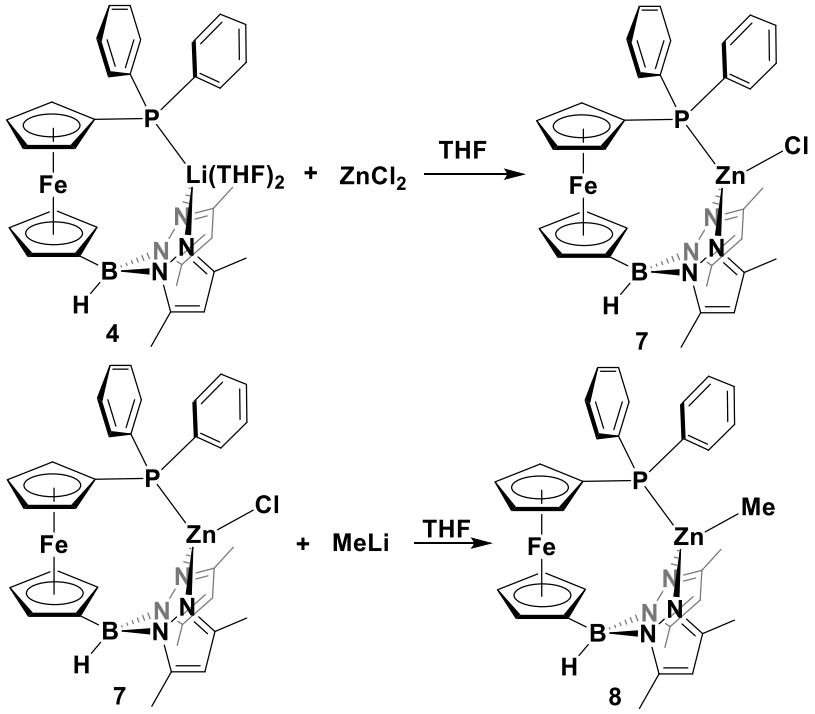

Scheme 2-3. Synthesis of zinc complexes.

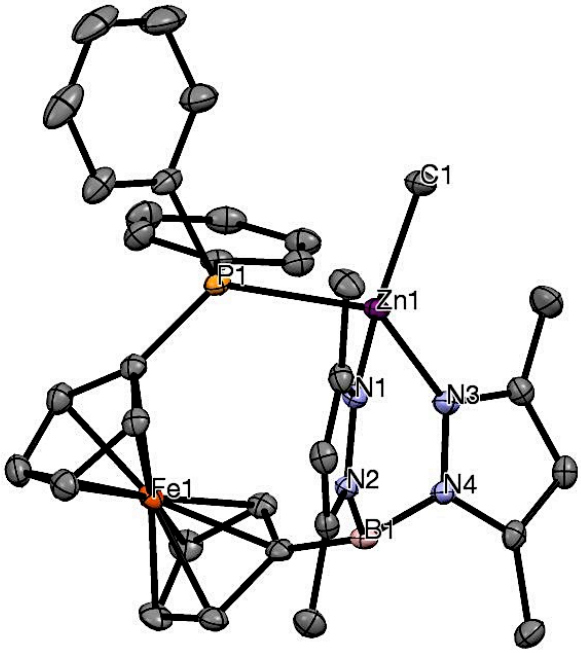

Figure 2-6. Molecular structure drawing of ($fc^{P,B}$)ZnMe with thermal ellipsoids at 50% probability; hydrogen atoms are omitted for clarity. Selected distances (Å) and angles (°): P(1)-Zn(1), 2.5519(4); C(1)-Zn(1), 1.9908(17); N(1)-Zn(1), 2.0234(13); N(3)-Zn(1), 2.0465(13); P(1)-Zn(1)-C(1), 101.05(5); P(1)-Zn(1)-N(1), 101.28(4); N(1)-Zn(1)-N(3), 92.11(5); C(1)-Zn(1)-N(1), 126.95(7); C(1)-Zn(1)-N(3), 121.08(7); P(1)-Zn(1)-N(3), 113.41(4).

2.4 Redox behavior of nickel and zinc heteroscorpionate complexes

To investigate the redox activity of the nickel systems, cyclic voltammetry (CV) was performed on ($fc^{P,B}$)NiCl and ($fc^{P,B}$)NiMe. The cyclic voltammogram of ($fc^{P,B}$)NiCl (Table 2-1, Figures A27-A31) showed a reversible and a quasi-reversible redox process at -0.03 V and -1.58 V vs. Fc/Fc^+, respectively. Complex ($fc^{P,B}$)NiMe showed an irreversible oxidation event at 0.18 V vs. Fc/Fc^+ in THF followed by a quasi-reversible redox process of the oxidized species with a redox potential of 0.42 V vs. Fc/Fc^+ (Figure 2-7, Table 2-1).

Table 2-1. Redox potentials for compounds **5-8**.

Compound	$E_{1/2}$ (V vs. Fc/Fc^+)
$(fc^{P,B})NiCl$	-0.03, -1.58
$(fc^{P,B})NiMe$	0.18,* 0.42
$(fc^{P,B})ZnCl$	-0.07
$(fc^{P,B})ZnMe$	-0.18

*E_{pa} (V vs. Fc/Fc^+).

Redox inactive analogues of the nickel complexes, $(fc^{P,B})ZnCl$ and $(fc^{P,B})ZnMe$, were prepared and characterized in order to assign the $fc^{P,B}$ and nickel(II) redox events unambiguously. Complex $(fc^{P,B})ZnCl$ (Figures A35-A37) displayed a reversible event with a redox potential of -0.07 V vs. Fc/Fc^+. Based on this information, the redox events in $(fc^{P,B})NiCl$ at potentials of -0.03 V and -1.576 V can be attributed to Fe(II)/Fe(III) and Ni(II)/Ni(I), respectively (Scheme 2-4). Complex $(fc^{P,B})ZnMe$ (Figure 2-7) showed a reversible event with a redox potential of -0.18 V vs. Fc/Fc^+, supporting the assignment of Fe(II)/Fe(III) couple as the first oxidation event in $(fc^{P,B})NiMe$. Although $(fc^{P,B})NiMe$ might be expected to oxidize at a lower potential than $(fc^{P,B})NiCl$, this is not the case. Our group has observed similar results in the case of mono(1,1'-diamidoferrocene) uranium (IV) complexes, where increasing the electron density at the uranium center did not yield expected trends in the oxidation of the ferrocene ligand.[43] Similarly, Kaim et. al. reported the characterization of 1,1'-bis(diphenylphosphino)ferrocene osmium(II) and ruthenium(II) complexes by cyclic voltammetry; the ferrocene ligands showed a reversible redox process at 0.39 V and 0.38 V vs. Fc/Fc^+, respectively, whereas the oxidation of osmium(II) and ruthenium(II) occurred at potentials over 1 V.[44]

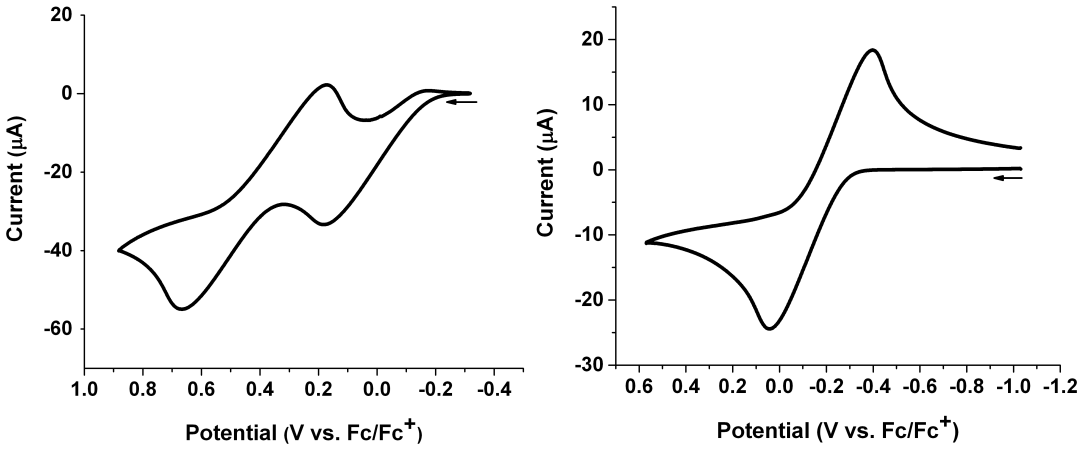

Figure 2-7. Cyclic voltammograms recorded with a glassy carbon electrode at 100 mV/s in THF, 0.10 M [TBA][PF_6] containing 5.0 mM ($fc^{P,B}$)NiMe (left) and ($fc^{P,B}$)ZnMe (right).

Chemical oxidation of ($fc^{P,B}$)NiMe with one equivalent of [Fc][PF_6] in THF resulted in the formation of insoluble green solids with a 1:1 distribution of starting material and ferrocene remaining in solution. Increasing the number of equivalents of oxidant to two resulted in the complete consumption of starting material. Attempts to grow X-ray quality crystals and to characterize the green solids were unsuccessful due to their very poor solubility in most common organic solvents.

Based on the chemical oxidation and cyclic voltammetry results, the possible identities for the oxidation products of complex ($fc^{P,B}$)NiMe are proposed in Scheme 2-4. The first irreversible oxidation (Figure 2-7) can be attributed either to the ferrocene moiety or the nickel center in compound **6**; the comparison with ($fc^{P,B}$)NiCl supports the first case, while DFT results support both assignments (see below). We also propose that this redox event is followed by the homolytic cleavage of the nickel-carbon bond to yield a cationic $[fc(II)Ni(II)]^+$ complex. The

ferrocene backbone of $[fc(II)Ni(II)]^+$ likely undergoes a quasi-reversible redox process, attributable to second event observed for $(fc^{P,B})$NiMe.

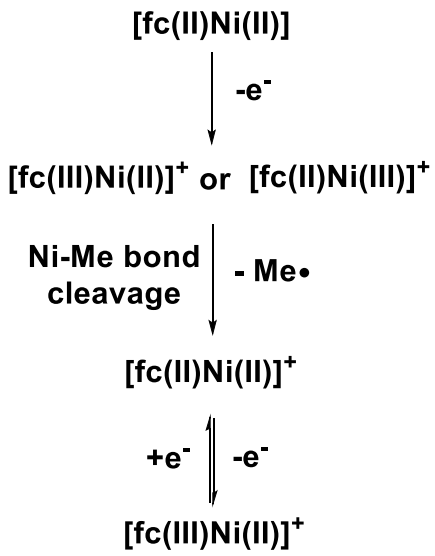

Scheme 2-4. Proposed oxidation pathway for $(fc^{P,B})$NiMe ([fc(II)Ni(II)] = $(fc^{P,B})$NiMe).

2.5 DFT calculations

In order to understand further the redox properties of $(fc^{P,B})$NiMe, geometry optimizations of the full molecules were carried out for all four compounds. The optimized structures are in good agreement with the experimental data (Tables A2, A3). From a qualitative point of view, the frontier molecular orbitals support the findings of the electrochemical study. For zinc complexes, as expected, the occupied frontier molecular orbitals are ferrocene based (Figure 1-8 and A49, A50). This situation changes for the nickel complexes: while the SOMO of $(fc^{P,B})$NiCl is heavily ferrocene based and has only a small contribution of nickel d orbitals (1.5%), the HOMO of $(fc^{P,B})$NiMe has a substantial contribution from nickel d orbitals (29%

total contribution). The calculations also support the nickel(II)/(I) reduction observed for ($fc^{P,B}$)NiCl since the unoccupied frontier molecular orbitals are nickel based (Figure A47).

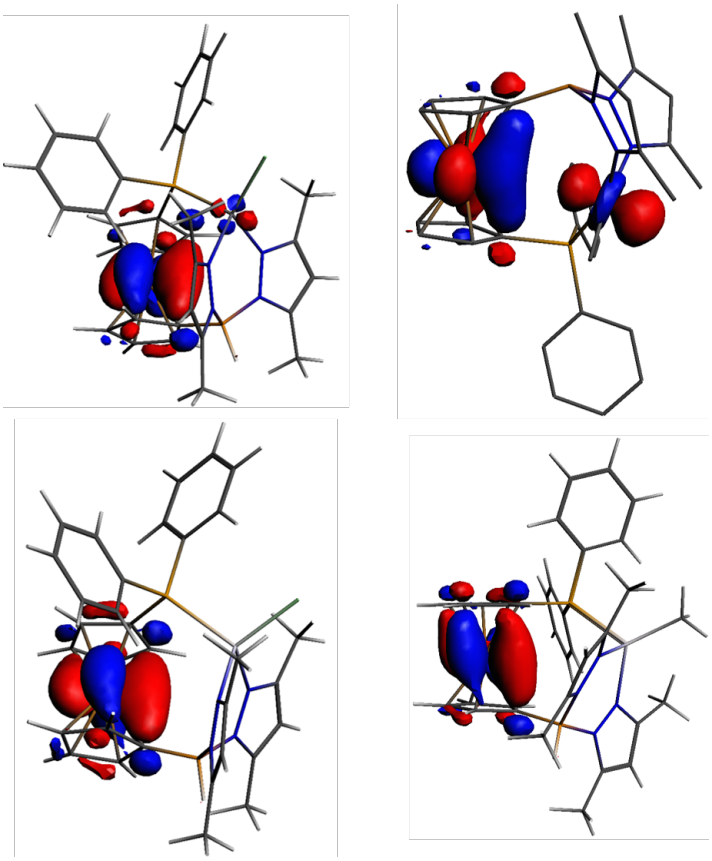

Figure 2-8. Molecular orbitals: SOMO-1 for ($fc^{P,B}$)NiCl (top left), HOMO for ($fc^{P,B}$)NiMe (top right), HOMO for ($fc^{P,B}$)ZnCl (bottom left), HOMO for ($fc^{P,B}$)ZnMe (bottom right).

2.6 Conclusions

Combining the stereoelectronic versatility of poly(pyrazolyl)borates and the redox activity of ferrocene resulted in the formation of a new type of a redox active heteroscorpionate compound, ($fc^{P,B}$)Li(THF)$_2$, and the corresponding nickel and zinc complexes. The redox activity of the nickel and zinc products was studied using cyclic voltammetry. The nickel complexes

showed a combination of reversible and irreversible redox processes that can be attributed to the redox active nature of both nickel and iron metal centers. In contrast, the zinc complexes showed only a single, iron based, reversible redox process consistent with the redox inactive nature of zinc. These assignments were supported by DFT calculation results.

Since both the electrochemical and chemical reactivity studies indicated that ($fc^{P,B}$)NiMe could not be oxidized in a straightforward manner, its application to redox switchable catalysis was not possible. However, a study of the ferrocene-based heteroscorpionate zinc(II) complexes as redox-switchable pre-catalysts is currently under investigation.

2.7 Experimental section

Synthesis of fc(PPh_2)$B(OMe)_2$. Compound fc(PPh_3)Br (1.00 g, 2.23 mmol) was dissolved in 100 mL of THF and cooled to -78 °C. *n*-Butyl lithium (2.5 M in hexanes, 1.07 mL, 2.68 mmol) was added dropwise over a period of 10 min. The resulting yellow slurry was stirred at -78 °C for 15 min. The reaction mixture was removed from the cold well, immediately quenched with $B(OMe)_3$ (1.27 mL, 11.2 mmol), and stirred for 1 h at ambient temperature. Volatile substances were removed under reduced pressure. The resulting yellow-orange oil was extracted in 15 mL of toluene and filtered through Celite. Toluene was removed under reduced pressure and the remaining orange oil was redissolved in 8 mL of *n*-pentane, filtered through Celite and stored at -40 °C overnight to afford a bright yellow solid (0.898 g, 91.1%). X-ray quality crystals were obtained from *n*-pentane at -40 °C upon prolonged standing. ^{1}H NMR (C_6D_6, 500 MHz, 298 K): δ (ppm) 3.61 (s, 6H, -OC*H*$_3$), 4.09 (t, 2H, Cp-*H*), 4.23 (m, 4H, Cp-*H*), 4.50 (t, 2H, Cp-*H*), 7.05 (m, 6H, *m*-Ph, *p*-Ph), 7.49 (m, 4H, *o*-Ph). ^{13}C NMR (C_6D_6, 126 MHz, 298 K): δ (ppm) 52.3 (d, -O*C*H$_3$), 72.0 (d, Cp-*C*), 73.8 (s, Cp-*C*), 73.9 (s, Cp-*C*), 76.3 (s, Cp-*C*),

77.5 (d, Cp-*C*), 134.3 (d, aromatic), 140.3 (d, aromatic). ^{11}B NMR (C_6D_6, 161 MHz, 298 K): δ (ppm) 28.8 (br s). ^{31}P NMR (C_6D_6, 121 MHz, 298 K): δ (ppm) -15.53 (s). Anal. Calcd: fc(PPh_2)B(OMe)$_2$ ($C_{24}H_{24}BFeO_2P$) C, 65.21; H, 5.47. Found: C, 65.19; H, 5.26.

Synthesis of [Li(OEt_2)][fc(PPh_2)(BH_3)]. Compound fc(PPh_2)B(OMe)$_2$ (0.839 g, 1.90 mmol) was dissolved in 50 mL of diethyl ether and cooled to -78 °C. Lithium aluminum hydride (0.072 g, 1.90 mmol) in 5 mL of diethyl ether was added dropwise over a period of 5 min. The reaction mixture was stirred at -78 °C for 30 min followed by 1 h at ambient temperature. The reaction solution was filtered through a glass frit and volatiles removed under reduced pressure. The resulting yellow-orange solid was washed with 30 mL of hexanes, redissolved in diethyl ether and filtered through Celite. Reduction in volume of the solution and storage at -40 °C afforded orange crystalline material in two crops (0.746 g, 84.6%). X-ray quality crystals were obtained from THF/hexanes layering at -40 °C. ^{1}H NMR (C_6D_6, 300 MHz, 298 K): δ (ppm) 1.92 (br m, $^1J_{HB}$ = 75.2 Hz, 3H, BH_3), 4.08 (t, 4H, Cp-*H*), 4.29 (t, 2H, Cp-*H*), 4.35 (t, 2H, Cp-*H*), 7.02 (m, 6H, *m*-Ph, *p*-Ph), 7.62 (m, 4H, *o*-Ph). The complex was not soluble enough in C_6D_6 to obtain a ^{13}C NMR spectrum. ^{11}B NMR (C_6D_6, 161 MHz, 298 K): δ (ppm) -27.1 (q, $^1J_{HB}$ = 75.2 Hz). ^{31}P NMR (C_6D_6, 121 MHz, 298 K): δ (ppm) -17.1 (s). Anal. Calcd: [fc(PPh_2)(BH_3)]Li·(Et_2O) ($C_{26}H_{31}BFeLiOP$) C, 67.29; H, 6.73. Found: C, 66.96; H, 6.54.

Synthesis of [Li(THF)$_2$][fc(PPh_2)(BH[(3,5-Me)$_2$pz]$_2$)]. Compound [Li(OEt_2)][fc(PPh_2)(BH_3)] (0.439 g, 0.945 mmol) in 5 mL of THF was added to 3,5-dimethylpyrazole (0.181 g, 1.88 mmol) in 15 mL of toluene and stirred for 48 h at 50 °C. Volatile substances were removed under reduced pressure. The remaining solids were dissolved in hexanes and filtered through Celite. Volatiles were removed under reduced pressure and the remaining oil redissolved in THF. Prolonged standing under reduced pressure of the THF

solution affords the product as an orange solid (0.653 g, 95.7%). ^{1}H NMR (C_6D_6, 300 MHz, 298 K): δ (ppm) 2.08 (s, 6H, CC*H*$_3$), 2.59 (s, 6H, CC*H*$_3$), 3.97 (t, 2H, Cp-*H*), 4.06 (t, 2H, Cp-*H*), 4.18 (t, 2H, Cp-*H*), 4.39 (t, 2H, Cp-*H*), 5.87 (s, 2H, C*H*), 7.04 (m, 6H, *m*-Ph, *p*-Ph), 7.56 (m, 4H, *o*-Ph). ^{13}C NMR (C_6D_6, 126 MHz, 298 K): δ (ppm) 13.9 (s, C*C*H$_3$), 14.1 (s, C*C*H$_3$), 70.1 (s, Cp-*C*), 72.9 (d, Cp-*C*), 74.3 (d, Cp-*C*), 74.6 (s, Cp-*C*), 75.4 (d, Cp-*C*), 104.3 (s, *C*H), 134.4 (d, aromatic), 141.2 (d, aromatic), 145.1 (s, *C*CH$_3$), 147.0 (s, *C*CH$_3$). ^{11}B NMR (C_6D_6, 161 MHz, 298 K): δ(ppm) -8.2 (br s). ^{31}P NMR (C_6D_6, 121 MHz, 298 K): δ (ppm) -14.1 (s). Anal. Calcd: (fc^{P,B})Li·(THF)$_2$ ($C_{40}H_{49}BFeLiN_4O_2P$) C, 66.50; H, 6.84; N, 7.76. Found: C, 67.69; H, 6.62; N, 8.74.

Synthesis of (fc^{P,B})NiCl. To $NiCl_2$(DME) (0.451 g, 2.05 mmol) in 20 mL of THF (THF)$_2$·Li[fc(PPh$_2$)(BH[(3,5-Me)$_2$pz]$_2$)] (1.48 g, 2.05 mmol) was added dropwise over a period of 10 min in 10 mL of THF at ambient temperature. The reaction solution was stirred for 12 h. Volatile substances were removed under reduced pressure and the product extracted into 100 mL of toluene and filtered through Celite. Reduction in volume of the toluene solution to 60 mL afforded black crystalline material after 24 h at -40 °C. Decanting of the solution and washing of the remaining solids with 3 mL of hexanes yielded the product as black crystalline material (1.43 g, 92.1%). Crystals of (fc^{P,B})NiCl always contain a molecule of toluene per molecule of compound as supported by NMR spectroscopic data. X-ray quality crystals were obtained from toluene/hexanes layering at -40 °C. ^{1}H NMR (C_6D_6, 400 MHz, 298 K): δ (ppm) -8.36 (br s), -4.68 (br s), 1.87 (br s), 3.74 (s), 9.93 (br s), 11.45 (br s), 13.53 (br s), 18.64 (br s). μ_{eff} = 3.12 μ_B. Anal. Calcd: (fc^{P,B})NiCl·(C_7H_8) ($C_{39}H_{41}BClFeN_4NiP$) C, 61.83; H, 5.46; N, 7.40. Found: C, 61.72; H, 5.39; N, 7.32.

Synthesis of ($fc^{P,B}$)NiMe. To ($fc^{P,B}$)NiCl·(C_7H_8) (38 mg, 0.0502 mmol) in 5 mL of toluene $ZnMe_2$ (0.080 mL, 0.053 mmol, 0.667 M in toluene) was added dropwise via syringe at ambient temperature. The reaction solution was stirred for an hour. Volatile substances were removed under reduced pressure. The product was extracted into 5 mL of *n*-pentane and filtered through Celite. Reduction in volume to 2 mL yielded the product as orange crystalline material upon standing at -40 °C (20.0 mg, 61.8%). X-ray quality crystals were obtained from a 1:10 mixture of toluene/hexanes at -40 °C. ^{1}H NMR (C_6D_6, 300 MHz, 298 K): δ (ppm) 0.02 (d, 3H, NiC*H*$_3$), 1.93 (br s), 2.34 (s), 2.38 (br s), 4.01 (s), 4.15 (br s), 4.32 (s), 4.63 (br s), 5.39 (br s), 5.69 (br s), 6.80 (br s), 7.61 (br s). ^{1}H NMR (C_6D_6, 500 MHz, 361 K): δ (ppm) -0.04 (d, 3H, NiC*H*$_3$), 2.15 (br s, 6H, CC*H*$_3$), 2.31 (s, 6H, CC*H*$_3$), 4.06 (br s, 2H, Cp-*H*), 4.24 (t, 2H, Cp-*H*), 4.32 (t, 2H, Cp-*H*), 4.34 (t, 2H, Cp-*H*), 5.52 (s, 2H, C*H*), 6.96 (br s, 4H, *m*-Ph), 7.05 (m, 2H, *p*-Ph), 7.30 (m, 4H, *o*-Ph). ^{13}C NMR (C_6D_6, 126 MHz, 298 K): δ (ppm) -5.1 (d, Ni*C*H$_3$), 13.8 (br s, C*C*H$_3$), 14.0 (br s, C*C*H$_3$), 14.6 (br s, C*C*H$_3$), 15.3 (br s, C*C*H$_3$), 69.2 (br s, Cp-*C*), 69.6 (s, Cp-*C*), 70.0 (s, Cp-*C*), 70.4 (br s, Cp-*C*), 70.6 (br s, Cp-*C*), 72.7 (br s, Cp-*C*), 72.9 (br s, Cp-*C*), 73.7 (s, Cp-*C*), 73.8 (s, Cp-*C*), 106.9 (br s, *C*H), 107.3 (br s, *C*H), 129.4 (br s, aromatic), 130.4 (br s, aromatic), 133.3 (br s, aromatic), 133.6 (br s, aromatic), 146.2 (s, *C*CH$_3$), 148.8 (br s, *C*CH$_3$), 149.2 (br s, *C*CH$_3$). ^{11}B NMR (C_6D_6, 161 MHz, 298 K): δ (ppm) -7.8 (br s). ^{31}P NMR (C_6D_6, 121 MHz, 298 K): δ (ppm) 30.33 (s). Anal. Calcd: ($fc^{P,B}$)NiMe ($C_{33}H_{36}BFeN_4NiP$) C, 61.45; H, 5.63; N, 8.69. Found: C, 60.54; H, 5.91; N, 8.37.

Synthesis of ($fc^{P,B}$)ZnCl. To $ZnCl_2$ (18.5mg, 0.136 mmol) in 2 mL of THF [Li(THF)$_2$][fc(PPh$_2$)(BH[(3,5-Me)$_2$pz]$_2$)] (98.3 mg, 0.136 mmol) in 2 mL of THF was added dropwise. The reaction solution was stirred for one hour. Volatile substances were removed under reduced pressure and the desired product was extracted into 4 mL of toluene and filtered

through Celite. Reduction in volume of the toluene solution to 1 mL and layering of 3 mL of hexanes afforded orange crystalline material after 24 h at -40 °C (90.0 mg, 86.4%). Crystals of ($fc^{P,B}$)ZnCl always contain a molecule of toluene per molecule of compound as supported by NMR data. X-ray quality crystals were obtained from toluene at -40 °C. ^{1}H NMR (C_6D_6, 500 MHz, 298 K): δ (ppm) 2.24 (s, 6H, CC*H*$_3$), 2.47 (s, 6H, CC*H*$_3$), 3.55 (q, 2H, Cp-*H*), 3.93 (m, 4H, Cp-*H*), 4.04 (m, 2H, Cp-*H*), 5.68 (s, 2H, C*H*), 7.01 (m, 6H, *m*-Ph, *p*-Ph), 7.85 (m, 4H, *o*-Ph). ^{13}C NMR (C_6D_6, 126 MHz, 298 K): δ (ppm) 14.0 (s, C*C*H$_3$), 14.4 (s, C*C*H$_3$), 68.0 (d, Cp-*C*), 69.7 (s, Cp-*C*), 72.3 (d, Cp-*C*), 72.6 (d, Cp-*C*), 74.9 (s, Cp-*C*), 107.1 (s, -*C*H-), 129.3 (d, aromatic), 131.2 (s, aromatic), 131.2 (d, aromatic), 134.3 (d, aromatic), 147.6 (s, *C*CH$_3$), 150.2 (s, *C*CH$_3$). ^{11}B NMR (C_6D_6, 161 MHz, 298 K): δ (ppm) -9.3 (br s). ^{31}P NMR (C_6D_6, 121 MHz, 298 K): δ (ppm) -16.4 (s). Anal. Calcd: ($fc^{P,B}$)ZnCl ($C_{32}H_{33}BClFeN_4PZn$) C, 57.19; H, 4.95; N, 8.34. Found: C, 57.04; H, 4.54; N, 8.09.

Synthesis of ($fc^{P,B}$)ZnMe. To ($fc^{P,B}$)ZnCl (75.5 mg, 0.112 mmol) in 5 mL of THF at -78 °C MeLi (0.231 mL, 0.118 mmol, 0.51 M in THF) was added dropwise over a period of 1 min. The resulting reaction mixture was stirred at -78 °C for 10 min and 1 h at ambient temperature. Volatile substances were removed under reduced pressure. The desired product was extracted in 5 mL of hexanes and filtered through Celite. Reduction in volume to 2 mL afforded yellow crystalline material upon standing at -40 °C (41.0 mg, 56.2%). X-ray quality crystals were obtained from hexanes at -40 °C. ^{1}H NMR (C_6D_6, 500 MHz, 298 K): δ (ppm) -0.03 (d, 3H, ZnC*H*$_3$), 2.26 (s, 6H, CC*H*$_3$), 2.35 (s, 6H, CC*H*$_3$), 3.50 (q, 2H, Cp-*H*), 3.93 (t, 2H, Cp-*H*), 4.01 (t, 2H, Cp-*H*), 4.09 (m, 2H, Cp-*H*), 5.79 (s, 2H, C*H*), 7.02 (m, 6H, *m*-Ph, *p*-Ph), 7.58 (m, 4H, *o*-Ph). ^{13}C NMR (C_6D_6, 126 MHz, 298 K): δ (ppm) -9.5 (d, Zn*C*H$_3$) 14.7 (s, C*C*H$_3$), 14.7 (s, C*C*H$_3$), 70.0 (s, Cp-*C*), 70.6 (d, Cp-*C*), 72.4 (d, Cp-*C*), 73.3 (d, Cp-*C*), 75.4 (s, Cp-*C*), 107.3 (s, -*C*H-),

129.5 (d, aromatic), 130.8 (s, aromatic), 134.7 (d, aromatic), 135.2 (d, aromatic), 147.7 (s, *C*CH_3), 149.8 (s, *C*CH_3). ^{11}B NMR (C_6D_6, 161 MHz, 298 K): δ (ppm) -8.9 (br s). ^{31}P NMR (C_6D_6, 121 MHz, 298 K): δ (ppm) -16.2 (s). Anal. Calcd: ($fc^{P,B}$)ZnMe ($C_{33}H_{36}BFeN_4PZn$) C, 60.82; H, 5.57; N, 8.60. Found: C, 60.75; H, 5.34; N, 8.45.

2.8 Appendix A

2.8.1 NMR spectroscopy

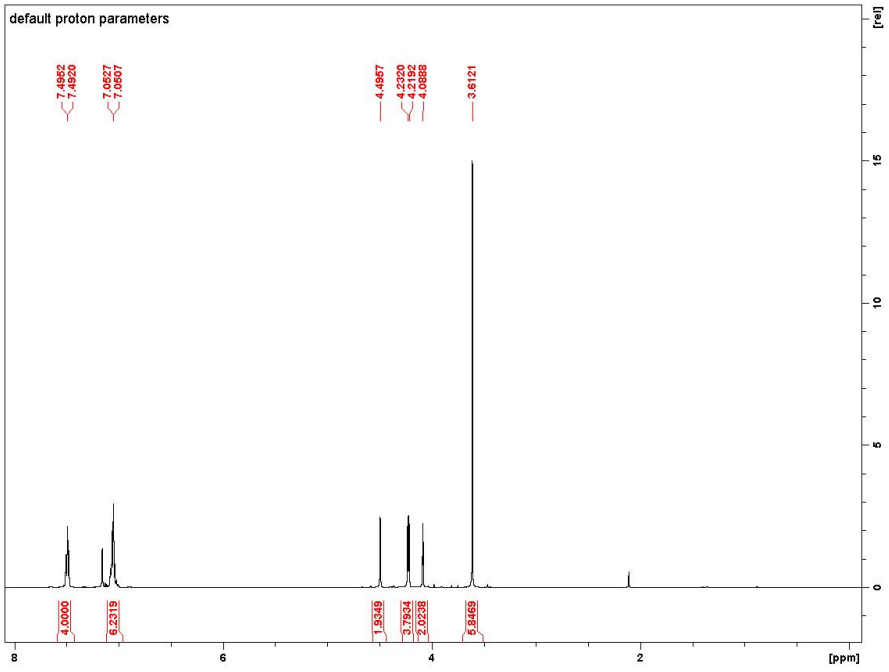

Figure A1. ^{1}H NMR spectrum (C_6D_6, 500 MHz, 298 K) of $fc(PPh_2)B(OMe)_2$.

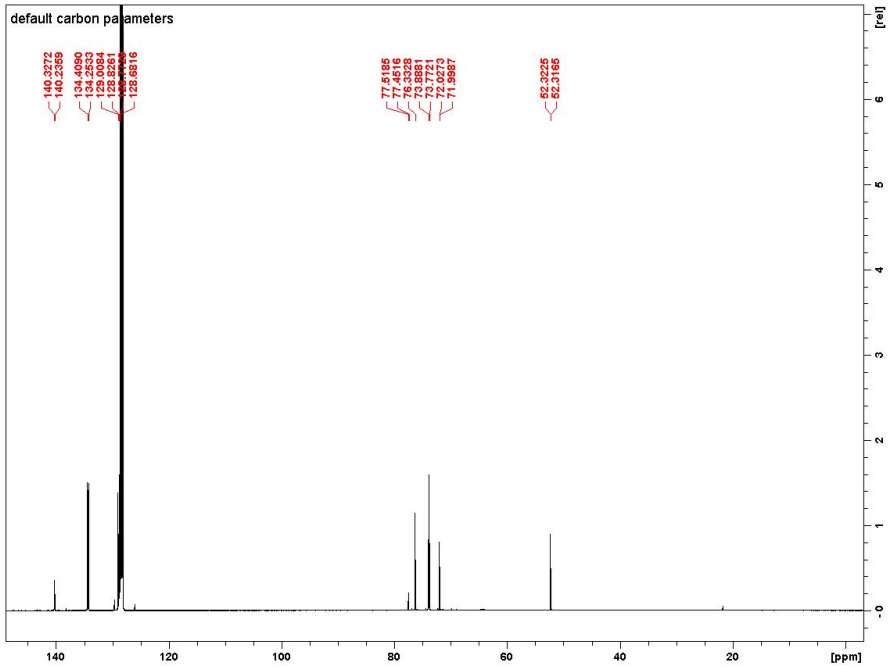

Figure A2. ^{13}C NMR spectrum (C_6D_6, 126 MHz, 298 K) of $fc(PPh_2)B(OMe)_2$.

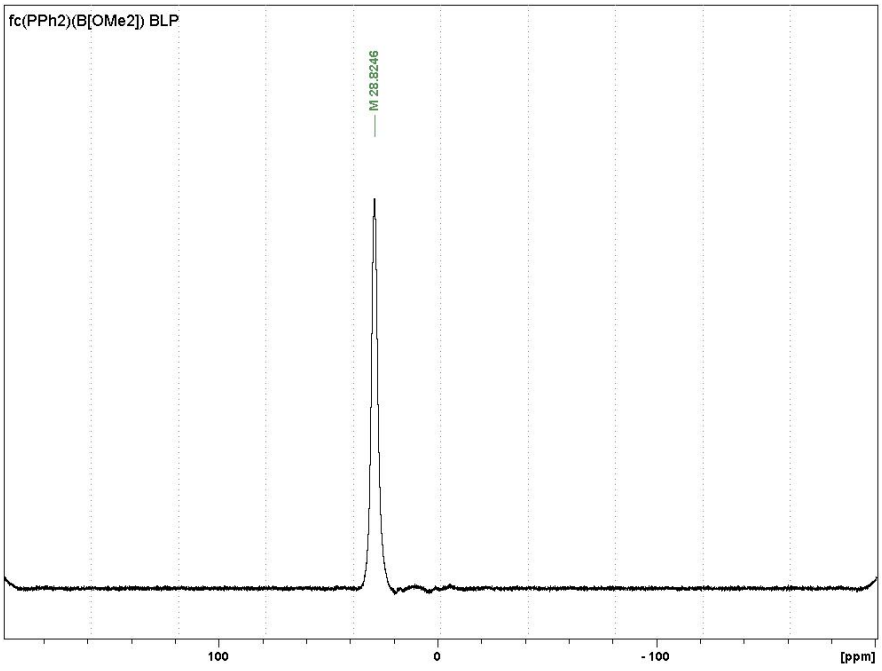

Figure A3. ^{11}B NMR spectrum (C_6D_6, 161 MHz, 298 K) of $fc(PPh_2)B(OMe)_2$.

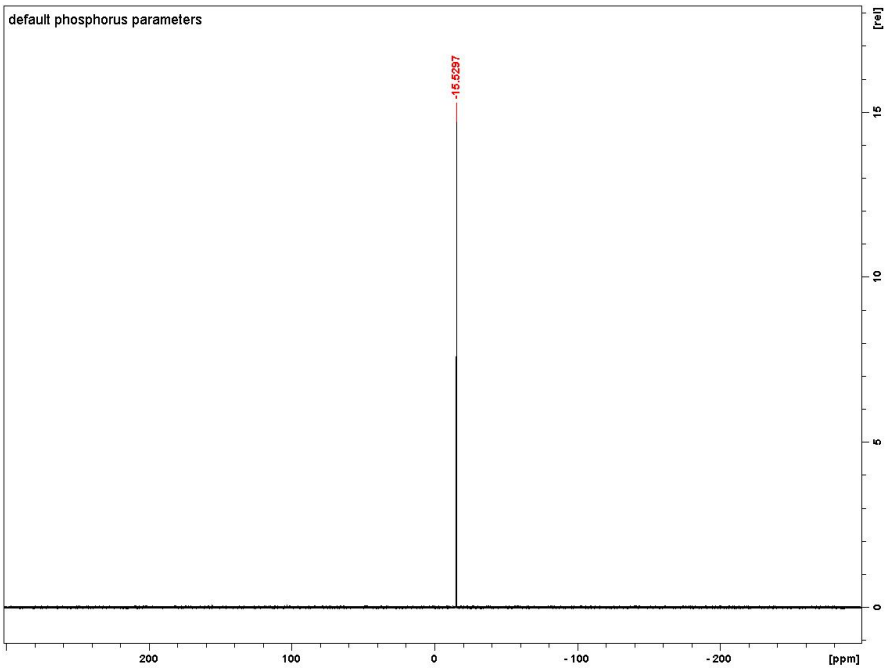

Figure A4. ^{31}P NMR spectrum (C_6D_6, 121 MHz, 298 K) of $fc(PPh_2)B(OMe)_2$.

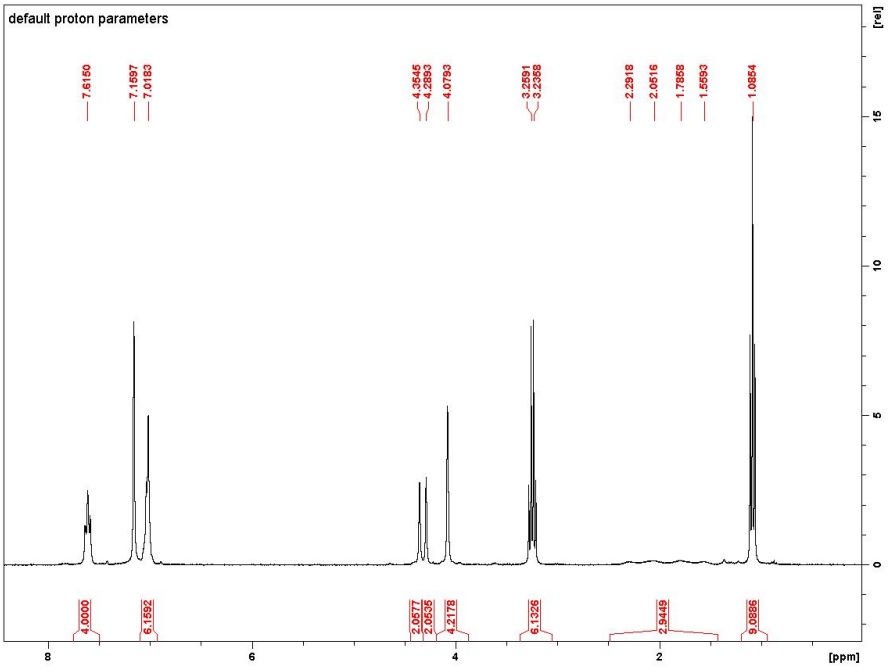

Figure A5. ^{1}H NMR spectrum (C_6D_6, 300 MHz, 298 K) of [Li(OEt$_2$)][fc(PPh$_2$)(BH$_3$)].

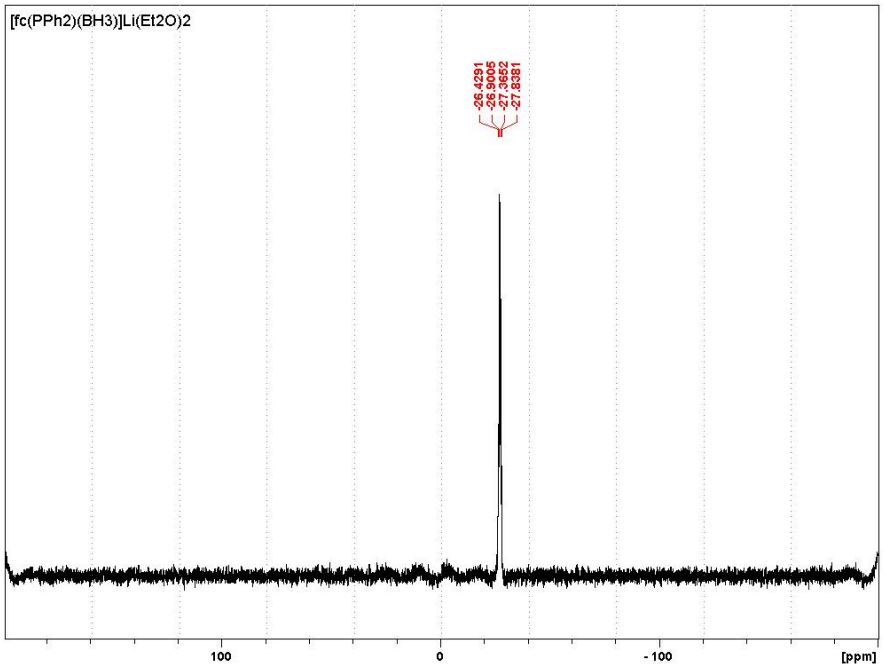

Figure A6. ^{11}B NMR spectrum (C_6D_6, 161 MHz, 298 K) of [Li(OEt$_2$)][fc(PPh$_2$)(BH$_3$)].

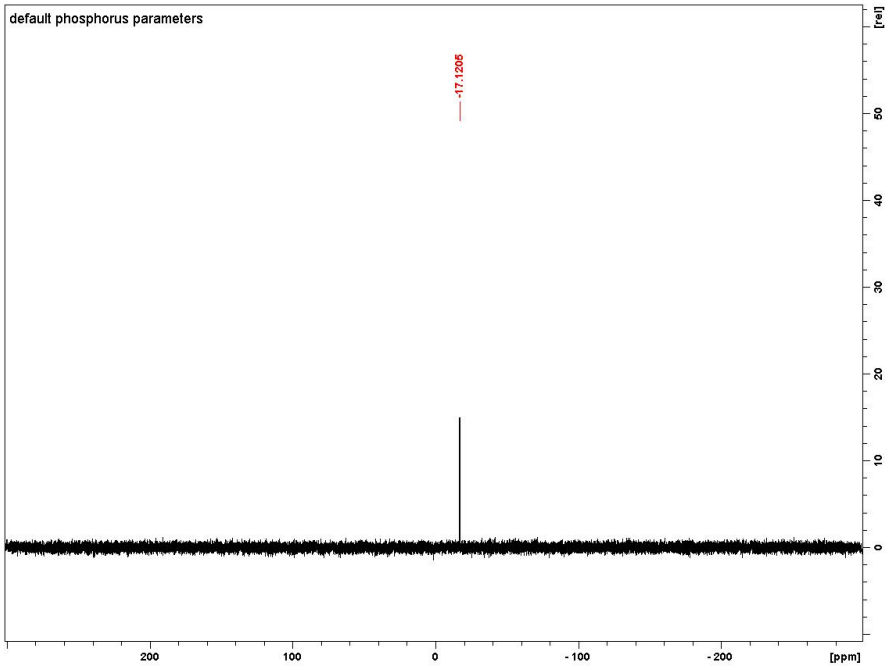

Figure A7. ^{31}P NMR spectrum (C_6D_6, 161 MHz, 298 K) of $[Li(OEt_2)][fc(PPh_2)(BH_3)]$.

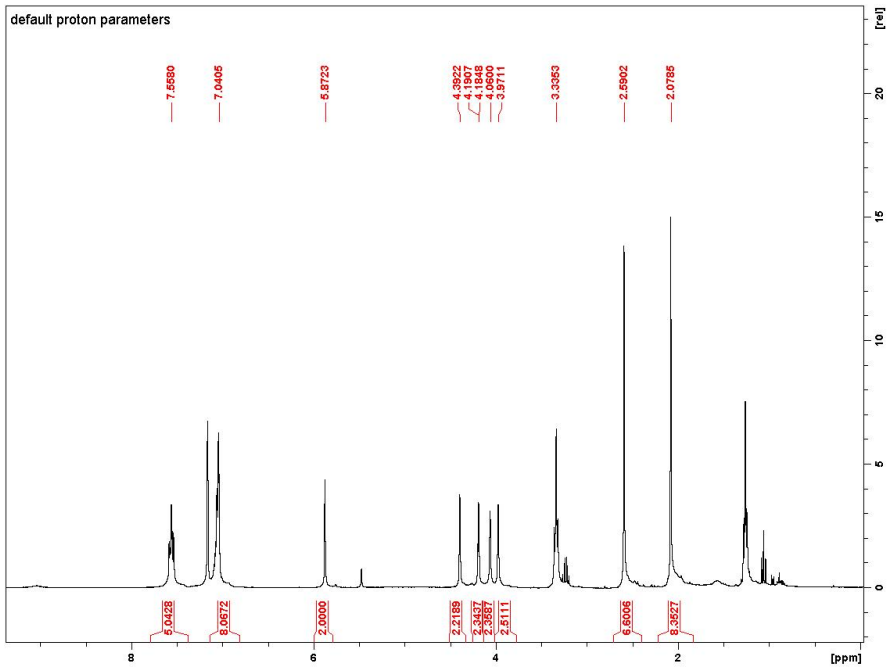

Figure A8. ^{1}H NMR spectrum (C_6D_6, 300 MHz, 298 K) of $[Li(THF)_2][fc(PPh_2)(BH[(3,5\text{-}Me)_2pz]_2)]$.

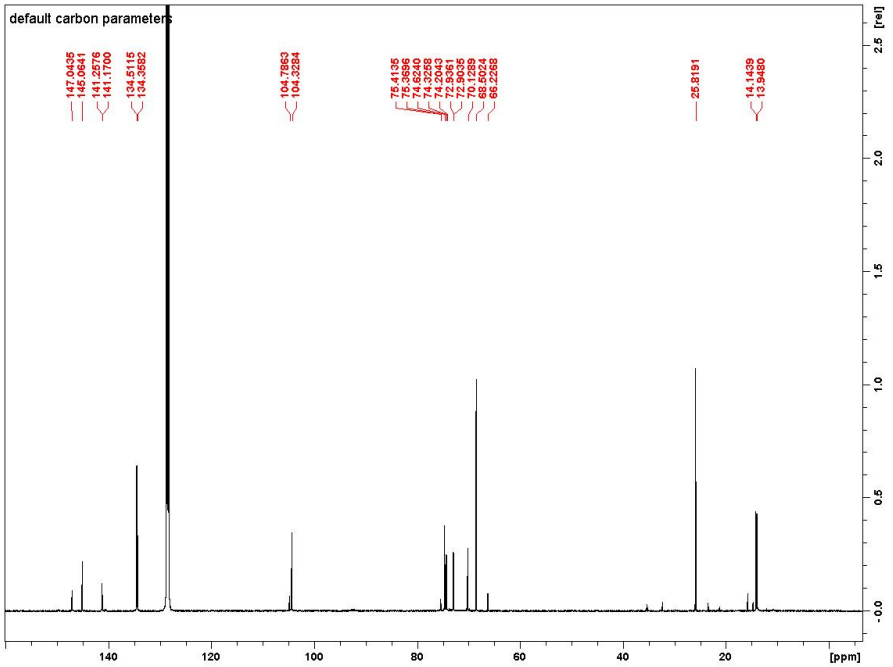

Figure A9. ^{13}C NMR spectrum (C_6D_6, 126 MHz, 298 K) of $[Li(THF)_2][fc(PPh_2)(BH[(3,5\text{-}Me)_2pz]_2)]$.

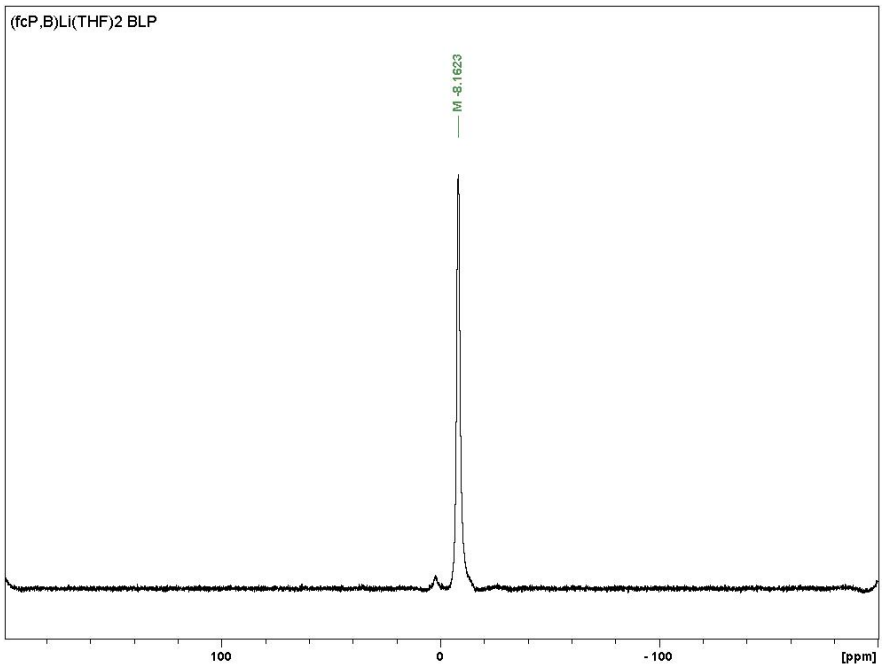

Figure A10. ^{11}B NMR spectrum (C_6D_6, 161 MHz, 298 K) of $[Li(THF)_2][fc(PPh_2)(BH[(3,5\text{-}Me)_2pz]_2)]$.

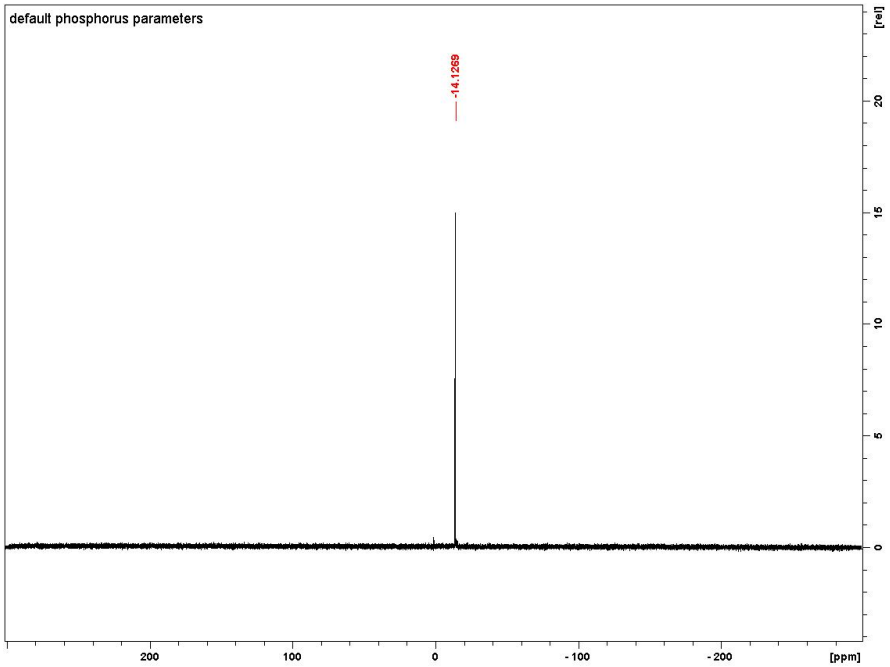

Figure A11. ^{31}P NMR spectrum (C_6D_6, 161 MHz, 298 K) of $[Li(THF)_2][fc(PPh_2)(BH[(3,5\text{-}Me)_2pz]_2)]$.

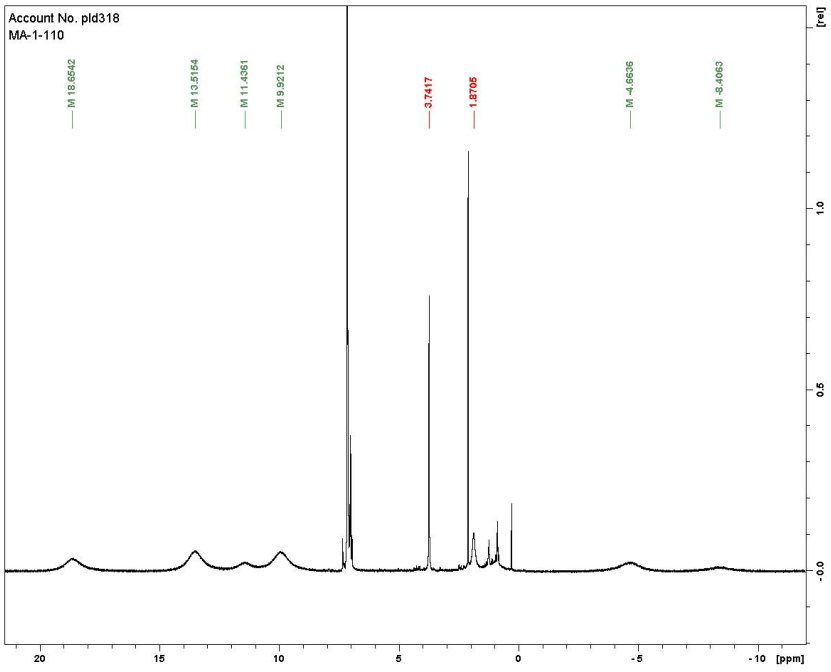

Figure A12. ^{1}H NMR spectrum (C_6D_6, 400 MHz, 298 K) of $(fc^{P,B})NiCl\cdot(C_7H_8)$.

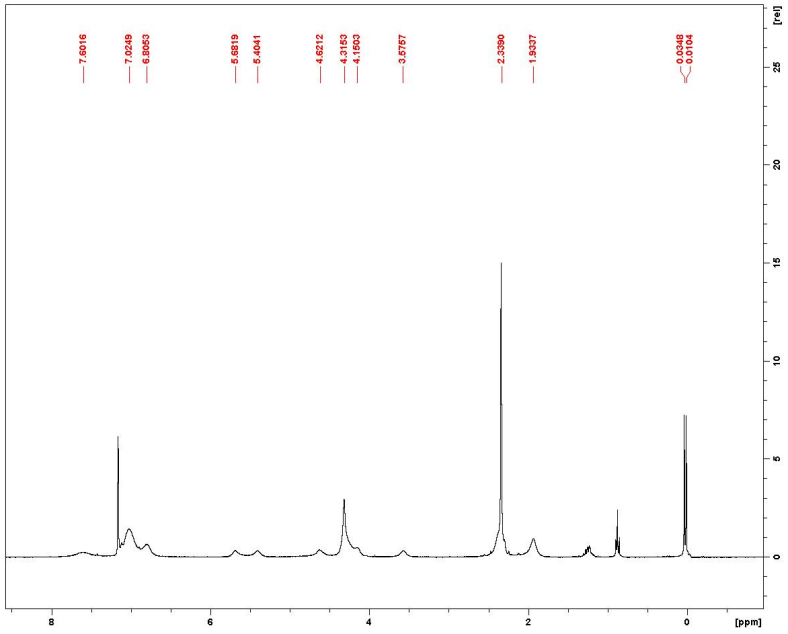

Figure A13. ^{1}H NMR spectrum (C_6D_6, 300 MHz, 298 K) of ($fc^{P,B}$)NiMe.

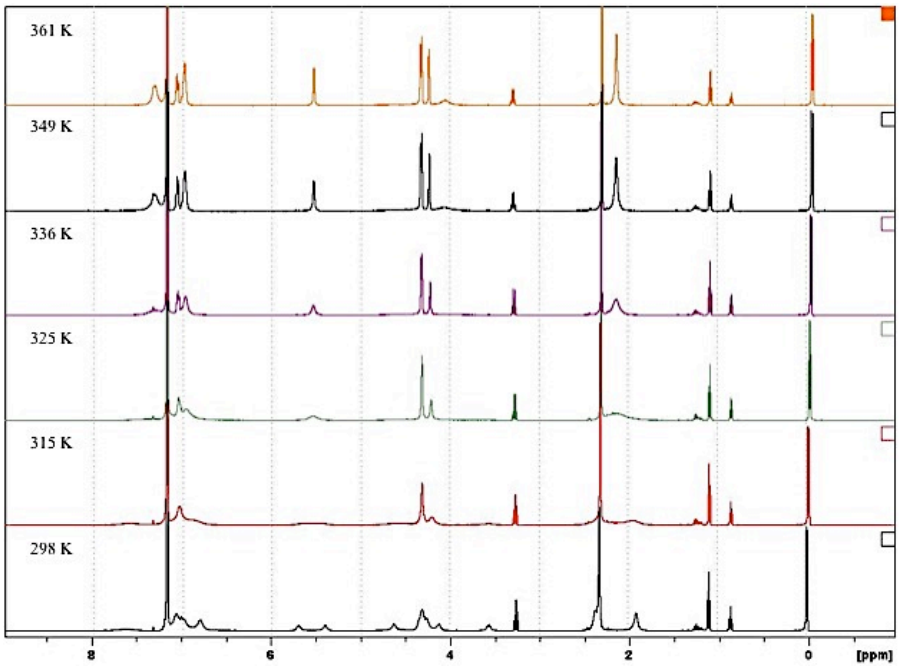

Figure A14. Variable temperature ^{1}H NMR spectra (C_6D_6, 500 MHz) of ($fc^{P,B}$)NiMe.

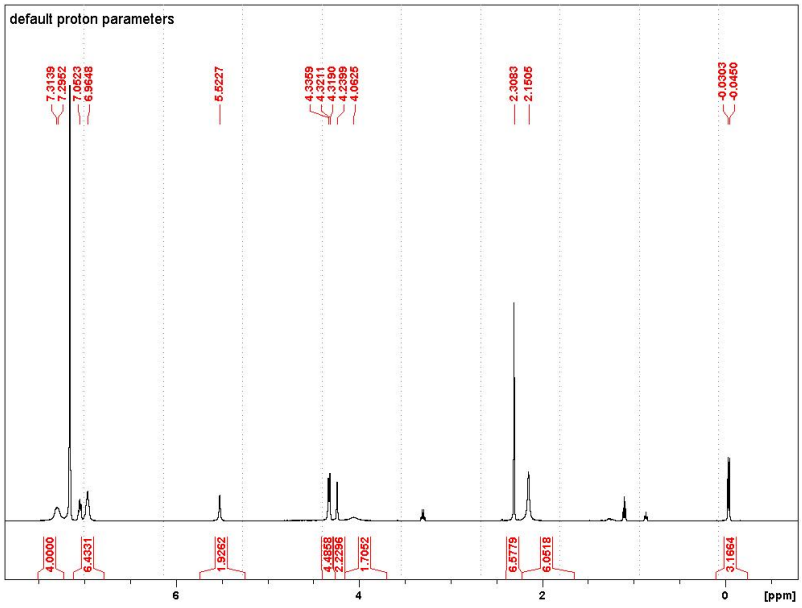

Figure A15. ^{1}H NMR spectrum (C_6D_6, 500 MHz, 361 K) of ($fc^{P,B}$)NiMe.

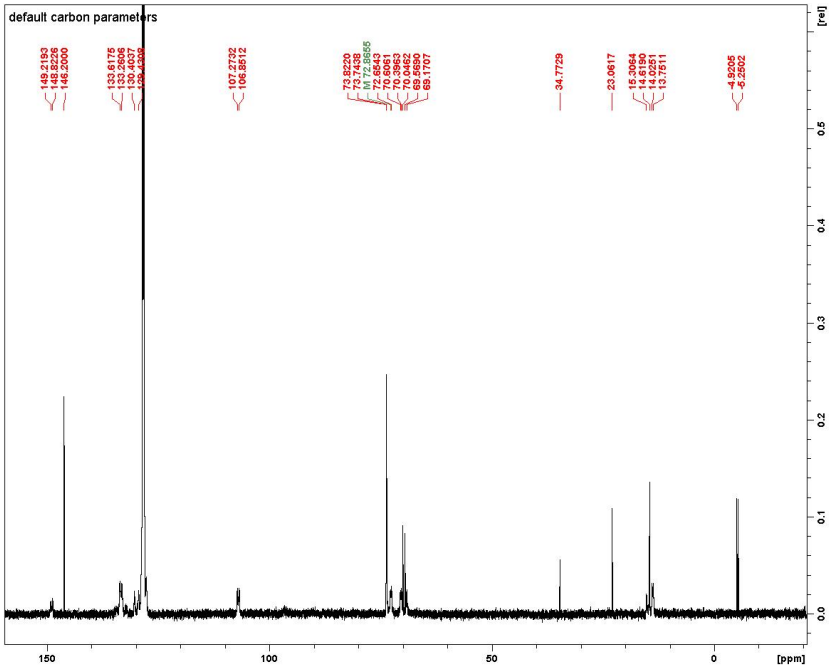

Figure A16. ^{13}C NMR spectrum (C_6D_6, 126 MHz, 298 K) of ($fc^{P,B}$)NiMe.

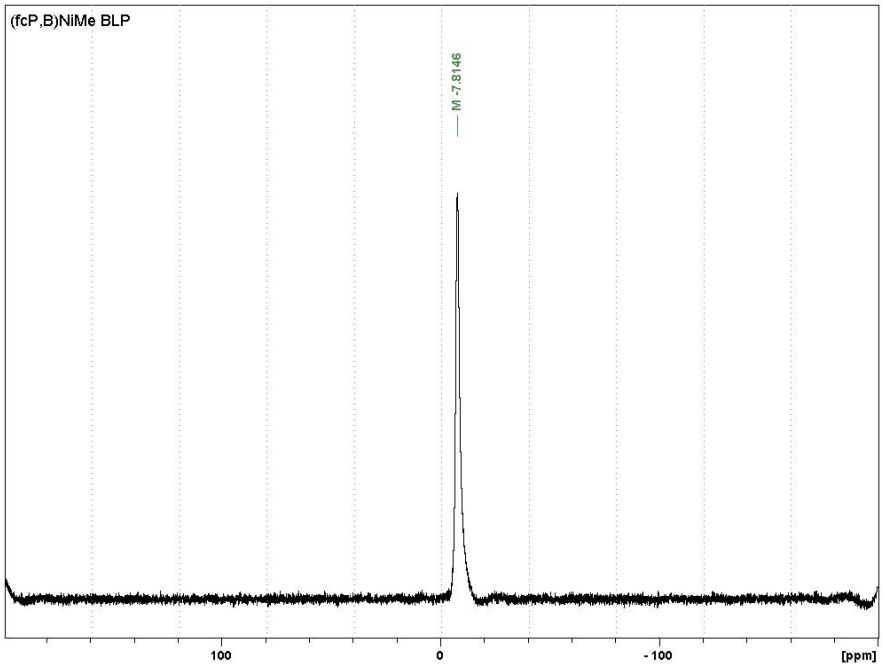

Figure A17. ^{11}B NMR spectrum (C_6D_6, 161 MHz, 298 K) of ($fc^{P,B}$)NiMe.

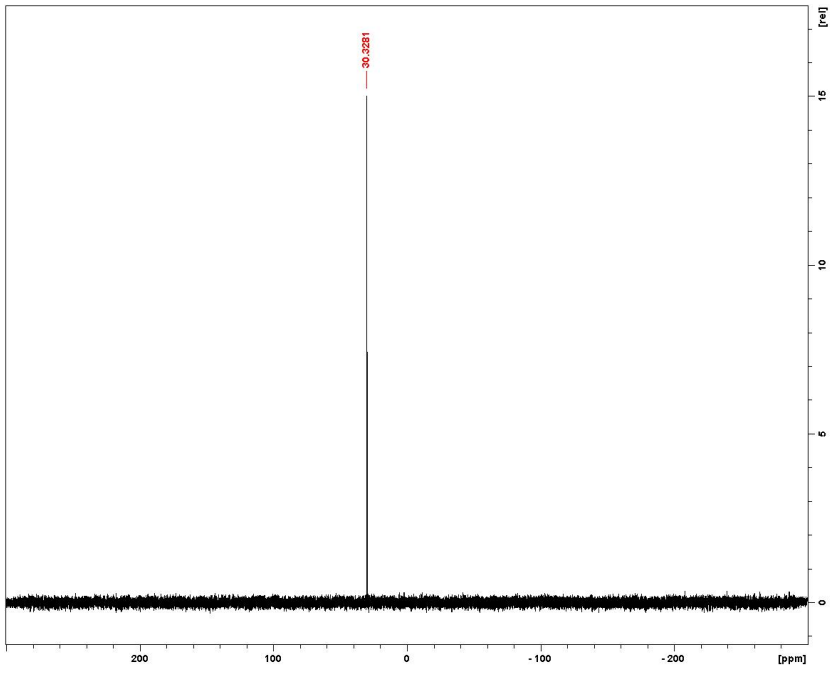

Figure A18. ^{31}P NMR spectrum (C_6D_6, 121 MHz, 298 K) of ($fc^{P,B}$)NiMe.

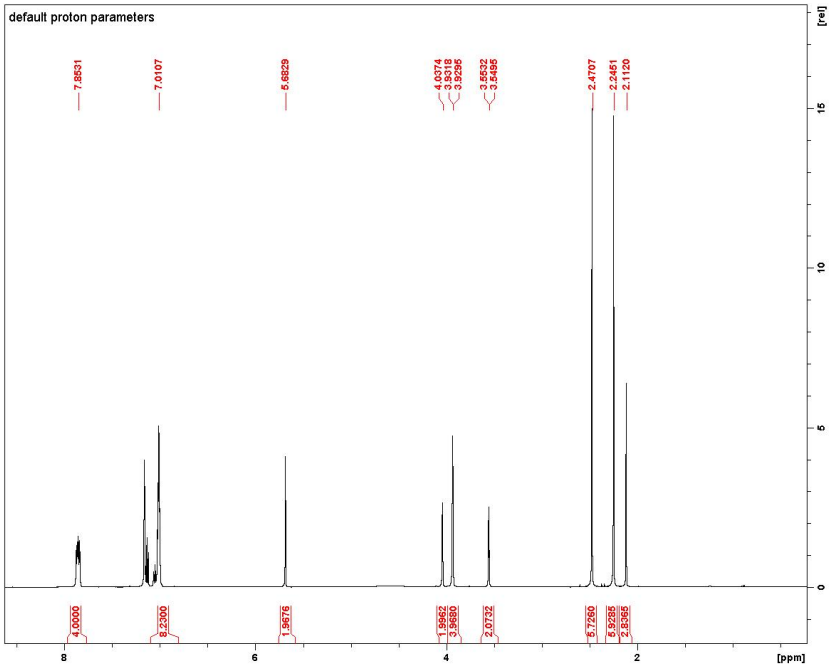

Figure A19. ^{1}H NMR spectrum (C_6D_6, 500 MHz, 298 K) of ($fc^{P,B}$)ZnCl·(C_7H_8).

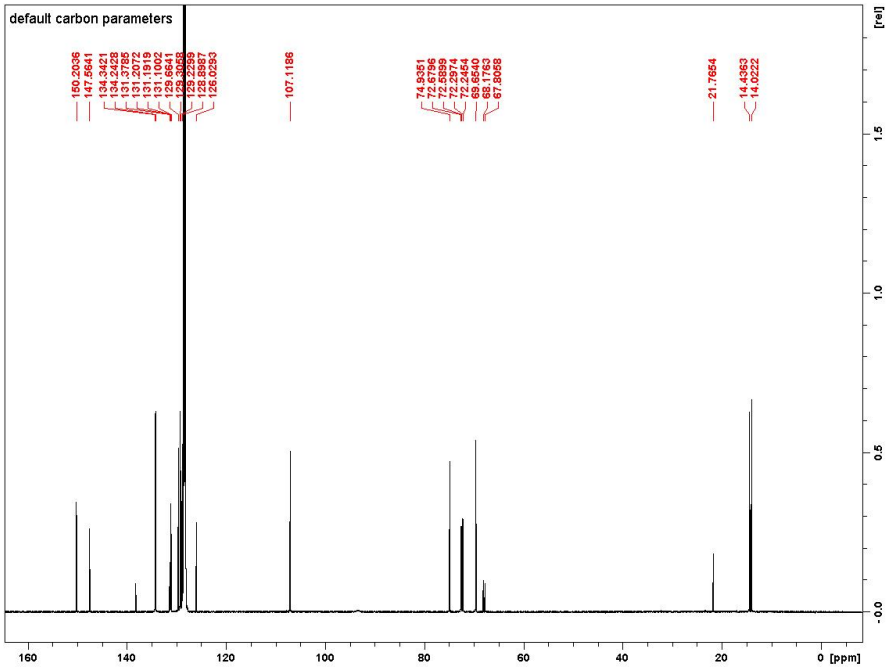

Figure A20. ^{13}C NMR spectrum (C_6D_6, 126 MHz, 298 K) of ($fc^{P,B}$)ZnCl·(C_7H_8).

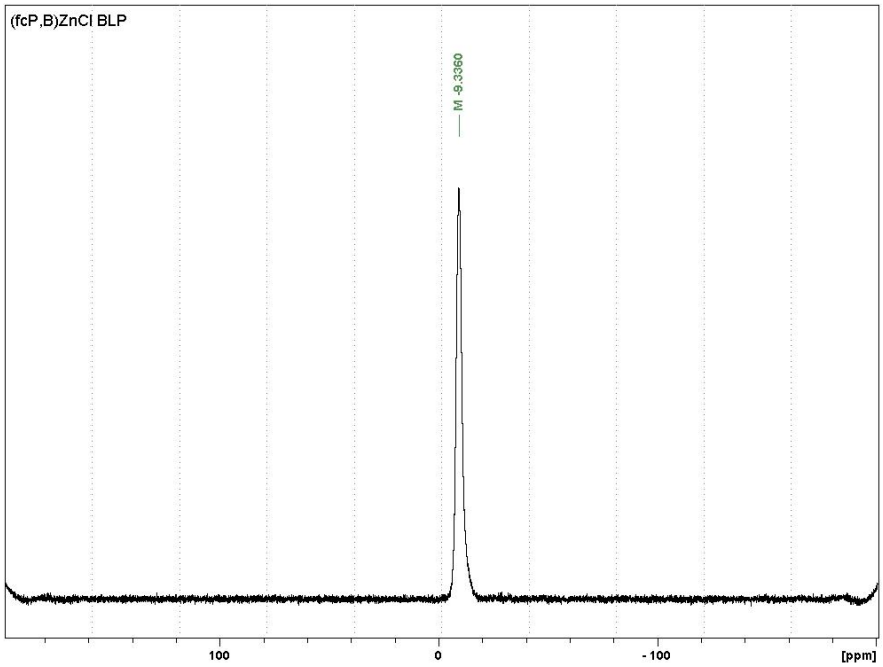

Figure A21. ^{11}B NMR spectrum (C_6D_6, 161 MHz, 298 K) of ($fc^{P,B}$)ZnCl·(C_7H_8).

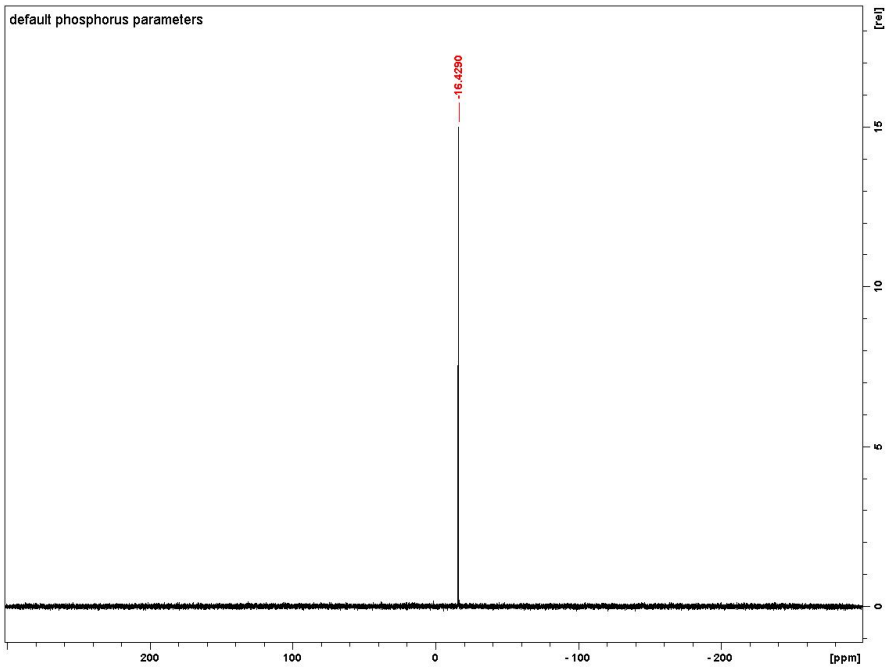

Figure A22. ^{31}P NMR spectrum (C_6D_6, 121 MHz, 298 K) of ($fc^{P,B}$)ZnCl·(C_7H_8).

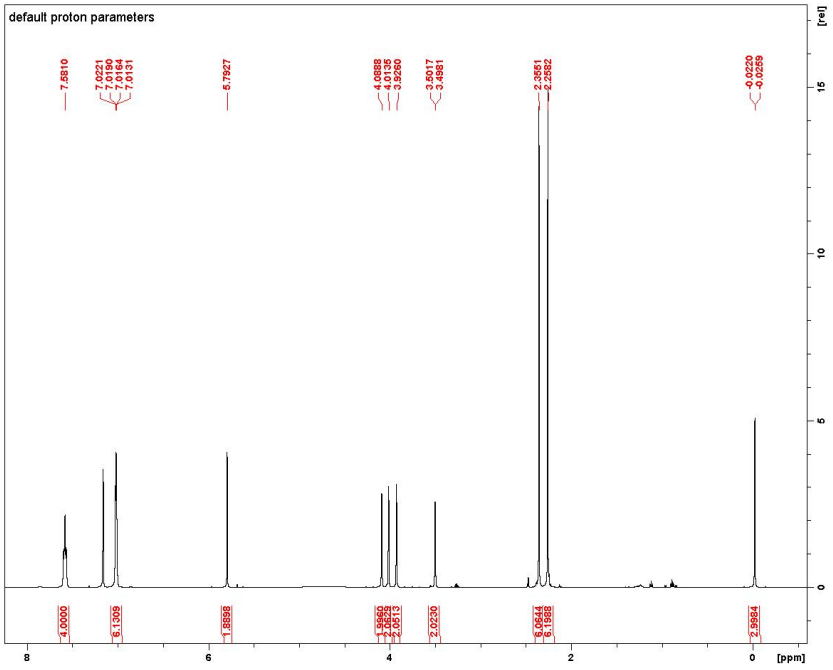

Figure A23. ^{1}H NMR spectrum (C_6D_6, 500 MHz, 298 K) of ($fc^{P,B}$)ZnMe.

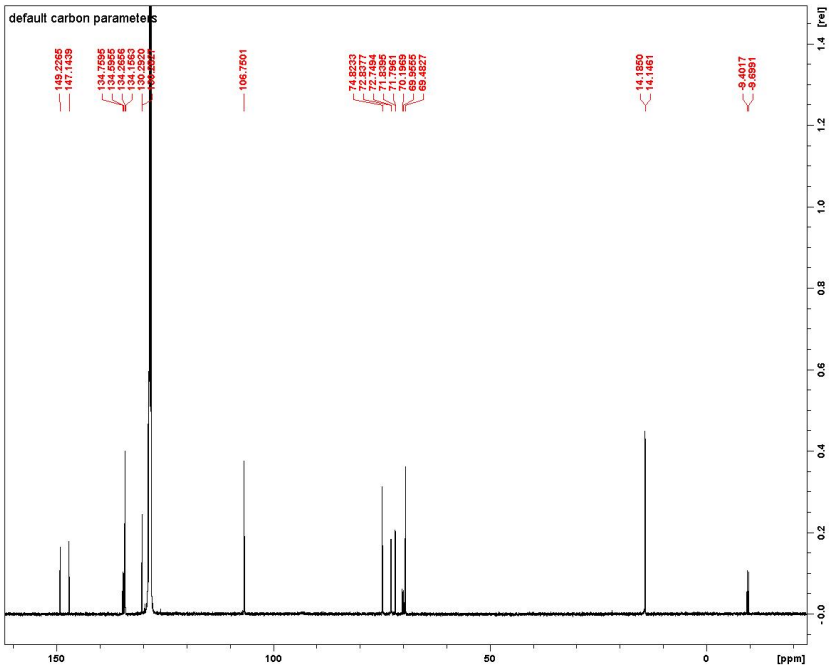

Figure A24. ^{13}C NMR spectrum (C_6D_6, 126 MHz, 298 K) of ($fc^{P,B}$)ZnMe.

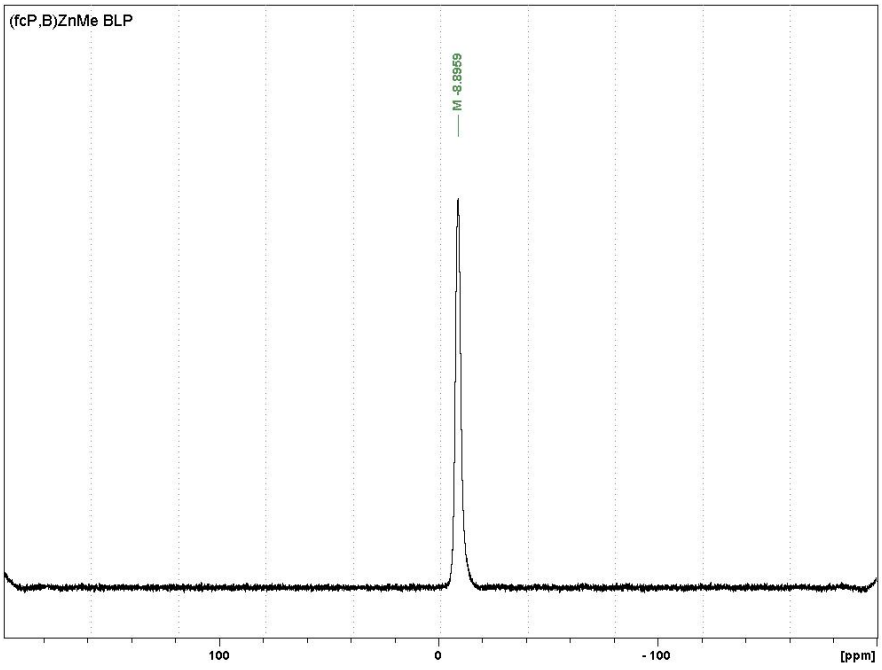

Figure A25. ^{11}B NMR spectrum (C_6D_6, 161 MHz, 298 K) of ($fc^{P,B}$)ZnMe.

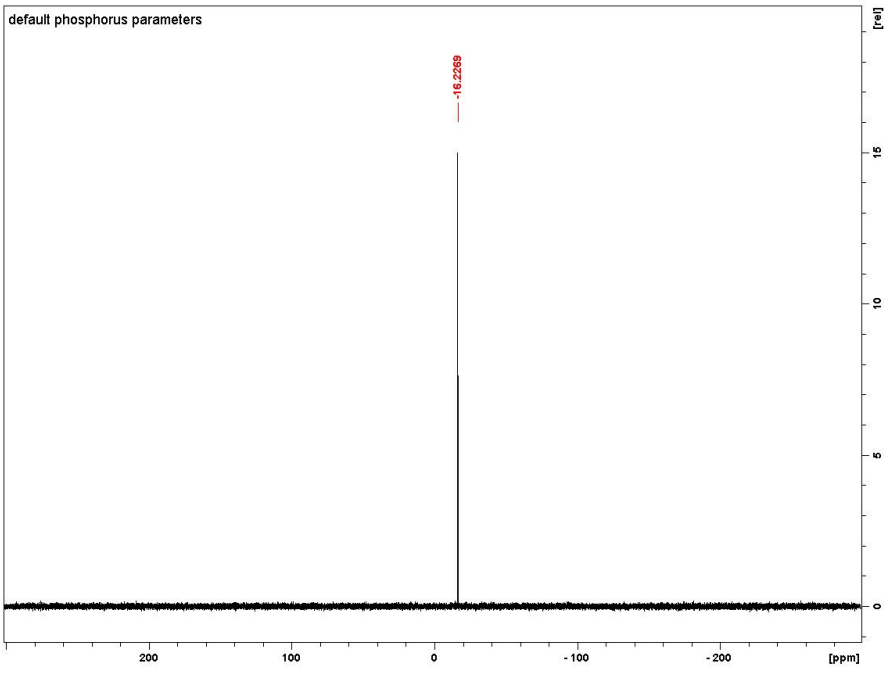

Figure A26. ^{31}P NMR spectrum (C_6D_6, 121 MHz, 298 K) of ($fc^{P,B}$)ZnMe.

2.8.2 Cyclic voltammetry data

Calculating i_{pc}/i_{pa}:

$$\frac{i_{pc}}{i_{pa}} = \frac{(i_{pc})_0}{i_{pa}} + 0.485\frac{(i_{sp})_0}{i_{pa}} + 0.086$$

The ratio of the peak currents, i_{pc}/i_{pa}, was determined by the equation above, because the actual baseline for measuring i_{pc} could not be determined in most cases. This was calculated from (a) the uncorrected cathodic peak current, $(i_{pc})_0$, with respect to the zero current baseline and (b) the current at the switching potential $(i_{sp})_0$.[7]

Table A1. Electrochemical details.

Analyte	$E_{1/2}$ (V)[a]	i_{pc}/i_{pa}
($fc^{P,B}$)NiCl	–0.026, –1.576	0.98, 0.84
($fc^{P,B}$)NiMe	0.419, 0.180*	0.48
($fc^{P,B}$)ZnCl	–0.068	1.03
($fc^{P,B}$)ZnMe	–0.177	1.06

[a] Potentials were referenced to the ferrocene/ferrocenium couple. *E_{pa}.

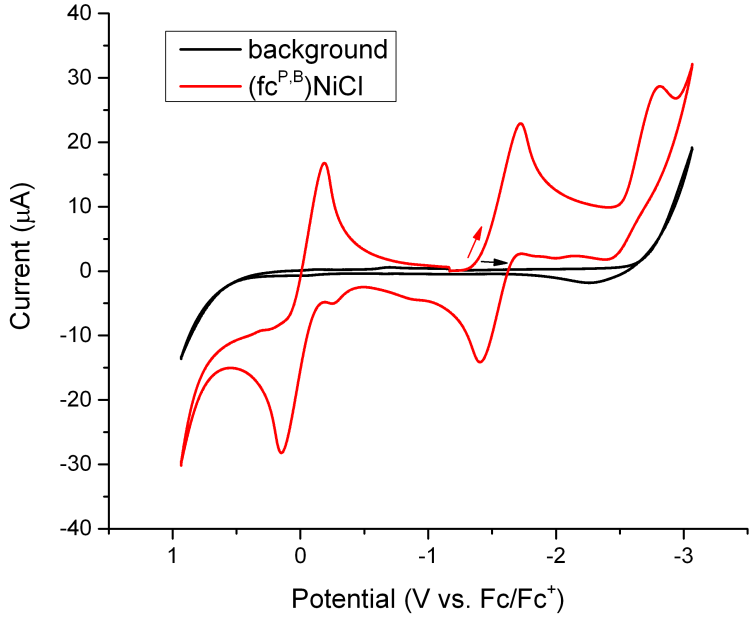

Figure A27. Cyclic voltammograms recorded with a glassy carbon electrode at 100 mV/s in THF, 0.10 M [TBA][PF_6] containing (a) no ($fc^{P,B}$)NiCl, (b) 5.0 mM ($fc^{P,B}$)NiCl.

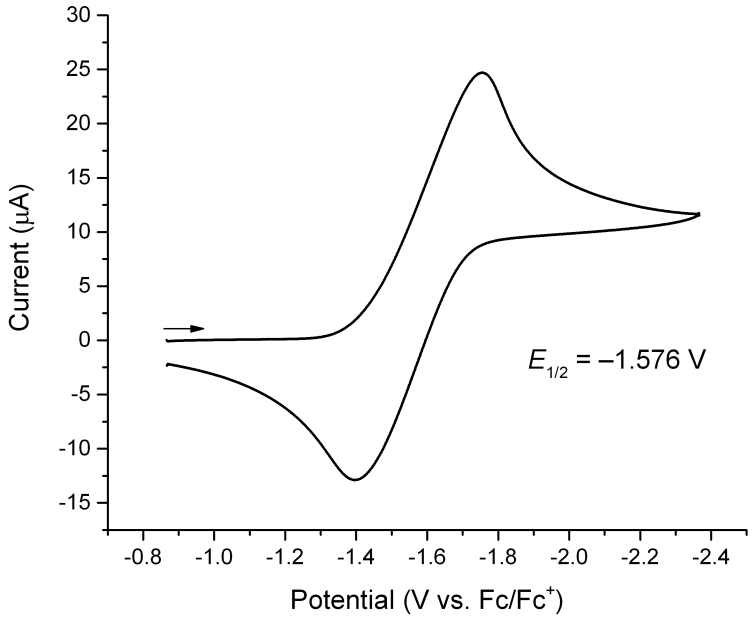

Figure A28. Cyclic voltammogram recorded with a glassy carbon electrode at 100 mV/s in THF, 0.10 M [TBA][PF_6] containing 5.0 mM ($fc^{P,B}$)NiCl. $E_{1/2}$ = -1.576 V, i_{pa}/i_{pc} = 0.84.

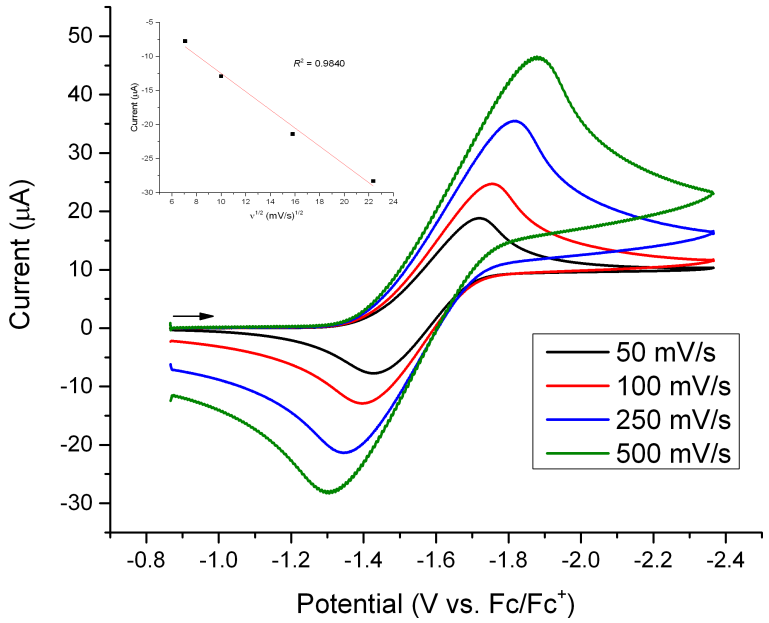

Figure A29. Cyclic voltammograms recorded with a glassy carbon electrode at 50, 100, 250, and 500 mV/s in THF, 0.10 M [TBA][PF_6] containing 5.0 mM ($fc^{P,B}$)NiCl.

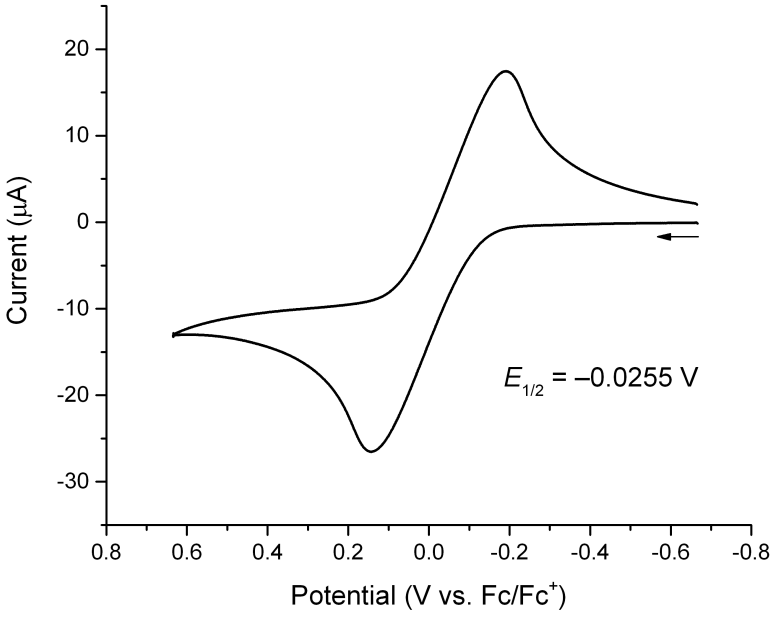

Figure A30. Cyclic voltammogram recorded with a glassy carbon electrode at 100 mV/s in THF, 0.10 M [TBA][PF_6] containing 5.0 mM ($fc^{P,B}$)NiCl. $E_{1/2}$ = -0.0255 V, i_{pc}/i_{pa} = 0.98.

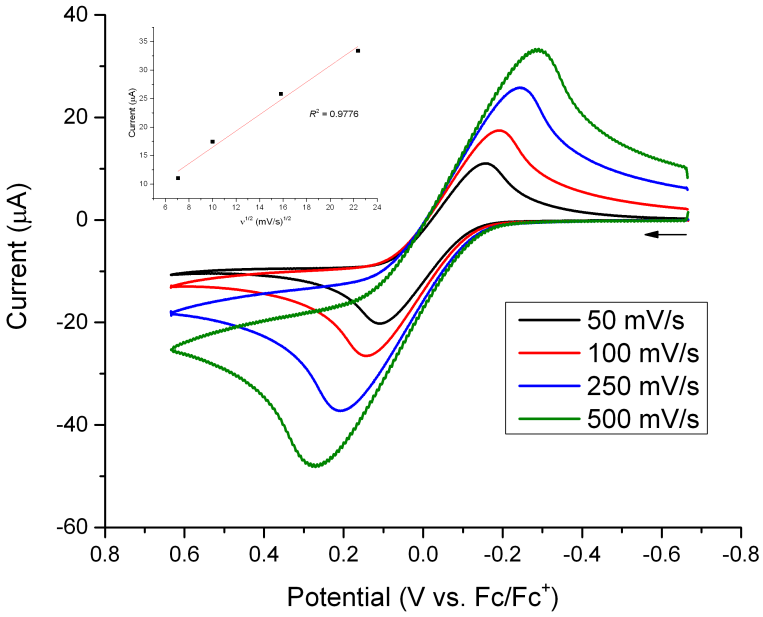

Figure A31. Cyclic voltammograms recorded with a glassy carbon electrode at 50, 100, 250, and 500 mV/s in THF, 0.10 M [TBA][PF_6] containing 5.0 mM ($fc^{P,B}$)NiCl.

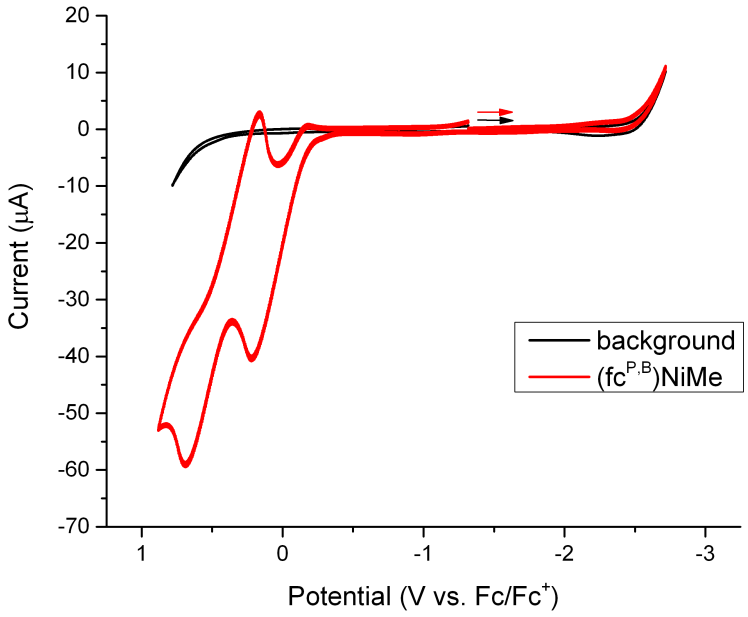

Figure A32. Cyclic voltammograms recorded with a glassy carbon electrode at 100 mV/s in THF, 0.10 M [TBA][PF_6] containing (a) no ($fc^{P,B}$)NiMe, (b) 5.0 mM ($fc^{P,B}$)NiMe.

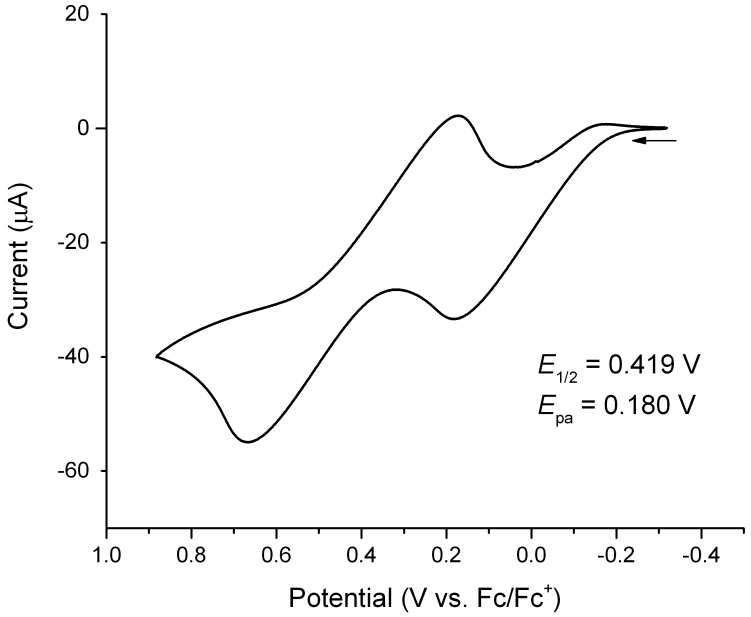

Figure A33. Cyclic voltammogram recorded with a glassy carbon electrode at 100 mV/s in THF, 0.10 M [TBA][PF_6] containing 5.0 mM ($fc^{P,B}$)NiMe. $E_{1/2}$ = 0.419 V, i_{pc}/i_{pa} = 0.48.

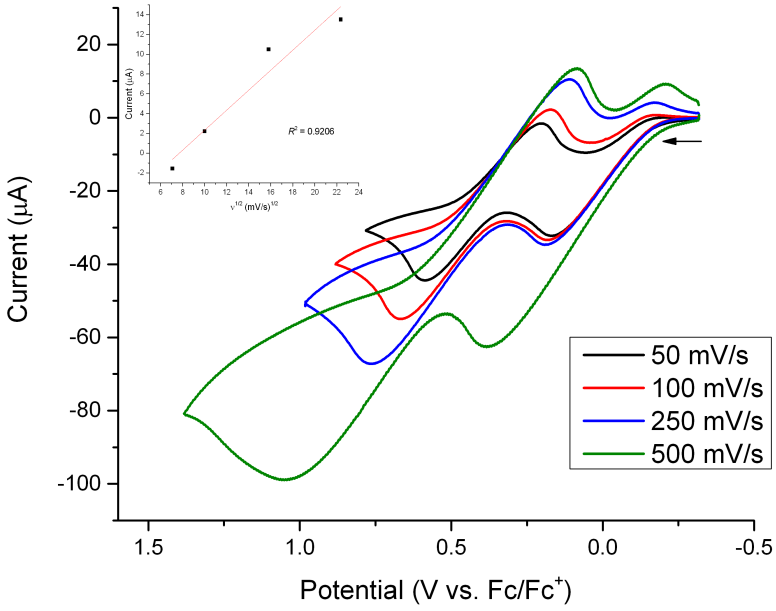

Figure A34. Cyclic voltammograms recorded with a glassy carbon electrode at 50, 100, 250, and 500 mV/s in THF, 0.10 M [TBA][PF_6] containing 5.0 mM ($fc^{P,B}$)NiMe.

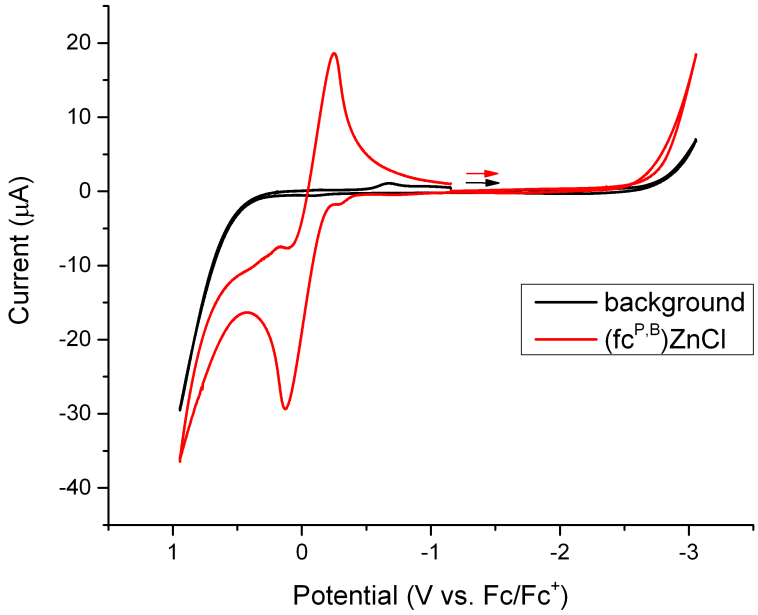

Figure A35. Cyclic voltammograms recorded with a glassy carbon electrode at 100 mV/s in THF, 0.10 M [TBA][PF_6] containing (a) no ($fc^{P,B}$)ZnCl, (b) 5.0 mM ($fc^{P,B}$)ZnCl.

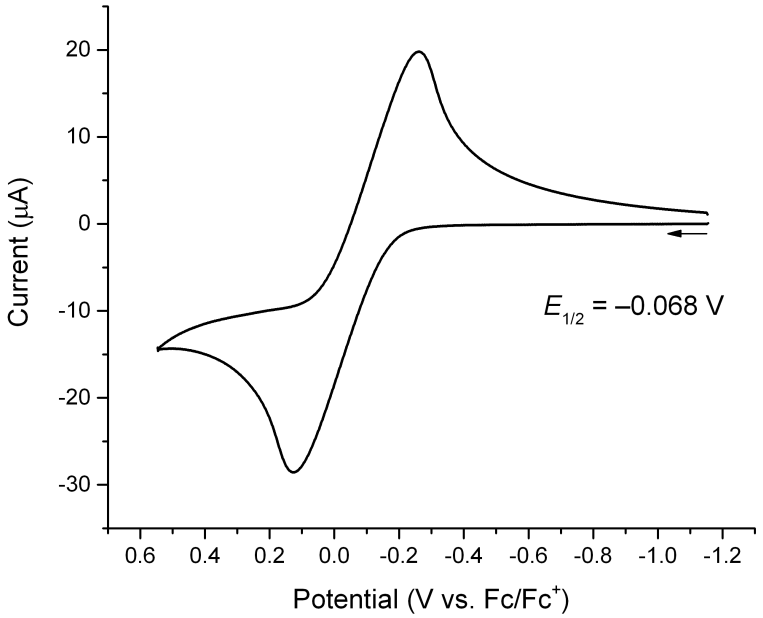

Figure A36. Cyclic voltammogram recorded with a glassy carbon electrode at 100 mV/s in THF, 0.10 M [TBA][PF_6] containing 5.0 mM ($fc^{P,B}$)ZnCl. $E_{1/2}$ = -0.068 V, i_{pc}/i_{pa} = 1.03.

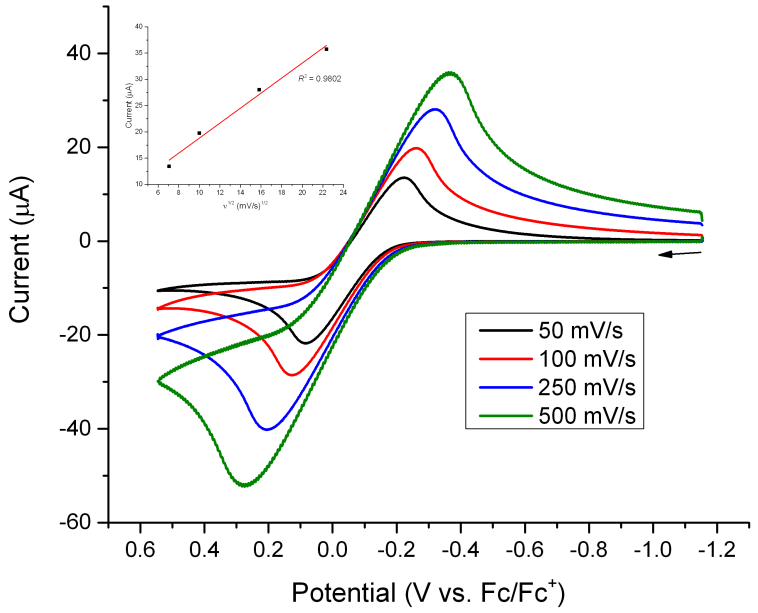

Figure A37. Cyclic voltammograms recorded with a glassy carbon electrode at 50, 100, 250, and 500 mV/s in THF, 0.10 M [TBA][PF_6] containing 5.0 mM ($fc^{P,B}$)ZnCl.

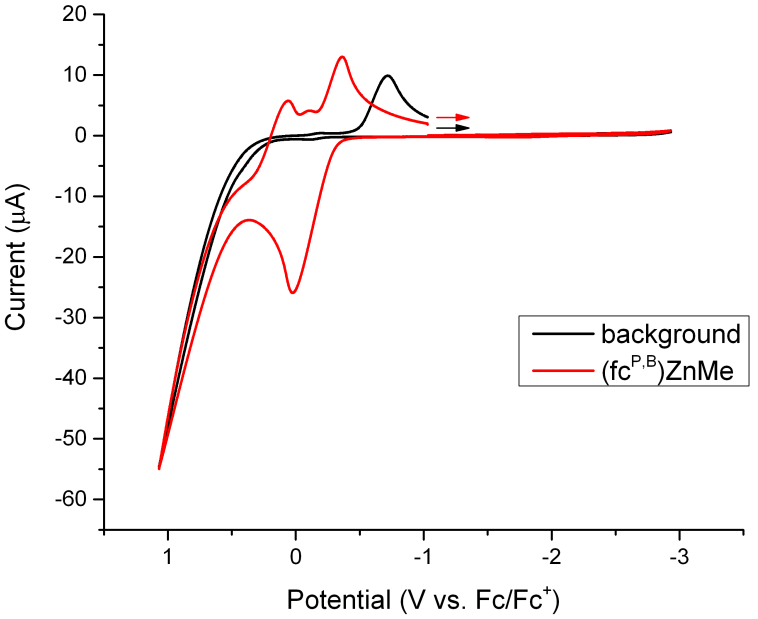

Figure A38. Cyclic voltammograms recorded with a glassy carbon electrode at 100 mV/s in THF, 0.10 M [TBA][PF_6] containing (a) no ($fc^{P,B}$)ZnMe, (b) 5.0 mM ($fc^{P,B}$)ZnMe.

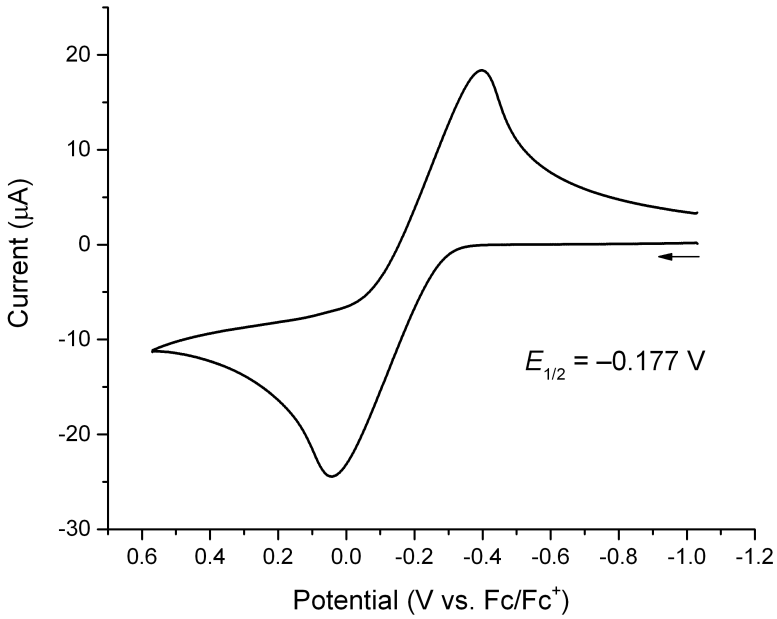

Figure A39. Cyclic voltammogram recorded with a glassy carbon electrode at 100 mV/s in THF, 0.10 M [TBA][PF_6] containing 5.0 mM ($fc^{P,B}$)ZnMe. $E_{1/2}$ = -0.177 V, i_{pc}/i_{pa} = 1.06.

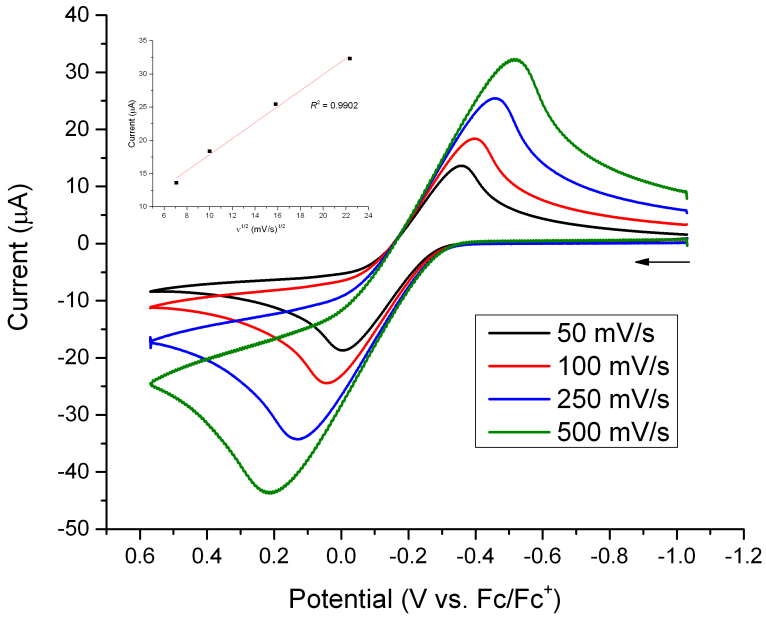

Figure A40. Cyclic voltammograms recorded with a glassy carbon electrode at 50, 100, 250, and 500 mV/s in THF, 0.10 M [TBA][PF_6] containing 5.0 mM ($fc^{P,B}$)ZnMe.

2.8.3 X-ray crystallographic data

fc(PPh$_2$)B(OMe)$_2$

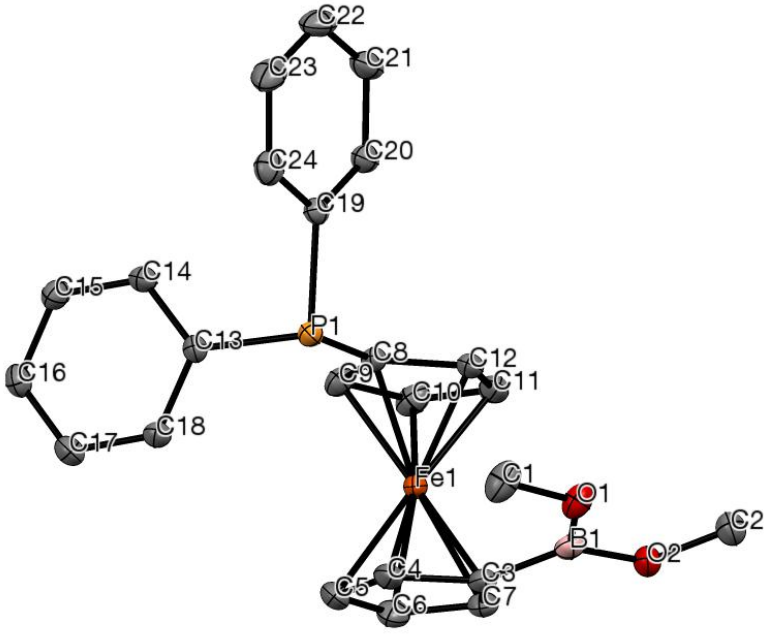

Figure A41. Thermal-ellipsoid (50% probability) representation of fc(PPh$_2$)B(OMe)$_2$ (code: pld1403). Hydrogen atoms were omitted for clarity.

Single crystals suitable for X-ray diffraction were grown from an *n*-pentane solution at -40 ºC. Crystal data for $C_{24}H_{24}BFeO_2P$; M_r = 442.06; monoclinic; space group Cc; *a* = 8.7001(7) Å; *b* = 16.5868(13) Å; *c* = 14.4047(11) Å; α = 90°; β = 92.8850(13)°; γ = 90°; V = 2076.1(3) Å^3; Z = 4; T = 100(2) K; λ = 0.71073 Å; μ = 0.821 mm^{-1}; d_{calc} = 1.414 g.cm^{-3}; 16452 reflections collected; 5809 unique (R_{int} = 0.0244); R_1 = 0.0249, wR_2 = 0.0608 for 5542 data with [I>2σ(I)] and R_1 = 0.0263, wR_2 = 0.0612 for all 5809 data. Residual electron density (e$^-$.Å^{-3}) max/min: 0.582/-0.164.

[fc(PPh$_2$)(BH$_3$)][Li(OEt$_2$)]

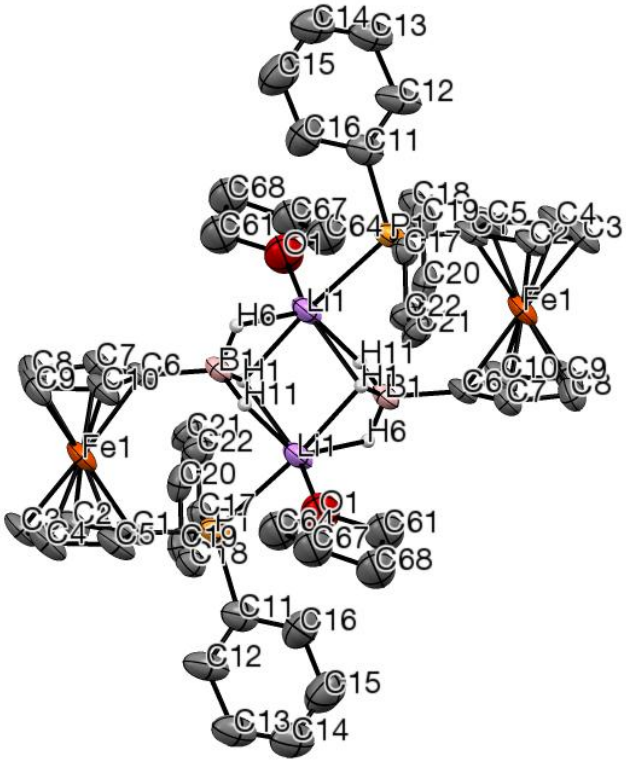

Figure A42. Thermal-ellipsoid (50% probability) representation of [fc(PPh$_2$)(BH$_3$)][Li(OEt$_2$)] (code: pld1365). Hydrogen atoms were omitted for clarity.

Single crystals suitable for X-ray diffraction were grown from a THF solution layered with hexanes at -40 ºC. Crystal data for $C_{52}H_{60.22}B_2Fe_2Li_2O_2P_2$; M_r = 926.37; orthorhombic; space group Pbca; *a* = 14.8935(14) Å; *b* = 12.4167(11) Å; *c* = 25.542(2) Å; α = 90°; β = 90°; γ = 90°; V = 4723.4(7) Å^3; Z = 4; T = 100(2) K; λ = 0.71073 Å; μ = 0.721 mm^{-1}; d_{calc} = 1.303 g.cm^{-3}; 57376 reflections collected; 5894 unique (R_{int} = 0.0721); R_1 = 0.0779, wR_2 = 0.1930 for 4133 data with [I>2σ(I)] and R_1 = 0.1093, wR_2 = 0.2127 for all 5894 data. Residual electron density (e$^-$.Å^{-3}) max/min: 0.839/-1.223.

($fc^{P,B}$)NiCl

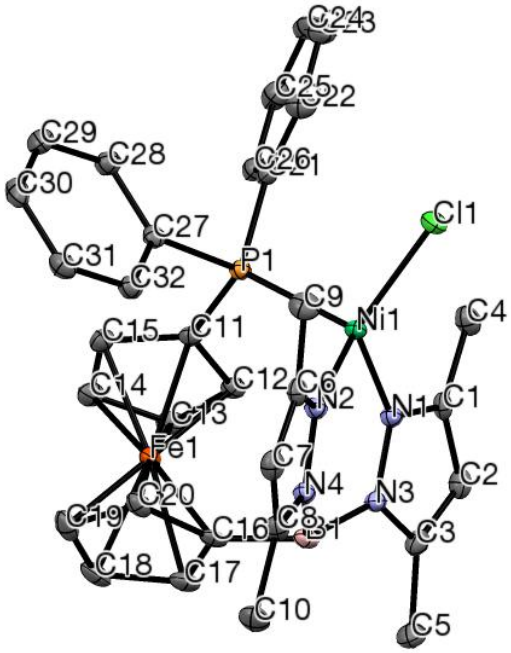

Figure A43. Thermal-ellipsoid (50% probability) representation of ($fc^{P,B}$)NiCl (code: pld1369). Hydrogen atoms were omitted for clarity.

Single crystals suitable for X-ray diffraction were grown from a toluene solution layered with hexanes at -40 ºC. Crystal data for $C_{39}H_{41}BCl\ FeN_4NiP$; M_r = 757.55; monoclinic; space group P2(1)/c; *a* = 11.0448(10) Å; *b* = 20.4296(19) Å; *c* = 15.7690(15) Å; α = 90°; β = 100.6910(11)°; γ = 90°; V = 3496.4(6) $Å^3$; Z = 4; T = 100(2) K; λ = 0.71073 Å; μ = 1.111 mm^{-1}; d_{calc} = 1.439 $g.cm^{-3}$; 34431 reflections collected; 6145 unique (R_{int} = 0.0285); R_1 = 0.0257, wR_2 = 0.0655 for 5495 data with [I>2σ(I)] and R_1 = 0.0302, wR_2 = 0.0674 for all 6145 data. Residual electron density ($e^-.Å^{-3}$) max/min: 0.384/-0.268.

(fc^{P,B})NiMe

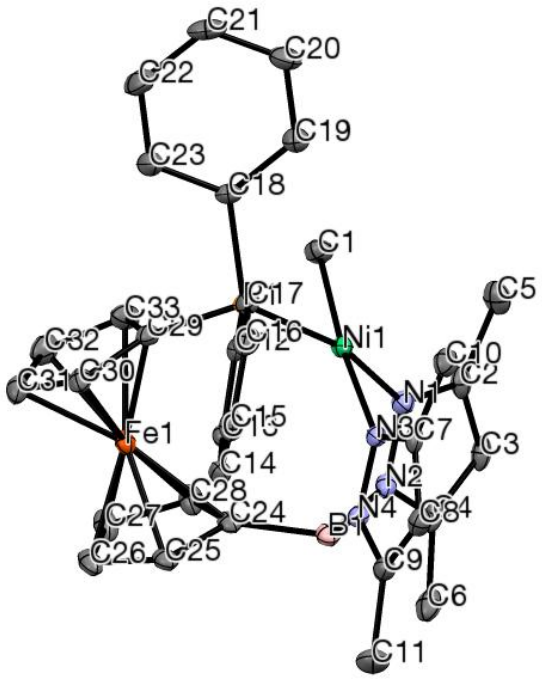

Figure A44. Thermal-ellipsoid (50% probability) representation of (fc^{P,B})NiMe (code: pld1406). Hydrogen atoms were omitted for clarity.

Single crystals suitable for X-ray diffraction were grown from a 1:10 mixture of toluene and hexanes at -40 ºC. Crystal data for $C_{73}H_{80}B_2Fe_2N_8Ni_2P_2$; M_r = 1382.13; orthorhombic; space group Pbcn; *a* = 24.5034(14) Å; *b* = 17.7143(10) Å; *c* = 16.2571(9) Å; α = 90°; β = 90°; γ = 90°; V = 7056.6(7) Å^3; Z = 4; T = 100(2) K; λ = 0.71073 Å; μ = 1.020 mm^{-1}; d_{calc} = 1.301 g.cm^{-3}; 80311 reflections collected; 6208 unique (R_{int} = 0.0304); R_1 = 0.0255, wR_2 = 0.0633 for 5711 data with [I>2σ(I)] and R_1 = 0.0292, wR_2 = 0.0653 for all 6208 data. Residual electron density (e$^-$.Å^{-3}) max/min: 0.312/-0.273.

(fc^{P,B})ZnCl

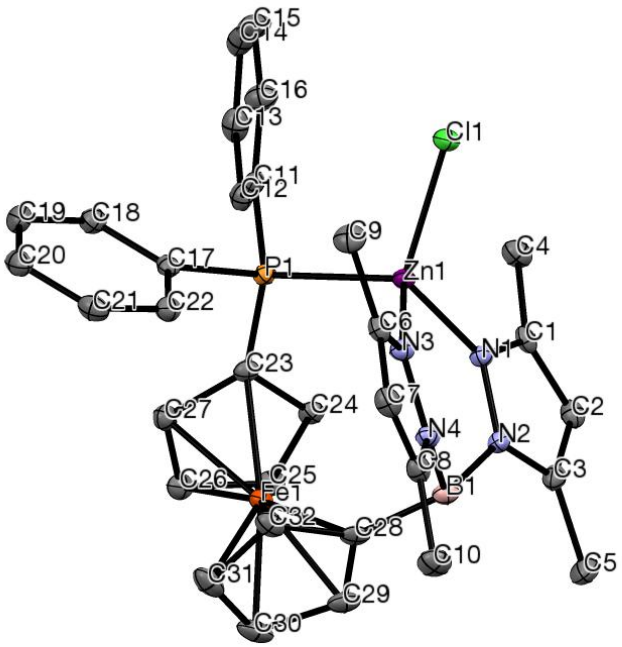

Figure A45. Thermal-ellipsoid (50% probability) representation of (fc^{P,B})ZnCl (code: pld1408). Hydrogen atoms were omitted for clarity.

Single crystals suitable for X-ray diffraction were grown from a toluene solution at -40 ºC. Crystal data for $C_{39}H_{41}BClFeN_4PZn$; M_r = 764.21; monoclinic; space group P2(1)/c; *a* = 11.0492(8) Å; *b* = 20.5575(14) Å; *c* = 15.6885(11) Å; α = 90°; β = 99.9460(11)°; γ = 90°;V = 3510.0(4) Å^3; Z = 4; T = 100(2) K; λ = 0.71073 Å; μ = 1.253 mm^{-1}; d_{calc} = 1.446 g.cm^{-3}; 33949 reflections collected; 6191 unique (R_{int} = 0.0238); R_1 = 0.0234, wR_2 = 0.0609 for 5700 data with [I>2σ(I)] and R_1 = 0.0263, wR_2 = 0.0620 for all 6191 data. Residual electron density (e$^-$.Å^{-3}) max/min: 0.348/-0.266.

($fc^{P,B}$)ZnMe

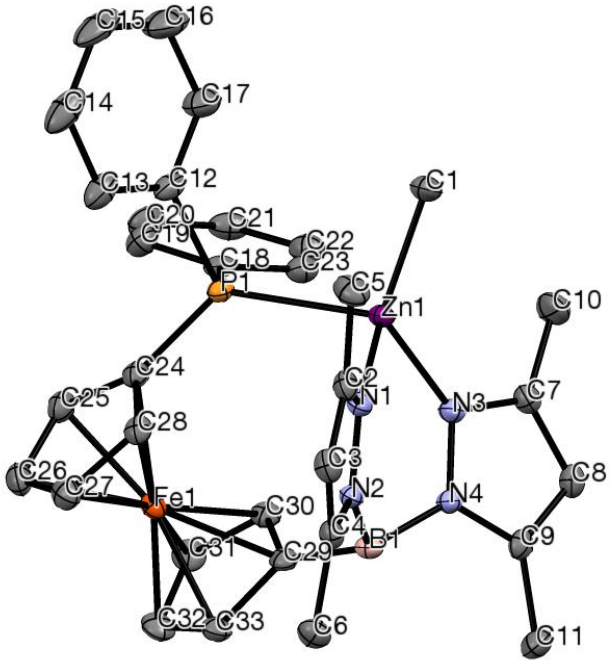

Figure A46. Thermal-ellipsoid (50% probability) representation of ($fc^{P,B}$)ZnMe (code: pld1407). Hydrogen atoms were omitted for clarity.

Single crystals suitable for X-ray diffraction were grown from a hexanes solution at -40 ºC. Crystal data for $C_{33}H_{36}BFeN_4PZn$; M_r = 651.66; triclinic; space group P-1; *a* = 10.1105(8) Å; *b* = 12.1986(9) Å; *c* = 13.4477(10) Å; α = 85.3940(12)°; β = 84.2210(12)°; γ = 67.7460(11)°; V = 1525.6(2) $Å^3$; Z = 2; T = 100(2) K; λ = 0.71073 Å; μ = 1.343 mm^{-1}; d_{calc} = 1.419 $g.cm^{-3}$; 18106 reflections collected; 5343 unique (R_{int} = 0.0164); R_1 = 0.0226, wR_2 = 0.0603 for 5000 data with [I>2σ(I)] and R_1 = 0.0245, wR_2 = 0.0614 for all 5343 data. Residual electron density ($e^-.Å^{-3}$) max/min: 0.340/-0.285.

2.8.4 DFT calculations

Table A2. Comparison of structural parameters derived from X-ray crystallography and DFT calculations, distance [Å] and angles [°] for nickel complexes.

(fc^{P,B})NiCl	***Exp.***	***ADF***	***(fc^{P,B})NiMe***	***Exp.***	***ADF***
Ni-Cl	2.21	2.24	Ni-C	1.95	1.96
Ni-P	2.33	2.33	Ni-P	2.13	2.15
Ni-N	1.96	2.01	Ni-N	1.94	1.98
Ni-N	1.96	2.01	Ni-N	1.95	1.97
PNiCl	105.6	107.9	PNiC	86.9	87.0
PNiN	109.0	107.8	PNiN	95.1	97.1
PNiN	102.6	104.3	PNiN	162.1	160.6
NBN	111.8	111.4	NBN	107.0	107.9

Table A3. Comparison of structural parameters derived from X-ray crystallography and DFT calculations, distance [Å] and angles [°] for zinc complexes.

(fc^{P,B})ZnCl	***Exp.***	***ADF***	***(fc^{P,B})ZnMe***	***Exp.***	***ADF***
Zn-Cl	2.23	2.27	Zn-C	1.99	2.02
Zn-P	2.40	2.48	Zn-P	2.55	2.60
Zn-N	1.99	2.06	Zn-N	2.05	2.12
Zn-N	1.98	2.06	Zn-N	2.02	2.11
PZnCl	107.6	110.2	PZnC	101.1	111.7
PZnN	106.5	108.4	PZnN	101.3	101.0
PZnN	113.3	113.1	PZnN	113.4	105.2
NBN	112.5	111.5	NBN	109.4	111.9

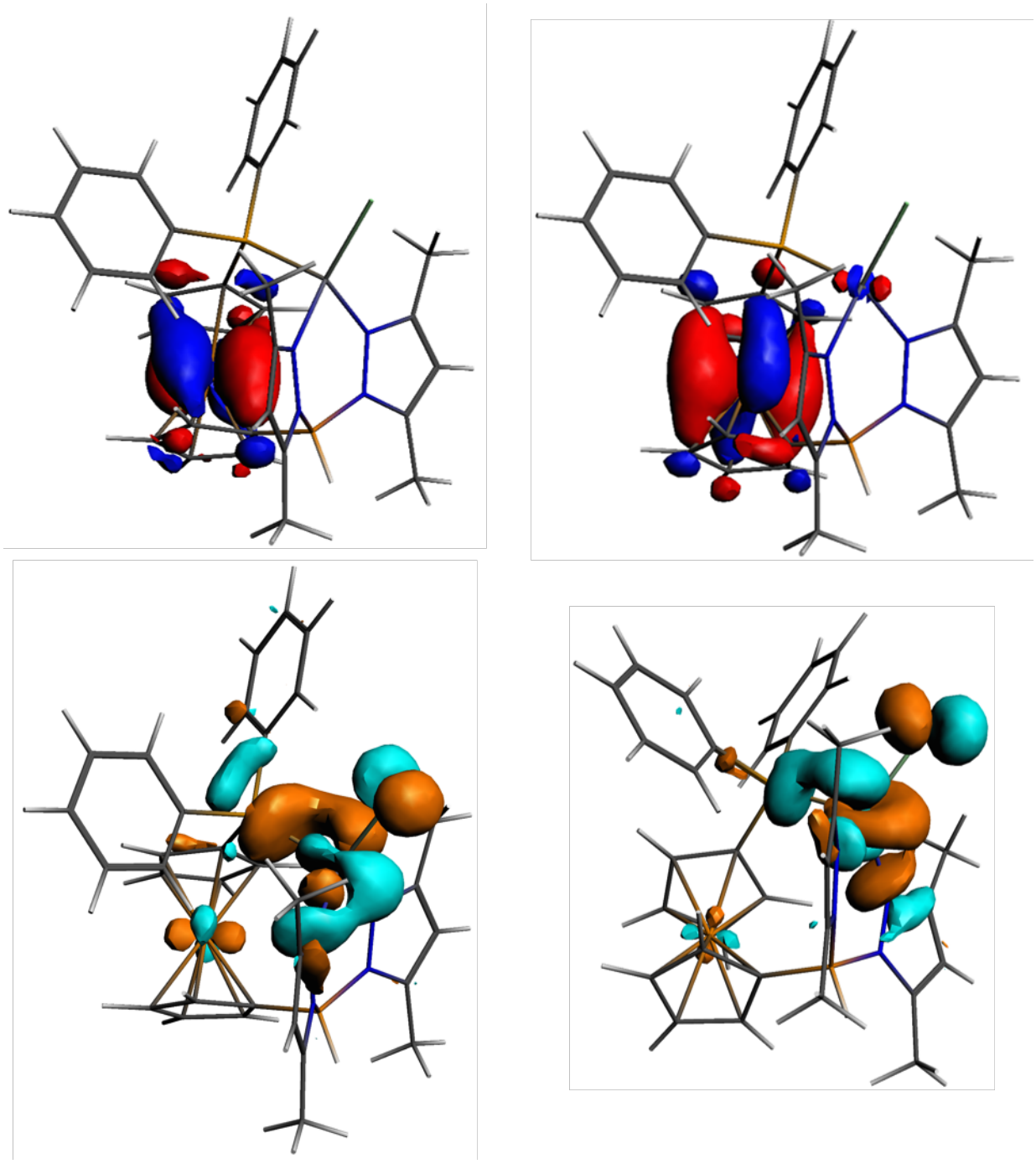

Figure A47. Frontier molecular orbitals for ($fc^{P,B}$)NiCl: SOMO-1 (top left), SOMO-2 (top right), LUMO (bottom left), LUMO+1 (bottom right).

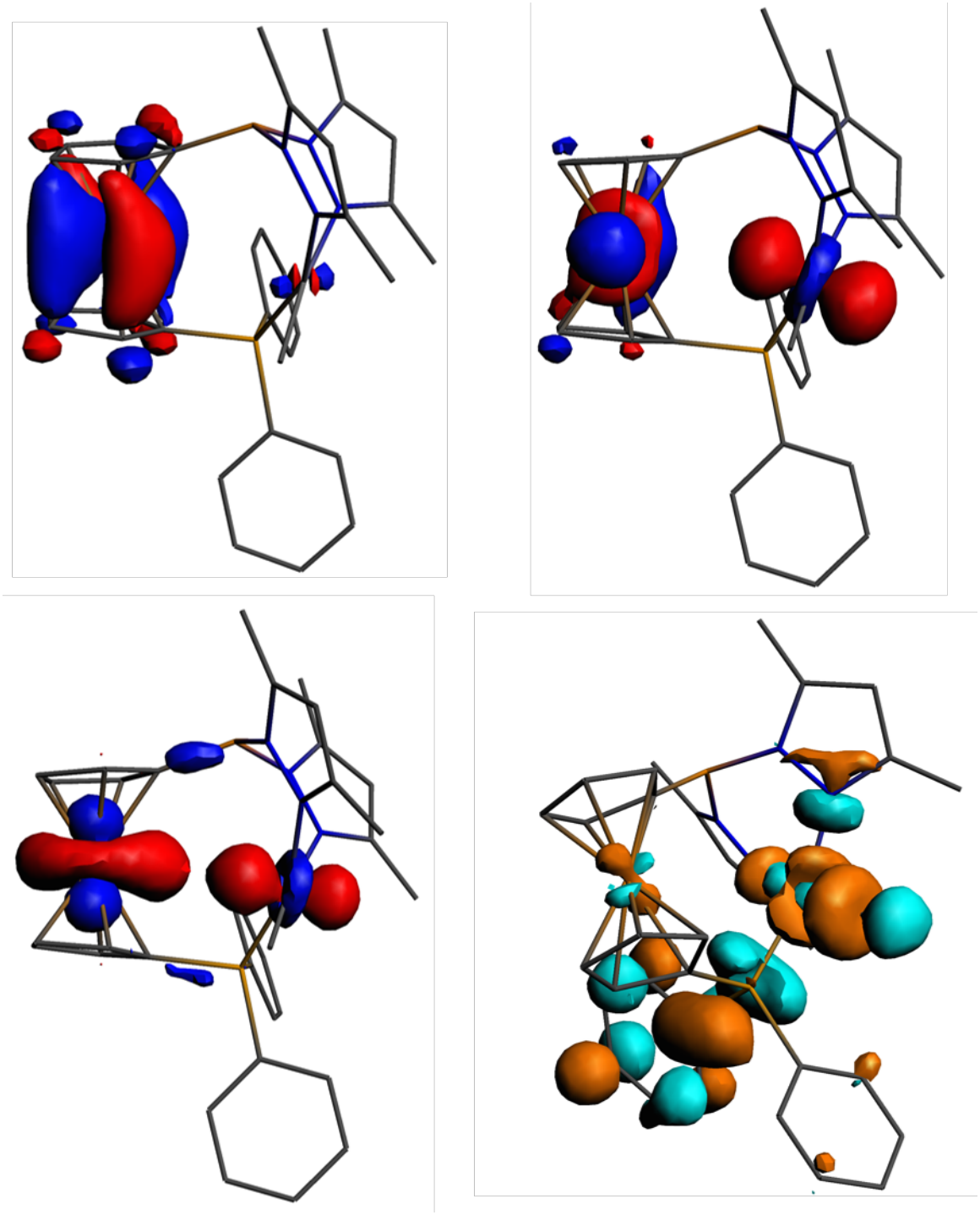

Figure A48. Frontier molecular orbitals for ($fc^{P,B}$)NiMe: HOMO-1 (top left), HOMO-2 (top right), HOMO-3 (bottom left), LUMO (bottom right).

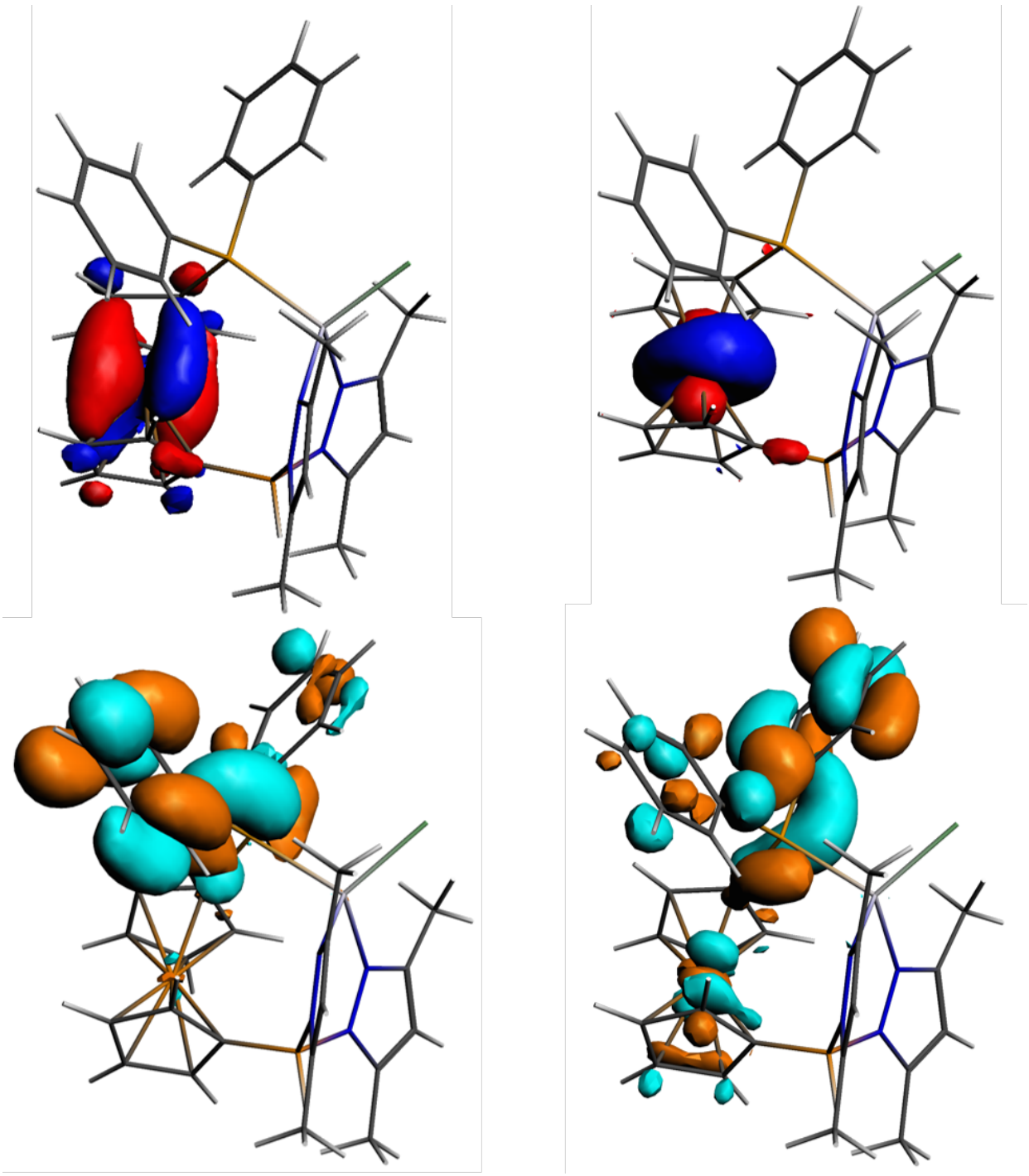

Figure A49. Frontier molecular orbitals for ($fc^{P,B}$)ZnCl: HOMO-1 (top left), HOMO-2 (top right), LUMO (bottom left), LUMO+1 (bottom right).

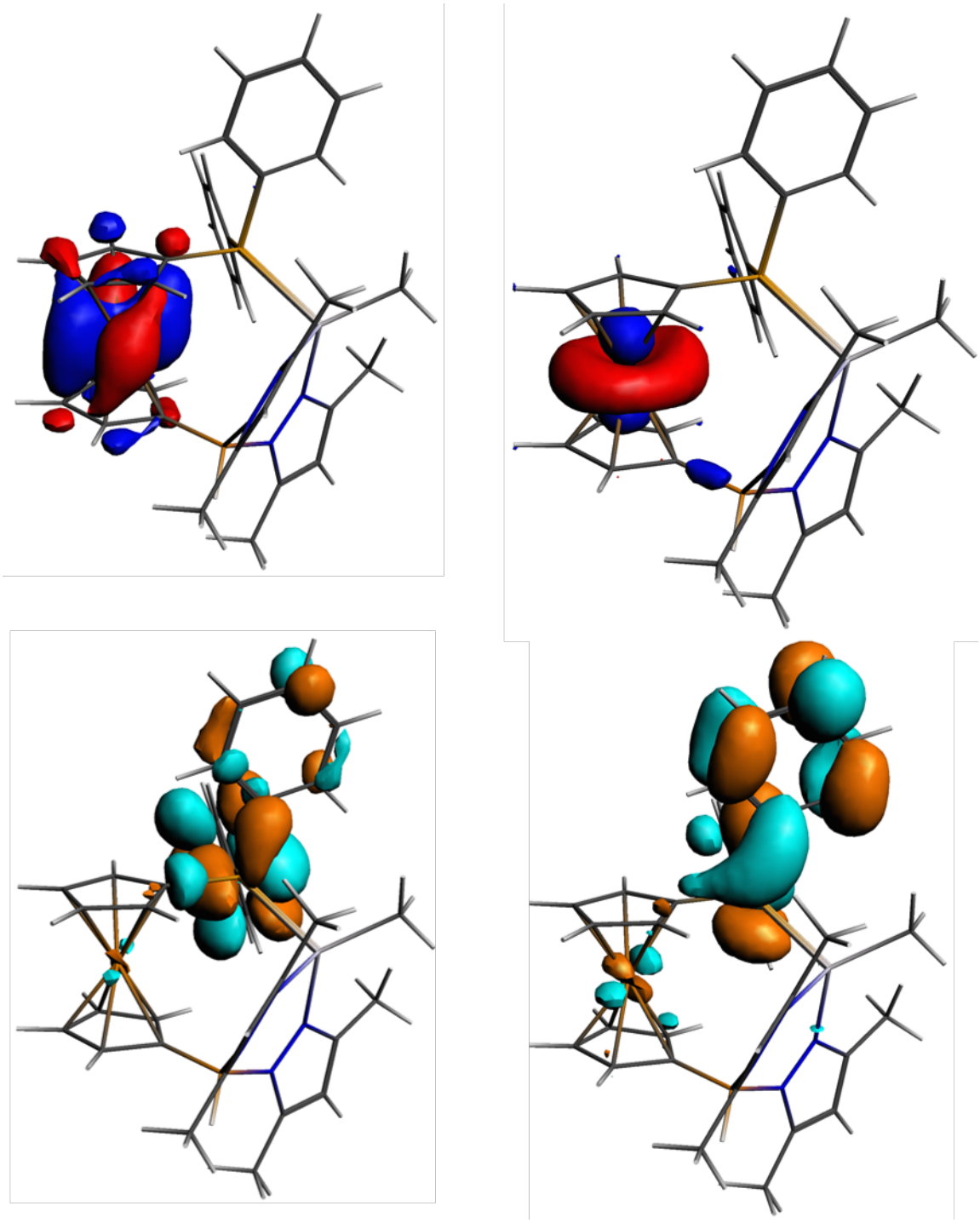

Figure A50. Frontier molecular orbitals for ($fc^{P,B}$)ZnMe: HOMO-1 (top left), HOMO-2 (top right), LUMO (bottom left), LUMO+1 (bottom right).

2.9 References

1. Trofimenko, S., *J. Am. Chem. Soc.* **1966,** *88*, 1842.

2. Trofimenko, S., *Chem. Rev.* **1993,** *93*, 943.

3. Trofimenko, S., *J. Chem. Ed.* **2005,** *82*, 1715.

4. Pettinari, C.; Pettinari, R., *Coord. Chem. Rev.* **2005,** *249*, 525.

5. Bigmore, H. R.; Lawrence, S. C.; Mountford, P.; Tredget, C. S., *Dalton Trans.* **2005**, 635.

6. Akita, M.; Hikichi, S., *Bull. Chem. Soc. Jpn.* **2002,** *75*, 1657.

7. Pettinari, C.; Marchetti, F.; Cerquetella, A.; Pettinari, R.; Monari, M.; Mac Leod, T. C. O.; Martins, L. s. M. D. R. S.; Pombeiro, A. J. L., *Organometallics* **2011,** *30*, 1616.

8. Cao, C.; Fraser, L. R.; Love, J. A., *J. Am. Chem. Soc.* **2005,** *127*, 17614.

9. Fraser, L. R.; Bird, J.; Wu, Q.; Cao, C.; Patrick, B. O.; Love, J. A., *Organometallics* **2007,** *26*, 5602.

10. Momin, A.; Bonnet, F.; Visseaux, M.; Maron, L.; Takats, J.; Ferguson, M. J.; Le Goff, X.-F.; Nief, F., *Chem. Commun.* **2011,** *47*, 12203.

11. Caballero, A.; Despagnet-Ayoub, E.; Mar Díaz-Requejo, M.; Díaz-Rodríguez, A.; González-Núñez, M. E.; Mello, R.; Muñoz, B. K.; Ojo, W.-S.; Asensio, G.; Etienne, M.; Pérez, P. J., *Science* **2011,** *332*, 835.

12. Lu, Z.; Williams, T. J., *Chem. Commun.* **2014,** *50*, 5391.

13. Hikichi, S.; Hanaue, K.; Fujimura, T.; Okuda, H.; Nakazawa, J.; Ohzu, Y.; Kobayashi, C.; Akita, M., *Dalton Trans.* **2013,** *42*, 3346.

14. Dias, H. V. R.; Lovely, C. J., *Chem. Rev.* **2008,** *108*, 3223.

15. Luca, O. R.; Crabtree, R. H., *Chem. Soc. Rev.* **2013,** *42*, 1440.

16. Fabrizi de Biani, F.; Jäkle, F.; Spiegler, M.; Wagner, M.; Zanello, P., *Inorg. Chem.* **1997,** *36*, 2103.

17. Guo, S.; Peters, F.; Fabrizi de Biani, F.; Bats, J. W.; Herdtweck, E.; Zanello, P.; Wagner, M., *Inorg. Chem.* **2001,** *40*, 4928.

18. Sirianni, E. R.; Yap, G. P. A.; Theopold, K. H., *Inorg. Chem.* **2014,** *53*, 9424.

19. Ilkhechi, A. H.; Bolte, M.; Lerner, H.-W.; Wagner, M., *J. Organomet. Chem.* **2005,** *690*, 1971.

20. Herdtweck, E.; Peters, F.; Scherer, W.; Wagner, M., *Polyhedron* **1998,** *17*, 1149.

21. Jäkle, F.; Polborn, K.; Wagner, M., *Chem. Ber.* **1996,** *129*, 603.

22. Lorkovic, I. M.; Duff, R. R.; Wrighton, M. S., *J. Am. Chem. Soc.* **1995,** *117*, 3617.

23. Wang, X.; Thevenon, A.; Brosmer, J. L.; Yu, I.; Khan, S. I.; Mehrkhodavandi, P.; Diaconescu, P. L., *J. Am. Chem. Soc.* **2014,** *136*, 11264.

24. Broderick, E. M.; Guo, N.; Vogel, C. S.; Xu, C.; Sutter, J.; Miller, J. T.; Meyer, K.; Mehrkhodavandi, P.; Diaconescu, P. L., *J. Am. Chem. Soc.* **2011,** *133*, 9278.

25. Diaconescu, P. L., *Comments Inorg. Chem.* **2010,** *31*, 196.

26. Broderick, E. M.; Guo, N.; Wu, T.; Vogel, C. S.; Xu, C.; Sutter, J.; Miller, J. T.; Meyer, K.; Cantat, T.; Diaconescu, P. L., *Chem. Commun.* **2011,** *47*, 9897.

27. Pangborn, A. B.; Giardello, M. A.; Grubbs, R. H.; Rosen, R. K.; Timmers, F. J., *Organometallics* **1996,** *15*, 1518.

28. Evans, D. F., *J. Chem. Soc.* **1959**, 2003.

29. Schubert, E. M., *J. Chem. Ed.* **1992,** *69*, 62.

30. Butler, I. R.; Davies, R. L., *Synthesis* **1996,** *1996*, 1350.

31. ADF2013.01; SCM Scientific Computing & Modeling: Theoretical Chemistry, Vrije Universiteit, Amsterdam, The Netherlands.

32. Bebbington, M. W. P.; Bontemps, S.; Bouhadir, G.; Hanton, M. J.; Tooze, R. P.; van Rensburg, H.; Bourissou, D., *New J. Chem.* **2010,** *34*, 1556.

33. Scheibitz, M.; Li, H.; Schnorr, J.; Sánchez Perucha, A.; Bolte, M.; Lerner, H.-W.; Jäkle, F.; Wagner, M., *J. Am. Chem. Soc.* **2009,** *131*, 16319.

34. Yang, L.; Powell, D. R.; Houser, R. P., *Dalton Trans.* **2007**, 955.

35. Uehara, K.; Hikichi, S.; Akita, M., *J. Chem. Soc., Dalton Trans.* **2002**, 3529.

36. Brammer, L.; Stevens, E. D., *Acta Cryst. C* **1989,** *45*, 400.

37. Zeller, A.; Herdtweck, E.; Strassner, T., *Eur. J. Inorg. Chem.* **2003,** *2003*, 1802.

38. Abubekerov, M.; Gianetti, T. L.; Kunishita, A.; Arnold, J., *Dalton Trans.* **2013,** *42*, 10525.

39. Mou, Z.; Liu, B.; Wang, M.; Xie, H.; Li, P.; Li, L.; Li, S.; Cui, D., *Chem. Commun.* **2014,** *50*, 11411.

40. Klitzke, J. S.; Roisnel, T.; Carpentier, J.-F.; Casagrande Jr, O. L., *Inorg. Chim. Acta* **2009,** *362*, 4585.

41. Looney, A.; Han, R.; Gorrell, I. B.; Cornebise, M.; Yoon, K.; Parkin, G.; Rheingold, A. L., *Organometallics* **1995,** *14*, 274.

42. Wilson, E. E.; Oliver, A. G.; Hughes, R. P.; Ashfeld, B. L., *Organometallics* **2011,** *30*, 5214.

43. Duhović, S.; Oria, J. V.; Odoh, S. O.; Schreckenbach, G.; Batista, E. R.; Diaconescu, P. L., *Organometallics* **2013,** *32*, 6012.

44. Kaim, W.; Sixt, T.; Weber, M.; Fiedler, J., *J. Organomet. Chem.* **2001,** *637-639*, 167.

CHAPTER 3: SWITCHABLE POLYMERIZATION OF NORBORNENE DERIVATIVES BY A FERROCENE-PALLADIUM(II) HETEROSCORPIONATE COMPLEX

3.1 Introduction

Vinyl polynorbornenes are important materials for optical applications due to their excellent thermal stability, high glass transition temperatures, small birefringence, and dielectric loss.[1-5] However, polynorbornenes are brittle, even at high molecular weights, display poor adhesion to common substrates, poor solubility in common organic solvents, and cannot be melt processed due to decomposition.[6-9] Modifying the norbornene monomers with functional groups increases the solubility of the resulting polymers and improves their processability.[10] The substitution of norbornenes, typically at the 5-position, can be achieved via a Diels-Alder reaction, in some cases, directly from dicyclopentadiene and a dienophile.[11] Polymers obtained from the substituted monomers show improved adhesive and mechanical properties while retaining similar optical properties as the unsubstituted polynorbornenes.[1, 4, 12]

Amongst transition metal catalysts, palladium-based systems are highly active toward norbornene polymerization and produce high molecular weight vinyl polynorbornenes.[1, 13-20] Most palladium catalysts feature bidentate or monodentate supporting ligands since an open coordination sphere is necessary for monomer coordination.[9-10, 13-15, 21-25] Commonly employed systems also require the use of strong Lewis acids/alkylating reagents (i.e. methylalumoxane, fluorinated arylboranes/alkyl aluminum complexes) as co-catalysts to generate a metal-alkyl fragment and an empty coordination site.[1, 7] The resulting catalytic species are typically not stable in the absence of monomer, and in certain cases, have further complications arising from

the possible monomer/co-catalyst interactions.[15, 26] Alternatively, in cases when an open coordination sphere cannot be readily obtained, such as allyl palladium complexes, the use of hemilabile supporting ligands has been reported.[27] Weakly coordinating components of these ligands can be readily displaced by more nucleophilic olefins. On the other hand, the use of a tridentate supporting ligand would severely limit the availability of an empty coordination site. A possible solution is the incorporation of a labile component into the ligand framework, similar to those in hemilabile ligands, resulting in an effective polymerization system without the need for a co-catalyst. Additionally, controlling the lability of a supporting ligand can be accomplished by a method similar to the one utilized in redox-switchable hemilabile ligands.[28] An appropriate placement of a redox-active group into a ligand framework provides a method of influencing both the electronic and steric properties of the transition metal complex through oxidation of the ligand. Because of our interest in redox active ferrocene-based chelating ligands,[29-33] we set out to investigate the effects of the redox switch on the lability of the ferrocene-chelating heteroscorpionate ligand in the palladium methyl complex, [fc(PPh_2)(BH[(3,5-$Me)_2$pz]$_2$)]PdMe (($fc^{P,B}$)PdMe, fc = 1,1'-ferrocenediyl, pz = pyrazole), in the presence of norbornene derivatives. Herein, we report the first palladium system supported by a tridentate ligand modified by an on/off redox switch for the addition polymerization of norbornene and norbornene derivatives.

3.2 Synthesis and characterization of palladium complexes

The palladium complex (COD)PdMeCl was prepared via transmetallation of (COD)$PdCl_2$ with trimethylaluminum, instead of using alkyl tin reagents,[34] in a mixture of THF and diethyl ether, similarly to the synthesis of [Pd_2(μ-Cl)$_2$$Me_2$($PEt_3$)$_2$].[34] The characterization of

the desired product was accomplished by ^{1}H NMR spectroscopy (Figure B1), which was consistent with previously published results.[35]

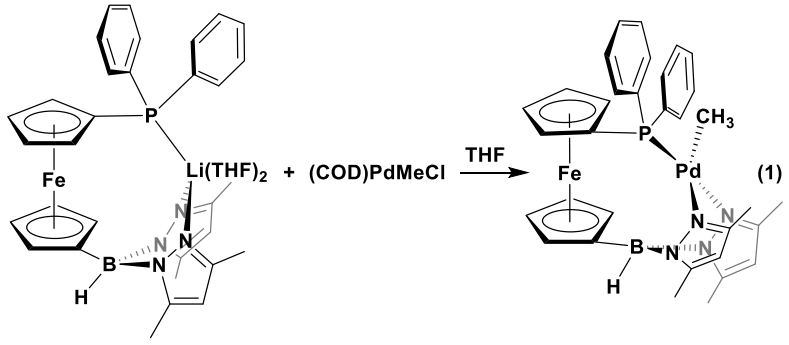

Addition of $(fc^{P,B})Li(THF)_2$ to (COD)PdMeCl in THF led to the isolation of $(fc^{P,B})PdMe\cdot(C_7H_8)$ as red crystals in 77.1% yield (Eq 1). The solid-state molecular structure of $(fc^{P,B})PdMe$ was determined using single-crystal X-ray diffraction (Figure 3-1). The coordination environment around the palladium center is in a distorted square planar geometry ($\tau = 0.16$)[36] similar to the nickel analogue, $(fc^{P,B})NiMe$.[37] The metal-donor atom distances (P(1)-Pd(1), 2.2107(4) Å; C(1)-Pd(1), 2.0454(18) Å; N(3)-Pd(1), 2.0938(14) Å; N(1)-Pd(1), 2.1097(14) Å) are comparable with values reported for similar complexes: 1-(mesityl)-3-(2-hydroxyphenyl)-4,5-dihydro-imidazolyl methyl triphenylphosphine palladium(II) (Pd-P, 2.2858(9) Å; Pd-C, 2.041(3) Å),[38] $(Tp^{Me,Me})$Pd(methallyl) ($Tp^{Me,Me}$ = hydrotris(3,5-dimethylpyrazolyl)borate, Pd-N, 2.090(2) and 2.086(2) Å).[39] However, unlike for the nickel analogue, the resonance signals in the corresponding ^{1}H NMR spectrum (Figure B2) are sharp, easily discernable, and are consistent with a diamagnetic complex.

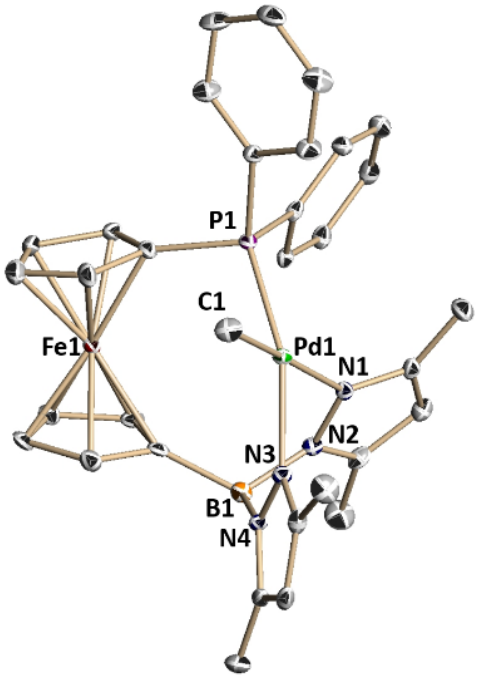

Figure 3-1. Molecular structure drawing of ($fc^{P,B}$)PdMe with thermal ellipsoids at 50% probability; hydrogen atoms are omitted for clarity. Selected distances (Å) and angles (°): P(1)-Pd(1), 2.2107(4); C(1)-Pd(1), 2.0454(18); N(1)-Pd(1), 2.1097(14); N(3)-Pd(1), 2.0938(14); P(1)-Pd(1)-C(1), 88.41(5); C(1)-Pd(1)-N(3) 91.71(7); P(1)-Pd(1)-N(1), 95.98(4); N(1)-Pd(1)-N(3), 84.99(5); C(1)-Pd(1)-N(1), 174.78(6); C(1)-Pd(1)-P(1), 88.39(4); N(3)-Pd(1)-P(1), 161.95(4).

Electrochemical studies performed on ($fc^{P,B}$)PdMe show a quasi-reversible curve with a redox potential of -0.27 V vs. Fc/Fc^{+} (Figure 3-2), suggesting that ferrocenium salts may be used as chemical oxidants. On an NMR scale, the oxidation of the palladium complex with one equivalent of acetyl ferrocenium tetrakis(3,5-bis(trifluoromethyl)phenyl)borate ([^{Ac}Fc][BAr^{F}]) results in the appearance of paramagnetically shifted and broadened signals in the ^{1}H NMR spectrum (Figure B8). The ^{11}B NMR spectrum (Figure B10) shows a significant upfield shift of the signal corresponding to the ($fc^{P,B}$)PdMe complex, from -7.6 to -65.2 ppm, upon oxidation.

However, the oxidized complex is ^{31}P NMR silent. Reduction with one equivalent of cobaltocene (Cp_2Co) restores the original complex, ($fc^{P,B}$)PdMe, with no appearance of decomposition or side products (Figures B6-7). On a larger scale, the addition of ($fc^{P,B}$)PdMe to a suspension of [^{Ac}Fc][BAr^F] in toluene resulted in the isolation of [($fc^{P,B}$)PdMe][BAr^F] as dark brown solids in 84% yield (Eq 2). The presence of the [BAr^F] counter ion was confirmed by the presence of a singlet at δ = -6.1 and -62.2 ppm in the ^{11}B and ^{19}F NMR spectra (Figures B9-10), respectively. Attempts to grow X-ray quality crystals from various neat solvents and solvent combinations were unsuccessful and only dark brown oils were obtained. However, besides spectroscopic characterization, elemental analysis also agrees with the formulation of [($fc^{P,B}$)PdMe][BAr^F].

$$(fc^{P,B})PdMe + [^{Ac}Fc][BAr^F] \xrightarrow{THF} [(fc^{P,B})PdMe][BAr^F] \quad (2)$$

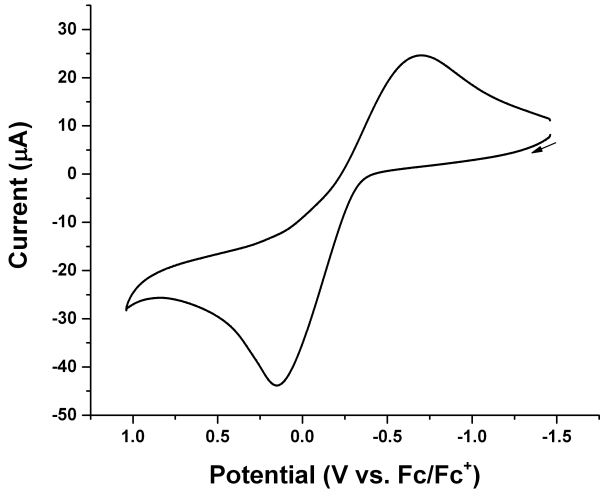

Figure 3-2. Cyclic voltammogram recorded with a glassy carbon electrode at 100 mV/s in THF, 0.10 M [^{n}Bu$_4$N][PF_6] containing 5.0 mM ($fc^{P,B}$)PdMe.

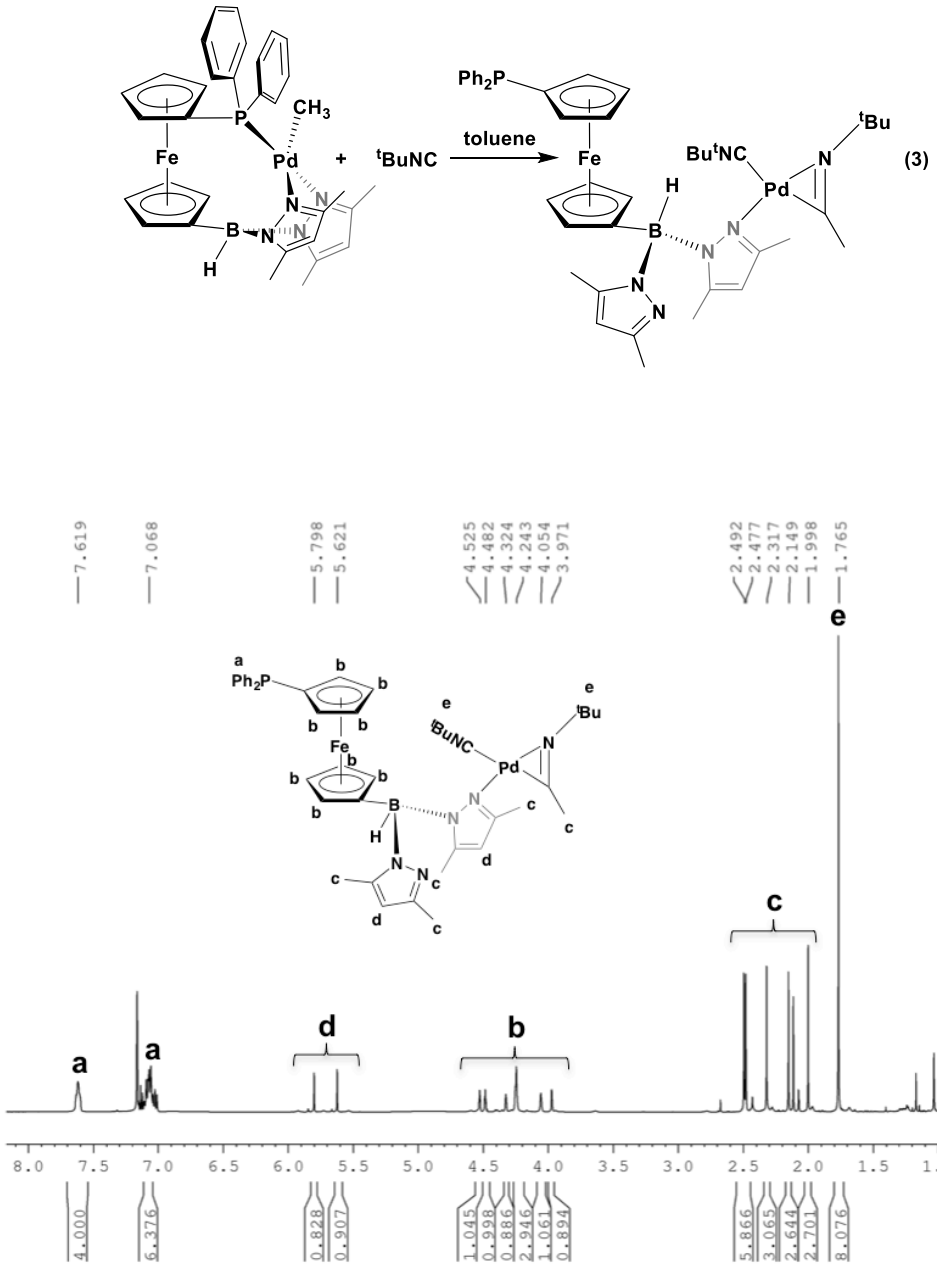

Figure 3-3. ^{1}H NMR spectrum (C_6D_6, 500 MHz, 298 K) of ($fc^{P,B}$)Pd[C(Me)N^{t}Bu](CN^{t}Bu).

Knowing the strength of the palladium-phosphorus and palladium-nitrogen bonds in ($fc^{P,B}$)PdMe is necessary for understanding its catalytic activity. Addition of four equivalents of *tert*-butyl isocyanide (^{t}BuNC) to ($fc^{P,B}$)PdMe resulted in the isolation of

($fc^{P,B}$)Pd[C(Me)N^{t}Bu](CN^{t}Bu)·(C_7H_8) as an orange crystalline material (Eq 3). The new compound is the product of a migratory insertion of one equivalent of ^{t}BuNC into the palladium-carbon bond and the coordination of a second equivalent of ^{t}BuNC to the palladium metal center.[40-41] The two pyrazoles are not chemically equivalent in the ^{1}H NMR spectrum (Figure 3-3), suggesting that only one of them is coordinated to palladium. The phosphine is in a solution state equilibrium between a free and palladium bound phosphine as observed by two peaks at -14.9 ppm and 9.4 ppm, respectively, in the ^{31}P NMR spectrum (Figure B15).[42] However, no reaction occurs upon the addition of benzonitrile or ferrocenyldiphenylphosphine to ($fc^{P,B}$)PdMe, suggesting that weaker nucleophiles cannot displace the supporting ligand. Similarly, addition of acetonitrile to [($fc^{P,B}$)PdMe][BAr^F] results in no reaction. However, oxidation ($fc^{P,B}$)PdMe with [^{Ac}Fc][BAr^F] in the presence of ferrocenyldiphenylphosphine results in the disappearance of the two ^{31}P NMR singlets at 30.5 ppm and -16.1 ppm (Figure B11) that correspond to the two ferrocene compounds, and the appearance of a singlet at 24.0 ppm (Figure B12) corresponding to a palladium bound $FcPPh_2$.[43]

3.3 Polymerization of norbornene and norbornene derivatives

The reduced ferrocene complex, ($fc^{P,B}$)PdMe, in the presence of norbornene showed no polymerization activity even when heating up to 100 °C in benzene. This absence of activity suggests that norbornene is too weak of a nucleophile to compete for a coordination site with the supporting ligand. On the other hand, in the presence of a stronger nucleophile, such as *tert*-butyl isocyanide, the phosphine of the supporting ligand is almost entirely displaced. Reducing the nucleophilic character of the supporting ligand through the oxidation of the ferrocene moiety, as

was observed in the case of ferrocenyldiphenylphosphine coordination, promotes monomer coordination.

The oxidation of the ferrrocene backbone with [^{Ac}Fc][BAr^{F}] turns "on" the activity of the (fc^{P,B})PdMe complex toward the polymerization of norbornene. The polymerization of 100 equivalents of norbornene (**NB**) reaches completion within an hour at 70 °C. However, the poor solubility of norbornene homopolymers in common organic solvents prevents their characterization by gel permeation chromatography (GPC) on regular instruments and complicates the in situ investigation of the "on/off" redox switch. To overcome these complications, the norbornene derivatives 5-butyl-bicyclo[2.2.1]hept-2-ene (NBa), 5-(triethoxysilyl)-bicyclo[2.2.1]hept-2-ene (NBb), 5-(trimethylsily)-bicyclo[2.2.1]hept-2-ene (NBc), and 5-cyclohexyl-bicyclo[2.2.1]hept-2-ene (NBd, Figure 3-4) were prepared by Scott Shepard and their polymerization results are summarized in Table 3-1. The polymerization of ca. 100 equivalents of the substituted norbornenes was monitored by ^{1}H NMR spectroscopy, until no further monomer conversion was observed. The obtained polymers were characterized by gel permeation chromatography (GPC). A large discrepancy was found between the experimental and theoretical values of the molecular weights, suggesting a poorly controlled polymerization process, with the *Đ* (*Đ* = M_w/M_n) values ranging from 1.5 to 3.6. A similar wide distribution of *Đ* values is observed in the literature for the polymerization of norbornenes by group 10 metals.[1, 6, 11, 13-14, 25] The polymerization activity for palladium complexes toward norbornene is largely dependent on the coordination environment around the metal center and the substituents on the monomer and can vary greatly from just a few numbers to several millions.[16, 18, 24, 44] By comparison, the oxidized ferrocene heteroscorpionate complex shows a relatively low activity with turnover frequencies ranging from 12.5 to 81 $mol_{nb}\, mol_{Pd}^{-1}\, h^{-1}$.

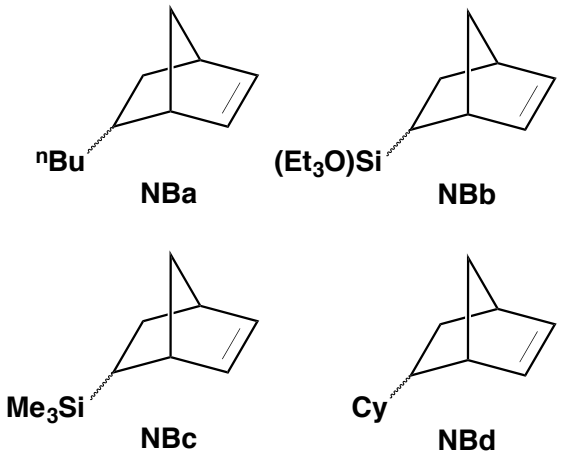

Figure 3-4. Norbornene derivatives NBa-d.

The in situ redox switch was performed with 5-triethoxysilyl norbornene. Starting with the oxidized complex [($fc^{P,B}$)PdMe][BAr^F] in the presence of 100 equivalents of monomer results in the polymerization of 35 equivalents in 20 min at 70 °C (Table 3-1, entry 6). The addition of one equivalent of Cp_2Co relative to the palladium complex severely reduces the catalytic activity. The polymerization of five equivalents of NBb observed during this time can be attributed to a small number of catalytically active complex present in solution, due to the slow rate of reduction of the palladium compound by Cp_2Co, which takes up to 30 min at ambient temperature to reach completion. No further conversion upon heating of the reaction solution at 70 °C for 20 min is observed once the reduction process is complete. The oxidation with [^{Ac}Fc][BAr^F] restores the catalytic activity (Figure 3-5). The slow rate of reduction of the catalyst would account for the shoulder peak observed in the GPC graph of the isolated polymer (Figure B37).

To gain a better understanding of how the redox switches affect the polymerization reaction, the influence of ligand oxidation upon electron donating abilities of individual

ferrocene substituents was considered. The oxidation of ferrocenyldiphenylphosphine reduces the electron donating ability of the phosphine donor, resulting in the increase of the CO stretching frequency by several wave numbers in rhenium carbonyl complexes.[45] Alternatively, oxidation of a ferrocene containing tris(pyrazolyl)borate molybdenum carbonyl complex resulted in virtually no change in the stretching frequency of the carbonyl ligands.[46] Based on these literature reports and our experimental results, we propose that the oxidation of the ferrocene-chelating heteroscorpionate increases the lability of the phosphine moiety allowing monomer coordination and migratory insertion into the metal-alkyl fragment, while the (pyrazolyl)borate portion remains unaffected. Since the displacement of the phosphine in the reduced complex by norbornene does not occur, the polymerization process is halted with this catalyst.

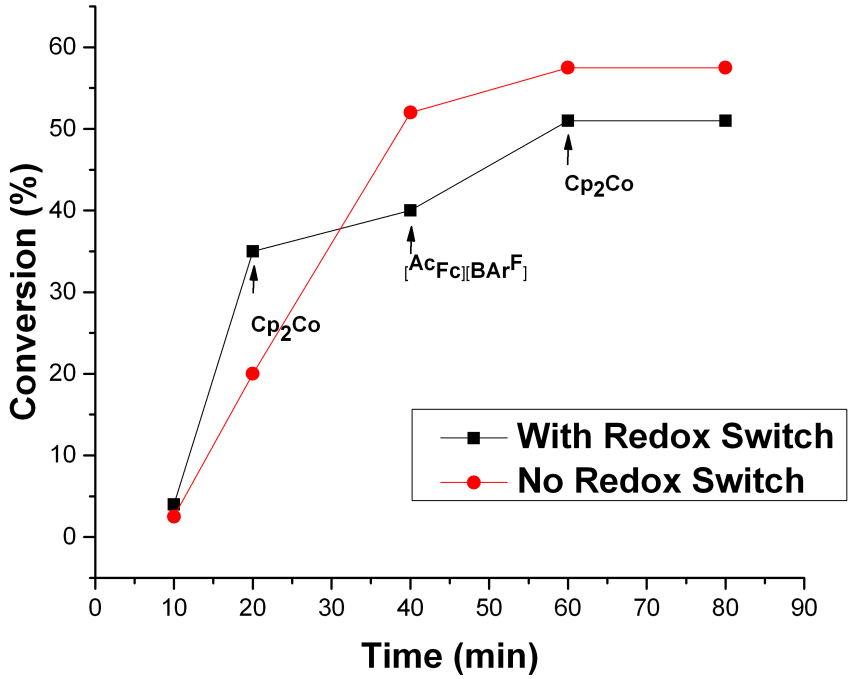

Figure 3-5. Comparison of 5-(triethoxysilyl)-bicyclo[2.2.1]hept-2-ene polymerization using a redox switch and not using a redox switch using [($fc^{P,B}$)PdMe][BAr^F] as a catalyst.

The involvement of alternative mechanisms in the polymerization of norbornene was also considered. In principle, "naked" Pd^{2+} might be generated in situ through loss of the supporting ligands; such species yield high molecular weight polynorbornenes.[47] However, the influence of the redox switch on the polymerization of norbornene suggests that the supporting ligand remains attached to palladium throughout the polymerization process. Alternatively, polymerization of norbornene by a cationic mechanism yields oligomeric materials with low molecular weights.[48] The reaction of norbornenes with [^{Ac}Fc][BAr^F] (Figure B25-28) under similar polymerization conditions as those used for [(fc^{P,B})PdMe][BAr^F] yielded no isolable polymeric material, suggesting that cationic polymerization by the oxidant is not a viable mechanism in this system.

Table 3-1. Polymerization of norbornene derivatives by in situ generated [(fc^{P,B})PdMe][BAr^F].

entry	monomer	time (h)	conversion (%)	$M_{n,\,theo}$	$M_{n,\,exp}$	*Đ*	TOF
1	NB	1	78	-	-	-	64
2	NBa	1	79	12.2	30.6	3.63	81
3	NBb	1	58	14.9	37.0	2.52	58
4	NBc	0.5	33	5.8	8.8	2.10	70
5	NBd	2	27	4.4	1.4	1.46	12.5
6	NBb	1.33	49	13.0	30.5	3.04	38.3

Conditions: monomer (0.50 mmol), catalyst (0.005 mmol), oxidant (0.005 mmol), d_6-benzene as a solvent (0.5 mL) and 1,3,5-trimethoxybenzene (0.10 mmol) as an internal standard. All experiments were performed at 70 °C, except for entry 5, performed at 100 °C. M_n are reported in 10^3 g/mol; $Đ = M_w/M_n$, TOF = (mol_{NB} in polymer) mol_{Pd}^{-1} h^{-1}. In the case of entry 1, the isolated yield is reported instead of conversion.

3.4 Conclusions

The application of a ferrocene-chelating heteroscorpionate ligand in palladium catalyzed norbornene polymerization was investigated. Compound [($fc^{P,B}$)PdMe][BAr^F] shows a reversible on/off switch toward the polymerization of norbornene derivatives. While the reduced state of the catalyst, ($fc^{P,B}$)PdMe, shows no activity, the oxidized complex, [($fc^{P,B}$)PdMe][BAr^F], exhibits activity toward norbornene polymerization.

3.5 Experimental section

Synthesis of (COD)PdMeCl. A suspension of (COD)$PdCl_2$ (247.7 mg, 0.868 mmol) in 6 mL of Et_2O/THF (1:2 vol %) was cooled to -78 °C. Trimethylaluminum (125.1 mg, 1.735 mmol) in 1 mL of hexanes was added slowly, the reaction mixture was removed from the cold well, and stirred at ambient temperature until the solution became colorless. Methanol was added to solvolyse the aluminum by-products and volatile substances were removed under reduced pressure. The desired product was extracted with THF and filtered through Celite. THF was removed under reduced pressure and the resulting off-white solids were washed with Et_2O (2 × 2 mL) to afford the final product (185.3 mg, 80.5 %). This procedure was carried out multiple times in similar scales with yields ranging from 50-80%. ^{1}H NMR ($CDCl_3$, 500 MHz, 298 K): δ (ppm) 1.18 (s, 3H, PdCH_3), 2.47 (m, 4H, CH_2), 2.58 (m, 2H, CH_2), 2.65 (m, 2H, CH_2), 5.15 (t, 2H, C*H*), 5.91 (t, 2H, C*H*).

Synthesis of ($fc^{P,B}$)PdMe. To (COD)PdMeCl (155.1 mg, 0.585 mmol) in 10 mL of THF, ($fc^{P,B}$)Li$(THF)_2$ (384.3 mg, 0.532 mmol) in 5 mL of THF was added dropwise. The reaction solution was stirred for 16 h at ambient temperature. Volatile substances were removed under reduced pressure and the desired product was extracted into 10 mL of toluene and filtered

through Celite. Reduction in volume of the toluene solution to 4 mL and layering with 4 mL of hexanes afforded red crystalline material after 24 h at -35 °C. Decanting of the solution and washing of the remaining solids with hexanes (3 × 2 mL) and cold toluene (3 × 1 mL) yields the product as a red crystalline material (321.9 mg, 77.1 %) in two crops. Crystals of ($fc^{P,B}$)PdMe always contain one molecule of toluene per molecule of compound as supported by NMR spectroscopic data. X-ray quality crystals were obtained from toluene at -35 °C. ^{1}H NMR (C_6D_6, 500 MHz, 298 K): δ (ppm) 0.99 (d, 3H, PdC*H*$_3$), 1.65 (s, 3H, CC*H*$_3$), 2.30 (s, 3H, CC*H*$_3$), 2.35 (s, 3H, CC*H*$_3$), 2.42 (s, 3H, CC*H*$_3$), 3.18 (s, 1H, Cp-*H*), 3.95 (s, 1H, Cp-*H*), 4.04 (s, 1H, Cp-*H*), 4.18 (s, 1H, Cp-*H*), 4.21 (s, 1H, Cp-*H*), 4.30 (s, 1H, Cp-*H*), 4.43 (s, 1H, Cp-*H*), 5.04 (s, 1H, Cp-*H*), 5.56 (s, 1H, C*H*), 5.73 (s, 1H, C*H*), 6.92 (t, 2H, *p*-Ph), 7.05 (m, 4H, *m*-Ph), 7.41 (t, 2H, *o*-Ph), 7.57 (t, 2H, *o*-Ph). ^{13}C NMR (C_6D_6, 126 MHz, 298 K): δ (ppm) -0.98 (d, Pd*C*H$_3$), 14.2 (s, C*C*H$_3$), 14.3 (d, C*C*H$_3$), 14.4 (s, C*C*H$_3$), 15.3 (s, C*C*H$_3$), 68.9 (s, Cp-*C*), 69.5 (s, Cp-*C*), 70.8 (d, Cp-*C*), 72.4 (d, Cp-*C*), 73.8 (d, Cp-*C*), 74.7 (s, Cp-*C*), 74.9 (d, Cp-*C*), 80.2 (s, Cp-*C*), 105.8 (s, -*C*H-), 106.7 (d, -*C*H-), 132.2 (s, aromatic), 132.6 (s, aromatic), 133.6 (s, aromatic), 133.7 (s, aromatic), 133.9 (s, aromatic), 134.0 (s, aromatic), 134.1 (s, aromatic), 134.2 (s, aromatic), 145.4 (s, *C*CH$_3$), 146.4 (d, *C*CH$_3$), 147.9 (s, *C*CH$_3$), 148.8 (d, *C*CH$_3$). ^{11}B NMR (C_6D_6, 161 MHz, 298 K): δ (ppm) -7.6 (br s). ^{31}P[^{1}H] NMR (C_6D_6, 121 MHz, 298 K): δ (ppm) 30.5 (s). Anal. Calcd: ($fc^{P,B}$)PdMe·(C_7H_8) ($C_{40}H_{44}BFeN_4PPd$) C, 61.21; H, 5.65; N, 7.14. Found: C, 60.82; H, 5.00; N, 6.56.

Synthesis of [($fc^{P,B}$)PdMe][BAr^{F}]. To [^{Ac}Fc][BAr^{F}] (75.9 mg, 0.069 mmol) was added ($fc^{P,B}$)PdMe·(C_7H_8) (49.6 mg, 0.063 mmol) in 5 mL of toluene. The reaction solution was stirred for 10 min and filtered through Celite. The solution volume was reduced to 1 mL, diluted to 10 mL with hexanes, and stored at -35 °C for 30 min. Decanting of the solution and washing of the

remaining brown oil with cold hexanes (2 × 4 mL) yields the product as a brown solid after an hour under reduced pressure (84.3 mg, 81.2 %). ^{1}H NMR (C_6D_6, 500 MHz, 298 K): δ (ppm) -9.71 (br s), -3.28 (s), -1.82 (s), 1.68 (s), 3.58 (br s), 4.68 (s), 4.84 (s), 7.42 (s), 7.91 (s), 8.60 (s), 10.04 (s), 12.43 (br s). ^{11}B NMR (C_6D_6, 161 MHz, 298 K): δ (ppm) -65.2 (br s), -6.1 (s). ^{19}F NMR (C_6D_6, 282 MHz, 298 K): δ (ppm) -62.2 (s). Anal. Calcd: [($fc^{P,B}$)PdMe][BAr^{F}]·(C_7H_8) ($C_{72}H_{56}B_2F_{24}FeN_4PPd$) C, 52.47; H, 3.43; N, 3.40. Found: C, 51.97; H, 2.74; N, 3.25.

Synthesis of ($fc^{P,B}$)Pd[C(Me)N^{t}Bu](CN^{t}Bu). To ($fc^{P,B}$)PdMe·(C_7H_8) (113.3 mg, 0.144 mmol) in 5 mL of dichloromethane at -78 °C was added CN^{t}Bu (0.065 mL, 0.577 mmol) via syringe. The reaction mixture was stirred for 1 h at -78 °C before volatile substances were removed under reduced pressure. The desired product was extracted in 3 mL of diethyl ether and filtered through Celite. Diethyl ether was removed under reduced pressure and the remaining solids were dissolved in 1.5 mL of toluene containing 2 drops of tBuNC. Hexanes (1 mL) was layered on top and the solution was stored overnight at -35 °C. Decanting of the solution and washing of the remaining solids with hexanes (3 × 1 mL) yielded the final product as an orange crystalline material (97.5 mg, 71.2%). Crystals of ($fc^{P,B}$)Pd[C(Me)N^{t}Bu](CN^{t}Bu) always contain one molecule of toluene per molecule of compound as supported by NMR spectroscopic data. ^{1}H NMR (C_6D_6, 500 MHz, 298 K): δ (ppm) 0.79 (s, 9H, C(CH_3)$_3$), 1.76 (s, 9H, C(CH_3)$_3$), 2.00 (s, 3H, CH_3), 2.15 (s, 3H, CH_3), 2.32 (s, 3H, CH_3), 2.48 (s, 3H, CH_3), 2.49 (s, 3H, CH_3), 3.97 (m, 1H, Cp-*H*), 4.05 (m, 1H, Cp-*H*), 4.24 (m, 3H, Cp-*H*), 4.32 (m, 1H, Cp-*H*), 4.48 (m, 1H, Cp-*H*), 4.52 (m, 1H, Cp-*H*), 5.62 (s, 1H, C*H*), 5.80 (s, 1H, C*H*), 7.07 (m, 6H, *m*-Ph, *p*-Ph), 7.62 (m, 4H, *o*-Ph). ^{13}C NMR (C_6D_6, 126 MHz, 298 K): δ (ppm) 13.7 (s, CCH_3), 14.8 (s, CCH_3), 15.0 (s, CCH_3), 15.8 (s, CCH_3), 29.7 (s, C(CH_3)$_3$), 32.2 (s, C(CH_3)$_3$), 34.4 (s, C(CH_3)=NC(CH_3)$_3$), 56.5 (s, C(CH_3)$_3$), 68.7 (s, C(CH_3)=NC(CH_3)$_3$), 71.0 (s, Cp-*C*), 72.7 (d, Cp-*C*), 73.0 (d, Cp-*C*), 73.6 (s,

Cp-*C*), 73.8 (s, Cp-*C*), 74.8 (s, Cp-*C*), 74.9 (s, Cp-*C*), 75.3 (s, Cp-*C*), 75.6 (s, Cp-*C*), 105.3 (s, *C*H), 106.5 (s, *C*H), 134.3 (s, aromatic), 134.4 (s, aromatic), 134.5 (s, aromatic), 134.6 (s, aromatic), 145.0 (s, *C*CH_3), 145.4 (s, *C*CH_3), 147.0 (s, *C*CH_3), 149.1 (s, *C*CH_3), 166.4 *C*(CH_3)=N$C(CH_3)_3$). ^{11}B NMR (C_6D_6, 161 MHz, 298 K): δ (ppm) 7.2 (br s). ^{31}P[^{1}H] NMR (C_6D_6, 121 MHz, 298 K): δ (ppm) -14.9 (s), 9.4 (s). Anal. Calcd: ($fc^{P,B}$)Pd[C(Me)N^{t}Bu](CN^{t}Bu)·(C_7H_8) ($C_{50}H_{62}BFeN_6PPd$) C, 63.14; H, 6.57; N, 8.84. Found: C, 62.62; H, 6.49; N, 8.86.

General Procedure for the Synthesis of Substituted Norbornenes. A pressure reactor was charged with dicyclopentadiene (20.0 mmol) and the corresponding olefin (44.0 mmol). The reactor was purged with nitrogen and sealed. The reactor was then heated to 220-240 °C for two hours before being allowed to cool to ambient temperature. The reactor was opened and the resulting tan oil was distilled at 2.5 torr to afford a colorless liquid.

Synthesis of 5-butyl-bicyclo[2.2.1]hept-2-ene (NBa). Distilled at 35 °C and 2.5 torr to afford a colorless liquid (44.0%), 18.2% exo, 81.8% endo. ^{1}H NMR ($CDCl_3$, 500 MHz, 298 K): δ (ppm) 0.47-0.50 (m, 1H), 0.87 (m, 3H), 1.07 (m, 2H), 1.20-1.46 (m, 6H), 1.82 (m, 1H), 1.96 (m, 1H), 2.50 (s, 1H), 2.75(s, 1H), 5.54-6.11 (m, 2H, olefinic). ^{13}C NMR ($CDCl_3$, 500 MHz, 298 K): δ (ppm) 137.1, 137.0, 136.3, 133.4, 132.6, 132.5, 54.4, 49.7, 48.3, 46.5, 45.8, 45.6, 45.4, 42.7, 42.1, 41.6, 38.9, 36.9, 36.5, 34.7, 33.2, 32.6, 31.3, 31.1, 23.1, 14.2.

Synthesis of 5-(triethoxysilyl)-bicyclo[2.2.1]hept-2-ene (NBb). Distilled at 65 °C and 2.5 torr to afford a colorless liquid (46.8%) as a mixture of exo and endo isomers. ^{1}H NMR ($CDCl_3$, 500 MHz, 298 K): δ (ppm) 0.46 (m, 1H), 1.07 (m, 1H), 1.23 (m, 9H), 1.35 (m, 1H), 1.76 (m, 1H), 1.88 (m, 1H), 2.92 (m, 2H), 3.76-3.86 (m, 6H), 5.92-6.13 (m, 2H, olefinic). ^{13}C NMR ($CDCl_3$, 500 MHz, 298 K): δ (ppm) 137.9, 135.4, 134.8, 133.8, 58.6, 58.4, 47.1, 44.3, 42.9, 42.6, 42.3, 27.1, 26.4, 20.9, 20.4, 18.5, 18.4.

Synthesis of 5-(trimethylsily)-bicyclo[2.2.1]hept-2-ene (NBc). Distilled at 30 °C and 2.5 torr to afford a colorless liquid (37.7%) as a mixture of exo and endo isomers. ^{1}H NMR ($CDCl_3$, 500 MHz, 298 K): δ (ppm) -0.09-0.00 (s, 9H), 0.31 (m, 1H), 0.90-1.14 (m, 2H), 1.29-1.51 (m, 2H), 1.85 (m, 1H), 2.72-2.93 (m, 1H), 3.21 (m, 1H), 5.48-6.16 (m, 2H, olefinic). ^{13}C NMR ($CDCl_3$, 500 MHz, 298 K): δ (ppm) 138.7, 135.6, 134.1, 51.7, 47.0, 44.9, 43.0, 42.62, 42.57, 27.3, 27.1, 25.4, 25.3, -1.3, -1.8.

Synthesis of 5-cyclohexyl-bicyclo[2.2.1]hept-2-ene (NBd). Distilled at 76°C at 2.5 torr to afford a colorless liquid (7.53%) ^{1}H NMR ($CDCl_3$, 500 MHz, 298 K): δ (ppm) 0.60 (m, 2H), 0.83-1.00 (m, 2H), 1.12-1.20 (m, 4H), 1.26 (s, 1H), 1.36 (m, 1H), 1.65 (m, 4H), 1.77 (m, 2H), 2.74-2.87 (s, 2H), 5.90-6.10 (m, 2H, olefinic). ^{13}C NMR ($CDCl_3$, 500 MHz, 298 K): δ (ppm) 137.1, 136.5, 132.4, 49.4, 46.0, 45.8, 45.5, 44.0, 43.1, 43.0, 42.5, 42.4, 41.9, 33.0, 32.8, 32.6, 32.5, 31.6, 31.2, 26.95, 29.93, 26.7, 26.6, 26.5, 26.5, 26.4.

NMR Scale Polymerizations. In a small vial, ($fc^{P,B}$)PdMe (5 μmol) was added to one equivalent of [^{Ac}Fc][BAr^F] in 0.2 mL of C_6D_6 and stirred until the oxidant was consumed. To the oxidized complex was added an external standard, 1,3,5-trimethoxybenzene (0.1 mmol), and monomer (0.5 mmol); the total solution volume was increased to 0.5 mL of C_6D_6. The contents of the vial were stirred and the homogeneous solution was transferred to a J. Young NMR tube equipped with a Teflon valve. The NMR tube was sealed, taken out of the box and placed in an oil bath. The polymerization was monitored by ^{1}H NMR spectroscopy until the conversion has stopped or reached completion. The contents of the NMR tube were diluted with 1 mL of dichloromethane and poured into 10 mL of methanol to yield white solids. The product was collected on a glass frit, washed with additional 5 mL of methanol and kept under reduced pressure until it reached a consistent weight. For the control experiments, [^{Ac}Fc][BAr^F] or Cp_2Co

(5 μmol) was used instead of ($fc^{P,B}$)PdMe while the rest of the conditions above were kept the same.

3.6 Appendix B

3.6.1 NMR spectroscopy

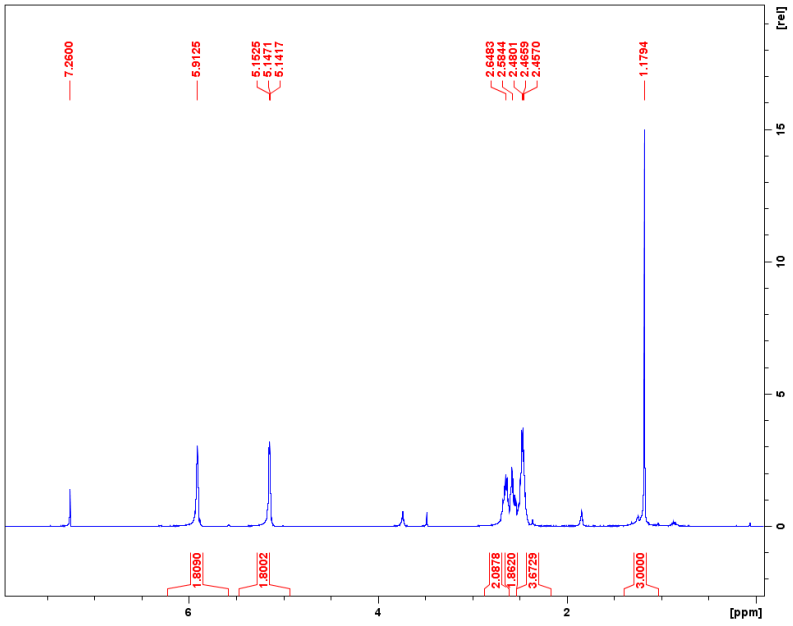

Figure B1. ^{1}H NMR spectrum ($CDCl_3$, 500 MHz, 298 K) of (COD)PdMeCl.

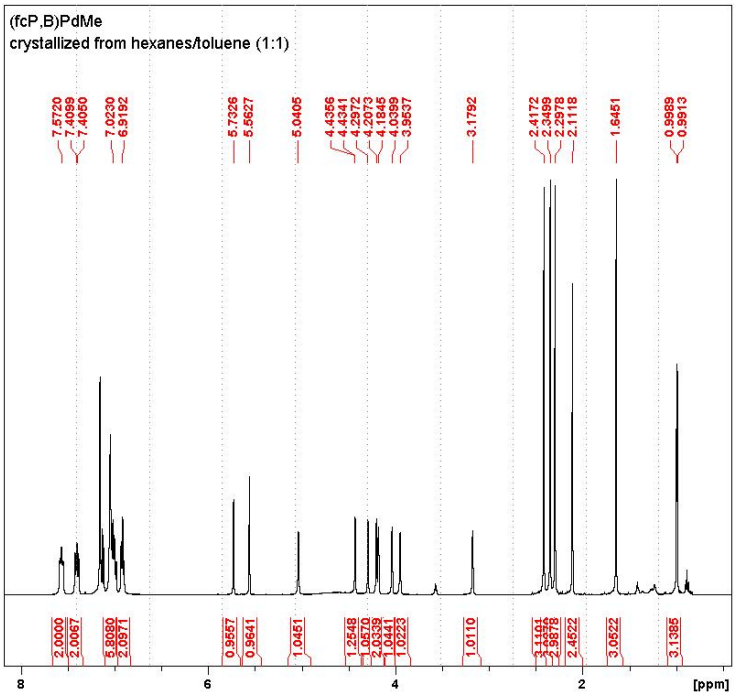

Figure B2. ^{1}H NMR spectrum (C_6D_6, 500 MHz, 298 K) of ($fc^{P,B}$)PdMe·(C_7H_8).

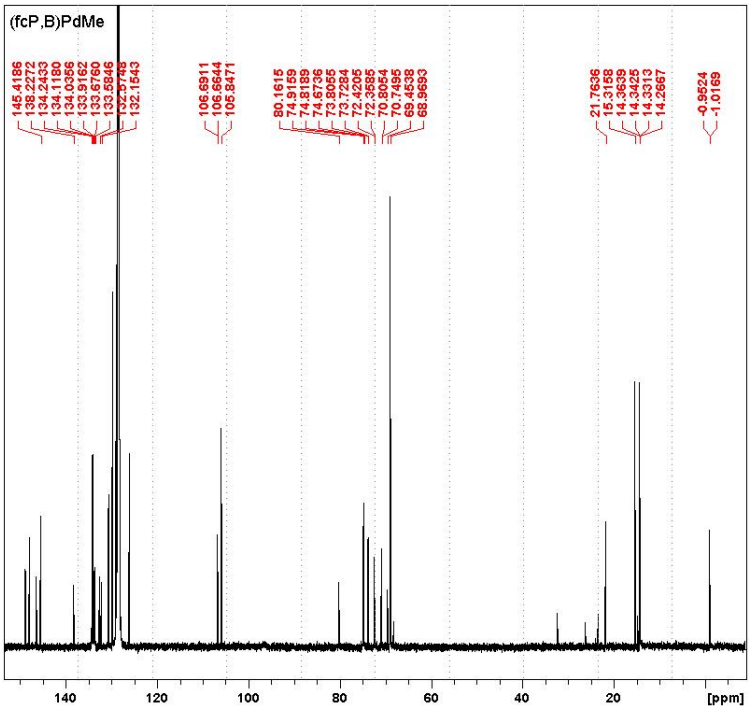

Figure B3. NMR spectrum (C_6D_6, 126 MHz, 298 K) of ($fc^{P,B}$)PdMe·(C_7H_8).

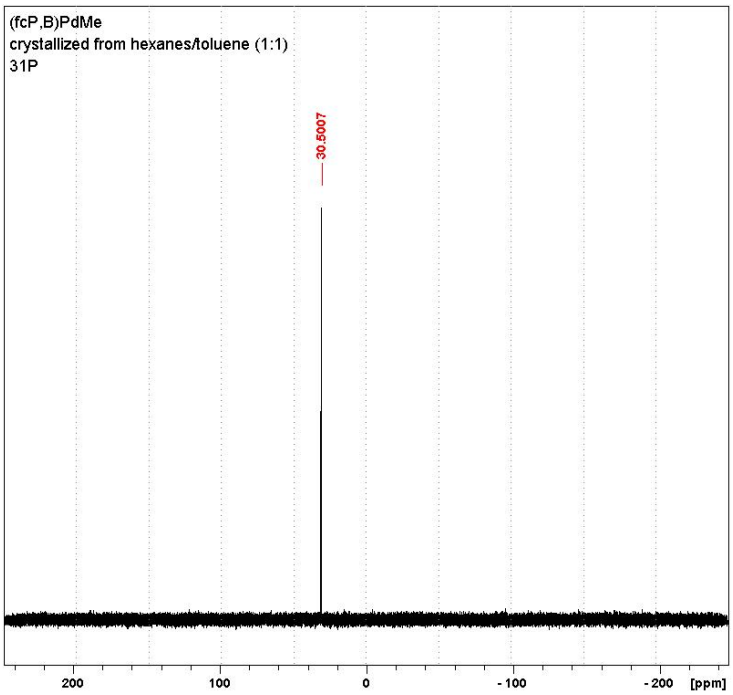

Figure B4. $^{31}P\{^{1}H\}$ NMR spectrum (C_6D_6, 202 MHz, 298 K) of ($fc^{P,B}$)PdMe·(C_7H_8).

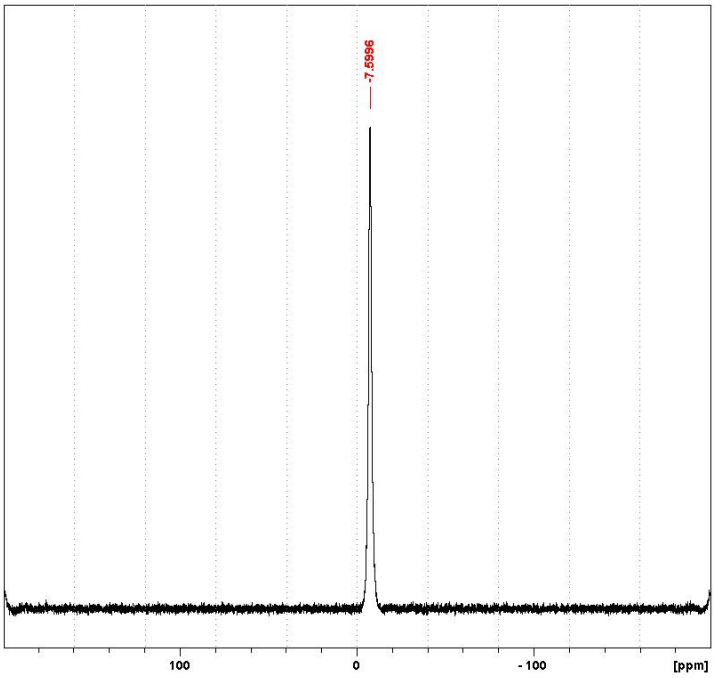

Figure B5. ^{11}B NMR spectrum (C_6D_6, 161 MHz, 298 K) of ($fc^{P,B}$)PdMe·(C_7H_8).

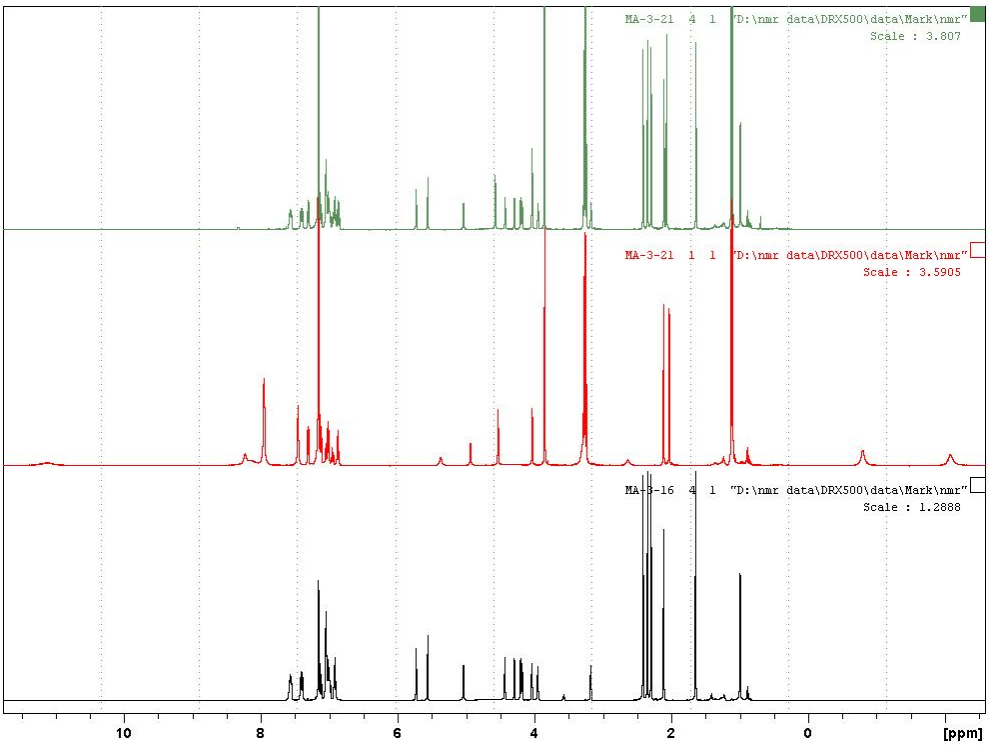

Figure B6. ^{1}H NMR spectra (C_6D_6, 500 MHz, 298 K) of ($fc^{P,B}$)PdMe (bottom), ($fc^{P,B}$)PdMe + [AcFc][BAr^F] (middle), ($fc^{P,B}$)PdMe + [AcFc][BAr^F] + Cp_2Co (top).

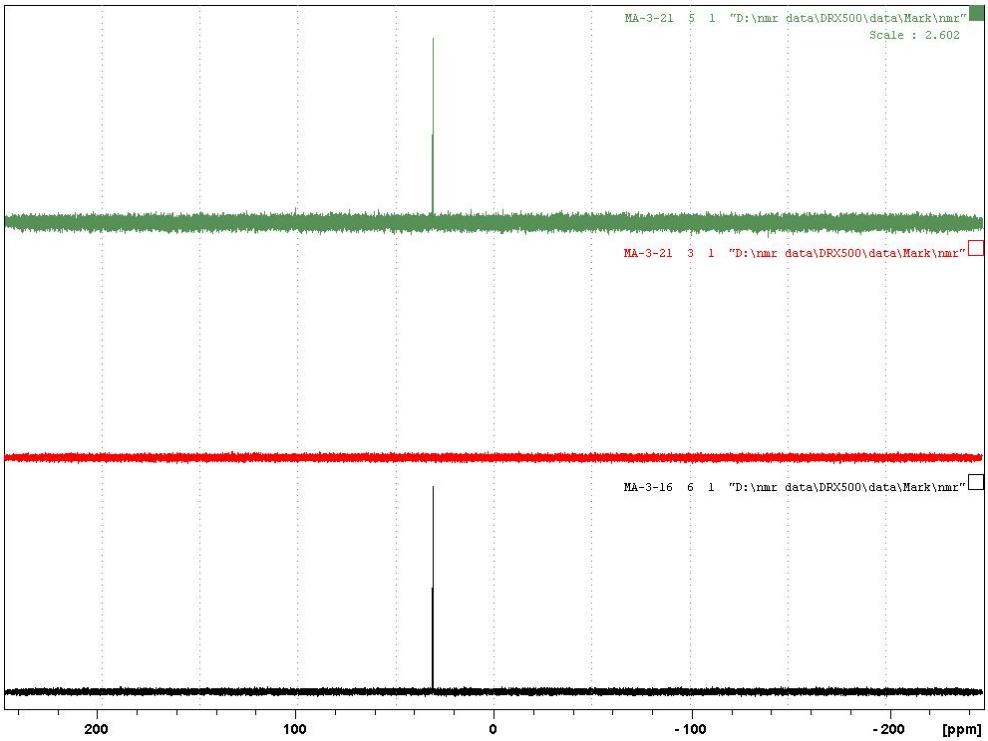

Figure B7. $^{31}P\{^{1}H\}$ NMR spectra (C_6D_6, 202 MHz, 298 K) of ($fc^{P,B}$)PdMe (bottom), ($fc^{P,B}$)PdMe + [AcFc][BAr^F] (middle), ($fc^{P,B}$)PdMe + [AcFc][BAr^F] + Cp_2Co (top).

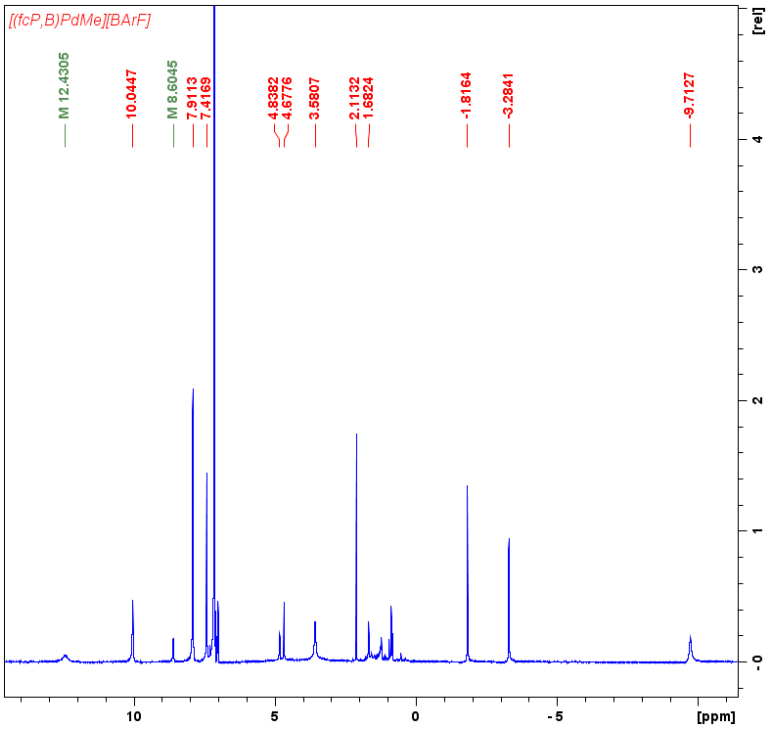

Figure B8. ^{1}H NMR spectrum (C_6D_6, 500 MHz, 298 K) of [($fc^{P,B}$)PdMe][BAr^{F}]·(C_7H_8).

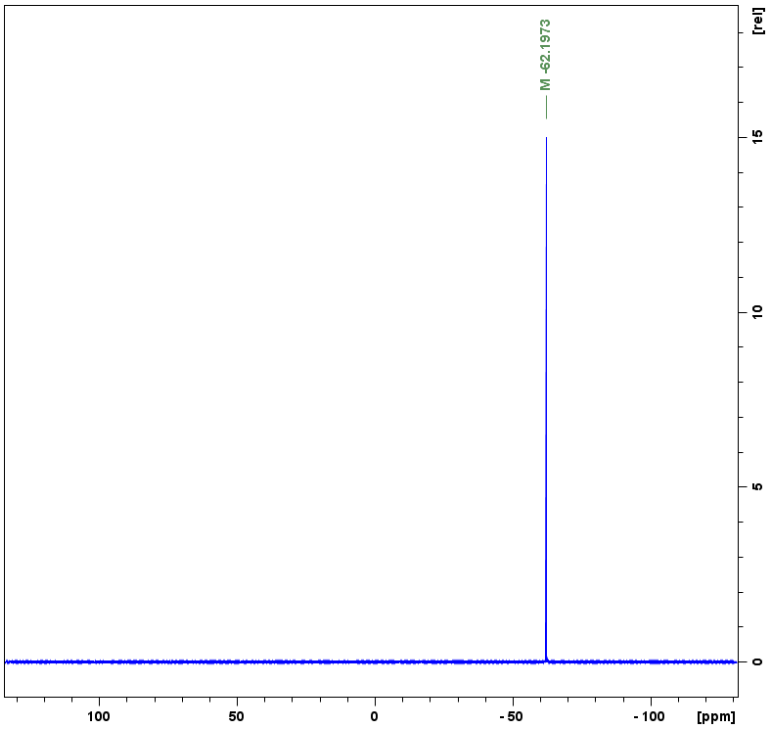

Figure B9. ^{19}F NMR spectrum (C_6D_6, 282 MHz, 298 K) of [($fc^{P,B}$)PdMe][BAr^{F}]·(C_7H_8).

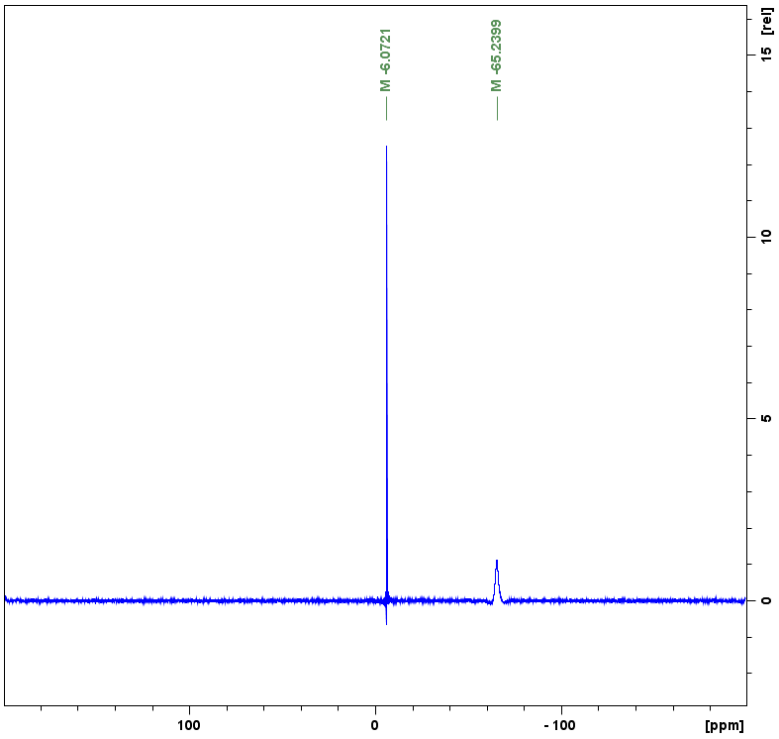

Figure B10. ^{11}B NMR spectrum (C_6D_6, 161 MHz, 298 K) of [(fc^{P,B})PdMe][BAr^{F}]·(C_7H_8).

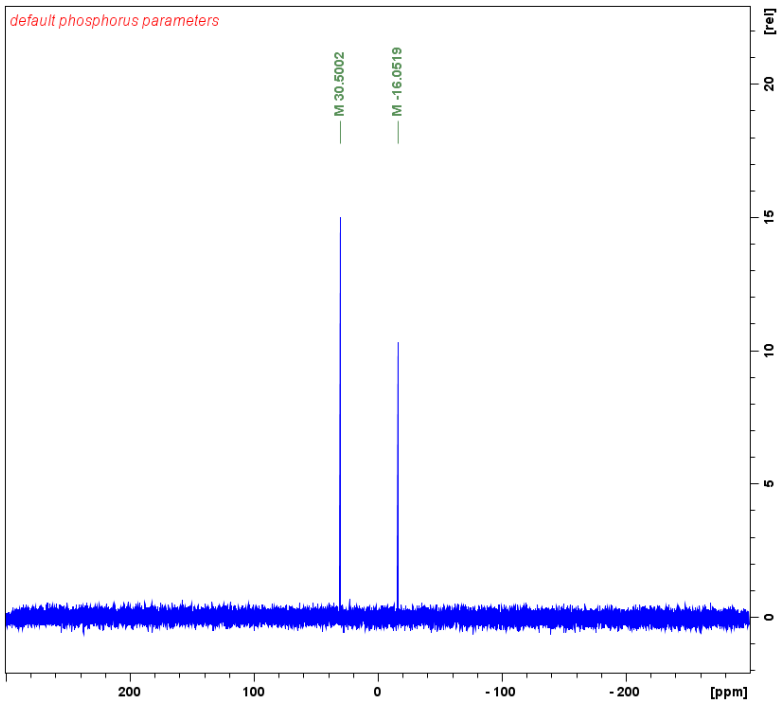

Figure B11. ^{31}P{^{1}H} NMR spectrum (C_6D_6, 121 MHz, 298 K) of (fc^{P,B})PdMe and $FcPPh_2$.

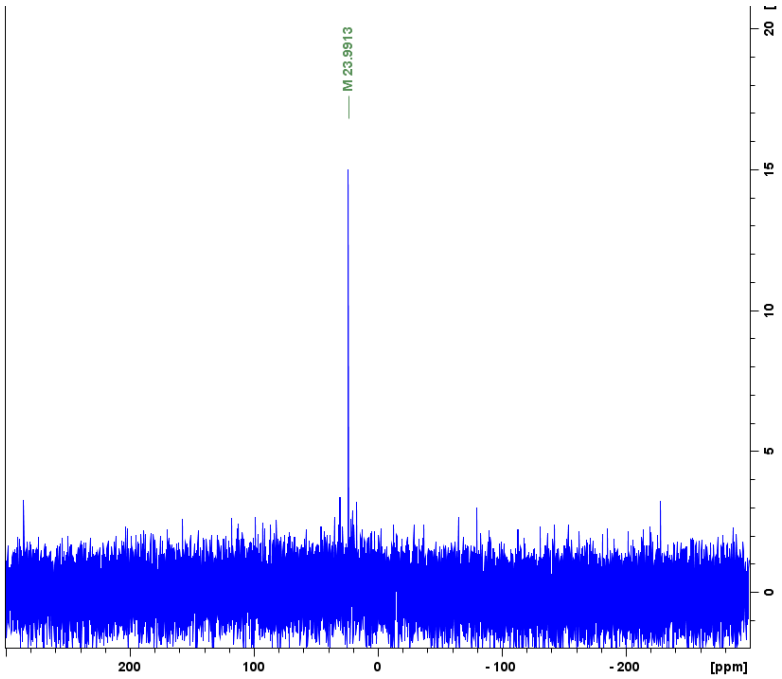

Figure B12. $^{31}P\{^{1}H\}$ NMR spectrum (C_6D_6, 121 MHz, 298 K) of [($fc^{P,B}$)PdMe($FcPPh_2$)][BAr^F].

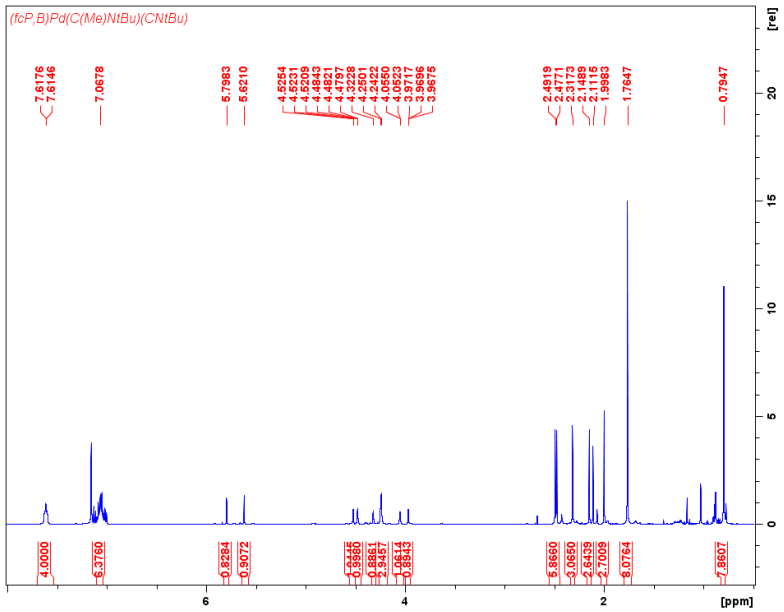

Figure B13. ^{1}H NMR spectrum (C_6D_6, 500 MHz, 298 K) of ($fc^{P,B}$)Pd[C(Me)NtBu](CNtBu).

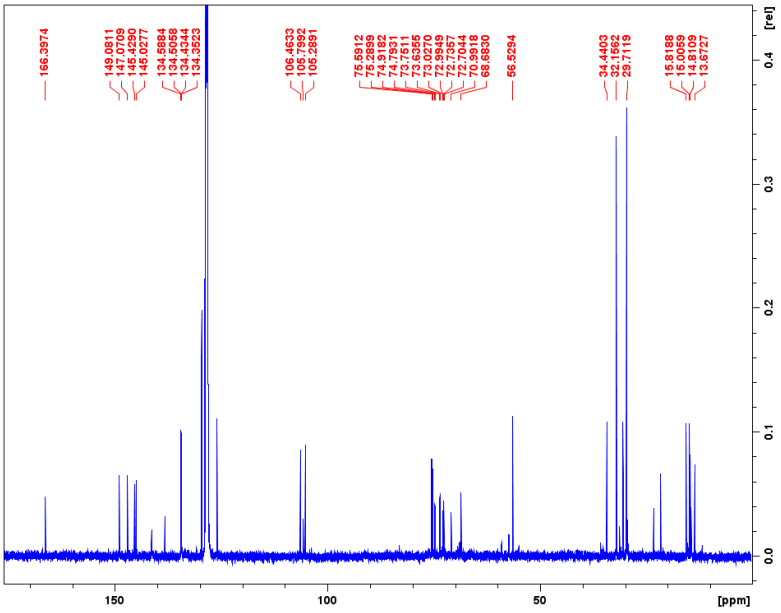

Figure B14. ^{13}C NMR spectrum (C_6D_6, 126 MHz, 298 K) of ($fc^{P,B}$)Pd[C(Me)NtBu] (CNtBu).

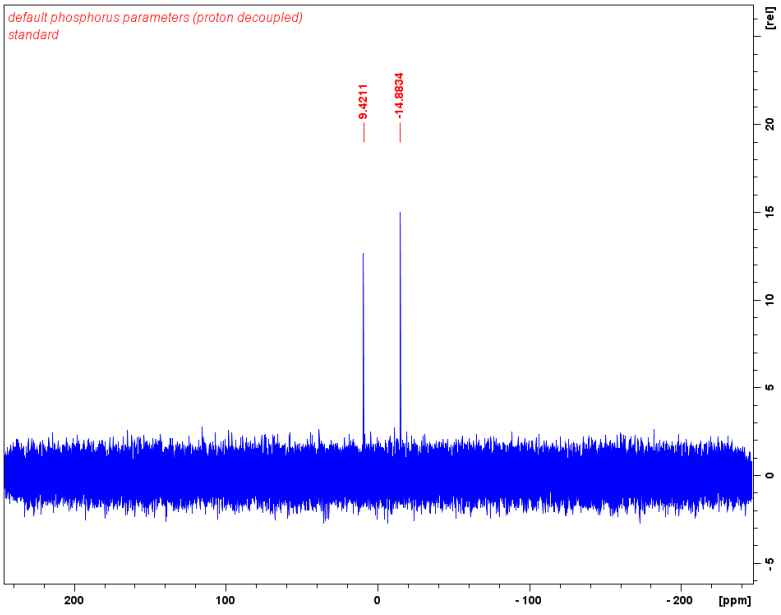

Figure B15. $^{31}P\{^{1}H\}$ NMR spectrum (C_6D_6, 202 MHz, 298 K) of ($fc^{P,B}$)Pd[C(Me)NtBu] (CNtBu).

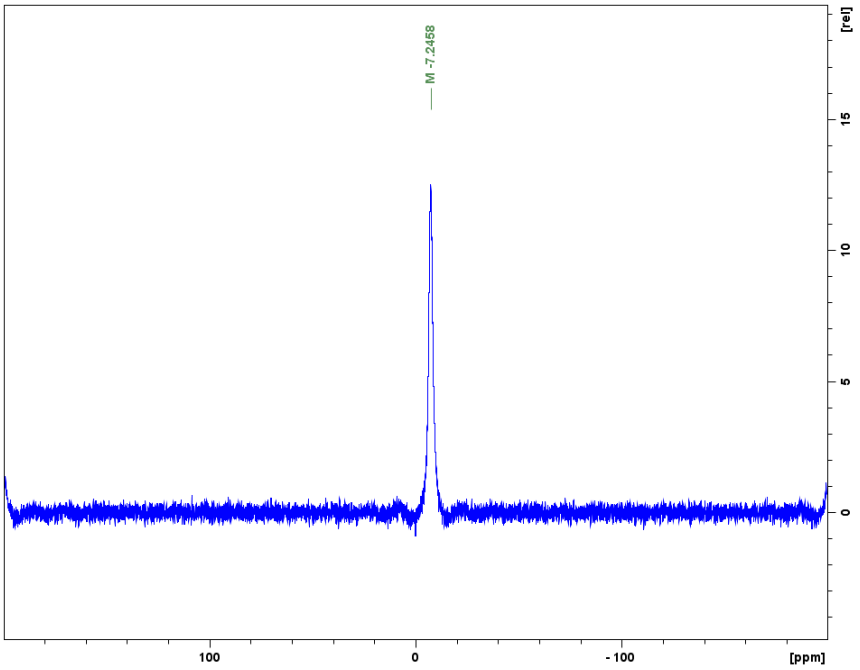

Figure B16. ^{11}B NMR spectrum (C_6D_6, 161 MHz, 298 K) of ($fc^{P,B}$)Pd[C(Me)NtBu] (CNtBu).

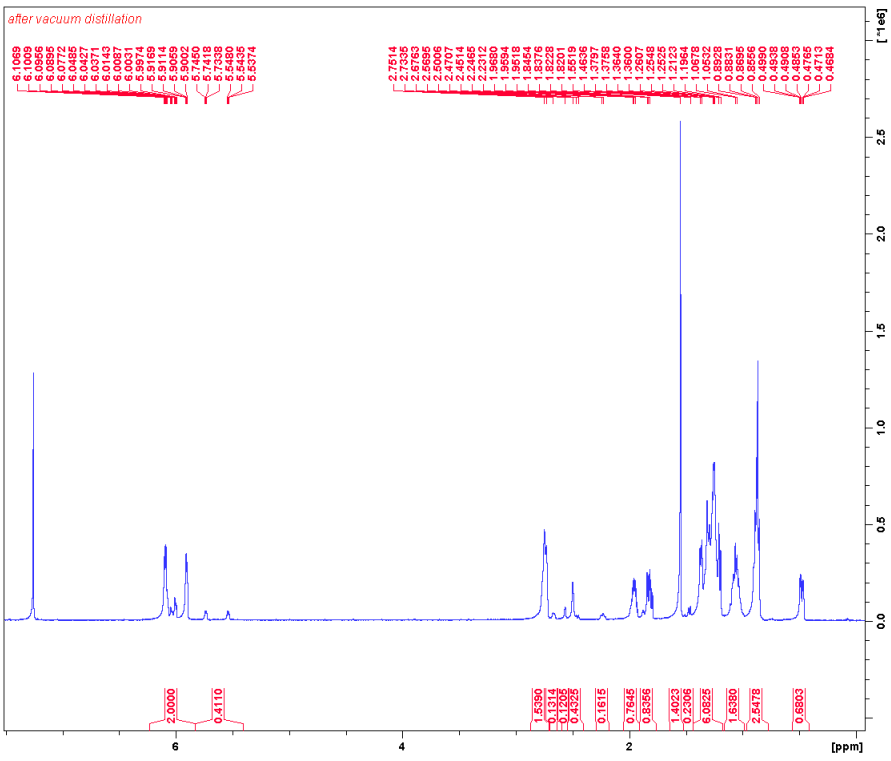

Figure B17. ^{1}H NMR Spectrum ($CDCl_3$, 500 MHz, 298 K) of 5-butyl-bicyclo[2.2.1]hept-2-ene.

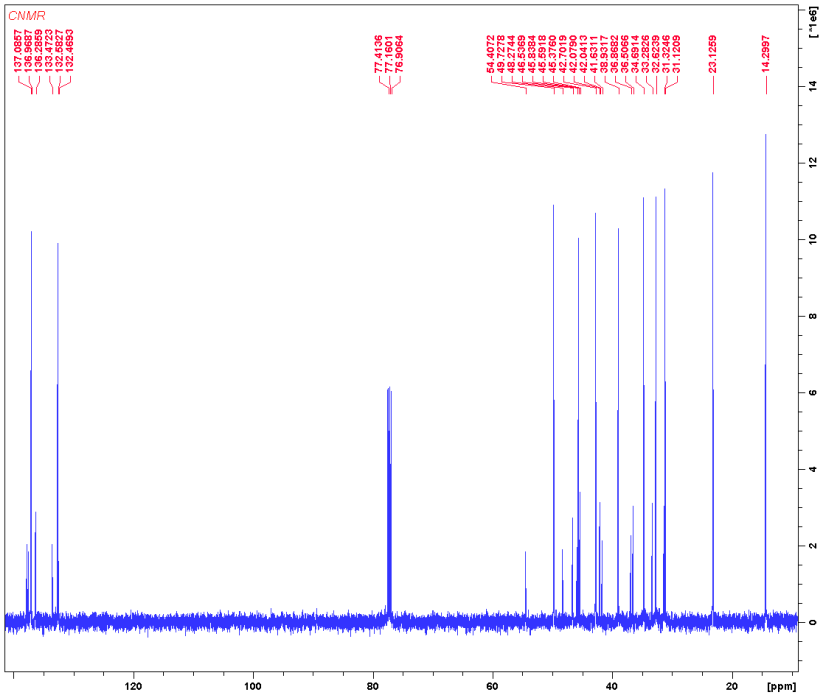

Figure B18. ^{13}C NMR Spectrum ($CDCl_3$, 500 MHz, 298 K) of 5-butyl-bicyclo[2.2.1]hept-2-ene.

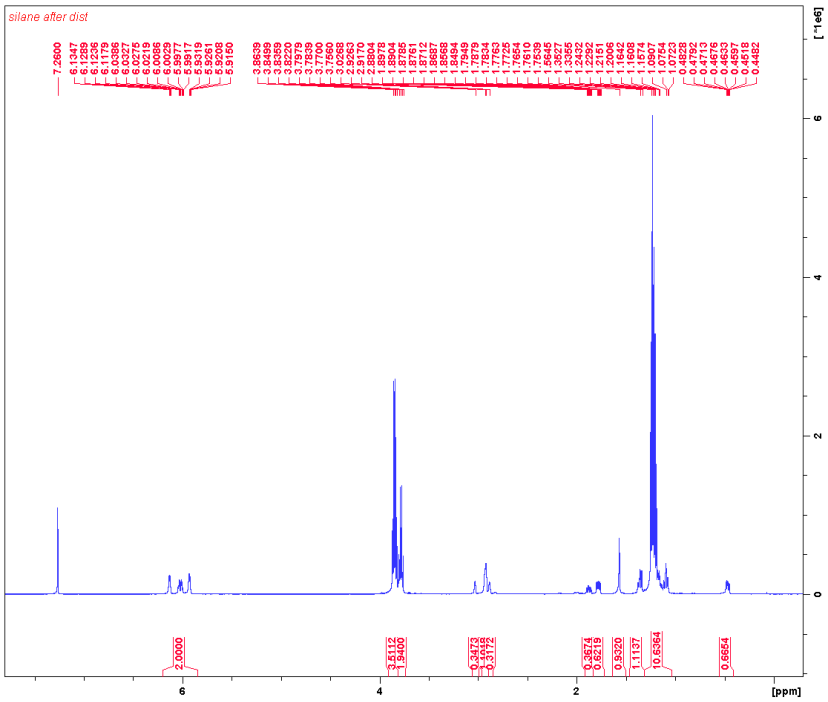

Figure B19. ^{1}H NMR Spectrum ($CDCl_3$, 500 MHz, 298 K) of 5-(triethoxysilyl)-bicyclo[2.2.1]hept-2-ene.

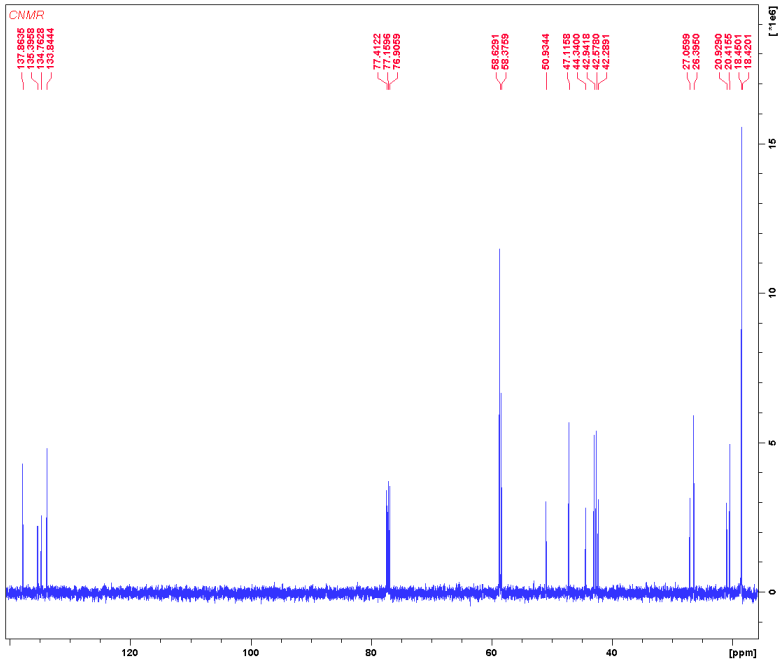

Figure B20. ^{13}C NMR Spectrum ($CDCl_3$, 500 MHz, 298 K) of 5-(triethoxysilyl)-bicyclo[2.2.1]hept-2-ene.

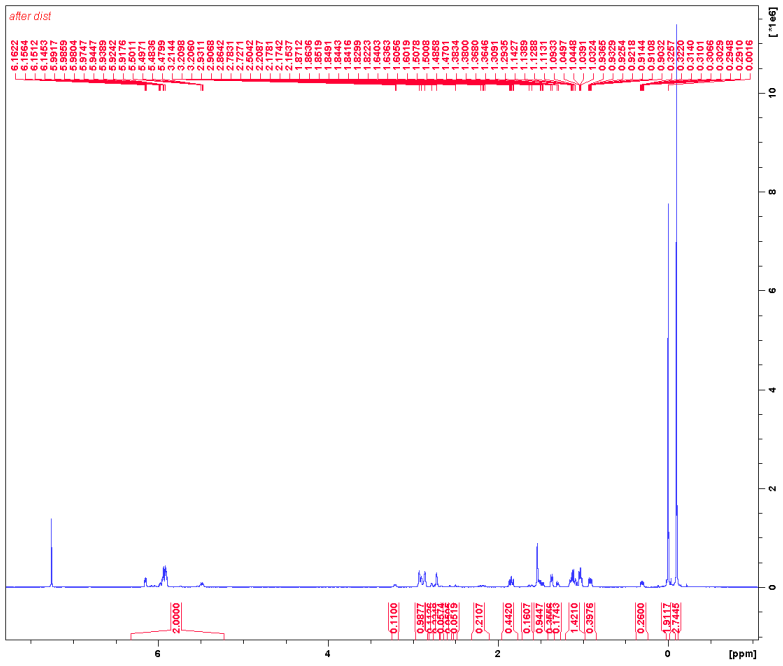

Figure B21. ^{1}H NMR Spectrum ($CDCl_3$, 500 MHz, 298 K) of 5-(trimethylsily)-bicyclo[2.2.1]hept-2-ene.

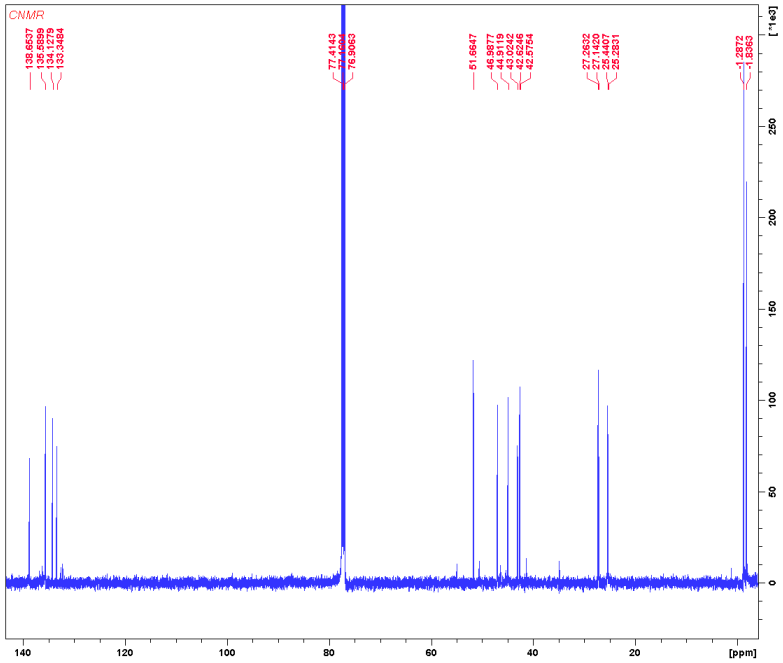

Figure B22. ^{13}C NMR Spectrum ($CDCl_3$, 500 MHz, 298 K) of 5-(trimethylsily)-bicyclo[2.2.1]hept-2-ene.

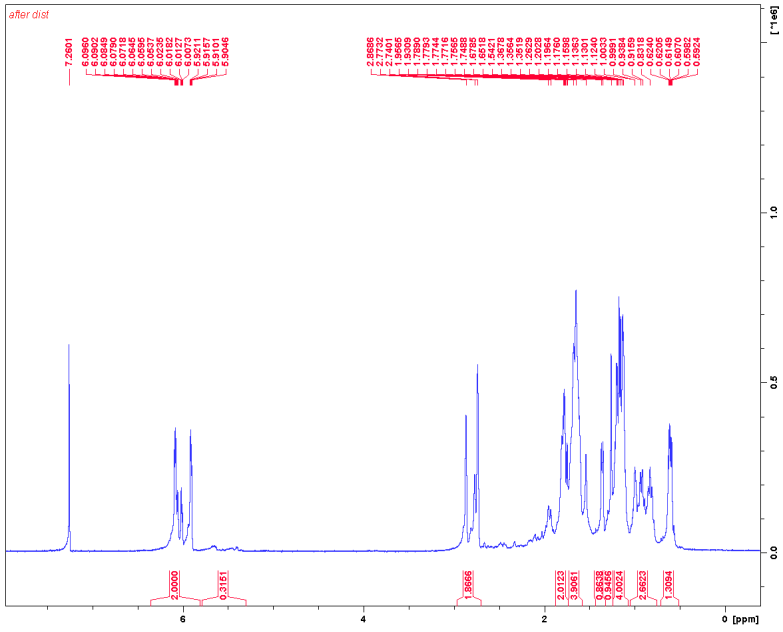

Figure B23. ^{1}H NMR Spectrum ($CDCl_3$, 500 MHz, 298 K) of 5-cyclohexyl-bicyclo[2.2.1]hept-2-ene:

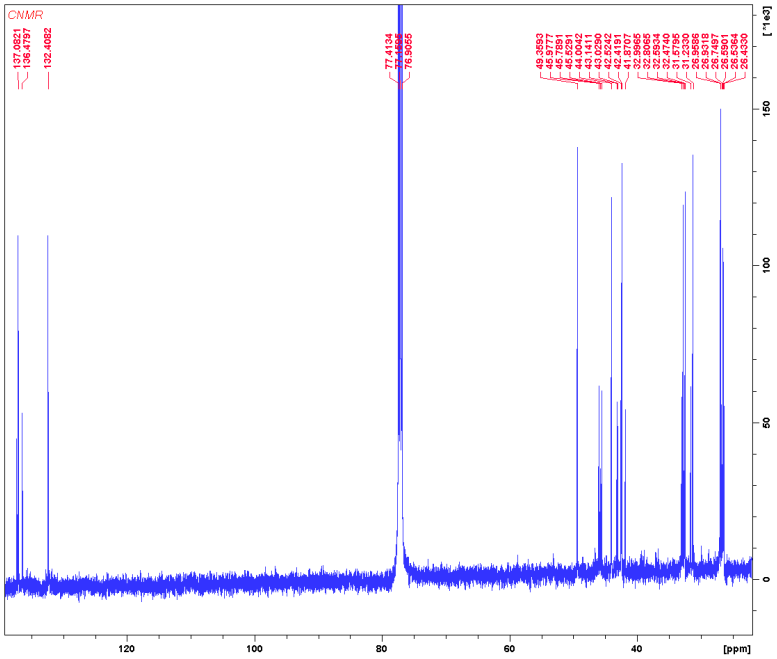

Figure B24. ^{13}C NMR Spectrum ($CDCl_3$, 500 MHz, 298 K) of 5-cyclohexyl-bicyclo[2.2.1]hept-2-ene.

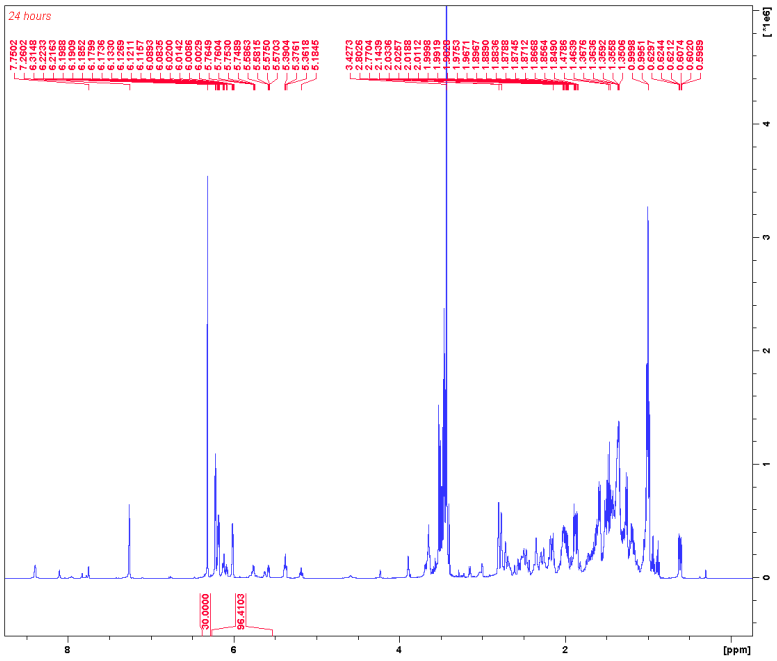

Figure B25. Control experiment of 50 equivalents of 5-butyl-bicyclo[2.2.1]hept-2-ene with 5 equivalents of $^{Ac}FcBAr^{F}$ at 70°C for 24 hours. 1,3,5-Trimethoxybenzene was used as an internal standard.

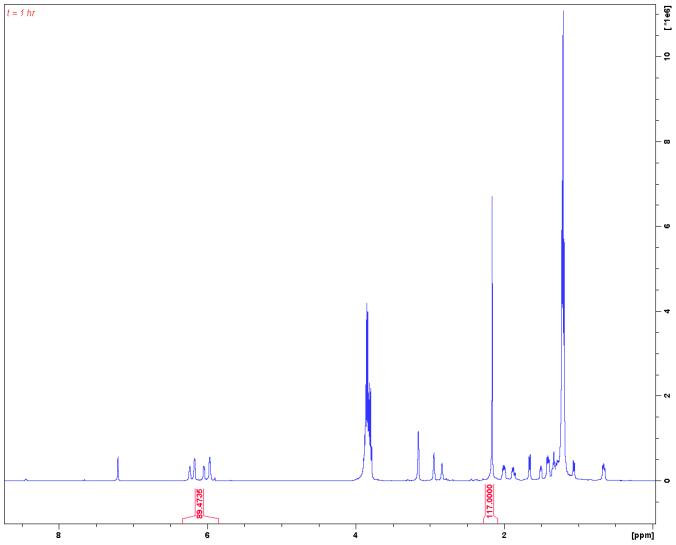

Figure B26. Control experiment of 50 equivalents of 5-(triethoxysilyl)-bicyclo[2.2.1]hept-2-ene with 5 equivalents of ^{Ac}FcBAr^{F} at 70°C for 1 hour. Hexamethylbenzene was used as an internal standard. No polymeric material was obtained upon pouring the reaction solution into methanol.

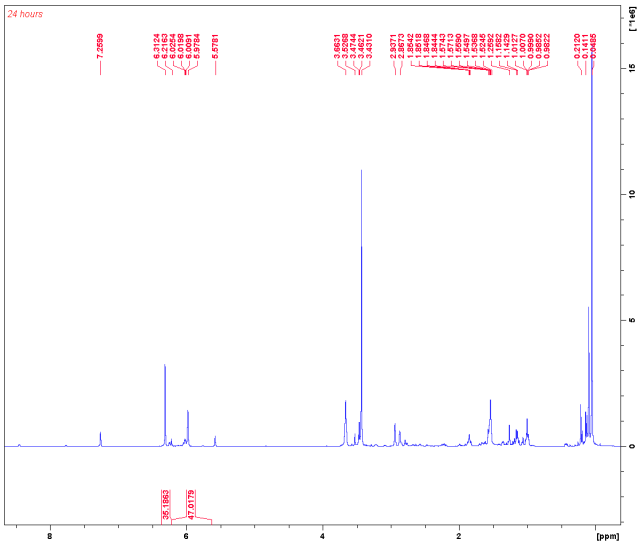

Figure B27. Control experiment of 50 equivalents of 5-(trimethylsilyl)-bicyclo[2.2.1]hept-2-ene with 5 equivalents of ^{Ac}FcBAr^{F} at 70°C for 24 hours. 1,3,5-Trimethoxybenzene was used as an internal standard. No polymeric material was obtained upon pouring the reaction solution into methanol.

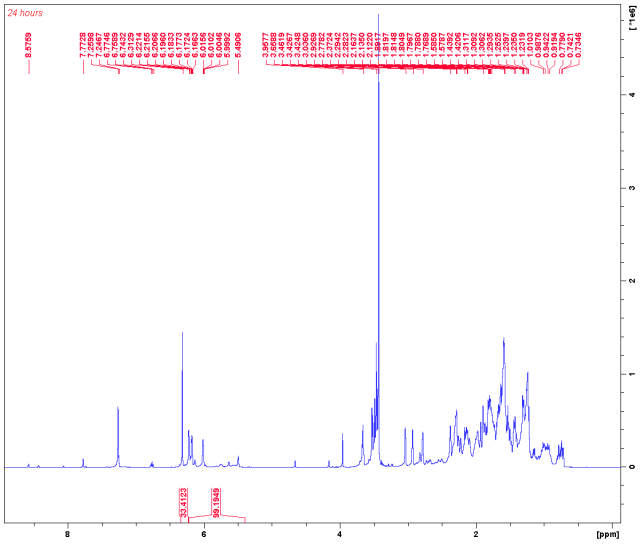

Figure B28. Control experiment of 50 equivalents of 5-cyclohexyl-bicyclo[2.2.1]hept-2-ene with 5 equivalents of ^{Ac}FcBAr^{F} at 100°C for 24 hours. 1,3,5-Trimethoxybenzene was used as an internal standard. No polymeric material was obtained upon pouring the reaction solution into methanol.

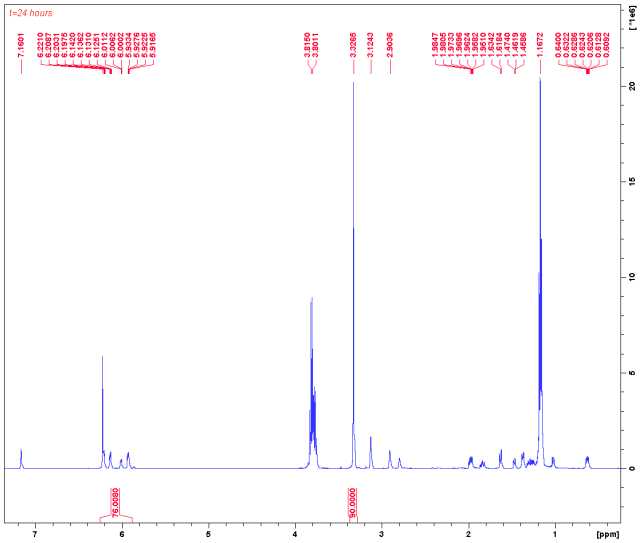

Figure B29. Control experiment of 50 equivalents of 5-(triethoxysilyl)-bicyclo[2.2.1]hept-2-ene with 5 equivalents of $CoCp_2$ at 70 °C for 24 hours. 1,3,5-Trimethoxybenzene was used as an internal standard. No polymeric material was obtained upon pouring the reaction solution into methanol.

3.6.2 Cyclic voltammetry data

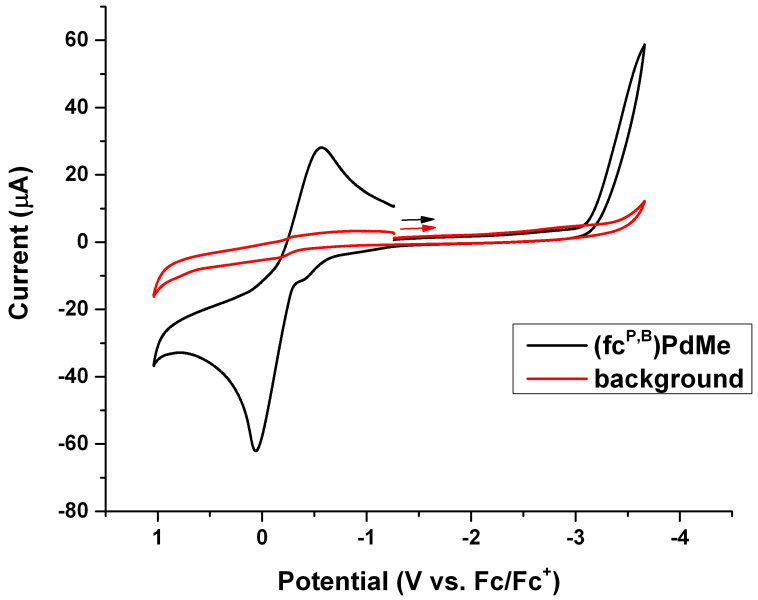

Figure B30. Cyclic voltammograms recorded with a glassy carbon electrode at 100 mV/s in THF, 0.10 M [TBA][PF_6] containing (a) no ($fc^{P,B}$)PdMe, (b) 5.0 mM ($fc^{P,B}$)PdMe.

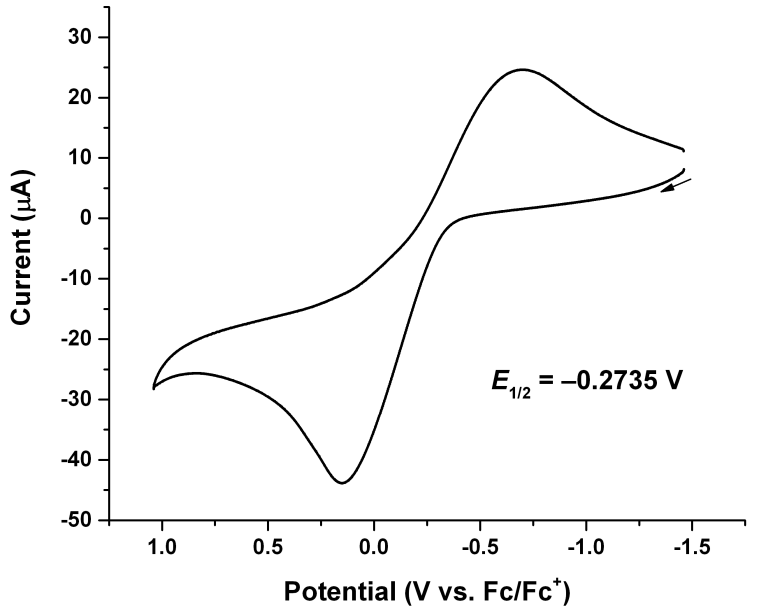

Figure B31. Cyclic voltammogram recorded with a glassy carbon electrode at 100 mV/s in THF, 0.10 M [TBA][PF_6] containing 5.0 mM ($fc^{P,B}$)PdMe. $E_{1/2}$ = -0.2735 V, i_{pa}/i_{pc} = 0.91.

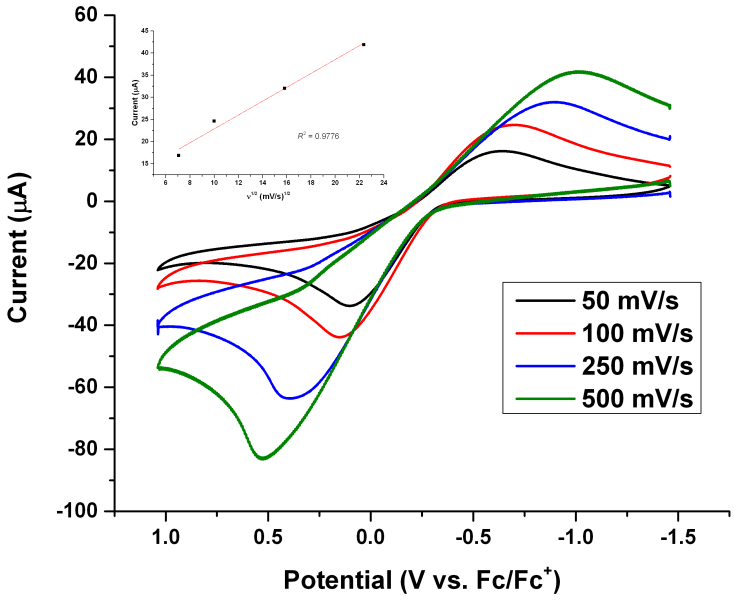

Figure B32. Cyclic voltammograms recorded with a glassy carbon electrode at 50, 100, 250, and 500 mV/s in THF, 0.10 M [TBA][PF_6] containing 5.0 mM ($fc^{P,B}$)PdMe.

3.6.3 Gel Permeation Chromatography

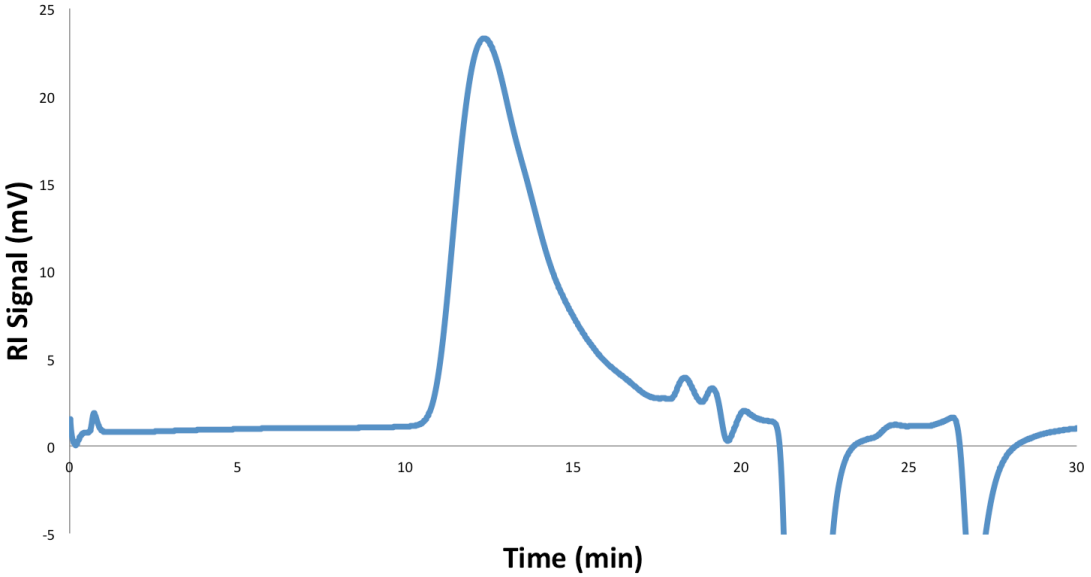

Figure B33. Polymerization of 81 equivalents of 5-butyl-bicyclo[2.2.1]hept-2-ene; M_n = 30648, M_w = 111148, $Đ$ = 3.627.

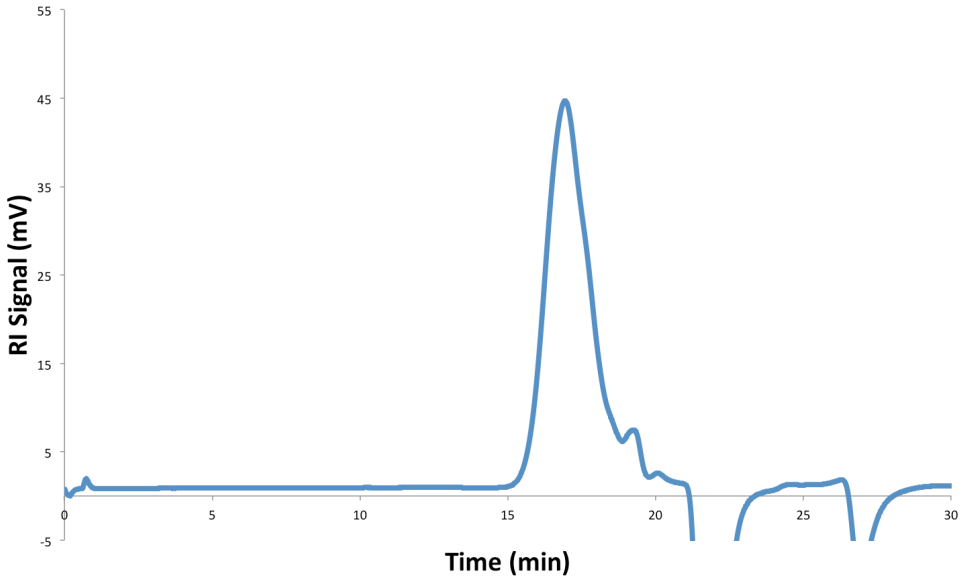

Figure B34. Polymerization of 25 equivalents of 5-cyclohexyl-bicyclo[2.2.1]hept-2-ene; M_n = 1439, M_w = 2105, $Đ$ = 1.462.

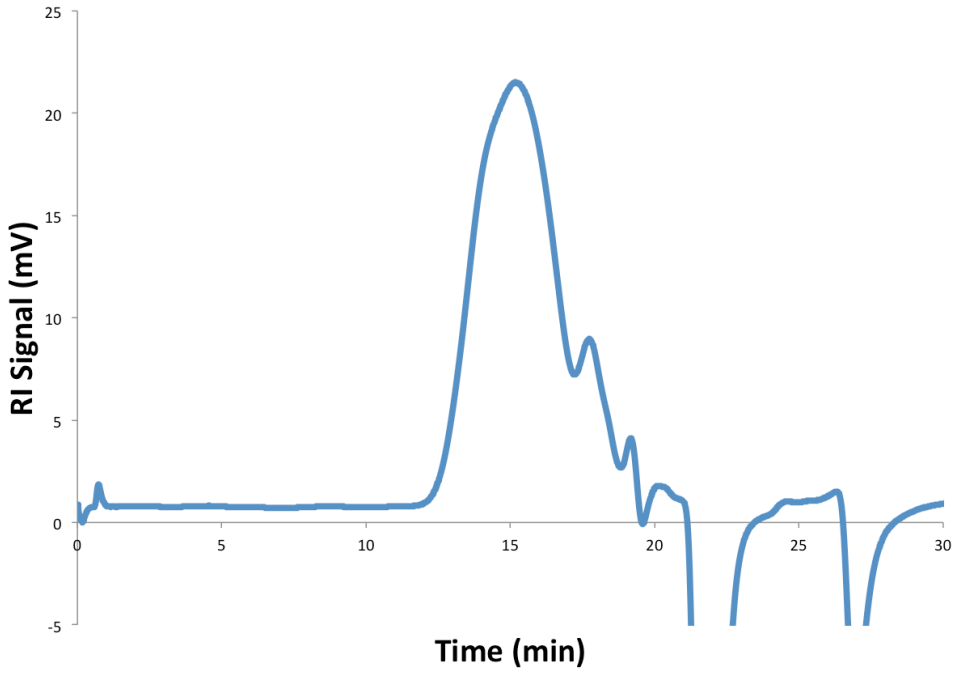

Figure B35. Polymerization of 35 equivalents of 5-(trimethylsilyl)-bicyclo[2.2.1] hept-2-ene; M_n = 8849, M_w = 18595, $Đ$ = 2.101.

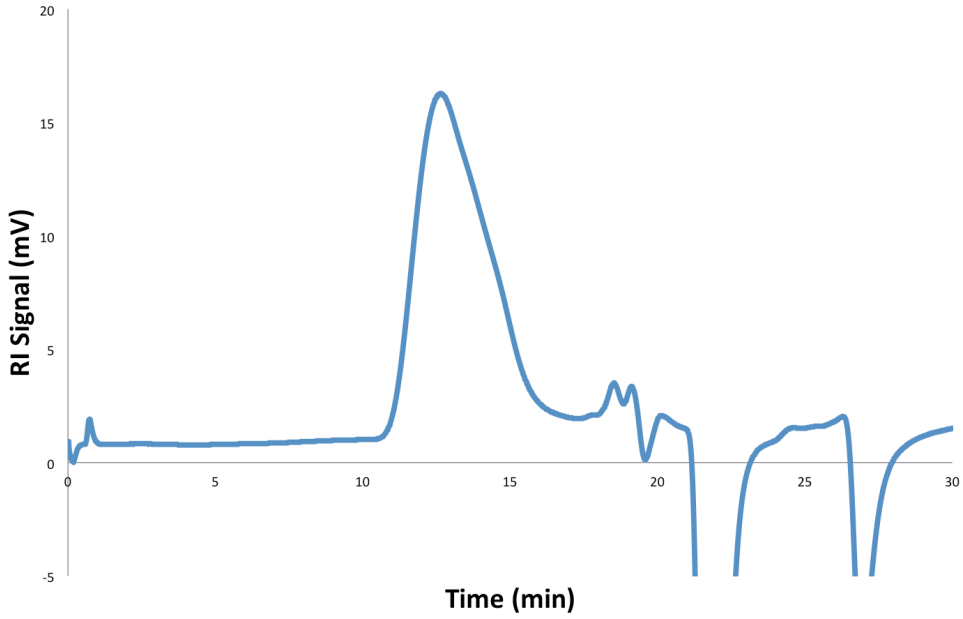

Figure B36. Polymerization of 58 equivalents of 5-(triethoxysilyl)-bicyclo[2.2.1] hept-2-ene; M_n = 37016, M_w = 93447, $Đ$ = 2.525.

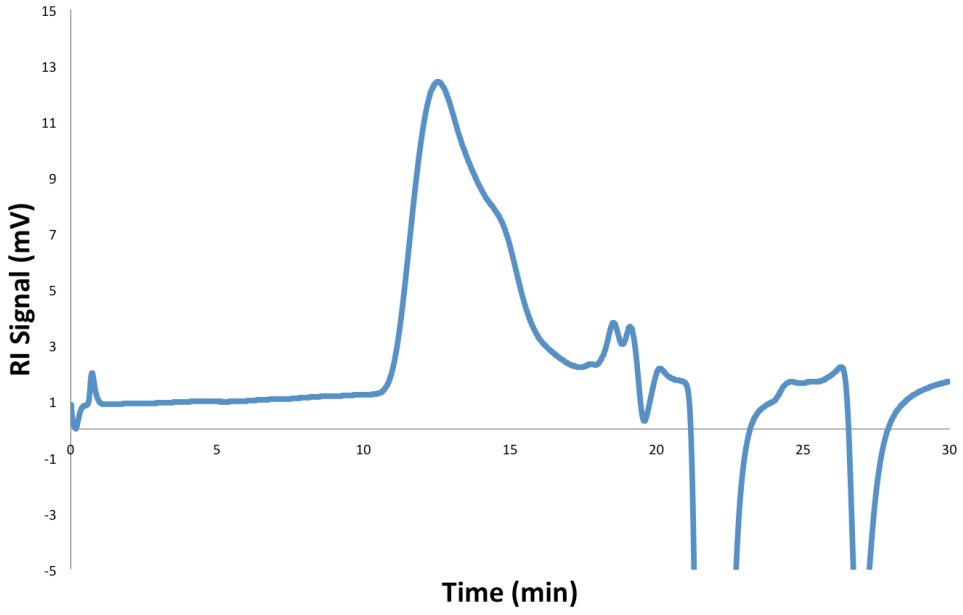

Figure B37. In situ redox controlled polymerization of 51 equivalents of 5-(triethoxysilyl)-bicyclo[2.2.1]hept-2-ene; M_n = 37016, M_w = 93447, $Đ$ = 2.525.

3.6.4 X-ray crystallographic data

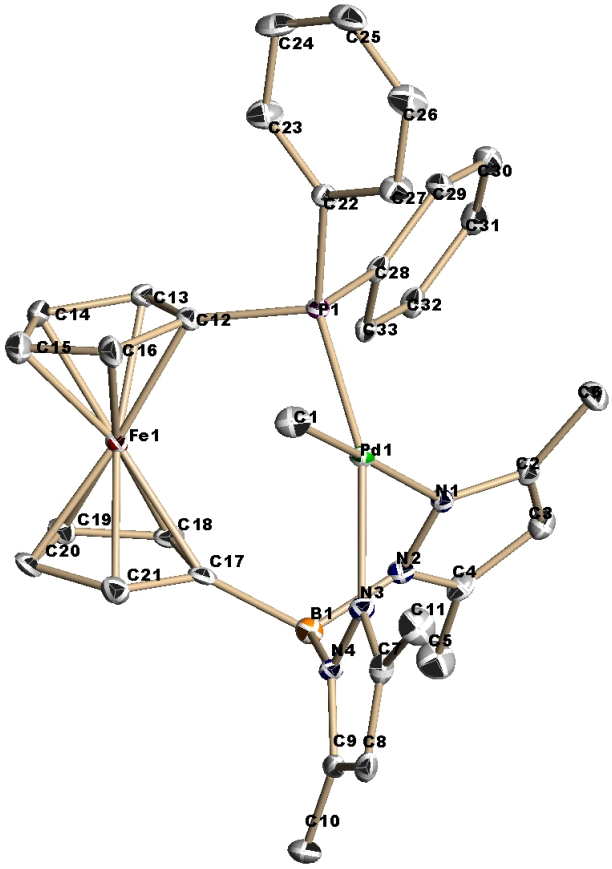

Figure B38. Molecular structure drawing of ($fc^{P,B}$)PdMe with thermal ellipsoids at 50% probability; hydrogen atoms are omitted for clarity.

Crystal data for $C_{36.50}H_{39}BFeN_4PPd$; M_r = 737.75; orthorhombic; space group Pbcn; *a* = 24.688(2) Å; *b* = 17.7025(14) Å; *c* = 16.2002(13) Å; α = 90°; β = 90°; γ = 90°; V = 7080.0(10) $Å^3$; Z = 8; T = 100(2) K; λ = 0.71073 Å; μ = 0.993 mm^{-1}; d_{calc} = 1.384 $g{\cdot}cm^{-3}$; 86374 reflections collected; 8931 unique (R_{int} = 0.0267); giving R_1 = 0.0271, wR_2 = 0.0652 for 8032 data with [I>2σ(I)] and R_1 = 0.0328, wR_2 = 0.0676 for all 8931 data. Residual electron density ($e^{-}{\cdot}Å^{-3}$) max/min: 0.903/-0.507.

3.7 References

1. He, X.; Liu, Y.; Chen, L.; Chen, Y.; Chen, D., *J. Polym. Sci. A Polym. Chem.* **2012,** *50*, 4695.

2. Janiak, C.; Lassahn, P. G., *J. Mol. Catal. A: Chem.* **2001,** *166*, 193.

3. Ahmed, S.; Bidstrup, S. A.; Kohl, P. A.; Ludovice, P. J., *J. Phys. Chem. B* **1998,** *102*, 9783.

4. Grove, N. R.; Kohl, P. A.; Bidstrup Allen, S. A.; Jayaraman, S.; Shick, R., *J. Polym. Sci., Part B: Polym. Phys.* **1999,** *37*, 3003.

5. Heinz, B. S.; Alt, F. P.; Heitz, W., *Macromol. Rapid Comm.* **1998,** *19*, 251.

6. Haselwander, T. F. A.; Heitz, W.; Krügel, S. A.; Wendorff, J. H., *Macromol. Chem. Phys.* **1996,** *197*, 3435.

7. Blank, F.; Janiak, C., *Coord. Chem. Rev.* **2009,** *253*, 827.

8. Wu, Q.; Lu, Y., *J. Polym. Sci., Part A: Polym. Chem.* **2002,** *40*, 1421.

9. Huo, P.; Liu, W.; He, X.; Wei, Z.; Chen, Y., *Polym. Chem.* **2014,** *5*, 1210.

10. Blank, F.; Vieth, J. K.; Ruiz, J.; Rodríguez, V.; Janiak, C., *J. Organomet. Chem.* **2011,** *696*, 473.

11. Lee, E. J.; Won, W. K.; Lee, B.; Kye, Y. H.; Lee, I. M., *Bull. Korean Chem. Soc.* **2013,** *34*, 2720.

12. Kang, M.; Sen, A., *Organometallics* **2004,** *23*, 5396.

13. Hu, T.; Li, Y.-G.; Li, Y.-S.; Hu, N.-H., *J. Mol. Catal. A: Chem.* **2006,** *253*, 155.

14. Tian, J.; Zhu, H.; Liu, J.; Chen, D.; He, X., *Appl. Organomet. Chem.* **2014,** *28*, 702.

15. Hennis, A. D.; Polley, J. D.; Long, G. S.; Sen, A.; Yandulov, D.; Lipian, J.; Benedikt, G. M.; Rhodes, L. F.; Huffman, J., *Organometallics* **2001,** *20*, 2802.

16. Walter, M. D.; Moorhouse, R. A.; Urbin, S. A.; White, P. S.; Brookhart, M., *J. Am. Chem. Soc.* **2009,** *131*, 9055.

17. Casares, J. A.; Espinet, P.; Salas, G., *Organometallics* **2008,** *27*, 3761.

18. Yamashita, M.; Takamiya, I.; Jin, K.; Nozaki, K., *Organometallics* **2006,** *25*, 4588.

19. Blank, F.; Scherer, H.; Janiak, C., *J. Mol. Cat. A: Chem.* **2010,** *330*, 1.

20. Blank, F.; Scherer, H.; Ruiz, J.; Rodriguez, V.; Janiak, C., *Dalton Trans.* **2010,** *39*, 3609.

21. Mehler, C.; Risse, W., *Macromolecules* **1992,** *25*, 4226.

22. Mehler, C.; Risse, W., *Makromol. Chem.-Rapid* **1991,** *12*, 255.

23. Heinz, B. S.; Heitz, W.; Krügel, S. A.; Raubacher, F.; Wendorff, J. H., *Acta Polym.* **1997,** *48*, 385.

24. Kim, D.-G.; Bell, A.; Register, R. A., *ACS Macro Lett.* **2015,** *4*, 327.

25. Xiang, P.; Ye, Z., *J. Organomet. Chem.* **2015,** *798, Part 2*, 429.

26. Commarieu, B.; Claverie, J. P., *Chem. Sci.* **2015,** *6*, 2172.

27. Mecking, S.; Keim, W., *Organometallics* **1996,** *15*, 2650.

28. Allgeier, A. M.; Mirkin, C. A., *Angew. Chem. Int. Ed.* **1998,** *37*, 894.

29. Wang, X.; Brosmer, J. L.; Thevenon, A.; Diaconescu, P. L., *Organometallics* **2015,** *34*, 4700.

30. Quan, S. M.; Diaconescu, P. L., *Chem. Commun.* **2015,** *51*, 9643

31. Wang, X.; Thevenon, A.; Brosmer, J. L.; Yu, I.; Khan, S. I.; Mehrkhodavandi, P.; Diaconescu, P. L., *J. Am. Chem. Soc.* **2014,** *136*, 11264.

32. Broderick, E. M.; Guo, N.; Wu, T.; Vogel, C. S.; Xu, C.; Sutter, J.; Miller, J. T.; Meyer, K.; Cantat, T.; Diaconescu, P. L., *Chem. Commun.* **2011,** *47*, 9897.

33. Broderick, E. M.; Guo, N.; Vogel, C. S.; Xu, C.; Sutter, J.; Miller, J. T.; Meyer, K.; Mehrkhodavandi, P.; Diaconescu, P. L., *J. Am. Chem. Soc.* **2011,** *133*, 9278.

34. Ladipo, F. T.; Anderson, G. K., *Organometallics* **1994,** *13*, 303.

35. Salo, E. V.; Guan, Z., *Organometallics* **2003,** *22*, 5033.

36. Yang, L.; Powell, D. R.; Houser, R. P., *Dalton Trans.* **2007**, 955.

37. Abubekerov, M.; Diaconescu, P. L., *Inorg. Chem.* **2015,** *54*, 1778.

38. Waltman, A. W.; Grubbs, R. H., *Organometallics* **2004,** *23*, 3105.

39. Rheingold, A. L.; Liable-Sands, L. M.; Incarvito, C. L.; Trofimenko, S., *J. Chem. Soc., Dalton Trans.* **2002**, 2297.

40. Delis, J. G. P.; Aubel, P. G.; Vrieze, K.; van Leeuwen, P. W. N. M.; Veldman, N.; Spek, A. L.; van Neer, F. J. R., *Organometallics* **1997,** *16*, 2948.

41. Delis, J. G. P.; Aubel, P. G.; van Leeuwen, P. W. N. M.; Vrieze, K.; Veldman, N.; Spek, A. L., *J. Chem. Soc., Chem. Commun.* **1995**, 2233.

42. Yamamoto, Y.; Tanase, T.; Ukaji, H.; Hasegawa, M.; Igoshi, T.; Yoshimura, K., *J. Organomet. Chem.* **1995,** *498*, C23.

43. Otto, S., *J. Chem. Cryst.* **2001,** *31*, 185.

44. Hennis, A. D.; Polley, J. D.; Long, G. S.; Sen, A.; Yandulov, D.; Lipian, J.; Benedikt, G. M.; Rhodes, L. F.; Huffman, J., *Organometallics* **2001,** *20*, 2802.

45. Miller, T. M.; Ahmed, K. J.; Wrighton, M. S., *Inorg. Chem.* **1989,** *28*, 2347.

46. Fabrizi de Biani, F.; Jäkle, F.; Spiegler, M.; Wagner, M.; Zanello, P., *Inorg. Chem.* **1997,** *36*, 2103.

47. Lassahn, P.-G.; Lozan, V.; Wu, B.; Weller, A. S.; Janiak, C., *Dalton Trans.* **2003**, 4437.

48. Gaylord, N. G.; Mandal, B. M.; Martan, M., *J. Polym. Science: Polym. Lett. Ed.* **1976,** *14*, 555.

49. Pangborn, A. B.; Giardello, M. A.; Grubbs, R. H.; Rosen, R. K.; Timmers, F. J., *Organometallics* **1996,** *15*, 1518.

CHAPTER 4: PREPARATION OF MULTIBLOCK COPOLYMERS VIA STEP-WISE ADDITION POLYMERIZATION OF L-LACTIDE AND TRIMETHYLENE CARBONATE

4.1 Introduction

Growing concerns over the environmental damage caused by petroleum-based plastic waste[1] and the associated health effects due to petroleum processing[2] necessitate a shift to environmentally benign commodity plastics.[3-6] As a result, biodegradable plastics obtained from bio-renewable sources, in particular poly(L-lactide) (PLA),[7-8] have received much attention in the past decades.[3, 9-11] Currently, applications of PLA vary widely from specialty plastics in biomedical devices[12-15] to commodity plastics in food packaging.[14-16] The mechanical properties of PLA resemble those of polystyrene;[11] it is a hard material with good tensile strength and high modulus.[10] Unfortunately, due to its low toughness, its overall applications are limited.[17] A potential way of enhancing the toughness of PLA is through copolymerization with 1,3-trimethylene carbonate (TMC), which gives a soft and amorphous homopolymer.[18] In this regard, Guerin et al.[19] and Leng et al.[20] performed extensive studies on the influence of block TMC incorporation into PLA. These reports concluded that a ca. 20% weight of TMC into TMC/LA block copolymers is optimal. The resulting thermoplastic elastomers,[19-20] of PLA-*b*-PTMC and PLA-*b*-PTMC-*b*-PLA compositions,[19] were shown to display both moderate elongation at break and moderate Young's modulus values. However, these copolymers were always prepared via initial TMC polymerization followed by the sequential addition of LA, in the presence of various organic and metal-based catalysts,[19-29] but not the reverse. As a result, only a small number of LA/TMC block combinations have been investigated and the influence of

more complicated block structures on the mechanical properties of these copolymers is rather underexplored.[19] In the course of studying the redox switchable reactivity[30-44] of the ferrocene-chelating heteroscorpionate zinc complex {[fc(PPh_2)(BH[(3,5-$Me)_2$pz]$_2$)]Zn(μ-OCH_2Ph)}$_2$ ([($fc^{P,B}$)Zn(μ-OCH_2Ph)]$_2$)[35] toward various monomers, we discovered that it can perform the ring-opening polymerization (ROP) of LA and TMC regardless of the addition order. Based on our interest in the ROP of cyclic esters and carbonates, we set out to prepare multiblock copolymers of L-lactide and 1,3-trimethylene carbonate to examine their physical, thermal, and mechanical properties, and we discuss our results herein.

4.2 Solution state behavior of the zinc benzoxide complex

Because of the unique behavior of [($fc^{P,B}$)Zn(μ-OCH_2Ph)] toward the ROP of LA and TMC, i.e., its ability to polymerize TMC after LA, we began by studying the solid state molecular structure and the solution behavior of the metal complex. The isolation of [($fc^{P,B}$)Zn(μ-OCH_2Ph)]$_2$ as yellow crystals in 68.5% yield (Eq 1) was achieved via the addition of ($fc^{P,B}$)ZnCl·(C_7H_8)[35] to in situ generated $KOCH_2Ph$ in THF.

The solid state molecular structure of [($fc^{P,B}$)Zn(μ-OCH_2Ph)]$_2$ was determined using single-crystal X-ray diffraction (Figure 4-1). The coordination environment around each zinc center is a distorted tetrahedron ($\tau = 0.75$).[45] The supporting ligands are bound in a κ^2 fashion via the pyrazole nitrogens, while the phosphine moieties are not coordinated and the benzoxide groups are in a bridging position between the two metal centers.

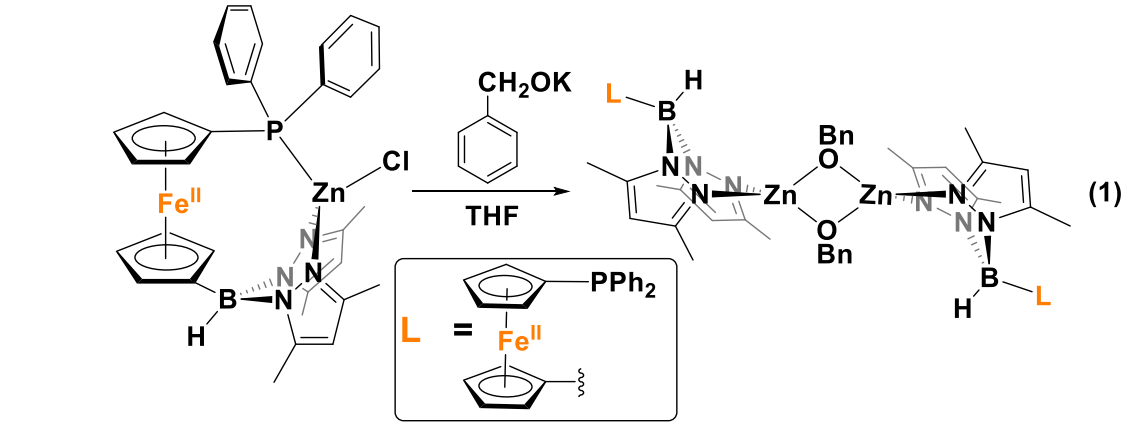

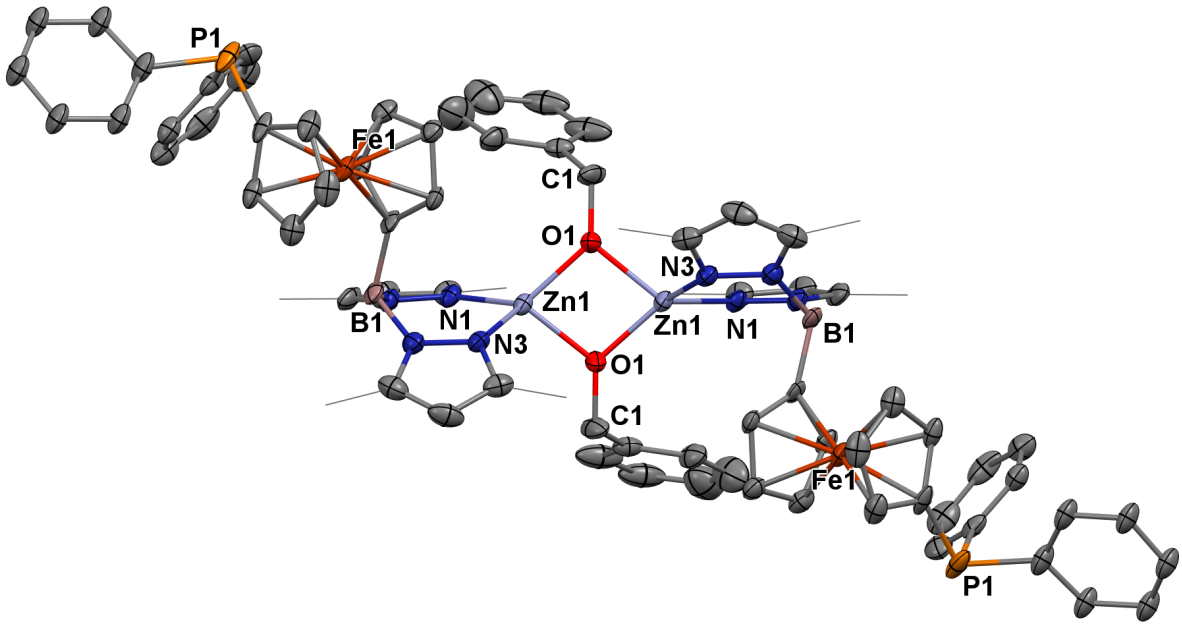

Figure 4-1. Molecular structure drawing of $[(fc^{P,B})Zn(\mu\text{-}OCH_2Ph)]_2$ with thermal ellipsoids at 50% probability; hydrogen atoms and disordered counterparts are omitted for clarity.

In solution, a single species is observed by NMR spectroscopy (Figures C1-4), with the resonance signals similar to those of previously reported $(fc^{P,B})Zn$ complexes.[35] For example, the $^{31}P\{^1H\}$ NMR spectrum of $[(fc^{P,B})Zn(\mu\text{-}OCH_2Ph)]_2$ shows a singlet at δ = -15.5 ppm. Similar

chemical shifts of δ = -16.4 and -15.5 ppm were observed for a coordinated phosphine in ($fc^{P,B}$)ZnCl and a free phosphine in fc(PPh_2)[$B(OMe_3)_2$], respectively.[35] Such minor differences in the $^{31}P\{^1H\}$ NMR spectra between free and zinc(II)-coordinated phosphines are commonly observed and are attributed to weak interactions between the soft phosphine ligands and the oxophilic zinc(II) centers.[46] Diffusion ordered spectroscopy (DOSY) NMR[47] experiments were conducted with ($fc^{P,B}$)ZnCl and [($fc^{P,B}$)Zn(μ-OCH_2Ph)]$_2$ (Figures C15-16) to determine if the latter exists as a dimer in solution. Based on the Stokes-Einstein relationship,[47] the ratio of the radii of [($fc^{P,B}$)Zn(μ-OCH_2Ph)]$_2$ to ($fc^{P,B}$)ZnCl is 1.63. This value is somewhat below the expected value of 2 for the dimer, as derived from the comparison of volumes from the solid state structures. However, ^1H Nuclear Overhauser Effect Spectroscopy (NOESY) studies of [($fc^{P,B}$)Zn(μ-OCH_2Ph)]$_2$ show a binding motif similar to that observed in the solid state structure. Interactions between the protons of the pyrazole methyl groups and the benzoxide ligand are observed in the 2D plot, while the interactions between the phosphine phenyl groups and the benzoxide are not observed (Figures C10-11). Additionally, a variable temperature NMR study was performed. The spectra of [($fc^{P,B}$)Zn(μ-OCH_2Ph)]$_2$ show no significant changes in the range of 298 – 352 K (Figure C9), suggesting that the speciation of the complex remains the same in solution even at elevated temperatures. The addition of an excess of a hard Lewis base, such as pyridine, to [($fc^{P,B}$)Zn(μ-OCH_2Ph)]$_2$ in C_6D_6 yields a simple mixture of the two compounds at ambient temperature (Figure C14). A lack of an interaction between the zinc complex and pyridine suggests that Lewis bases, similar to monomers prior to being ring opened, do not disrupt the dimeric structure of the zinc complex.

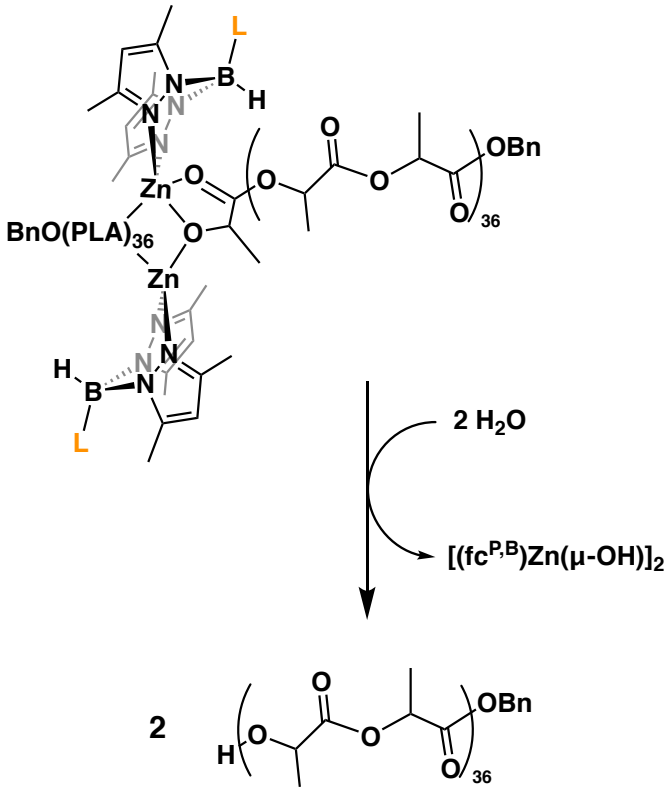

Figure 4-2. Illustration of L-lactide polymerization quenching undertaken for the DOSY NMR experiment.

The stability of $[(fc^{P,B})Zn(\mu\text{-}OCH_2Ph)]_2$ was evaluated both in the presence and absence of a substrate. In the absence of a monomer, $[(fc^{P,B})Zn(\mu\text{-}OCH_2Ph)]_2$ slowly decomposes in benzene at ambient temperature, reaching 7.0% decomposition after 24 h (Figure C26). Heating the compound at 100 °C in benzene results in 34% decomposition after 1.5 h (Figure C27). However, in the presence of a monomer, no decomposition is observed, even at elevated temperatures (70 °C) for 3 h (Figure C28).

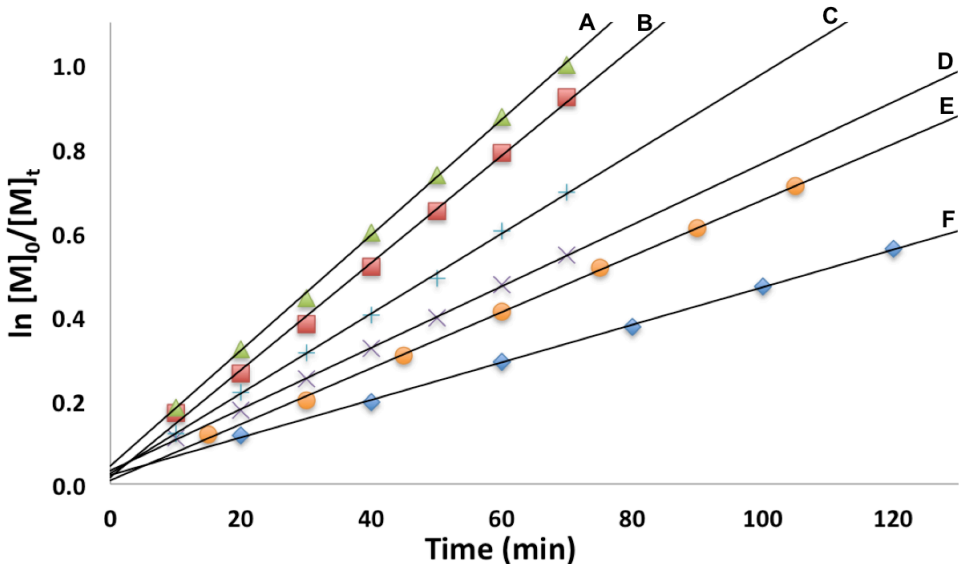

Figure 4-3. Semilogorithmic plots of L-lactide conversion with time in C_6H_6 at 70 °C with $[(fc^{P,B})Zn(\mu\text{-}OCH_2Ph)]_2$ as a catalyst ($[LA]_0$ = 0.313 M: A, [Zn] = 4.69 mM, [LA]/[Zn] = 67; B, [Zn] = 3.91 mM, [LA]/[Zn] = 80; C, [Zn] = 3.13 mM, [LA]/[Zn] = 100; D, [Zn] = 2.34 mM, [LA]/[Zn] = 133; E, [Zn] = 1.88 mM, [LA]/[Zn] = 167; F, [Zn] = 1.56 mM, [LA]/[Zn] = 200).

Next, we looked at the identity of the catalytically active species in the case of each monomer. In order to evaluate if it remains a dimer during polymerizations, an attempt to characterize the product corresponding to the ring-opening of a single equivalent of monomer was made. Due to its slow rate of polymerization at ambient temperature, L-lactide was chosen as the model substrate. On an NMR scale, addition of two equivalents of L-lactide to $[(fc^{P,B})Zn(\mu\text{-}OCH_2Ph)]_2$ resulted in the formation of a single major species (Figure C12) after two hours at ambient temperature. Performing a DOSY NMR experiment on this product yielded a slower diffusion rate than for the parent complex (Figure C17), consistent with the retention of the dimeric state post incorporation of one equivalent of L-lactide per metal center. These results are reproduced during quenching experiments of L-lactide polymerizations (Figure 4-2). A

DOSY NMR experiment performed with $[(fc^{P,B})Zn(PLA)_{36}(OCH_2Ph)]_2$ yielded a diffusion rate of 1.04×10^{-6} m/s^2 (Figure C20). Water was then added to the same sample resulting in the hydrolysis of the polymer chains from the zinc catalyst and the formation of $[(fc^{P,B})Zn(\mu\text{-}OH)]_2$. The free polymers, $PhCH_2O(PLA)_{36}H$, displayed a diffusion rate of 2.00×10^{-6} m/s^2 (Figure C21). Since the diffusion rate of a molecule is inversely proportional to its hydrodynamic radius, two polymer chains bound together by a catalyst will diffuse at half the rate of a single polymer chain. The doubling of the diffusion rate upon hydrolysis of the active polymerization species is consistent with the liberation of polymer chains from a dimeric species. Similar results were obtained in the case of TMC polymerization (Figures C18-19) suggesting that the catalytically active species is a dimer in both cases.

The conversion of L-lactide was monitored by ^{1}H NMR spectroscopy for varying concentrations of monomer, in benzene at 70 °C. In all cases, first-order kinetics were observed via the semilogarithmic plots of several polymerizations (Figure 4-3). The order in pre-catalyst was determined via the logarithmic plot of the metal complex concentration against k_{app} (Figure 4-4) displaying first-order kinetics and yielding the following rate law (Eq 2):

$$-d[LA]/dt = k[Zn_2]^1[LA]^1 \qquad (2)$$

A first-order in both monomer and pre-catalyst is commonly observed for metal mediated ring-opening polymerizations. In particular, a clear order in catalyst is consistent with a well-behaved system in solution and the retention of the dimeric state by the catalyst throughout the polymerization process.[48-49]

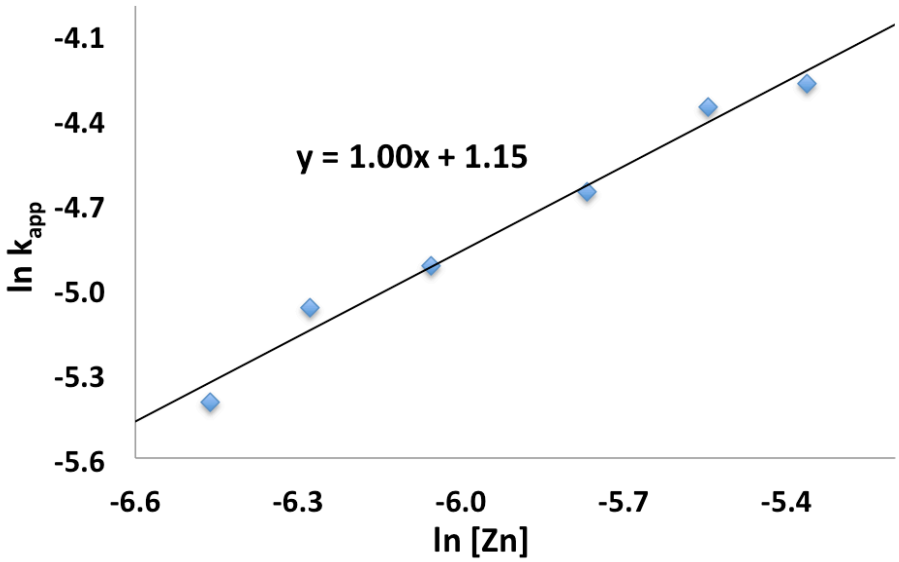

Figure 4-4. Plot of ln k_{app} vs. ln [Zn] for the polymerization of L-lactide with [($fc^{P,B}$)Zn(μ-OCH_2Ph)]$_2$ as a catalyst (C_6H_6 , 70 °C, $[LA]_0$ = 0.313 M).

4.3 Preparation and determination of physical, mechanical, and thermal properties of the multiblock copolymers

We looked at the preparation of LA/TMC homopolymers as well as, in keeping with the ca. 20% by weight optimal composition, the preparation of a variety of multiblock copolymers. In all cases, the multiblock copolymers were prepared via the sequential addition of monomer to the growing polymer chain. Utilizing our system, the copolymerization of TMC and LA is not limited by the order of monomer addition. The percent by weight composition of TMC was kept within 15-20%, and the number average molecular weight was kept at ca. 50,000 g/mol. We reasoned that attempting to maintain these variable relatively constant would allow us to probe the influence that the copolymer microstructure has on the physical properties of the corresponding materials.

Polymerization of ca. 100 equivalents of TMC (Table 4-1, entry 2) reaches completion at room temperature within one hour. Polymerization of L-lactide at room temperature is much slower and requires up to 24 hours for the same number of equivalents to reach completion. Raising the temperature to 70 °C results in a complete conversion within an hour. In both cases, the polymerizations are well controlled. The molecular weights increase with conversion while retaining low dispersity (*Đ*) values (Figures C43-44 and Tables C1-2).

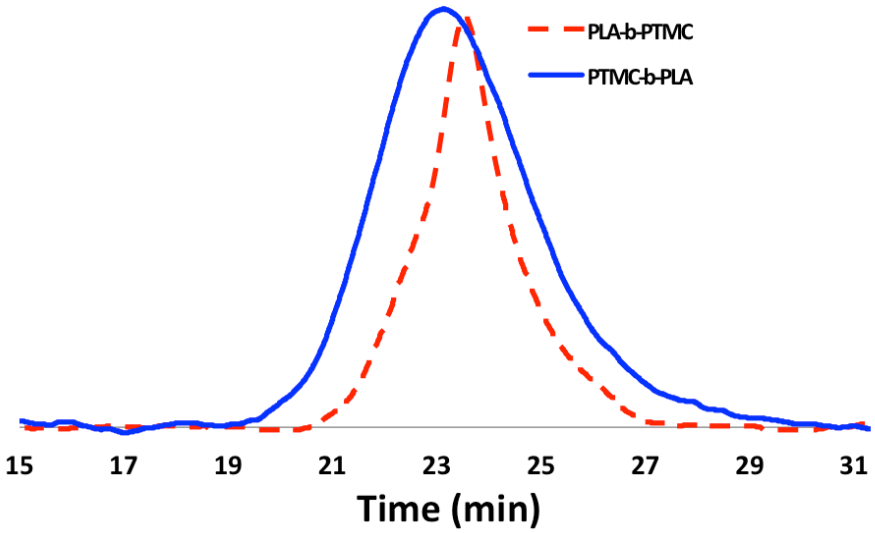

Figure 4-5. GPC traces of PLA-*b*-PTMC (Table 4-1, entry 3) and PTMC-*b*-PLA (Table 4-1, entry 4) copolymers.

Although the homopolymerization of TMC proceeds quickly at ambient temperature, elevated temperatures are required to polymerize it after L-lactide due to the nature of the intermediate formed after the ring-opening of lactide that features a five-membered chelate.[30, 50-55] This difference in shifting the polymerization of TMC from room temperature, as in the case of PLA-*b*-PTMC (Table 4-1, entry 3), to elevated temperatures, as in the case of PTMC-*b*-PLA

(Table 4-1, entry 4), manifests itself in the broadening of the molecular weight distributions (Figure 4-5). As a result, the dispersity values are larger for the copolymers subjected to TMC polymerization at elevated temperatures, ranging from 1.45 to 1.69 (Table 4-1, entries 4-9), then for the polymers that were not (Table 4-1, entries 2-3).

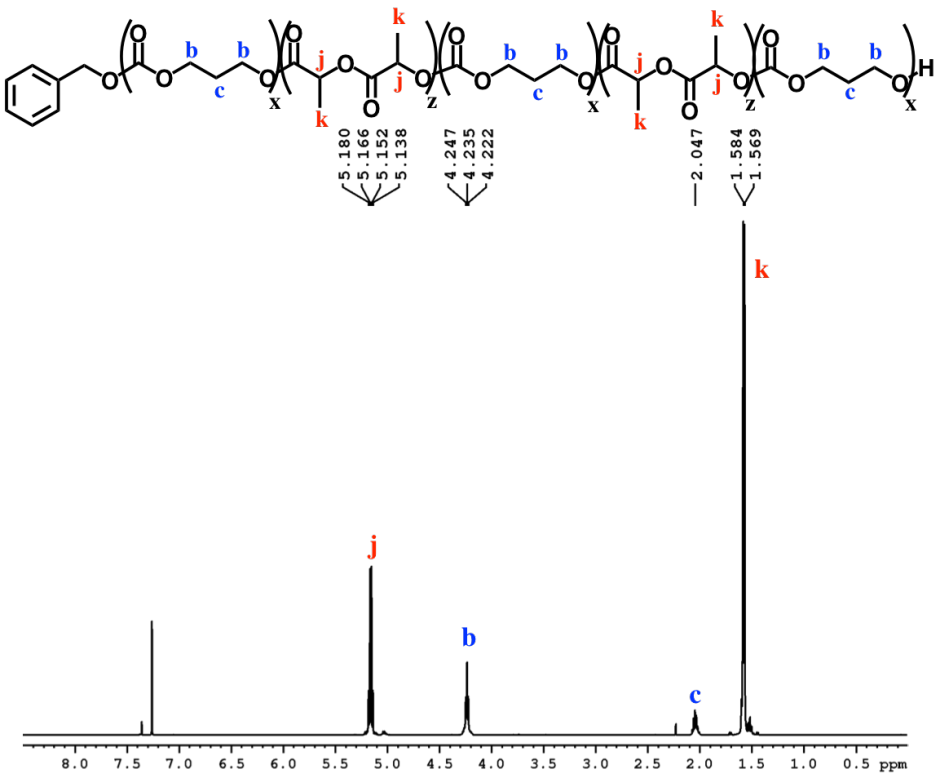

Figure 4-6. ^{1}H NMR spectrum ($CDCl_3$, 500 MHz, 298 K) of PTMC-b-PLA-b-PTMC-b-PLA-b-PTMC (Table 4-1, entry 8).

The block structures of the polymers are consistent with observations from the ^{1}H NMR spectra. In all cases, the copolymers appear as mixtures of the corresponding homopolymers (Figures 4-6 and C31-C40), a defining characteristic of true block copolymers.[20] Alternatively, both gradient and random block copolymers of TMC and LA yield broadened peaks for PTMC

and a distribution of peaks in the methine region of PLA.[20] The junctions of the copolymer[19, 56] can also be clearly observed in the ^{13}C NMR spectrum of the pentablock copolymers (Figures 4-7 and C41).[19-20] DOSY NMR experiments carried out with the triblock and pentablock copolymers (Figures C22-25) show the same diffusion rate for both the PLA and the PTMC segments in all cases, further supporting a block copolymer formation. Additionally, ^{1}H NMR spectra of aliquots collected during the preparation of the PLA-*b*-PTMC-*b*-PLA-*b*-PTMC-*b*-PLA copolymer show the stepwise growth of each block (Figure C42). Similarly, the corresponding GPC traces of the same aliquots show an increase in molecular weight with every additional block (Figure 4-8). The benzoxide end group is clearly observed and diffuses at the same rate as the polymers in DOSY NMR spectra for both homopolymers, both in the case of the polymers still attached to the catalyst and in free polymers (Figures C18-21). The downfield shift in ^{1}H NMR spectra of the benzoxide methylene protons from 4.03 ppm in the parent complex to 4.72 ppm and 4.94 ppm in the ring-opening polymerization products of LA and TMC, respectively, is also indicative of the participation of the benzoxide group in the ring-opening process of the monomers.[19] The experiments described above suggest that these polymerization processes proceed via a living mechanism.[57]

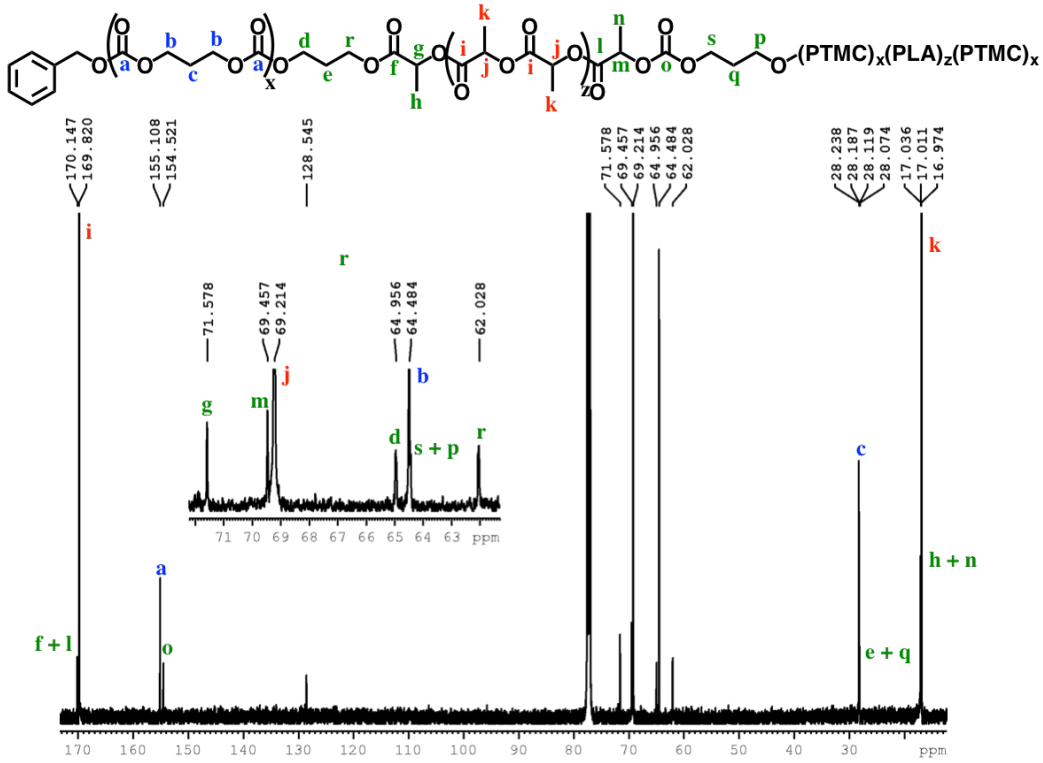

Figure 4-7. $^{13}C\{H\}$ NMR spectrum ($CDCl_3$, 500 MHz, 298 K) of the PTMC-b-PLA-b-PTMC-b-PLA-b-PTMC copolymer.

The differential scanning calorimetry (DSC) curves, obtained by Kevin Swartz, for the newly synthesized block copolymers display T_g and T_m values corresponding to isotactic PLA only (Table 4-2, Figures C60-66). Even at high sample loadings, the T_g corresponding to PTMC could not be detected (Figure C59), likely due to the relatively low content of PTMC in each copolymer. Only when we examined copolymers with a ca. 40% weight composition of TMC, could we detect the T_g corresponding to PTMC (Table 4-2, entry 11; Figure C69). In general, both the T_g and the T_m values are observed to decrease with the increasing number of blocks in the polymer. This depression of the T_g and T_m values is a known phenomenon in poly(L-lactide) chemistry;[58] the inclusion of amorphous polymer segments influences the crystallization behavior of the semicrystalline PLA fragments and improves the polymer chain mobility.[59-61]

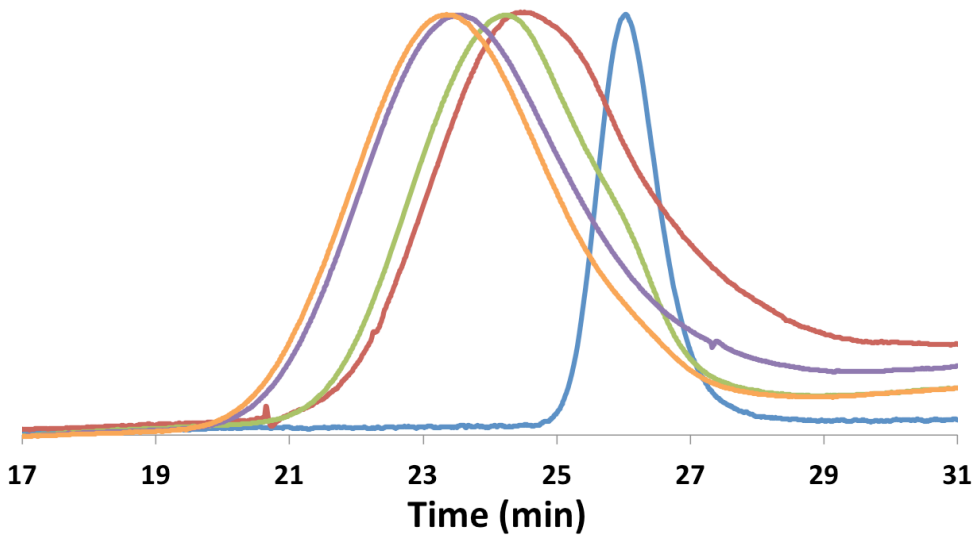

Figure 4-8. GPC traces corresponding to the stepwise preparation of PLA-*b*-PTMC-*b*-PLA-*b*-PTMC-*b*-PLA (M_n are reported in 10^3 g/mol; $Đ = M_w/M_n$): PLA (blue, M_n = 13.5, $Đ$ = 1.09); PTMC-*b*-PLA (red, M_n = 20.0, $Đ$ = 1.25); PLA-*b*-PTMC-*b*-PLA (green, M_n = 32.9, $Đ$ = 1.29); PTMC-*b*-PLA-*b*-PTMC-*b*-PLA (purple, M_n = 40.0, $Đ$ = 1.42); PLA-*b*-PTMC-*b*-PLA-*b*-PTMC-*b*-PLA (orange, M_n = 45.1, $Đ$ = 1.43).

Kevin Swartz and Zhixin Xie determined the mechanical properties of the polymers via dynamic mechanical analysis (DMA, Table 4-2, Figures C70-77) on multiple samples of each copolymer prepared via a solvent casting method. The PLA homopolymer displayed a Young's modulus of 1733 MPa and an elongation at break value of 11% (Table 4-2, entry 1). The copolymers display lower Young's modulus values than PLA, consistent with the addition of a soft PTMC fragment,[62] and, in most cases, display an order of magnitude improved elongation at break values. The diblock copolymers showed a lower Young's modulus and a minor improvement in the elongation at break of up to 23% (Table 4-2, entries 2-3). As the number of blocks increases to three or more, we observed a decrease in the Young's moduli while the

elongation at break values were drastically improved up to 250% (Table 4-2, entries 4-8). Therefore, increasing the number of blocks while maintaining a consistent monomer composition results in copolymers with improved elasticity. Particularly in the case of the pentablock copolymers, the materials possess low Young's moduli and high elongation at break values while maintaining thermal properties similar to the rest of the block copolymers.

Table 4-1: Addition copolymerization of L-lactide and 1,3-trimethylene carbonate.

Entry	Polymer	PTMC (wt%)	PLA (wt%)	Mn (TMC, NMR)	Mn (LA, NMR)	Mn (NMR)	Mn (GPC)	*Đ*
1	PLA	-	100	-	-	40.7	39.8	1.14
2	PTMC	100	-	-	-	10.4	9.0	1.01
3	PLA-*b*-PTMC	19	81	10.0	43.7	53.7	55.5	1.12
4	PTMC-*b*-PLA	17	83	8.0	39.5	47.5	47.0	1.60
5	PTMC-*b*-PLA-*b*-PTMC	18	82	8.7	40.8	49.5	43.2	1.67
6	PLA-*b*-PTMC-*b*-PLA	17	83	9.0	43.7	52.7	55.6	1.46
7	PLA-*b*-PTMC-*b*-PLA-*b*-PTMC	19	81	10.2	42.9	53.1	48.2	1.49
8	PTMC-*b*-PLA-*b*-PTMC-*b*-PLA-*b*-PTMC	18	82	9.8	45.2	55.0	58.9	1.49
9	PLA-*b*-PTMC-*b*-PLA-*b*-PTMC-*b*-PLA	19	81	10.0	42.3	52.3	53.2	1.69
10	PLA-*b*-PTMC-*b*-PLA	10	90	5.2	47.5	52.7	50.8	1.29
11	PLA-*b*-PTMC-*b*-PLA	30	70	15.9	36.8	52.7	48.9	1.42
12	PLA-*b*-PTMC-*b*-PLA	39	61	22.1	34.5	56.6	51.2	1.68

Conditions: benzene as a solvent (1.5 mL) and hexamethylbenzene as an internal standard. All experiments were performed at 70 °C, except for those corresponding to entry 2 and the first blocks of entries 3, 5, 7, and 8, which were performed at ambient temperature. The order of block preparation is illustrated from right to left in the final copolymer. The respective monomer loading (Figures C31-40) is distributed evenly between the blocks of each type. M_n are reported in 10^3 g/mol; $Đ = M_w/M_n$.

Table 4-2: Polymer thermal and mechanical properties.

Entry	Polymer structure	PTMC (wt%)	T_g[a] (°C)	T_g[a] (°C)	T_m[a] (°C)	E[b] (MPa)	σ[c] (MPa)	ε[d] (%)
1	PLA	0	-	55	173	1733 ± 108	49 ± 3	11 ± 4
2	PLA-*b*-PTMC	19	-	42	173	865 ± 85	36 ± 5	18 ± 3
3	PTMC-*b*-PLA	17	-	37	164	763 ± 135	37 ± 5	23 ± 4
4	PTMC-*b*-PLA-*b*-PTMC	18	-	35	161	521 ± 30	24 ± 2	250 ± 32
5	PLA-*b*-PTMC-*b*-PLA	17	-	35	165	382 ± 61	12 ± 4	220 ± 44
6	PLA-*b*-PTMC-*b*-PLA-*b*-PTMC	19	-	34	165	471 ± 147	27 ± 0	210 ± 47
7	PTMC-*b*-PLA-*b*-PTMC-*b*-PLA-*b*-PTMC	18	-	34	160	334 ± 70	21 ± 2	180 ± 23
8	PLA-*b*-PTMC-*b*-PLA-*b*-PTMC-*b*-PLA	19	-	34	153	303 ± 44	20 ± 1	250 ± 32
9	PLA-*b*-PTMC-*b*-PLA	10	-	43	163	545 ± 145	41 ± 2	18 ± 3
10	PLA-*b*-PTMC-*b*-PLA	30	-	40	161	332 ± 48	22 ± 4	81 ± 11
11	PLA-*b*-PTMC-*b*-PLA	39	-13	9	157	364 ± 64	21 ± 4	260 ± 13

[a] Glass transition temperatures and melting points were determined using DSC. [b] Young's modulus. [c] Ultimate tensile strength. [d] Elongation at break. Material properties corresponding to entries 2 and 3 are averages of two different batches of materials (Figures C71-72).

An inverse relationship between Young's modulus and elongation at break values was observed by Guerin et al. upon increasing the percent composition of TMC in their copolymers.[19] We also prepared several triblock copolymers with different percent compositions of TMC (Table 4-1, entries 10-12; Table 4-2, entries 9-11) to study the effects of varying the TMC concentration in our copolymers. Lowering the TMC percent composition to 10% yielded a brittle material similar to PLA but with a lower Young's modulus than that of the homopolymer. On the other hand, when the TMC composition in the copolymer was increased to ca. 30% and 40% by weight we observed a similar inverse relationship between the Young's modulus and the elongation at break of the materials. Based on these results, a further increase in the PTMC

composition would have a negative impact on the Young's modulus of the materials at the expense of an increased elongation at break. The copolymers with increased TMC loadings also show a drastic deviation in the glass transition temperature from the 20% weight PTMC multiblock copolymers. Therefore, multiblock copolymers derived from consistent monomer ratios yield materials with a unique combination of thermal and mechanical properties for various specialty applications.

4.4 DFT calculations

To gain a better understanding of the mechanism, we turned to density functional theory. All calculations were carried out with the GAUSSIAN09 program package[63] on the Extreme Science and Engineering Discovery Environment (XSEDE)[64] by Dr. Junnian Wei. The methyl groups on the pyrazole substituents were replaced by hydrogen atoms and the phenyl groups on PPh_2 were replaced by methyl groups to simplify the calculation (for more details about calculations, see the supporting information). First, possible monomeric and dimeric structures of the zinc benzoxide complexes were optimized and their energies compared (Figure C82). The energy of the dimer $[(fc^{P,B})Zn(\mu\text{-}OCH_2Ph)]_2$ was lower by 3.3 kcal/mol than that of the corresponding monomer, $(fc^{P,B})Zn(OCH_2Ph)$, in agreement with the experimental observations.

Since the energy difference between the dimeric and the monomeric species was small, the free energy surfaces for the reaction with LA and TMC were thus computed for both the monomer and the dimer (Figures C83-84) to compare the initiation step. For LA, although the monomer shows a lower activation barrier than the dimer (by 2.7 kcal/mol) for the alkoxide nucleophilic attack ($TS_{I\text{-}II}$), the energy for the ring-opening step ($TS_{II\text{-}III}$) and the overall activation barrier are lower for the dimeric species than for the monomer by 4.2 and 4.4

kcal/mol, respectively; furthermore, the two zinc centers participate in the process synergistically when the reaction occurs with the dimer. Similarly, for the initiation of TMC, both activation barriers were lower for the dimer (by 3.1 and 1.6 kcal/mol). These results are again in agreement with the experimental observations discussed above that the dimeric zinc complex facilitates the polymerization.

The copolymerization steps were then considered. Since the insertion of TMC leads to a product that has a similar structure as the step before, each following insertion should be similar to the initiation step, making the homopolymerization and copolymerization possible. However, after the insertion of LA, the resulting product contains a five-membered ring, in which the bond between the Zn center and the carbonyl group cannot be ignored. Thus, the insertions of a second LA or TMC molecule, respectively, after the insertion of the first LA were considered. As shown in Figure 4-9, the dimeric species significantly lowers the overall activation barriers, thus making the propagations possible after the insertion of LA. We would like to note that we are treating the results shown in Figure 4-9 from a qualitative point of view that allows us to compare the behavior of LA versus TMC. The large number of atoms involved and the simplifications necessary in order to get the respective transition states and intermediates to converge in a reasonable amount of time likely resulted in obtaining energies for the products that are positive with respect to the starting materials.

It is interesting to observe that after the insertion of LA, the insertion of another LA is easier than the insertion of TMC. Based on these results, we can envision that although the homopolymerization of TMC is much easier than that of LA, during the copolymerization of LA and TMC in one pot, LA would be consumed first (Figure C45).

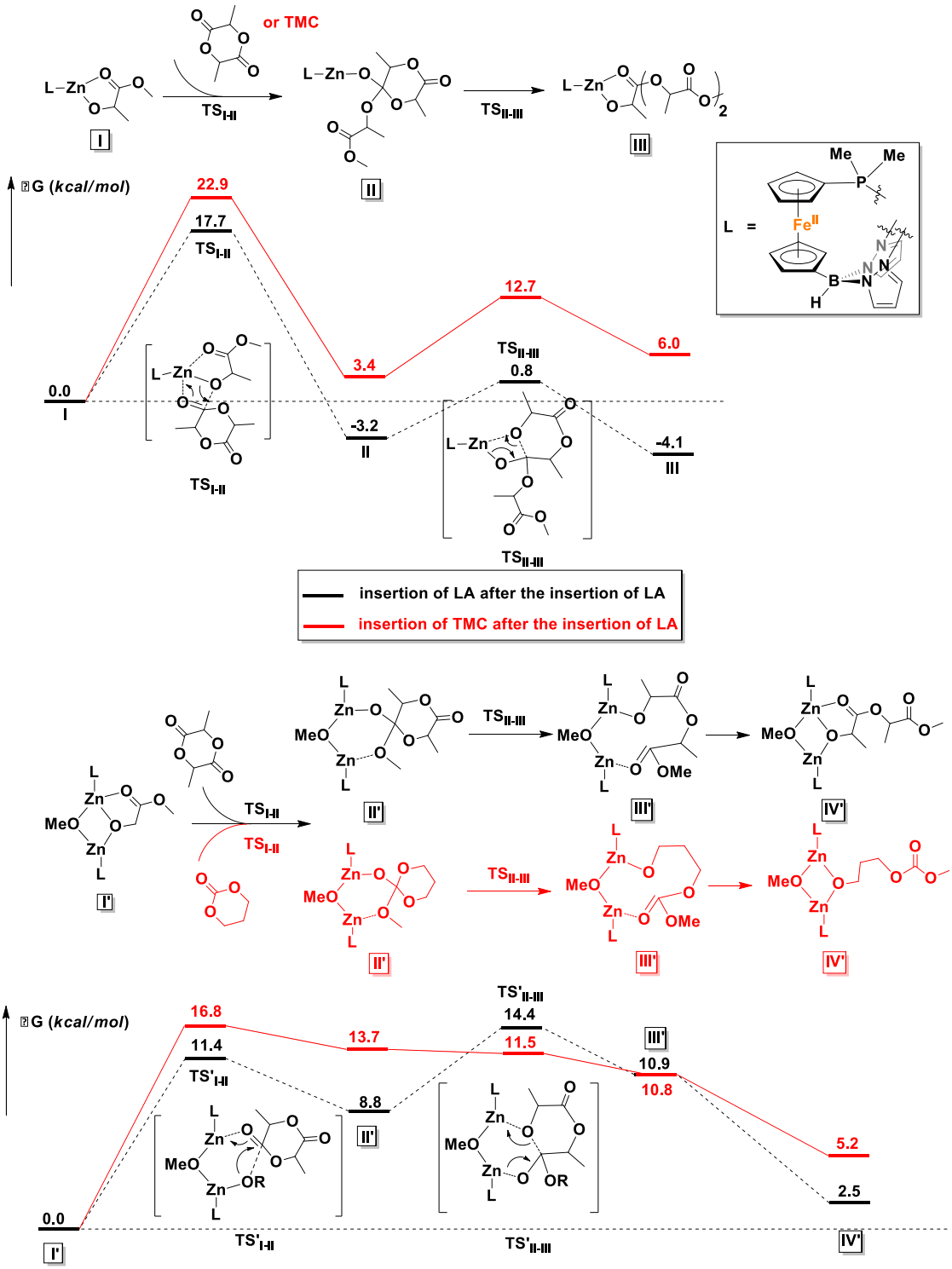

Figure 4-9. Comparison of reaction coordinates for propagation catalyzed by a monomeric (top) or dimeric (bottom) form of the zinc complex.

4.5 Conclusions

This chapter discusses the ring-opening copolymerization of LA and TMC to obtain pentablock copolymers, by the multiple step-wise addition of either monomer to the other, without the need for synthesizing tailored initiators or using any other additives. These reactions were possible with a dimeric zinc catalyst, $[(fc^{P,B})Zn(\mu\text{-}OCH_2Ph)]_2$. The solution state behavior of $[(fc^{P,B})Zn(\mu\text{-}OCH_2Ph)]_2$ in the presence and absence of LA and TMC was thoroughly investigated in order to understand why this catalyst does not have the limitations of previously reported compounds that cannot polymerize TMC after LA. Utilizing diffusion ordered NMR spectroscopy, as well as other spectroscopic techniques, the retention of the dimeric state of the zinc complex in solution was confirmed. It was also found that the zinc complex reacts as a dimer when catalyzing the ROP of L-lactide and 1,3-trimethylene carbonate. A combination of molecular weight versus conversion, end group analysis, chain extension, and kinetics experiments, as well as great control over the polymer molecular weights, suggests that these polymerization processes proceed via a living mechanism.

The preparation of various multiblock copolymers was achieved by a simple step-wise addition of the cyclic ester and carbonate in the presence of the catalyst. The physical, thermal, and mechanical properties of the isolated copolymers were determined using NMR spectroscopy, GPC, DSC, and DMA. In all cases, the block-like structures of the isolated polymers could be observed by NMR spectroscopy and the theoretical molecular weights agreed well with the GPC results. Furthermore, a clear trend in the influence of the block structures on the thermal and mechanical properties was observed; with an increasing number of blocks, a decrease in the glass transition temperatures, melting point temperatures, and the Young's modulus was observed. This study shows that multiblock copolymers derived from consistent monomer ratios yield

materials with a unique combination of thermal and mechanical properties that may be used for various specialty applications.

To gain further insight into the polymerization mechanism, density functional theory calculations were performed. The retention of the dimeric state of the zinc complex during the polymerization process was supported by the results that also indicated that the dimer is instrumental in lowering the activation barrier of TMC after LA polymerization. However, obtaining an accurate description of the polymerization processes during copolymerization was hindered by the large and complex nature of our system.

4.6 Experimental section

Synthesis of $[(fc^{P,B})Zn(\mu\text{-}OCH_2Ph)]_2$. To KCH_2Ph (82.4 mg, 0.633 mmol) in 5 mL of THF at -78 °C was added $HOCH_2Ph$ (66.0 μL, 0.633 mmol) drop-wise via syringe until the solution became colorless. A THF solution of $(fc^{P,B})ZnCl\cdot(C_7H_8)$ (483.7 mg, 0.633 mmol) was then added drop-wise and the reaction mixture stirred for 1 h at -78 °C. The reaction vessel was brought to ambient temperature and volatile substances were removed under reduced pressure. The desired product was extracted with 5 mL of toluene and filtered through Celite. Toluene was removed under reduced pressure and the remaining oily orange solids were dissolved in 5 mL of diethyl ether. After several minutes, a copious amount of yellow solids precipitated from diethyl ether. The solids were collected and washed with diethyl ether until the washings became pale yellow. The final product was isolated as yellow crystals in two crops from a THF/diethyl ether (1:2) mixture at -35 °C (354.2 mg, 68.5%). Crystals of $[(fc^{P,B})Zn(\mu\text{-}OCH_2Ph)]_2$ always contain two molecules of solvent per molecule of compound as a mixture of THF and diethyl ether as supported by NMR spectroscopic data. X-ray quality crystals were obtained from a THF/diethyl

ether layering at -35 °C. ^{1}H NMR (C_6D_6, 500 MHz, 298 K): δ (ppm) 2.00 (s, 6H, C*H*$_3$), 2.47 (s, 6H, C*H*$_3$), 3.74 (t, 2H, Cp-*H*), 3.91 (t, 2H, Cp-*H*), 4.03 (s, 2H, OC*H*$_2$Ph), 4.13 (q, 2H, Cp-*H*), 4.32 (t, 2H, Cp-*H*), 4.88 (br s, 1H, B*H*), 5.76 (s, 2H, C*H*), 6.69 (m, 2H, *o*-Ph), 6.81 (m, 2H, *m*-Ph), 6.87 (m, 1H, *p*-Ph), 7.04 (m, 6H, *m*-Ph, *p*-Ph), 7.53 (m, 4H, *o*-Ph). ^{13}C NMR (C_6D_6, 126 MHz, 298 K): δ (ppm) 13.5 (s, *C*H$_3$), 14.0 (d, *C*H$_3$), 69.9 (s, Cp-*C*), 70.5 (s, O*C*H$_2$Ph), 72.7 (d, Cp-*C*), 74.1 (s, Cp-*C*), 74.3 (d, Cp-*C*), 75.7 (d, Cp-*C*), 106.0 (s, *C*H), 127.3 (s, aromatic), 129.3 (s, aromatic), 134.4 (d, aromatic), 141.0 (d, aromatic), 144.3 (s, aromatic), 147.7 (s, *C*CH$_3$), 150.2 (s, *C*CH$_3$). ^{31}P{^{1}H} NMR (C_6D_6, 121 MHz, 298 K): δ (ppm) -15.5 (s). ^{11}B NMR (C_6D_6, 161 MHz, 298 K): δ (ppm) -7.2 (br s). Anal. Calcd: [(fc^{P,B})Zn(μ-OCH$_2$Ph)]$_2$·(THF)$_2$ ($C_{86}H_{96}B_2Fe_2N_8O_2P_2Zn_2$) C, 63.30; H, 5.93; N, 6.87. Found: C, 63.76; H, 5.87; N, 7.01.

Synthesis of [(fc^{P,B})Zn(μ-OH)]$_2$. To [(fc^{P,B})Zn(μ-OCH$_2$Ph)]$_2$ (101.5 mg, 62.1 mmol), outside of the glove-box, was added 5 mL of wet diethyl ether and the mixture was stirred for 30 min at ambient temperature. The solution volume was reduced to 2 mL and yellow solids were collected on a frit and washed with 2 x 1 mL of cold diethyl ether. After drying under a reduced pressure for several hours, the final product was isolated as a yellow powder (70.8 mg, 87.2%). ^{1}H NMR (C_6D_6, 500 MHz, 298 K): δ (ppm) -0.76 (s, 1H, O*H*), 2.24 (s, 6H, C*H*$_3$), 2.37 (s, 6H, C*H*$_3$), 3.40 (t, 2H, Cp-*H*), 3.48 (t, 2H, Cp-*H*), 3.99 (q, 2H, Cp-*H*), 4.21 (t, 2H, Cp-*H*), 4.69 (br s, 1H, B*H*), 5.76 (s, 2H, C*H*), 7.04 (m, 6H, *m*-Ph, *p*-Ph), 7.45 (m, 4H, *o*-Ph). ^{13}C NMR (C_6D_6, 126 MHz, 298 K): δ (ppm) 13.4 (s, *C*H$_3$), 13.7 (d, *C*H$_3$), 69.9 (s, Cp-*C*), 72.6 (d, Cp-*C*), 74.5 (s, Cp-*C*), 74.6 (d, Cp-*C*), 76.0 (d, Cp-*C*), 105.1 (s, *C*H), 134.3 (d, aromatic), 140.1 (d, aromatic), 146.6 (s, *C*CH$_3$), 148.6 (s, *C*CH$_3$). ^{31}P{^{1}H} NMR (C_6D_6, 203 MHz, 298 K): δ (ppm) -15.6 (s). ^{11}B NMR (C_6D_6, 161 MHz, 298 K): δ (ppm) -6.6 (br s). Anal. Calcd: [(fc^{P,B})Zn(μ-OH)]$_2$ ($C_{64}H_{68}B_2Fe_2N_8O_2P_2Zn_2$) C, 58.80; H, 5.24; N, 8.57. Found: C, 59.28; H, 5.26; N, 8.59.

In-situ generation of $[(fc^{P,B})Zn(LA)(OCH_2Ph)]_2$ and other NMR scale reactions. To a small vial, $[(fc^{P,B})Zn(\mu\text{-}OCH_2Ph)]_2$ (5 μmol), the appropriate amount of monomer, and 0.5 mL of C_6D_6 were added. The contents of the vial were stirred and the homogeneous solution was transferred to a J. Young NMR tube equipped with a Teflon valve. The NMR tube was sealed, taken out of the box and placed in an oil bath. Monomer consumption was monitored by ^1H NMR spectroscopy until the desired product was formed.

General polymerization procedure. To a Schlenk flask, sealed with a Teflon screw cap, $[(fc^{P,B})Zn(\mu\text{-}OCH_2Ph)]_2$ (2.5 μmol), an external standard, hexamethylbenzene (25 μmol), the appropriate amount of monomer, and up to 1.5 mL of C_6H_6 in total were added. The Schlenk flask was taken out of the glovebox and placed in an oil bath at 70 °C. Upon completion of each block, the reaction was cooled to room temperature and brought back into the glovebox for the addition of monomer comprising the next block. Typical reaction times for the complete conversion of 100 equivalents of L-lactide are 3 - 9 h in 0.5 – 1.5 mL of C_6H_6; 50 equivalents of TMC, after lactide, are polymerized over a period of 12 - 24 h in 0.5 – 1.5 mL of C_6H_6. The L-lactide and 1,3-trimethylene carbonate used in each polymerization experiment were distributed evenly across each block. Upon completion of the final block, the contents of the Schlenk flask were diluted with 1 mL of dichloromethane and poured into 15 mL of methanol to yield white solids. The product was collected on a glass frit, washed with additional 10 mL of methanol and kept under reduced pressure at 70 °C until it reached a consistent weight.

General kinetics procedure. In a glove box a Schlenk flask, sealed with a Teflon screw cap, equipped with a stir bar an appropriate amount of $[(fc^{P,B})Zn(\mu\text{-}OCH_2Ph)]_2$ and L-lactide were added with 1.6 mL as the final volume of C_6H_6. The flask was then taken out of the glove box and placed in an oil bath at 70 °C. At the appropriate time intervals the flask was removed

from the bath and cooled under a flowing stream of cold water prior to being brought back into the glove box. Inside the box, aliquots were poured into hexanes, dried to a constant weight under reduced pressure, and analyzed by ^{1}H NMR spectroscopy.

Dynamic Mechanical Analysis. Mechanical properties were measured on a TA Instruments RSAIII dynamic mechanical analyzer (DMA). Modulus tests were conducted at 20°C and a frequency of 1 Hz with samples of 6.0 mm wide and ~40 μm thick loaded onto the DMA with a 3 mm gap between the thin film grips. The stress−strain curves of the films were obtained at 20 °C at a stretching rate of 1 mm/s. The tested samples used were 6.0 mm wide and ~40 μm thick with a 3 mm gap between the thin film grips of the DMA. A minimum of three samples was tested per polymer. Young's modulus was determined using the non-dynamic single point analysis before the dynamic tests.

4.7 Appendix C

4.7.1 NMR spectroscopy

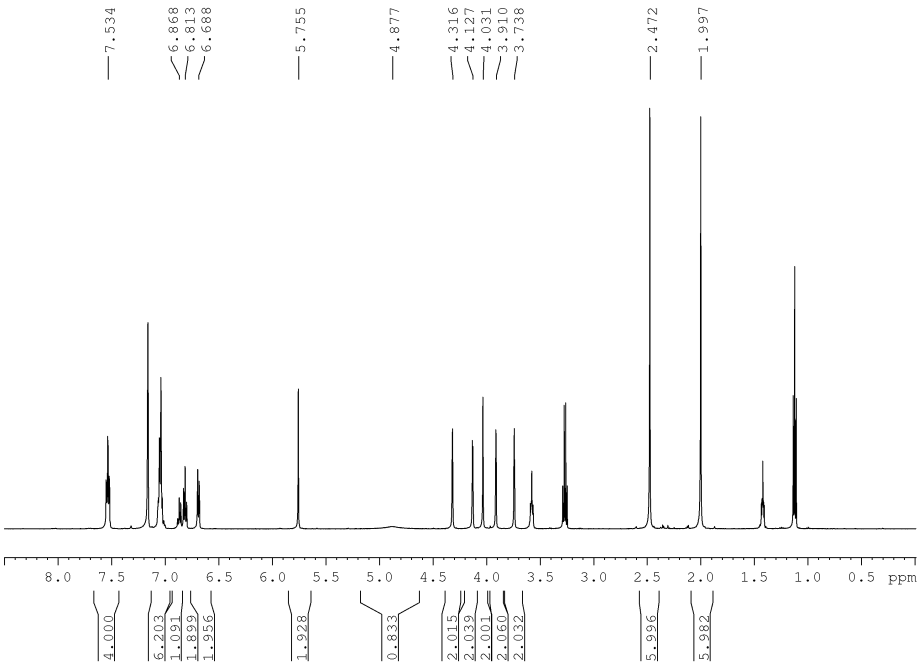

Figure C1. ^{1}H NMR spectrum (C_6D_6, 500 MHz, 298 K) of $[(fc^{P,B})Zn(\mu\text{-}OCH_2Ph)]_2$.

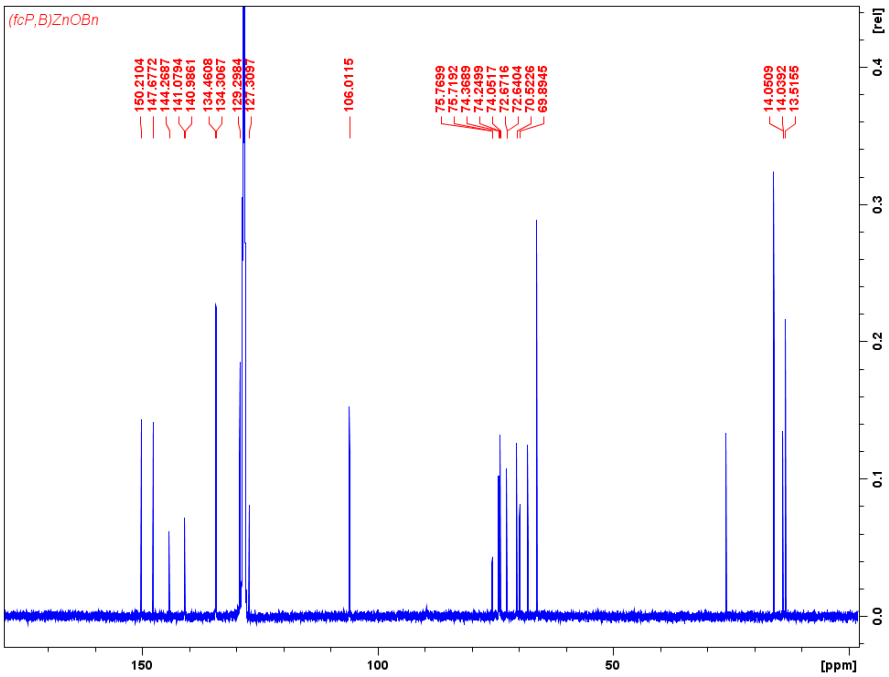

Figure C2. ^{13}C NMR spectrum (C_6D_6, 126 MHz, 298 K) of $[(fc^{P,B})Zn(\mu\text{-}OCH_2Ph)]_2$.

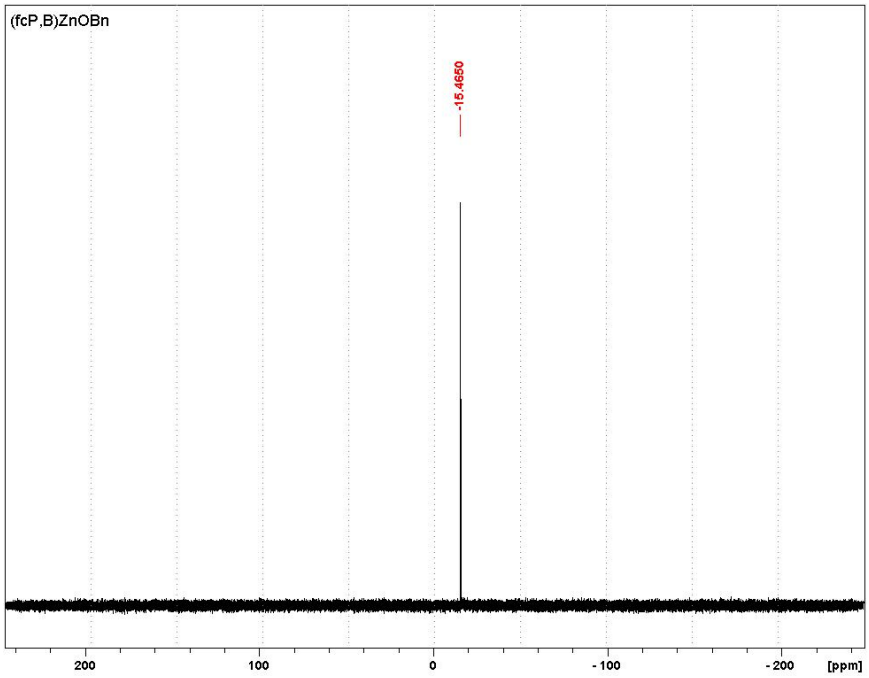

Figure C3. $^{31}P\{^{1}H\}$ NMR spectrum (C_6D_6, 203 MHz, 298 K) of $[(fc^{P,B})Zn(\mu\text{-}OCH_2Ph)]_2$.

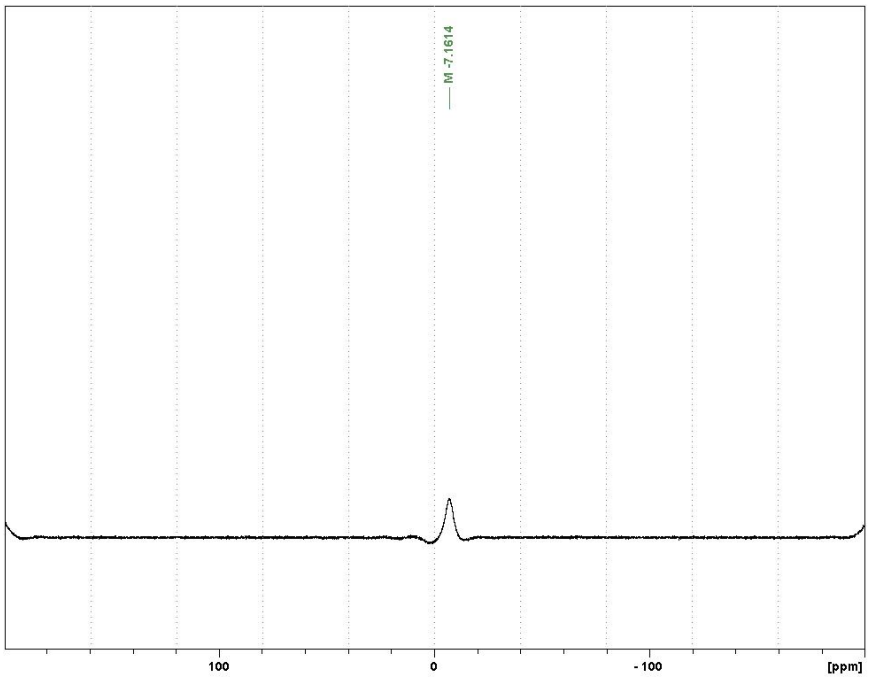

Figure C4. ^{11}B NMR spectrum (C_6D_6, 161 MHz, 298 K) of $[(fc^{P,B})Zn(\mu\text{-}OCH_2Ph)]_2$.

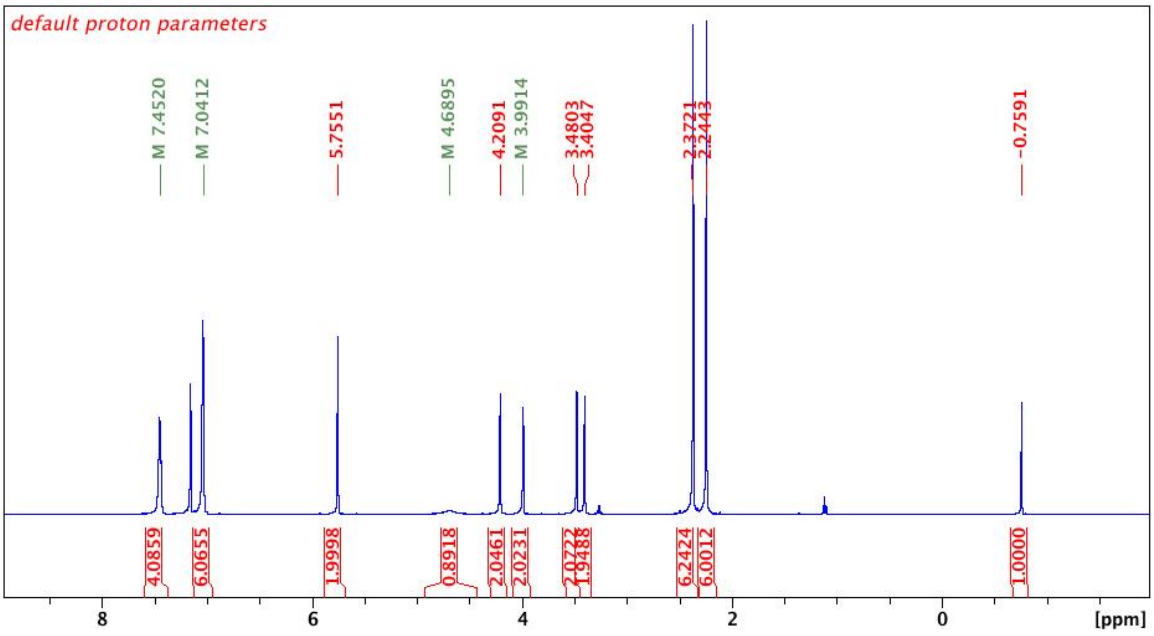

Figure C5. ^{1}H NMR spectrum (C_6D_6, 500 MHz, 298 K) of [(fc^{P,B})Zn(μ-OH)]$_2$.

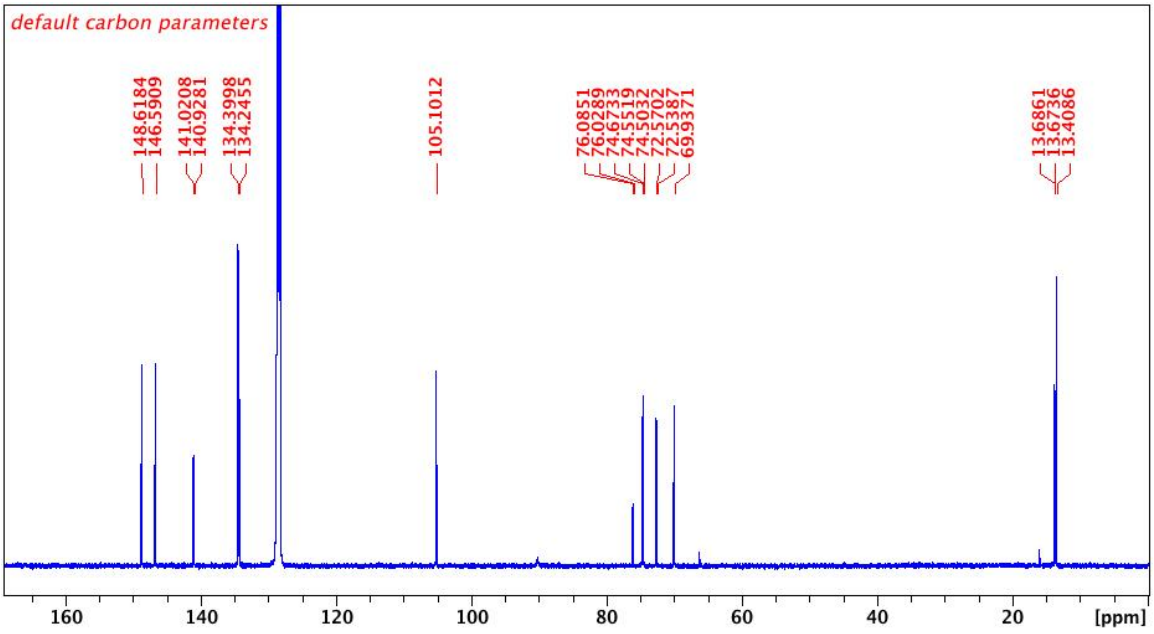

Figure C6. ^{13}C NMR spectrum (C_6D_6, 126 MHz, 298 K) of [(fc^{P,B})Zn(μ-OH)]$_2$.

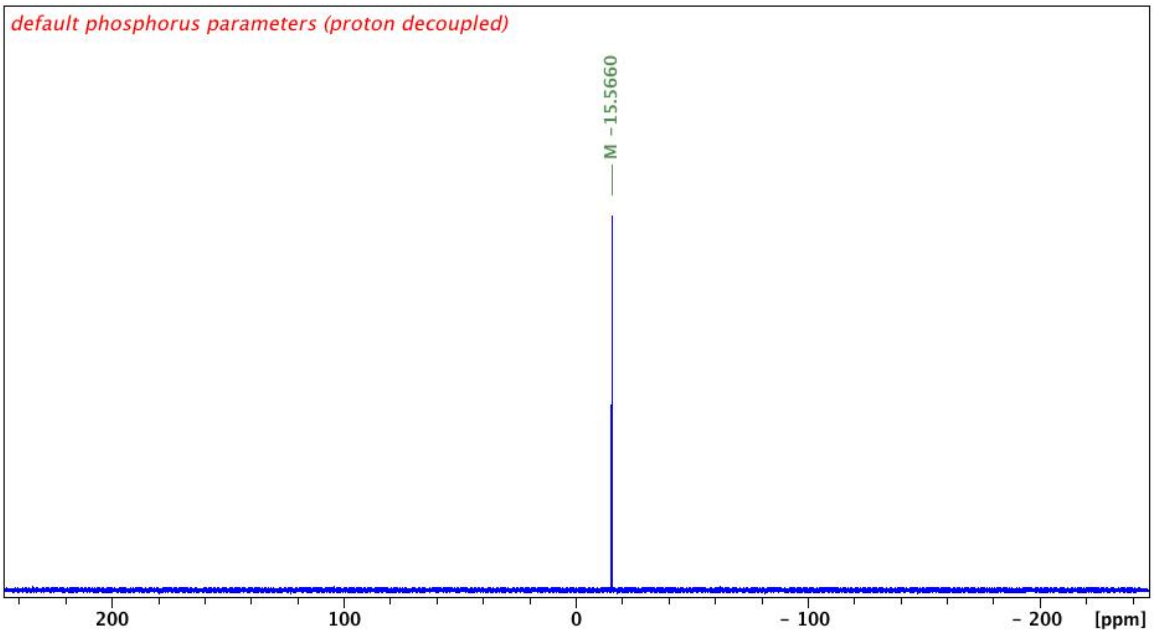

Figure C7. $^{31}P\{^{1}H\}$ NMR spectrum (C_6D_6, 203 MHz, 298 K) of $[(fc^{P,B})Zn(\mu\text{-}OH)]_2$.

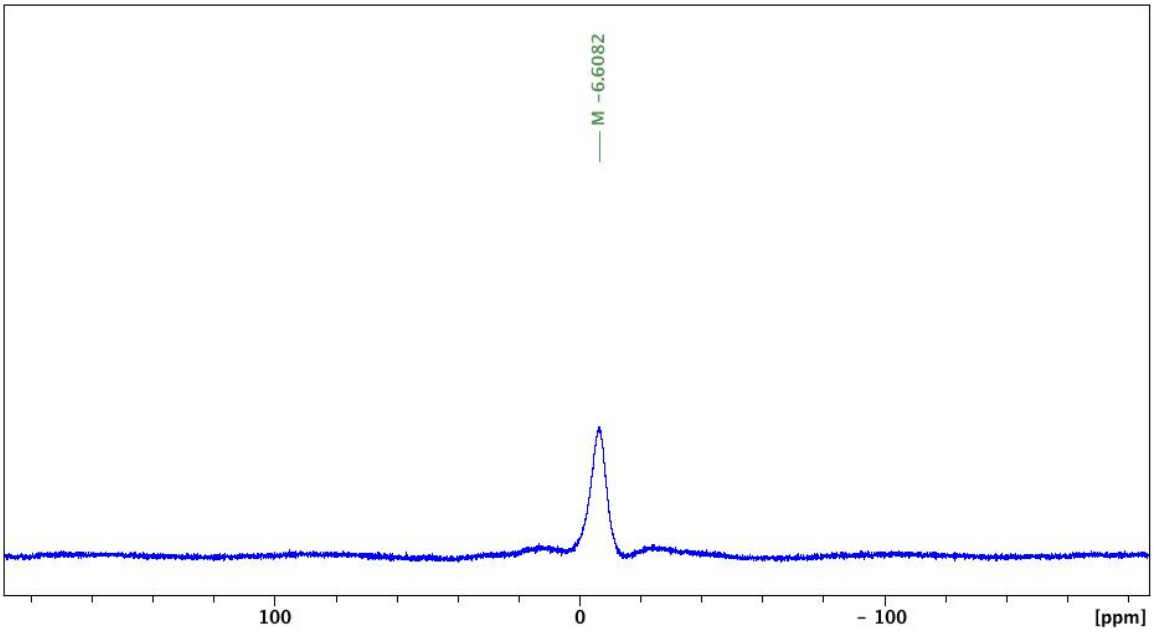

Figure C8. ^{11}B NMR spectrum (C_6D_6, 161 MHz, 298 K) of $[(fc^{P,B})Zn(\mu\text{-}OH)]_2$.

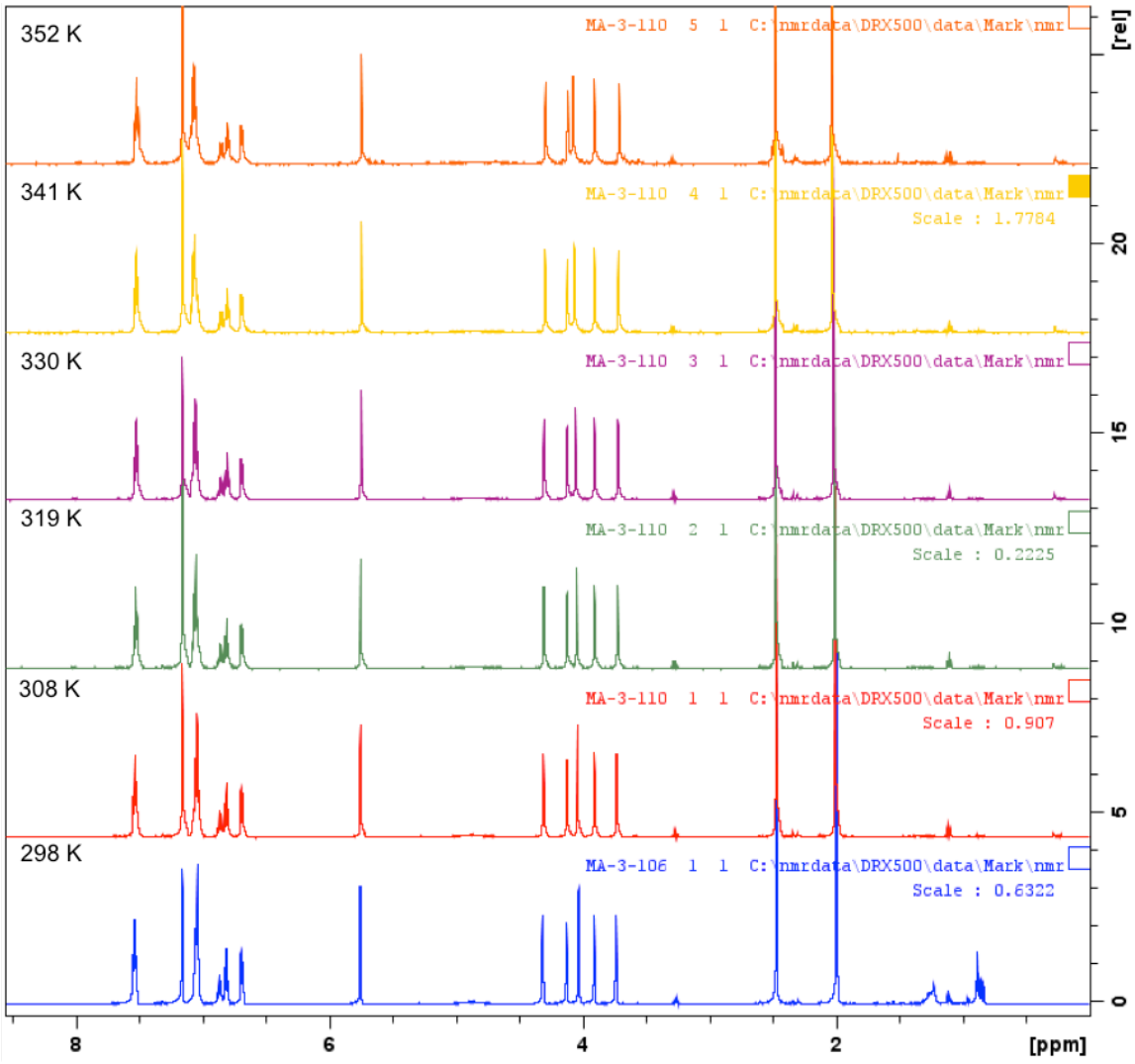

Figure C9. Variable temperature NMR (C_6D_6, 500 MHz) study of $[(fc^{P,B})Zn(\mu\text{-}OCH_2Ph)]_2$.

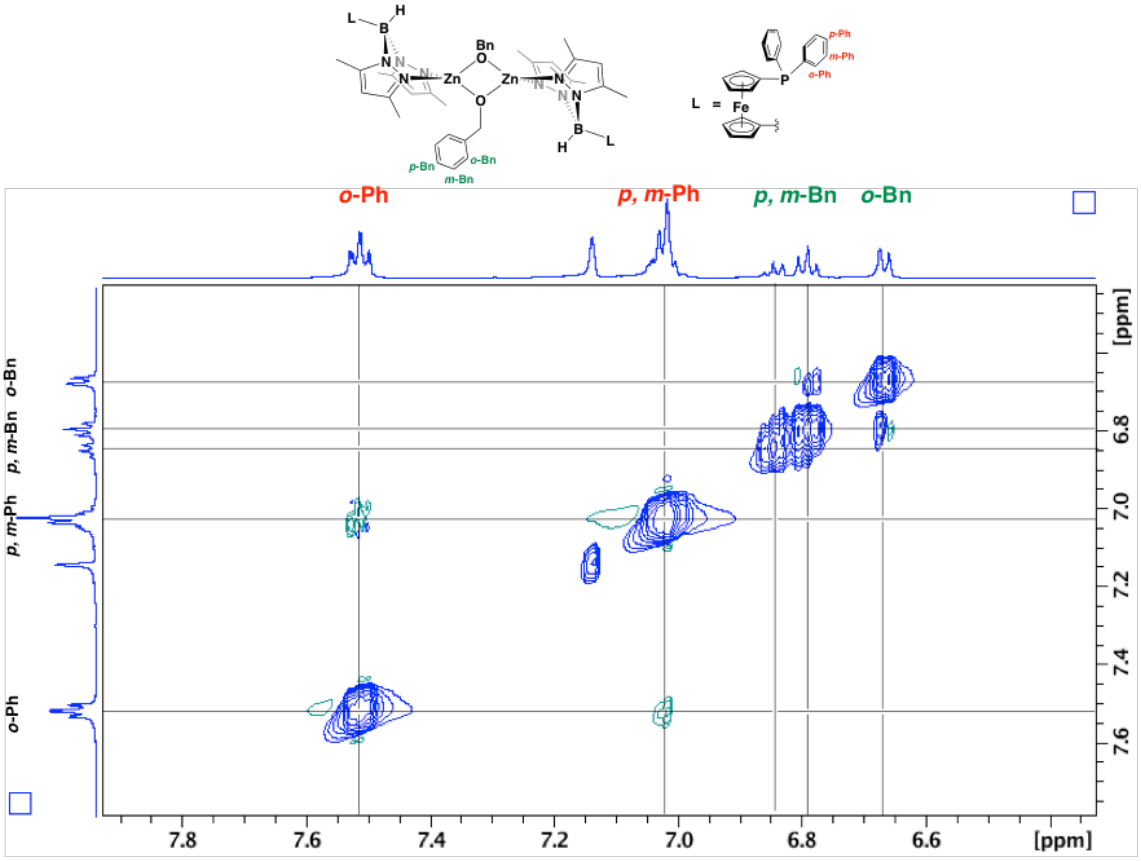

Figure C10. Selected region of ^{1}H NOESY NMR spectrum (C_6D_6, 500 MHz, 298 K) of $[(fc^{P,B})Zn(\mu\text{-}OCH_2Ph)]_2$.

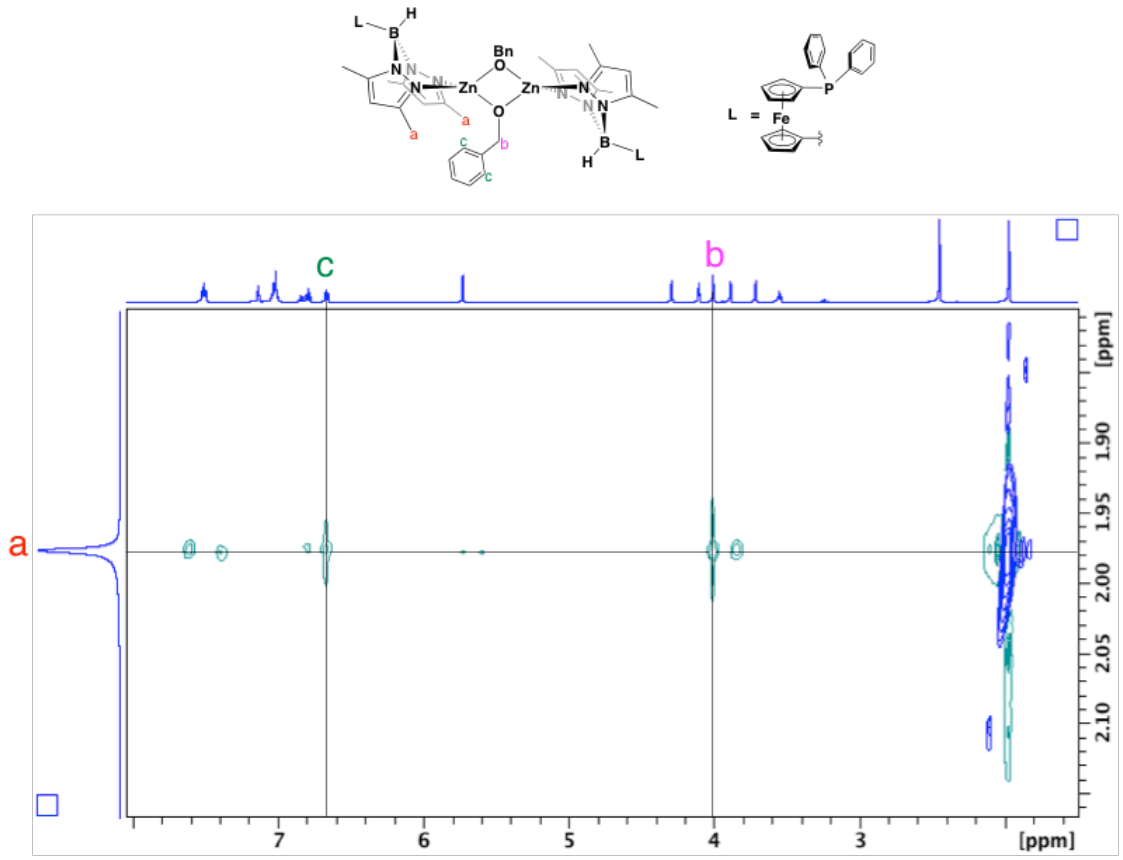

Figure C11. Selected region of ^{1}H NOESY NMR spectrum (C_6D_6, 500 MHz, 298 K) of $[(fc^{P,B})Zn(\mu\text{-}OCH_2Ph)]_2$.

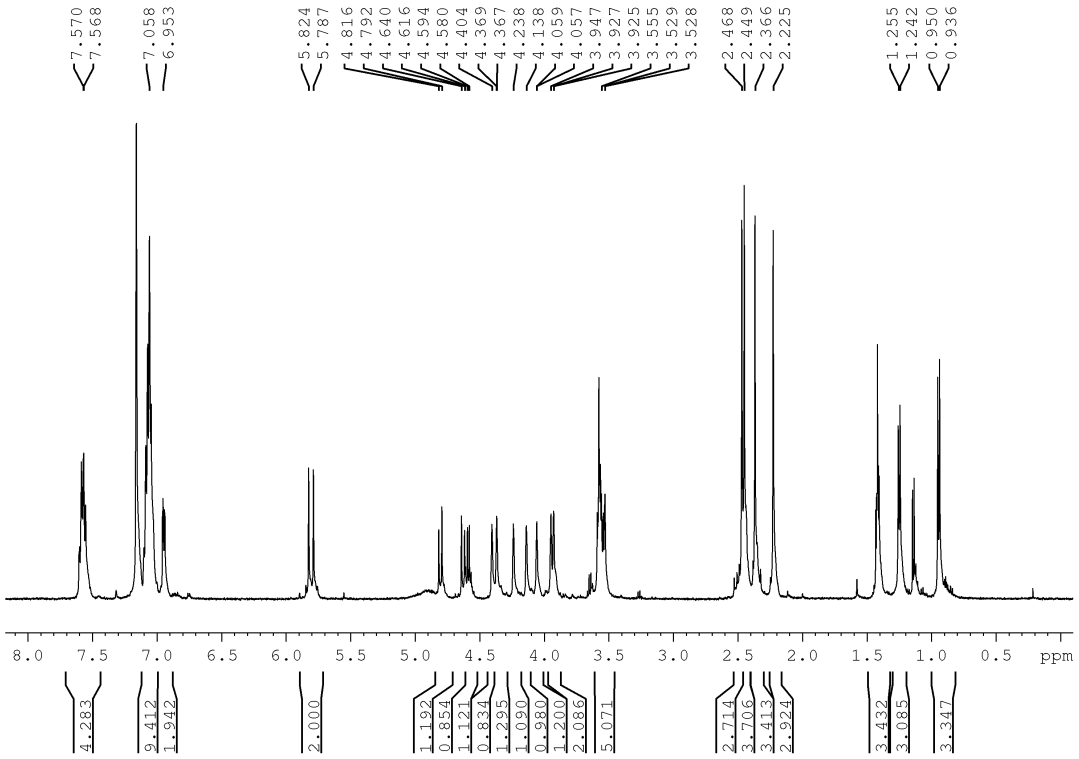

Figure C12. NMR scale reaction (C_6D_6, 500 MHz, 298 K) of $[(fc^{P,B})Zn(\mu\text{-}OCH_2Ph)]_2$ and L-lactide.

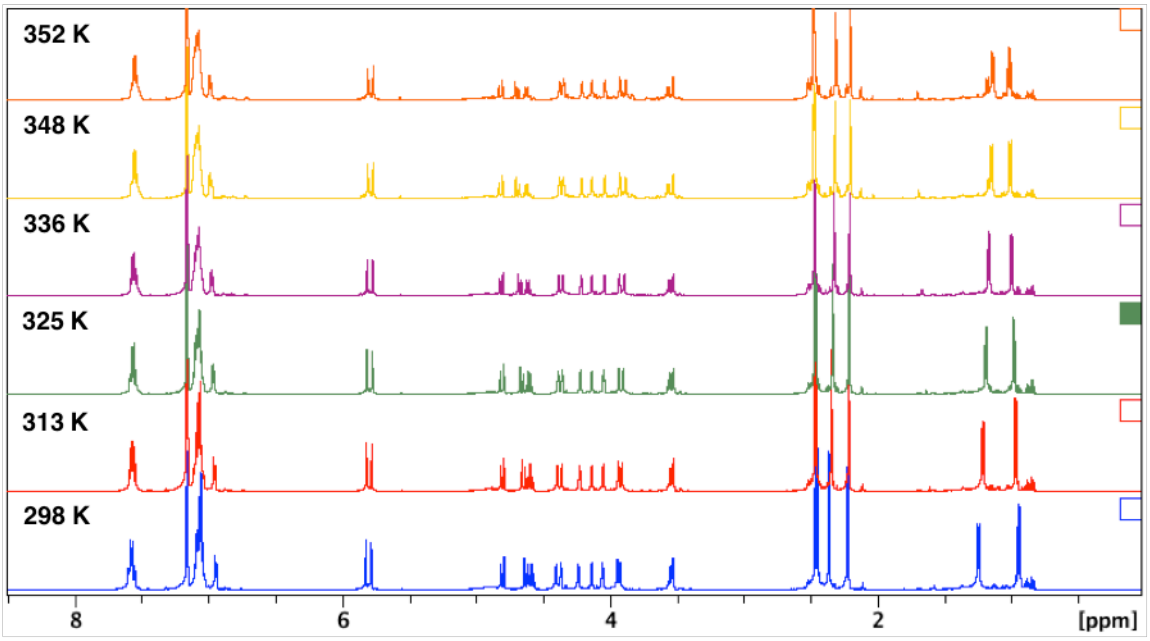

Figures C13. Variable temperature NMR (C_6D_6, 500 MHz) study of $[(fc^{P,B})Zn(LA)(OCH_2Ph)]_2$.

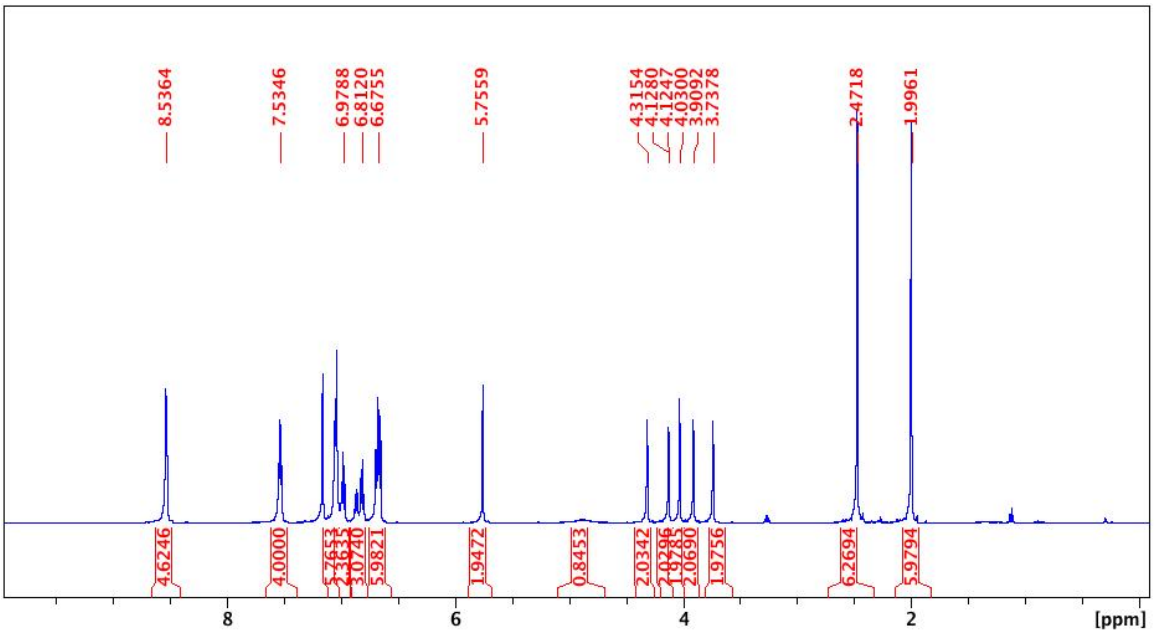

Figure C14. ^{1}H NMR spectrum (C_6D_6, 500 MHz, 298 K) of $[(fc^{P,B})Zn(\mu\text{-}OCH_2Ph)]_2$ in the presence of 5 equivalent of pyridine. No change in the signals corresponding to $[(fc^{P,B})Zn(\mu\text{-}OCH_2Ph)]_2$ is observed.

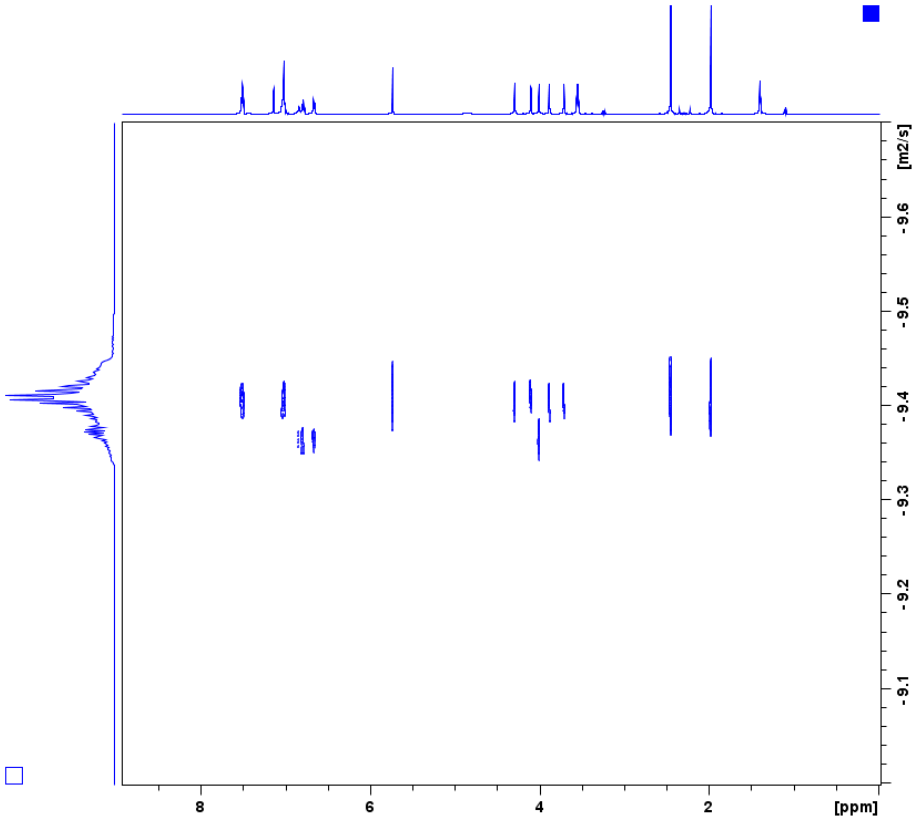

Figure C15. ^{1}H DOSY NMR spectrum (C_6D_6, 500 MHz, 298 K) of [($fc^{P,B}$)Zn(μ-OCH_2Ph)]$_2$. A minor difference in the diffusion rates of the –OCH_2Ph component vs. the heteroscorpionate supporting ligand is observed. Such drifts in the signals corresponding to the same molecule can be found in various DOSY spectra in the literature.

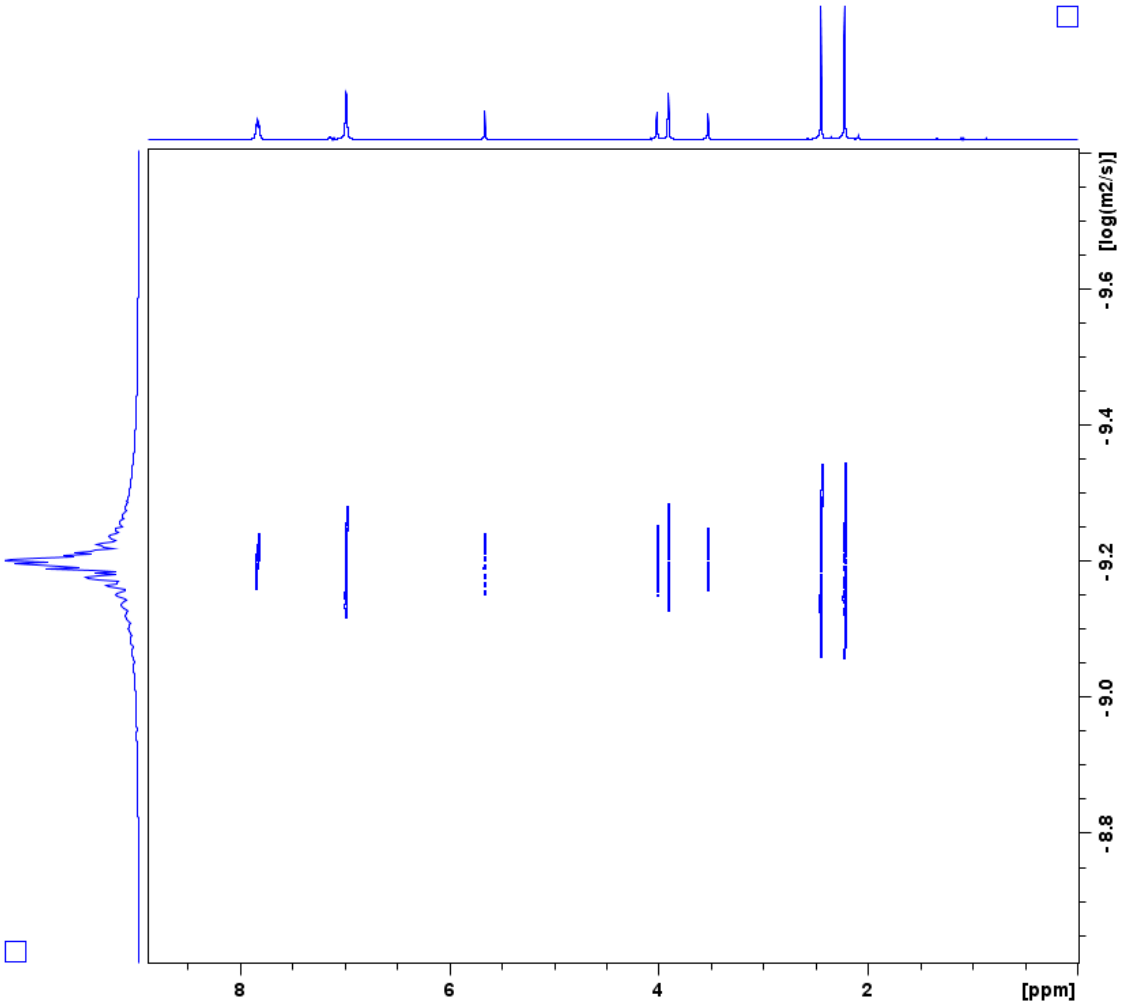

Figure C16. ^{1}H DOSY NMR spectrum (C_6D_6, 500 MHz, 298 K) of ($fc^{P,B}$)ZnCl.

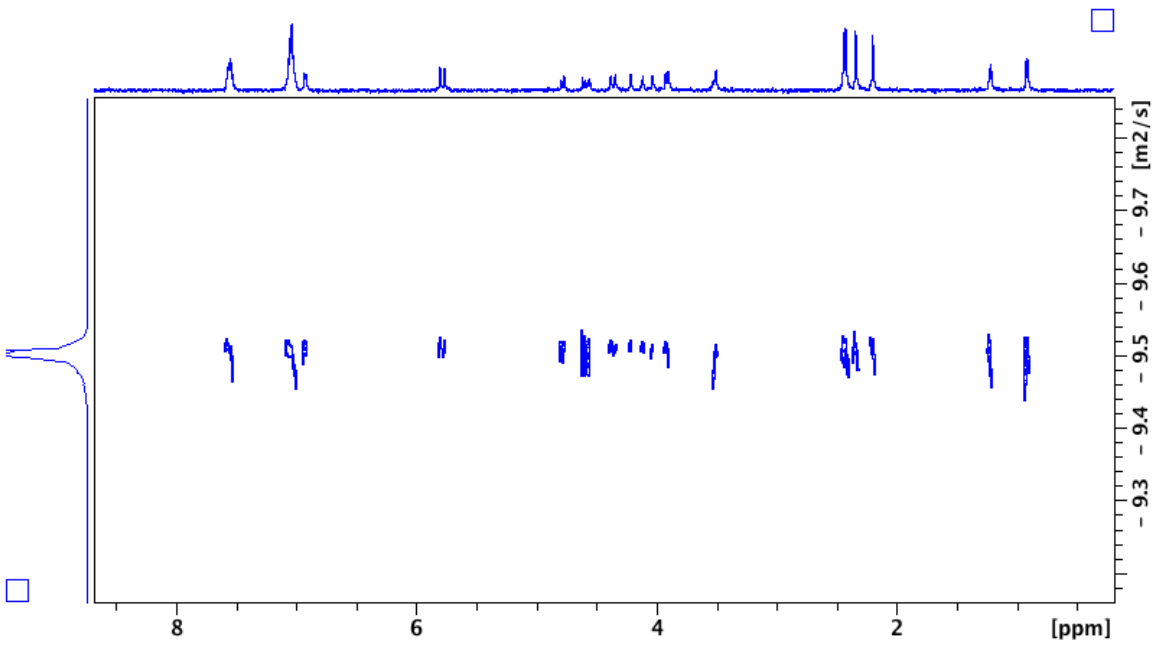

Figure C17. ^{1}H DOSY NMR spectrum (C_6D_6, 500 MHz, 298 K) of $[(fc^{P,B})Zn(LA)(OCH_2Ph)]_2$.

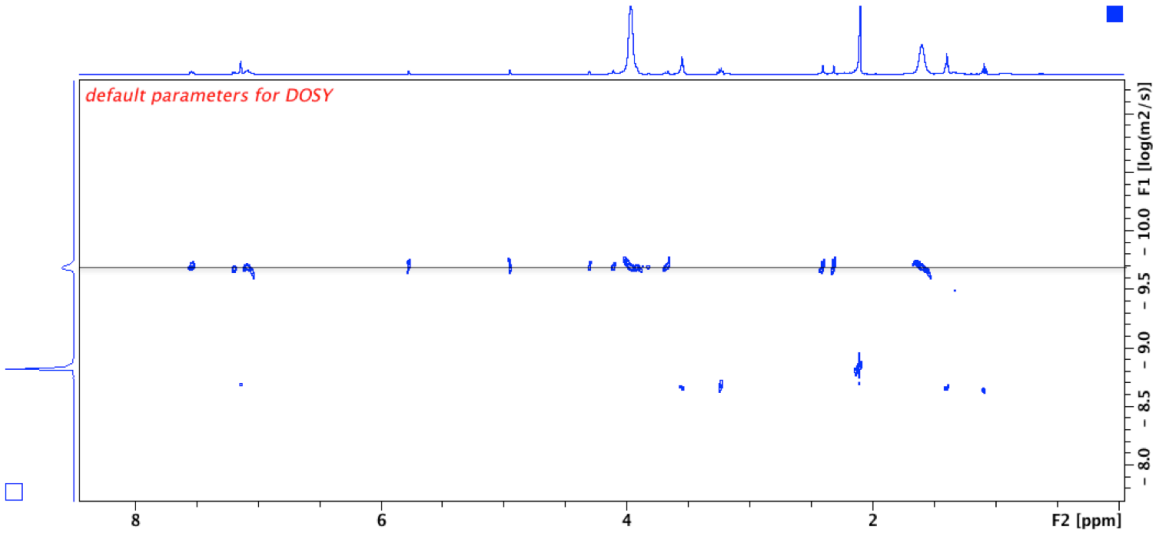

Figure C18. ^{1}H DOSY NMR spectrum (C_6D_6, 500 MHz, 298 K) of $[(fc^{P,B})Zn(PTMC)_{36}(OCH_2Ph)]_2$.

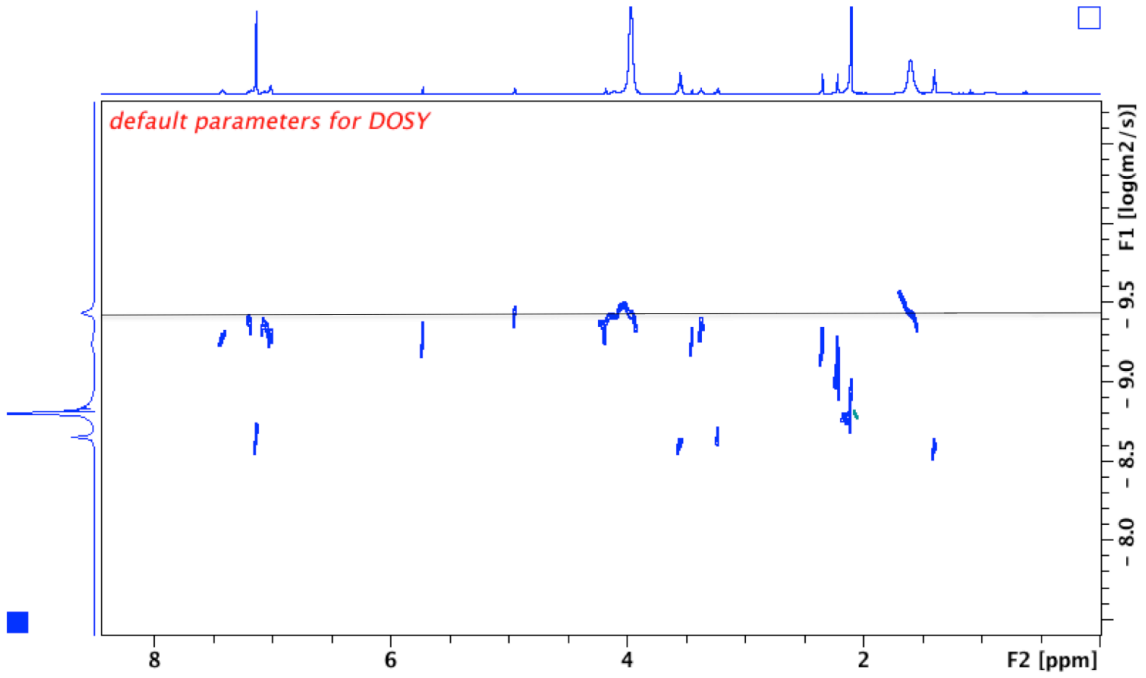

Figure C19. ^{1}H DOSY NMR spectrum (C_6D_6, 500 MHz, 298 K) of the $PhCH_2O(PTMC)_{36}H$ polymer.

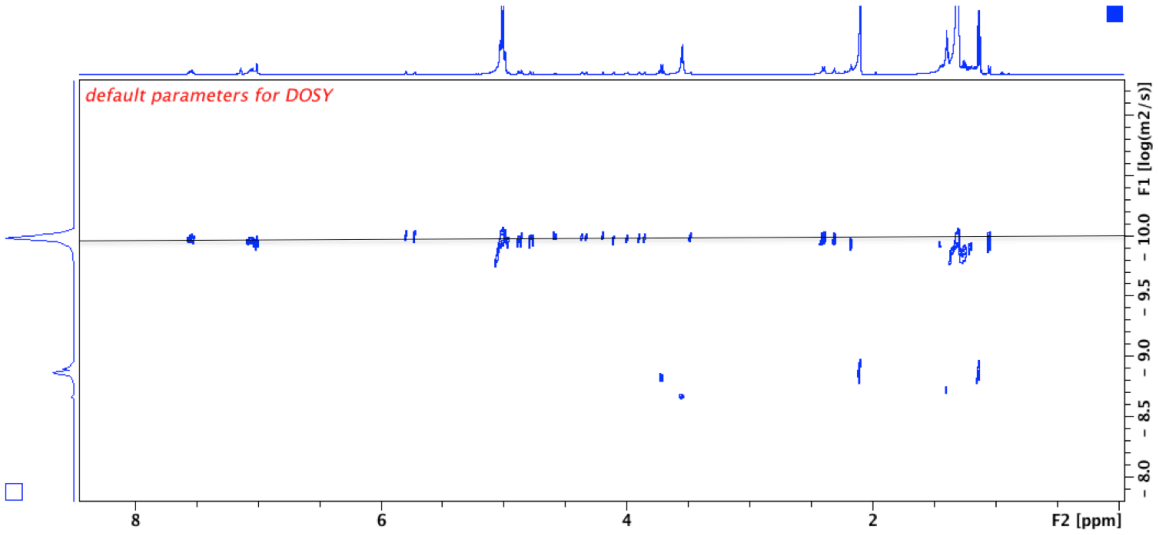

Figure C20. ^{1}H DOSY NMR spectrum (C_6D_6, 500 MHz, 298 K) of $[(fc^{P,B})Zn(PLA)_{36}(OCH_2Ph)]_2$.

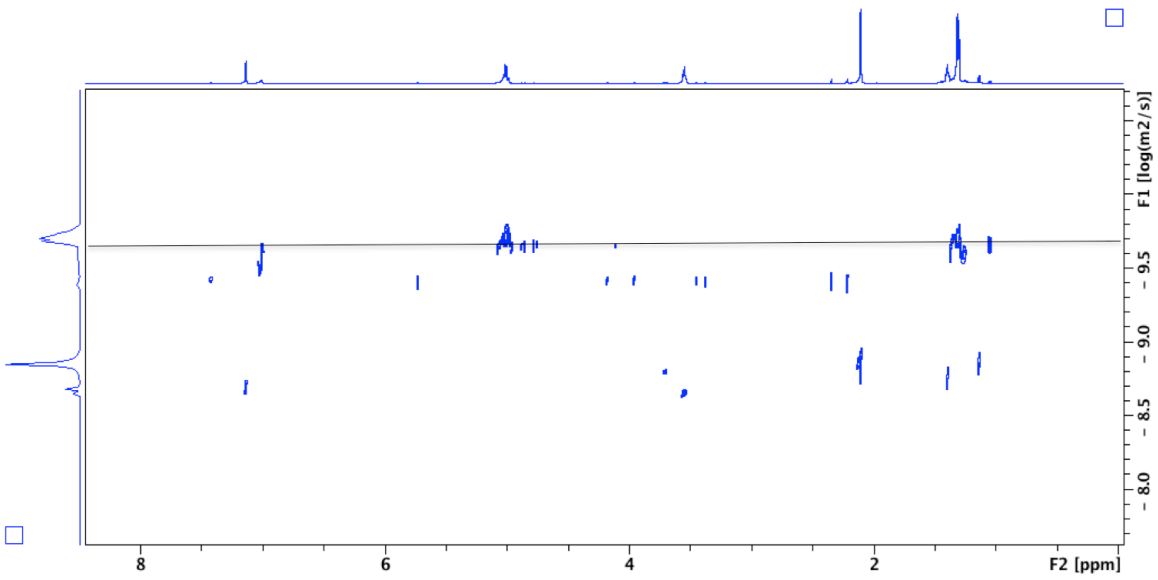

Figure C21. ^{1}H DOSY NMR spectrum (C_6D_6, 500 MHz, 298 K) of $PhCH_2O(PLA)_{36}H$.

$D[(fc^{P,B})ZnCl] = 6.38 \times 10^{-10}\ m^2/s$

$D = 3.92 \times 10^{-10}\ m^2/s$

$D\{[(fc^{P,B})Zn(LA)(OCH_2Ph)]_2\} = 3.16 \times 10^{-10}\ m^2/s$

$D\{[(fc^{P,B})Zn(PTMC)_{36}(OCH_2Ph)]_2\} = 2.07 \times 10^{-10}\ m^2/s$

$D[PhCH_2O(PTMC)_{36}H] = 3.80 \times 10^{-10}\ m^2/s$

$D\{[(fc^{P,B})Zn(PLA)_{36}(OCH_2Ph)]_2\} = 1.04 \times 10^{-10}\ m^2/s$

$D[PhCH_2O(PLA)_{36}H] = 2.00 \times 10^{-10}\ m^2/s$

The Stokes-Einstein equation shows the relationship between the hydrodynamic radius and the diffusion coefficient:

$D = (kT)/(6\pi\eta r_H)$

By comparing the diffusion coefficients of two compounds the ratios of the hydrodynamic radii can be determined.

$D_{(ZnCl)}/D_{(ZnOBn)2} = r_{(ZnOBn)2}/r_{(ZnCl)} = 1.63$

$D_{(ZnOBn)2}/D_{[Zn(LA)OBn]2} = r_{[Zn(LA)OBn]2}/r_{(ZnOBn)2} = 1.24$

$D_{(PhCH2O(PLA)36H)}/D_{[Zn(PLA)36(OCH2Ph)]2} = r_{[Zn(PLA)36(OCH2Ph)]2}/r_{(PhCH2O(PLA)36H)} = 1.92$

$D_{(PhCH2O(PTMC)36H)}/D_{[Zn(PTMC)36(OCH2Ph)]2} = r_{[Zn(PTMC)36(OCH2Ph)]2}/r_{(PhCH2O(PTMC)36H)} = 1.84$

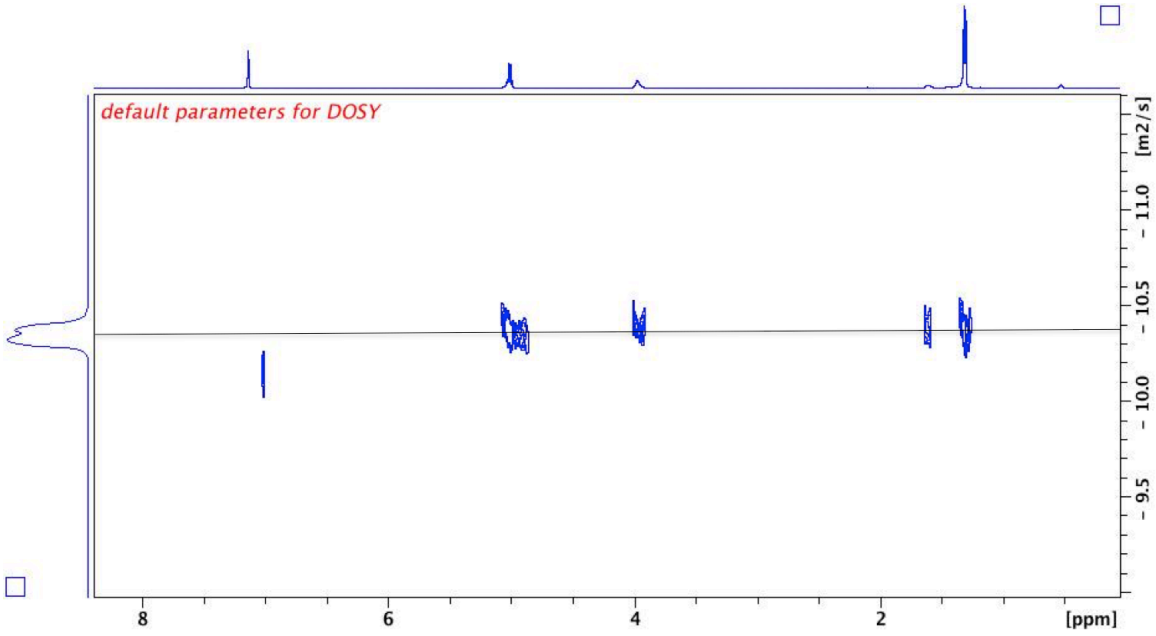

Figure C22. ^{1}H DOSY NMR spectrum (C_6D_6, 500 MHz, 298 K) of PLA-*b*-PTMC-*b*-PLA.

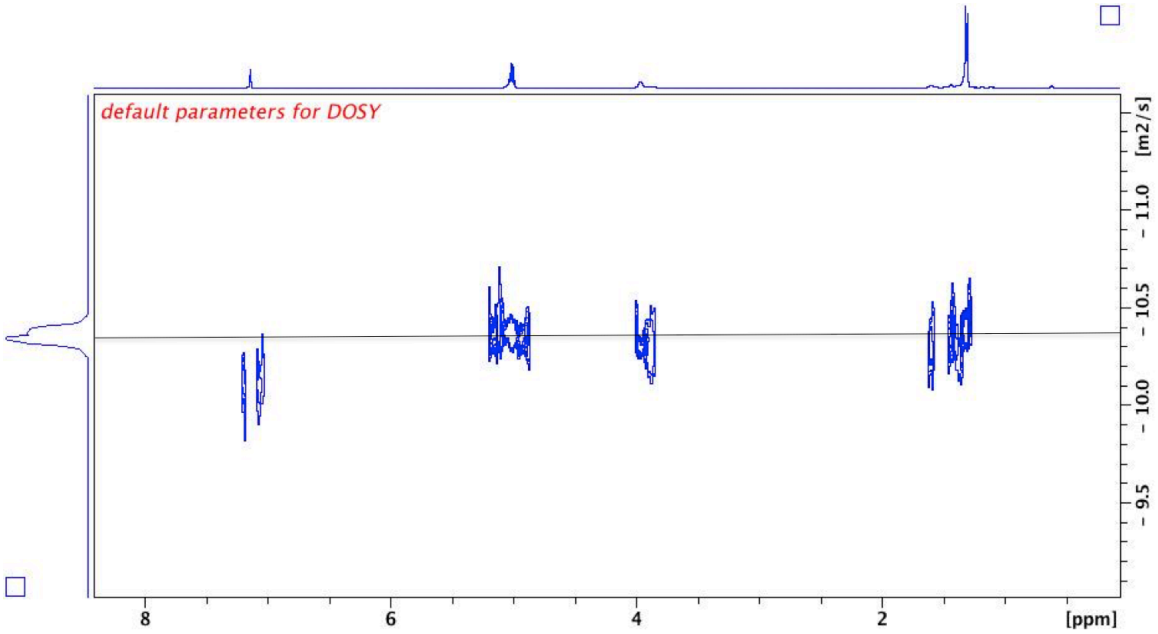

Figure C23. ^{1}H DOSY NMR spectrum (C_6D_6, 500 MHz, 298 K) of PTMC-*b*-PLA-*b*-PTMC.

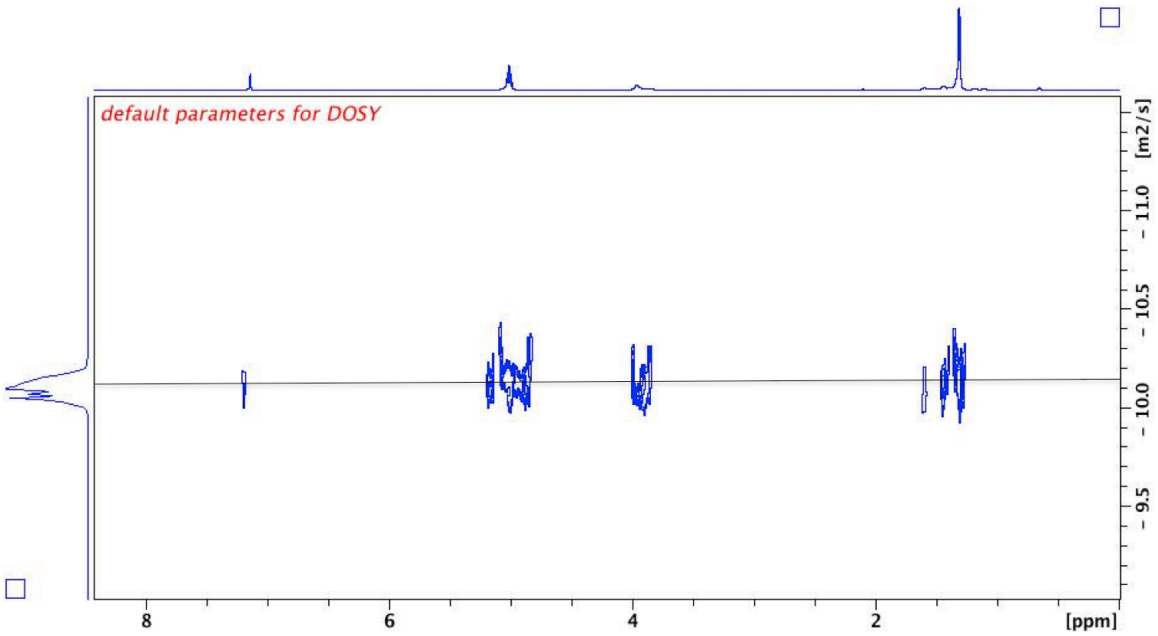

Figure C24. ^{1}H DOSY NMR spectrum (C_6D_6, 500 MHz, 298 K) of PTMC-*b*-PLA-*b*-PTMC-*b*-PLA-*b*-PTMC.

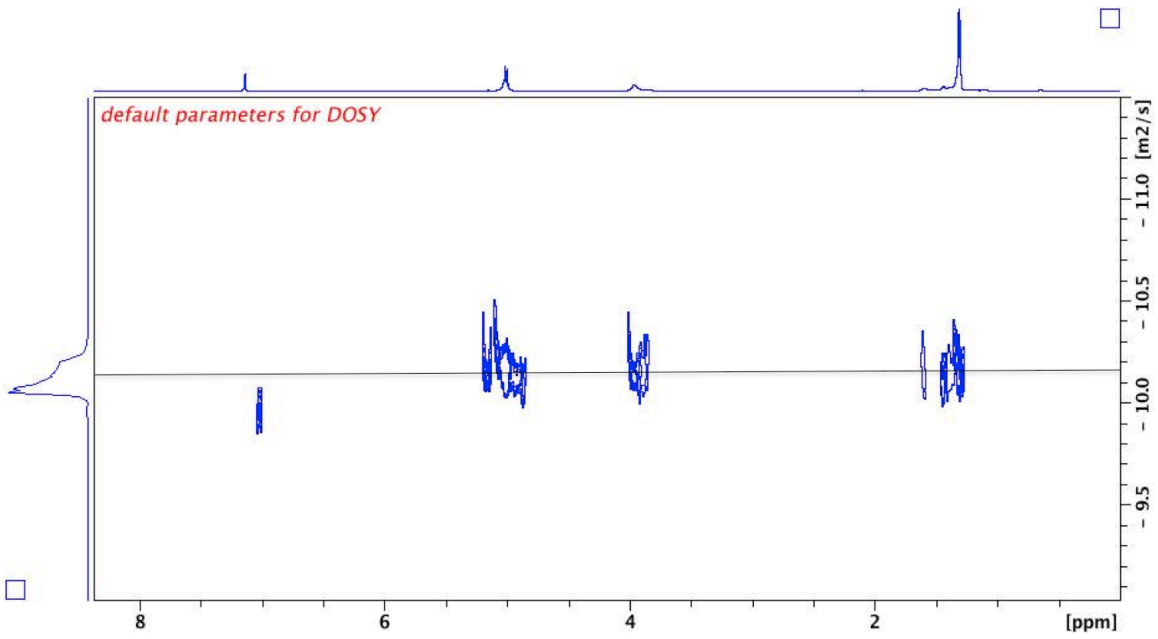

Figure C25. ^{1}H DOSY NMR spectrum (C_6D_6, 500 MHz, 298 K) of PLA-*b*-PTMC-*b*-PLA-*b*-PTMC-*b*-PLA.

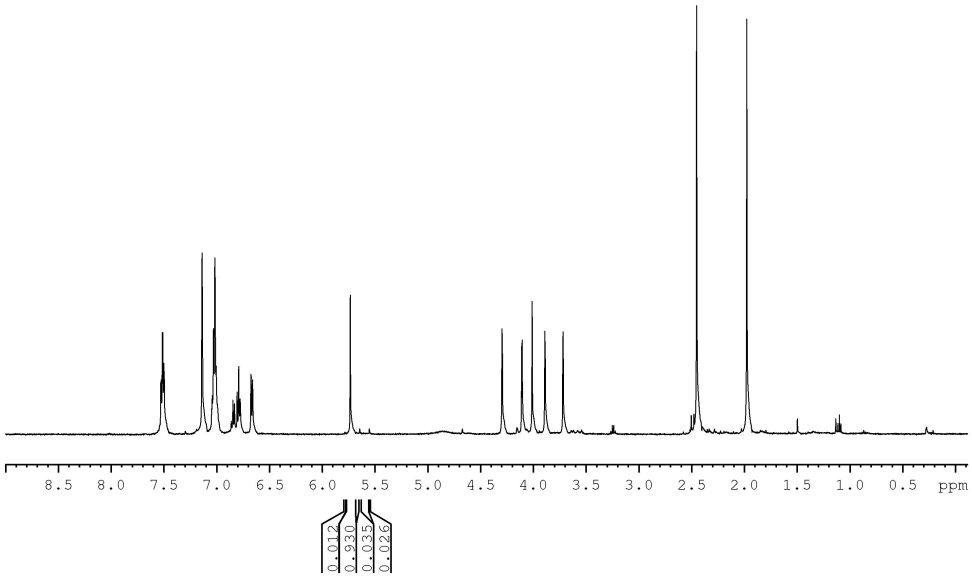

Figure C26. Thermal decomposition study (C_6D_6, 500 MHz, 298 K) of $[(fc^{P,B})Zn(\mu\text{-}OCH_2Ph)]_2$, 24 h at ambient temperature.

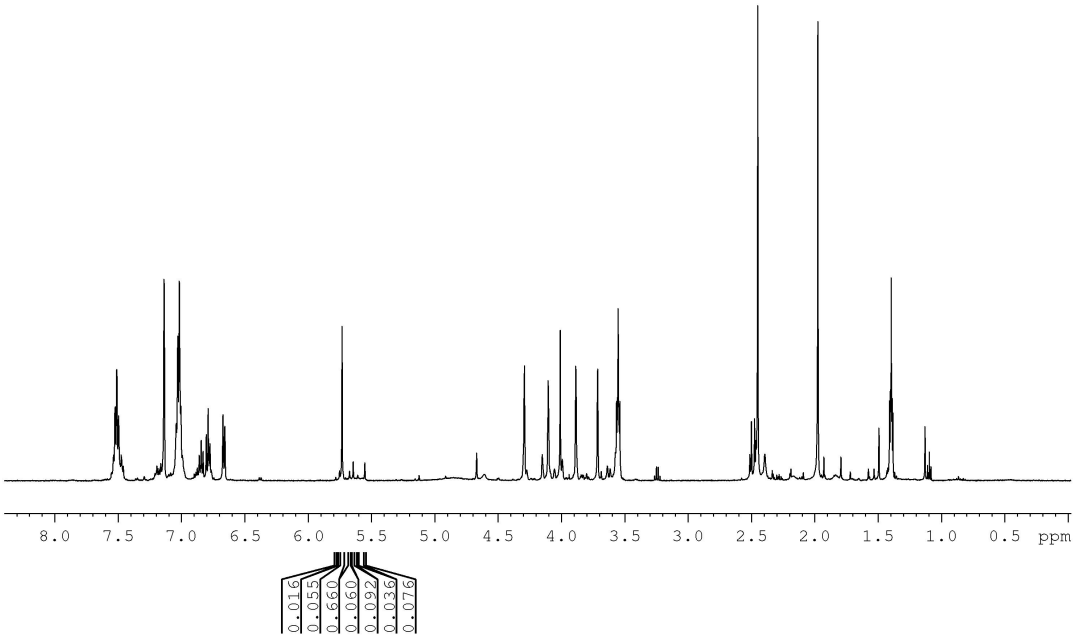

Figure C27. Thermal decomposition study (C_6D_6, 500 MHz, 298 K) of $[(fc^{P,B})Zn(\mu\text{-}OCH_2Ph)]_2$, 1.5 h at 70 °C.

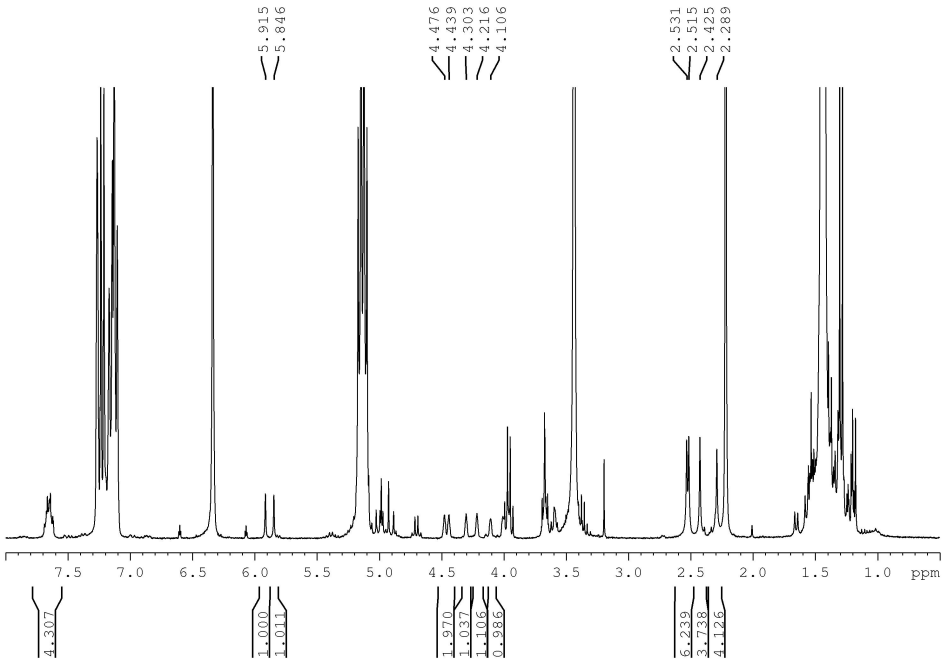

Figure C28. Thermal decomposition study (C_6D_6, 300 MHz, 298 K) of $[(fc^{P,B})Zn(\mu\text{-}OCH_2Ph)]_2$ in the presence of 100 equivalents of L-lactide, 3 h at 70 °C.

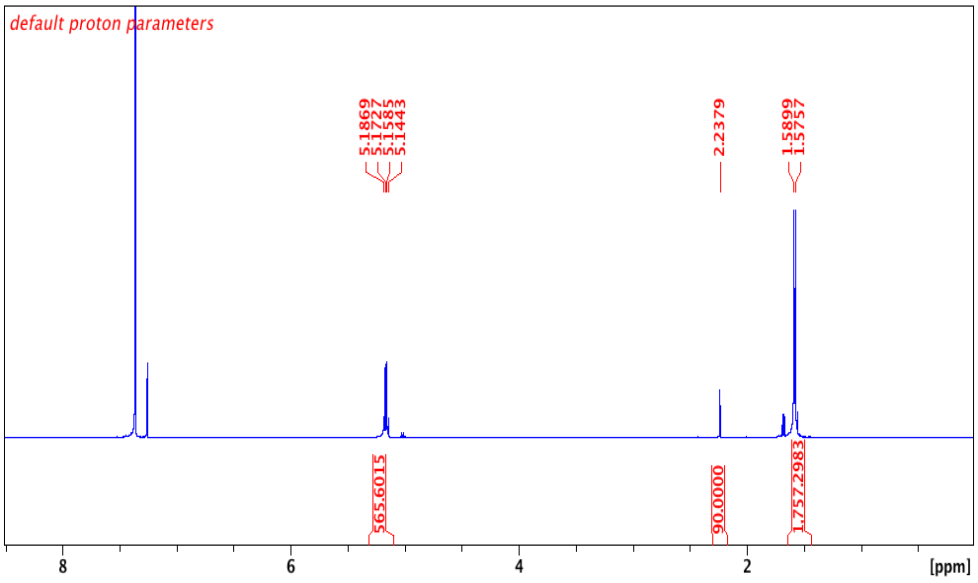

Figure C29. ^{1}H NMR spectrum ($CDCl_3$, 500 MHz, 298 K) of L-LA polymerization (Table 4-1, entry 1). Standard is hexamethylbenzene (HMB). $[(fc^{P,B})Zn(\mu\text{-}OCH_2Ph)]_2$: HMB: TMC: LA ratio is 1:10:566.

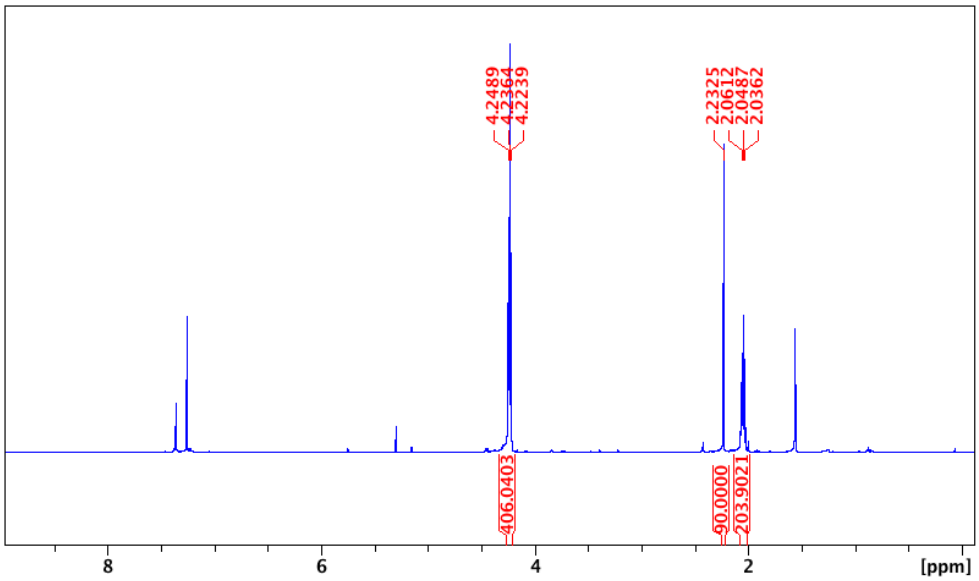

Figure C30. ^{1}H NMR spectrum ($CDCl_3$, 500 MHz, 298 K) of TMC polymerization (Table 4-1, entry 2). Standard is hexamethylbenzene (HMB). $[(fc^{P,B})Zn(\mu\text{-}OCH_2Ph)]_2$: HMB: TMC ratio is 1:10:202.

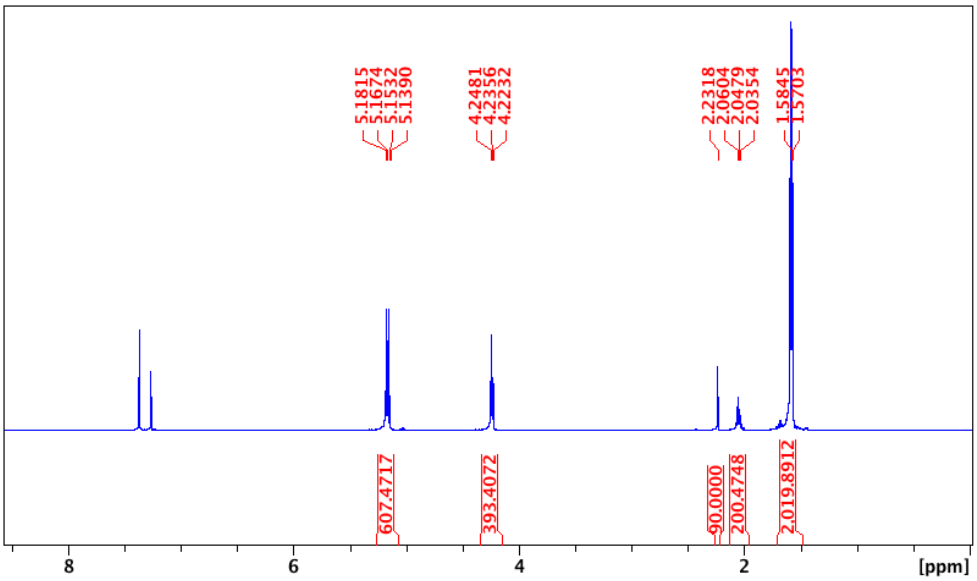

Figure C31. ^{1}H NMR spectrum ($CDCl_3$, 500 MHz, 298 K) of PLA-*b*-PTMC polymerization (Table 4-1, entry 3). Standard is hexamethylbenzene (HMB). $[(fc^{P,B})Zn(\mu\text{-}OCH_2Ph)]_2$: HMB: TMC: LA ratio is 1:10:196:608.

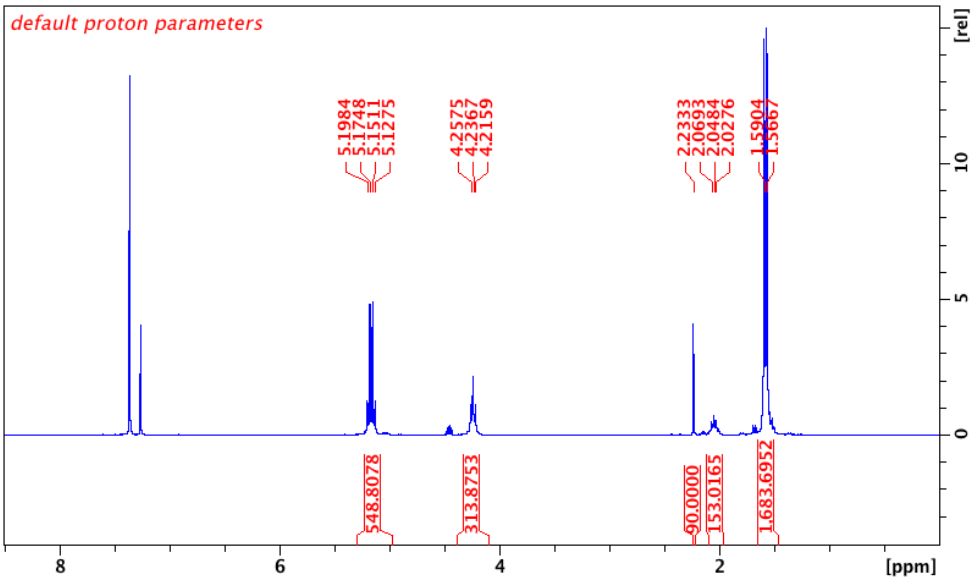

Figure C32. ^{1}H NMR spectrum ($CDCl_3$, 300 MHz, 298 K) of PTMC-*b*-PLA polymerization (Table 4-1, entry 4). Standard is hexamethylbenzene (HMB). $[(fc^{P,B})Zn(\mu\text{-}OCH_2Ph)]_2$: HMB: TMC: LA ratio is 1:10:158:550.

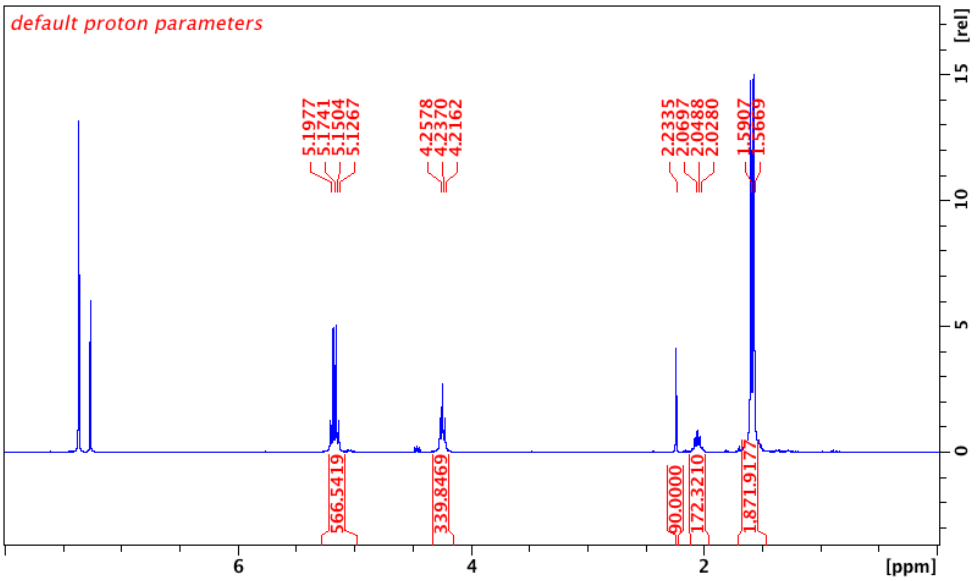

Figure C33. ^{1}H NMR spectrum ($CDCl_3$, 300 MHz, 298 K) of PTMC-*b*-PLA-*b*-PTMC polymerization (Table 4-1, entry 5). Standard is hexamethylbenzene (HMB). [(fc^{P,B})Zn(μ-OCH_2Ph)]$_2$: HMB: TMC: LA ratio is 1:10:170:566.

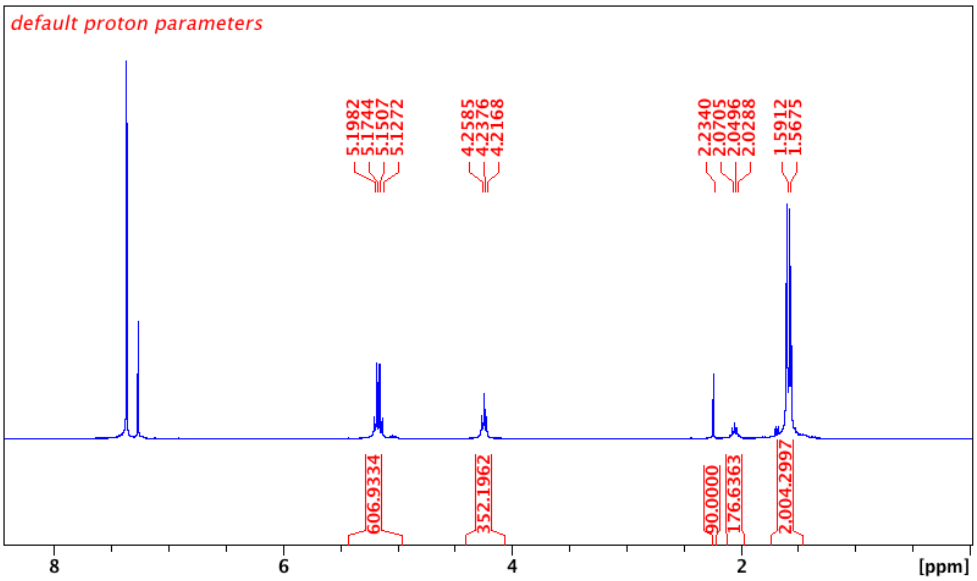

Figure C34. ^{1}H NMR spectrum ($CDCl_3$, 300 MHz, 298 K) of PLA-*b*-PTMC-*b*-PLA polymerization (Table 4-1, entry 6). Standard is hexamethylbenzene (HMB). [(fc^{P,B})Zn(μ-OCH_2Ph)]$_2$: HMB: TMC: LA ratio is 1:10:176:606.

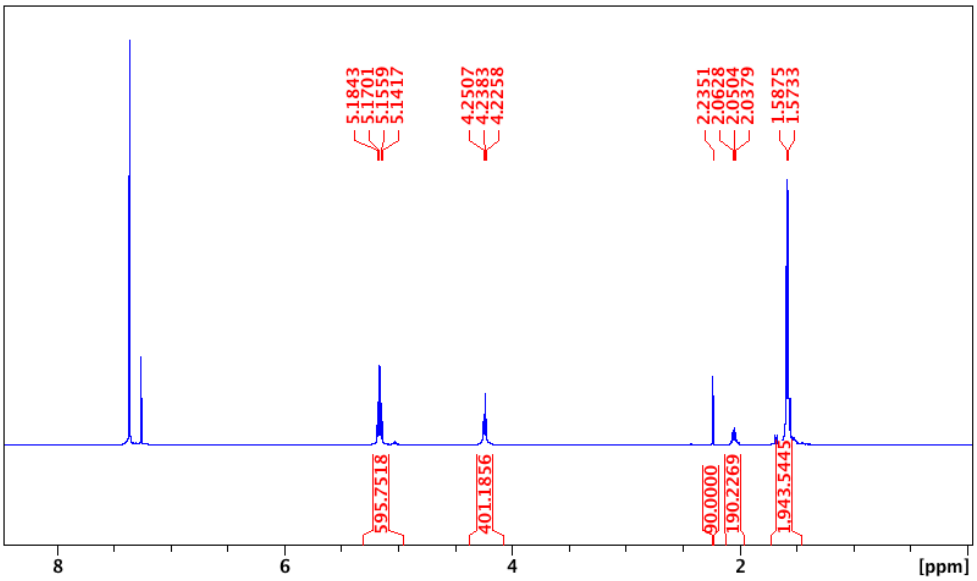

Figure C35. ^{1}H NMR spectrum ($CDCl_3$, 500 MHz, 298 K) of PLA-*b*-PTMC-*b*-PLA-*b*-PTMC polymerization (Table 4-1, entry 7). Standard is hexamethylbenzene (HMB). [($fc^{P,B}$)Zn(μ-OCH_2Ph)]$_2$: HMB: TMC: LA ratio is 1:10:200:596.

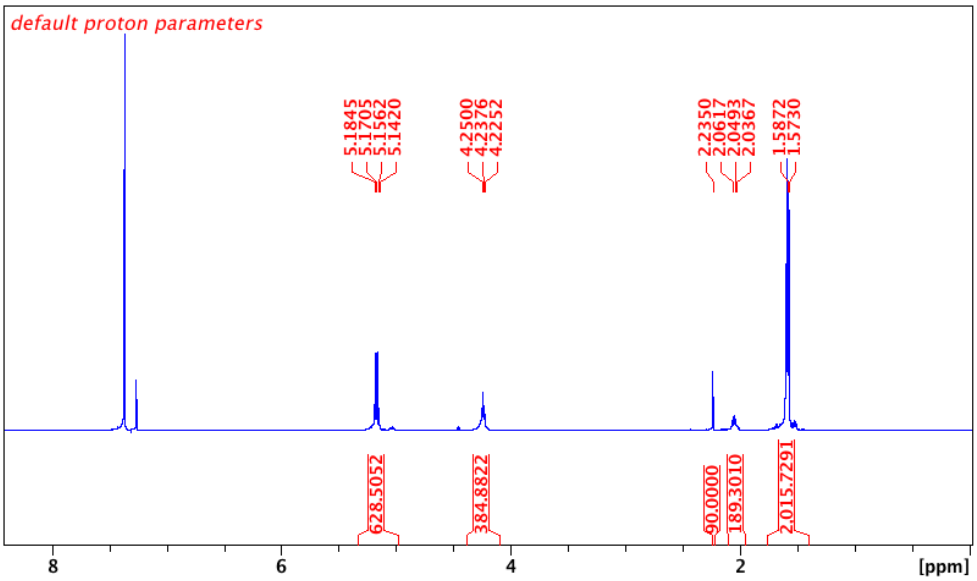

Figure C36. ^{1}H NMR spectrum ($CDCl_3$, 500 MHz, 298 K) of PTMC-*b*-PLA-*b*-PTMC-*b*-PLA-*b*-PTMC polymerization (Table 4-1, entry 8). Standard is hexamethylbenzene (HMB). [($fc^{P,B}$)Zn(μ-OCH_2Ph)]$_2$: HMB: TMC: LA ratio is 1:10:192:628.

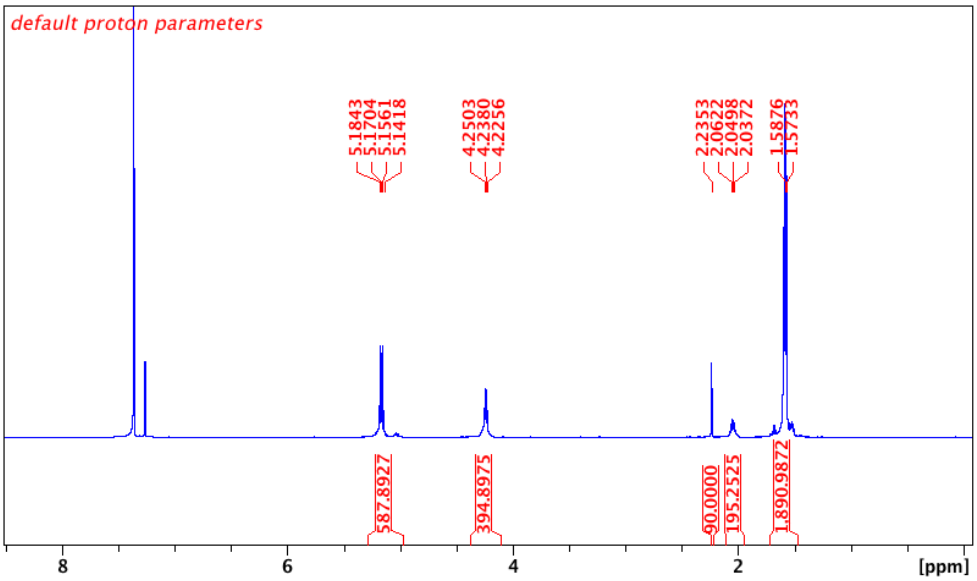

Figure C37. ^{1}H NMR spectrum ($CDCl_3$, 500 MHz, 298 K) of PLA-*b*-PTMC-*b*-PLA-*b*-PTMC-*b*-PLA polymerization (Table 4-1, entry 9). Standard is hexamethylbenzene (HMB). [(fc^{P,B})Zn(μ-OCH_2Ph)]$_2$: HMB: TMC: LA ratio is 1:10:198:588.

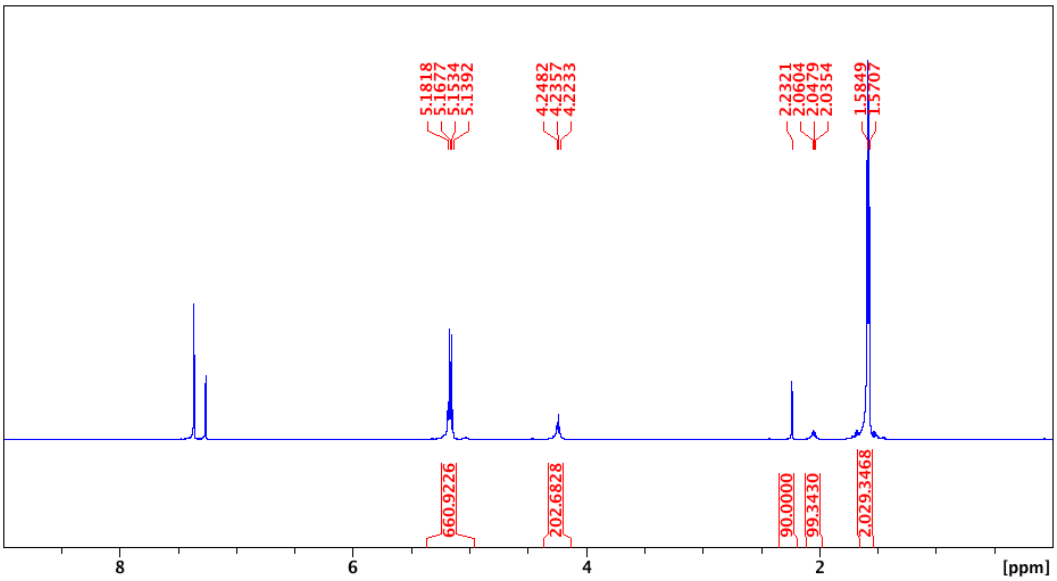

Figure C38. ^{1}H NMR spectrum ($CDCl_3$, 300 MHz, 298 K) of PLA-*b*-PTMC-*b*-PLA polymerization (Table 4-1, entry 10). Standard is hexamethylbenzene (HMB). [(fc^{P,B})Zn(μ-OCH_2Ph)]$_2$: HMB: TMC: LA ratio is 1:10:102:660.

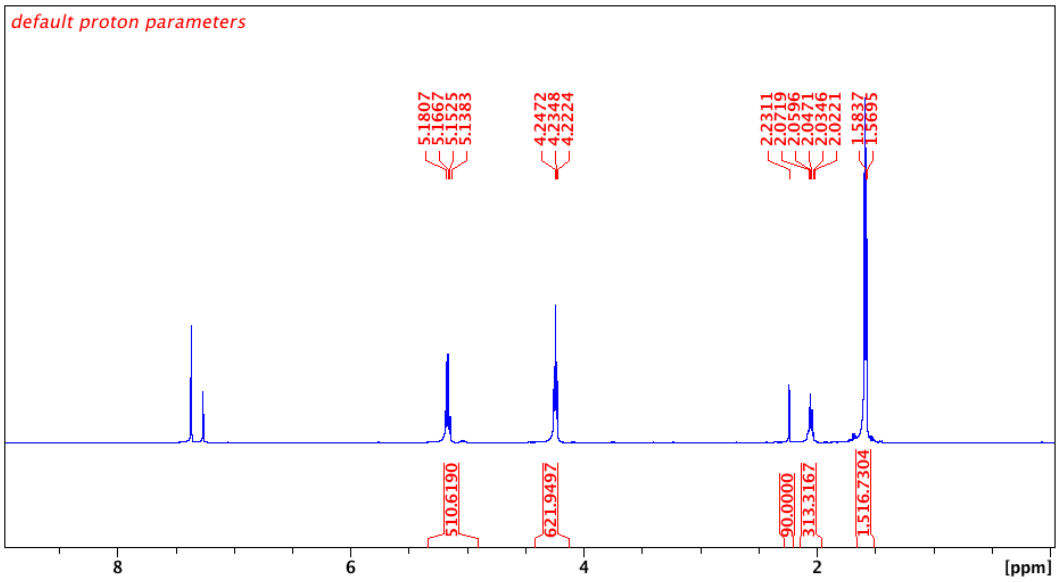

Figure C39. ^{1}H NMR spectrum ($CDCl_3$, 300 MHz, 298 K) of PLA-*b*-PTMC-*b*-PLA polymerization (Table 4-1, entry 11). Standard is hexamethylbenzene (HMB). [(fc^{P,B})Zn(μ-OCH_2Ph)]$_2$: HMB: TMC: LA ratio is 1:10:312:510.

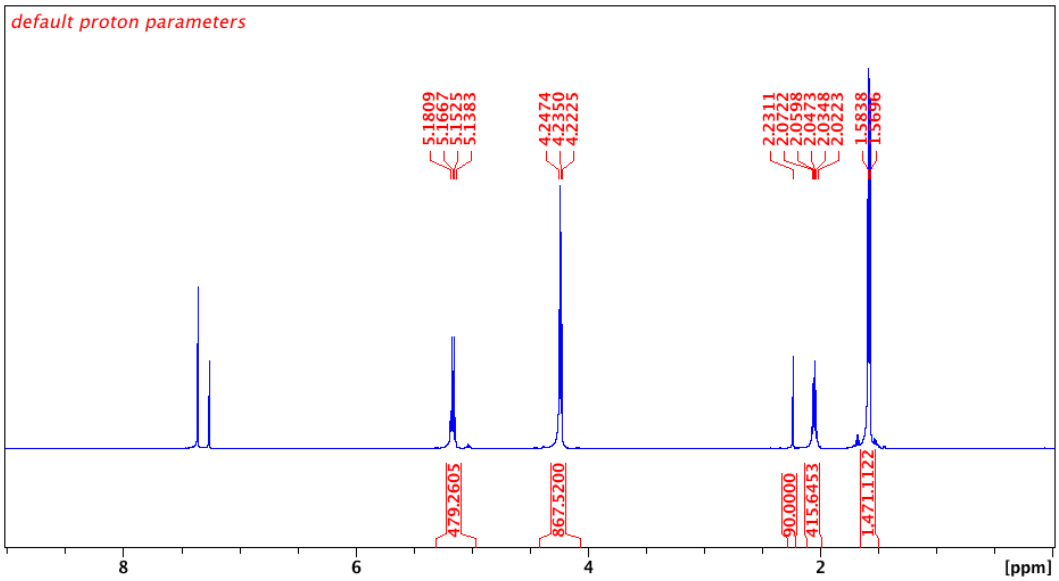

Figure C40. ^{1}H NMR spectrum ($CDCl_3$, 300 MHz, 298 K) of PLA-*b*-PTMC-*b*-PLA polymerization (Table 4-1, entry 12). Standard is hexamethylbenzene (HMB). [(fc^{P,B})Zn(μ-OCH_2Ph)]$_2$: HMB: TMC: LA ratio is 1:10:434:480.

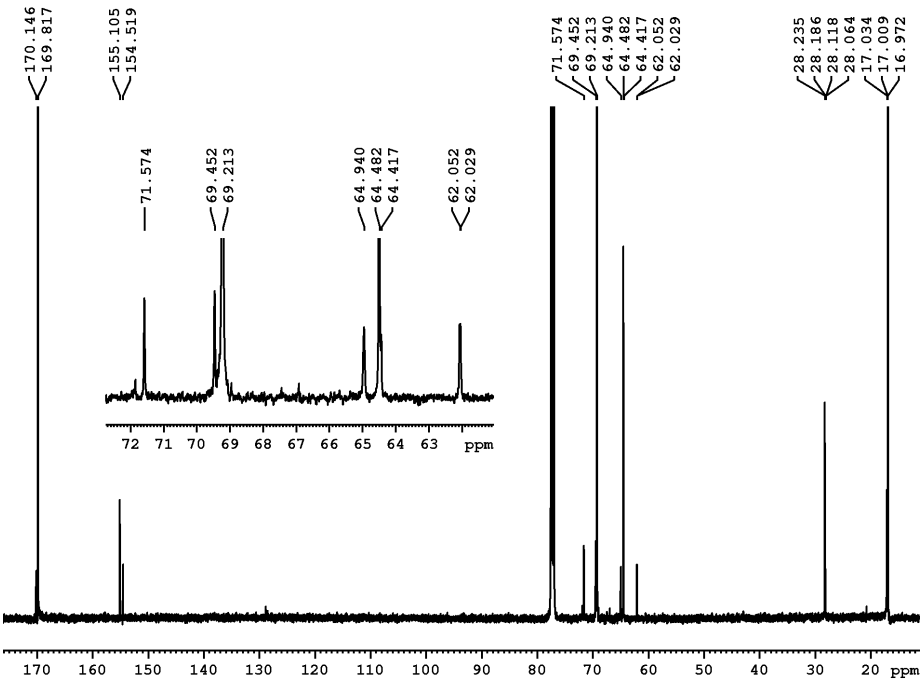

Figure C41. ^{13}C NMR spectrum ($CDCl_3$, 126 MHz, 298 K) of the PLA-*b*-PTMC-*b*-PLA-*b*-PTMC-*b*-PLA copolymer (Table 4-1, entry 9).

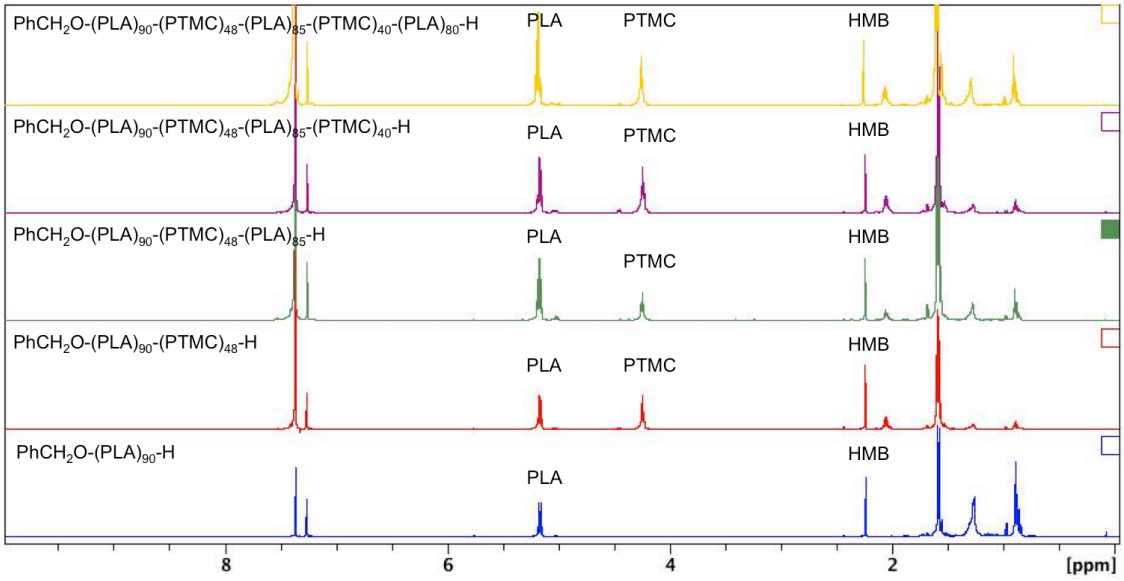

Figure C42. ^{1}H NMR spectra ($CDCl_3$, 500 MHz, 298 K) corresponding to the stepwise preparation of PLA-*b*-PTMC-*b*-PLA-*b*-PTMC-*b*-PLA in the presence of HMB as an internal standard.

4.7.2 Conversion studies

Table C1. Molecular weight versus conversion study of 1,3-trimethylene carbonate.

Time (min)	Conversion (%)	M_n (NMR)	M_n (GPC)	$Đ$
30	37	9,400	10,300	1.04
50	44	11,200	12,500	1.09
70	58	14,800	14,500	1.14
90	72	18,400	17,000	1.17

Conditions: benzene as a solvent (1.5 mL) and hexamethylbenzene as an internal standard. The experiment was performed at ambient temperature.

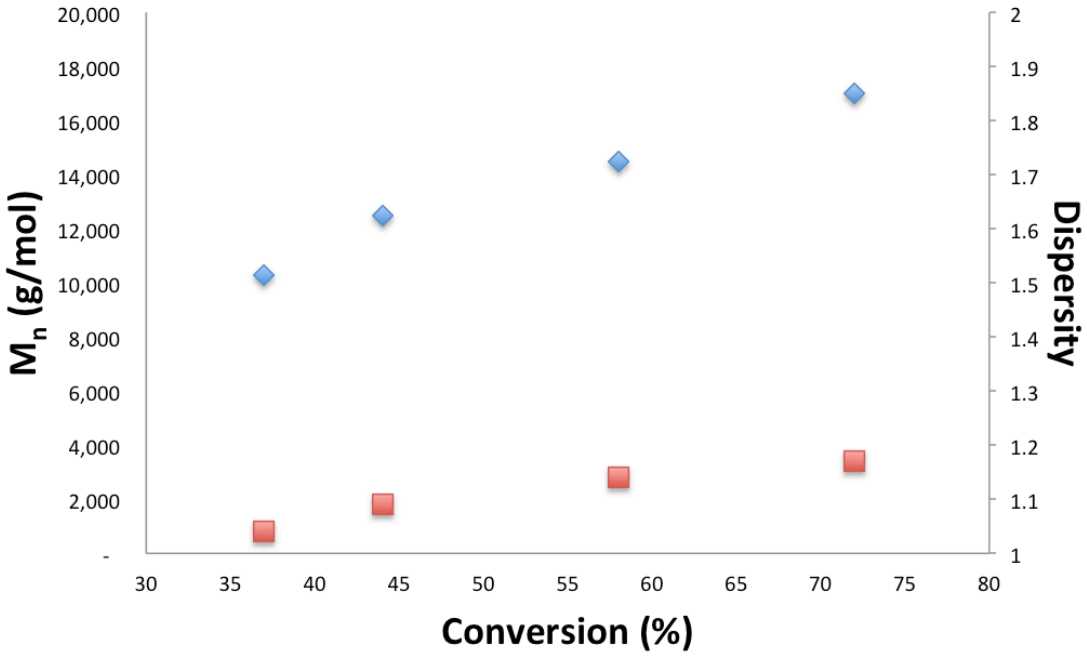

Figure C43. Conversion of 1,3-trimethylene carbonate versus M_n.

Table C2. Molecular weight versus conversion study of L-lactide.

Time (min)	Conversion (%)	M_n (NMR)	M_n (GPC)	*Đ*
10	18	8,100	8,800	1.06
20	31	13,500	13,500	1.09
30	42	19,700	20,400	1.08
40	52	24,100	25,400	1.01
50	60	27,700	28,700	1.03
60	69	31,200	31,700	1.02

Conditions: benzene as a solvent (1.5 mL) and hexamethylbenzene as an internal standard. The experiment was performed at 70 °C.

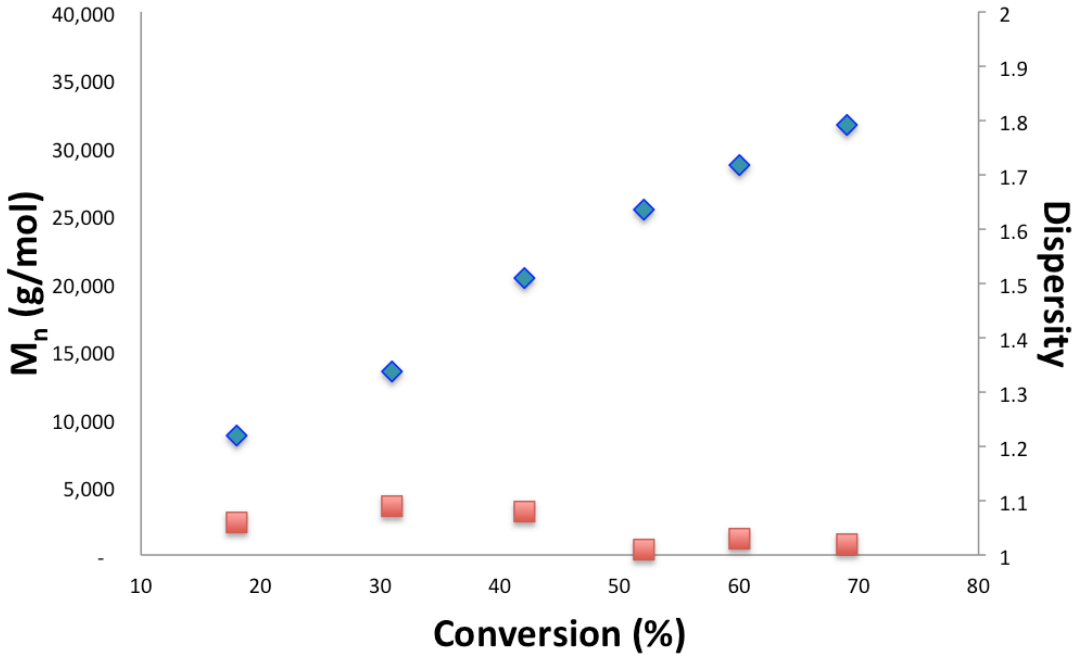

Figure C44. Conversion of L-lactide versus M_n.

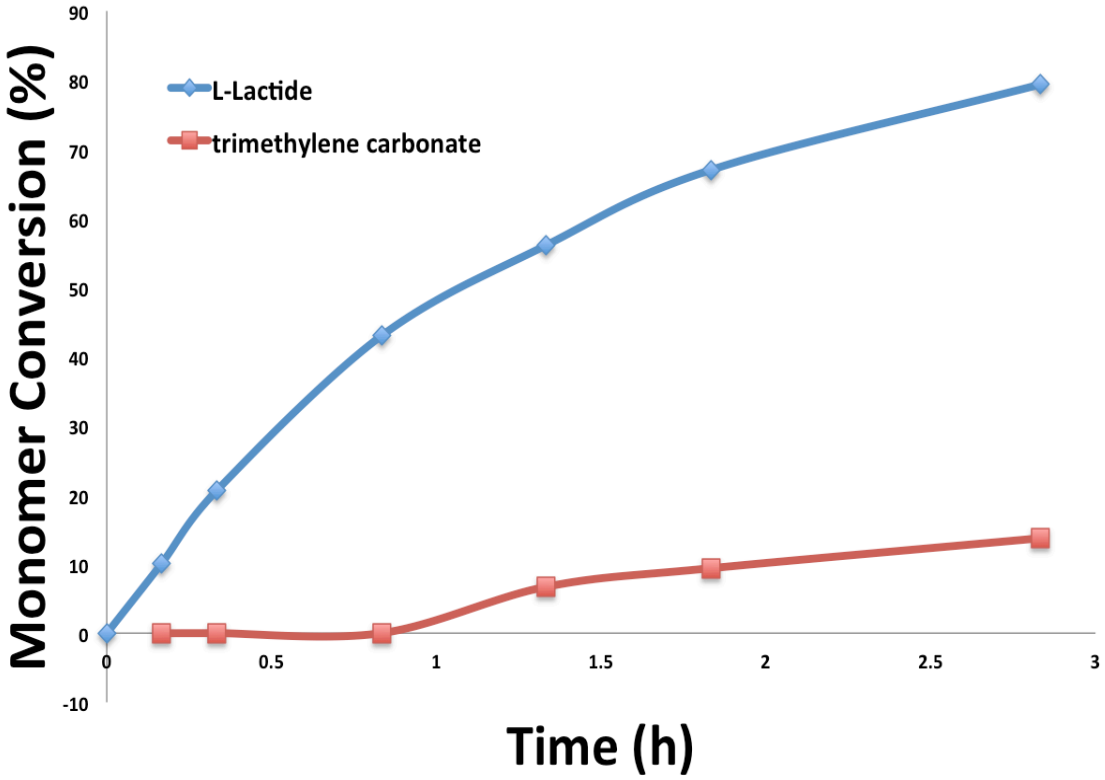

Figure C45. One pot polymerization of L-lactide (100 equivalents) and trimethylene carbonate (50 equivalents) in 0.5 mL of C_6D_6 at 50 °C.

4.7.3 Gel permeation chromatography

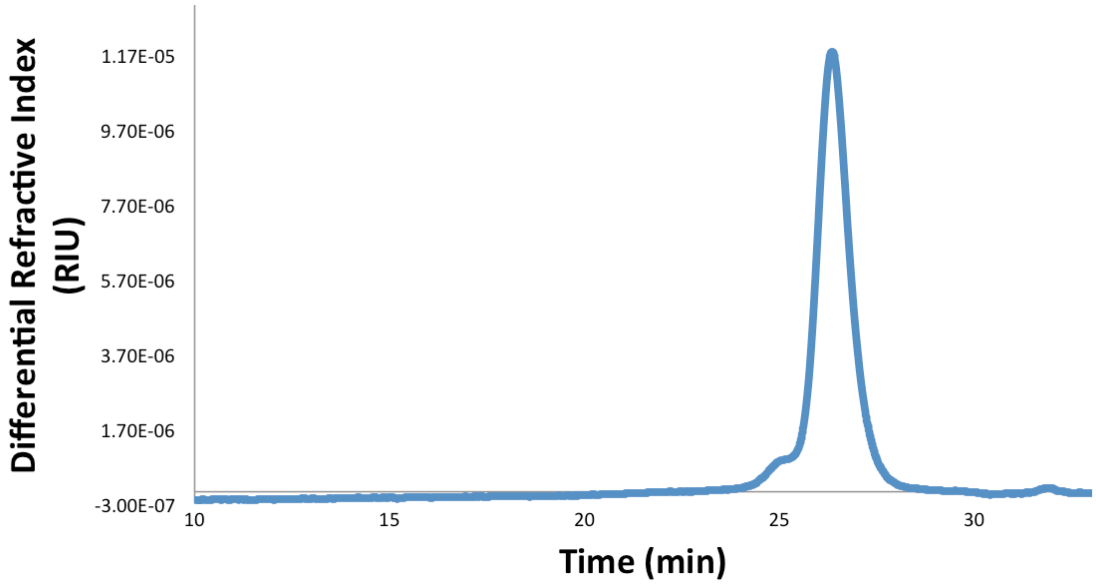

Figure C46. Polymerization of 101 equivalents of 1,3-trimethylene carbonate (Table 4-1, entry 2); M_n = 9,000; M_w =9,100; $Đ$ = 1.01.

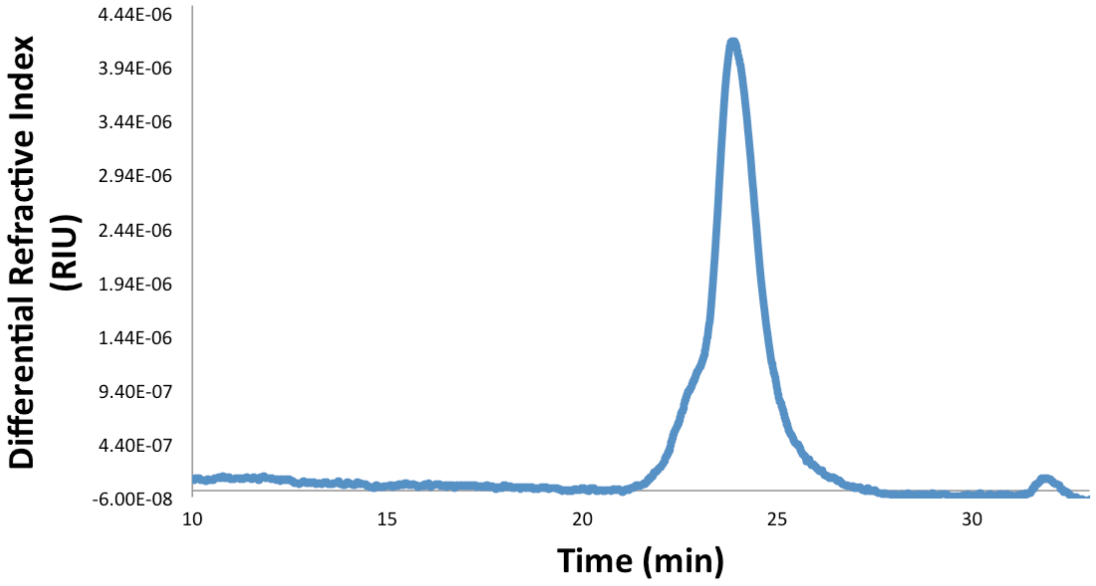

Figure C47. Polymerization of 283 equivalents of L-lactide (Table 4-1, entry 1); M_n = 39,800; M_w = 45,200; $Đ$ = 1.14.

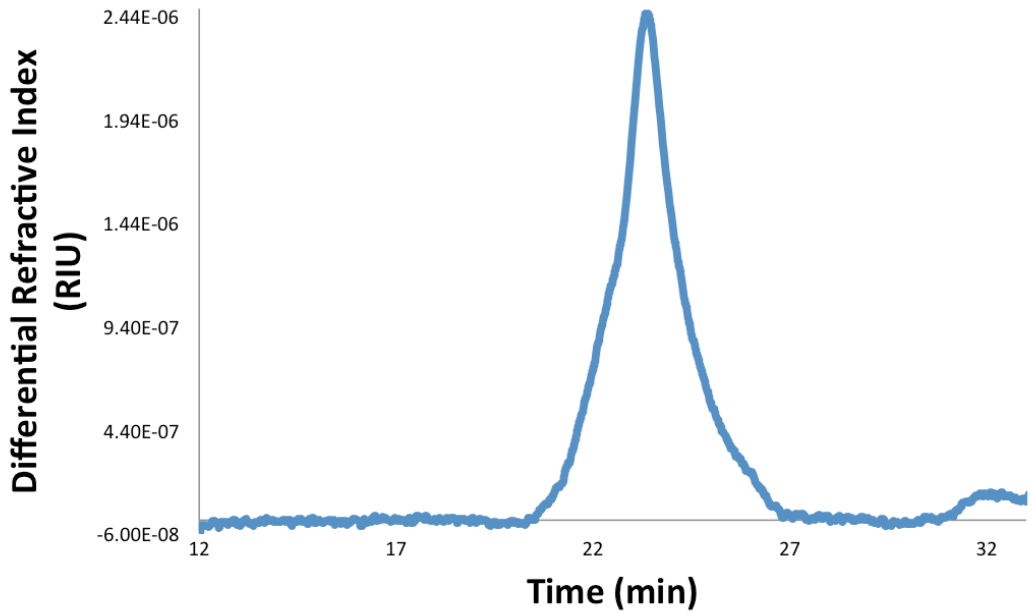

Figure C48. GPC trace of PLA-*b*-PTMC copolymer (Table 4-1, entry 3); M_n = 55,500; M_w = 61,800; $Đ$ = 1.12.

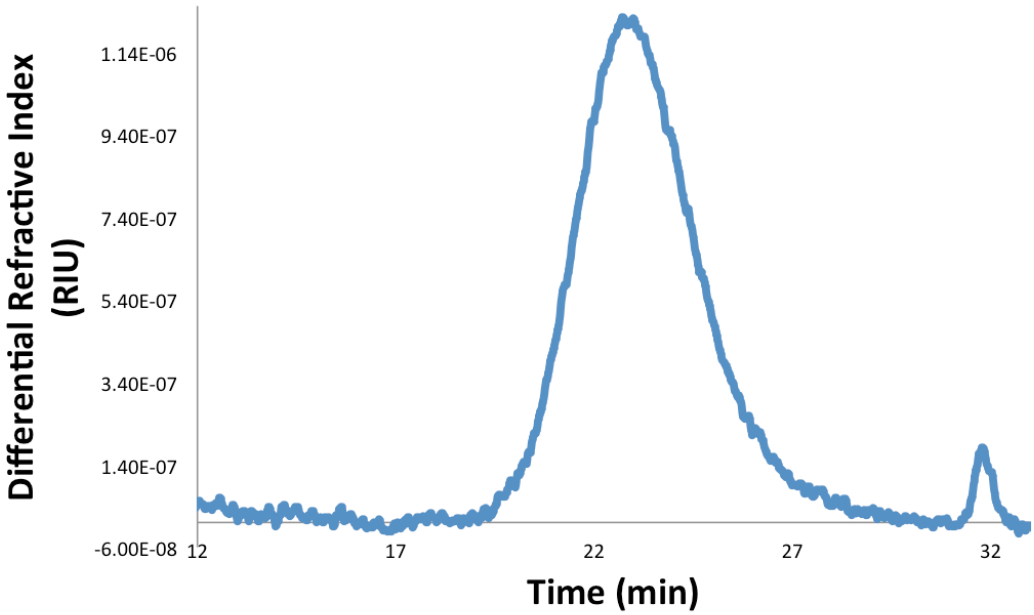

Figure C49. GPC trace of PTMC-*b*-PLA copolymer (Table 4-1, entry 4); M_n = 47,000; M_w = 75,000; $Đ$ = 1.60.

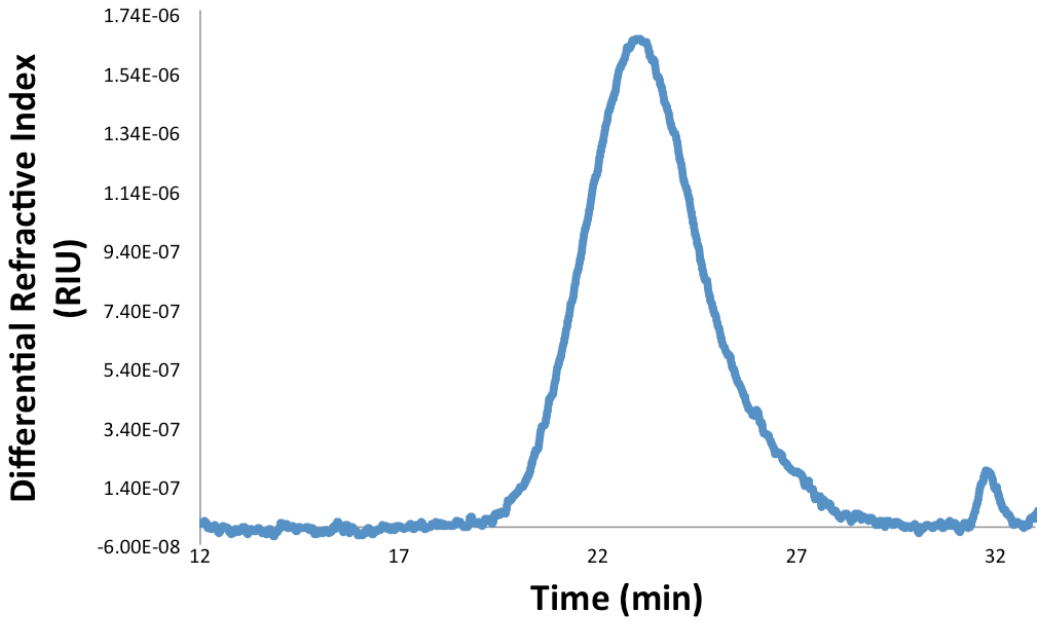

Figure C50. GPC trace of PTMC-*b*-PLA-*b*-PTMC copolymer (Table 4-1, entry 5); M_n = 43,200; M_w = 72,200; $Đ$ = 1.67.

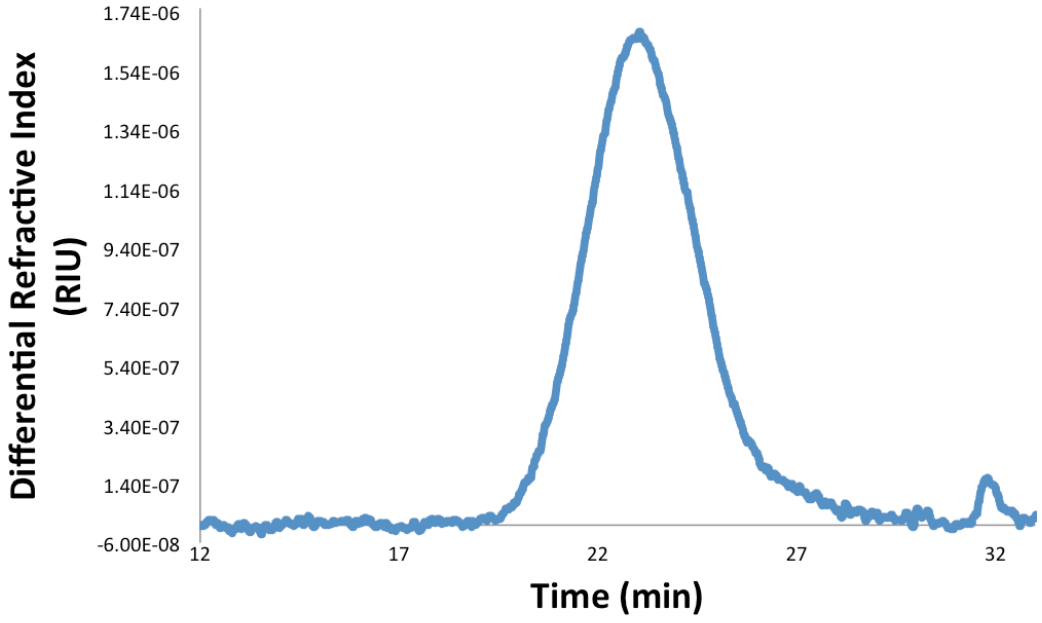

Figure C51. GPC trace of PLA-*b*-PTMC-*b*-PLA copolymer (Table 4-1, entry 6); M_n = 55,600; M_w = 81,400; $Đ$ = 1.46.

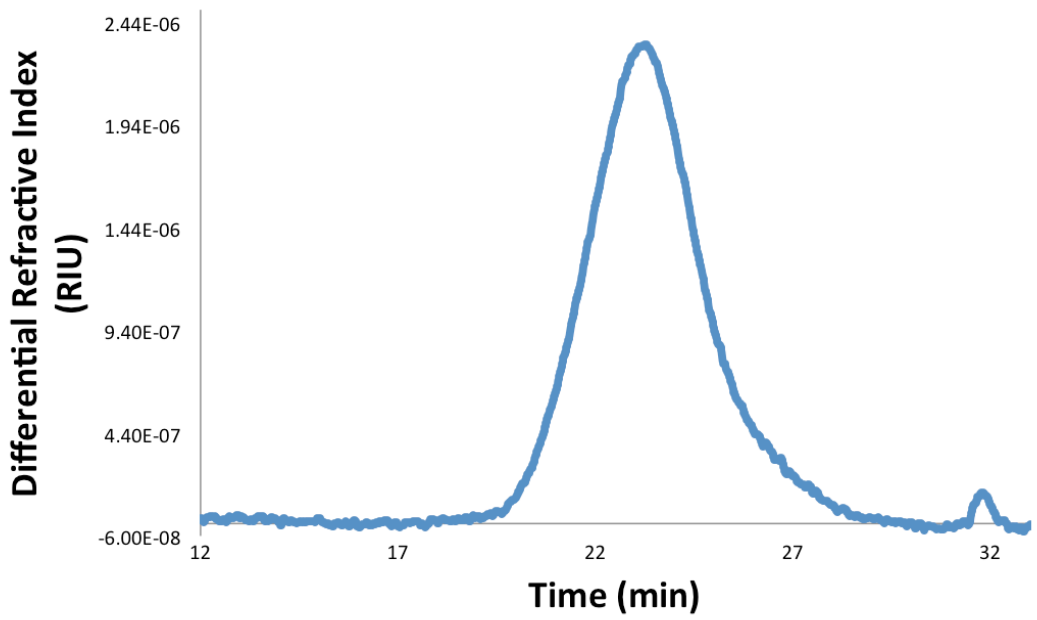

Figure C52. GPC trace of PLA-*b*-PTMC-*b*-PLA-*b*-PTMC copolymer (Table 4-1, entry 7); M_n = 48,200; M_w = 71,800; $Đ$ = 1.49.

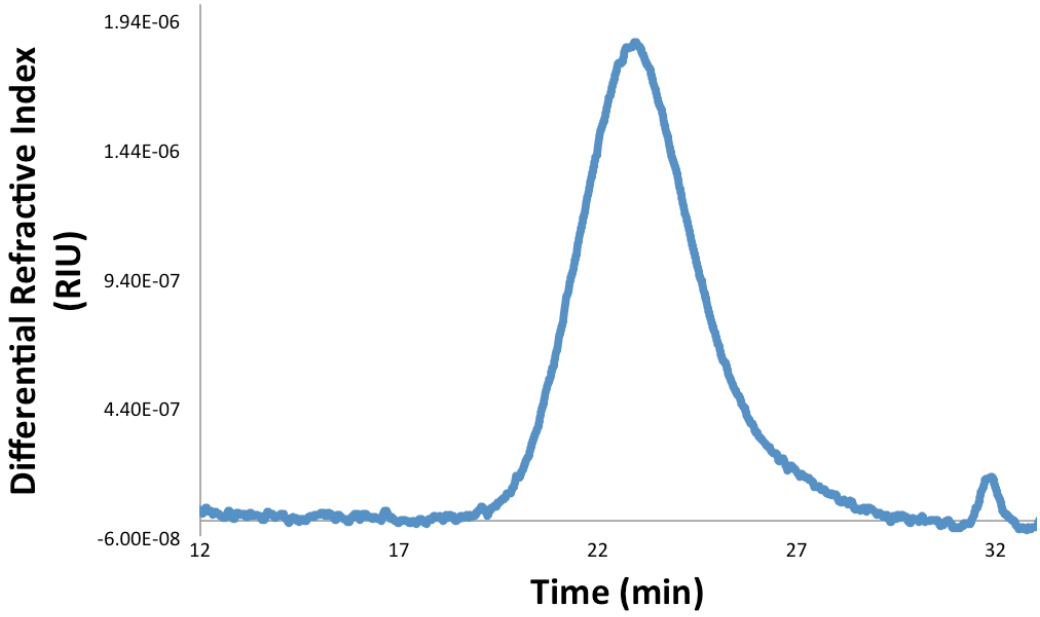

Figure C53. GPC trace of PTMC-*b*-PLA-*b*-PTMC-*b*-PLA-*b*-PTMC copolymer (Table 4-1, entry 8); M_n = 58,900; M_w = 87,900; $Đ$ = 1.49.

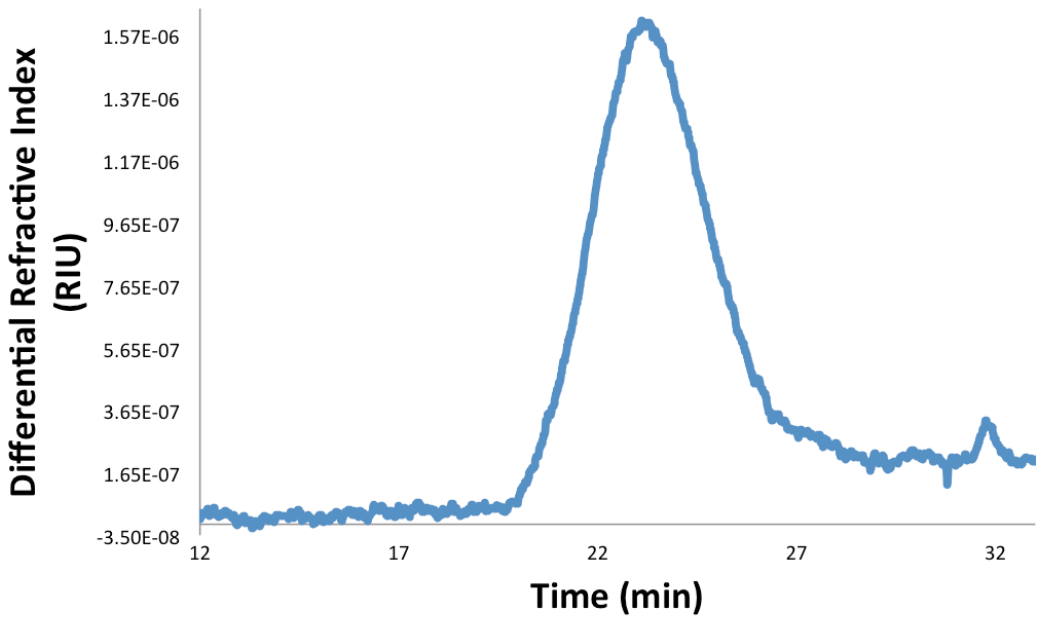

Figure C54. GPC trace of PLA-*b*-PTMC-*b*-PLA-*b*-PTMC-*b*-PLA copolymer (Table 4-1, entry 9); M_n = 53,200; M_w = 89,700; $Đ$ = 1.69.

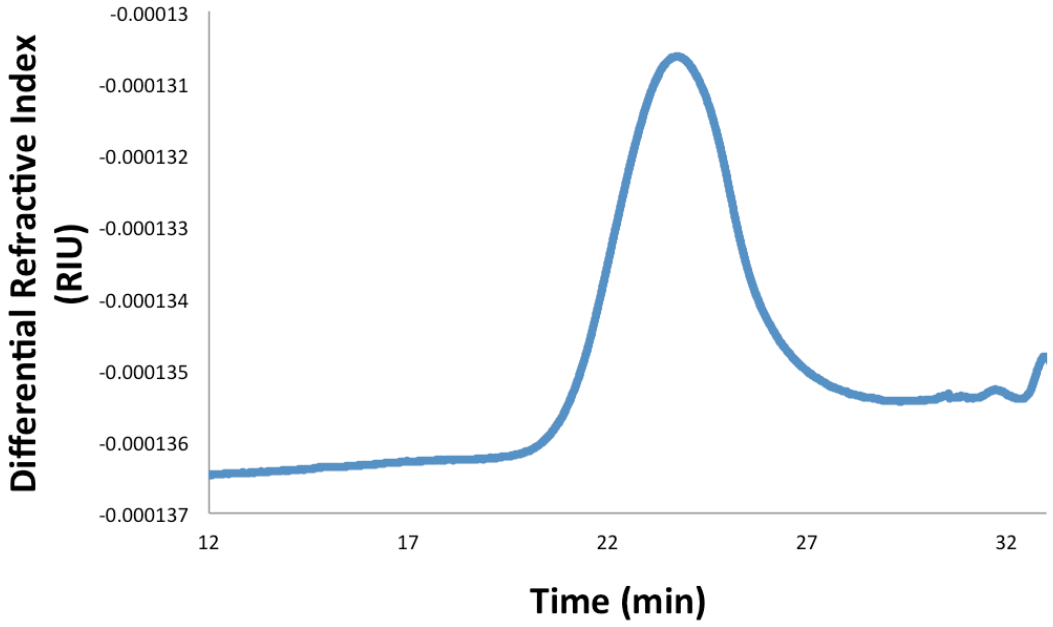

Figure C55. GPC trace of PLA-*b*-PTMC-*b*-PLA copolymer (Table 4-1, entry 10); M_n = 50,800; M_w = 65,800; $Đ$ = 1.29.

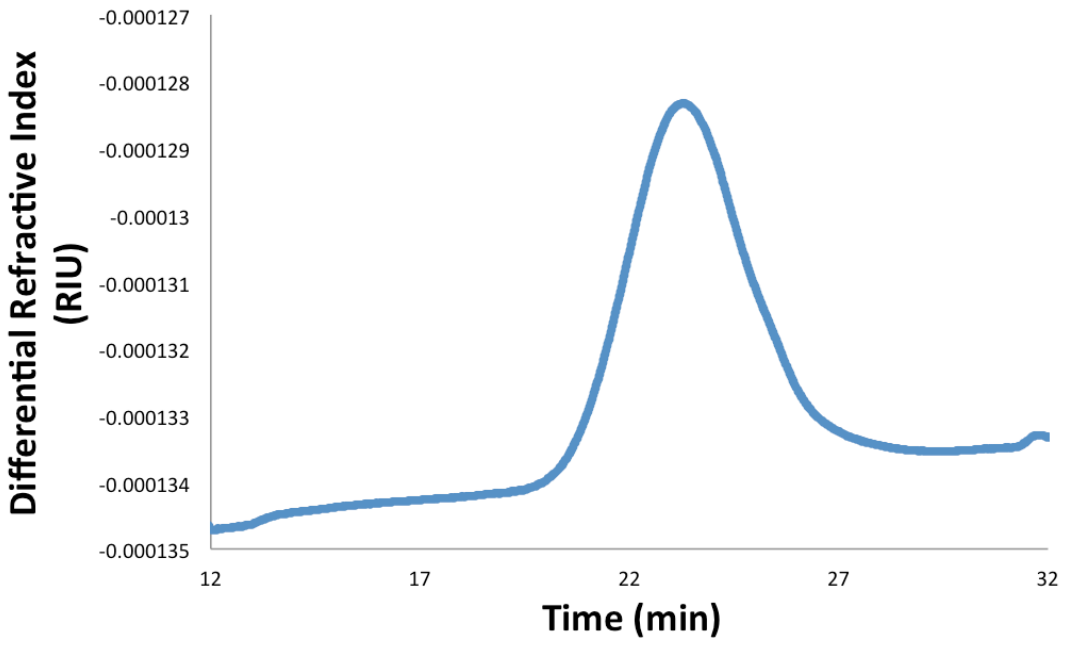

Figure C56. GPC trace of PLA-*b*-PTMC-*b*-PLA copolymer (Table 4-1, entry 11); M_n = 48,900; M_w = 69,400; $Đ$ = 1.42.

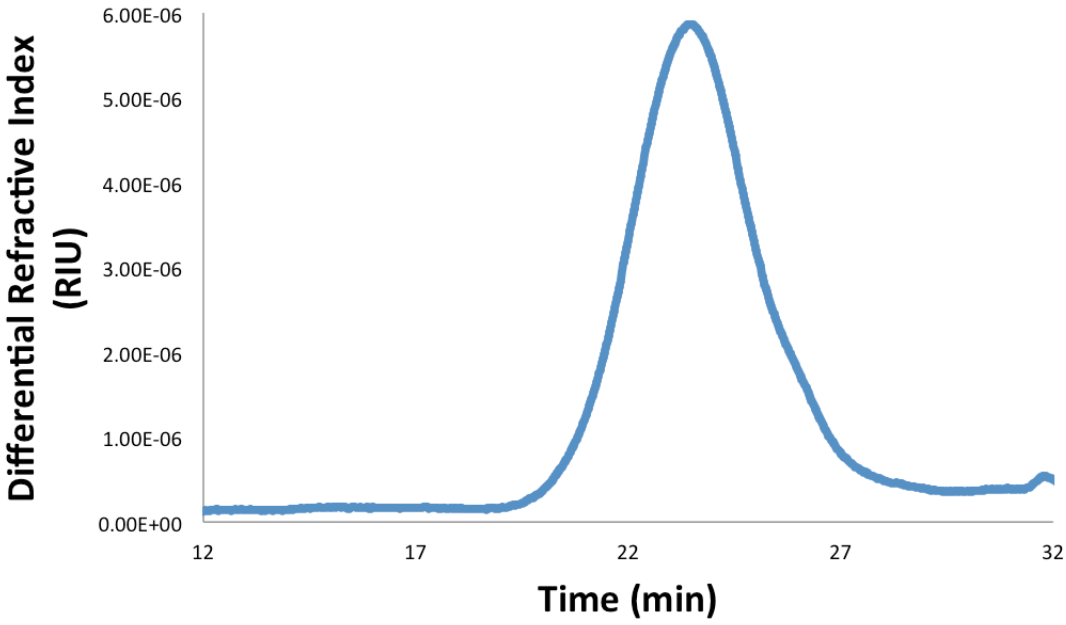

Figure C57. GPC trace of PLA-*b*-PTMC-*b*-PLA copolymer (Table 4-1, entry 12); M_n = 51,200; M_w = 86,000; $Đ$ = 1.68.

4.7.4 Differential scanning calorimetry

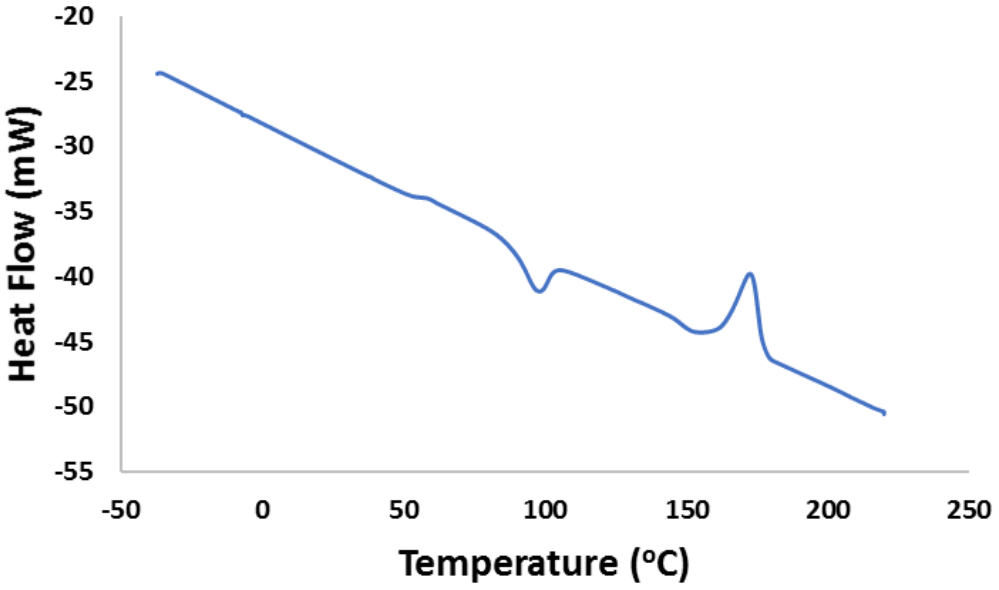

Figure C58. DSC curve (third heating run) of a PLA sample (M_n (GPC) = 39,800; Table 4-1, entry 1).

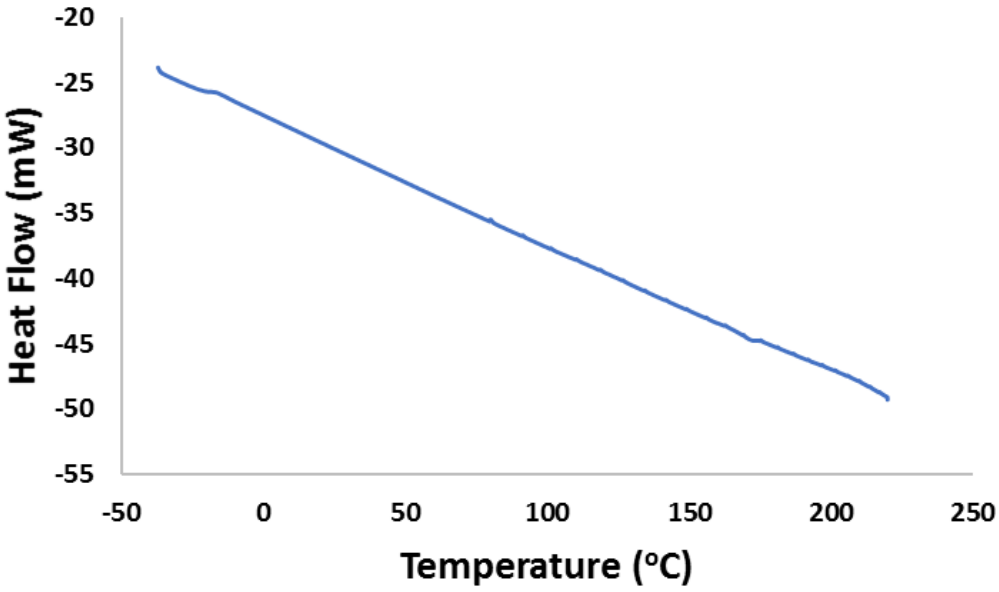

Figure C59. DSC curve (third heating run) of a PTMC sample (M_n (GPC) = 9,000; Table 4-1, entry 2).

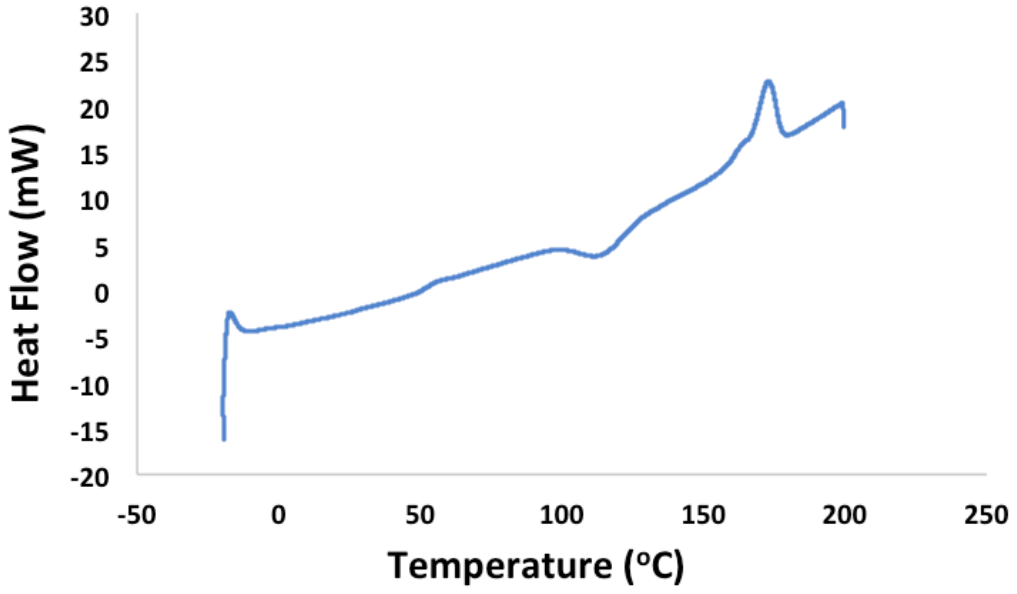

Figure C60. DSC curve (third heating run) of a PLA-*b*-PTMC sample (M_n (GPC) = 55,500; Table 4-1, entry 3).

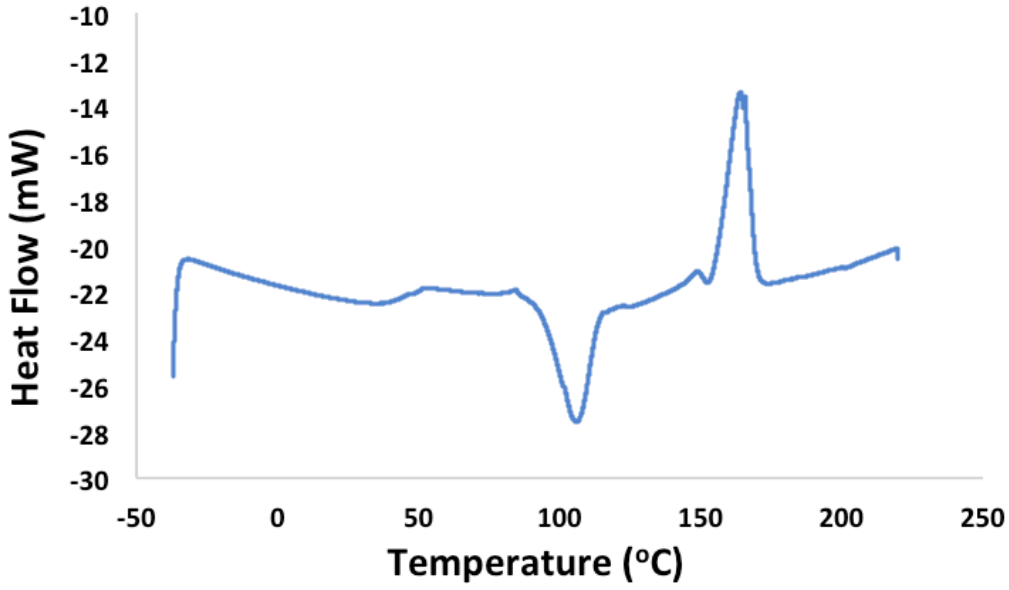

Figure C61. DSC curve (third heating run) of a PTMC-*b*-PLA sample (M_n (GPC) = 47,000; Table 4-1, entry 4).

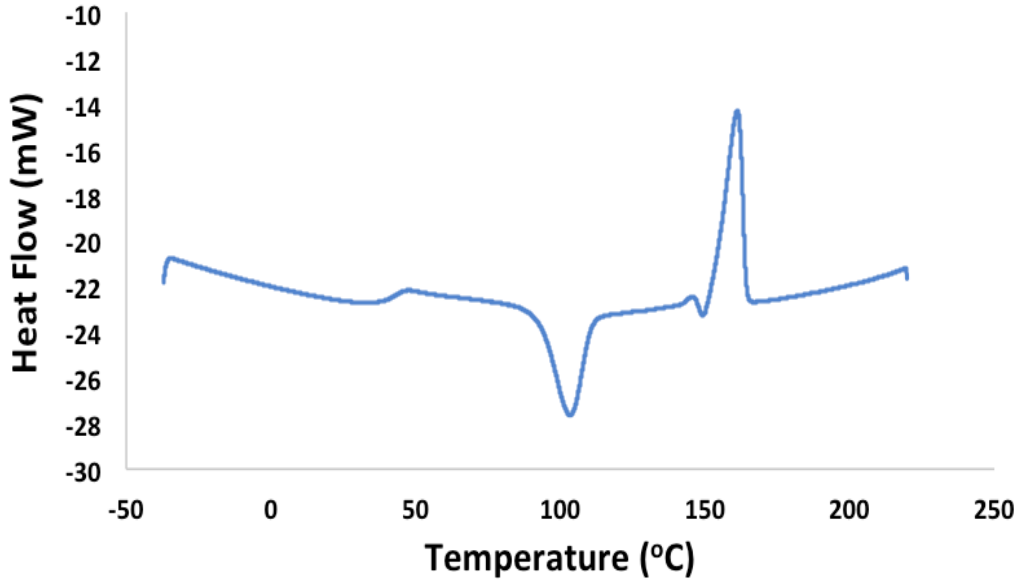

Figure C62. DSC curve (third heating run) of a PTMC-*b*-PLA-*b*-PTMC sample (M_n (GPC) = 43,200; Table 4-1, entry 5).

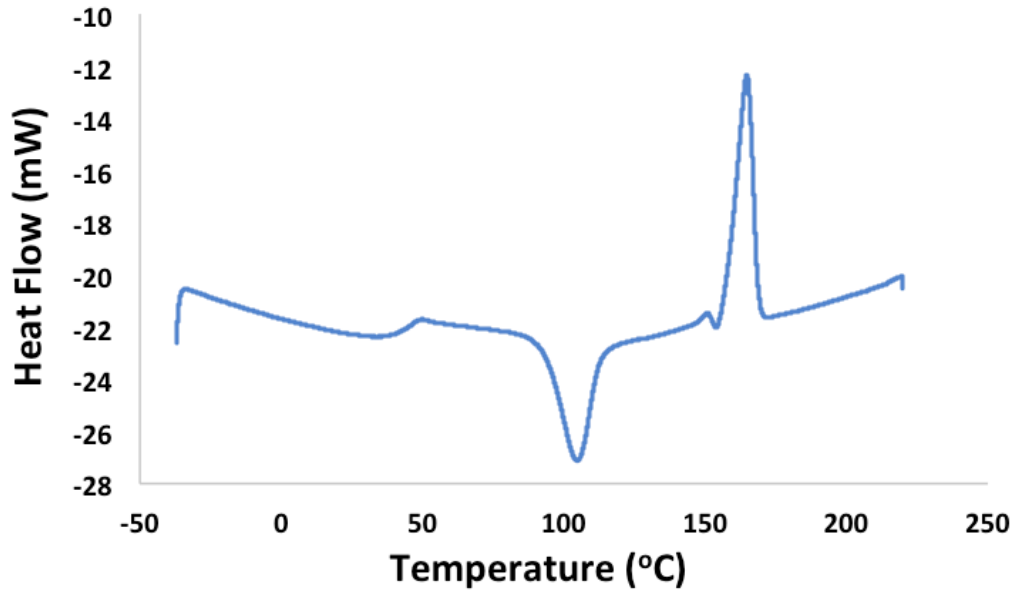

Figure C63. DSC curve (third heating run) of a PLA-*b*-PTMC-*b*-PLA sample (M_n (GPC) = 55,600; Table 4-1, entry 6).

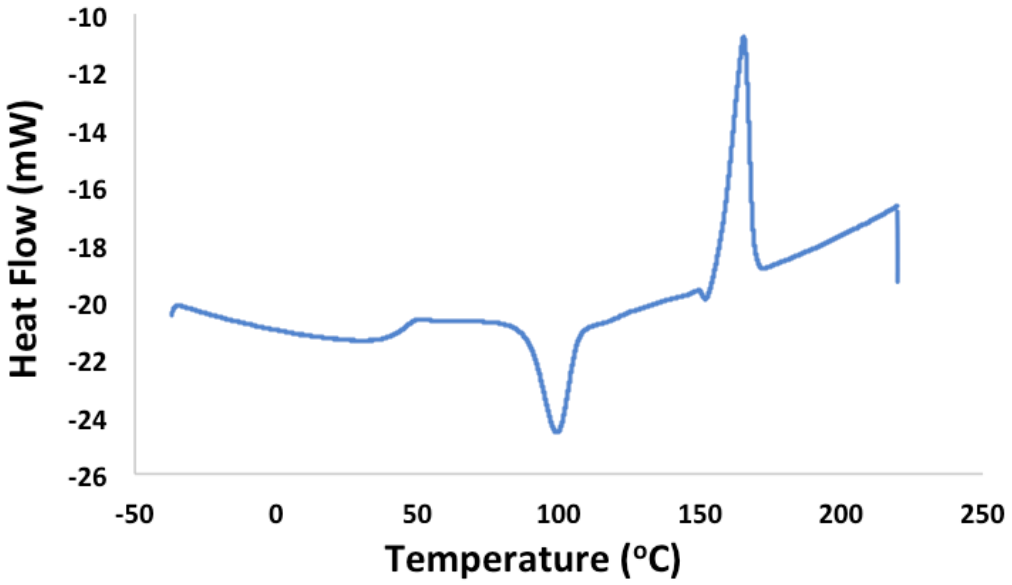

Figure C64. DSC curve (third heating run) of a PLA-*b*-PTMC-*b*-PLA-*b*-PTMC sample (M_n (GPC) = 48,200; Table 4-1, entry 7).

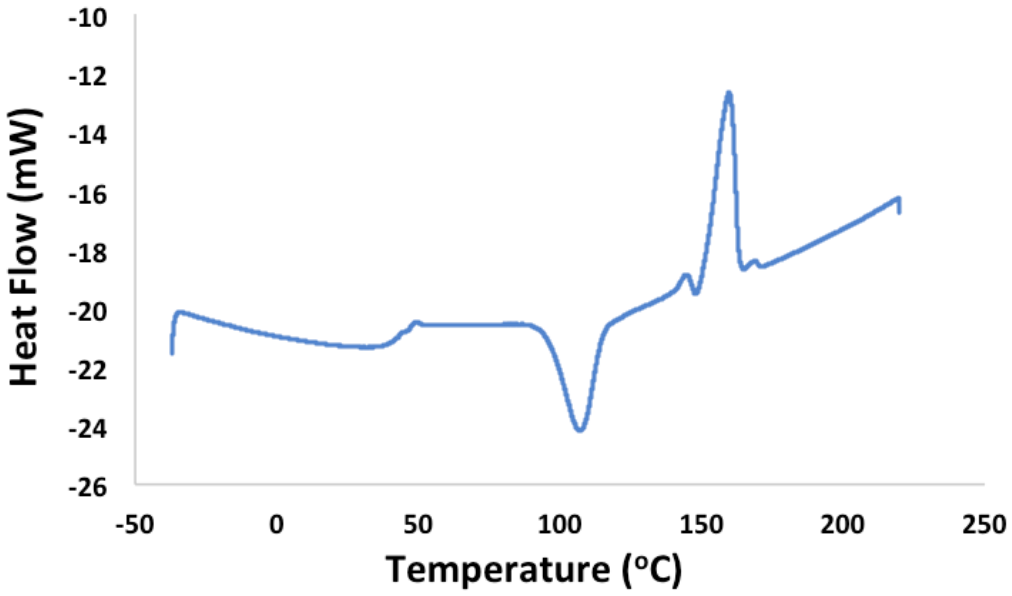

Figure C65. DSC curve (third heating run) of a PTMC-*b*-PLA-*b*-PTMC-*b*-PLA-*b*-PTMC sample (M_n (GPC) = 58,900; Table 4-1, entry 8).

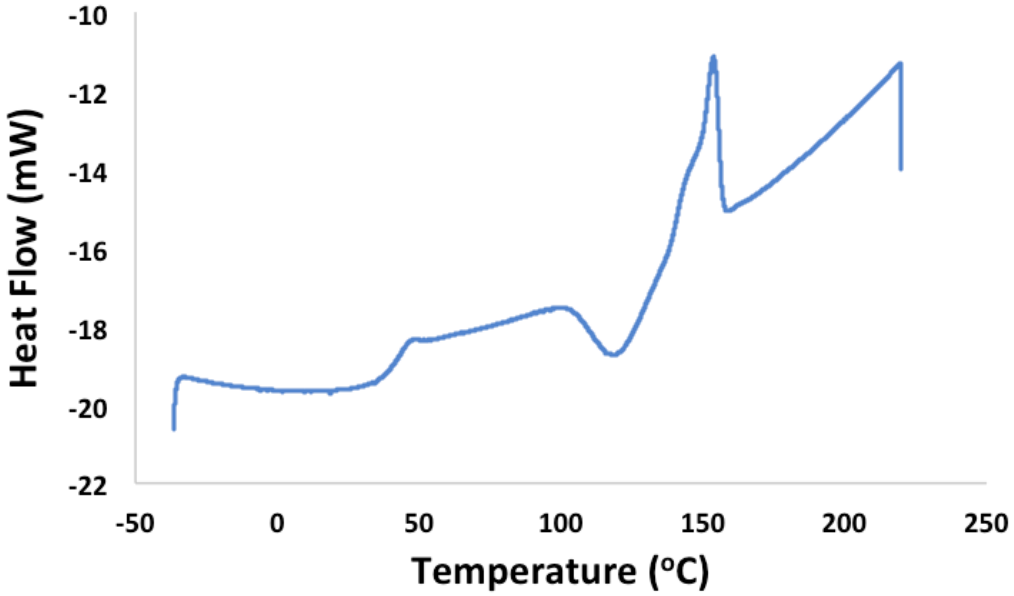

Figure C66. DSC curve (third heating run) of a PLA-*b*-PTMC-*b*-PLA-*b*-PTMC-*b*-PLA sample (M_n (GPC) = 53,200; Table 4-1, entry 9).

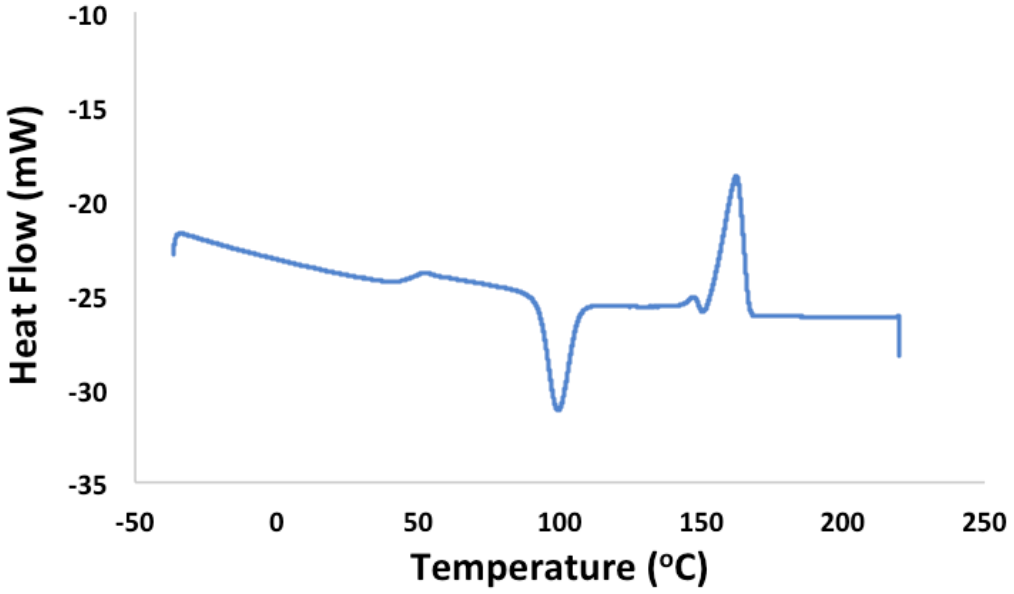

Figure C67. DSC curve (third heating run) of a PLA-*b*-PTMC-*b*-PLA sample (M_n (GPC) = 50,800; Table 4-1, entry 10).

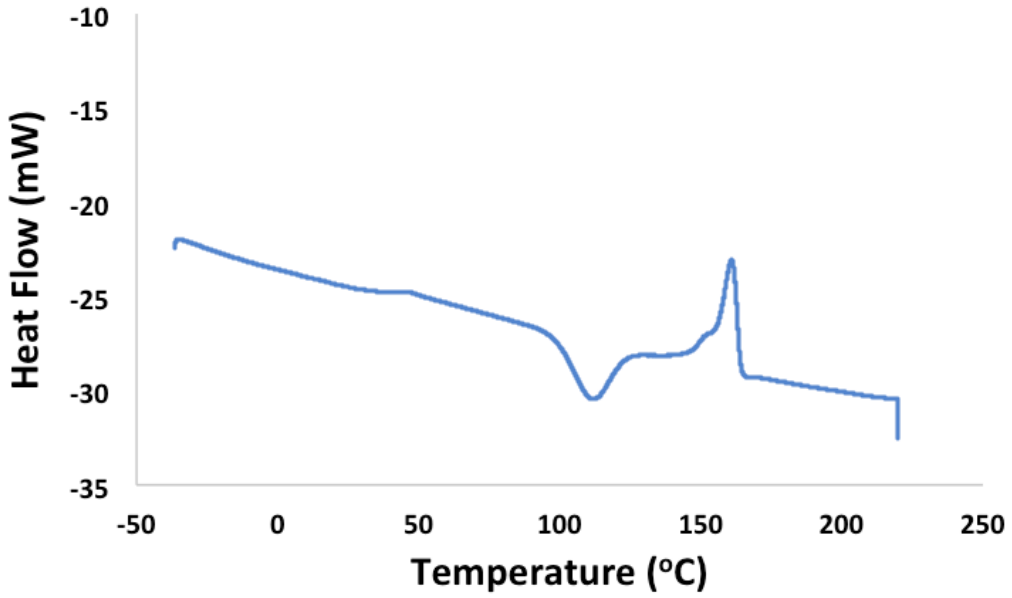

Figure C68. DSC curve (third heating run) of a PLA-*b*-PTMC-*b*-PLA sample (M_n (GPC) = 48,900; Table 4-1, entry 11).

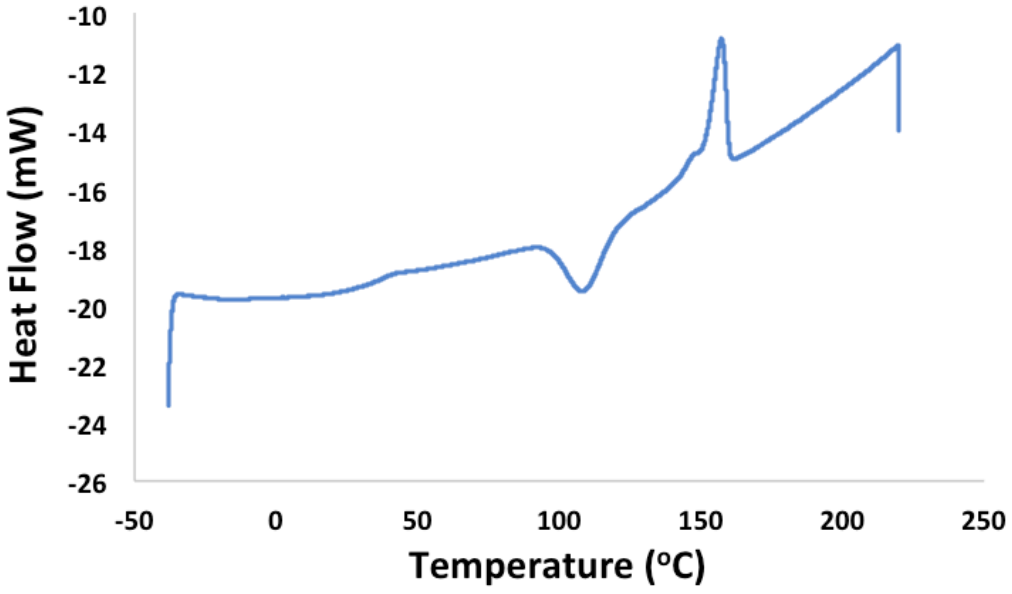

Figure C69. DSC curve (third heating run) of a PLA-*b*-PTMC-*b*-PLA sample (M_n (GPC) = 51,200; Table 4-1, entry 12).

4.7.5 Dynamic mechanical analysis

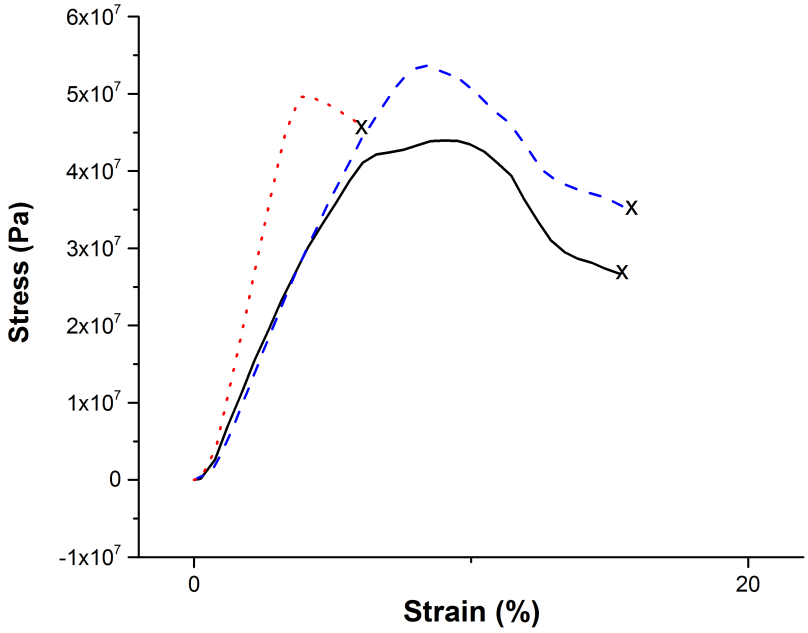

Figure C70. Stress vs. strain curve of a PLA sample (M_n (GPC) = 39,800; Table 4-1, entry 2).

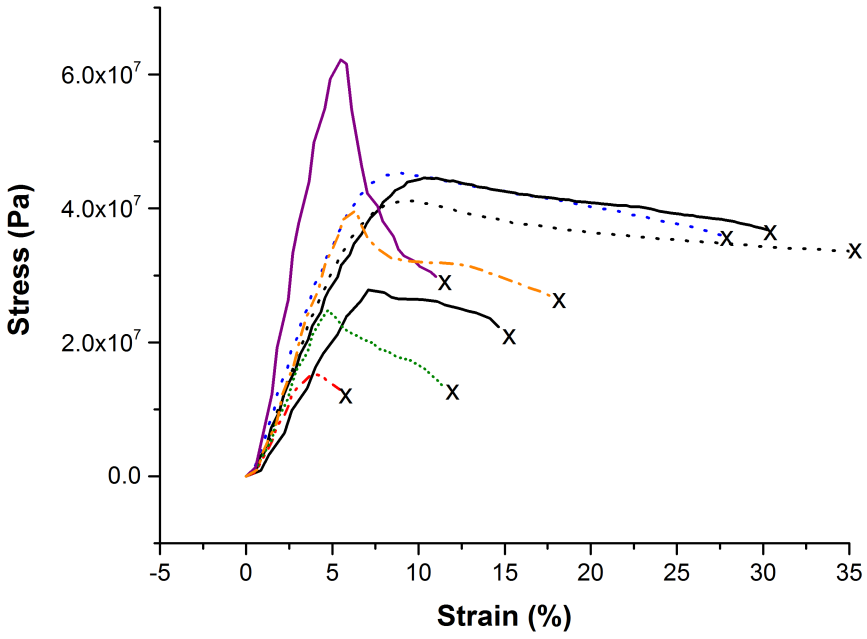

Figure C71. Stress vs. strain curve of a PLA-*b*-PTMC sample (M_n (GPC) = 55,500; Table 4-1, entry 3) and PLA-*b*-PTMC sample (M_n (GPC) = 53,400).

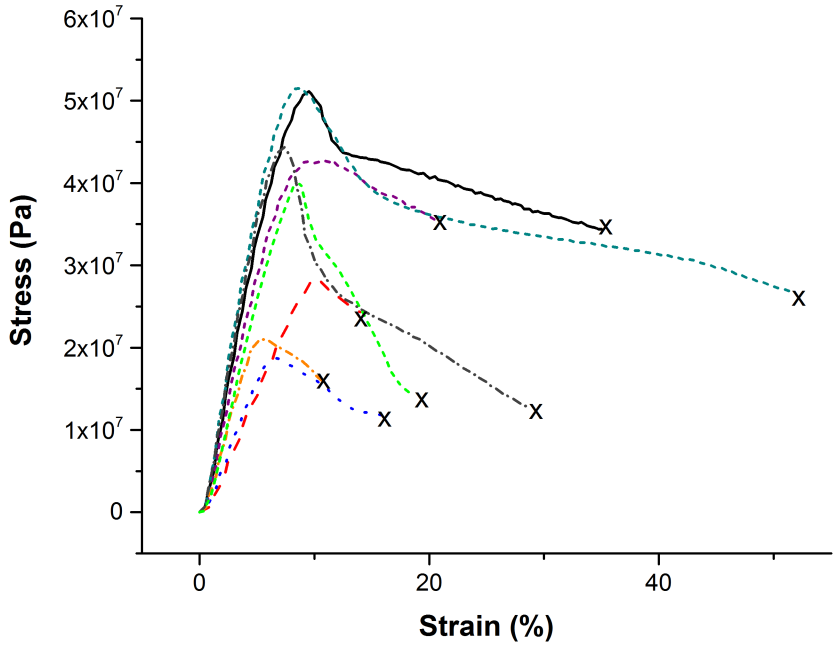

Figure C72. Stress vs. strain curve of a PTMC-*b*-PLA sample (M_n (GPC) = 47,000; Table 4-1, entry 4) and PTMC-*b*-PLA sample (M_n (GPC) = 59,000).

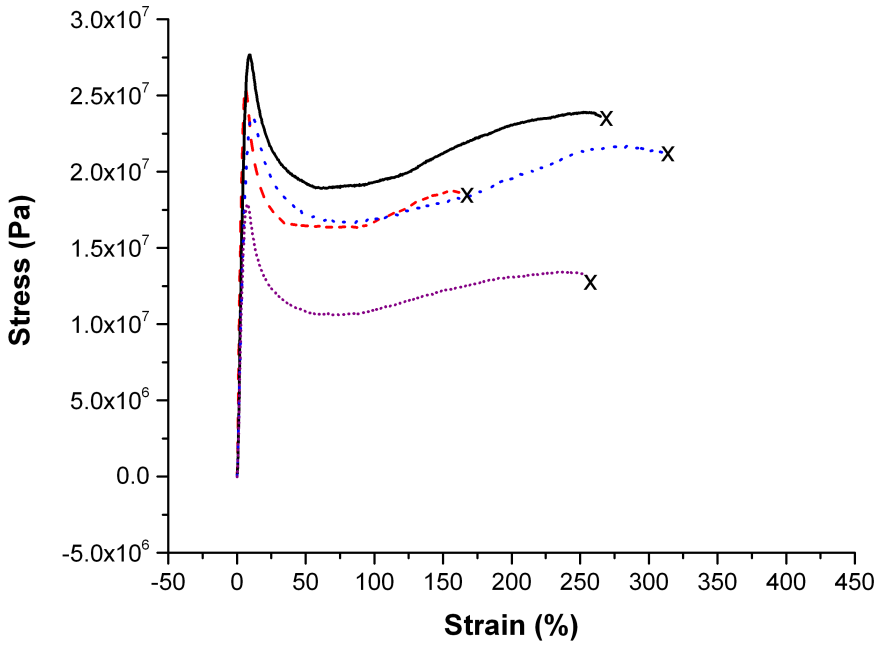

Figure C73. Stress vs. strain curve of a PTMC-*b*-PLA-*b*-PTMC sample (M_n (GPC) = 43,200; Table 4-1, entry 5).

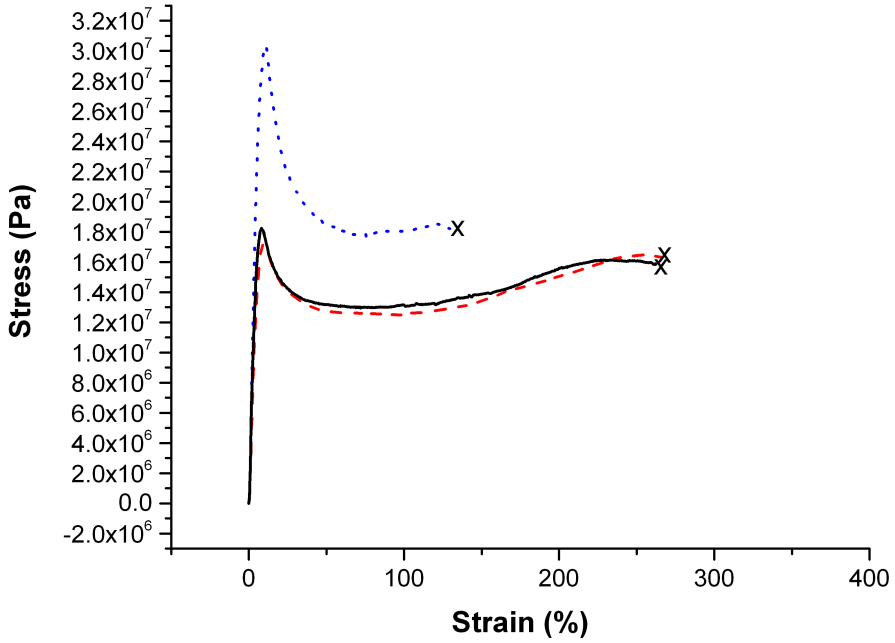

Figure C74. Stress vs. strain curve of a PLA-*b*-PTMC-*b*-PLA sample (M_n (GPC) = 55,600; Table 4-1, entry 6).

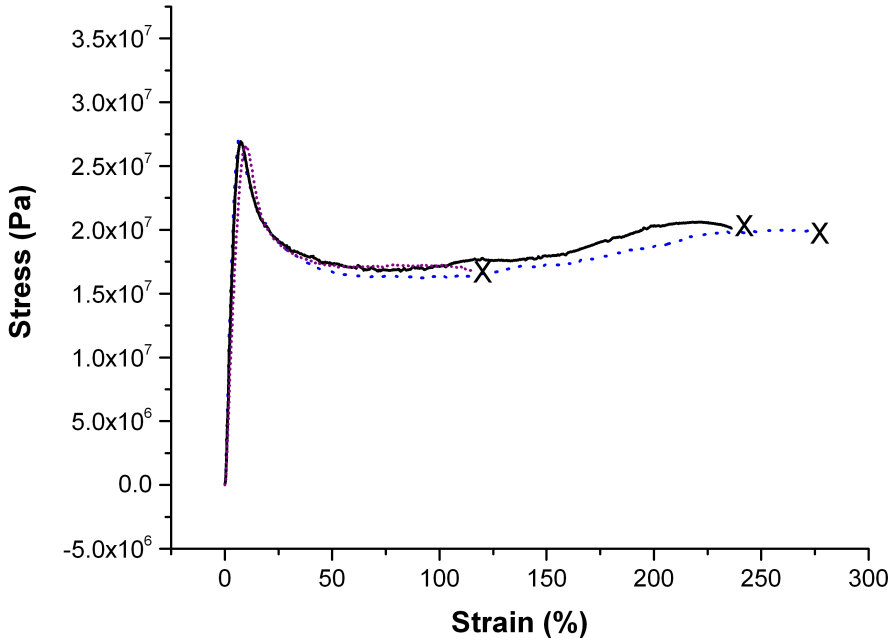

Figure C75. Stress vs. strain curve of a PTMC-*b*-PLA-*b*-PTMC-*b*-PLA sample (M_n (GPC) = 48,200; Table 4-1, entry 7).

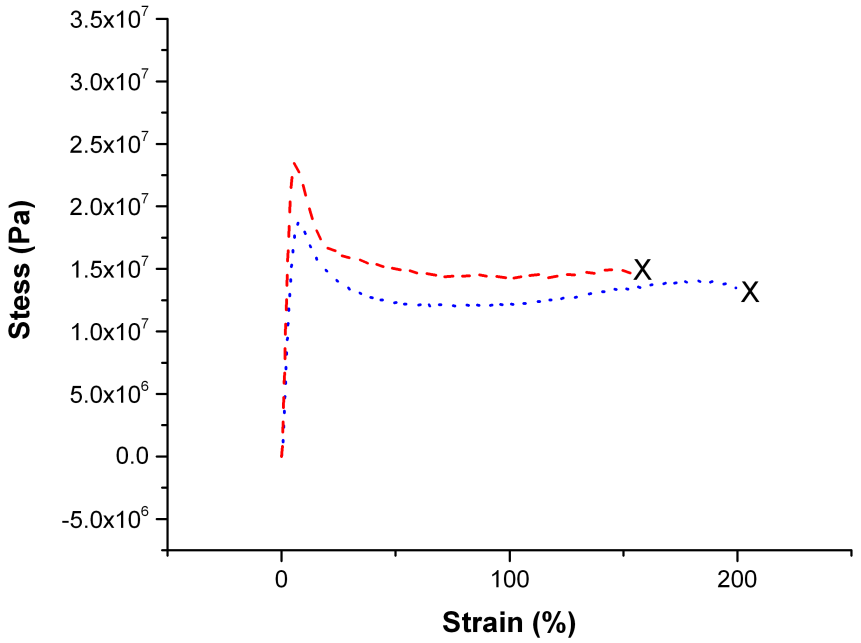

Figure C76. Stress vs. strain curve of a PTMC-*b*-PLA-*b*-PTMC-*b*-PLA-*b*-PTMC sample (M_n (GPC) = 58,900; Table 4-1, entry 8).

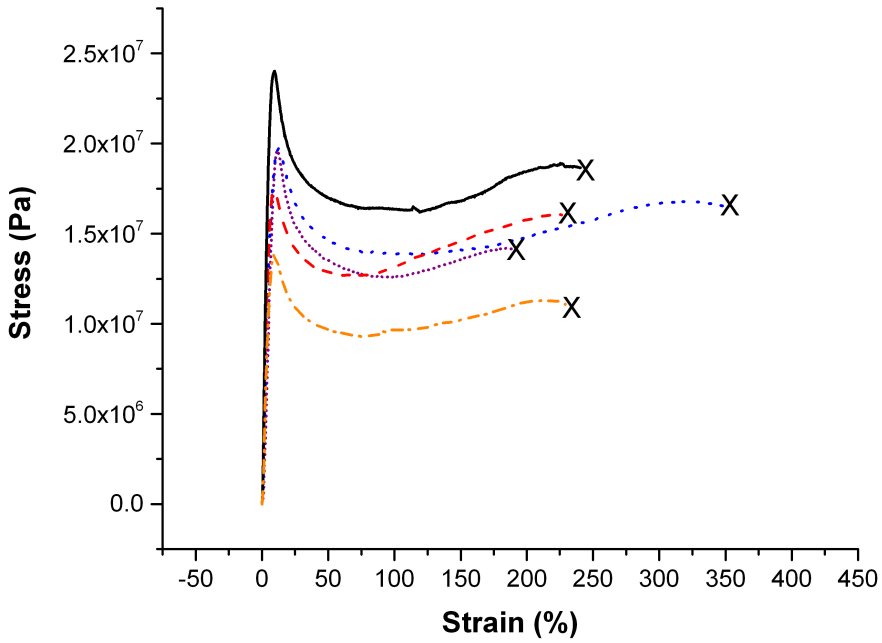

Figure C77. Stress vs. strain curve of a PLA-*b*-PTMC-*b*-PLA-*b*-PTMC-*b*-PLA sample (M_n (GPC) = 53,200; Table 4-1, entry 9).

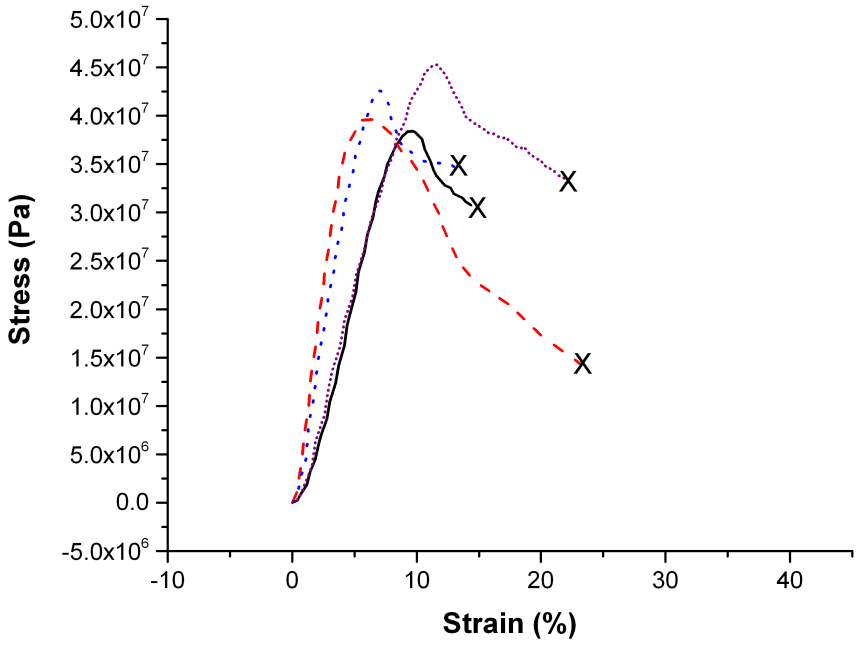

Figure C78. Stress vs. strain curve of a PLA-*b*-PTMC-*b*-PLA sample (M_n (GPC) = 50,800; Table 4-1, entry 10).

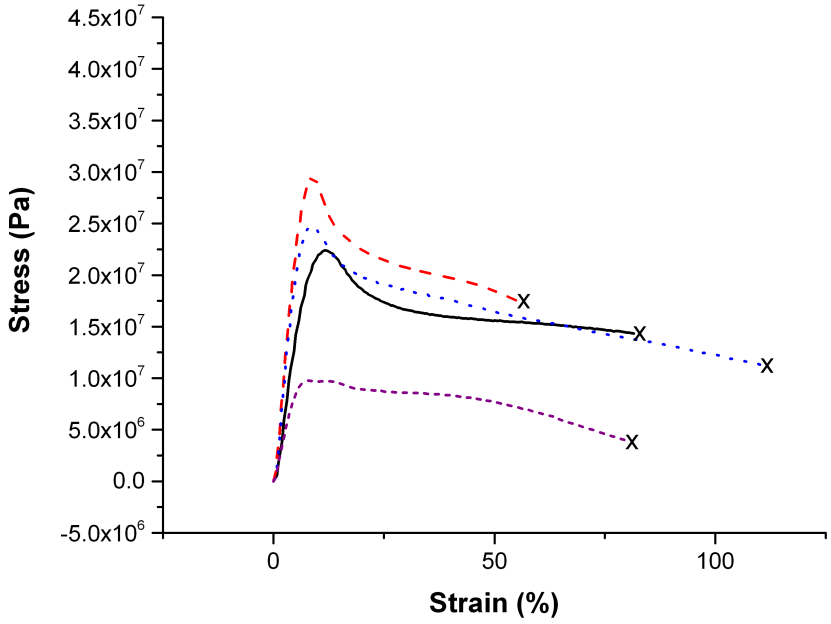

Figure C79. Stress vs. strain curve of a PLA-*b*-PTMC-*b*-PLA sample (M_n (GPC) = 48,900; Table 4-1, entry 11).

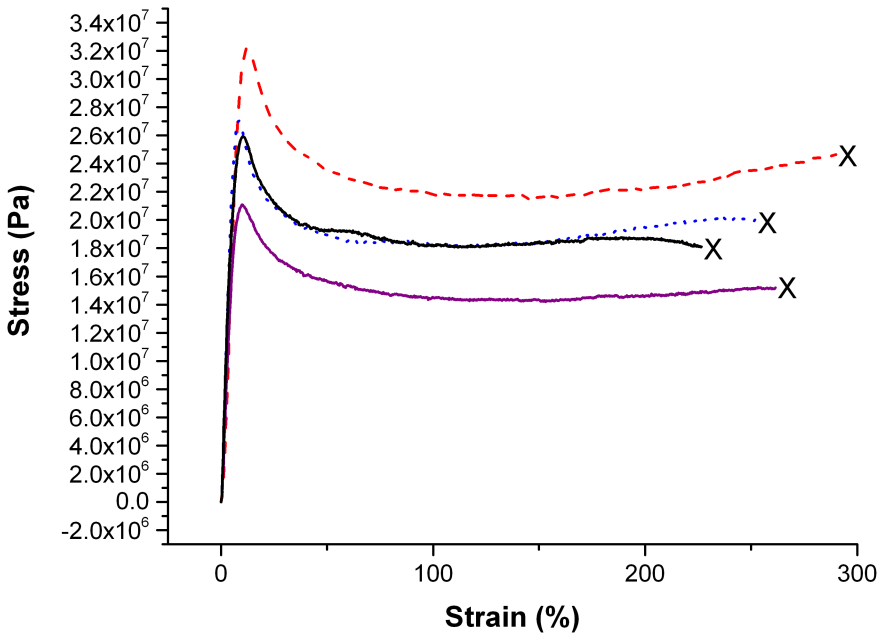

Figure C80. Stress vs. strain curve of a PLA-*b*-PTMC-*b*-PLA sample (M_n (GPC) = 51,200; Table 4-1, entry 12).

4.7.6 X-ray crystallographic data

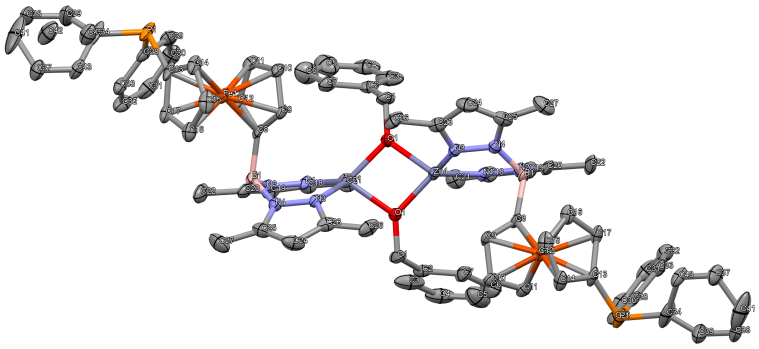

Figure C81. Molecular structure drawing of $[(fc^{P,B})Zn(\mu\text{-}OCH_2Ph)]_2$ with thermal ellipsoids at 50% probability; hydrogen atoms are omitted for clarity. Selected distances (Å) and angles (°): N(1)-Zn(1), 1.970(4); N(3)-Zn(1), 2.019(4); O(1)-Zn(1), 1.946(3), 1.981(4); N(1)-Zn(1)-N(3), 99.44(17); O(1)-Zn(1)-O(1) 80.26(16); N(3)-Zn(1)-O(1), 104.43(16), 131.00(17); N(1)-Zn(1)-O(1), 118.28(17), 124.18(16).

Crystal data for $C_{78}H_{78}B_2Fe_2N_8O_2P_2Zn_2$; M_r = 1485.48; Monoclinic; space group P2/c; *a* = 13.855(4) Å; *b* = 9.378(2) Å; *c* = 30.742(8) Å; α = 90°; β = 101.648(3)°; γ = 90°; V = 3912.1(17) $Å^3$; Z = 2; T = 100(2) K; λ = 0.71073 Å; μ = 1.058 mm^{-1}; d_{calc} = 1.261g·cm^{-3}; 39551 reflections collected; 9416 unique (R_{int} = 0.0667); giving R_1 = 0.0797, wR_2 = 0.2105 for 7205 data with [I>2σ(I)] and R_1 = 0.0983, wR_2 = 0.2187 for all 9416 data. Residual electron density (e^{-}·$Å^{-3}$) max/min: 1.873/-1.188.

4.7.7 DFT calculations

All calculations were carried out with the GAUSSIAN 09[2] program package on the Extreme Science and Engineering Discovery Environment (XSEDE). The methyl groups on the pyrazole substituents were replaced by hydrogen atoms and the phenyl groups on PPh2 were replaced by methyl groups to simplify the calculation. It should be noted that using a dispersion correction is important and the D3 version of Grimme's dispersion[3] was applied.

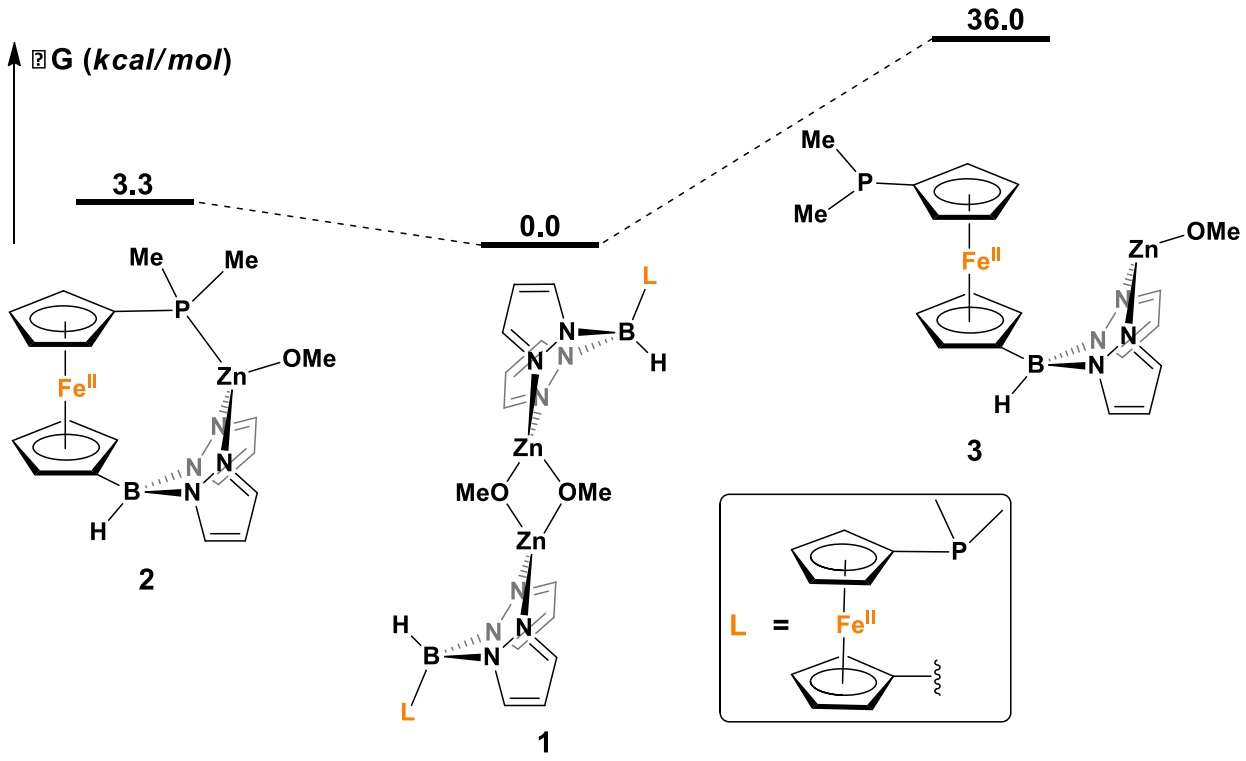

Figure C82. Comparison between the energies of the dimeric zinc complex and two monomeric forms.

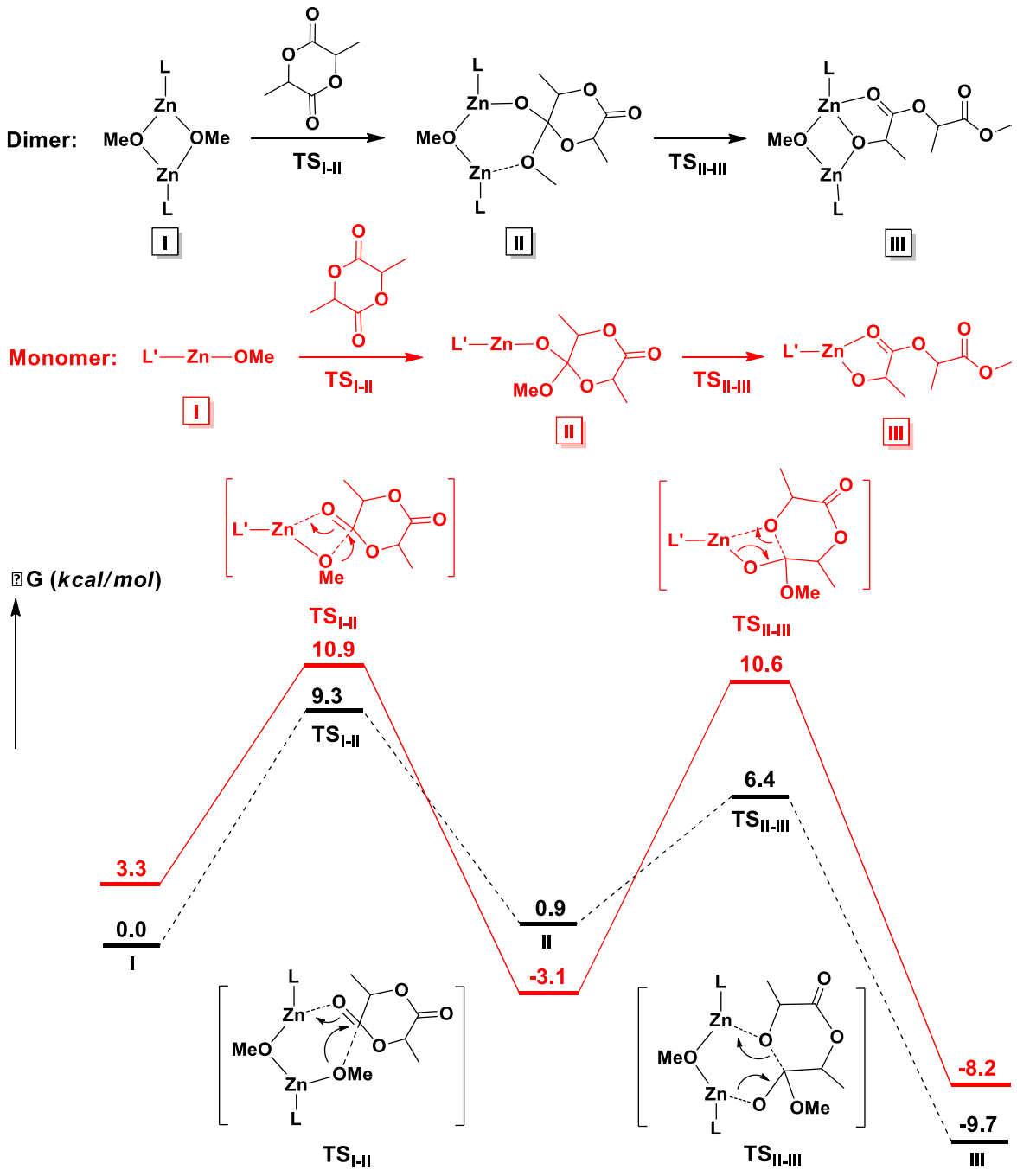

Figure C83. Comparison of the initiation steps of LA polymerization catalyzed by a monomeric (red) or dimeric (black) form of the zinc complex.

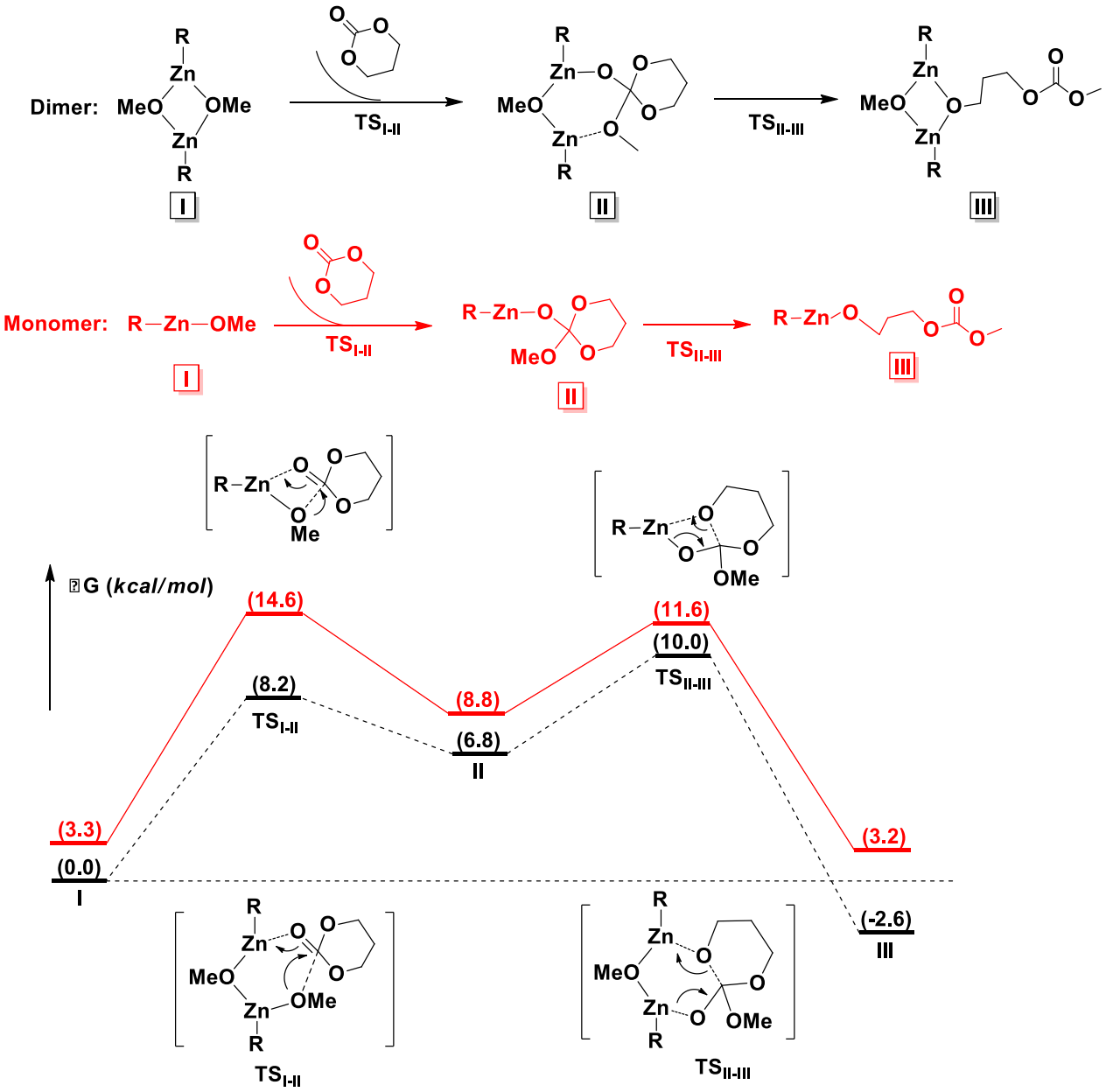

Figure C84. Comparison of the initiation steps of TMC polymerization catalyzed by a monomeric (red) or dimeric (black) form of the zinc complex.

Table C3. Energies, enthalpies, and free energies of the structures calculated at the PBE1PBE/SDD, 6-311+G(d,p) (PCM, GD3, benzene)//B3LYP/LANL2DZ, 6-31G(d) level.

Structures	correction of H	correction of G	G	E with corrections	new G with corrections
lactide	0.151554	0.105907	-534.250539	-533.935059	-533.829152
trimethylene carbonate	0.111273	0.074079	-381.634182	-381.4101659	-381.3360869
1	0.875728	0.70951	-3175.387086	-3497.86323	-3497.15372
2	0.436398	0.345477	-1587.679245	-1748.919683	-1748.574206
3	0.436644	0.344288	-1587.660442	-1748.892456	-1748.548168
TSI-II^{monomer}-LA	0.589366	0.478011	-2121.90727	-2282.86919	-2282.391179
II^{monomer}-LA	0.591557	0.481052	-2121.921651	-2282.894573	-2282.413521
TSII-III^{monomer}-LA	0.58906	0.479528	-2121.905148	-2282.871218	-2282.39169
III^{monomer}-LA	0.591123	0.476715	-2121.941604	-2282.898472	-2282.421757
TSI-II^{dimer}-LA	1.028291	0.842812	-3709.600812	-4031.810914	-4030.968102
II^{dimer}-LA	1.030228	0.846358	-3709.610079	-4031.827784	-4030.981426
TSII-III^{dimer}-LA	1.029558	0.838501	-3709.602191	-4031.811084	-4030.972583
III^{dimer}-LA	1.030265	0.841752	-3709.641343	-4031.840047	-4030.998295
TSI-II^{monomer}-TMC	0.548666	0.446324	-1969.292661	-2130.338613	-2129.892289
II^{monomer}-TMC	0.550803	0.447984	-1969.298916	-2130.349591	-2129.901607
TSII-III^{monomer}-TMC	0.549183	0.448359	-1969.298147	-2130.34546	-2129.897101
III^{monomer}-TMC	0.550702	0.445793	-1969.306127	-2130.356265	-2129.910472
TSI-II^{dimer}-TMC	0.988222	0.811889	-3556.991913	-3879.288584	-3878.476695
II^{dimer}-TMC	0.989541	0.813922	-3556.994991	-3879.292875	-3878.478953
TSII-III^{dimer}-TMC	0.988158	0.811071	-3556.991928	-3879.28486	-3878.473789
III^{dimer}-TMC	0.989914	0.804174	-3557.015624	-3879.298082	-3878.493908
Cat^{monomer}-propagation	0.514005	0.413133	-1854.818974	-2015.915846	-2015.502713
TSI-II^{monomer}-propagation-LA	0.666528	0.54449	-2389.028178	-2549.84817	-2549.30368
II^{monomer}-propagation-LA	0.668844	0.546174	-2389.049481	-2549.88321	-2549.337036
TSII-III^{monomer}-propagation-LA	0.666657	0.545564	-2389.031229	-2549.876085	-2549.330521
III^{monomer}-propagation-LA	0.667879	0.537682	-2389.06437	-2549.876085	-2549.338403

TSI-II^{monomer}-propagation-TMC	0.625781	0.511976	-2236.41156	-2397.314263	-2396.802287
II^{monomer}-propagation-TMC	0.628223	0.51387	-2236.433189	-2397.347309	-2396.833439
TSII-III^{monomer}-propagation-TMC	0.626479	0.512416	-2236.420035	-2397.330991	-2396.818575
III^{monomer}-propagation-TMC	0.62831	0.511968	-2236.4261	-2397.341203	-2396.829235
Cat^{dimer}-propagation	0.923049	0.750067	-3403.230614	-3725.575668	-3724.825601
TSI-II^{dimer}-propagation-LA	1.076096	0.88247	-3937.437068	-4259.51908	-4258.63661
II^{dimer}- propagation-LA	1.077715	0.885663	-3937.440182	-4259.526353	-4258.64069
TSII-III^{dimer}-propagation-LA	1.075994	0.882083	-3937.428402	-4259.513895	-4258.631812
III^{dimer}-propagation-LA	1.077382	0.883962	-3937.432711	-4259.521379	-4258.637417
IV^{dimer}-propagation-LA	1.077412	0.87887	-3937.459297	-4259.52969	-4258.65082
TSI-II^{dimer}-propagation-TMC	1.035662	0.849595	-3784.822131	-4106.984541	-4106.134946
II^{dimer}- propagation-TMC	1.037218	0.850853	-3784.826982	-4106.991026	-4106.140173
TSII-III^{dimer}-propagation-TMC	1.035811	0.848165	-3784.826779	-4106.991833	-4106.143668
III^{dimer}-propagation-TMC	1.036798	0.847828	-3784.829799	-4106.99265	-4106.144822
IV^{dimer}-propagation-TMC	1.037851	0.844254	-3784.843767	-4106.998055	-4106.153801

4.8 References

1. Gregory, M. R., *Phil. Trans. R. Soc. B* **2009,** *364* (1526), 2013-2025.

2. Halden, R. U., *Annu. Rev. Public Health* **2010,** *31*, 179-194.

3. Chen, G.-Q.; Patel, M. K., *Chem. Rev.* **2012,** *112* (4), 2082-2099.

4. Bogaert, J.-C.; Coszach, P., *Macromol. Symp.* **2000,** *153* (1), 287-303.

5. Drumright, R. E.; Gruber, P. R.; Henton, D. E., *Adv. Mater.* **2000,** *12* (23), 1841-1846.

6. Zhu, Y.; Romain, C.; Williams, C. K., *Nature* **2016,** *540* (7633), 354-362.

7. Lunt, J., *Polym. Degrad. Stab.* **1998,** *59* (1), 145-152.

8. Vink, E. T. H.; Rábago, K. R.; Glassner, D. A.; Gruber, P. R., *Polym. Degrad. Stab.* **2003,** *80* (3), 403-419.

9. Dechy-Cabaret, O.; Martin-Vaca, B.; Bourissou, D., *Chem. Rev.* **2004,** *104* (12), 6147-6176.

10. Nair, L. S.; Laurencin, C. T., *Prog. Polym. Sci.* **2007,** *32* (8–9), 762-798.

11. Platel, R. H.; Hodgson, L. M.; Williams, C. K., *Polym. Rev.* **2008,** *48* (1), 11-63.

12. Hayashi, T., *Prog. Polym. Sci.* **1994,** *19* (4), 663-702.

13. Middleton, J. C.; Tipton, A. J., *Biomaterials* **2000,** *21* (23), 2335-2346.

14. Ikada, Y.; Tsuji, H., *Macromol. Rapid Commun.* **2000,** *21* (3), 117-132.

15. Amass, W.; Amass, A.; Tighe, B., *Polym. Int.* **1998,** *47* (2), 89-144.

16. Chiellini, E.; Solaro, R., *Adv. Mater.* **1996,** *8* (4), 305-313.

17. Becker, J. M.; Pounder, R. J.; Dove, A. P., *Macromol. Rapid Commun.* **2010,** *31* (22), 1923-1937.

18. Pêgo, A. P.; Grijpma, D. W.; Feijen, J., *Polymer* **2003,** *44* (21), 6495-6504.

19. Guerin, W.; Helou, M.; Carpentier, J.-F.; Slawinski, M.; Brusson, J.-M.; Guillaume, S. M., *Polym. Chem.* **2013,** *4* (4), 1095-1106.

20. Leng, X.; Wei, Z.; Ren, Y.; Bian, Y.; Wang, Q.; Li, Y., *RSC Adv.* **2016,** *6* (46), 40371-40382.

21. Lemmouchi, Y.; Perry, M. C.; Amass, A. J.; Chakraborty, K.; Schacht, E., *J. Polym. Sci. A Polym. Chem.* **2008,** *46* (16), 5348-5362.

22. Darensbourg, D. J.; Choi, W.; Karroonnirun, O.; Bhuvanesh, N., *Macromolecules* **2008,** *41* (10), 3493-3502.

23. Nakayama, Y.; Yasuda, H.; Yamamoto, K.; Tsutsumi, C.; Jerome, R.; Lecomte, P., *React. Funct. Polym.* **2005,** *63* (2), 95-105.

24. Grijpma, D. W.; Joziasse, C. A. P.; Pennings, A. J., *Macromol. Rapid Commun.* **1993,** *14* (3), 155-161.

25. Kim, J.-H.; Lee, S. Y.; Chung, D. J., *Polym. J.* **2000,** *32* (12), 1056-1059.

26. Pospiech, D.; Komber, H.; Jehnichen, D.; Häussler, L.; Eckstein, K.; Scheibner, H.; Janke, A.; Kricheldorf, H. R.; Petermann, O., *Biomacromolecules* **2005,** *6* (1), 439-446.

27. Tyson, T.; Finne-Wistrand, A.; Albertsson, A.-C., *Biomacromolecules* **2009,** *10* (1), 149-154.

28. Kricheldorf, H. R.; Rost, S., *Macromolecules* **2005,** *38* (20), 8220-8226.

29. Wang, L.; Kefalidis, C. E.; Sinbandhit, S.; Dorcet, V.; Carpentier, J.-F.; Maron, L.; Sarazin, Y., *Chem. Eur. J.* **2013,** *19* (40), 13463-13478.

30. Wei, J.; Riffel, M. N.; Diaconescu, P. L., *Macromolecules* **2017,** *50* (5), 1847-1861.

31. Shepard, S. M.; Diaconescu, P. L., *Organometallics* **2016,** *35* (15), 2446–2453.

32. Quan, S. M.; Wang, X.; Zhang, R.; Diaconescu, P. L., *Macromolecules* **2016,** *49* (18), 6768-6778.

33. Huang, W.; Diaconescu, P. L., *Inorg. Chem.* **2016,** *55* (20), 10013–10023.

34. Abubekerov, M.; Shepard, S. M.; Diaconescu, P. L., *Eur. J. Inorg. Chem.* **2016,** *2016* (15-16), 2634-2640.

35. Abubekerov, M.; Diaconescu, P. L., *Inorg. Chem.* **2015,** *54* (4), 1778–1784.

36. Wang, X.; Thevenon, A.; Brosmer, J. L.; Yu, I.; Khan, S. I.; Mehrkhodavandi, P.; Diaconescu, P. L., *J. Am. Chem. Soc.* **2014,** *136* (32), 11264-11267.

37. Broderick, E. M.; Guo, N.; Wu, T.; Vogel, C. S.; Xu, C.; Sutter, J.; Miller, J. T.; Meyer, K.; Cantat, T.; Diaconescu, P. L., *Chem. Commun.* **2011,** *47*, 9897-9899.

38. Broderick, E. M.; Guo, N.; Vogel, C. S.; Xu, C.; Sutter, J.; Miller, J. T.; Meyer, K.; Mehrkhodavandi, P.; Diaconescu, P. L., *J. Am. Chem. Soc.* **2011,** *133* (24), 9278–9281.

39. Biernesser, A. B.; Delle Chiaie, K. R.; Curley, J. B.; Byers, J. A., *Angew. Chem. Int. Ed.* **2016,** *55* (17), 5251–5254.

40. Biernesser, A. B.; Li, B.; Byers, J. A., *J. Am. Chem. Soc.* **2013,** *135* (44), 16553-16560.

41. Hermans, C.; Rong, W.; Spaniol, T. P.; Okuda, J., *Dalton Trans.* **2016,** *45* (19), 8127-8133.

42. Sauer, A.; Buffet, J.-C.; Spaniol, T. P.; Nagae, H.; Mashima, K.; Okuda, J., *ChemCatChem* **2013,** *5* (5), 1088-1091.

43. Teator, A. J.; Lastovickova, D. N.; Bielawski, C. W., *Chem. Rev.* **2016,** *116* (4), 1969-1992.

44. Tennyson, A. G.; Lynch, V. M.; Bielawski, C. W., *J. Am. Chem. Soc.* **2010,** *132* (27), 9420-9429.

45. Yang, L.; Powell, D. R.; Houser, R. P., *Dalton Trans.* **2007,** (9), 955-964.

46. Fliedel, C.; Rosa, V.; Alves, F. M.; Martins, A. M.; Aviles, T.; Dagorne, S., *Dalton Trans.* **2015,** *44* (27), 12376-12387.

47. Li, D.; Kagan, G.; Hopson, R.; Williard, P. G., *J. Am. Chem. Soc.* **2009,** *131* (15), 5627-5634.

48. Chamberlain, B. M.; Cheng, M.; Moore, D. R.; Ovitt, T. M.; Lobkovsky, E. B.; Coates, G. W., *J. Am. Chem. Soc.* **2001,** *123* (14), 3229-3238.

49. Ouhadi, T.; Hamitou, A.; Jerome, R.; Teyssie, P., *Macromolecules* **1976,** *9* (6), 927-931.

50. Lewiński, J.; Horeglad, P.; Wójcik, K.; Justyniak, I., *Organometallics* **2005,** *24* (19), 4588-4593.

51. Horeglad, P.; Cybularczyk, M.; Trzaskowski, B.; Żukowska, G. Z.; Dranka, M.; Zachara, J., *Organometallics* **2015,** *34* (14), 3480-3496.

52. Klitzke, J. S.; Roisnel, T.; Kirillov, E.; Casagrande, O. d. L.; Carpentier, J.-F., *Organometallics* **2014,** *33* (20), 5693-5707.

53. Phomphrai, K.; Chumsaeng, P.; Sangtrirutnugul, P.; Kongsaeree, P.; Pohmakotr, M., *Dalton Trans.* **2010,** *39* (7), 1865-1871.

54. Nomura, N.; Ishii, R.; Yamamoto, Y.; Kondo, T., *Chem. Eur. J.* **2007,** *13* (16), 4433-4451.

55. Kremer, A. B.; Andrews, R. J.; Milner, M. J.; Zhang, X. R.; Ebrahimi, T.; Patrick, B. O.; Diaconescu, P. L.; Mehrkhodavandi, P., *Inorg. Chem.* **2017,** *56* (3), 1375-1385.

56. Dobrzynski, P.; Kasperczyk, J., *J. Polym. Sci. A Polym. Chem.* **2006,** *44* (10), 3184-3201.

57. Darling, T. R.; Davis, T. P.; Fryd, M.; Gridnev, A. A.; Haddleton, D. M.; Ittel, S. D.; Matheson, R. R.; Moad, G.; Rizzardo, E., *J. Polym. Sci. A Polym. Chem.* **2000,** *38* (10), 1706-1708.

58. Nagarajan, S.; Deepthi, K.; Gowd, E. B., *Polymer* **2016,** *105*, 422-430.

59. Liang, Y.-y.; Tang, H.; Zhong, G.-j.; Li, Z.-m., *Chin. J. Polym. Sci.* **2014,** *32* (9), 1176-1187.

60. Zhang, Y.; Wang, Z.; Jiang, F.; Bai, J.; Wang, Z., *Soft Matter* **2013,** *9* (24), 5771-5778.

61. Jacobsen, S.; Fritz, H. G., *Polym. Eng. Sci.* **1999,** *39* (7), 1303-1310.

62. Zhu, K. J.; Hendren, R. W.; Jensen, K.; Pitt, C. G., *Macromolecules* **1991,** *24* (8), 1736-1740.

63. Frisch, M. J., In *Gaussian 09 (Revision D.01)*, Gaussian Inc.: Wallingford, CT, 2010 (see the SI for the full reference).

64. Towns, J.; Cockerill, T.; Dahan, M.; Foster, I.; Gaither, K.; Grimshaw, A.; Hazlewood, V.; Lathrop, S.; Lifka, D.; Peterson, G. D.; Roskies, R.; Scott, J. R.; Wilkens-Diehr, N., *Computing in Science and Engineering* **2014,** *16* (5), 62-74.

65. Pangborn, A. B.; Giardello, M. A.; Grubbs, R. H.; Rosen, R. K.; Timmers, F. J., *Organometallics* **1996,** *15* (5), 1518-1520.

66. Matsuo, J.; Aoki, K.; Sanda, F.; Endo, T., *Macromolecules* **1998,** *31* (14), 4432-4438.

CHAPTER 5: INFLUENCE OF THE OXIDATION STATE OF THE FERROCENE HETEROSCORPIONATE ZINC(II) COMPLEXES ON THE POLYMERIZATION OF CYCLIC ESTERS AND CARBONATES

5.1 Introduction

Aliphatic polyesters and polycarbonates derived from L-lactide, ε-caprolactone, δ-valerolactone, and trimethylene carbonate are biodegradable plastics with applications in the biomedical field, food packaging, and other specialty applications.[1-9] Utilizing discrete metal complexes for the ring-opening polymerization of these cyclic monomers provides a great degree of control over the microstructure of the resulting polymers. In particular, neutral zinc alkoxide complexes show high activity toward the ring-opening polymerization of cyclic esters and carbonates. Due to the "living" nature of these processes, polymers with high molecular weights and low dispersities are typically obtained.[10-21] Additionally, utilizing zinc in polymerizations is advantageous due to the low cost, high abundance, and biocompatibility of the metal, allowing for a wide application of the resulting biodegradable plastics.

The prevalent use of zinc in ring-opening polymerizations of cyclic esters and carbonates is matched by the use of hard N/O-based supporting ligands. However, only a few reports could be found using soft donor ligands, such as phosphines, to stabilize the active zinc metal center.[22-24] Such interactions can be beneficial due to the hemilabile nature of the zinc-phosphine bond and may result in highly active polymerization systems. The use of redox-active ligands in combination with zinc for ring-opening polymerizations is even less common than the use of soft-donor ligands despite their potential benefits.[25] Redox-active ligands provide a means of affecting the reactivity of the metal through changes in the oxidation state of the ligand. For

example, in redox-switchable hemilabile ligands, the incorporation of a redox active group into the ligand framework, in close proximity to a substitutionally labile component, allows the control of the strength of the ligand-metal bond, leading to the dissociation of the ligand fragment upon oxidation.[26-30] In addition, the electronic and steric environment of the transition metal can be controlled without directly affecting its oxidation state.[31]

We previously reported the influence of a redox switch on the lability of [fc(PPh_2)(BH[(3,5-$Me)_2$pz]$_2$)] (($fc^{P,B}$), fc = 1,1'-ferrocenediyl, pz = pyrazole) in a palladium methyl complex in the presence of norbornene.[32] Upon the oxidation of the ferrocene backbone, the phosphine moiety displayed hemilabile behavior, resulting in norbornene polymerization. We reasoned that using the same ligand to support a more oxophilic metal, such as zinc(II), may yield a beneficial hemilabile interaction between the phosphine and the metal in the reduced state of the supporting ligand. In this case, the oxidation of the ligand could result in the loss of the zinc-phosphine interaction, similar to redox-switchable hemilabile ligands, and in altering the reactivity of a catalyst. Earlier, we have described the preparation as well as the characterization of [($fc^{P,B}$)Zn(μ-OCH_2Ph)]$_2$ (Chapter 3). However, in the case of the reduced species, a direct zinc-phosphine interaction was not observed. Despite this finding, and because of our interest in redox-switchable catalytic processes,[32-41] we set out to investigate the influence of the redox state of $fc^{P,B}$ on the zinc mediated ring-opening polymerization of cyclic esters and carbonates. Additionally, an investigation into redox and polymerization activity of a monomeric ferrocene-chelating heteroscorpionate zinc complex, ($fc^{P,B}$)Zn(OPh), is reported.

5.2 Synthesis and characterization of the oxidized zinc benzoxide complex

We previously described the preparation as well as an investigation of the solution state behavior of $[(fc^{P,B})Zn(\mu\text{-}OCH_2Ph)]_2$ (Chapter 4). However, the influence of the redox state of the supporting ligand on the activity of this compound was not investigated.

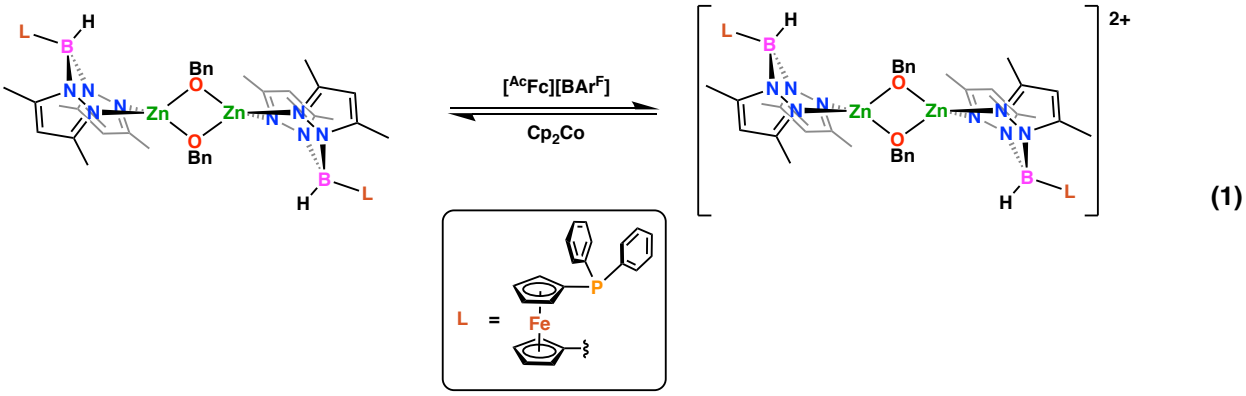

(1)

Electrochemical studies performed on $[(fc^{P,B})Zn(\mu\text{-}OCH_2Ph)]_2$ show a reversible curve with a redox potential of -0.024 V vs. Fc/Fc^+ (Figure D30), suggesting that ferrocenium salts may be used as chemical oxidants. On an NMR scale, the oxidation of the zinc complex with one equivalent of acetyl ferrocenium tetrakis(3,5-bis(trifluoromethyl)phenyl)borate ($[^{Ac}Fc][BAr^F]$) in C_6D_6 results in the formation of insoluble red solids and acetyl ferrocene, with only the latter observed by NMR spectroscopy. Reduction with one equivalent of cobaltocene (Cp_2Co) restores the original complex, $[(fc^{P,B})Zn(\mu\text{-}OCH_2Ph)]_2$, with no apparent decomposition or side products (Eq 1, Figures D1-2). On a larger scale, the addition of one equivalent of $[^{Ac}Fc][BAr^F]$ to $[(fc^{P,B})Zn(\mu\text{-}OCH_2Ph)]_2$ led to the isolation of red solids. Attempts at characterizing the oxidation product by NMR spectroscopy were unsuccessful; the complex is insoluble in hydrocarbon solvents and rapidly reacts with non-hydrocarbon solvents (THF, chloroform). The reaction product of THF-d_8 with $[(fc^{P,B})Zn(\mu\text{-}OCH_2Ph)]_2[BAr^F]_2$ is a paramagnetic complex, which is ^{31}P NMR silent, similar to the previously reported $[(fc^{P,B})PdMe][BAr^F]$.[32] The ^{11}B NMR spectrum (Figure D4) shows a minor shift from δ = -7.2 to -7.8 ppm upon oxidation. The presence of the

[BAr^F] counter ion was confirmed by the presence of a singlet at δ = -5.9 and -63.5 ppm in the ^{11}B and ^{19}F NMR spectra (Figures D4-5), respectively. Attempts to grow X-ray quality crystals of the oxidized complex from various neat solvents and solvent combinations were unsuccessful and only dark red oils were obtained. However, elemental analysis agrees with the formulation of $[(fc^{P,B})Zn(\mu\text{-}OCH_2Ph)]_2[BAr^F]_2$.

The lack of a signal in the ^{31}P NMR spectrum of the oxidized complex prompted a further investigation into the electronic state of this complex, performed by Matthias Miehlich. Due to the difficulty of characterizing the oxidized complex in solution we turned to ^{57}Fe Mössbauer spectroscopy. At 80 K, with no applied magnetic field, the reduced complex shows a doublet with an isomer shift (δ = 0.54(1) mm/s) and quadrupole splitting (ΔE^Q = 2.34(1) mm/s) consistent with a low spin iron(II) complex (Figure 5-1). Surprisingly, under the same conditions, the oxidized complex also displays a doublet with an isomer shift (δ = 0.54(1) mm/s) and quadrupole splitting (ΔE^Q = 2.26(1) mm/s) consistent with a low spin iron(II) complex (Figure 5-1). Attempts at acquiring an X-band EPR spectrum (in perpendicular mode), both in the solid and solution states, at liquid nitrogen, liquid helium, and ambient temperature, under a variety of different conditions, were unsuccessful. Similar Mössbauer and EPR spectroscopy results were reported for oxidized arylphosphinoferrocenes by Durfey et al., and were attributed to either oxidation of the phosphorus lone pair or the aryl groups. The presence of an unpaired electron in close proximity to the phosphorus atom would be consistent with the lack of signal in the ^{31}P NMR spectrum of the oxidized complex. Ligand based oxidations of ferrocenes, as opposed to iron, have also been reported for various phenyphosphinoferrocenes and ferrocenylpyrrole species; although the inability to observe an EPR signal for these species remains puzzling. Isolated products of chemical oxidations displayed low-spin iron(II) species,

evidenced by ^{57}Fe Mössbauer spectroscopy in the case of the ferrocenylpyrrole complex, and a mix of low-spin iron(II) and low-spin iron(III) species in the case of phenyphosphinoferrocenes. However, the ^{31}P NMR spectra for the oxidized phenylphosphinoferrocenes typically display broadened, but detectible signals.

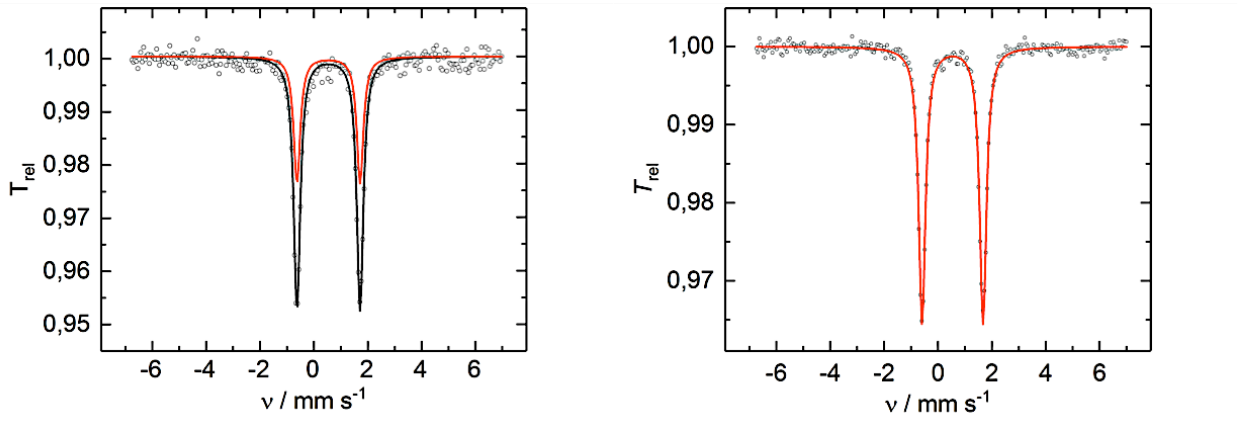

Figure 5-1. Zero-field ^{57}Fe Mössbauer spectra of $[(fc^{P,B})Zn(\mu\text{-}OCH_2Ph)]_2$ (left) and $[(fc^{P,B})Zn(\mu\text{-}OCH_2Ph)]_2[BAr^F]_2$ (right), recorded as solid samples at 80 K.

5.3 Electronic structure calculations

To better understand the observed oxidation state of Fe in the cation Dr. Vojtěch Vlček investigated the highest occupied valence states from which the electrons are removed. Common local and semilocal density functionals cannot however address this problem due to the improper description of the highly correlated *d* orbitals in Fe. The mean field description (i.e., the common exchange-correlation potential in DFT) fails to capture the physics of the localized states due to a self-interaction error.[47-48] This leads to spurious delocalization of orbitals and incorrect charge transfer and oxidation energies.[49-50]

We verify that (semi)-local functionals contradict indeed the experimental data. We illustrate this by the density of electronic states obtained with the common GGA functional (shown in Figure 5-2). Projection of the corresponding wave-functions onto the atomic orbitals reveals the character of individual states and their mutual hybridization. The top valence region (close to the HOMO at - 3.3 eV) is dominated by the localized *d* states of iron. An Fe *d* state contribution is also found in lower energy states, but these do not energetically participate in the oxidation process. Note that the phosphorus *p* states are significantly separated in energy from the top valence region by as much as 0.9 eV. Hence, the GGA results suggest that the Fe atoms are oxidized, in contradiction to experiment.

This conundrum is resolved by mitigating the self-interaction error of the localized states. We resort to the established approach of correcting the DFT picture by use of a site- and orbital-specific potential energy derived from the Hubbard model Hamiltonian.[51] We estimated the potential for the Fe *d* states from first principles using linear response theory[46] and obtained U = 7.7 eV. Such a high value leads to significant changes in the density of states (Figure 5-2). We see that the Fe *d* states are pushed down in energy and significantly hybridize with the valence region below - 5 eV. The frontier orbitals are at - 4.7 eV with a major contribution from phosphorus *p* states. Indeed, the HOMO and HOMO-1 isosurfaces are found mostly around the P atoms (Figure 5-3).

The ground state geometry of the molecule is different when optimized for the cation or neutral systems. This leads to a slight variation of the U parameter by 0.3 eV, but the character of the top valence state is not affected: for U > 4 eV (i.e., much smaller than the variation due to changes in the geometry), the top valence orbital becomes dominated by phosphorus *p* states.

The GGA+U calculations thus show that Fe remains in its +II state and the phosphine groups are oxidized.

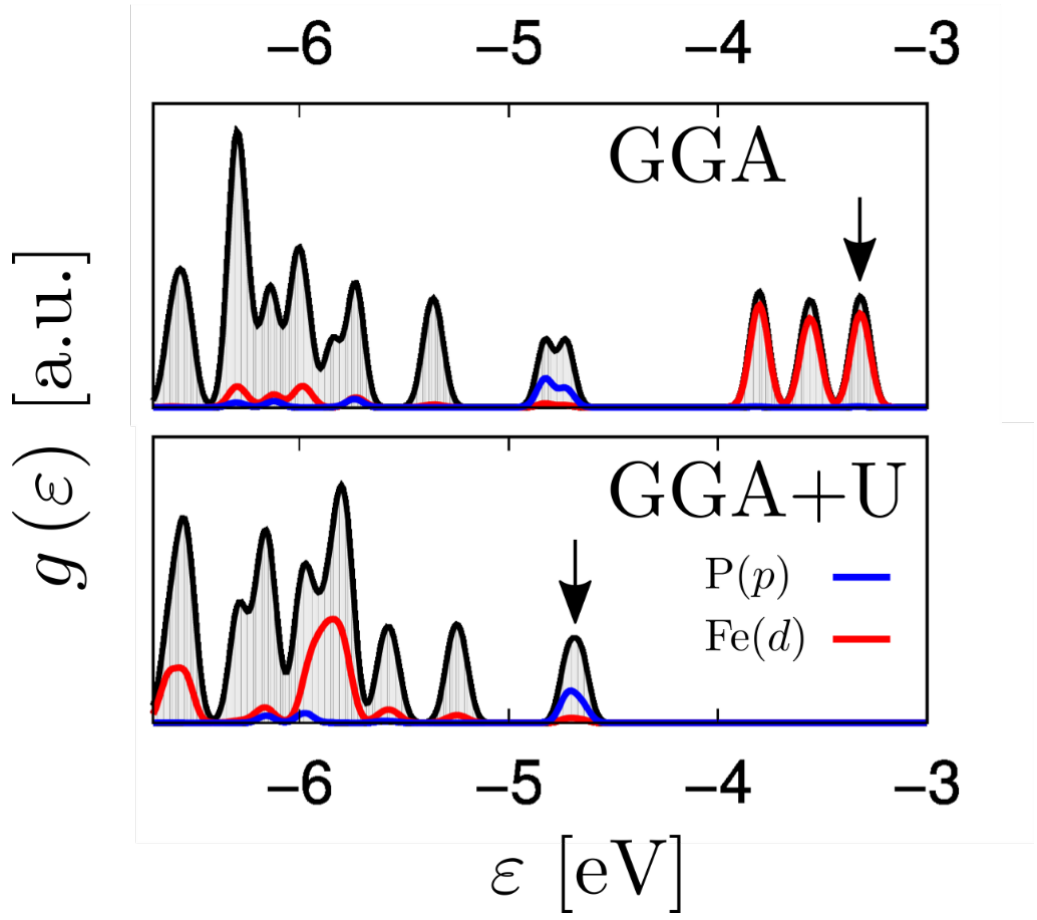

Figure 5-2. Total density of states *g*(*e*) for the top valence region. The highest occupied orbital is indicated by a black arrow. Contributions of the atomic-like *p* and *d* orbitals of P and Fe are shown by colors. Note that due to strong hybridization multiple atomic orbitals contribute to each molecular state.

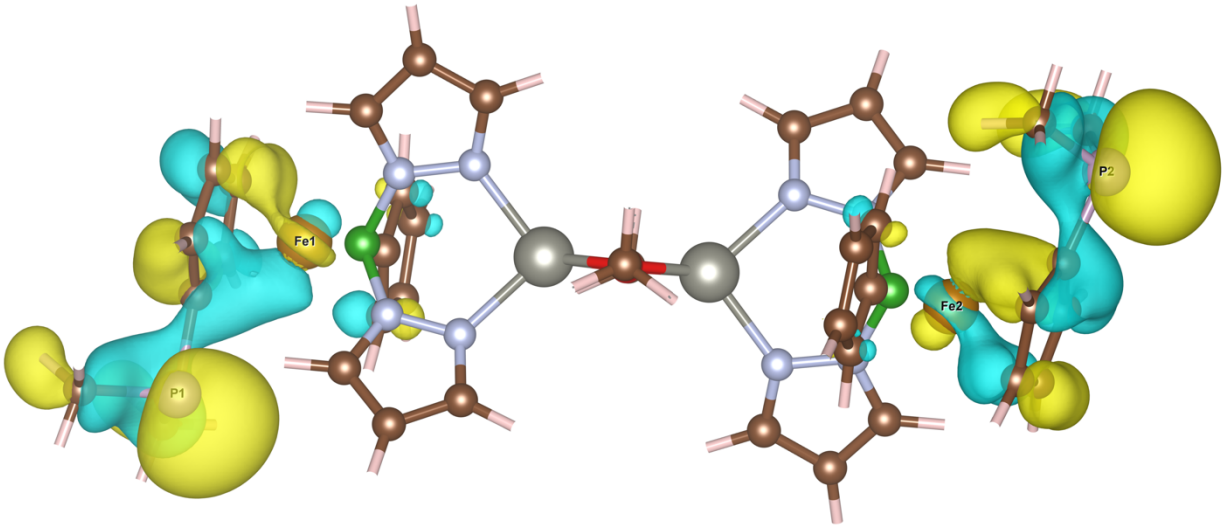

Figure 5-3. Isosurface for the HOMO and HOMO-1 orbitals. Yellow and light blue coloring represents the positive and negative real parts of the wavefunction. For clarity, the hydrogen atoms were removed from the figure.

5.4 Polymerization of cyclic esters and carbonates

The influence of the ligand oxidation state on the reactivity of the zinc complex was examined through the ring-opening polymerization of cyclic esters and carbonates. Due to the difficulty in isolating and manipulating the oxidized complex, it was generated in situ immediately prior to use through the addition of two equivalents of $[^{Ac}Fc][BAr^{F}]$ to $[(fc^{P,B})Zn(\mu\text{-}OCH_2Ph)]_2$. The role of the oxidant as a potential polymerization catalyst was ruled out based on control experiments, showing no activity under polymerization conditions for L-lactide, trimethylene carbonate, and δ-valerolactone (Figure D14-15, D17) and only a minor conversion for ε-caprolactone (Figure D16). In all cases, the polymerizations are well-controlled processes with the molecular weights of the resulting polymers increasing linearly with conversion while the dispersity values remain narrow (Tables D1-6, Figures D43-48).

Polymerizations of ca. 200 equivalents of L-lactide (LA) showed faster conversion for the reduced complex at various temperatures. At ambient temperature, a 60% conversion was obtained after 24 h for the reduced complex, while the oxidized complex reached only 17% conversion. Such a low conversion could be attributed to both the poor solubility of L-lactide and, particularly, to the insolubility of the oxidized complex in benzene at ambient temperature. Performing the polymerizations at 70 °C resulted in much shorter reaction times for both complexes (Table 5-1, entries 1-2); a complete conversion was observed for the reduced complex and 91% conversion for the oxidized complex in 3 h. The molecular weights for the isolated polymers obtained from the oxidized and reduced complexes agree well with the corresponding theoretical molecular weights. The dispersity values ($Đ$) are within a 1.0 – 1.15 range, suggesting that the polymerization process is well controlled.

Contrary to the L-lactide case, the oxidation of the ligand had no observable influence on the rates of polymerization of ε-caprolactone (CL, Table 5-1, entries 3-4). Polymerizations of ca. 200 equivalents of ε-caprolactone at ambient temperature reached completion for both the oxidized and the reduced complex in 24 h. On the other hand, carrying out the polymerizations at 70 °C results in complete consumption of the monomer within 30 min for both complexes. Similar to L-lactide, the molecular weights of the polymers, obtained by gel permeation chromatography, from both the oxidized and reduced complexes agree well with the theoretical values. However, the dispersity values ($Đ$) are slightly narrower and fall between 1.0-1.1.

The most pronounced difference between the oxidized and the reduced complex was observed for the polymerization of trimethylene carbonate (TMC, Table 5-1, entries 5-6) and δ-valerolactone (VL, Table 5-1, entries 7-8). The complete conversion of ca. 200 equivalents of TMC was accomplished in under 15 minutes at ambient temperature utilizing the oxidized

complex and up to 90 min for the reduced complex. Similarly, the conversion of ca. 200 equivalents of VL plateaus at 92% for the oxidized complex after 20 min at ambient temperature while the same conversion is obtained for the reduced species after 60 min. Further conversion of VL cannot be obtained with increased time or elevated temperatures. All polymers show an excellent agreement between NMR and GPC molecular weights and display narrow dispersity values.

Table 5-1: Polymerization of cyclic esters and carbonates by $[(fc^{P,B})Zn(\mu\text{-}OCH_2Ph)]_2$ (**2**) and the in situ generated $[(fc^{P,B})Zn(\mu\text{-}OCH_2Ph)]_2[BAr^F]_2$ (**3**).

Entry	Compound	Monomer	Time (min)	Conversion (%)	M_n (NMR)	M_n (GPC)	*Đ*
1	**2**	LA	180	>99	1.40	1.38	1.14
2	**3**	LA	180	91	1.32	1.35	1.02
3	**2**	CL	30	>99	0.90	0.89	1.09
4	**3**	CL	30	>99	1.07	1.06	1.08
5	**2**	TMC	90	98	1.00	1.00	1.14
6	**3**	TMC	15	>99	0.79	0.81	1.02
7	**2**	VL	60	92	1.02	1.04	1.01
8	**3**	VL	20	92	1.01	1.05	1.04

Conditions: monomer (0.50 mmol), catalyst (0.0025 mmol), oxidant (0.005 mmol), d_6-benzene as a solvent (0.5 mL), and hexamethylbenzene (0.025 mmol) as an internal standard. Entries 1-4 were carried out at 70 °C and entries 5-8 were performed at ambient temperature; M_n are reported in 10^4 g/mol; $Đ = M_w/M_n$.

Literature examples of L-lactide and ε-caprolactone polymerization by zinc complexes are rather common,[52-58] while examples of trimethylene carbonate and δ-valerolactone polymerizations are not as prevalent.[59-61] In comparison to other heteroscorpionate complexes, tris(pyrazolyl)borate complexes, and ligands with similar tripodal frameworks, both the oxidized and the reduced complexes display moderate activity for the polymerization of L-lactide and ε-caprolactone.[52-58] Similarly, the reduced complex shows a moderate activity toward the polymerization of trimethylene carbonate and δ-valerolactone, while the oxidized complex shows high activity toward the same monomers.[59-61]

5.5 Synthesis and characterization of the zinc phenoxide complex

To investigate the possibility of redox-switchable hemilabile ligand behavior we have also prepared a monomeric zinc species containing a phosphorus-zinc interaction. The addition of NaOPh to ($fc^{P,B}$)ZnCl in methylene chloride resulted in the isolation of ($fc^{P,B}$)Zn(OPh) as orange crystals in 79.8% yield (Eq 2). The solid state molecular structure of ($fc^{P,B}$)Zn(OPh) (Figure 5-4) in crystals of ($fc^{P,B}$)Zn(OPh) • (Et_2O) was determined using single-crystal X-ray diffraction. The coordination environment around the zinc center has a distorted tetrahedral geometry with a τ value of 0.88. Unlike in the case of the [($fc^{P,B}$)Zn(μ-OCH_2Ph)]$_2$ complex, the phenoxide ligands do not bridge resulting in a monomeric species.

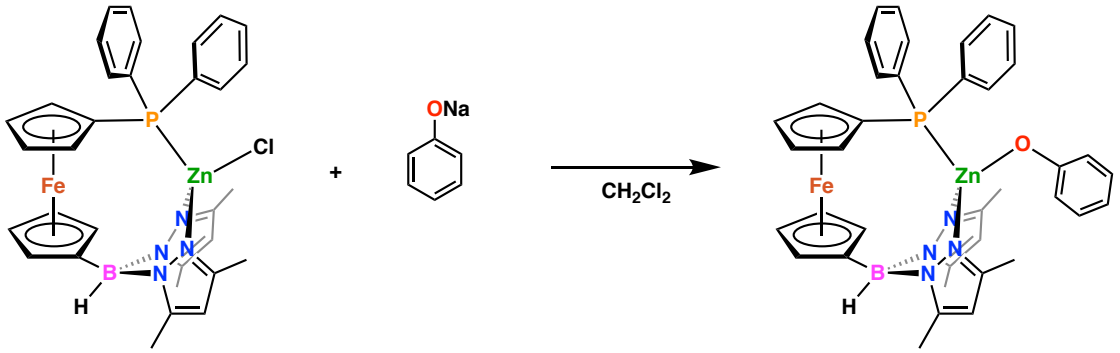

(2)

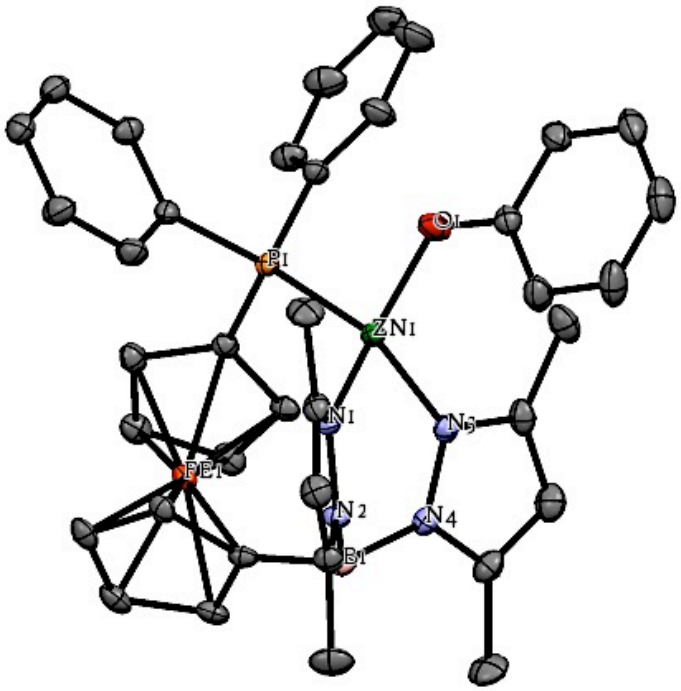

Figure 5-4. Molecular structure drawing of ($fc^{P,B}$)Zn(OPh) in crystals of ($fc^{P,B}$)Zn(OPh) • (Et_2O) with thermal ellipsoids at 50% probability; hydrogen atoms are omitted for clarity. Selected distances (Å) and angles (°): O(1)-Zn(1), 1.9065(); N(1)-Zn(1), 2.0067(); N(3)-Zn(1), 1.9903(); P(1)-Zn(1), 2.3985(); N(1)-Zn(1)-N(3), 107.77(); N(1)-Zn(1)-N(3), 95.50(); N(1)-Zn(1)-O(1), 115.52(); O(1)-Zn(1)-P(1), 99.82(); N(3)-Zn(1)-O(1), 118.66(); N(1)-Zn(1)-P(1), 120.62().

Electrochemically ($fc^{P,B}$)Zn(OPh) shows a reversible curve with a half-potential of -0.065 V vs. Fc/Fc^{+} (Figure D33). On an NMR scale, oxidation of ($fc^{P,B}$)Zn(OPh) with 1.1 equivalents of [^{Ac}Fc][BAr^{F}] in C_6D_6 results in the formation of insoluble red solids, just like in the case of [($fc^{P,B}$)Zn(μ-OCH_2Ph)]$_2$. However, the complete oxidation of the starting material does not occur and a mixture of ($fc^{P,B}$)Zn(OPh) and ^{Ac}Fc is observed spectroscopically (Figure D22). Similarly, utilizing excess $AgBF_4$ did not result in complete oxidation of ($fc^{P,B}$)Zn(OPh), which could still be observed as broad peaks in the ^{1}H NMR spectrum due to the presence of silver solid in the sample (Figure D23).

5.6 Polymerization of cyclic esters and carbonates

Despite the lack of redox-switchable behavior, we looked into the polymerization activity of the reduced species. Although the ($fc^{P,B}$)Zn(OPh) is a monomeric complex, its propensity to form a dimeric species during polymerization of cyclic esters and carbonates must be considered. Since [($fc^{P,B}$)Zn(μ-OCH_2Ph)]$_2$ remains a dimeric species during ROP of cyclic esters and carbonates it's worth considering that ($fc^{P,B}$)Zn(OPh) would prefer to dimerize after a single ring-opening of a monomer. To test this theory, the polymerization of ca. ten equivalents of L-lactide in the presence of ($fc^{P,B}$)Zn(OPh) was monitored spectroscopically (Figure D24). The rate of polymerization is substantially slower compared to [($fc^{P,B}$)Zn(μ-OCH_2Ph)]$_2$, reaching only 65% conversion of the ten equivalents after 5 h at 100 °C (Figure D25). However, after the polymerization onset the signals corresponding to ($fc^{P,B}$)Zn(OPh) do not shift in the ^{1}H NMR spectra (Figure D24), which prompted a further look into the polymerization process by Diffusion Ordered Spectroscopy (DOSY) NMR. We have previously used this technique to illustrate that our zinc polymerization systems show the same diffusion rate for the catalyst and

the polymer. In this case, the diffusion rate of PLA was substantially different from ($fc^{P,B}$)Zn(OPh) suggesting that it does not participate in the polymerization process (Figure D26). Similar results are obtained in the case of a cyclic carbonate, trimethylene carbonate. The formation of PTMC is observed at a slow rate, but without any change observed in for ($fc^{P,B}$)Zn(OPh) (Figures D27-D28), suggesting that an impurity or a decomposition product may be responsible for monomer conversion.

5.7 DFT calculations

To gain a better understanding of the influence of the ligand oxidation on the activity of the catalyst, we turned to density functional theory. All calculations were carried out with the GAUSSIAN09 program package[62] on the Extreme Science and Engineering Discovery Environment (XSEDE)[63] by Dr. Junnian Wei. The methyl groups of the pyrazole substituents were replaced by hydrogen atoms and the phenyl groups of PPh_2 were replaced by methyl groups to simplify the calculations (for more details about calculations, see the supporting information). Lactide was chosen as the model substrate for the DFT calculations. We previously reported a computational study comparing the energies of possible monomeric and dimeric structures of the zinc benzoxide complexes and showed that the dimer [($fc^{P,B}$)Zn(μ-OCH_2Ph)]$_2$ was more stable (by 3.3 kcal/mol) than the corresponding monomer, ($fc^{P,B}$)Zn(OCH_2Ph). In the oxidized state, the dimeric species [($fc^{P,B}$)Zn(μ-OCH_2Ph)]$_2^{2+}$ was greatly favored (20.1 kcal/mol) over the corresponding monomer (Figure 5-5). This preference was maintained even after the insertion of the first lactide, with the dimeric intermediate being 12.7 kcal/mol lower in energy than a monomeric intermediate (Figure 5-6). These results suggest that the active species in the reactions involving the oxidized complexes is a dimer.

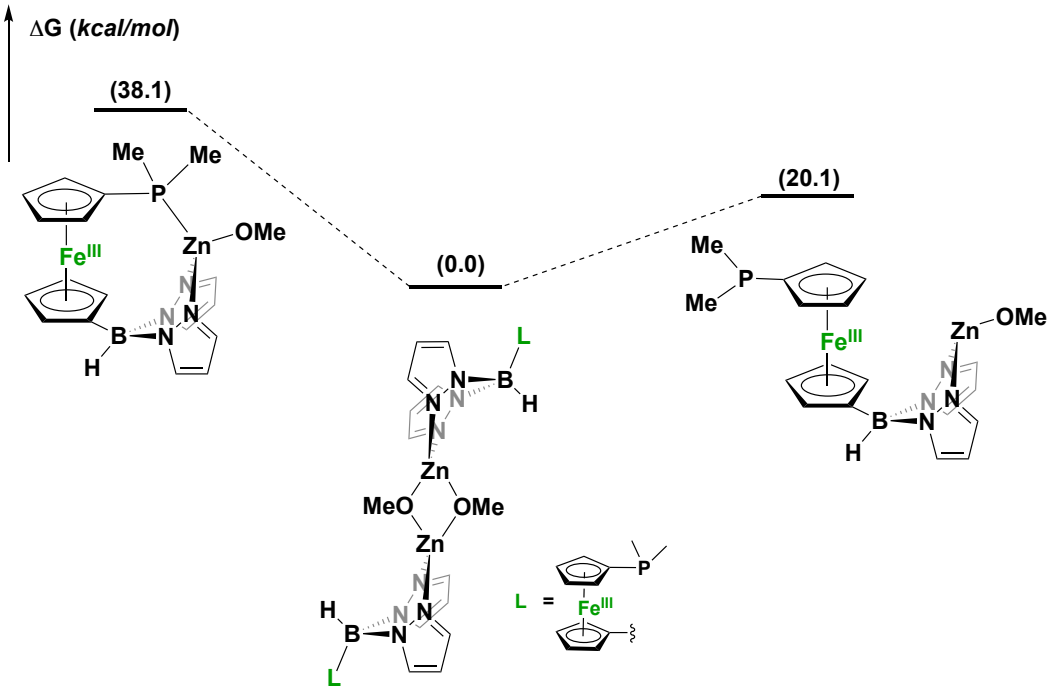

Figure 5-5. Optimized structures for $[(fc^{P,B})Zn(\mu\text{-}OCH_2Ph)]_2[BAr^F]_2$.

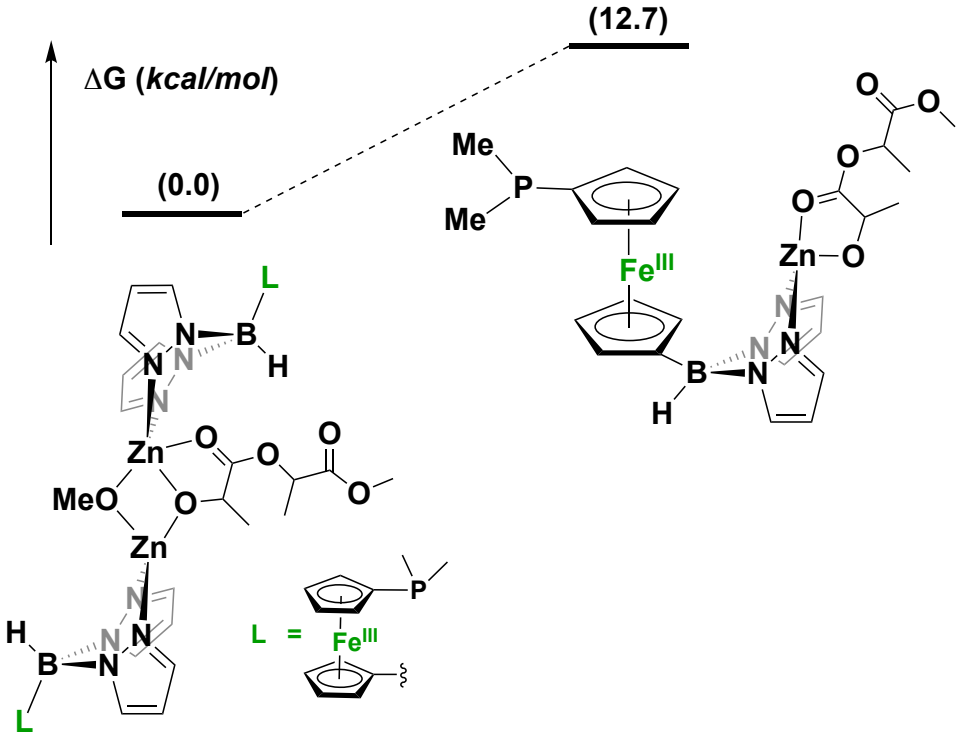

Figure 5-6. Optimized structures of the product obtained after the first lactide ring-opening event.

5.8 Conclusions

The application of a ferrocene-chelating heteroscorpionate ligand in zinc catalyzed ring-opening polymerization of cyclic esters and trimethylene carbonate was investigated. Different polymerization rates for $[(fc^{P,B})Zn(\mu\text{-}OCH_2Ph)]_2$ and the corresponding oxidized complex, namely $[(fc^{P,B})Zn(\mu\text{-}OCH_2Ph)]_2[BAr^F]_2$, toward the same set of monomers were observed. The differences in the observed reactivity are likely attributed to the difference in charge distributions between the neutral and the cationic zinc species. The lack of selectivity is attributed to the lack of the zinc-phosphine interaction in both the reduced and oxidized states of the zinc-benzoxide species. However, the monomeric zinc-phenoxide species, which retains the phosphine-zinc interaction, was found inactive towards ring-opening polymerization of L-lactide and trimethylene carbonate. Based on the results of this investigation, a development and application of a monomeric zinc-alkoxide species, bearing a ferrocene-chelating heteroscorpionate derivative, towards ring-opening polymerization of cyclic esters and carbonates is currently under investigation.

5.9 Experimental Section

Synthesis of $[(fc^{P,B})Zn(\mu\text{-}OCH_2Ph)]_2[BAr^F]_2$. To solid $[^{Ac}Fc][BAr^F]$ (67.8 mg, 0.062 mmol) was added $[(fc^{P,B})Zn(\mu\text{-}OCH_2Ph)]_2$ (55.8 mg, 0.068 mmol) in 4 mL of toluene/trifluorotoluene (1:1 vol %). The reaction mixture was stirred for 30 min at ambient temperature. The toluene solution was decanted and the remaining oily red solids were washed with 2 × 2 mL of toluene. The product was isolated as a red solid after an hour under reduced pressure (77.8 mg, 78.0%). ^{1}H NMR (THF-d_8, 500 MHz, 298 K): δ (ppm) 2.24 (s), 2.39 (s), 4.40 (s), 4.43 (s), 4.63 (s), 4.66 (s), 6.07 (s), 7.09 (t), 7.14 (s), 7.28 (t), 7.58 (s), 7.71 (m), 7.79 (s),

8.95 (br s), 10.64 (br s). ^{11}B NMR (THF-d_8, 161 MHz, 298 K): δ (ppm) -5.9 (s), -7.8 (br s). ^{19}F NMR (THF-d_8, 376 MHz, 298 K): δ (ppm) -63.5 (s). Anal. Calcd: [($fc^{P,B}$)Zn(OCH_2Ph)][BAr^F] ($C_{71}H_{52}B_2F_{24}FeN_4OPZn$) C, 53.07; H, 3.26; N, 3.49. Found: C, 53.17; H, 3.32; N, 3.54.

Synthesis of ($fc^{P,B}$)Zn(OPh). To ($fc^{P,B}$)ZnCl·(C_7H_8) (121.1 mg, 0.158 mmol) in 4 mL of methylene chloride was added solid NaOPh (27.6 mg, 0.238 mmol) and the suspension stirred for 1 h at ambient temperature. The reaction mixture was filtered through Celite and volatile substances were removed under reduced pressure. The remaining oily solids were dissolved in 2 mL of diethyl ether and stored at -35 °C for several hours. Decanting of the solution and washing with cold diethyl ether yielded the product as orange crystals (101.4 mg, 79.8%). X-ray quality crystals were obtained from diethyl ether at -35 °C. Crystals of ($fc^{P,B}$)Zn(OPh) always contain a molecule of diethyl ether per molecule of compound as supported by NMR data. ^{1}H NMR (C_6D_6, 500 MHz, 298 K): δ (ppm) 2.21 (s, 6H, C*H*$_3$), 2.27 (s, 6H, C*H*$_3$), 3.53 (q, 2H, Cp-*H*), 3.93(t, 2H, Cp-*H*), 4.00 (t, 2H, Cp-*H*), 4.04 (t, 2H, Cp-*H*), 4.70 (br s, 1H, B*H*), 5.69 (s, 2H, C*H*), 6.68 (m, 1H, *p*-Ph), 6.89 (m, 2H, *m*-Ph), 7.02 (m, 6H, *m*-Ph, *p*-Ph), 7.15 (m, 2H, *o*-Ph), 7.98 (m, 4H, *o*-Ph). ^{13}C NMR (C_6D_6, 126 MHz, 298 K): δ (ppm) 13.3 (s, *C*H$_3$), 14.0 (s, *C*H$_3$), 68.1 (d, Cp-*C*), 68.2 (s, Cp-*C*), 69.6 (s, Cp-*C*), 72.2 (d, Cp-*C*), 72.6 (s, Cp-*C*), 75.1 (s, Cp-*C*), 106.8 (s, *C*H), 115.4 (s, aromatic), 119.4 (s, aromatic), 129.3 (d, aromatic), 130.2 (s, aromatic), 131.2 (d, aromatic), 131.4 (d, aromatic), 134.5 (d, aromatic), 147.9 (s, *C*CH$_3$), 150.1 (s, *C*CH$_3$), 168.0 (d, aromatic). ^{31}P{^{1}H} NMR (C_6D_6, 203 MHz, 298 K): δ (ppm) -15.5 (s). ^{11}B NMR (C_6D_6, 161 MHz, 298 K): δ (ppm) -7.0 (br s). Anal. Calcd: ($fc^{P,B}$)Zn(OPh)·(Et_2O) ($C_{42}H_{48}BFeN_4O_2PZn$) C, 62.75; H, 6.02; N, 6.97. Found: C, 61.83; H, 5.81; N, 6.75.

NMR scale polymerizations. To a small vial, [($fc^{P,B}$)Zn(μ-OCH_2Ph)]$_2$ (2.5 μmol), an external standard, hexamethylbenzene (0.025 mmol), the monomer (0.5 mmol), and 0.5 mL of

C_6D_6 were added. The contents of the vial were stirred and the homogeneous solution was transferred to a J. Young NMR tube equipped with a Teflon valve. The NMR tube was sealed, taken out of the box and placed in an oil bath. The polymerization was monitored by ^1H NMR spectroscopy until the conversion stopped or reached completion. The contents of the NMR tube were diluted with 0.5 mL of dichloromethane and poured into 10 mL of methanol to yield white solids. The product was collected on a glass frit, washed with additional 5 mL of methanol and kept under reduced pressure until it reached a consistent weight. For the control experiments, $[^{Ac}Fc][BAr^F]$ (5 μmol) was used instead of $[(fc^{P,B})Zn(\mu\text{-}OCH_2Ph)]_2$ under similar conditions as above (Figures D14-17).

5.10 Appendix D

5.10.1 NMR spectroscopy

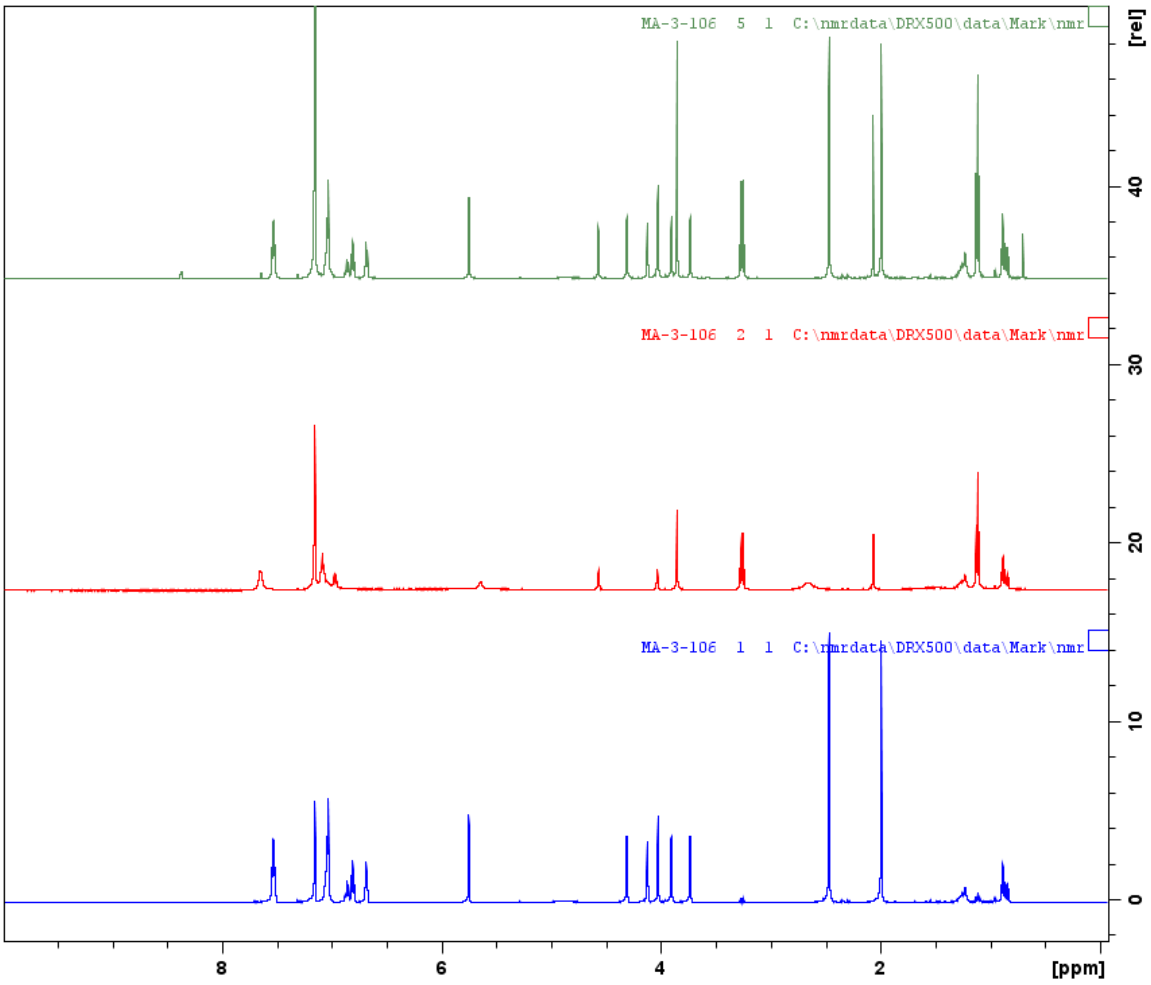

Figure D1. ^{1}H NMR spectra (C_6D_6, 500 MHz, 298 K) of $[(fc^{P,B})Zn(\mu\text{-}OCH_2Ph)]_2$ (bottom), $[(fc^{P,B})Zn(\mu\text{-}OCH_2Ph)]_2$ + $[AcFc][BAr^F]$ (middle), $[(fc^{P,B})Zn(\mu\text{-}OCH_2Ph)]_2$ + $[AcFc][BAr^F]$ + Cp_2Co (top).

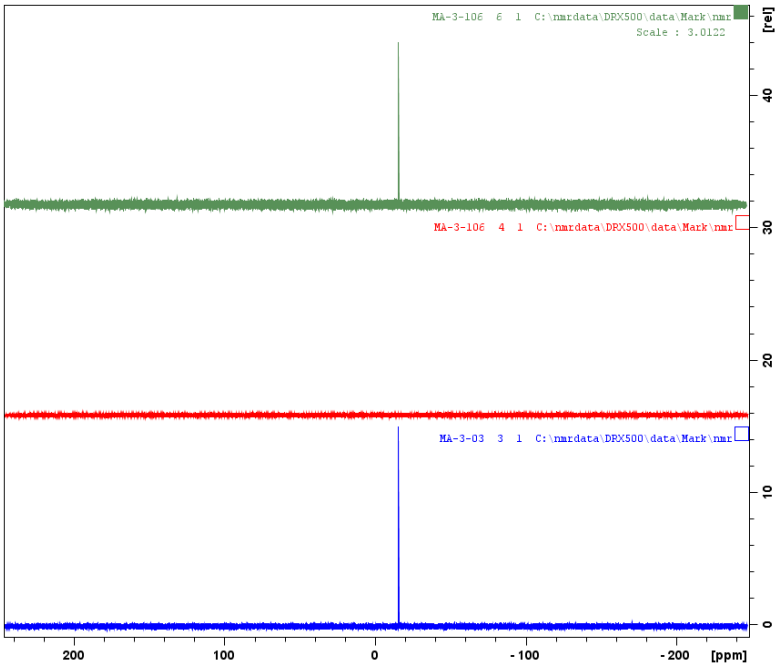

Figure D2. $^{31}P\{^{1}H\}$ NMR spectra (C_6D_6, 202 MHz, 298 K) of $[(fc^{P,B})Zn(\mu\text{-}OCH_2Ph)]_2$ (bottom), $[(fc^{P,B})Zn(\mu\text{-}OCH_2Ph)]_2$ + $[AcFc][BAr^F]$ (middle), $[(fc^{P,B})Zn(\mu\text{-}OCH_2Ph)]_2$ + $[AcFc][BAr^F]$ + Cp_2Co (top).

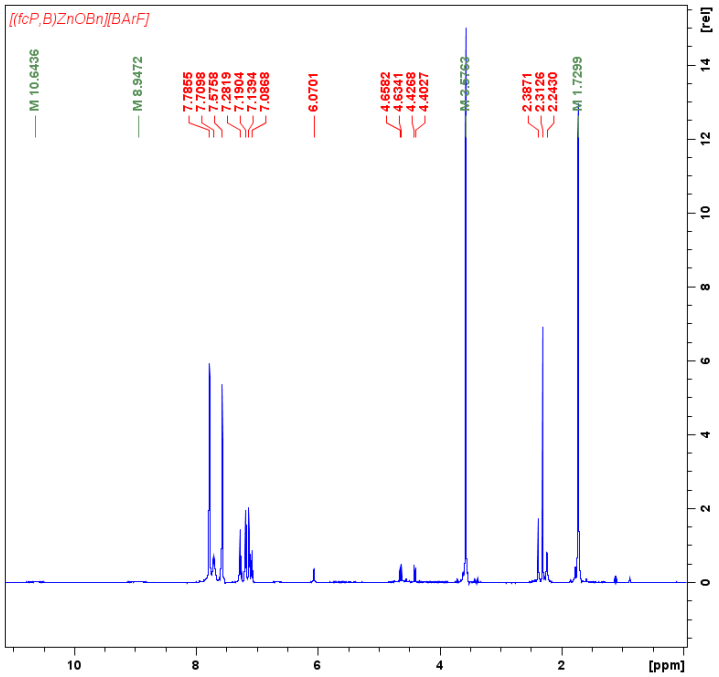

Figure D3. ^{1}H NMR spectrum (THF-d_8, 500 MHz, 298 K) of $[(fc^{P,B})Zn(\mu\text{-}OCH_2Ph)]_2[BAr^F]_2$.

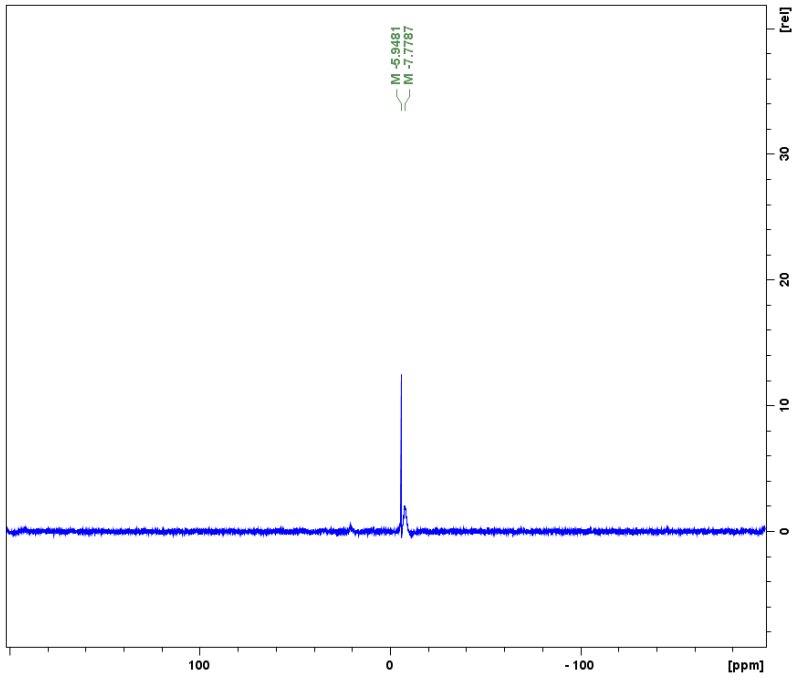

Figure D4. ^{11}B NMR spectrum (THF-d_8, 161 MHz, 298 K) of $[(fc^{P,B})Zn(\mu\text{-}OCH_2Ph)]_2[BAr^F]_2$.

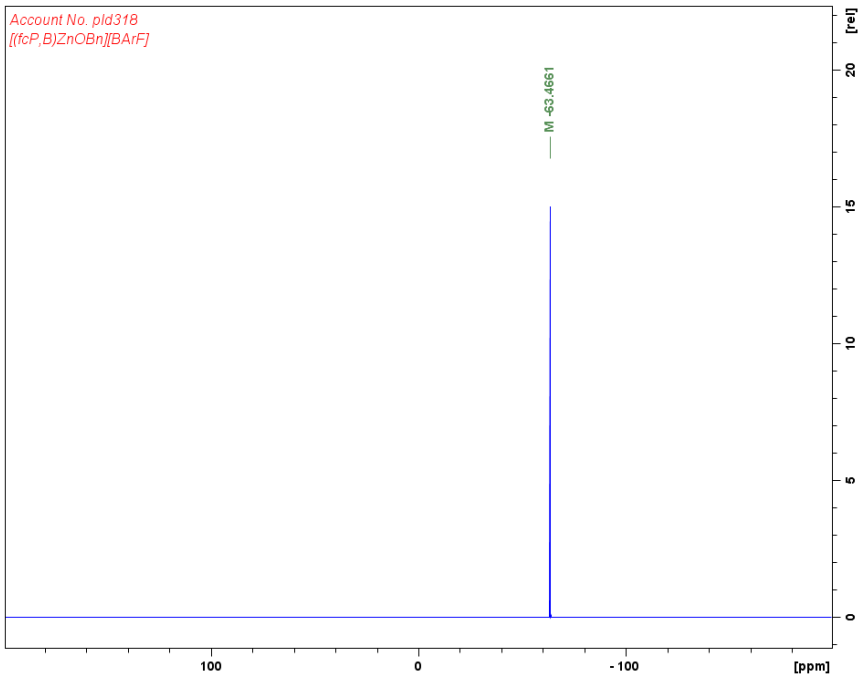

Figure D5. ^{19}F NMR spectrum (THF-d_8, 376 MHz, 298 K) of $[(fc^{P,B})Zn(\mu\text{-}OCH_2Ph)]_2[BAr^F]_2$.

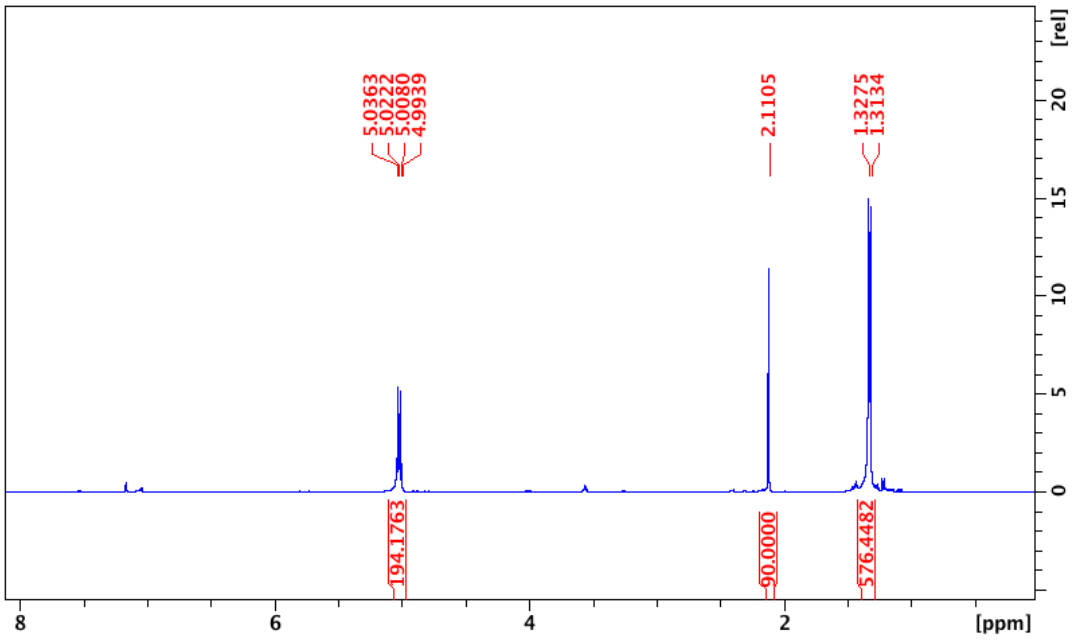

Figure D6. ^{1}H NMR spectrum (C_6D_6, 500 MHz, 298 K) of L-lactide (LA) polymerization. Standard is hexamethylbenzene (HMB). Compound 2: HMB: LA ratio is 1:10:194.

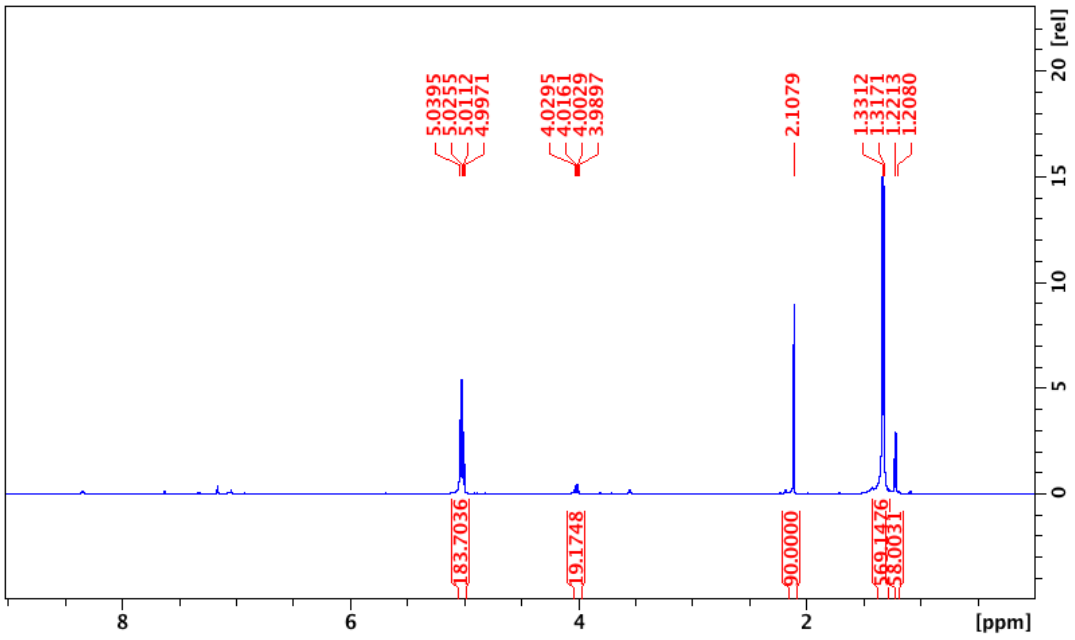

Figure D7. ^{1}H NMR spectrum (C_6D_6, 500 MHz, 298 K) of L-lactide (LA) polymerization. Standard is hexamethylbenzene (HMB). Compound 3: HMB: LA ratio is 1:10:184.

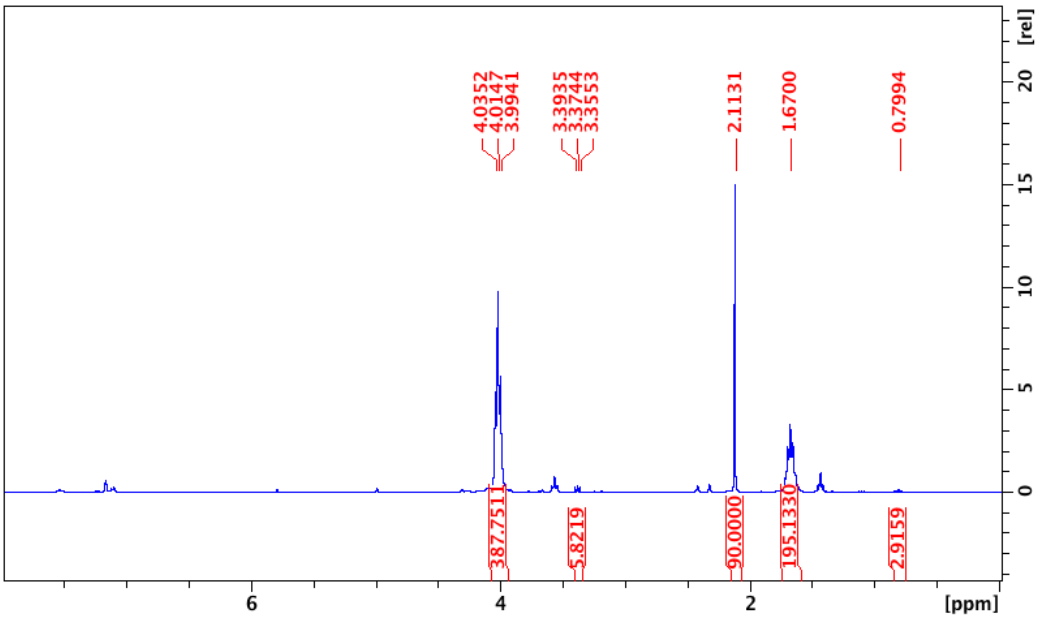

Figure D8. ^{1}H NMR spectrum (C_6D_6, 500 MHz, 298 K) of trimethylene carbonate (TMC) polymerization. Standard is hexamethylbenzene (HMB). Compound 2: HMB: TMC ratio is 1:10:194.

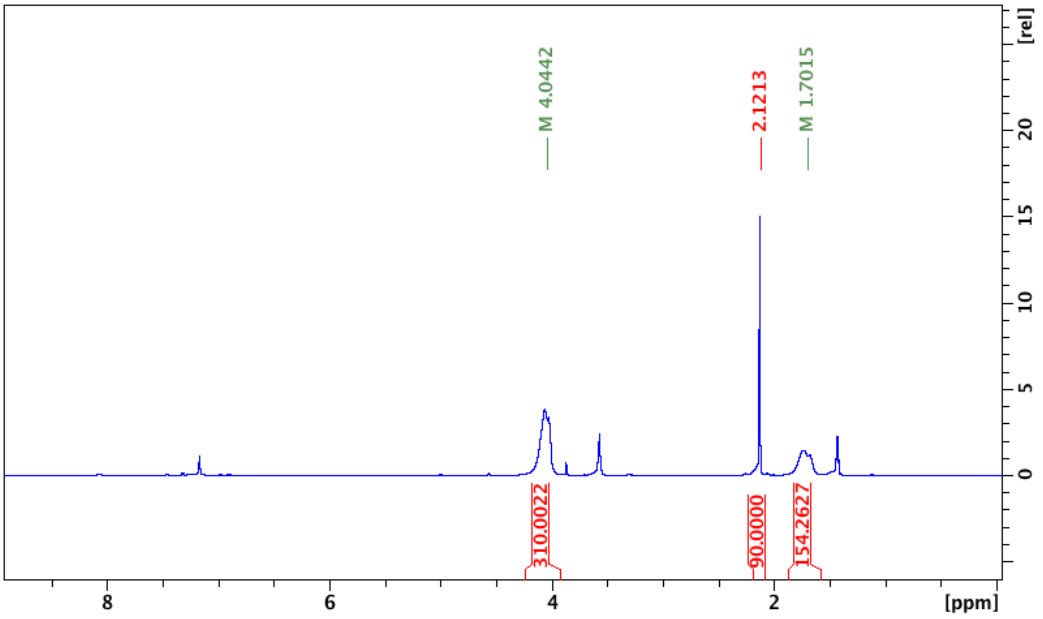

Figure D9. ^{1}H NMR spectrum (C_6D_6, 500 MHz, 298 K) of trimethylene carbonate (TMC) polymerization. Standard is hexamethylbenzene (HMB). Compound 3: HMB: TMC ratio is 1:10:156.

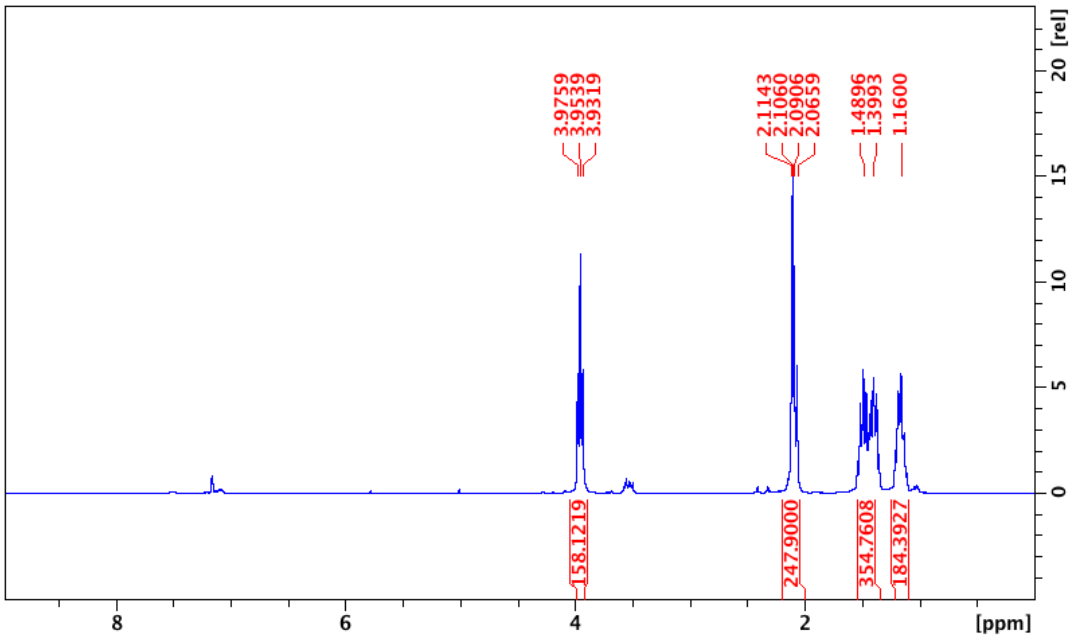

Figure D10. ^{1}H NMR spectrum (C_6D_6, 300 MHz, 298 K) of ε-caprolactone (CL) polymerization. Standard is hexamethylbenzene (HMB). Compound 2: HMB: CL ratio is 1:10:158.

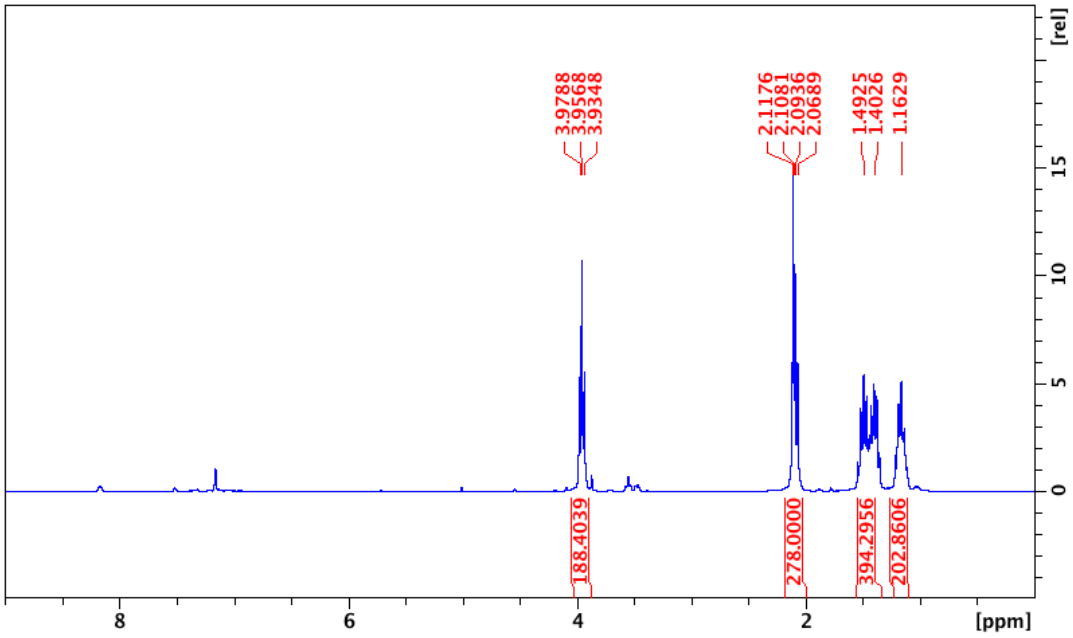

Figure D11. ^{1}H NMR spectrum (C_6D_6, 300 MHz, 298 K) of ε-caprolactone (CL) polymerization. Standard is hexamethylbenzene (HMB). Compound 3: HMB: CL ratio is 1:10:188.

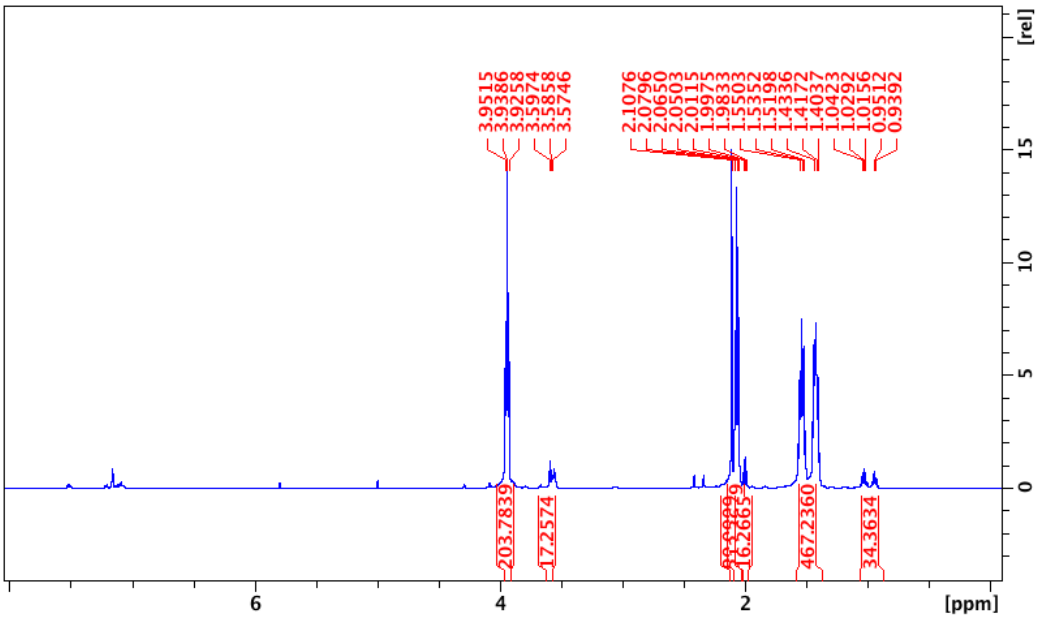

Figure D12. ^{1}H NMR spectrum (C_6D_6, 500 MHz, 298 K) of δ-valerolactone (VL) polymerization. Standard is hexamethylbenzene (HMB). Compound 2: HMB: VL ratio is 1:10:204.

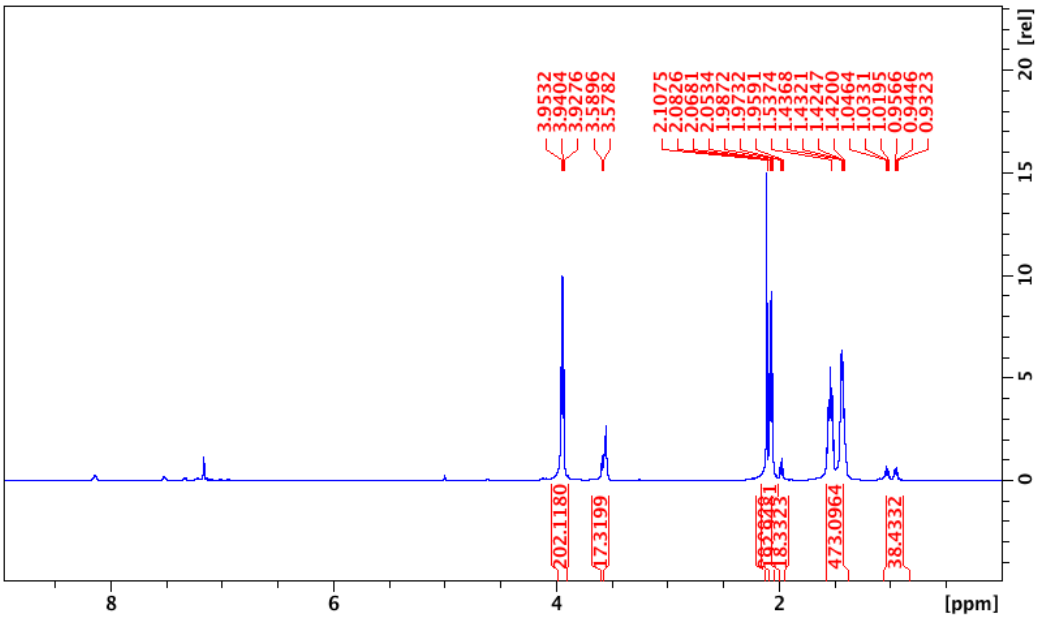

Figure D13. ^{1}H NMR spectrum (C_6D_6, 500 MHz, 298 K) of δ-valerolactone (VL) polymerization. Standard is hexamethylbenzene (HMB). Compound 3: HMB: VL ratio is 1:10:202.

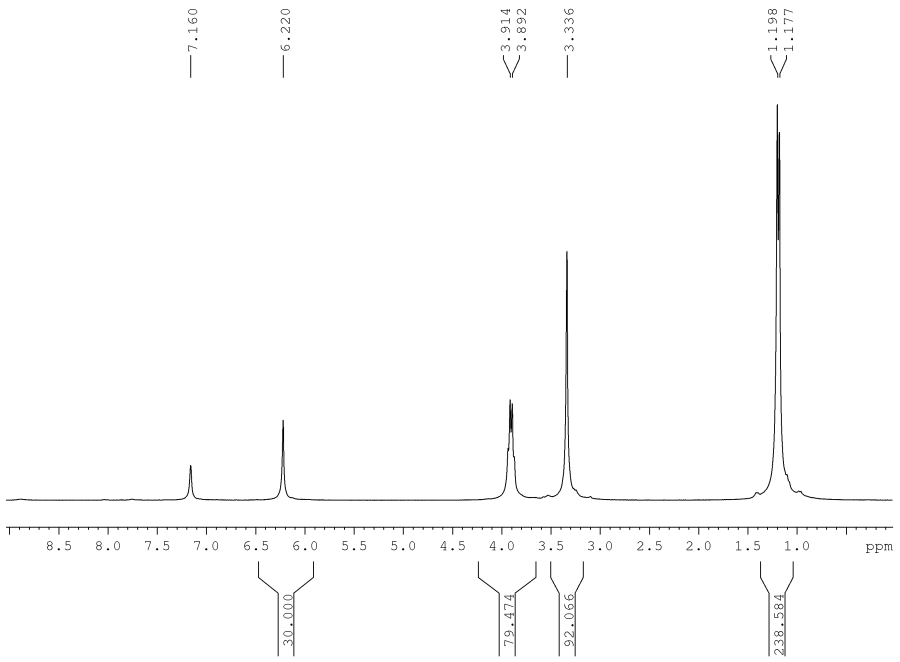

Figure D14. Control experiment of 40 equivalents of L-lactide (LA) with 5 equivalents of [^{Ac}Fc][BAr^{F}] at 70 °C for three hours.

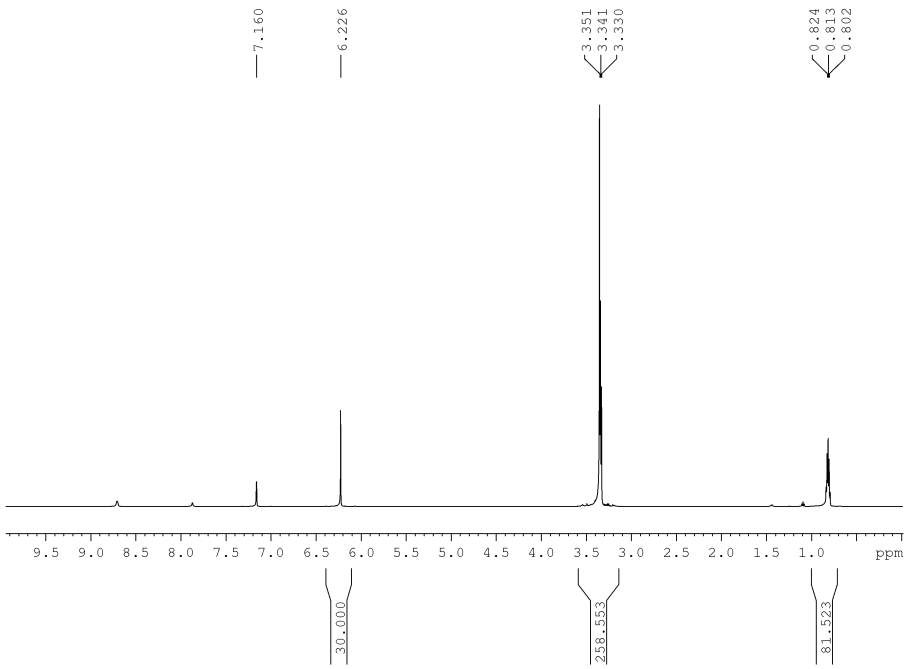

Figure D15. Control experiment of 40 equivalents of trimethylene carbonate (TMC) with 5 equivalents of [^{Ac}Fc][BAr^{F}] at ambient temperature for 2 hours.

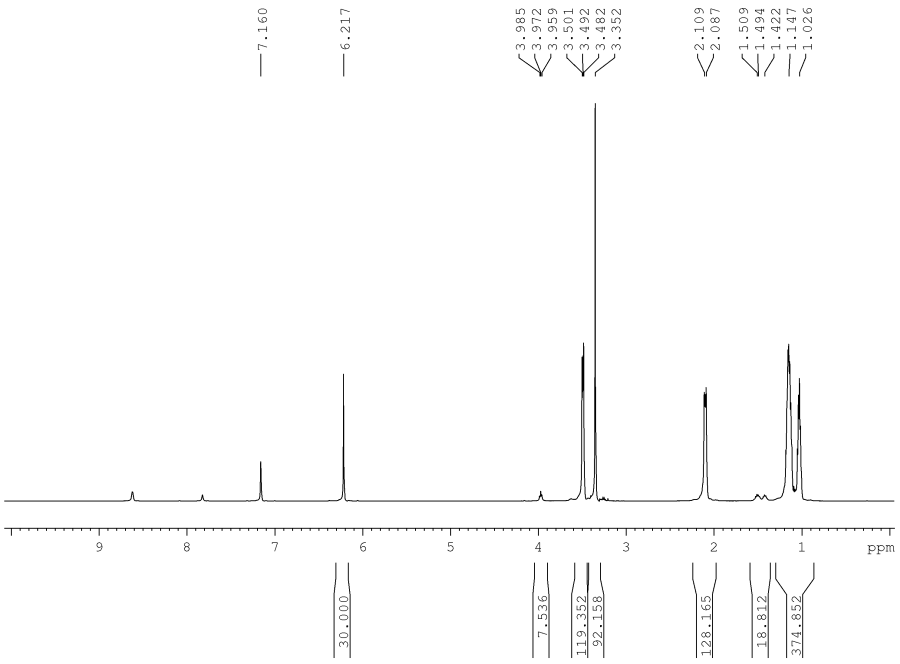

Figure D16. Control experiment of 64 equivalents of ε-caprolactone (CL) with 5 equivalents of [^{Ac}Fc][BAr^{F}] at 70°C for 1 hour.

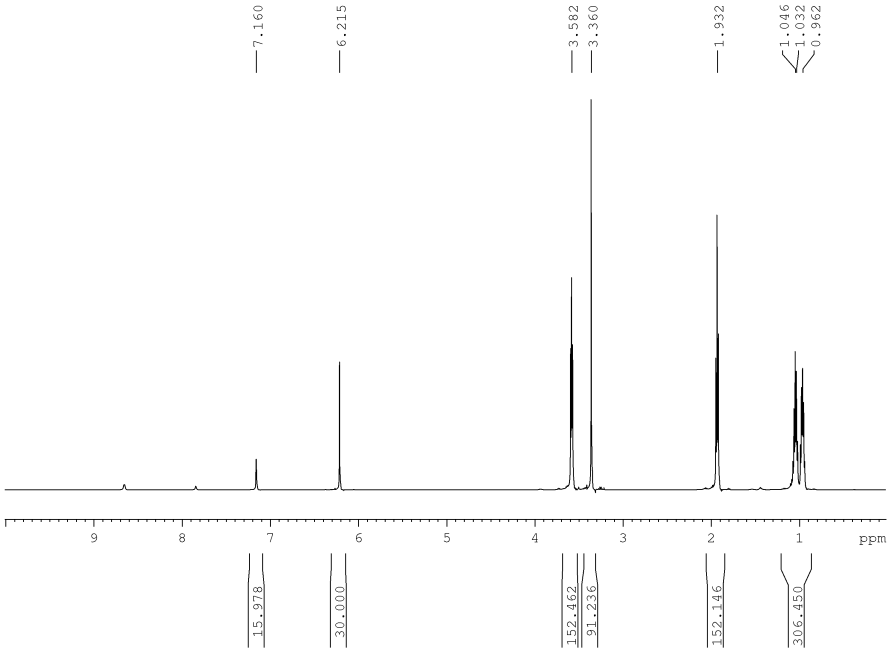

Figure D17. Control experiment of 76 equivalents of δ-valerolactone (VL) with 5 equivalents of [^{Ac}Fc][BAr^{F}] at ambient temperature for 2 hours.

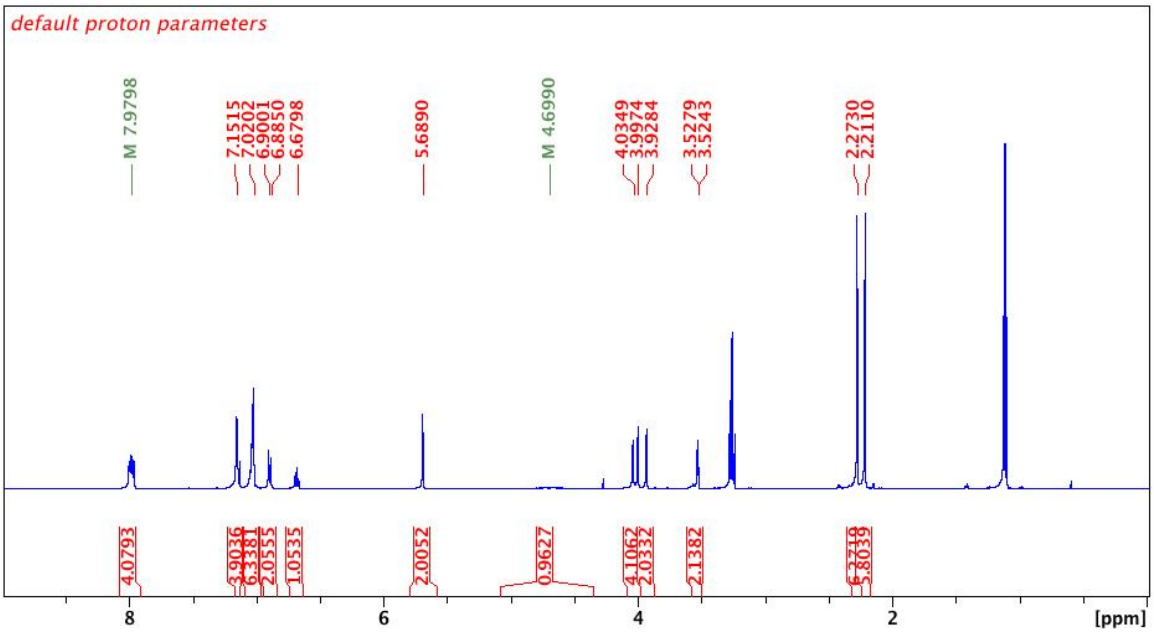

Figure D18. ^{1}H NMR spectrum (C_6D_6, 500 MHz, 298 K) of ($fc^{P,B}$)Zn(OPh).

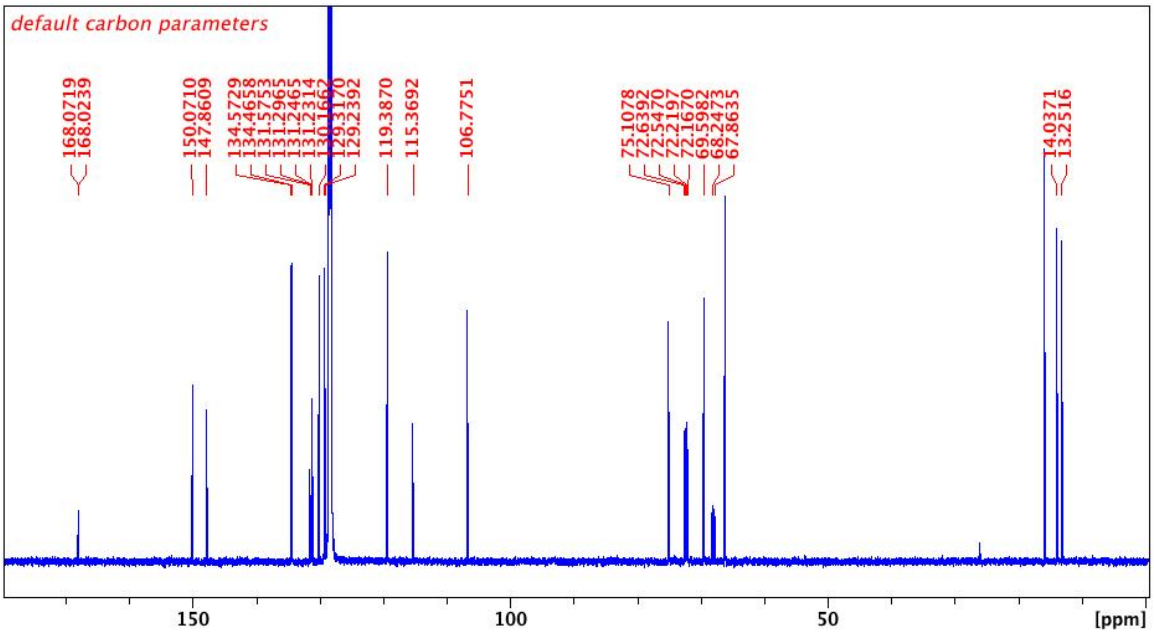

Figure D19. ^{13}C NMR spectrum (C_6D_6, 126 MHz, 298 K) of ($fc^{P,B}$)Zn(OPh).

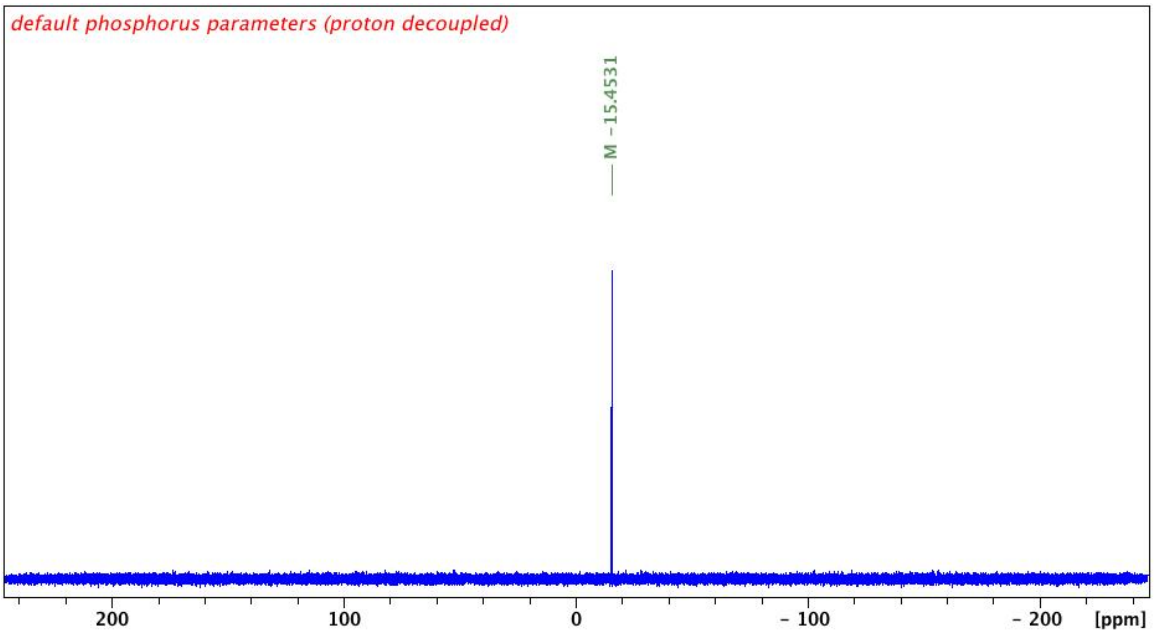

Figure D20. $^{31}P\{^{1}H\}$ NMR spectrum (C_6D_6, 203 MHz, 298 K) of ($fc^{P,B}$)Zn(OPh).

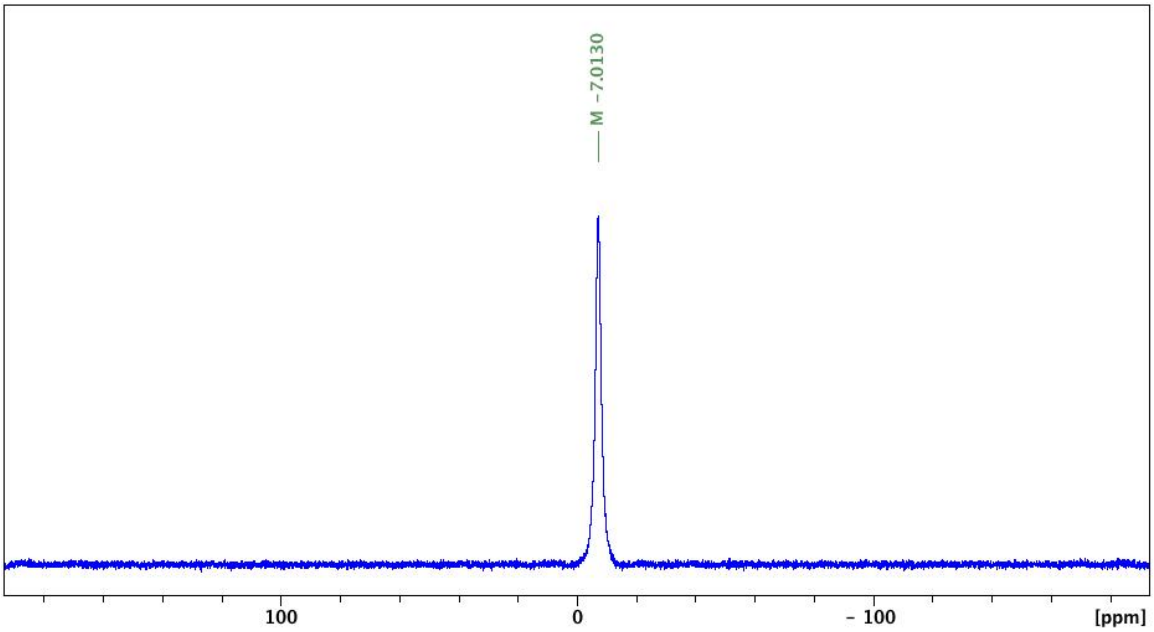

Figure D21. ^{11}B NMR spectrum (C_6D_6, 161 MHz, 298 K) of ($fc^{P,B}$)Zn(OPh).

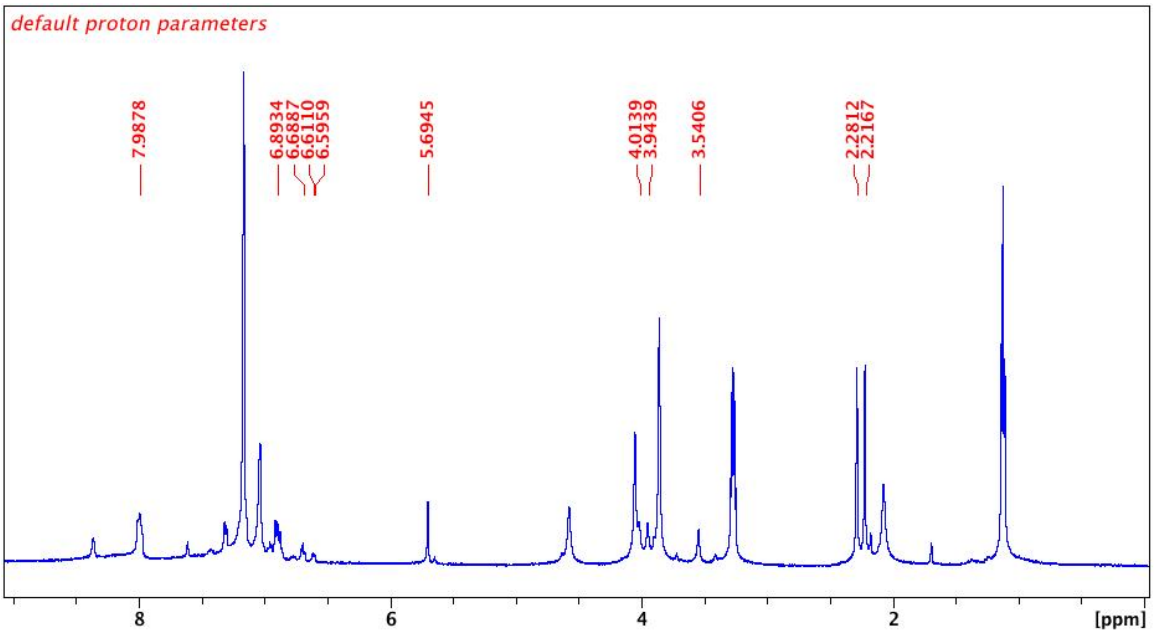

Figure D22. ^{1}H NMR spectrum (C_6D_6, 500 MHz, 298 K) of ($fc^{P,B}$)Zn(OPh) + [AcFc][BAr^{F}].

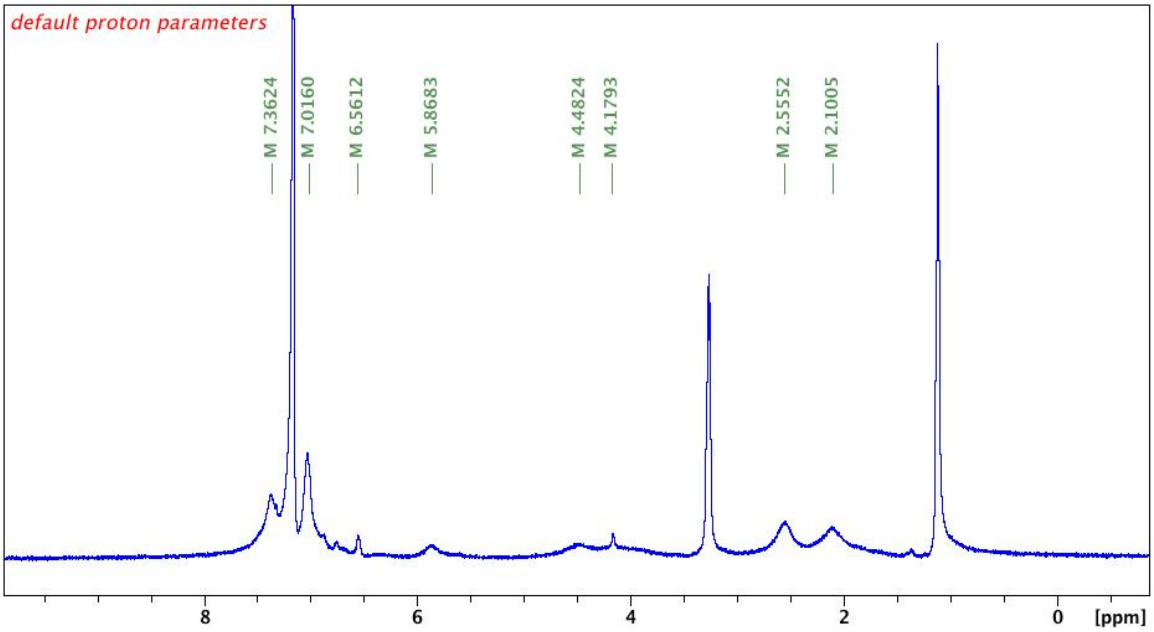

Figure D23. ^{1}H NMR spectrum (C_6D_6, 500 MHz, 298 K) of ($fc^{P,B}$)Zn(OPh) + $AgBF_4$.

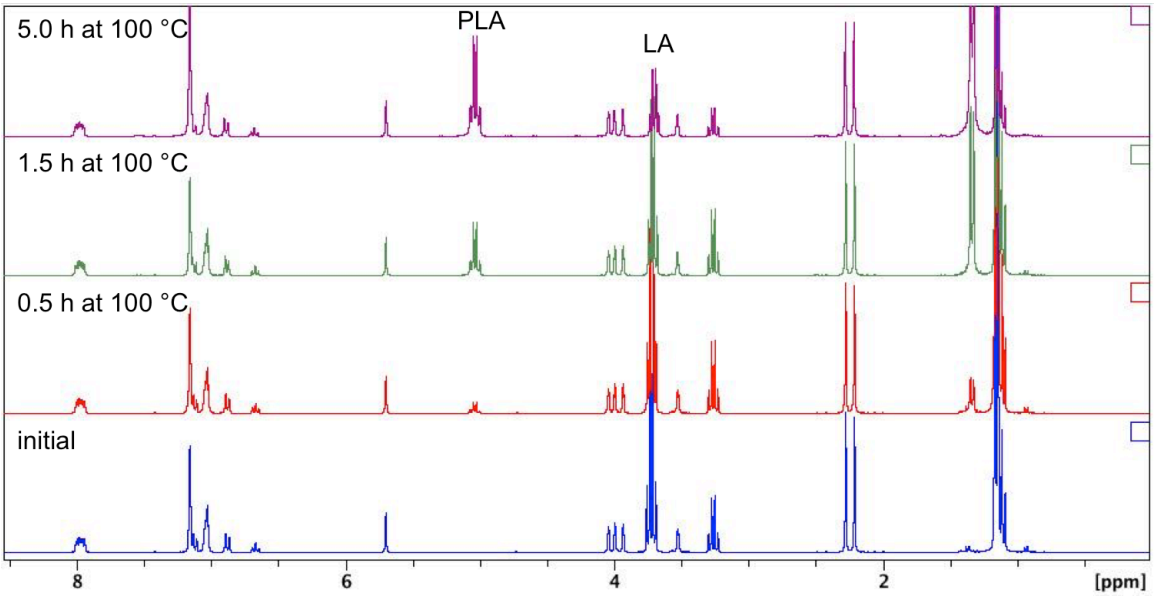

Figure D24. ^{1}H NMR spectra (C_6D_6, 500 MHz, 298 K) of L-lactide polymerization (10 equivalents) in the presence of ($fc^{P,B}$)Zn(OPh).

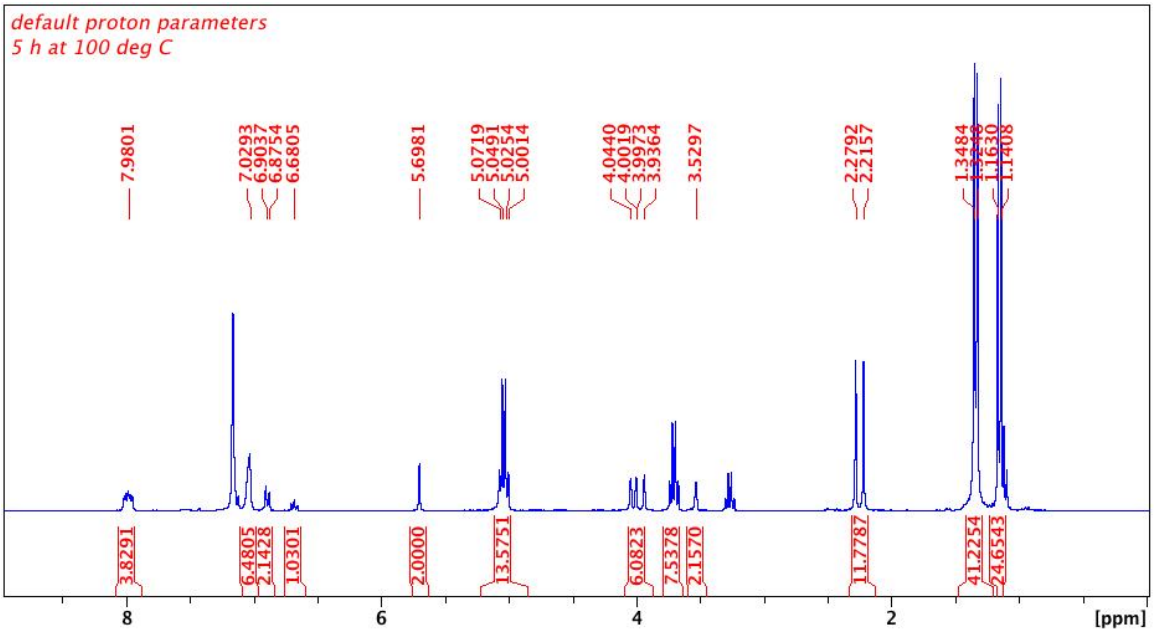

Figure D25. ^{1}H NMR spectrum (C_6D_6, 500 MHz, 298 K) of L-lactide polymerization (10 equivalents) in the presence of ($fc^{P,B}$)Zn(OPh) after 5 h at 100 °C.

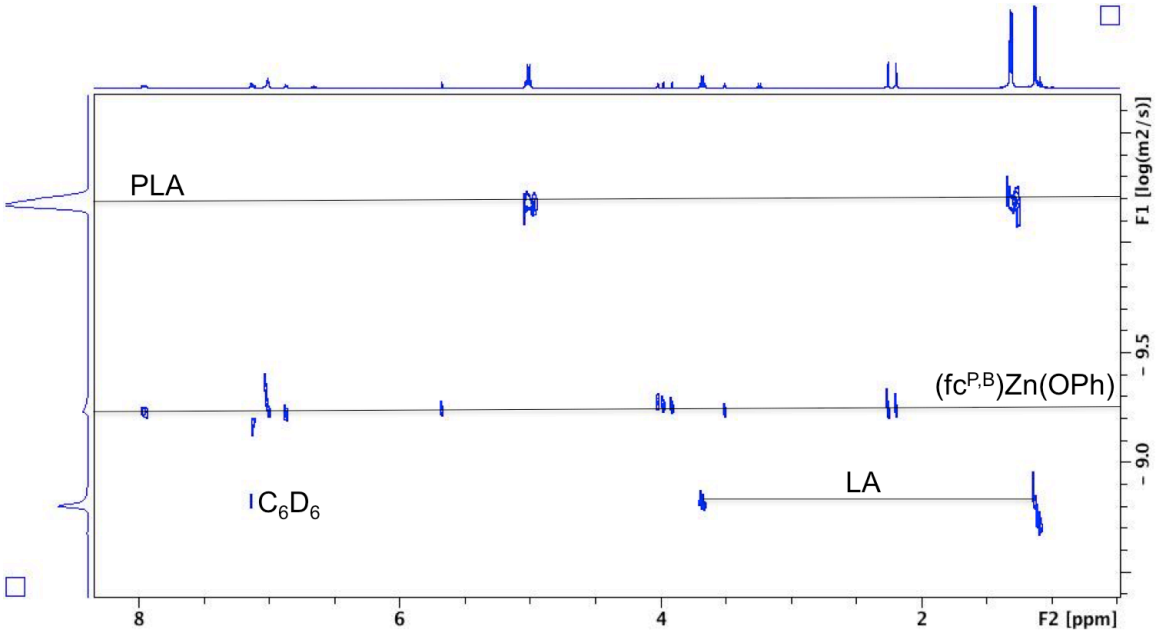

Figure D26. ^{1}H DOSY NMR spectrum (C_6D_6, 500 MHz, 298 K) of L-lactide polymerization (10 equivalents) in the presence of ($fc^{P,B}$)Zn(OPh) after 5 h at 100 °C .

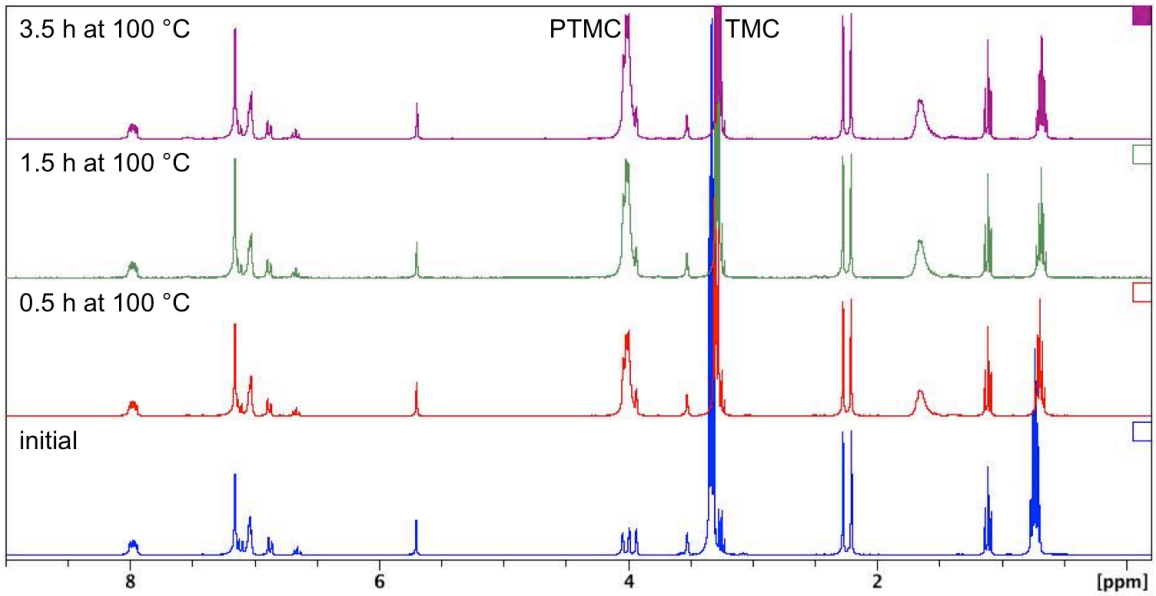

Figure D27. ^{1}H NMR spectra (C_6D_6, 500 MHz, 298 K) of trimethylene carbonate polymerization (13 equivalents) in the presence of ($fc^{P,B}$)Zn(OPh).

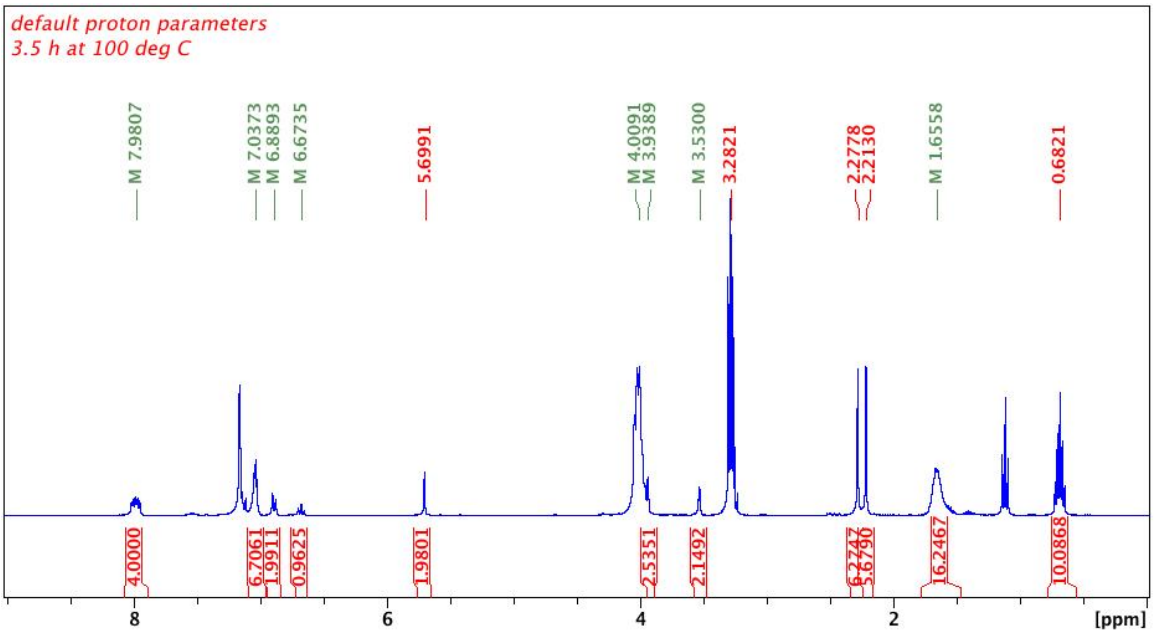

Figure D28. ^{1}H NMR spectrum (C_6D_6, 500 MHz, 298 K) of trimethylene carbonate polymerization (13 equivalents) in the presence of ($fc^{P,B}$)Zn(OPh) after 3.5 h at 100 °C.

5.10.2 Cyclic voltammetry data

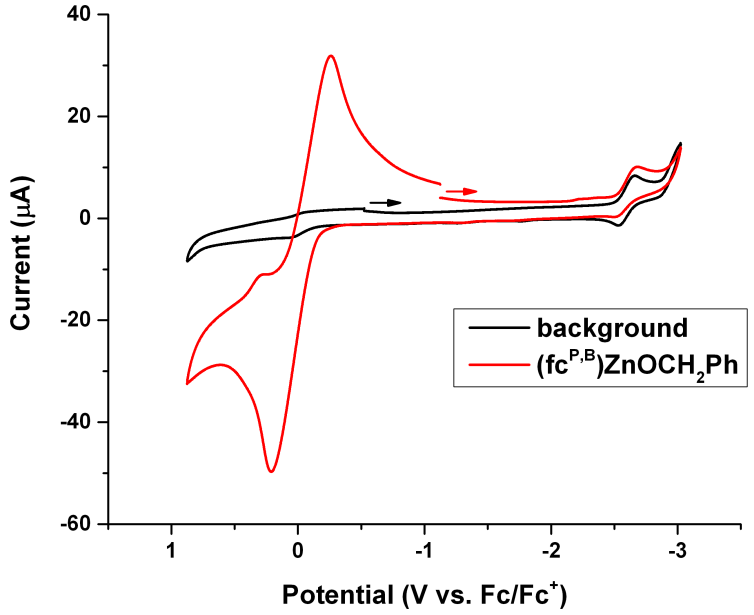

Figure D29. Cyclic voltammograms recorded with a glassy carbon electrode at 100 mV/s in THF, 0.10 M [TBA][PF_6] containing (a) no [($fc^{P,B}$)Zn(μ-OCH_2Ph)]$_2$, (b) 2.5 mM [($fc^{P,B}$)Zn(μ-OCH_2Ph)]$_2$.

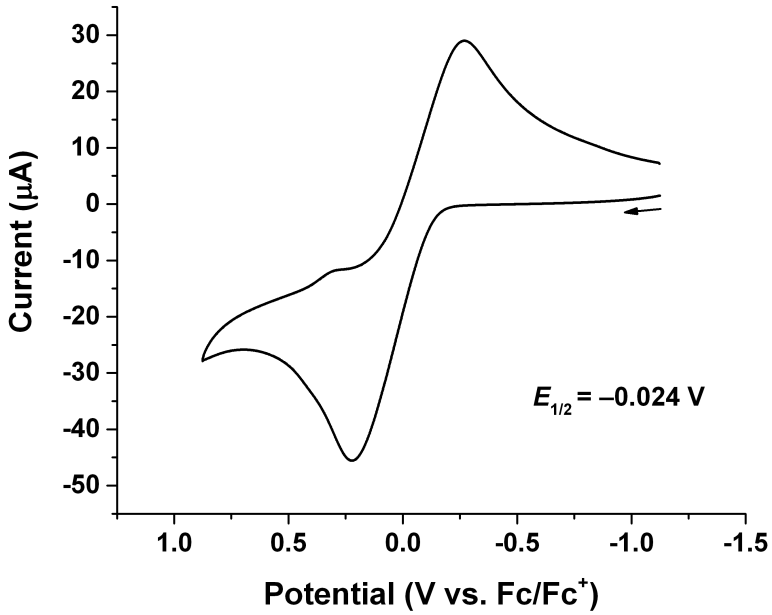

Figure D30. Cyclic voltammogram recorded with a glassy carbon electrode at 100 mV/s in THF, 0.10 M [TBA][PF_6] containing 2.5 mM [($fc^{P,B}$)Zn(μ-OCH_2Ph)]$_2$. $E_{1/2}$ = -0.024 V, i_{pa}/i_{pc} = 1.02.

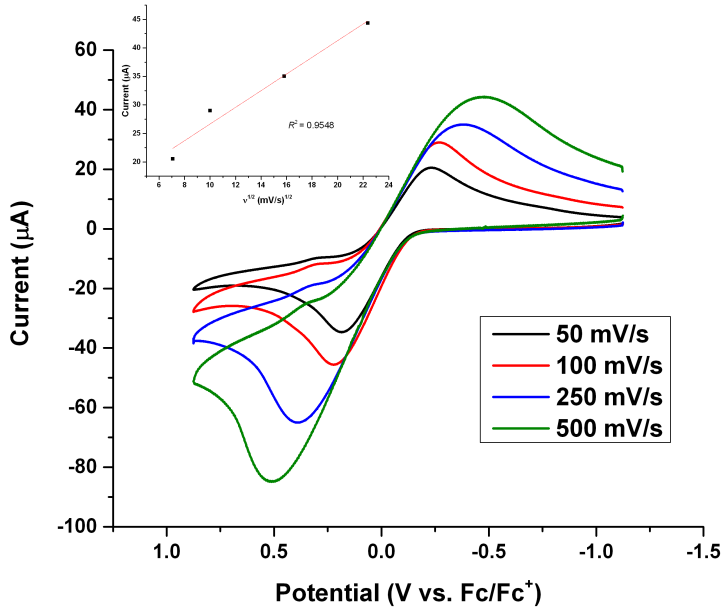

Figure D31. Cyclic voltammograms recorded with a glassy carbon electrode at 50, 100, 250, and 500 mV/s in THF, 0.10 M [TBA][PF_6] containing 2.5 mM [($fc^{P,B}$)Zn(μ-OCH_2Ph)]$_2$.

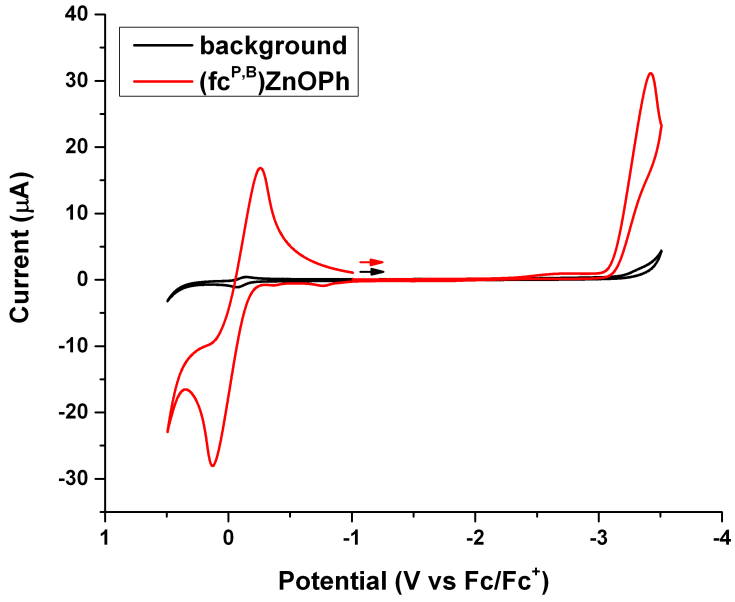

Figure D32. Cyclic voltammograms recorded with a glassy carbon electrode at 100 mV/s in THF, 0.10 M [TBA][PF_6] containing (a) no ($fc^{P,B}$)Zn(OPh), (b) 5.0 mM ($fc^{P,B}$)Zn(OPh).

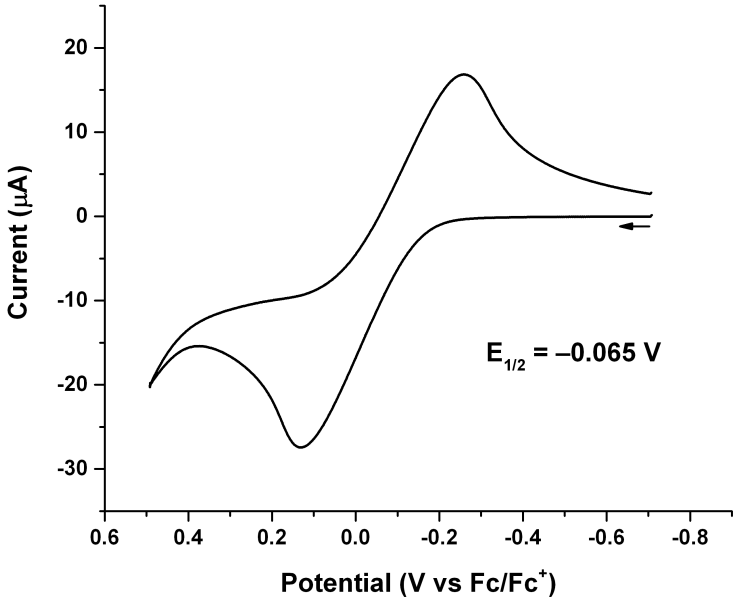

Figure D33. Cyclic voltammogram recorded with a glassy carbon electrode at 100 mV/s in THF, 0.10 M [TBA][PF_6] containing 5.0 mM ($fc^{P,B}$)Zn(OPh). $E_{1/2}$ = -0.065 V, i_{pa}/i_{pc} = 1.06.

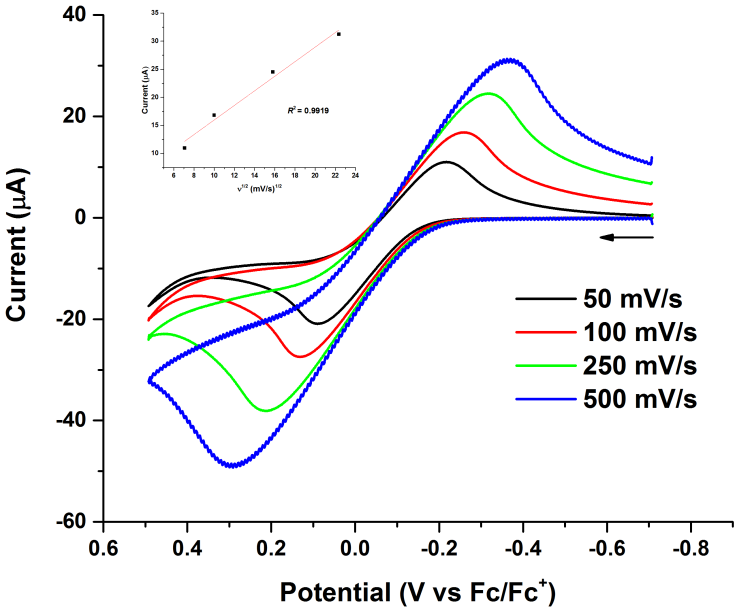

Figure D34. Cyclic voltammograms recorded with a glassy carbon electrode at 50, 100, 250, and 500 mV/s in THF, 0.10 M [TBA][PF_6] containing 5.0 mM ($fc^{P,B}$)Zn(OPh).

5.10.3 Gel permeation chromatography

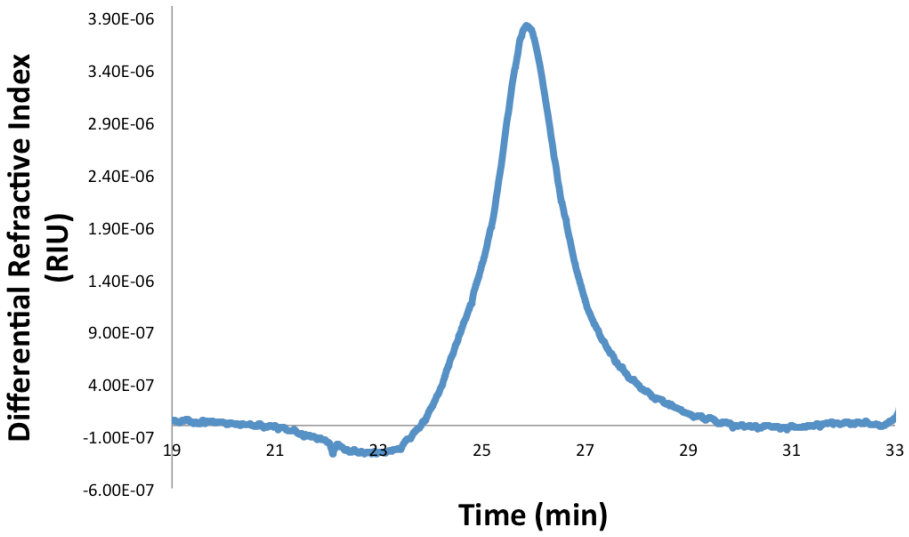

Figure D35. Polymerization of 194 equivalents of L-lactide by compound 2; M_n = 13,800; $Đ$ = 1.14.

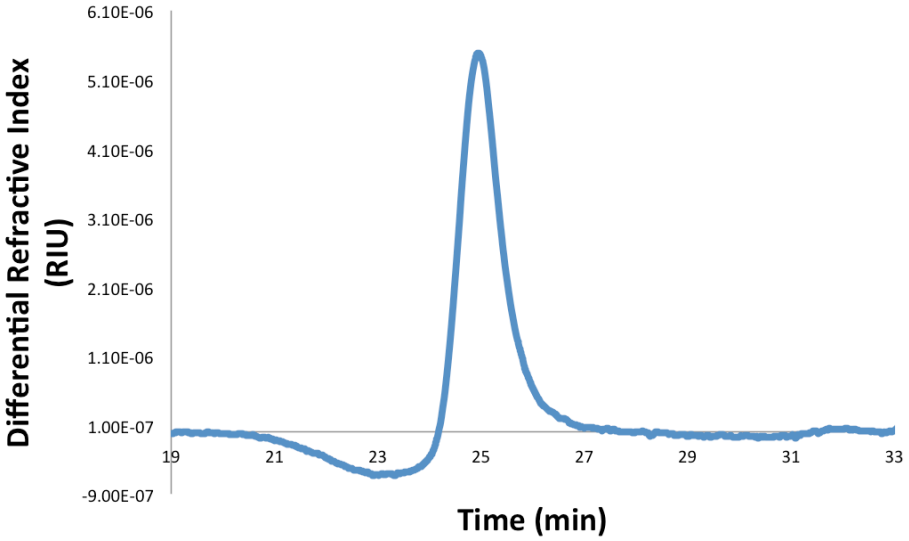

Figure D36. Polymerization of 184 equivalents of L-lactide by compound 3; M_n = 13,500; $Đ$ = 1.03.

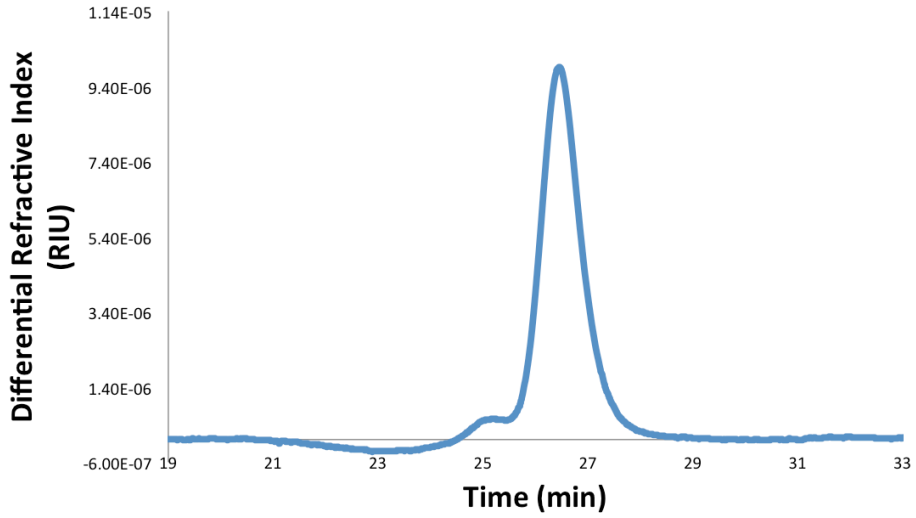

Figure D37. Polymerization of 194 equivalents of trimethylene carbonate by compound 2; M_n = 10,000; $Đ$ = 1.14.

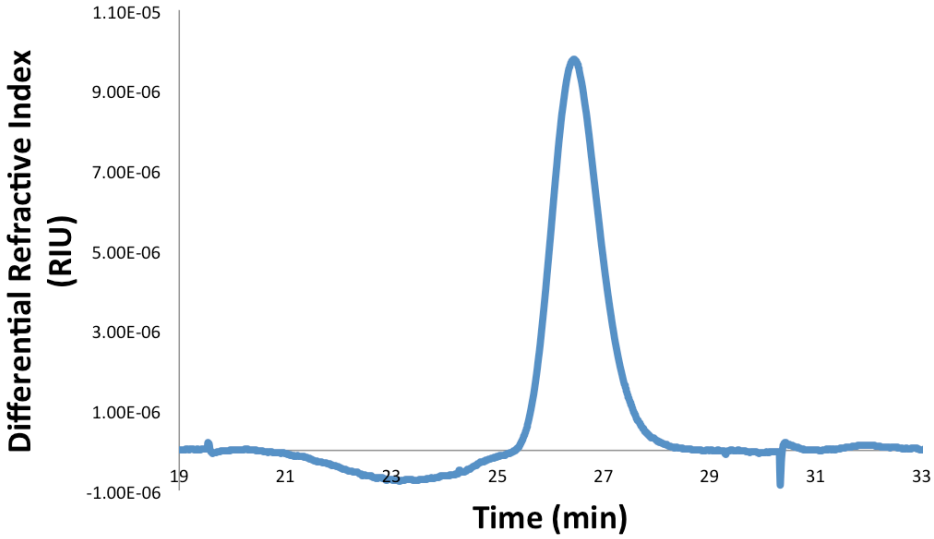

Figure D38. Polymerization of 156 equivalents of trimethylene carbonate by compound 3; M_n = 8,100; $Đ$ = 1.02.

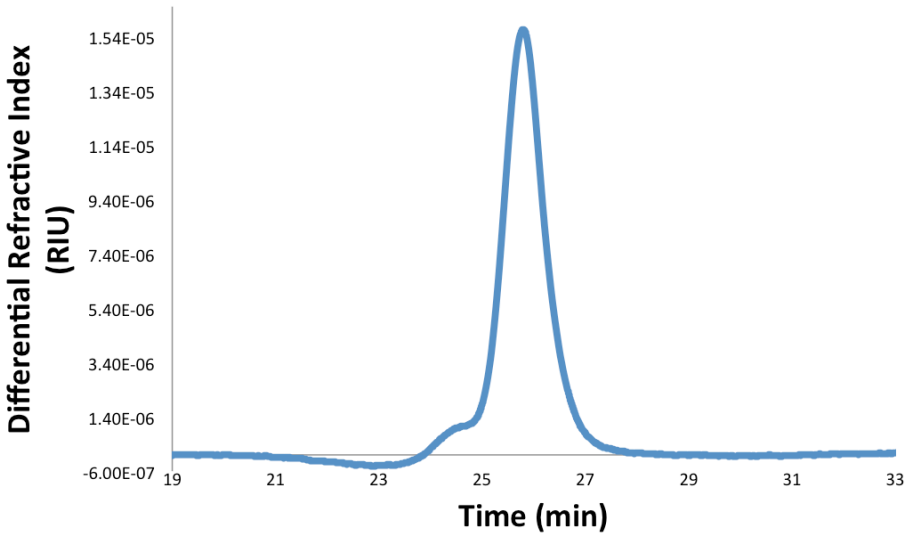

Figure D39. Polymerization of 158 equivalents of ε-caprolactone by compound 2; M_n = 8,900; $Đ$ = 1.09.

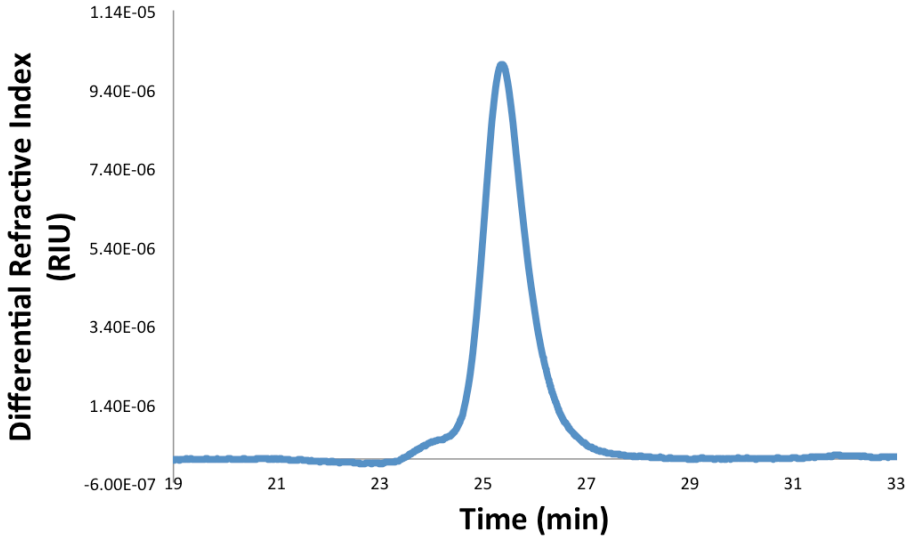

Figure D40. Polymerization of 188 equivalents of ε-caprolactone by compound 3; M_n = 10,500; $Đ$ = 1.08.

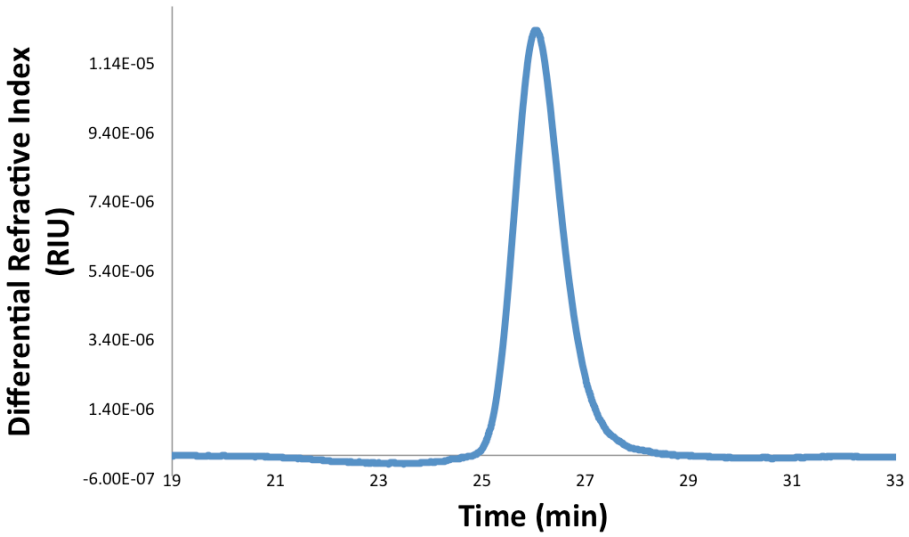

Figure D41. Polymerization of 204 equivalents of δ-valerolactone by compound 2; M_n = 10,400; $Đ$ = 1.01.

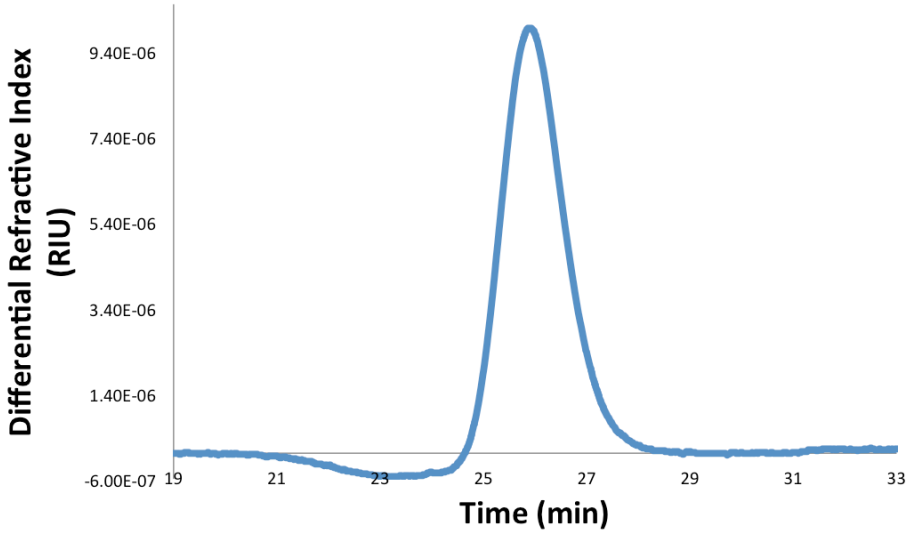

Figure D42. Polymerization of 202 equivalents of δ-valerolactone by compound 3; M_n = 10,500; $Đ$ = 1.04.

5.10.4 Conversion studies

Table D1. Molecular weight versus conversion study of L-lactide in the presence of $[(fc^{P,B})Zn(OCH_2Ph)]_2[BAr^F]_2$.

Time (min)	Conversion (%)	M_n (NMR)	M_n (GPC)	*Đ*
35	25	10,500	11,800	1.05
55	36	14,300	15,500	1.08
75	43	17,100	18,600	1.06
95	49	19,700	20,900	1.11
115	55	22,600	22,800	1.05

Conditions: benzene as a solvent (1.5 mL) and hexamethylbenzene as an internal standard. The experiment was performed at 70 °C.

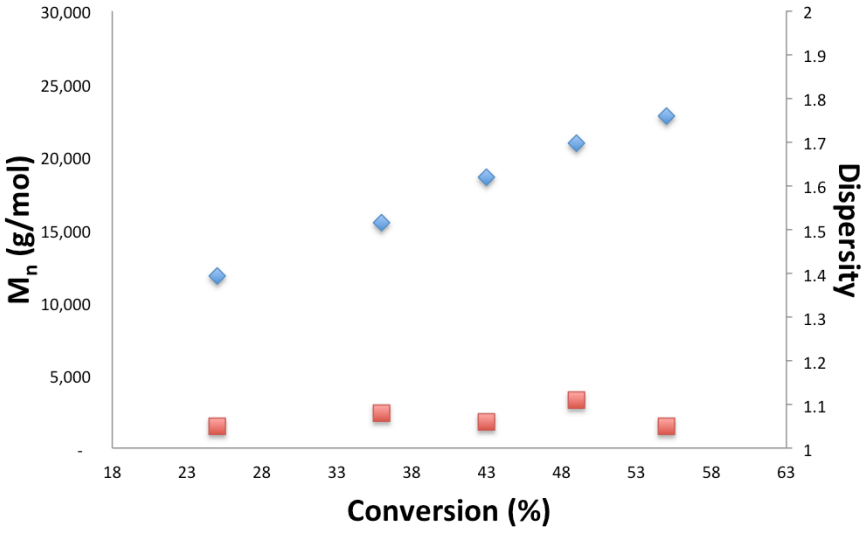

Figure D43. Conversion of L-lactide versus M_n in the presence of $[(fc^{P,B})Zn(OCH_2Ph)]_2[BAr^F]_2$.

Table D2. Molecular weight versus conversion study of trimethylene carbonate in the presence of $[(fc^{P,B})Zn(OCH_2Ph)]_2[BAr^F]_2$.

Time (min)	Conversion (%)	M_n (NMR)	M_n (GPC)	*Đ*
2	20	3,500	3,100	1.09
3	35	5,900	5,800	1.01
4	41	7,000	7,100	1.02
5	43	7,300	7,600	1.04
6	48	8,200	8,800	1.00
7	68	12,100	12,200	1.02

Conditions: benzene as a solvent (1.5 mL) and hexamethylbenzene as an internal standard. The experiment was performed at ambient temperature.

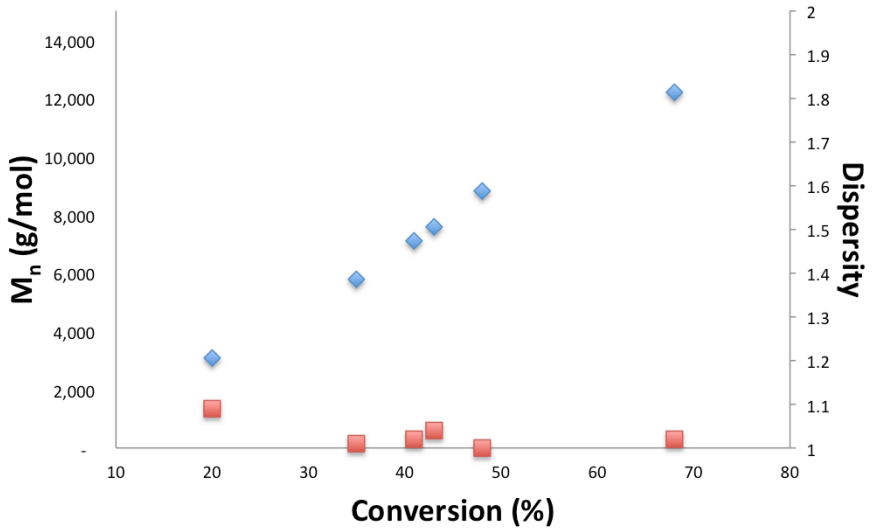

Figure D44. Conversion of trimethylene carbonate versus M_n in the presence of $[(fc^{P,B})Zn(OCH_2Ph)]_2[BAr^F]_2$.

Table D3. Molecular weight versus conversion study of δ-valerolactone in the presence of $[(fc^{P,B})Zn(OCH_2Ph)]_2$.

Time (min)	Conversion (%)	M_n (NMR)	M_n (GPC)	*Đ*
10	21	6,000	5,800	1.03
15	30	8,000	7,400	1.01
25	48	13,000	11,800	1.04
30	58	15,800	14,100	1.03
35	65	17,900	15,900	1.04
40	71	18,800	16,900	1.04

Conditions: benzene as a solvent (1.5 mL) and hexamethylbenzene as an internal standard. The experiment was performed at ambient temperature.

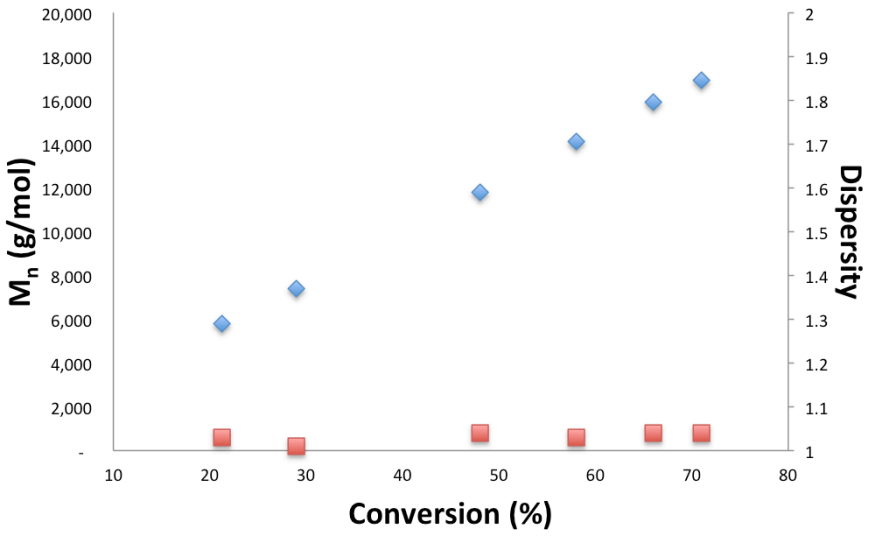

Figure D45. Conversion of δ-valerolactone versus M_n in the presence of $[(fc^{P,B})Zn(OCH_2Ph)]_2$.

Table D4. Molecular weight versus conversion study of δ-valerolactone in the presence of $[(fc^{P,B})Zn(OCH_2Ph)]_2[BAr^F]_2$.

Time (min)	Conversion (%)	M_n (NMR)	M_n (GPC)	*Đ*
2	27	8,300	8,900	1.1
4	36	10,900	11,900	1.04
6	40	12,100	13,200	1.04
8	44	13,500	14,700	1.04
10	49	15,000	16,300	1.02
12	56	16,700	17,700	1.03
14	61	17,800	18,500	1.02

Conditions: benzene as a solvent (1.5 mL) and hexamethylbenzene as an internal standard. The experiment was performed at ambient temperature.

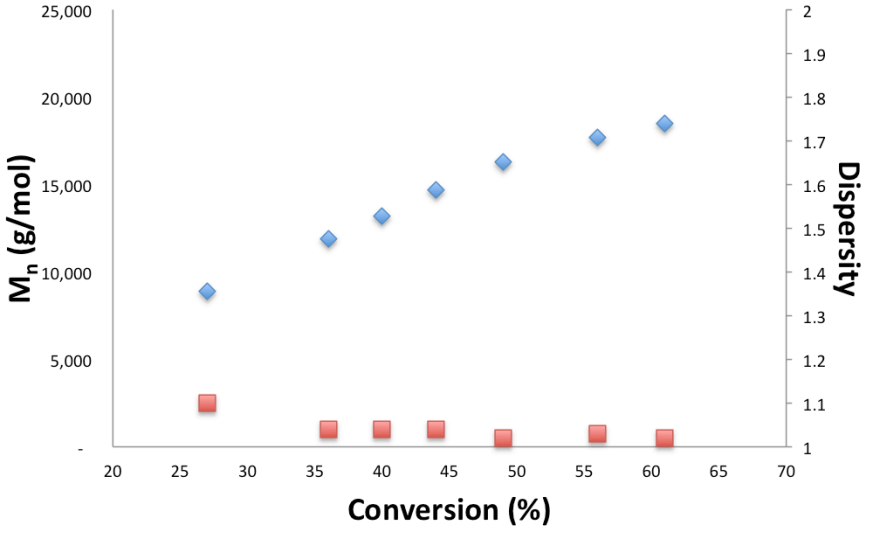

Figure D46. Conversion of δ-valerolactone versus M_n in the presence of $[(fc^{P,B})Zn(OCH_2Ph)]_2[BAr^F]_2$.

Table D5. Molecular weight versus conversion study of ε-caprolactone in the presence of $[(fc^{P,B})Zn(OCH_2Ph)]_2$.

Time (min)	Conversion (%)	M_n (NMR)	M_n (GPC)	*Đ*
60	15	5,100	5,100	1.01
120	25	8,900	8,300	1.02
180	32	11,300	10,100	1.01
240	43	15,100	14,000	1.01
300	52	18,100	16,400	1.01
360	57	19,800	18,100	1.01

Conditions: benzene as a solvent (1.5 mL) and hexamethylbenzene as an internal standard. The experiment was performed at ambient temperature.

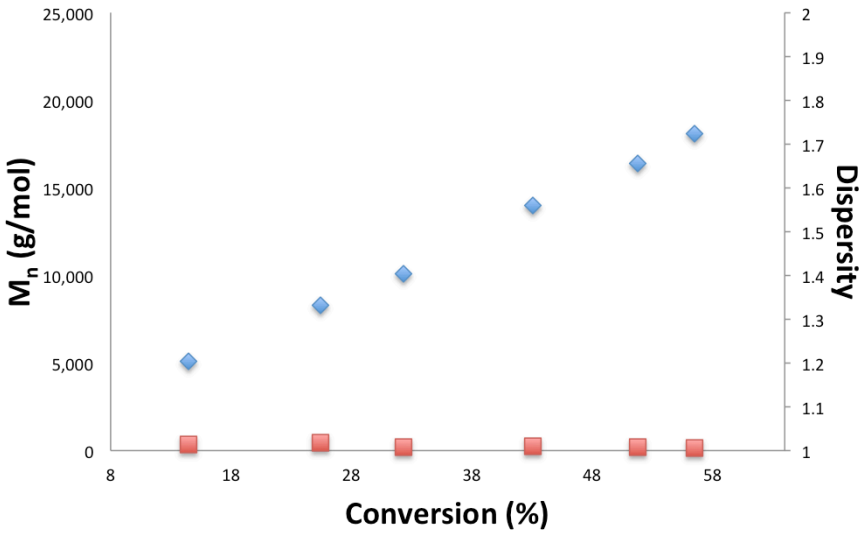

Figure D47. Conversion of ε-caprolactone versus M_n in the presence of $[(fc^{P,B})Zn(OCH_2Ph)]_2$.

Table D6. Molecular weight versus conversion study of ε-caprolactone in the presence of $[(fc^{P,B})Zn(OCH_2Ph)]_2[BAr^F]_2$.

Time (min)	Conversion (%)	M_n (NMR)	M_n (GPC)	*Đ*
60	17	6,000	5,700	1.06
120	30	10,500	9,300	1.09
180	46	16,100	16,200	1.03
240	57	19,900	20,000	1.04
300	68	23,800	23,800	1.02
360	75	26,200	26,300	1.02

Conditions: benzene as a solvent (1.5 mL) and hexamethylbenzene as an internal standard. The experiment was performed at ambient temperature.

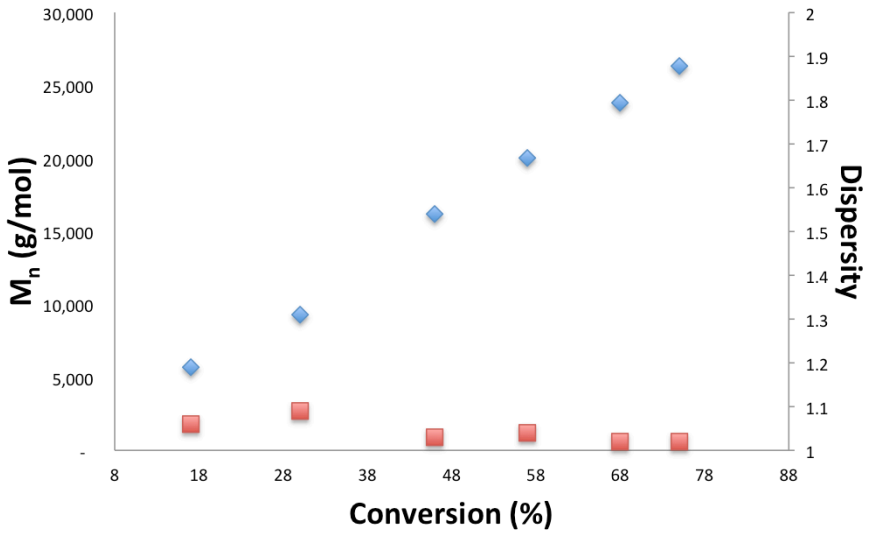

Figure D48. Conversion of ε-caprolactone versus M_n in the presence of $[(fc^{P,B})Zn(OCH_2Ph)]_2[BAr^F]_2$.

5.10.5 X-ray crystallographic data

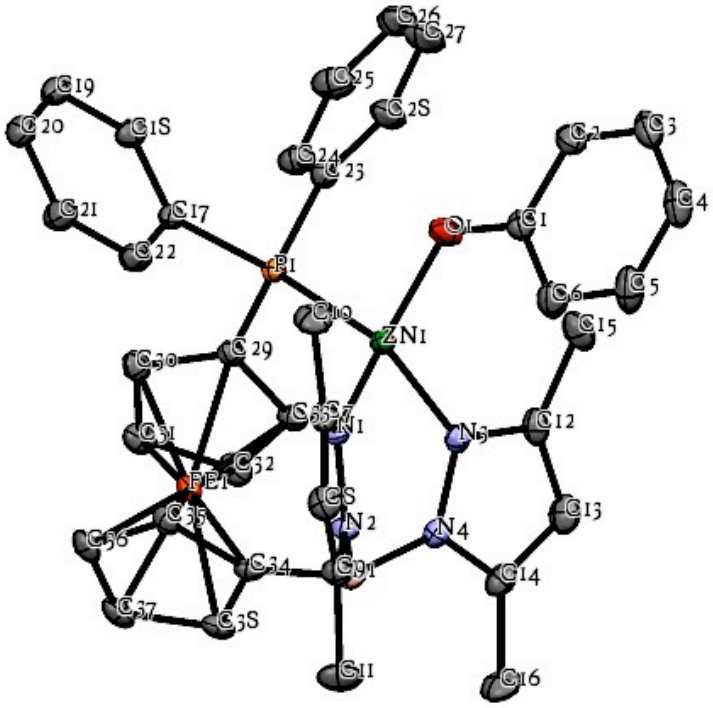

Figure D49. Molecular structure drawing of ($fc^{P,B}$)Zn(OPh) with thermal ellipsoids at 50% probability; hydrogen atoms are omitted for clarity.

5.11 References

1. Suriano, F.; Coulembier, O.; Hedrick, J. L.; Dubois, P., Functionalized cyclic carbonates: from synthesis and metal-free catalyzed ring-opening polymerization to applications. *Polym. Chem.* **2011,** *2* (3), 528-533.

2. Ulery, B. D.; Nair, L. S.; Laurencin, C. T., Biomedical applications of biodegradable polymers. *J. Polym. Sci. B Polym. Phys.* **2011,** *49* (12), 832-864.

3. Tian, H.; Tang, Z.; Zhuang, X.; Chen, X.; Jing, X., Biodegradable synthetic polymers: Preparation, functionalization and biomedical application. *Prog. Polym. Sci.* **2012,** *37* (2), 237-280.

4. Vert, M., Aliphatic Polyesters: Great Degradable Polymers That Cannot Do Everything. *Biomacromolecules* **2005,** *6* (2), 538-546.

5. Nair, L. S.; Laurencin, C. T., Biodegradable polymers as biomaterials. *Prog. Polym. Sci.* **2007,** *32* (8–9), 762-798.

6. Place, E. S.; George, J. H.; Williams, C. K.; Stevens, M. M., Synthetic polymer scaffolds for tissue engineering. *Chem. Soc. Rev.* **2009,** *38* (4), 1139-1151.

7. Ruzette, A.-V.; Leibler, L., Block copolymers in tomorrow's plastics. *Nat. Mater.* **2005,** *4* (1), 19-31.

8. Vroman, I.; Tighzert, L., Biodegradable Polymers. *Materials* **2009,** *2* (2), 307.

9. Oerlemans, C.; Bult, W.; Bos, M.; Storm, G.; Nijsen, J. F. W.; Hennink, W. E., Polymeric Micelles in Anticancer Therapy: Targeting, Imaging and Triggered Release. *Pharm. Res.* **2010,** *27* (12), 2569-2589.

10. Guillaume, S. M.; Carpentier, J.-F., Recent advances in metallo/organo-catalyzed immortal ring-opening polymerization of cyclic carbonates. *Catal. Sci. Technol.* **2012,** *2* (5), 898-906.

11. Ajellal, N.; Carpentier, J.-F.; Guillaume, C.; Guillaume, S. M.; Helou, M.; Poirier, V.; Sarazin, Y.; Trifonov, A., Metal-catalyzed immortal ring-opening polymerization of lactones, lactides and cyclic carbonates. *Dalton Trans.* **2010,** *39* (36), 8363-8376.

12. Helou, M.; Miserque, O.; Brusson, J.-M.; Carpentier, J.-F.; Guillaume, S. M., Metal Triflates as Highly Stable and Active Catalysts for the "Immortal" Ring-Opening Polymerization of Trimethylene Carbonate. *ChemCatChem* **2010,** *2* (3), 306-313.

13. Helou, M.; Miserque, O.; Brusson, J.-M.; Carpentier, J.-F.; Guillaume, S. M., Highly Effective and Green Catalytic Approach Toward α,ω-Dihydroxy-Telechelic Poly(trimethylenecarbonate). *Macromol. Rapid Commun.* **2009,** *30* (24), 2128-2135.

14. Williams, C. K.; Breyfogle, L. E.; Choi, S. K.; Nam, W.; Young, V. G.; Hillmyer, M. A.; Tolman, W. B., A Highly Active Zinc Catalyst for the Controlled Polymerization of Lactide. *J. Am. Chem. Soc.* **2003,** *125* (37), 11350-11359.

15. O'Keefe, B. J.; Hillmyer, M. A.; Tolman, W. B., Polymerization of lactide and related cyclic esters by discrete metal complexes. *J. Chem. Soc., Dalton Trans.* **2001,** (15), 2215-2224.

16. Dechy-Cabaret, O.; Martin-Vaca, B.; Bourissou, D., Controlled Ring-Opening Polymerization of Lactide and Glycolide. *Chem. Rev.* **2004,** *104* (12), 6147-6176.

17. Wu, J.; Yu, T.-L.; Chen, C.-T.; Lin, C.-C., Recent developments in main group metal complexes catalyzed/initiated polymerization of lactides and related cyclic esters. *Coord. Chem. Rev.* **2006,** *250* (5–6), 602-626.

18. Platel, R. H.; Hodgson, L. M.; Williams, C. K., Biocompatible Initiators for Lactide Polymerization. *Polym. Rev.* **2008,** *48* (1), 11-63.

19. Wheaton, C. A.; Hayes, P. G.; Ireland, B. J., Complexes of Mg, Ca and Zn as homogeneous catalysts for lactide polymerization. *Dalton Trans.* **2009,** (25), 4832-4846.

20. Arbaoui, A.; Redshaw, C., Metal catalysts for e-caprolactone polymerisation. *Polym. Chem.* **2010,** *1* (6), 801-826.

21. Huang, Y.; Wang, W.; Lin, C.-C.; Blake, M. P.; Clark, L.; Schwarz, A. D.; Mountford, P., Potassium, zinc, and magnesium complexes of a bulky OOO-tridentate bis(phenolate) ligand: synthesis, structures, and studies of cyclic ester polymerisation. *Dalton Trans.* **2013,** *42* (25), 9313-9324.

22. Fliedel, C.; Rosa, V.; Alves, F. M.; Martins, A. M.; Aviles, T.; Dagorne, S., P,O-Phosphinophenolate zinc(ii) species: synthesis, structure and use in the ring-opening polymerization (ROP) of lactide, ?-caprolactone and trimethylene carbonate. *Dalton Trans.* **2015,** *44* (27), 12376-12387.

23. D'Auria, I.; Lamberti, M.; Mazzeo, M.; Milione, S.; Roviello, G.; Pellecchia, C., Coordination Chemistry and Reactivity of Zinc Complexes Supported by a Phosphido Pincer Ligand. *Chem. Eur. J.* **2012,** *18* (8), 2349-2360.

24. Liang, L.-C.; Lee, W.-Y.; Tsai, T.-L.; Hsu, Y.-L.; Lee, T.-Y., Amido phosphine complexes of zinc: synthesis, structure, and catalytic ring-opening polymerization of ?-caprolactone. *Dalton Trans.* **2010,** *39* (37), 8748-8758.

25. Bakewell, C.; Fateh-Iravani, G.; Beh, D. W.; Myers, D.; Tabthong, S.; Hormnirun, P.; White, A. J. P.; Long, N.; Williams, C. K., Comparing a series of 8-quinolinolato complexes of

aluminium, titanium and zinc as initiators for the ring-opening polymerization of rac-lactide. *Dalton Trans.* **2015,** *44* (27), 12326-12337.

26. Singewald, E. T.; Mirkin, C. A.; Stern, C. L., A Redox-Switchable Hemilabile Ligand: Electrochemical Control of the Coordination Environment of a RhI Complex. *Angew. Chem. Int. Ed.* **1995,** *34* (15), 1624-1627.

27. Sassano, C. A.; Mirkin, C. A., Degenerate Exchange Reactions: A Novel and General Way To Determine the Thermodynamic Perturbations on Transition Metal Complexes That Result from Ligand Oxidation. *J. Am. Chem. Soc.* **1995,** *117* (45), 11379-11380.

28. Higgins, T. B.; Mirkin, C. A., Model compounds for polymeric redox-switchable hemilabile ligands. *Inorg. Chim. Acta* **1995,** *240* (1–2), 347-353.

29. Slone, C. S.; Mirkin, C. A.; Yap, G. P. A.; Guzei, I. A.; Rheingold, A. L., Oxidation-State-Dependent Reactivity and Catalytic Properties of a Rh(I) Complex Formed from a Redox-Switchable Hemilabile Ligand. *J. Am. Chem. Soc.* **1997,** *119* (44), 10743-10753.

30. Weinberger, D. A.; Higgins, T. B.; Mirkin, C. A.; Stern, C. L.; Liable-Sands, L. M.; Rheingold, A. L., Terthienyl and Poly-terthienyl Ligands as Redox-Switchable Hemilabile Ligands for Oxidation-State-Dependent Molecular Uptake and Release. *J. Am. Chem. Soc.* **2001,** *123*, 2503-2516.

31. Allgeier, A. M.; Mirkin, C. A., Ligand Design for Electrochemically Controlling Stoichiometric and Catalytic Reactivity of Transition Metals. *Angew. Chem. Int. Ed.* **1998,** *37* (7), 894-908.

32. Abubekerov, M.; Shepard, S. M.; Diaconescu, P. L., Switchable Polymerization of Norbornene Derivatives by a Ferrocene-Palladium(II) Heteroscorpionate Complex. *Eur. J. Inorg. Chem.* **2016,** *2016* (15-16), 2634-2640.

33. Wang, X.; Brosmer, J. L.; Thevenon, A.; Diaconescu, P. L., Highly Active Yttrium Catalysts for the Ring-Opening Polymerization of ε-Caprolactone and δ-Valerolactone. *Organometallics* **2015,** *34* (19), 4700–4706.

34. Quan, S. M.; Diaconescu, P. L., High activity of an indium alkoxide complex toward ring opening polymerization of cyclic esters. *Chem. Commun.* **2015,** *51*, 9643 - 9646.

35. Brosmer, J. L.; Diaconescu, P. L., Yttrium-Alkyl Complexes Supported by a Ferrocene-Based Phosphinimine Ligand. *Organometallics* **2015,** *34* (11), 2567–2572.

36. Abubekerov, M.; Diaconescu, P. L., Synthesis and Characterization of Ferrocene-Chelating Heteroscorpionate Complexes of Nickel(II) and Zinc(II). *Inorg. Chem.* **2015,** *54* (4), 1778–1784.

37. Wang, X.; Thevenon, A.; Brosmer, J. L.; Yu, I.; Khan, S. I.; Mehrkhodavandi, P.; Diaconescu, P. L., Redox Control of Group 4 Metal Ring-Opening Polymerization Activity toward l-Lactide and ε-Caprolactone. *J. Am. Chem. Soc.* **2014,** *136* (32), 11264-11267.

38. Upton, B. M.; Gipson, R. M.; Duhovic, S.; Lydon, B. R.; Matsumoto, N. M.; Maynard, H. D.; Diaconescu, P. L., Synthesis of ferrocene-functionalized monomers for biodegradable polymer formation. *Inorg. Chem. Front.* **2014,** *1* (3), 271 - 277.

39. Broderick, E. M.; Thuy-Boun, P. S.; Guo, N.; Vogel, C. S.; Sutter, J.; Miller, J. T.; Meyer, K.; Diaconescu, P. L., Synthesis and Characterization of Cerium and Yttrium Alkoxide Complexes Supported by Ferrocene-Based Chelating Ligands. *Inorg. Chem.* **2011,** *50* (7), 2870-2877.

40. Broderick, E. M.; Guo, N.; Wu, T.; Vogel, C. S.; Xu, C.; Sutter, J.; Miller, J. T.; Meyer, K.; Cantat, T.; Diaconescu, P. L., Redox control of a polymerization catalyst by changing the oxidation state of the metal center. *Chem. Commun.* **2011,** *47*, 9897-9899.

41. Broderick, E. M.; Guo, N.; Vogel, C. S.; Xu, C.; Sutter, J.; Miller, J. T.; Meyer, K.; Mehrkhodavandi, P.; Diaconescu, P. L., Redox Control of a Ring-Opening Polymerization Catalyst. *J. Am. Chem. Soc.* **2011,** *133* (24), 9278–9281.

42. Pangborn, A. B.; Giardello, M. A.; Grubbs, R. H.; Rosen, R. K.; Timmers, F. J., Safe and Convenient Procedure for Solvent Purification. *Organometallics* **1996,** *15* (5), 1518-1520.

43. Matsuo, J.; Aoki, K.; Sanda, F.; Endo, T., Substituent Effect on the Anionic Equilibrium Polymerization of Six-Membered Cyclic Carbonates. *Macromolecules* **1998,** *31* (14), 4432-4438.

44. Dhar, D.; Yee, G. M.; Spaeth, A. D.; Boyce, D. W.; Zhang, H.; Dereli, B.; Cramer, C. J.; Tolman, W. B., Perturbing the Copper(III)–Hydroxide Unit through Ligand Structural Variation. *J. Am. Chem. Soc.* **2016,** *138* (1), 356-368.

45. Paolo, G.; Stefano, B.; Nicola, B.; Matteo, C.; Roberto, C.; Carlo, C.; Davide, C.; Guido, L. C.; Matteo, C.; Ismaila, D.; Andrea Dal, C.; Stefano de, G.; Stefano, F.; Guido, F.; Ralph, G.; Uwe, G.; Christos, G.; Anton, K.; Michele, L.; Layla, M.-S.; Nicola, M.; Francesco, M.; Riccardo, M.; Stefano, P.; Alfredo, P.; Lorenzo, P.; Carlo, S.; Sandro, S.; Gabriele, S.; Ari, P. S.; Alexander, S.; Paolo, U.; Renata, M. W., QUANTUM ESPRESSO: a modular and open-source software project for quantum simulations of materials. *J. Phys. Condens. Matter* **2009,** *21* (39), 395502.

46. Cococcioni, M.; de Gironcoli, S., Linear response approach to the calculation of the effective interaction parameters in the $\mathrm{LDA}+\mathrm{U}$ method. *Phys. Rev. B* **2005,** *71* (3), 035105.

47. Perdew, J. P.; Zunger, A., Self-interaction correction to density-functional approximations for many-electron systems. *Phys. Rev. B* **1981,** *23* (10), 5048-5079.

48. Kümmel, S.; Kronik, L., Orbital-dependent density functionals: Theory and applications. *Rev. Mod. Phys.* **2008,** *80* (1), 3-60.

49. Cohen, A. J.; Mori-Sánchez, P.; Yang, W., Insights into Current Limitations of Density Functional Theory. *Science* **2008,** *321* (5890), 792-794.

50. Kulik, H. J., Perspective: Treating electron over-delocalization with the DFT+U method. *J. Chem. Phys.* **2015,** *142* (24), 240901.

51. Himmetoglu, B.; Floris, A.; de Gironcoli, S.; Cococcioni, M., Hubbard-corrected DFT energy functionals: The LDA+U description of correlated systems. *Int. J. Quantum Chem.* **2014,** *114* (1), 14-49.

52. Chisholm, M. H.; Eilerts, N. W.; Huffman, J. C.; Iyer, S. S.; Pacold, M.; Phomphrai, K., Molecular Design of Single-Site Metal Alkoxide Catalyst Precursors for Ring-Opening Polymerization Reactions Leading to Polyoxygenates. 1. Polylactide Formation by Achiral and Chiral Magnesium and Zinc Alkoxides, (h^3-L)MOR, Where L = Trispyrazolyl- and Trisindazolylborate Ligands. *J. Am. Chem. Soc.* **2000,** *122* (48), 11845-11854.

53. Honrado, M.; Otero, A.; Fernández-Baeza, J.; Sánchez-Barba, L. F.; Garcés, A.; Lara-Sánchez, A.; Rodríguez, A. M., Copolymerization of Cyclic Esters Controlled by Chiral NNO-Scorpionate Zinc Initiators. *Organometallics* **2016,** *35* (2), 189-197.

54. Lian, B.; Thomas, C. M.; Casagrande, O. L.; Lehmann, C. W.; Roisnel, T.; Carpentier, J.-F., Aluminum and Zinc Complexes Based on an Amino-Bis(pyrazolyl) Ligand: Synthesis, Structures, and Use in MMA and Lactide Polymerization. *Inorg. Chem.* **2007,** *46* (1), 328-340.

55. Alonso-Moreno, C.; Garcés, A.; Sánchez-Barba, L. F.; Fajardo, M.; Fernández-Baeza, J.; Otero, A.; Lara-Sánchez, A.; Antiñolo, A.; Broomfield, L.; López-Solera, M. I.; Rodríguez, A.

M., Discrete Heteroscorpionate Lithium and Zinc Alkyl Complexes. Synthesis, Structural Studies, and ROP of Cyclic Esters. *Organometallics* **2008,** *27* (6), 1310-1321.

56. Schofield, A. D.; Barros, M. L.; Cushion, M. G.; Schwarz, A. D.; Mountford, P., Sodium, magnesium and zinc complexes of mono(phenolate) heteroscorpionate ligands. *Dalton Trans.* **2009,** (1), 85-96.

57. Mou, Z.; Liu, B.; Wang, M.; Xie, H.; Li, P.; Li, L.; Li, S.; Cui, D., Isoselective ring-opening polymerization of rac-lactide initiated by achiral heteroscorpionate zwitterionic zinc complexes. *Chem. Commun.* **2014,** *50* (77), 11411-11414.

58. Garcés, A.; Sánchez-Barba, L. F.; Alonso-Moreno, C.; Fajardo, M.; Fernández-Baeza, J.; Otero, A.; Lara-Sánchez, A.; López-Solera, I.; Rodríguez, A. M., Hybrid Scorpionate/Cyclopentadienyl Magnesium and Zinc Complexes: Synthesis, Coordination Chemistry, and Ring-Opening Polymerization Studies on Cyclic Esters. *Inorg. Chem.* **2010,** *49* (6), 2859-2871.

59. Vivas, M.; Mejías, N.; Contreras, J., Ring-opening polymerization of lactones initiated by diphenylzinc–coinitiator systems. *Polym. Int.* **2003,** *52* (6), 1005-1009.

60. Gowda, R. R.; Chakraborty, D., Zinc acetate as a catalyst for the bulk ring opening polymerization of cyclic esters and lactide. *J. Mol. Catal. A: Chem.* **2010,** *333* (1–2), 167-172.

61. Helou, M.; Miserque, O.; Brusson, J.-M.; Carpentier, J.-F.; Guillaume, S. M., Ultraproductive, Zinc-Mediated, Immortal Ring-Opening Polymerization of Trimethylene Carbonate. *Chem. Eur. J.* **2008,** *14* (29), 8772-8775.

62. Frisch, M. J., In *Gaussian 09 (Revision D.01)*, Gaussian Inc.: Wallingford, CT, 2010 (see the SI for the full reference).

63. Towns, J.; Cockerill, T.; Dahan, M.; Foster, I.; Gaither, K.; Grimshaw, A.; Hazlewood, V.; Lathrop, S.; Lifka, D.; Peterson, G. D.; Roskies, R.; Scott, J. R.; Wilkens-Diehr, N., XSEDE: Accelerating Scientific Discovery. *Computing in Science and Engineering* **2014,** *16* (5), 62-74.

CHAPTER 6: FERROCENE-BIS(PHOSPHINIMINE) NICKEL(II) AND PALLADIUM(II) ALKYL COMPLEXES: INFLUENCE OF THE Fe-M (M = Ni, Pd) INTERACTION ON REDOX ACTIVITY AND OLEFIN COORDINATION

6.1 Introduction

Catalytic processes that can be switched by an external stimulus can offer an additional, 'bio-like' control of chemical transformations.[1-2] Early examples showed that switchable catalysts could be used to speed up or slow down the rate of a reaction according to the presence of a specific trigger,[3-12] which could be either a physical or a chemical stimulus,[1-2, 13] or to change the stereochemical[14-16] outcome of a reaction (on/off switches). In recent years, however, more advanced tasks have been accomplished, such as turning 'on' and 'off' different forms of the same pre-catalyst in order to promote complementary reactions that take place from a mixture of different building blocks.[17-23] Redox switchable catalysis uses redox reagents (chemical triggers) to turn on and off reactions. The earlier works of Wrighton et el.,[12] Long et al.,[3] and Plenio et al.[5] illustrated the influence of the redox states of ferrocenyl units, in supporting ligands, on catalysis. Our initial work focused extensively on utilizing ferrocene-based ligands for the redox control of ring-opening polymerizations (ROP) of cyclic esters. Starting with indium, yttrium,[4] and cerium[24] phosfen (phosfen = 1,1'-di(2-*tert*-butyl-6-diphenylphosphiniminophenoxy)ferrocene) complexes, an on/off activity for the polymerization of L-lactide was observed based on the oxidation state of the iron center. These early efforts culminated in the discovery of a system that displayed redox-controlled polymerization of several cyclic monomers: first in the case of L-lactide/ε-caprolactone with a titanium thiolfan complex, (thiolfan*)Ti(O^iPr)$_2$ (thiolfan* = 1,1'-di(2,4-di-*tert*-butyl-6-thiophenoxy)ferrocene),[18]

and then for L-lactide/cyclohexene oxide utilizing a zirconium salfan complex, (salfan)Zr(O^tBu)$_2$ (salfan = 1,1'-di(2-*tert*-butyl-6-*N*-methylmethylenephenoxy)ferrocene).[17]

Recently, there have been efforts by our group and others to expand the application of redox-controlled systems beyond ROP.[10] Such examples include ferrocene-based ligands capable of modulating monomer selectivity in palladium systems for olefin polymerization[25-27] and Buchwald-Hartwig cross-coupling reactions,[28] utilization of cobalt complexes for olefin hydroalkoxylation,[29] and of gold mesoionic carbenes for heterocycles synthesis.[30] However, in all cases of redox-controlled catalysis, the ferrocene unit is distant from the primary metal center and no direct interaction exists between iron in ferrocene and the metal involved in a substrate transformation.

Various bidentate ferrocene derived ligands reported in the literature containing phosphorus,[31-37] sulfur,[38-41] and nitrogen-based[42-53] substituents are known to promote direct iron-metal interactions. However, the use of these complexes in redox-switchable catalysis has not been investigated. For example, ferrocene-bis(phosphinimines) have been used as supporting ligands,[43, 54] but not in catalytic examples. Based on our interest in redox-switchable catalysis utilizing ferrocene derivatives, we decided to prepare ferrocene-bis(phosphinimine) nickel and palladium alkyl complexes containing iron-nickel and iron-palladium interactions and investigate their efficacy for redox-switchable olefin polymerization.

6.2 Preparation, characterization, and interaction with olefins of the ferrocence-bis(phosphinimine) complexes

Initial attempts to carry out a direct ligand substitution using fc($NPPh_3$)$_2$ to prepare the halide-alkyl complexes of nickel and palladium were unsuccessful (Scheme 6-1). However, the

addition of $NaBPh_4$ to $(PPh_3)_2NiCl(Ph)$ or (COD)PdCl(Me) (COD = 1,5-cyclooctadiene) in the presence of $fc(NPPh_3)_2$ in methylene chloride resulted in the isolation of $[fc(NPPh_3)_2NiPh][BPh_4]$ and $[fc(NPPh_3)_2PdMe][BPh_4]$ as red crystals in an 82.4% yield and orange crystalline material in 67.0% yield, respectively (Scheme 6-1). The solid-state molecular structures of $[fc(NPPh_3)_2NiPh][BPh_4]$ (Figure 6-1) and $[fc(NPPh_3)_2PdMe][BPh_4]$ (Figure 6-2) were investigated using single-crystal X-ray diffraction. The coordination environments around the nickel and palladium centers have a distorted square planar geometry with a τ value[63] of 0.18 and 0.16, respectively. The iron-nickel distance of 2.8244(6) Å is similar to that of a related complex $[fc(S_2)Ni(PMe_2Ph)]$ (2.886(1) Å)[41] and longer than those observed for the dicationic species $[fc(NIm)_2Ni(NCMe)][BF_4]_2$ (2.6268(4) Å) and $[fc(NIm)_2Ni(PMe_3)][BF_4]_2$ (2.7376(4) Å, $fc(NIm)_2$ = *N,N'*-bis(1,3-di-*iso*-propyl-4,5-dimethylimidazolin-2-ylidene)-1,1'-ferrocenediamine).[44] The palladium-iron distance of 2.7957(5) Å is comparable with values reported for the similar complexes $[fc(NIm)_2Pd(PMe_3)][BF_4]_2$ (2.7475(4) Å), $[fc(NIm)_2Pd(PMe_3)][BF_4]_2$ (2.7424(3) Å),[44] $[(dppf)Pd(PPh_3)][BF_4]_2$ (2.877(2) Å, dppf = 1,1'-bis(diphenylphosphino)ferrocene),[64] $[fc(S_2)Pd(PPh_3)]$ (2.878(1) Å)[39] and is longer than those observed for $[fc(NIm)_2Pd(NCMe)][BF_4]_2$ (2.6297(4) Å), $[fc(NIm)_2Pd(PPh_3)][BF_4]_2$ (2.6447(3) Å),[44] and $[fc(NPPh_3)_2Pd(Cl)][Cl]$ (2.67 Å).[43] The ^1H NMR spectrum of $[fc(NPPh_3)_2NiPh][BPh_4]$ is consistent with the presence in solution of a diamagnetic species and both the nickel and palladium complexes display a wide separation between the Cp signals (0.97 ppm and 1.46 ppm, respectively), consistent with the presence of an Fe-M (M = Ni, Pd) interaction.[43] In the ^{31}P NMR spectra, the chemical shifts of 37.5 ppm (nickel) and 30.2 ppm (palladium) are downfield compared to that of $fc(NPPh_3)_2$.[43] The presence of the borate counter ion was confirmed by

singlets at -5.7 ppm and -5.9 ppm for the nickel and palladium complexes, respectively, in the corresponding ^{11}B NMR spectra.

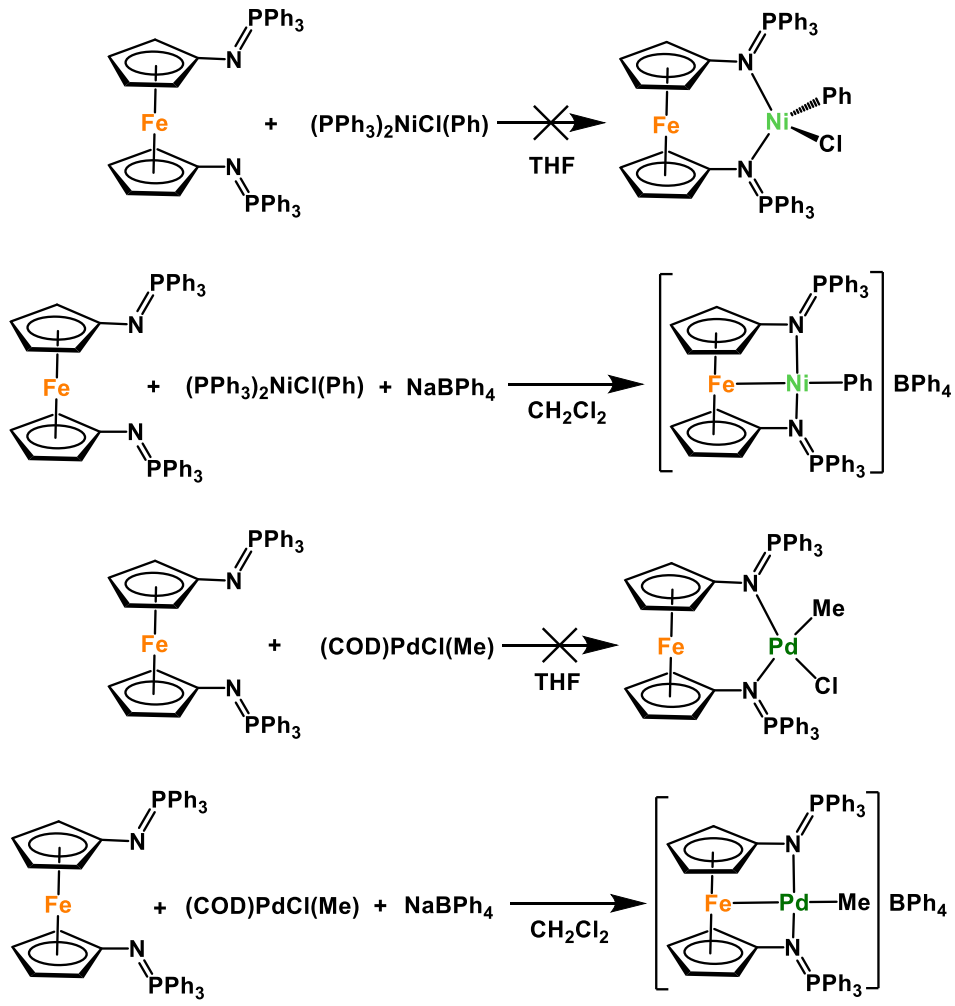

Scheme 6-1. The preparation of nickel and palladium ferrocene-bis(triphenylphosphinimine) complexes.

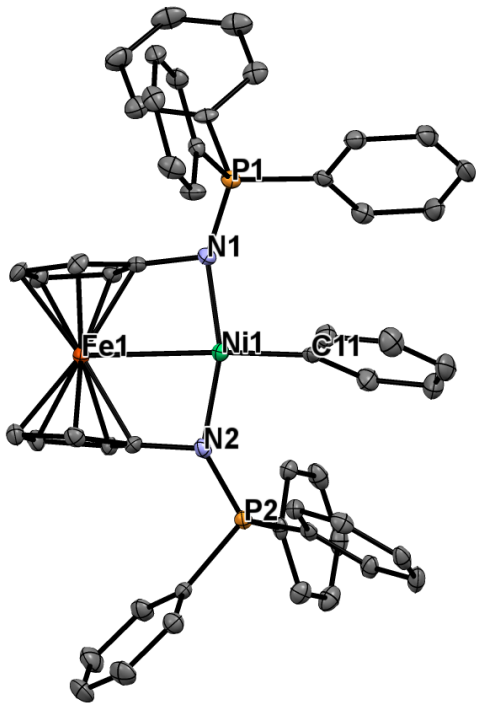

Figure 6-1. Molecular structure drawing of [fc($NPPh_3$)$_2$NiPh][BPh_4] with thermal ellipsoids at 50% probability; hydrogen, solvent, and borate atoms are omitted for clarity. Selected distances (Å) and angles (°): N(1)-P(1), 1.613(2); N(2)-P(2), 1.613(2); N(1)-Ni(1), 1.898(2); N(2)-Ni(1), 1.895(2); C(11)-Ni(1), 1.891(3); Fe(1)-Ni(1), 2.8244(6); C(11)-Ni(1)-N(1), 102.4(1); C(11)-Ni(1)-N(2), 97.2(1); N(1)-Ni(1)-Fe(1), 80.94(6); N(2)-Ni(1)-Fe(1), 79.52(6).

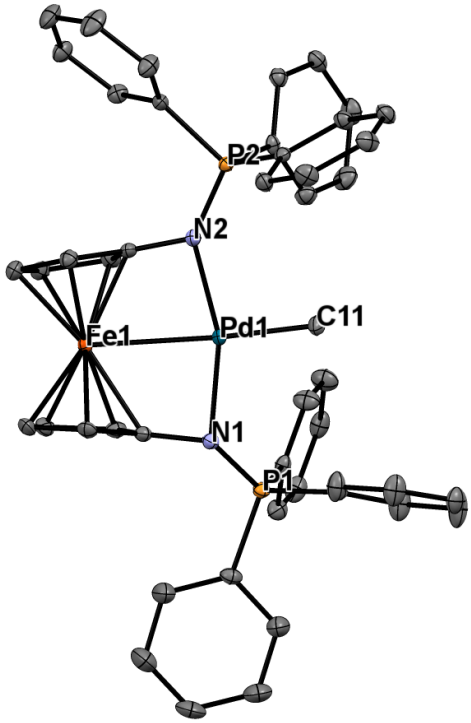

Figure 6-2. Molecular structure drawing of [fc($NPPh_3$)$_2$PdMe][BPh_4] with thermal ellipsoids at 50% probability; hydrogen, solvent, and borate atoms are omitted for clarity. Selected distances (Å) and angles (°): N(1)-P(1), 1.620(1); N(2)-P(2), 1.606(1); N(1)-Pd(1), 2.072(1); N(2)-Pd(1), 2.031(1); C(11)-Pd(1), 2.051(2); Fe(1)-Pd(1), 2.7957(5); C(11)-Pd(1)-N(1), 102.29(6); C(11)-Pd(1)-N(2), 97.14(7); N(1)-Pd(1)-Fe(1), 81.07(4); N(2)-Pd(1)-Fe(1), 79.46(4).

Electrochemical studies performed on [fc($NPPh_3$)$_2$NiPh][BPh_4] displayed a complicated and uninformative redox behavior (Figure E36). Attempts to perform a chemical oxidation using acetyl ferrocenium tetrakis(3,5-bis(trifluoromethyl)phenyl)borate ([^{Ac}Fc][BAr^F], Scheme 6-2 and Figure E26) or $AgBF_4$ (Figure E27) and a reduction using cobaltocene (Figure E24) on an NMR reaction scale did not result in the formation of any new species. Utilizing KC_8 as a reducing agent resulted only in the formation of nickel black and liberation of fc($NPPh_3$)$_2$ (Scheme 6-2,

Figure E25). On the other hand, electrochemical studies performed on [fc(NPPh$_3$)$_2$PdMe][BPh$_4$] (Figure E37) displayed several quasi-reversible redox processes in the range of 0 – 1.25 V (vs. Fc/Fc$^+$) suggesting that a more potent oxidant than a ferrocenium salt may be used. Similarly to the nickel case, utilizing [^{Ac}Fc][BAr^F] as an oxidant led to the formation of several minor species, with the starting material remaining the predominant species (Scheme 6-2, Figure E28). However, in the presence of excess AgBF$_4$, the formation of a single species was observed. Scaling up the reaction resulted in the isolation of [fc(NPPh$_3$)$_2$Pd(THF)][BF$_4$]$_2$ (Scheme 6-2) as dark golden plates in a 73.2% yield. The results of an X-ray diffraction study are displayed in Figure 3 along with selected distances and angles. The coordination environment around the palladium center is a distorted square planar geometry (τ = 0.14). The palladium-iron distance of 2.6493(8) Å is significantly shorter than in [fc(NPPh$_3$)$_2$PdMe][BPh$_4$] and is now comparable with those observed for [fc(NIm)$_2$Pd(NCMe)][BF$_4$]$_2$ (2.6297(4) Å), [fc(NIm)$_2$Pd(PPh$_3$)][BF$_4$]$_2$ (2.6447(3) Å),[44] and [fc(NPPh$_3$)$_2$Pd(Cl)][Cl] (2.67 Å).[43] In the ^{1}H NMR spectrum, the separation between the Cp signals (1.76 ppm) is slightly larger (1.46 ppm) than for the parent complex, [fc(NPPh$_3$)$_2$PdMe][BPh$_4$]. In the ^{31}P NMR spectrum, the chemical shift of 37.4 ppm is downfield from that of [fc(NPPh$_3$)$_2$PdMe][BPh$_4$] (30.2 ppm). The presence of the BF$_4$ ions was confirmed by ^{11}B NMR spectroscopy showing a singlet at -0.4 ppm and ^{19}F NMR spectroscopy showing two singlets at -152.0 and -152.1 ppm.

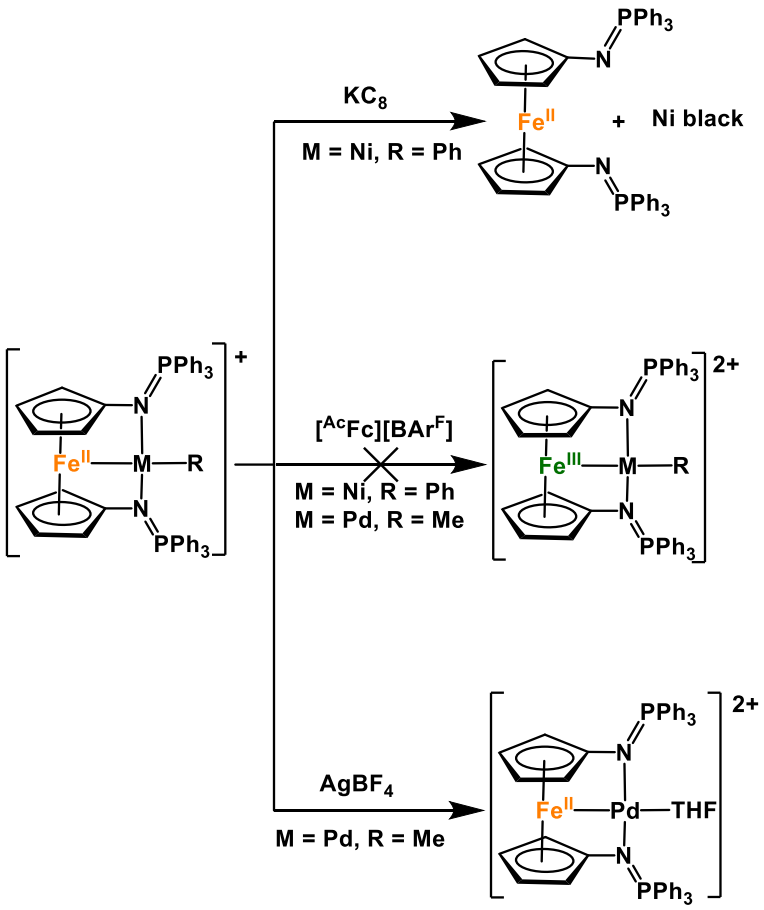

Scheme 6-2. Chemical oxidation and reduction of nickel and palladium ferrocene-bis(triphenylphosphinimine) complexes.

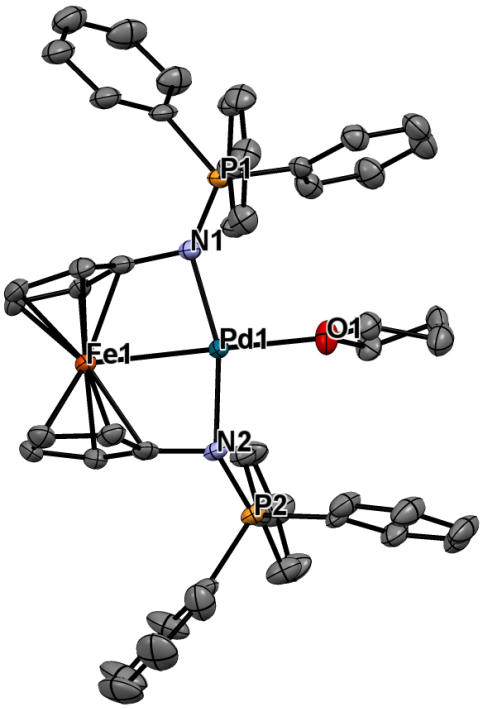

Figure 6-3. Molecular structure drawing of $[fc(NPPh_3)_2Pd(THF)][BF_4]_2$ with thermal ellipsoids at 50% probability; hydrogen, solvent, and borate atoms are omitted for clarity. Selected distances (Å) and angles (°): N(1)-P(1), 1.618(4); N(2)-P(2), 1.613(4); N(1)-Pd(1), 2.040(4); N(2)-Pd(1), 2.042(4); O(1)-Pd(1), 2.142(3); Fe(1)-Pd(1), 2.6493(8); O(1)-Pd(1)-N(1), 99.9(1); O(1)-Pd(1)-N(2), 97.7(1); N(1)-Pd(1)-Fe(1), 80.9(1); N(2)-Pd(1)-Fe(1), 81.5(1).

Next, we looked at the strength of the Fe-M (M = Ni, Pd) interaction. Previous reports by Cabrera et al.[31] and Jess et al.[44] showed that the Fe-M interactions in similar complexes are weak enough that a small molecule, such as acetonitrile, can disrupt them. The resulting acetonitrile adducts, in the case of palladium complexes, are non-symmetrical species that can be readily detected by heteronuclear NMR spectroscopy. Consequently, solutions of $[fc(NPPh_3)_2NiPh][BPh_4]$ and $[fc(NPPh_3)_2PdMe][BPh_4]$ in a mixture of acetonitrile and

methylene chloride (1:1 vol %) both display singlets with no apparent shift, suggesting that the acetonitrile-palladium and acetonitrile-nickel interactions are not sufficient enough to overcome the metal-metal interactions in these complexes.

Due to the lack of redox activity in [fc(NPPh$_3$)$_2$NiPh][BPh$_4$], we did not investigate its reactivity with olefins. On the other hand, although [fc(NPPh$_3$)$_2$PdMe)[BPh$_4$] did not show a reversible redox process, we wanted to determine whether the complex would be more robust during a polymerization process. However, we did not observe any polymerization activity at ambient temperature for norbornene, styrene, 1-hexene, and ethylene (1.0 atm), suggesting that the palladium-olefin interactions are also too weak to overcome the iron-palladium interaction. Elevating the reaction temperature resulted in the rapid formation of palladium black and no additional reactivity.

The lack of activity of [fc(NPPh$_3$)$_2$PdMe][BPh$_4$] toward olefin polymerization prompted an investigation into alternative phosphinimine ligands. It is possible that a more electron rich derivative, such as the analogous tricyclohexylphosphinimine, would yield a palladium complex with a weaker Fe-Pd interaction.[43] However, we could not prepare [fc(NPCy$_3$)$_2$PdMe][BPh$_4$] (Scheme E1) although we used various methods, possibly due to the large steric bulk of the supporting ligand disfavoring the formation of a square planar fc(NPCy$_3$)$_2$PdCl(Me) intermediate. Alternatively, we prepared a new ferrocene-bis(phosphinimine) derivative, fc(PEt$_3$)$_2$ (Scheme 6-3), combining a more electron rich phosphine and a reduced steric environment compared with the fc(NPPh$_3$)$_2$ analogue. The reduction of the steric environment manifests itself in the isolation of a stable halide-alkyl complex, fc(NPEt$_3$)$_2$PdCl(Me) (Scheme 6-3) that was not achieved either with fc(NPPh$_3$)$_2$ or fc(NPCy$_3$)$_2$. The lack of symmetry in fc(NPCy$_3$)$_2$PdCl(Me) is clearly observed by a multitude of signals, specifically, the presence of

eight separate signals (3.70 – 5.56 ppm) for the Cp protons in the ^{1}H NMR spectrum and two singlets (43.4 and 45.1 ppm) in the ^{31}P NMR spectrum.

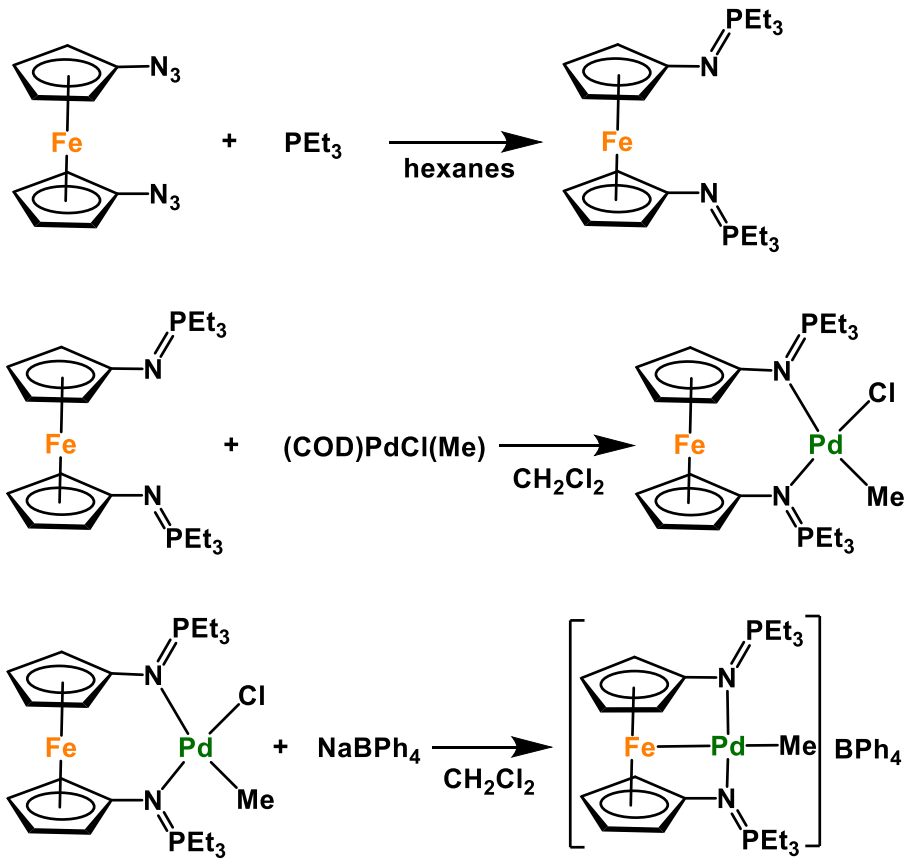

Scheme 6-3. The preparation of nickel and palladium ferrocene-bis(triethylphosphinimine) complexes.

Chloride abstraction from fc(NPEt$_3$)$_2$PdCl(Me) was accomplished with NaBPh$_4$ affording [fc(NPEt$_3$)$_2$PdMe][BPh$_4$] (Scheme 6-3) as an orange crystalline material in a 79.3% yield. The solid-state molecular structure of [fc(NPEt$_3$)$_2$PdMe][BPh$_4$] (Figure 6-4) was determined using single-crystal X-ray diffraction. The coordination environment around the palladium center is in a slightly distorted square planar geometry with a τ value of 0.20. The iron-palladium distance of

2.7806(5) Å is similar to that of [fc(NPPh$_3$)$_2$PdMe][BPh$_4$] (2.7957(5) Å). The ^{1}H NMR spectrum of [fc(NPEt$_3$)$_2$PdMe][BPh$_4$] shows a wide separation of 1.66 ppm between the signals of the Cp protons. A downfield shift in the resonance signal of [fc(NPEt$_3$)$_2$PdMe][BPh$_4$] (57.3 ppm) compared to both fc(NPEt$_3$)$_2$ (28.9 ppm) and fc(NPEt$_3$)$_2$PdCl(Me) (43.4 and 45.1 ppm) was observed in the ^{31}P NMR spectra. The BPh$_4$ ion appears at -5.7 ppm in the ^{11}B NMR spectrum, similar to the fc(NPPh$_3$)$_2$ nickel and palladium analogues.

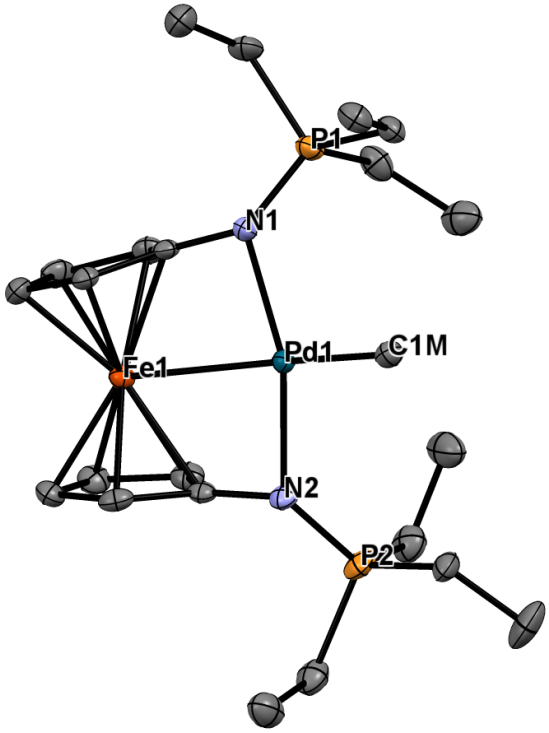

Figure 6-4. Molecular structure drawing of [fc(NPEt$_3$)$_2$PdMe][BPh$_4$] with thermal ellipsoids at 50% probability; hydrogen, solvent, and borate atoms are omitted for clarity. Selected distances (Å) and angles (°): N(1)-P(1), 1.624(2); N(2)-P(2), 1.612(2); N(1)-Pd(1), 2.054(2); N(2)-Pd(1), 2.046(2); C(1)M-Pd(1), 2.056(2); Fe(1)-Pd(1), 2.7806(5); C(1)M-Pd(1)-N(1), 99.4(1); C(1)M-Pd(1)-N(2), 98.35(9); N(1)-Pd(1)-Fe(1), 80.90(6); N(2)-Pd(1)-Fe(1), 81.02(6).

Electrochemical studies performed with $[fc(NPEt_3)_2PdMe][BPh_4]$ displayed irreversible redox events similar to those for $[fc(NPPh_3)_2PdMe][BPh_4]$ (Figure E39). Attempts to perform a chemical oxidation using excess $AgBF_4$ only resulted in a partial counter ion exchange while a new palladium species was not observed. The addition of acetonitrile to a methylene chloride solution of $[fc(NPEt_3)_2PdMe][BPh_4]$ yielded the same results as were observed for $[fc(NPPh_3)_2NiPh][BPh_4]$ and $[fc(NPPh_3)_2PdMe][BPh_4]$. No change in the chemical shift or formation of a non-symmetrical species was observed in the ^{31}P NMR spectrum. Furthermore, the species is thermally sensitive and gradually decomposes at ambient temperature to form a new major species (Figures E33-34). A loss of the methyl group and the widening in the Cp proton separation was observed in the ^{1}H NMR spectrum as well as a further downfield shift of the signal in the ^{31}P NMR spectrum (Figures E34), reminiscent of the formation of $[fc(NPPh_3)_2Pd(THF)][BF_4]_2$ from $[fc(NPPh_3)_2PdMe][BPh_4]$. Decomposition was also clearly observed in the presence of styrene while no olefin-palladium interaction was observed at ambient temperature (Figure E35). Increasing the temperature only accelerated the rate of decomposition of the palladium-methyl species.

6.3 DFT calculations

The extent of the Fe-M interaction can also be determined from DFT calculations. Geometry optimizations for $[fc(NPPh_3)_2NiPh]^+$, $[fc(NPPh_3)_2PdMe]^+$, and $[fc(NPEt_3)_2PdMe]^+$ were performed for the present study employing ADF2013.01, [59-61] using the PW91 functional[62] and no frozen electron cores. Although the counterion was omitted, all the atoms of the cations were included. The optimized Fe-M distances (Table 6-1) are close to each other and to the

values obtained experimentally (Table E1). The calculated Mayer bond orders[65-66] are around 0.2 and are similar to the values obtained for other palladium complexes that show Fe-Pd interactions.[31-32, 35, 45]

Each of the analyzed compounds showed several molecular orbitals that indicate bonding interactions between iron and nickel or palladium (Figure 6-5 for selected orbitals and see the supporting information for more MOs for all three complexes, Figures E44, E46, and E48). Some of these orbitals are lying relatively deep, especially for the palladium complexes, for example, HOMO-16 and HOMO-25 for $[fc(NPPh_3)_2PdMe]^+$ and HOMO-13 for $[fc(NPEt_3)_2PdMe]^+$. Interestingly, the palladium complexes also contain p type iron-metal interactions, however, both the bonding and antibonding components are occupied (Figures E46 and E48).

In order to understand further the Fe→Pd interaction, natural bond orbital analysis was carried out using NBO 6.0[67] and the natural localized molecular orbitals (NLMOs) were generated (Figures E45, E47, and E49). All three metal complexes have two NLMOs with a bond order (BO) larger than 0.02: NLMO89 (BO = 0.04) and NLMO95 (BO = 0.03) for $[fc(NPPh_3)_2NiPh]^+$, NLMO93 (BO = 0.03) and NLMO219 (BO = 0.06) for $[fc(NPPh_3)_2PdMe)]^+$, and NLMO69 (BO = 0.03) and NLMO147 (BO = 0.06) for $[fc(NPEt_3)_2PdMe]^+$.

Topological analysis of the electron density was performed via Bader's atoms in molecule (AIM) theory.[68-69] AIM identifies bonds by calculating (3, −1) critical points, and it differentiates between covalent bonds and weak interactions, such as hydrogen bonds, van der Waals, and donor-acceptor interactions, by the value of the Laplacian (∇^2_ρ). If $\nabla^2_\rho < 0$, the interaction is considered covalent. If $\nabla^2_\rho > 0$, the interaction is a weak interaction. AIM has been used to calculate bond critical points between two metal centers[70] and in ferrocene complexes.[71]

All three $[fc(NPPh_3)_2NiPh]^+$, $[fc(NPPh_3)_2PdMe]^+$, and $[fc(NPEt_3)_2PdMe]^+$ species show Fe-M bond critical points (Table 6-1) consistent with a weak, non-covalent interaction (see the supporting information for details).

Table 6-1. Computational parameters for $[fc(NPPh_3)_2NiPh]^+$, $[fc(NPPh_3)_2PdMe]^+$, and $[fc(NPEt_3)_2PdMe]^+$.

	Ni	**Pd (PPh_3)**	**Pd (PEt_3)**
Fe-M (Å)	2.81	2.82	2.84
Fe-M Mayer Bond Order	0.21	0.27	0.27
Mulliken Charges			
Fe	-0.15	-0.13	-0.13
M	0.29	0.66	0.75
Hirshfeld Charges			
Fe	0.02	0.02	0.02
M	0.25	0.40	0.40
Wiberg bond index	0.09	0.10	0.10
NLMO Bond Order	0.09	0.09	0.09
Natural Charge			
Fe	0.14	0.17	0.17
M	0.70	0.58	0.58
Bader Charge			
Fe	0.66	0.71	0.71
M	0.59	0.39	0.39
r at Fe-M BCP[a]	0.03	0.03	0.03
Laplacian (∇^2_ρ) at Fe-M BCP	0.04	0.05	0.05

[a] BCP is an Fe-M bond critical point (3, -1) identified by Bader analysis.

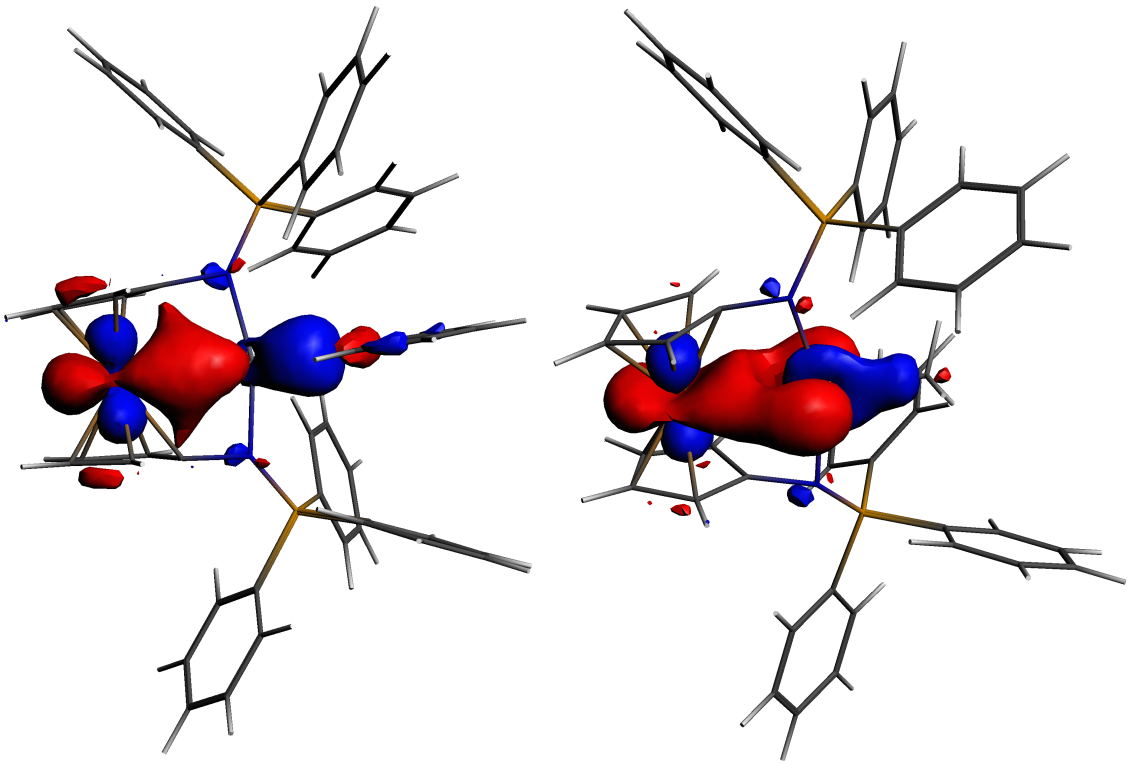

Figure 6-5. Frontier molecular orbitals: HOMO-6 for $[fc(NPPh_3)_2NiPh]^+$ (left) and HOMO-4 for $[fc(NPPh_3)_2PdMe]^+$ (right); isosurface value = 0.03.

6.4 Conclusions

The preparation of ferrocene-bis(phosphinimine) nickel and palladium alkyl complexes, via halide abstraction, was described. The ferrocene ligands are bound in a κ^3 fashion featuring iron-nickel and iron-palladium interactions. Electrochemically, only irreversible redox processes were observed for the palladium species. Chemically, $[fc(NPPh_3)_2NiPh][BPh_4]$ and $[fc(NPEt_3)_2PdMe][BPh_4]$ were redox inactive, while $[fc(NPPh_3)_2PdMe][BPh_4]$ underwent an irreversible oxidation resulting in the loss of the alkyl group. Attempts at disrupting the iron-palladium interactions using weak nucleophiles, such as acetonitrile and olefins, were

unsuccessful. Although DFT calculations indicate that these interactions are relatively weak, they are important to the overall electronic stabilization of each metal complex, especially in the case of palladium. Based on the results of this study, the ferrocene-bis(phosphinimine) nickel and palladium alkyl complexes discussed herein are not viable for applications in redox-switchable olefin polymerization.

6.5 Experimental section

Synthesis of [fc(NPPh$_3$)$_2$NiPh][BPh$_4$]. A solution of fc(NPPh$_3$)$_2$ (316.9 mg, 0.413 mmol) and (PPh$_3$)$_2$NiClPh (261.5 mg, 0.375 mmol) in 10 mL of methylene chloride was added to a suspension of NaBPh$_4$ (128.6 mg, 0.375 mmol) in 5 mL of methylene chloride at 0 °C. The reaction mixture was stirred for 1 h at 0 °C followed by a filtration through a Celite plug. Volatile substances were removed under a reduced pressure and the remaining solids were washed with diethyl ether (5 × 10 mL). The remaining solids were dissolved in 3 mL of methylene chloride, layered with 9 mL of diethyl ether, and stored for several hours at -35 °C. Decanting of the solution and washing with cold diethyl ether yielded the product as a red crystalline material. Recrystallization from methylene chloride/diethyl ether (1:3 vol %) layering at ambient temperature and washing with diethyl ether yielded analytically pure product (406.1 mg, 82.4%). X-ray quality crystals were obtained from methylene chloride/diethyl ether (1:3 vol %) layering at ambient temperature. Crystals of [fc(NPPh$_3$)$_2$NiPh][BPh$_4$] always contain a mixture of methylene chloride and diethyl ether per molecule of compound as supported by NMR data. ^{1}H NMR (CDCl$_3$, 500 MHz, 298 K): δ (ppm) 3.39 (t, 4H, Cp-*H*), 4.36 (t, 4H, Cp-*H*), 5.77 (t, 2H, Ni-(*m*-Ph)), 5.92 (t, 1H, Ni-(*p*-Ph)), 6.69 (d, 2H, Ni-(*o*-Ph)), 6.89 (t, 4H, B-(*p*-Ph)), 7.05 (t, 8H, B-(*m*-Ph)), 7.31-7.57 (m, 38H, B-(*o*-Ph), P-(*o*-Ph), P-(*m*-Ph), P-(*p*-Ph)). ^{13}C NMR

($CDCl_3$, 126 MHz, 298 K): δ (ppm) 69.0 (d, Cp-*C*), 72.4 (s, Cp-*C*), 80.6 (d, Cp-*C*), 121.6 (s, aromatic), 121.7 (s, aromatic), 124.8 (d, aromatic), 125.6 (m, aromatic), 125.7 (s, aromatic),127.9 (d, aromatic), 133.2 (s, aromatic), 133.5 (d, aromatic), 136.6 (s, aromatic), 138.9 (s, aromatic), 141.9 (s, aromatic), 164.5 (q, $^1J_{CB}$ = 49.9 Hz ,B-*C*). ^{11}B NMR ($CDCl_3$, 161 MHz, 298 K): δ (ppm) -5.7 (s). $^{31}P\{^1H\}$ NMR ($CDCl_3$, 203 MHz, 298 K): δ (ppm) 37.5 (s). Anal. Calcd: $[fc(NPPh_3)_2NiPh][BPh_4]\cdot(Et_2O)_{0.5}(CH_2Cl_2)_1$ ($C_{79}H_{70}BCl_2FeN_2NiO_{0.5}P_2$) C, 72.23; H, 5.37; N, 2.13. Found: C, 72.60; H, 5.33; N, 1.96.

Synthesis of $[fc(NPPh_3)_2PdMe][BPh_4]$. A solution of $fc(NPPh_3)_2$ (293.0 mg, 0.398 mmol) and (COD)PdCl(Me) (101.3 mg, 0.382 mmol) in 6 mL of methylene chloride was added to a suspension of $NaBPh_4$ (130.8 mg, 0.382 mmol) in 4 mL of methylene chloride at ambient temperature. The reaction mixture was stirred for 30 min at ambient temperature followed by a filtration through a Celite plug. Volatile substances were removed under a reduced pressure and the remaining solids were were dissolved in 3 mL of THF. Orange crystalline material forms from THF after several hours at ambient temperature. Decanting of the solution and washing with cold THF yielded the product as an orange crystalline material (319.6 mg, 67.0%). X-ray quality crystals were obtained from methylene chloride/diethyl ether vapor diffusion. Crystals of $[fc(NPPh_3)_2PdMe][BPh_4]$ always contain a molecule of THF per molecule of compound as supported by NMR data. ^{1}H NMR (CD_2Cl_2, 500 MHz, 298 K): δ (ppm) -0.07 (s, 3H, Pd-CH_3), 3.12 (s, 4H, Cp-*H*), 4.58 (s, 4H, Cp-*H*), 6.86 (t, 4H, B-(*p*-Ph)), 7.01 (t, 8H, B-(*m*-Ph)), 7.31 (br s, 8H, B-(*o*-Ph)), 7.53 (m, 12H, P-(*o*-Ph)), 7.67 (t, 6H, P-(*p*-Ph)), 7.73 (m, 12H, P-(*m*-Ph)). ^{13}C NMR (CD_2Cl_2, 126 MHz, 298 K): δ (ppm) -4.7 (t, Pd-*C*H_3), 68.2 (d, Cp-*C*), 72.6 (s, Cp-*C*), 88.3 (d, Cp-*C*), 122.2 (s, aromatic), 126.1 (q, aromatic), 126.9 (d, aromatic), 129.5 (d, aromatic), 133.8 (d, aromatic), 134.0 (d, aromatic), 136.5 (s, aromatic), 164.6 (q, $^1J_{CB}$ = 49.4 Hz, B-*C*). ^{11}B

NMR (CD_2Cl_2, 161 MHz, 298 K): δ (ppm) -5.9 (s). $^{31}P\{^1H\}$ NMR (CD_2Cl_2, 203 MHz, 298 K): δ (ppm) 30.2 (s). Anal. Calcd: $[fc(NPPh_3)_2PdMe][BPh_4]\cdot(THF)_1$ ($C_{75}H_{69}BFeN_2OP_2Pd$) C, 72.10; H, 5.57; N, 2.24. Found: C, 72.13; H, 5.61; N, 2.29.

Synthesis of $[fc(NPPh_3)_2Pd(THF)][BF_4]_2$. To a suspension of $AgBF_4$ (54.4 mg, 0.279 mmol) in 2 mL of methylene chloride was added $[fc(NPPh_3)_2PdMe][BPh_4]$ (116.3 mg, 0.093 mmol) in 5 mL of methylene chloride at ambient temperature. The reaction solution was stirred for 10 min at ambient temperature before being filtered through a Celite plug. The filtrate was concentrated to 2 mL followed by the addition of a few drop of THF, layering with 2 mL of diethyl ether, and stored overnight at -35 °C. Decanting of the solution and washing with cold diethyl ether yielded the product as dark golden plates (79.9 mg, 73.2%). X-ray quality crystals were obtained from a methylene chloride/THF (1:2 vol %) layering at ambient temperature. Crystals of $[fc(NPPh_3)_2Pd(THF)][BF_4]_2$ always contain a molecule of methylene chloride per molecule of compound as supported by NMR spectroscopic data. ^1H NMR (CD_2Cl_2, 500 MHz, 298 K): δ (ppm) 1.61 (m, 4H, CH_2), 3.53 (m, 4H, OCH_2), 3.63 (t, 4H, Cp-*H*), 5.39 (t, 4H, Cp-*H*), 7.66 (m, 12H, *o*-Ph), 7.75 (m, 18H, *m*-Ph, *p*-Ph). ^{13}C NMR (CD_2Cl_2, 126 MHz, 298 K): δ (ppm) 25.9 (s, *C*H_2), 69.1 (s, O*C*H_2), 73.2 (d, Cp-*C*), 83.8 (s, Cp-*C*), 106.9 (d, Cp-*C*), 123.9 (d, aromatic), 130.8 (d, aromatic), 133.3 (d, aromatic), 135.4 (d, aromatic). ^{11}B NMR (CD_2Cl_2, 161 MHz, 298 K): δ (ppm) -0.4 (br s). ^{19}F NMR spectrum (CD_2Cl_2, 282 MHz, 298 K) of $[fc(NPPh_3)_2Pd(THF)][BF_4]_2$: δ (ppm) -152.0 (br s), -152.1 (br s). $^{31}P\{^1H\}$ NMR (CD_2Cl_2, 203 MHz, 298 K): δ (ppm) 37.4 (s). Anal. Calcd: $[fc(NPPh_3)_2Pd(THF)][(BF_4)_2]\cdot(CH_2Cl_2)_1$ ($C_{51}H_{48}B_2Cl_2F_8FeN_2OP_2Pd$) C, 52.19; H, 4.12; N, 2.39. Found: C, 51.54; H, 4.35; N, 2.26.

Synthesis of $Fc(NPEt_3)_2$. To $fc(N_3)_2$ (194.0 mg, 0.724 mmol) in 8 mL of hexanes was added PEt_3 (0.21 mL, 1.45 mmol) in 8 mL of hexanes drop-wise under subdued light. The

reaction solution was stirred for 1 h at ambient temperature. The hexanes solution was decanted and volatile substances were removed under a reduced pressure. The remaining orange crystalline solids were dissolved in 2 mL of diethyl ether, layered with 2 mL of hexanes, and stored for 18 h at -35 °C. Decanting of the solution and washing with 2 mL of cold hexanes yielded the product as red crystals (295.1 mg, 90.9%). ^{1}H NMR ($CDCl_3$, 500 MHz, 298 K): δ (ppm) 1.13 (m, 18H, CH_2CH_3), 1.85 (m, 12H, CH_2CH_3), 3.66 (t, 4H, Cp-*H*), 3.74 (t, 4H, Cp-*H*). ^{13}C NMR ($CDCl_3$, 126 MHz, 298 K): δ (ppm) 6.6 (d, CH_2CH_3), 18.0 (d, CH_2CH_3), 61.3 (d, Cp-*C*), 64.8 (s, Cp-*C*), 111.6 (s, Cp-*C*). ^{31}P{^{1}H} ($CDCl_3$, 203 MHz, 298 K): δ (ppm) 28.9 (s). Anal. Calcd: fc$(NPEt_3)_2$ ($C_{22}H_{38}FeN_2P_2$) C, 58.94; H, 8.54; N, 6.25. Found: C, 59.15; H, 8.55; N, 6.18.

Synthesis of fc$(NPEt_3)_2$PdCl(Me). To (COD)PdCl(Me) (80.2 mg, 0.303 mmol) in 3 mL of methylene chloride was added fc$(NPEt_3)_2$ (123.3 mg, 0.275 mmol) in 4 mL of methylene chloride and the reaction mixture was stirred for 1 h at ambient temperature. The reaction mixture was filered through Celite, volatile substances were removed under a reduced pressure, the product extracted with 5 mL of toluene. Removal of toluene under a reduced pressure yielded the product as an orange oil (120.9 mg, 72.6%). ^{1}H NMR (C_6D_6, 500 MHz, 298 K): δ (ppm) 0.72 (m, 9H, CH_2CH_3), 0.81 (m, 9H, CH_2CH_3), 1.21 (s, 3H, Pd-CH_3), 1.45 (m, 3H, CH_2CH_3), 1.70 (m, 6H, CH_2CH_3), 2.39 (m, 3H, CH_2CH_3), 3.75 (br s, 1H, Cp-*H*), 3.77 (br s, 1H, Cp-*H*), 3.80 (br s, 1H, Cp-*H*), 3.88 (br s, 1H, Cp-*H*), 4.05 (br s, 1H, Cp-*H*), 4.08 (br s, 1H, Cp-*H*), 5.19 (br s, 1H, Cp-*H*), 5.52 (br s, 1H, Cp-*H*). ^{13}C NMR (C_6D_6, 126 MHz, 298 K): δ (ppm) -9.8 (t, Pd-CH_3), 6.8 (d, CH_2CH_3), 7.2 (d, CH_2CH_3), 18.3 (d, CH_2CH_3), 18.8 (d, CH_2CH_3), 63.1 (s, Cp-*C*), 63.7 (s, Cp-*C*), 65.4 (s, Cp-*C*), 65.8 (s, Cp-*C*), 67.0 (s, Cp-*C*), 67.1 (s, Cp-*C*), 68.1 (s, Cp-*C*), 70.1 (s, Cp-*C*), 109.1 (d, Cp-*C*), 109.3 (m, Cp-*C*). ^{31}P{^{1}H} NMR (C_6D_6, 203 MHz, 298 K): δ (ppm) 43.3 (s), 45.1 (s). HRMS (m/z) $[M + 2H - \cdot Cl - \cdot CH_3]^{2+}$ calcd: ($C_{22}H_{40}FeN_2P_2Pd$) 556.10509. Found:

556.10930. High-resolution mass spectrometry was performed instead of elemental analysis due to the viscous, oily nature of the compound, which has a tendency to retain fractional equivalents of solvents and 1,5-cyclooctadiene.

Synthesis of [fc(NPEt$_3$)$_2$PdMe][BPh$_4$]. To fc(NPEt$_3$)$_2$PdCl(Me) (156.5 mg, 0.258 mmol) in 8 mL of methylene chloride was added solid NaBPh$_4$ (88.5 mg, 0.258 mmol) and the resulting suspension stirred for 30 min at ambient temperature. The reaction mixture was filtered through Celite followed by removal of volatile substances under reduced pressure. The remaining solids were dissolved in 2 mL of methylene chloride and layered with 6 mL of diethyl ether. Orange crystalline material forms after several hours at ambient temperature. Decanting of the solution and washing with diethyl ether yielded the product as an orange crystalline material (181.8 mg, 79.3%). X-ray quality crystals were obtained from methylene chloride/diethyl ether vapor diffusion. Crystals of [fc(NPEt$_3$)$_2$PdMe][BPh$_4$] always contain a molecule of methylene chloride per molecule of compound as supported by NMR spectroscopic data. ^{1}H NMR (CDCl$_3$, 500 MHz, 298 K): δ (ppm) 0.91 (s, 3H, Pd-C*H*$_3$), 1.09 (m, 18H, CH$_2$C*H*$_3$), 1.82 (m, 12H, C*H*$_2$CH$_3$), 2.97 (t, 4H, Cp-*H*), 4.63 (t, 4H, Cp-*H*), 6.89 (t, 4H, B-(*p*-Ph)), 7.04 (t, 8H, B-(*m*-Ph)), 7.41 (br s, 8H, B-(*o*-Ph)). ^{13}C NMR (CDCl$_3$, 126 MHz, 298 K): δ (ppm) -11.1 (t, Pd-*C*H$_3$), 6.1 (d, CH$_2$*C*H$_3$), 18.1 (d, *C*H$_2$CH$_3$), 67.5 (d, Cp-*C*), 72.5 (s, Cp-*C*), 87.6 (d, Cp-*C*), 121.8 (s, aromatic), 125.6 (q, aromatic), 136.5 (s, aromatic), 164.4 (q, $^1J_{CB}$ = 49.3 Hz, B-*C*). ^{11}B NMR (CDCl$_3$, 161 MHz, 298 K): δ (ppm) -5.7 (s). ^{31}P{^{1}H} NMR (CDCl$_3$, 203 MHz, 298 K): δ (ppm) 57.3 (s). Anal. Calcd: [fc(NPEt$_3$)$_2$PdMe][BPh$_4$]·(CH$_2$Cl$_2$)$_1$ (C$_{48}$H$_{63}$BCl$_2$FeN$_2$P$_2$Pd) C, 59.19; H, 6.52; N, 2.88. Found: C, 59.77; H, 6.55; N, 2.84.

6.6 Appendix E

6.6.1 NMR spectra

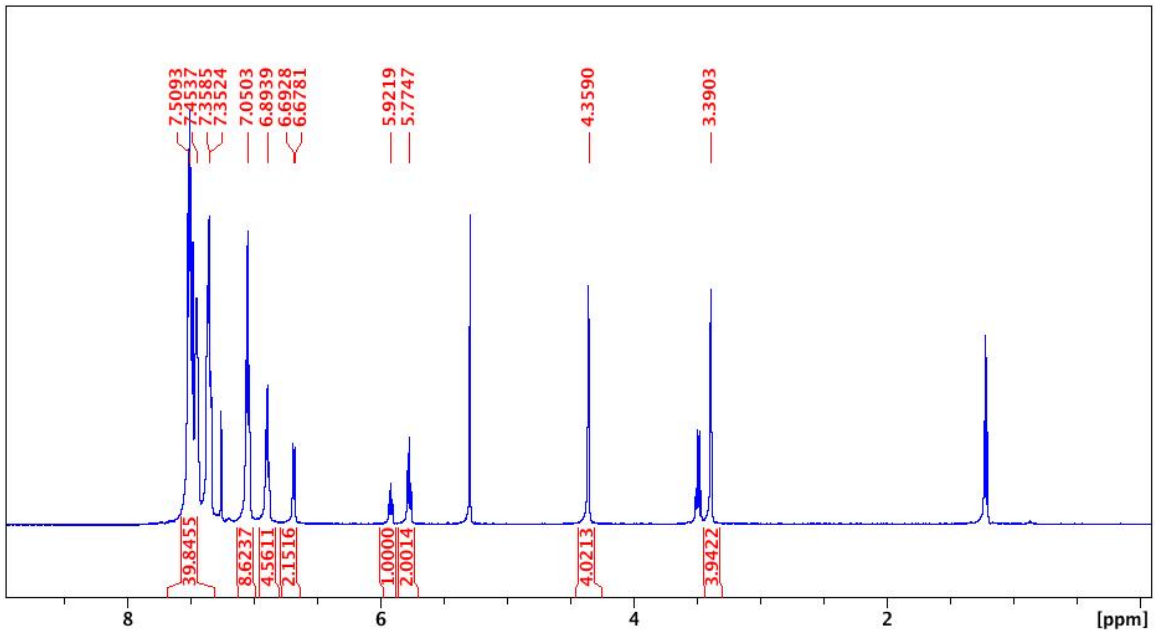

Figure E1. ^{1}H NMR spectrum ($CDCl_3$, 500 MHz, 298 K) of $[fc(NPPh_3)_2NiPh][BPh_4]$.

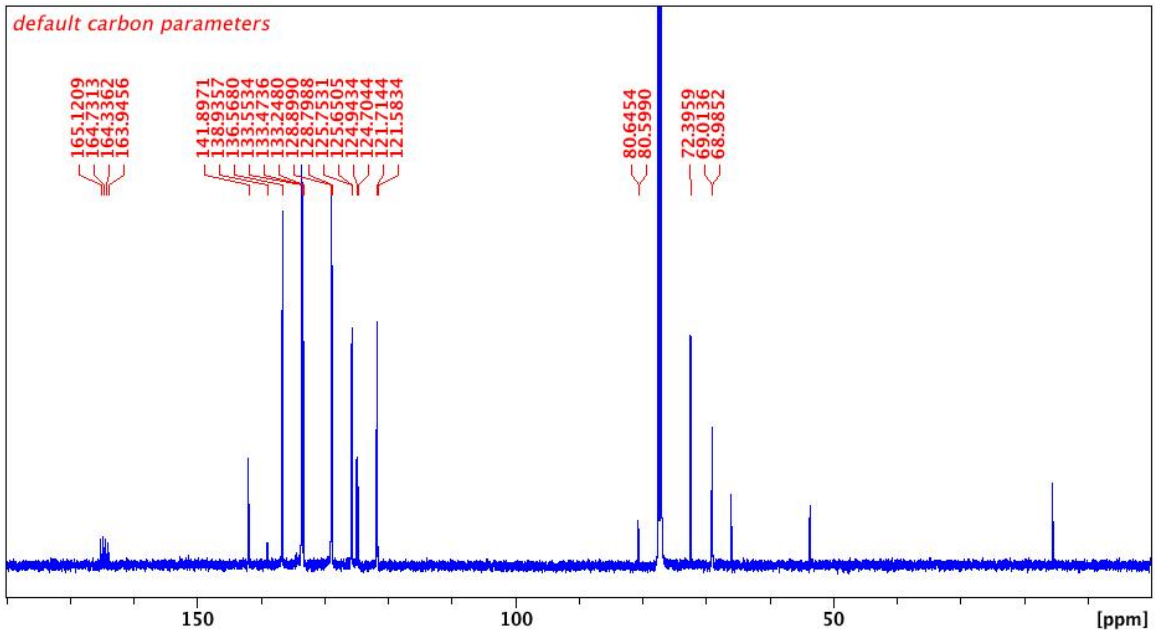

Figure E2. ^{13}C NMR spectrum ($CDCl_3$, 126 MHz, 298 K) of $[fc(NPPh_3)_2NiPh][BPh_4]$.

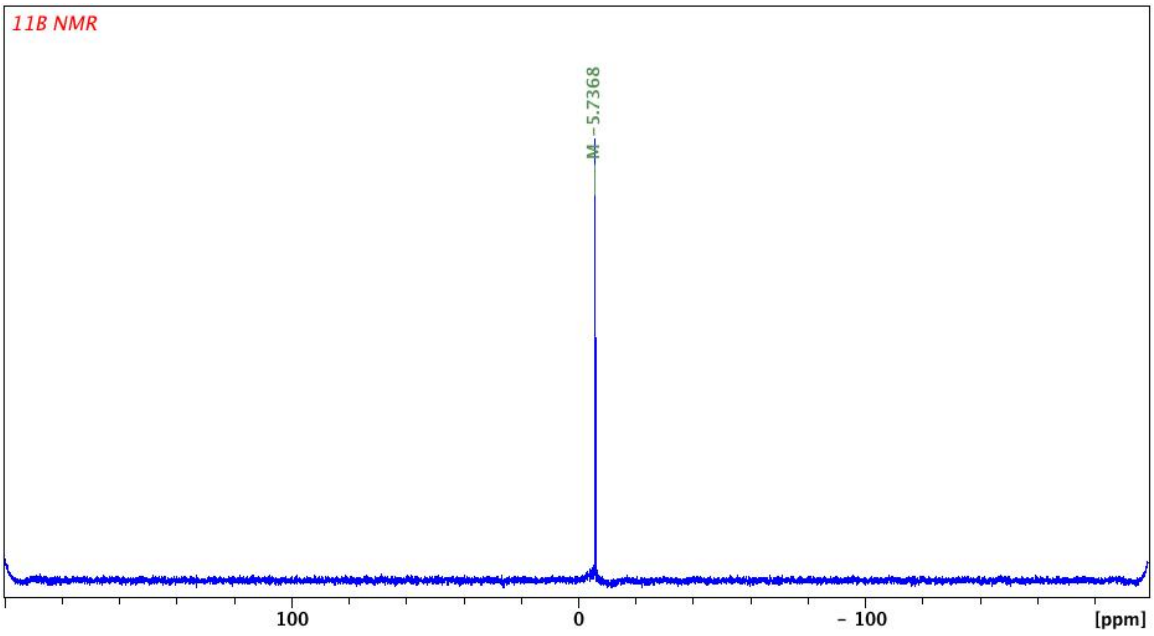

Figure E3. ^{11}B NMR spectrum ($CDCl_3$, 161 MHz, 298 K) of $[fc(NPPh_3)_2NiPh][BPh_4]$.

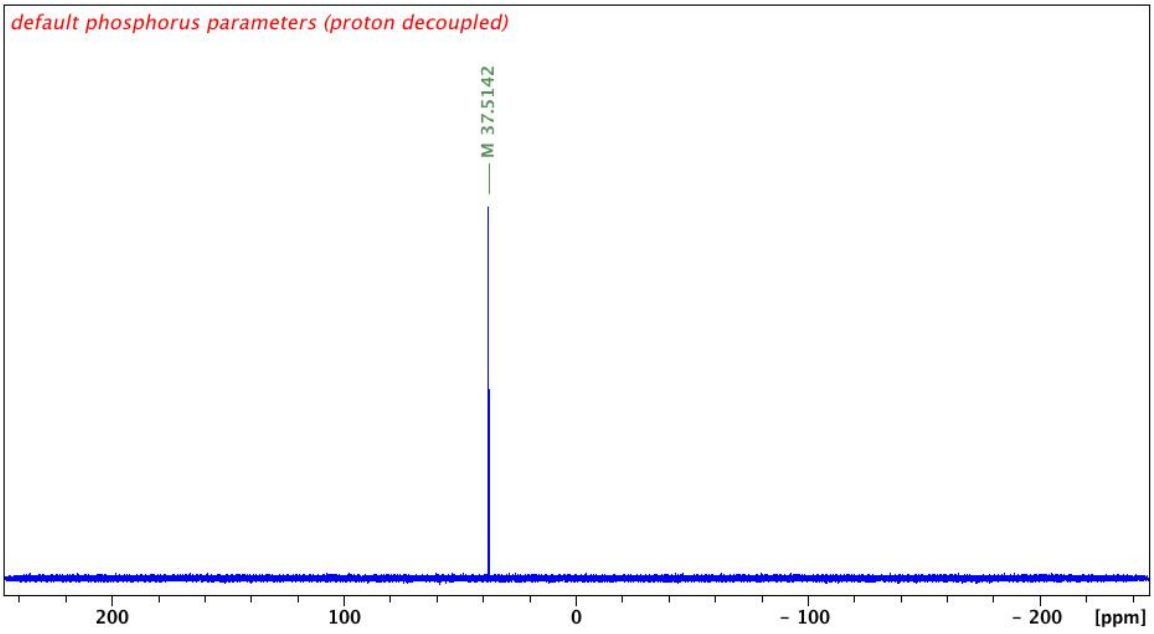

Figure E4. $^{31}P\{^1H\}$ NMR spectrum ($CDCl_3$, 203 MHz, 298 K) of $[fc(NPPh_3)_2NiPh][BPh_4]$.

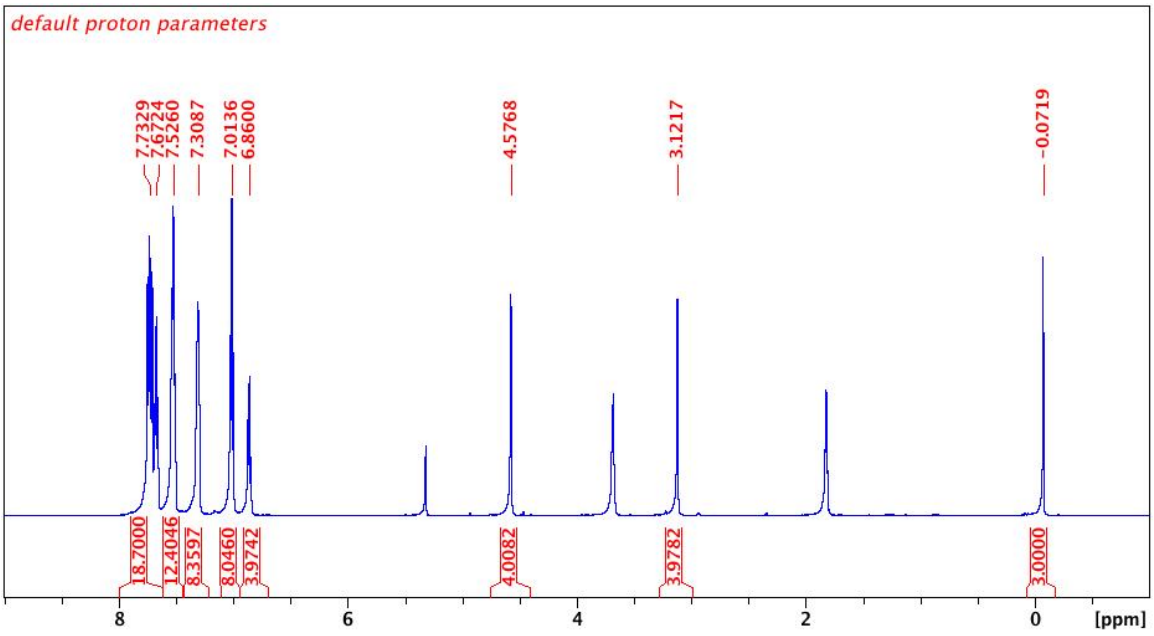

Figure E5. ^{1}H NMR spectrum (CD_2Cl_2, 500 MHz, 298 K) of [fc(NPPh$_3$)$_2$PdMe][BPh$_4$].

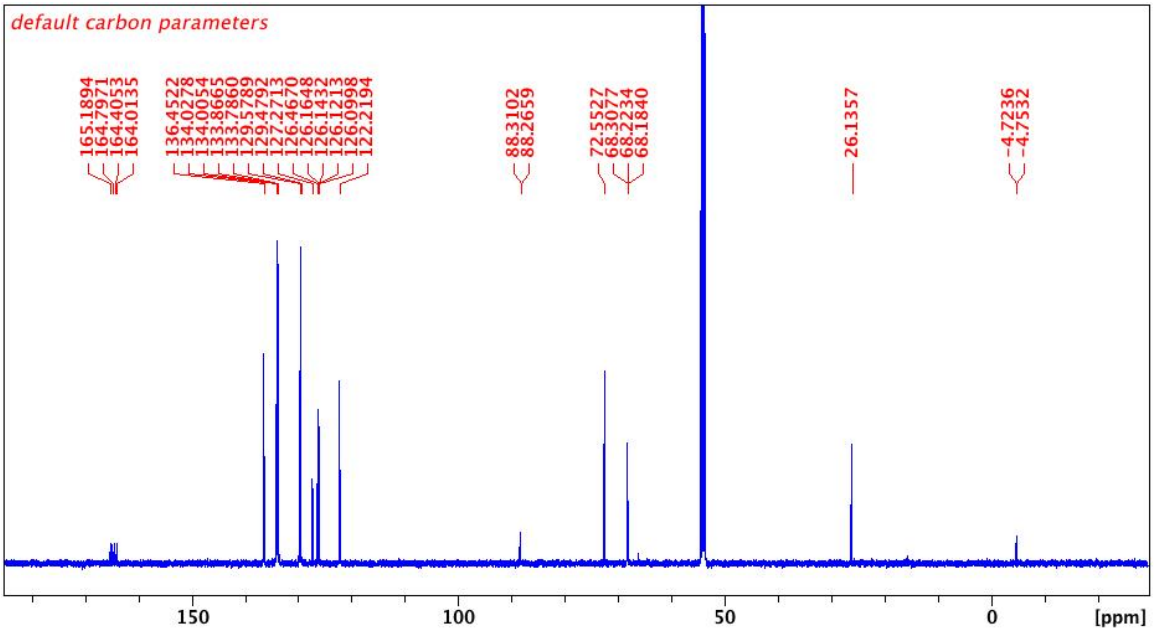

Figure E6. ^{13}C NMR spectrum (CD_2Cl_2, 126 MHz, 298 K) of [fc(NPPh$_3$)$_2$PdMe][BPh$_4$].

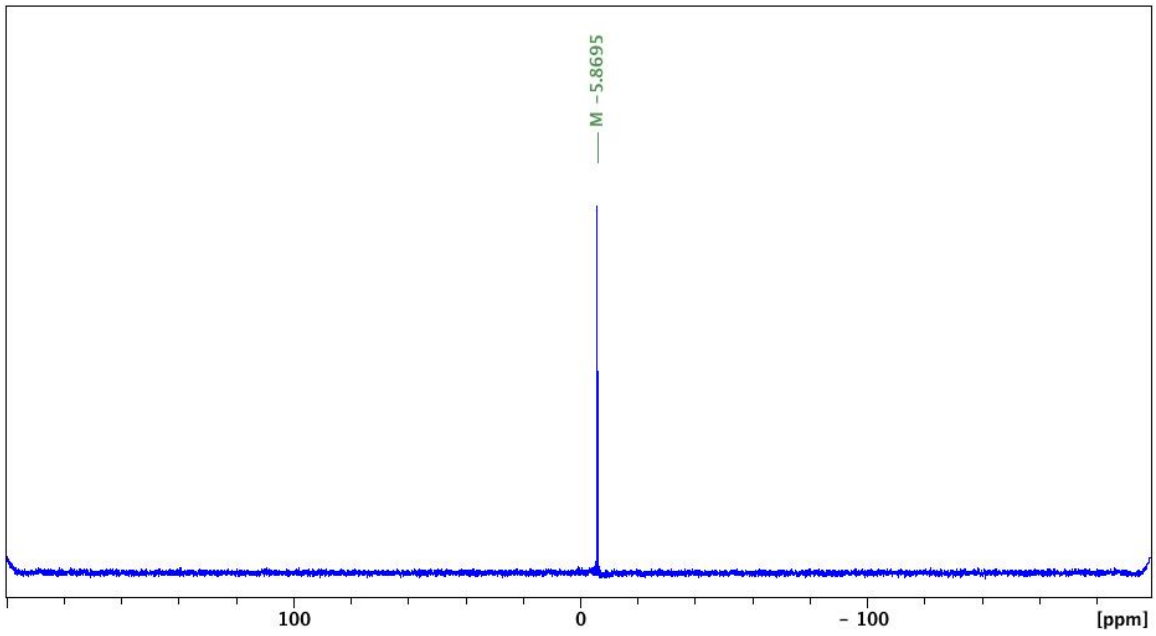

Figure E7. ^{11}B NMR spectrum (CD_2Cl_2, 161 MHz, 298 K) of [fc(NPPh$_3$)$_2$PdMe][BPh$_4$].

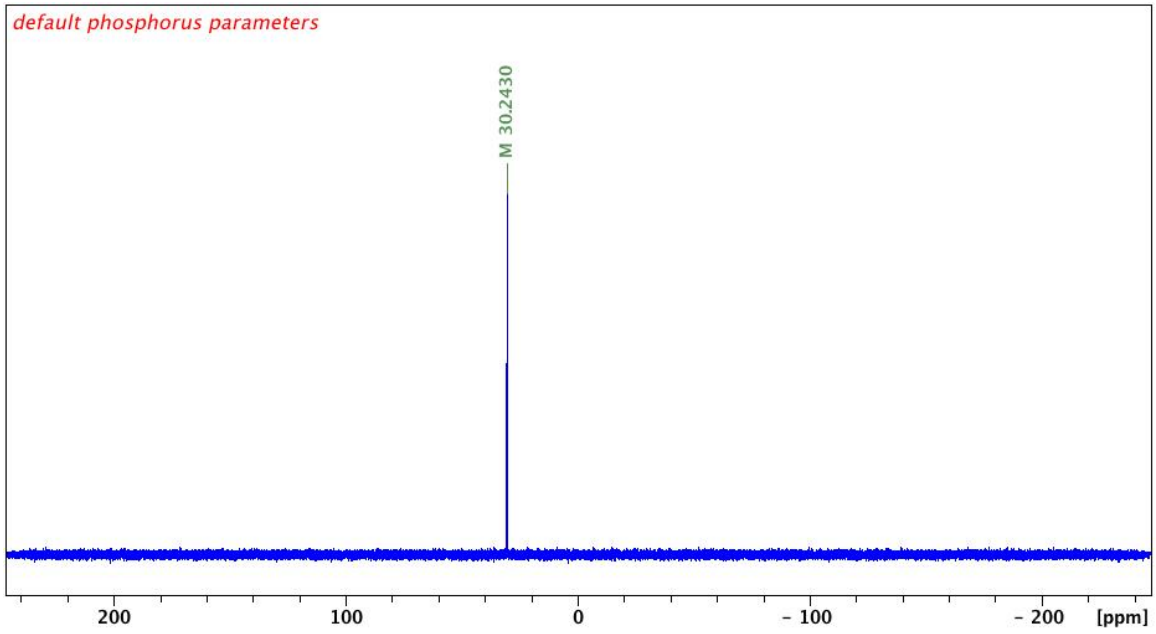

Figure E8. $^{31}P\{^1H\}$ NMR spectrum (CD_2Cl_2, 203 MHz, 298 K) of [fc(NPPh$_3$)$_2$PdMe][BPh$_4$].

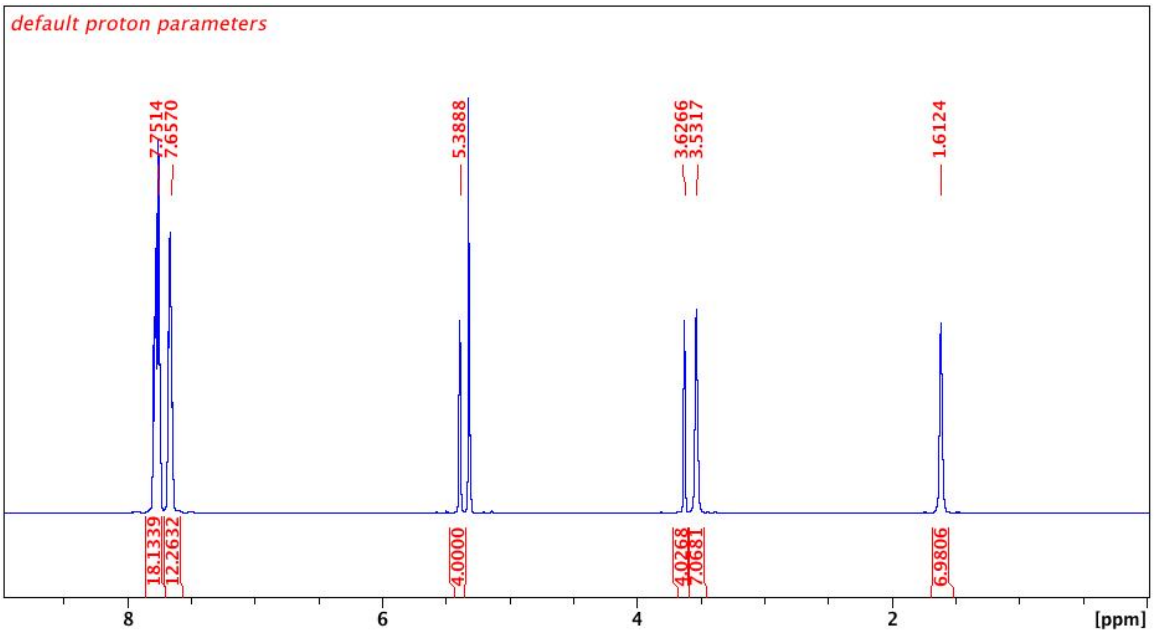

Figure E9. ^{1}H NMR spectrum (CD_2Cl_2, 500 MHz, 298 K) of $[fc(NPPh_3)_2Pd(THF)][BF_4]_2$.

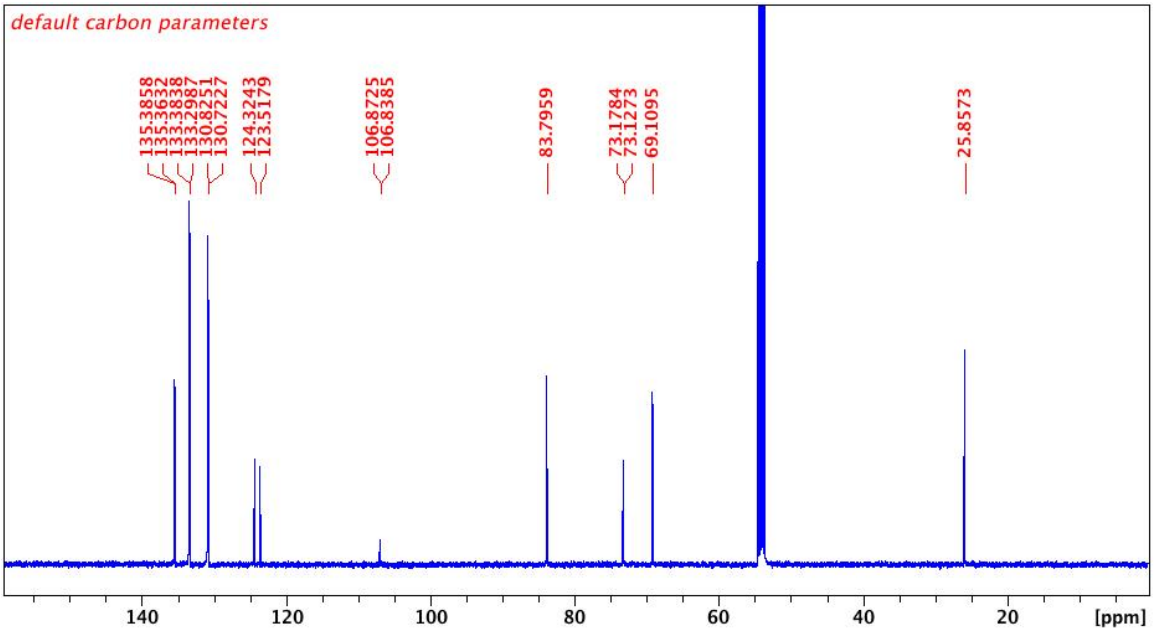

Figure E10. ^{13}C NMR spectrum (CD_2Cl_2, 126 MHz, 298 K) of $[fc(NPPh_3)_2Pd(THF)][BF_4]_2$.

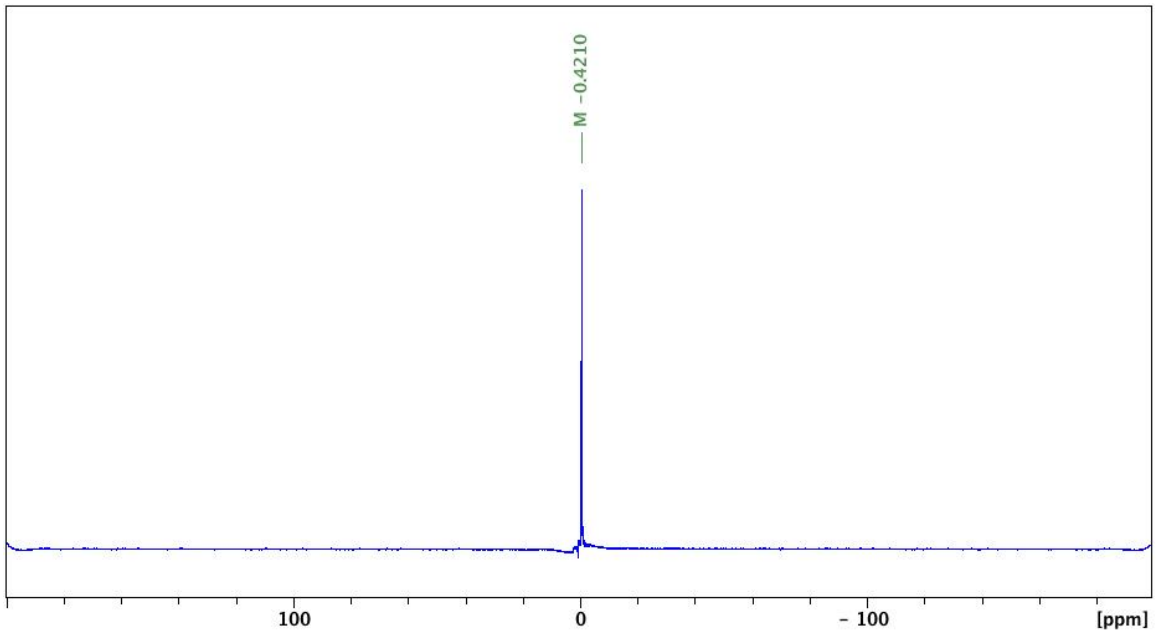

Figure E11. ^{11}B NMR spectrum (CD_2Cl_2, 161 MHz, 298 K) of $[fc(NPPh_3)_2Pd(THF)][BF_4]_2$.

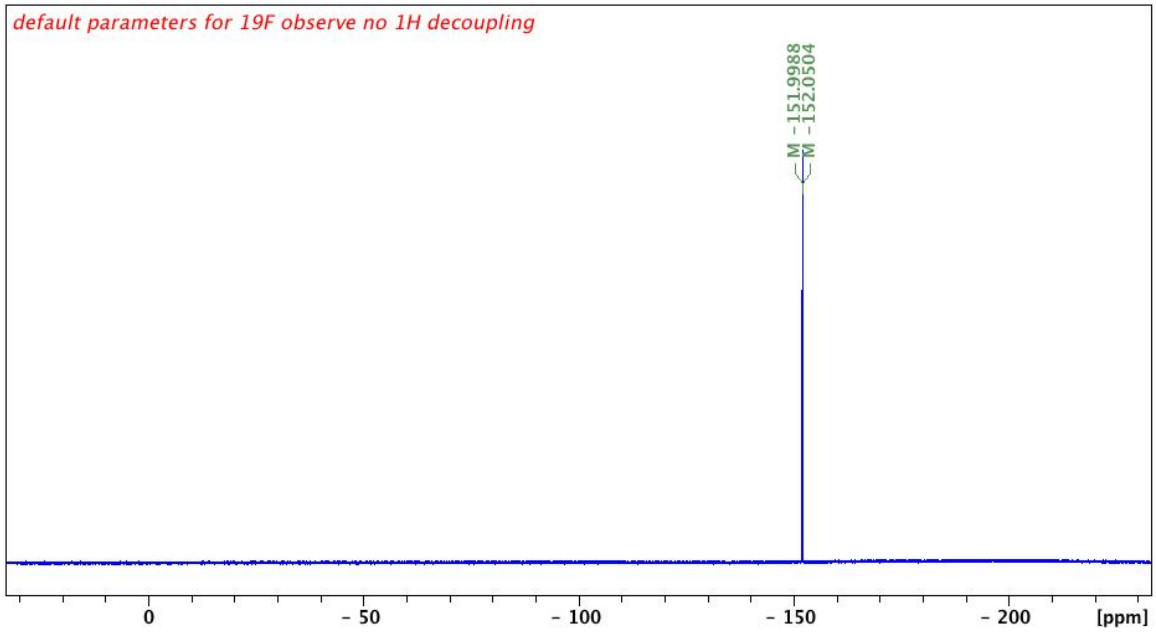

Figure E12. ^{19}F NMR spectrum (CD_2Cl_2, 282 MHz, 298 K) of $[fc(NPPh_3)_2Pd(THF)][BF_4]_2$.

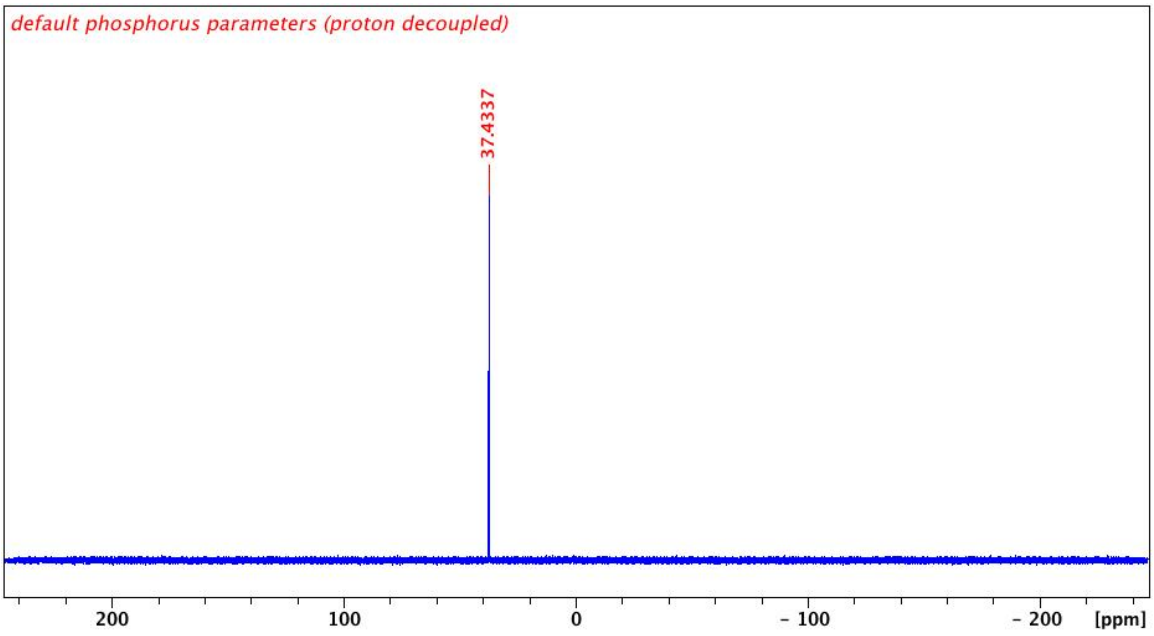

Figure E13. $^{31}P\{^{1}H\}$ NMR spectrum (CD_2Cl_2, 203 MHz, 298 K) of $[fc(NPPh_3)_2Pd(THF)][BF_4]_2$.

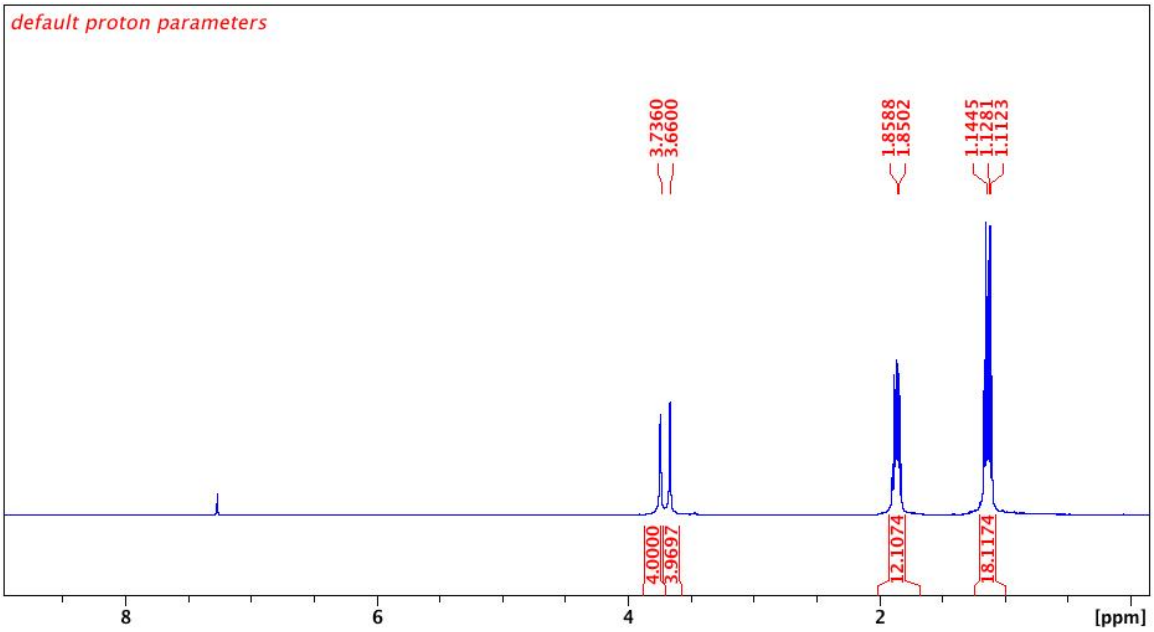

Figure E14. ^{1}H NMR spectrum ($CDCl_3$, 500 MHz, 298 K) of $fc(NPEt_3)_2$.

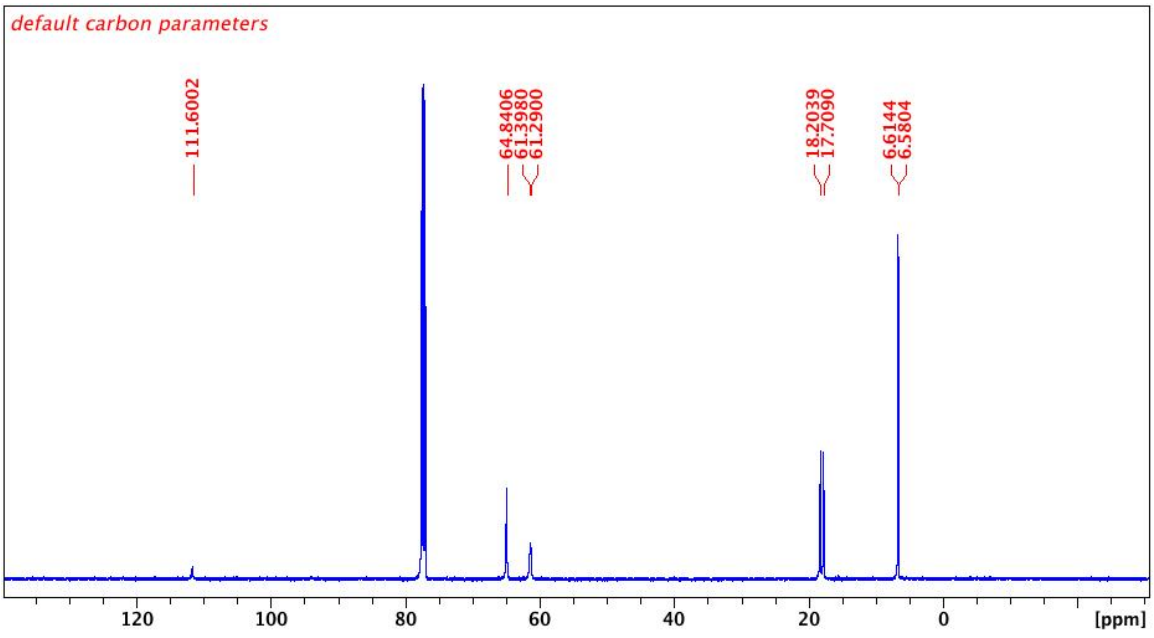

Figure E15. ^{13}C NMR spectrum ($CDCl_3$, 126 MHz, 298 K) of $fc(NPEt_3)_2$.

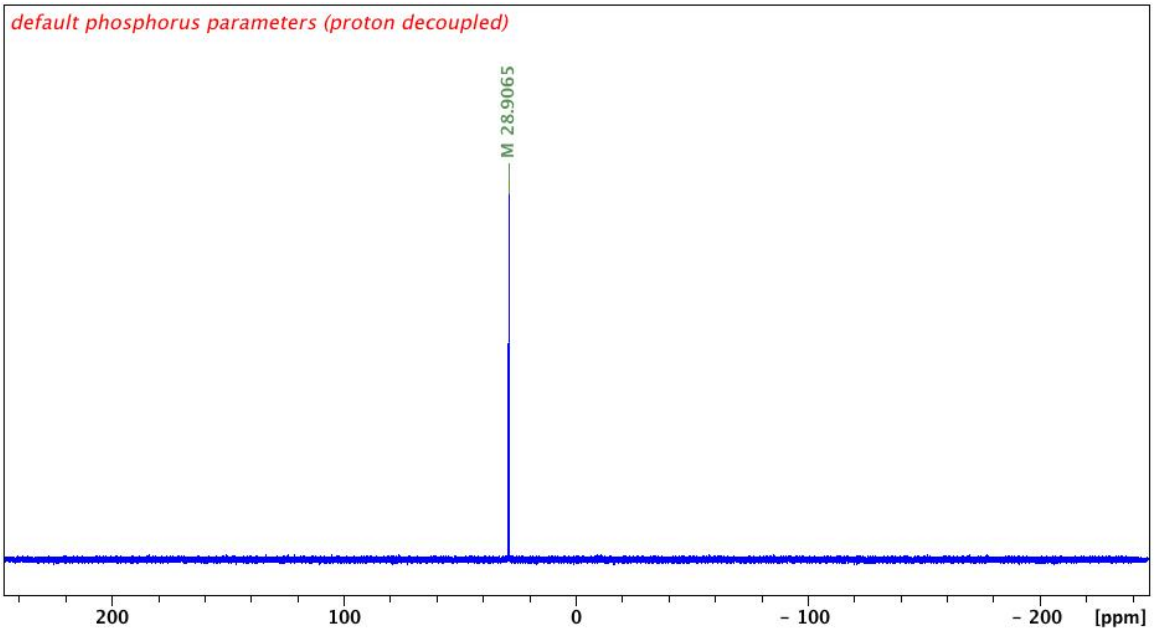

Figure E16. $^{31}P\{^1H\}$ NMR spectrum ($CDCl_3$, 203 MHz, 298 K) of $fc(NPEt_3)_2$.

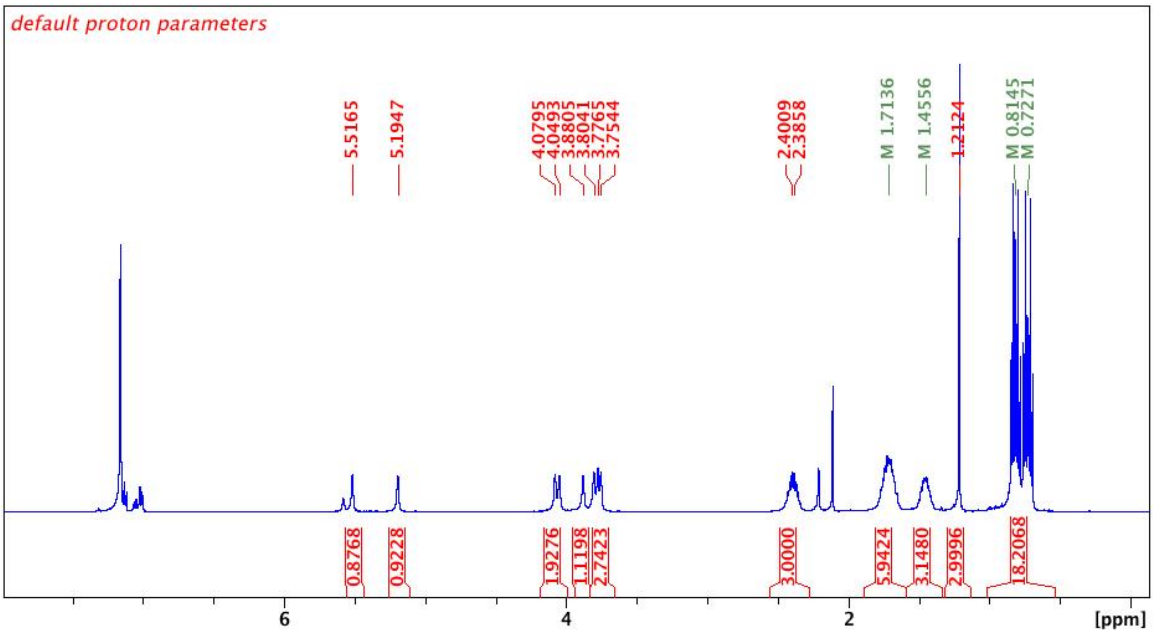

Figure E17. ^{1}H NMR spectrum (C_6D_6, 500 MHz, 298 K) of fc(NPEt$_3$)$_2$PdCl(Me).

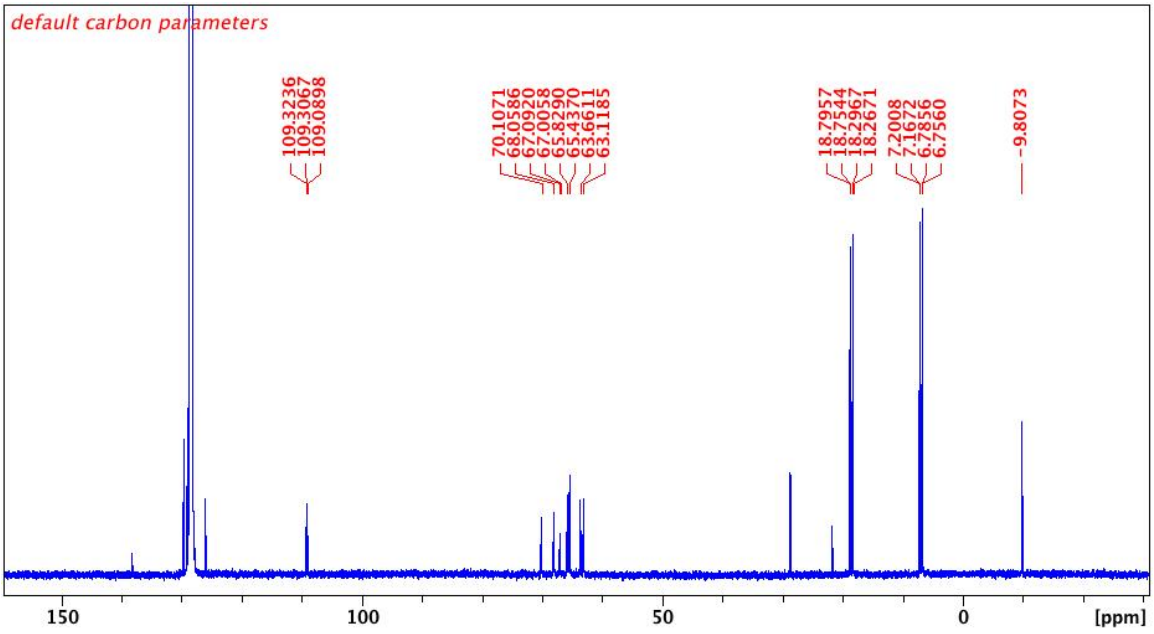

Figure E18. ^{13}C NMR spectrum (C_6D_6, 126 MHz, 298 K) of fc(NPEt$_3$)$_2$PdCl(Me).

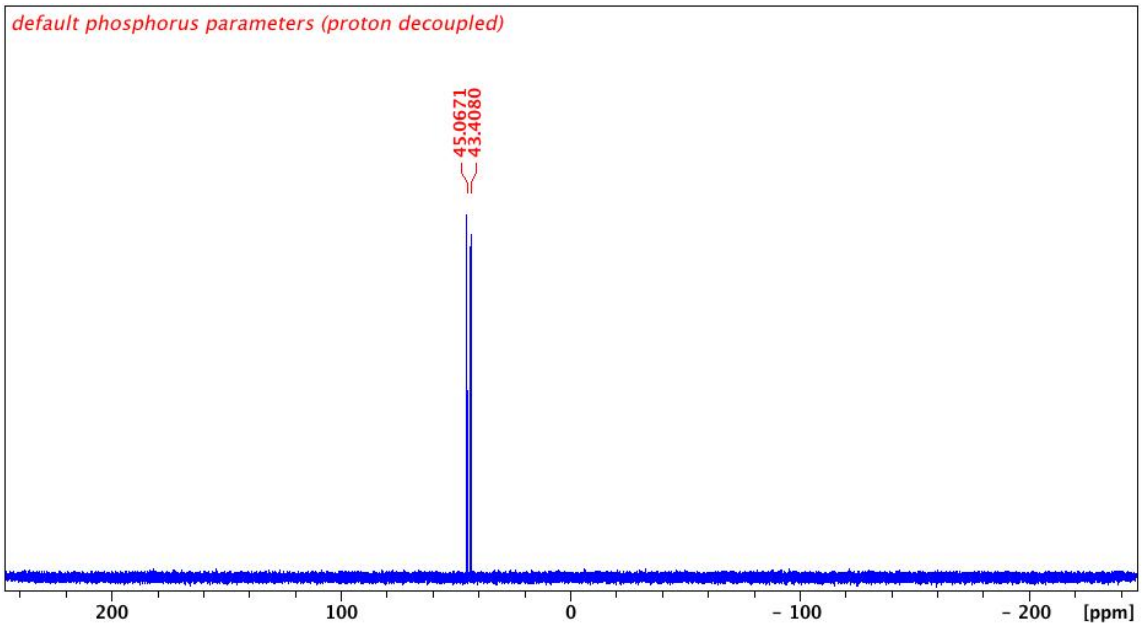

Figure E19. $^{31}P\{^{1}H\}$ NMR spectrum (C_6D_6, 203 MHz, 298 K) of $fc(NPEt_3)_2PdCl(Me)$.

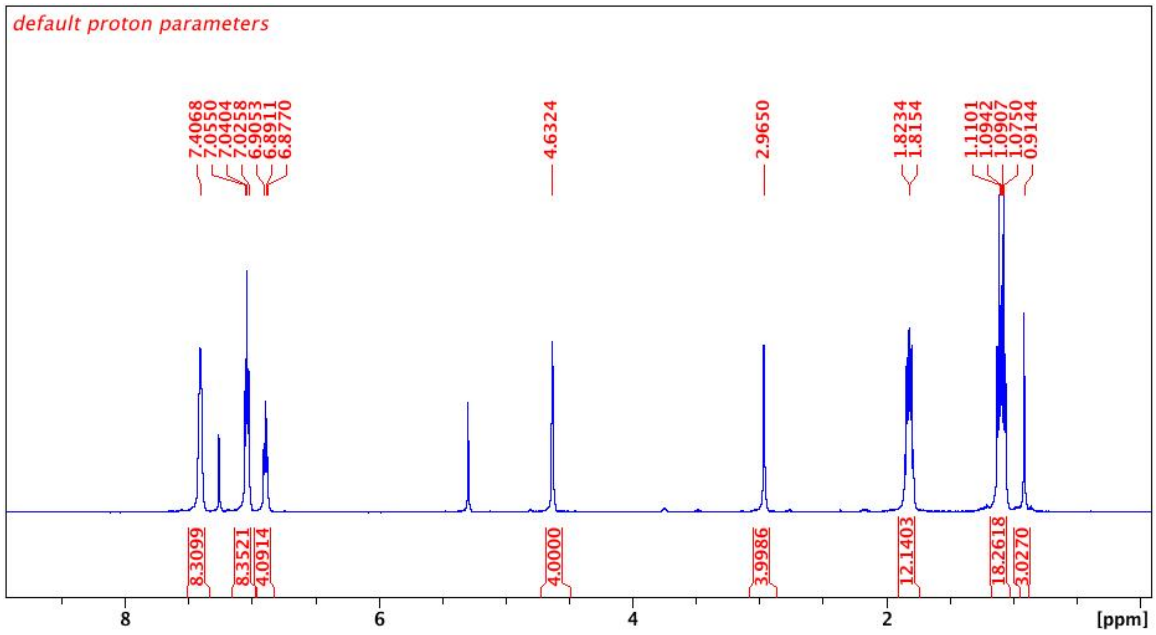

Figure E20. ^{1}H NMR spectrum ($CDCl_3$, 500 MHz, 298 K) of $[fc(NPEt_3)_2PdMe][BPh_4]$.

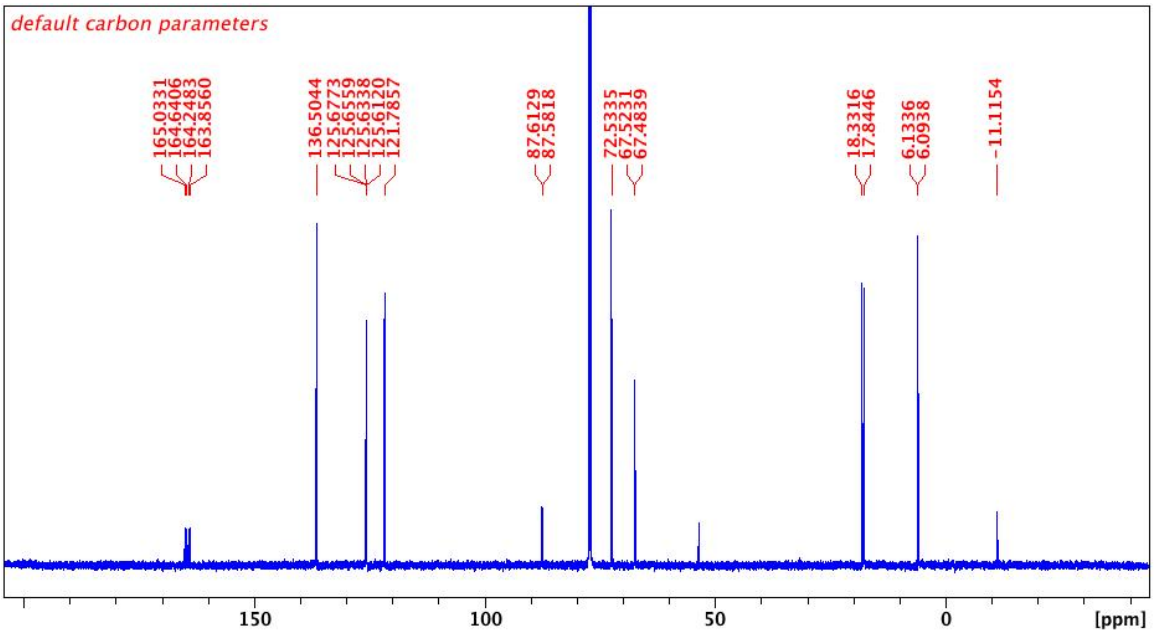

Figure E21. ^{13}C NMR spectrum ($CDCl_3$, 126 MHz, 298 K) of $[fc(NPEt_3)_2PdMe][BPh_4]$.

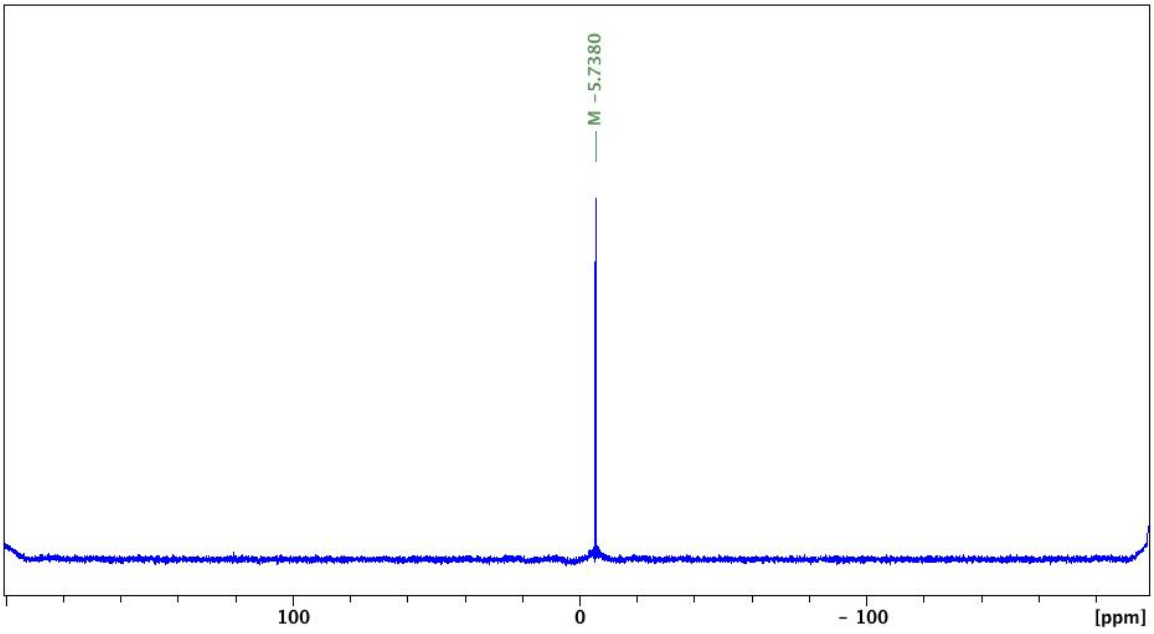

Figure E22. ^{11}B NMR spectrum ($CDCl_3$, 161 MHz, 298 K) of $[fc(NPEt_3)_2PdMe][BPh_4]$.

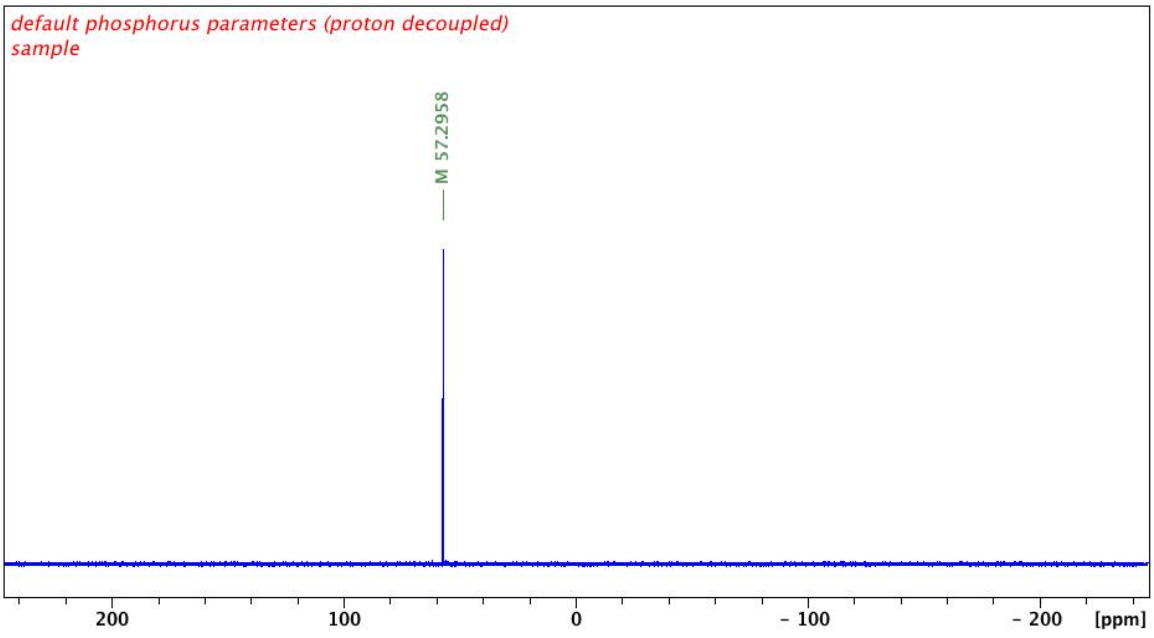

Figure E23. $^{31}P\{^{1}H\}$ NMR spectrum ($CDCl_3$, 203 MHz, 298 K) of $[fc(NPEt_3)_2PdMe][BPh_4]$.

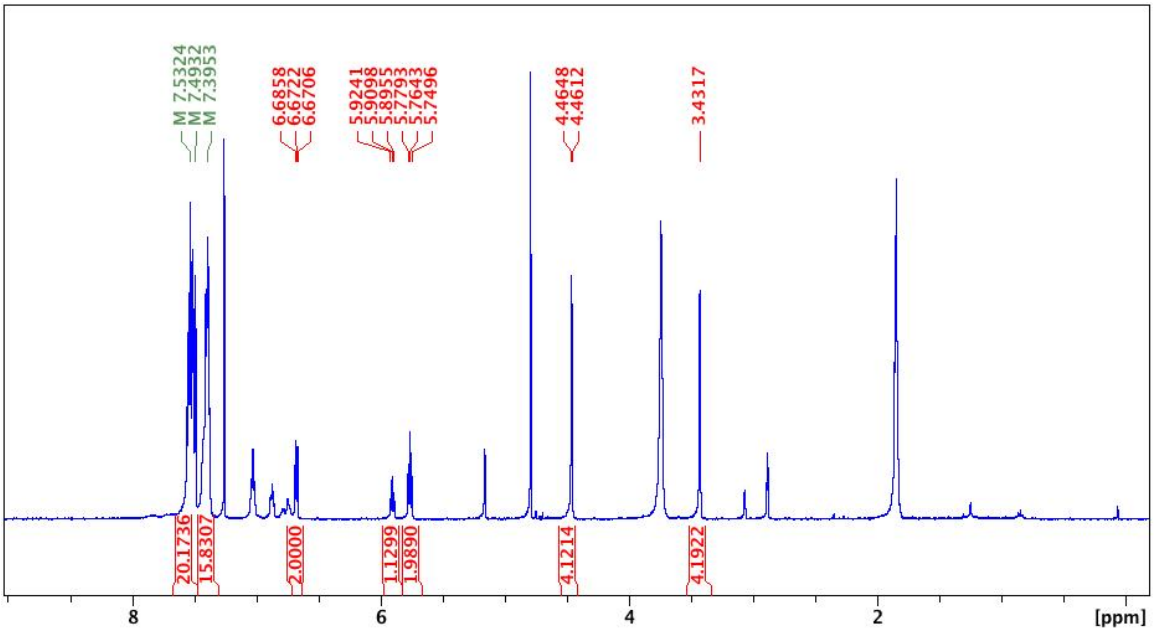

Figure E24. ^{1}H NMR spectrum ($CDCl_3$, 500 MHz, 298 K) of the reaction mixture of $[fc(NPPh_3)_2NiPh][BPh_4]$ in the presence of 1.4 equivalents of Cp_2Co in THF, after 15 minutes at ambient temperature.

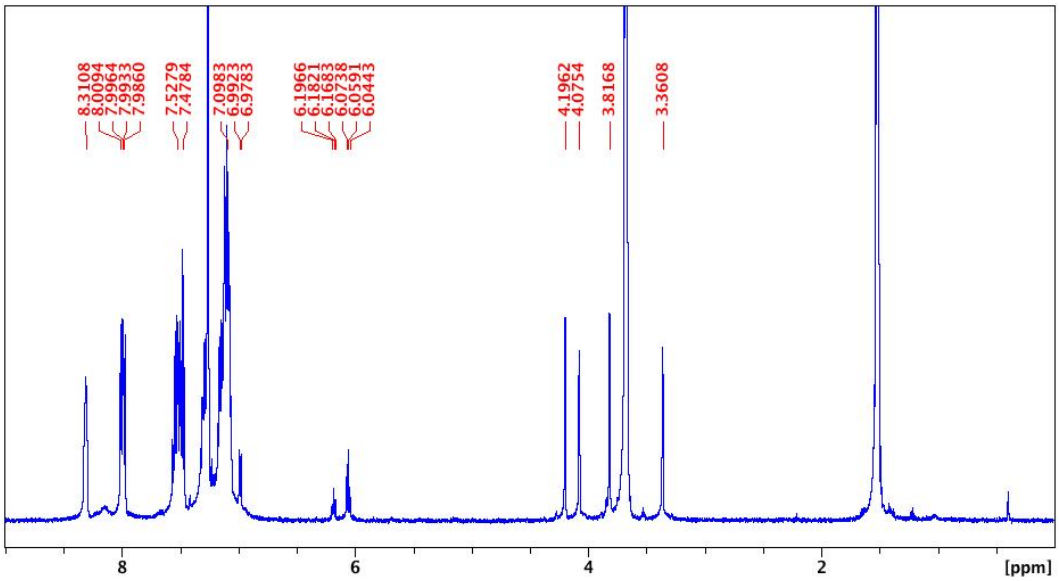

Figure E25. ^{1}H NMR spectrum (C_6D_6, 500 MHz, 298 K) of the reaction mixture of $[fc(NPPh_3)_2NiPh][BPh_4]$ with 1.2 equivalents of KC_8 after 1 minute in THF at ambient temperature, containing unreacted $[fc(NPPh_3)_2NiPh][BPh_4]$ and $fc(NPPh_3)_2$.

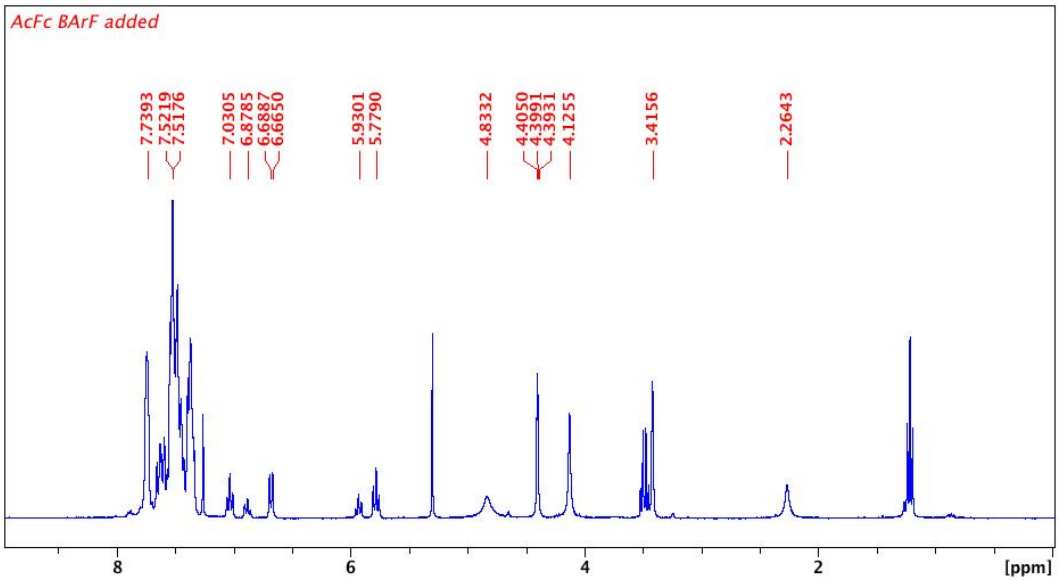

Figure E26. ^{1}H NMR spectrum ($CDCl_3$, 300 MHz, 298 K) of an NMR scale reaction of $[fc(NPPh_3)_2NiPh][BPh_4]$ with 1 equivalent of $[^{Ac}Fc][BAr^{F}]$, after 15 minutes at ambient temperature.

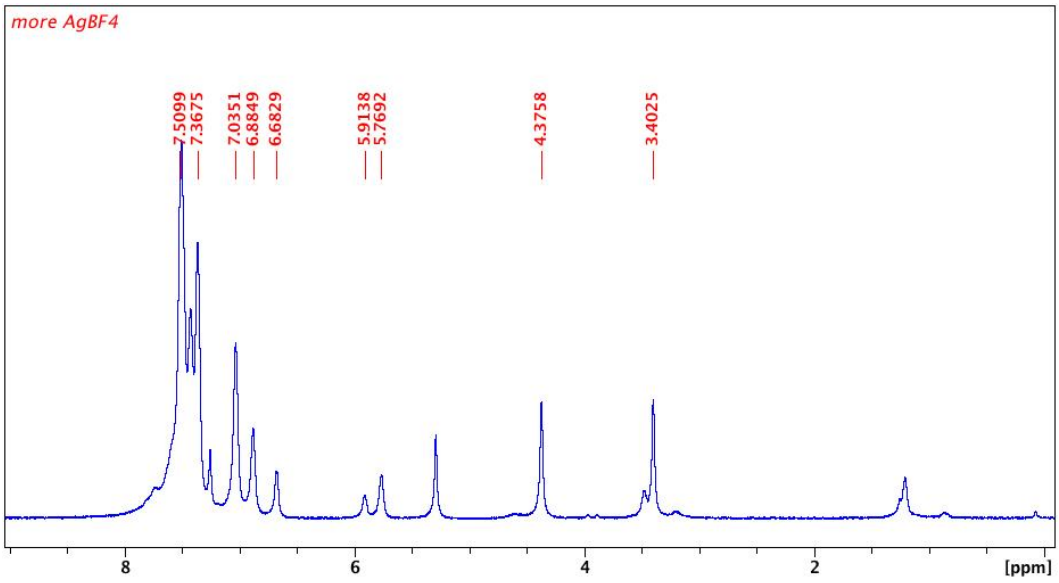

Figure E27. ^{1}H NMR spectrum ($CDCl_3$, 500 MHz, 298 K) of an NMR scale reaction of [fc($NPPh_3$)$_2$NiPh][BPh_4] with an excess of $AgBF_4$ after 30 minutes at ambient temperature.

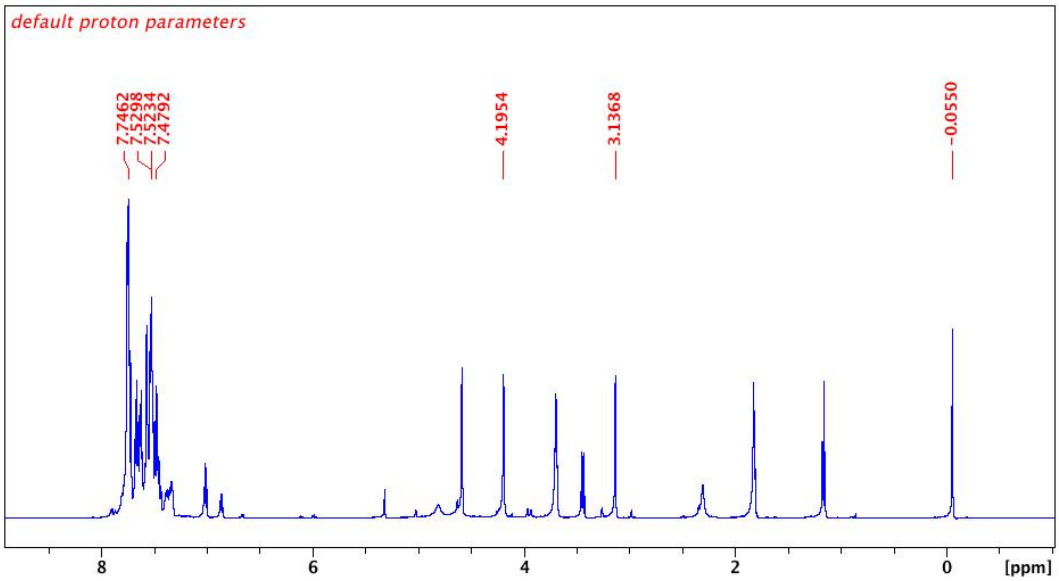

Figure E28. ^{1}H NMR spectrum (CD_2Cl_2, 500 MHz, 298 K) of a NMR scale reaction of [fc($NPPh_3$)$_2$PdMe][BPh_4] with 1 equivalent of [^{Ac}Fc][BAr^{F}] after 30 minutes at ambient temperature.

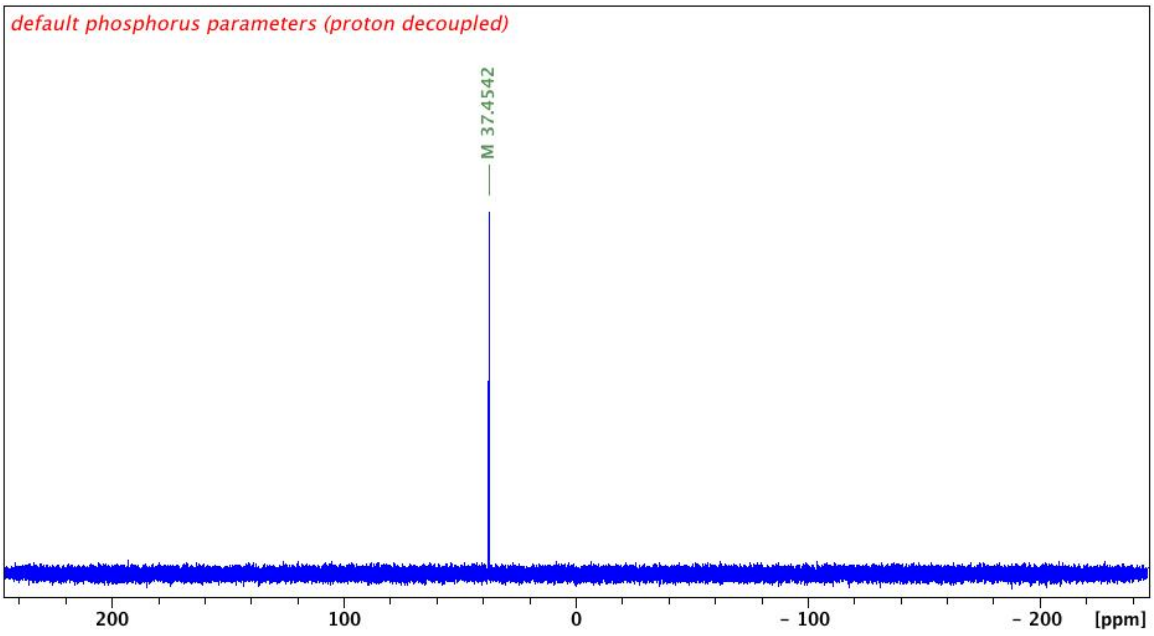

Figure E29. $^{31}P\{^{1}H\}$ NMR spectrum (CH_2Cl_2/MeCN (1:1 vol %), 203 MHz, 298 K) of $[fc(NPPh_3)_2NiPh][BPh_4]$.

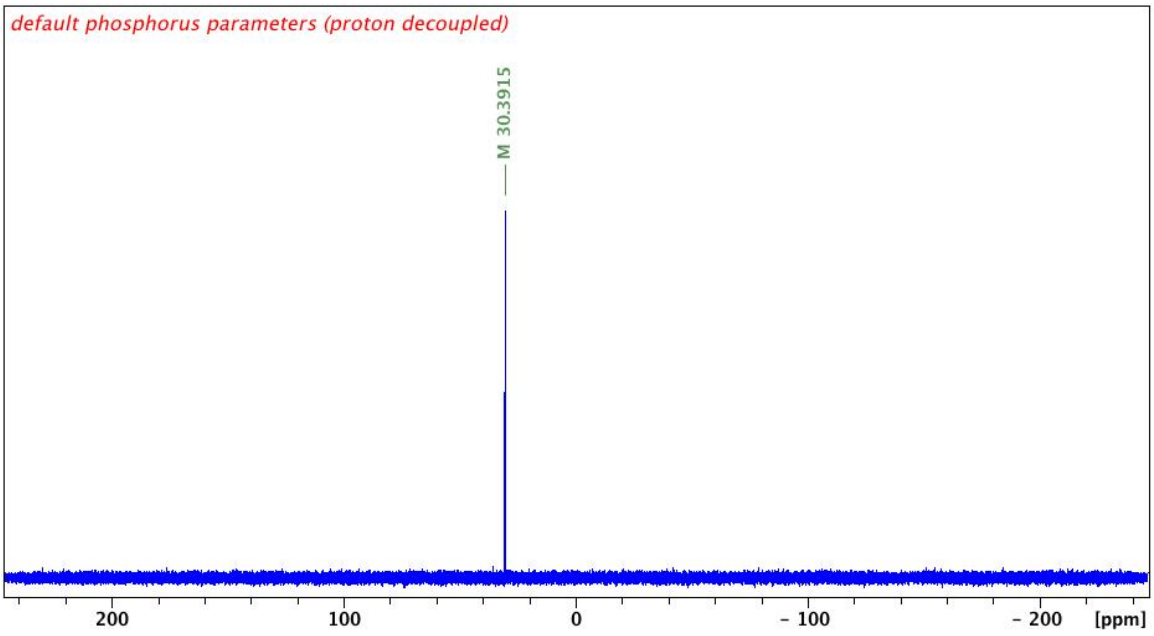

Figure E30. $^{31}P\{^{1}H\}$ NMR spectrum (CH_2Cl_2/MeCN (1:1 vol %), 203 MHz, 298 K) of $[fc(NPPh_3)_2PdMe][BPh_4]$.

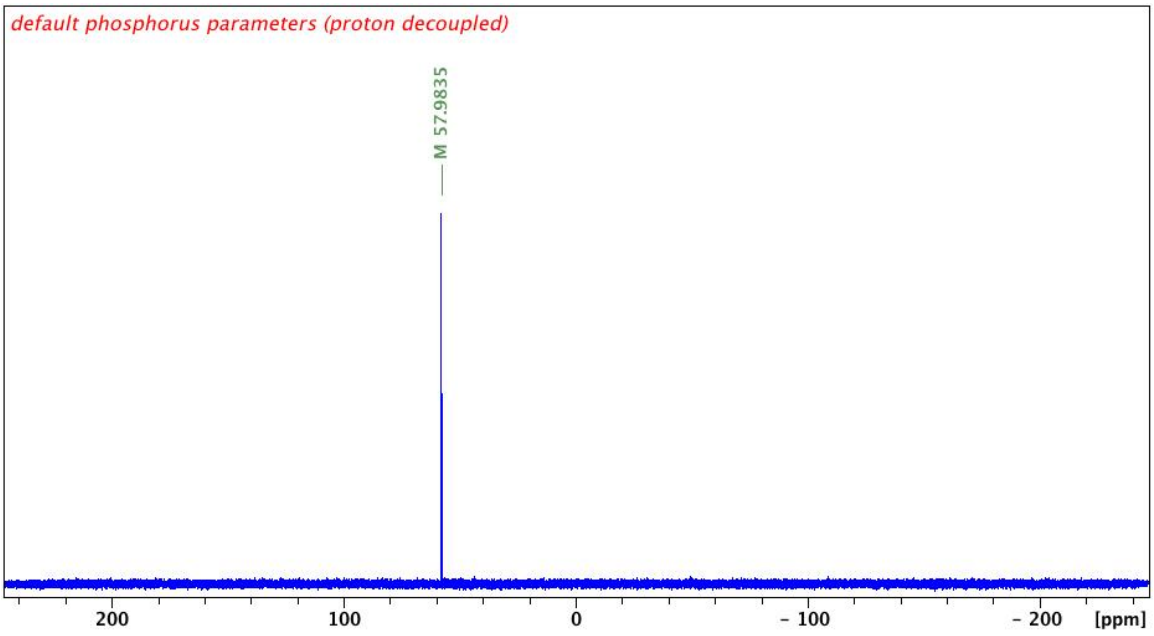

Figure E31. $^{31}P\{^{1}H\}$ NMR spectrum (CH_2Cl_2/MeCN (1:1 vol %), 203 MHz, 298 K) of $[fc(NPEt_3)_2PdMe][BPh_4]$.

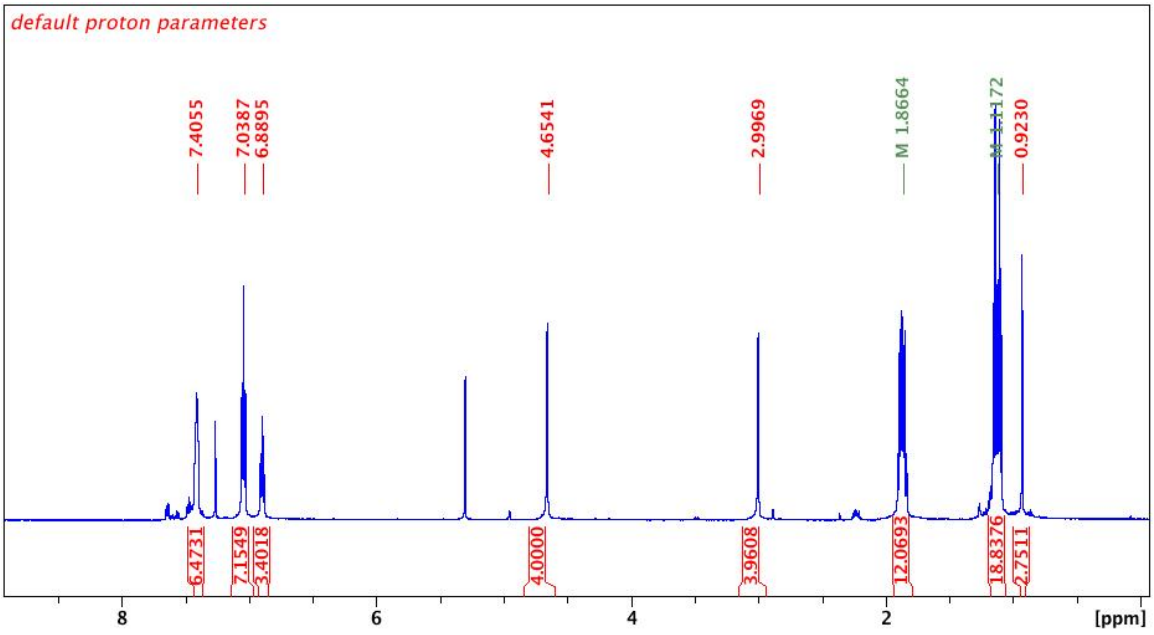

Figure E32. ^{1}H NMR spectrum ($CDCl_3$, 500 MHz, 298 K) of an NMR scale reaction of $[fc(NPEt_3)_2PdMe][BPh_4]$ with excess $AgBF_4$ after 30 min at ambient temperature.

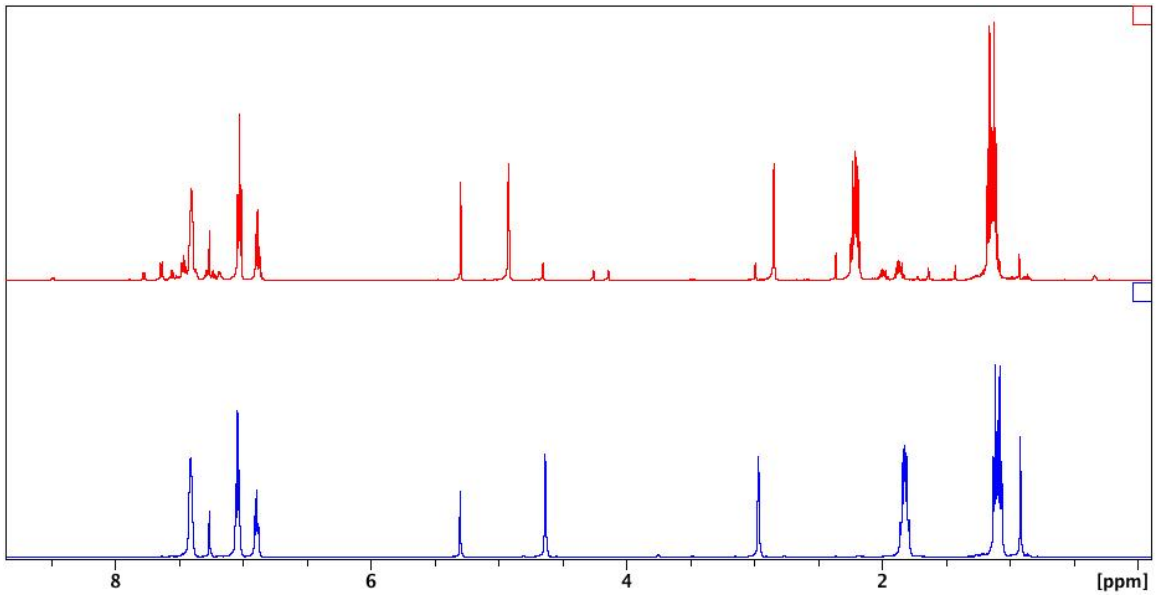

Figure E33. ^{1}H NMR spectra ($CDCl_3$, 500 MHz, 298 K) of $[fc(NPEt_3)_2PdMe][BPh_4]$ (bottom) and its decomposition (top) after 16 hours at ambient temperature, in $CDCl_3$.

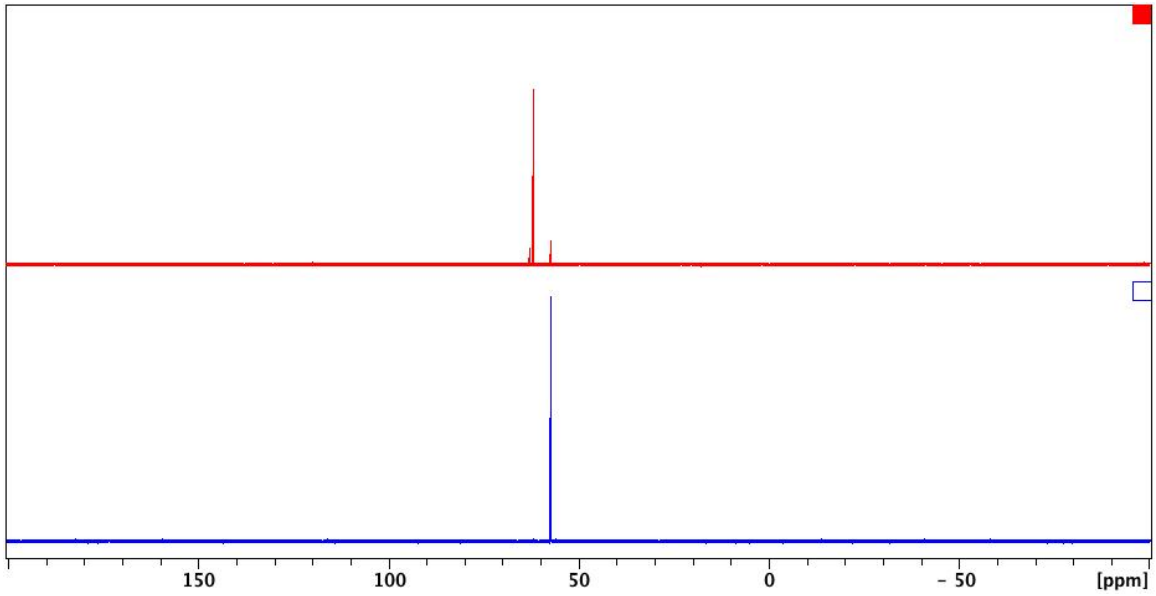

Figure E34. ^{31}P NMR spectra ($CDCl_3$, 203 MHz, 298 K) of $[fc(NPEt_3)_2PdMe][BPh_4]$ (bottom) and its decomposition (top) after 16 hours at ambient temperature, in $CDCl_3$.

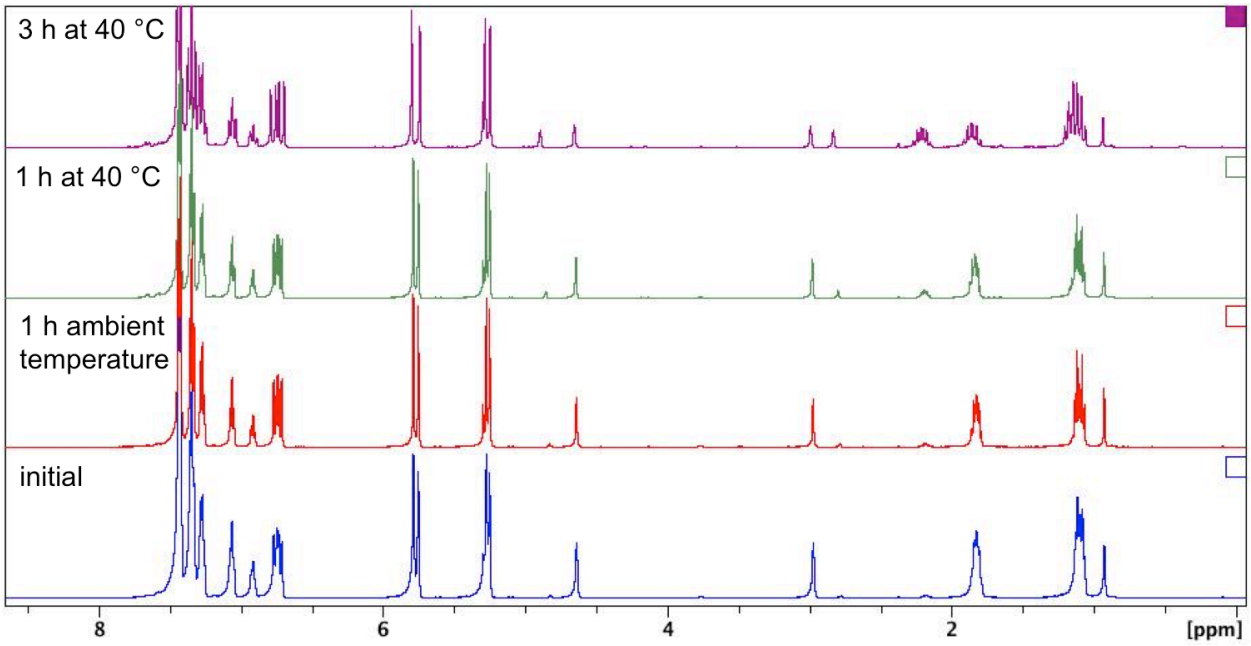

Figure E35. ^{1}H NMR spectra ($CDCl_3$, 500 MHz, 298 K) of $[fc(NPEt_3)_2PdMe][BPh_4]$ decomposition in the presence of 16 equivalents of styrene, in $CDCl_3$.

6.6.2 Additional figures

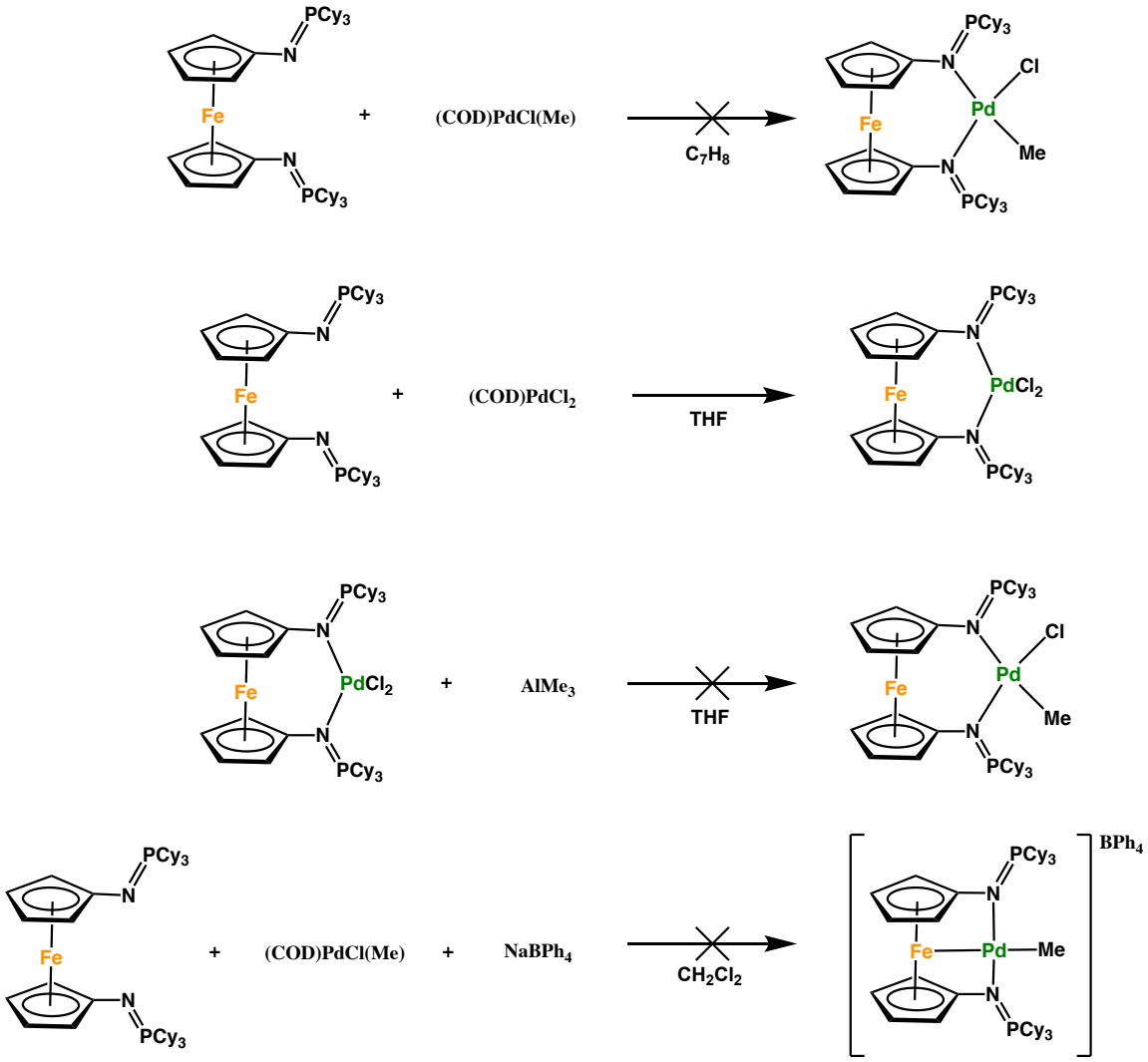

Scheme E1. Attempts to prepare ferrocene-bis(tricyclohexyl)phosphinimine complexes of palladium.

6.6.3 Cyclic voltammetry data

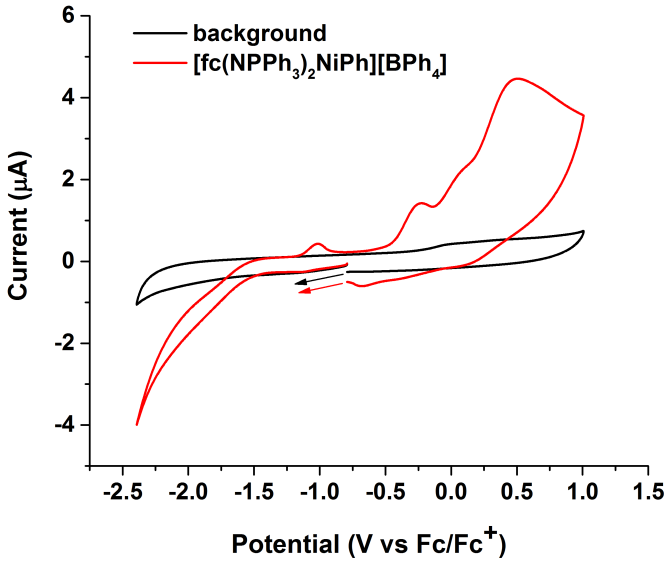

Figure E36. Cyclic voltammograms recorded with a glassy carbon electrode at 100 mV/s in methylene chloride, 0.10 M [TPA][BAr^F] containing no [fc($NPPh_3$)$_2$NiPh][BPh_4] (black trace) and 5.0 mM [fc($NPPh_3$)$_2$NiPh][BPh_4] (red trace).

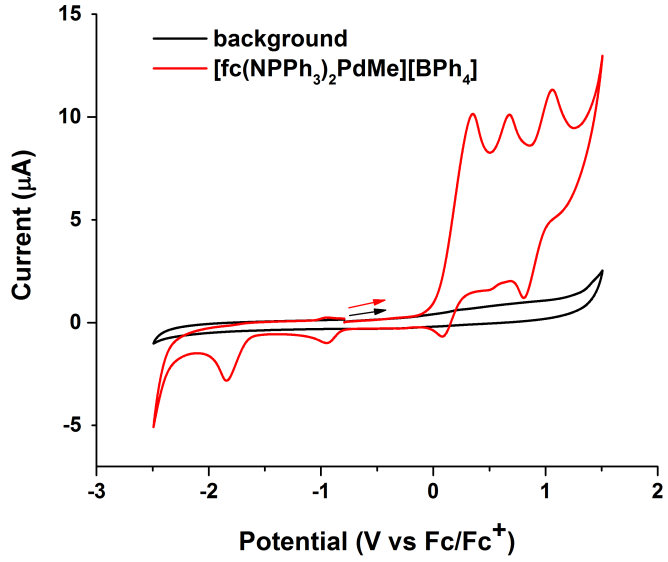

Figure E37. Cyclic voltammograms recorded with a glassy carbon electrode at 100 mV/s in methylene chloride, 0.10 M [TBA][PF_6] containing no [fc($NPPh_3$)$_2$PdMe][BPh_4] (black trace) and 5.0 mM [fc($NPPh_3$)$_2$PdMe][BPh_4] (red trace).

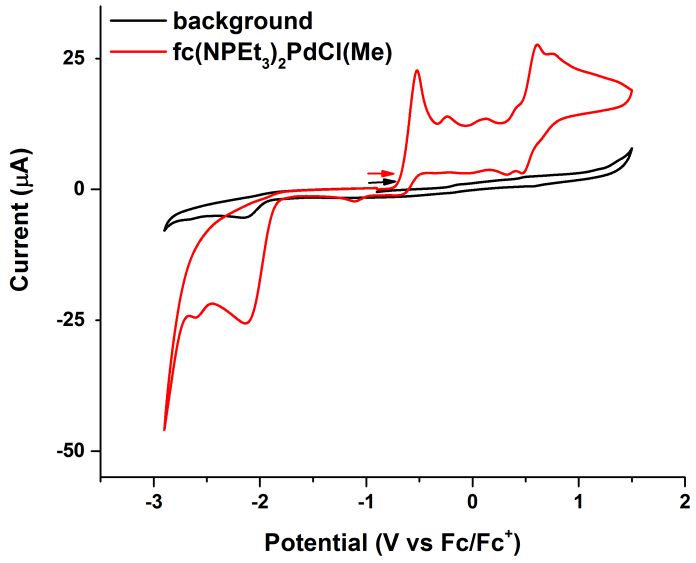

Figure E38. Cyclic voltammograms recorded with a glassy carbon electrode at 100 mV/s in methylene chloride, 0.10 M [TBA][PF_6] containing no fc($NPEt_3$)$_2$PdCl(Me) (black trace) and 5.0 mM fc($NPEt_3$)$_2$PdCl(Me) (red trace).

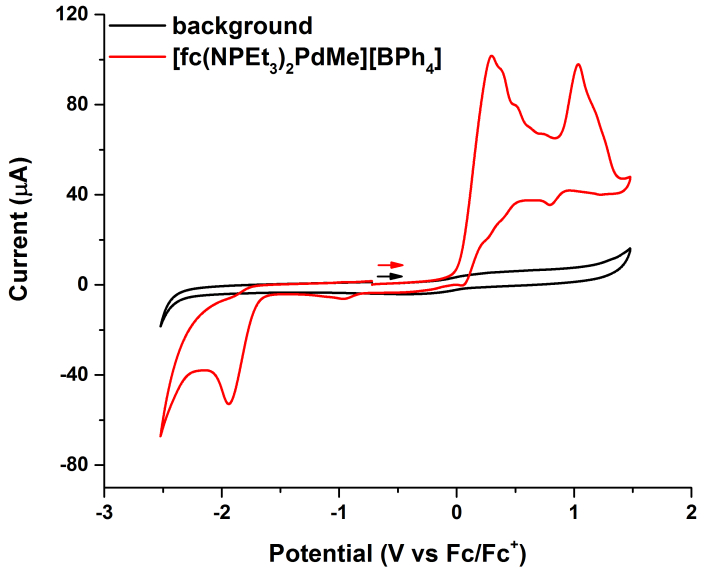

Figure E39. Cyclic voltammograms recorded with a glassy carbon electrode at 100 mV/s in methylene chloride, 0.10 M [TBA][PF_6] containing no [fc($NPEt_3$)$_2$PdMe][BPh_4] (black trace) and 5.0 mM [fc($NPEt_3$)$_2$PdMe][BPh_4] (red trace).

6.6.4 X-ray crystallographic data

[fc(NPPh$_3$)$_2$NiPh][BPh$_4$]

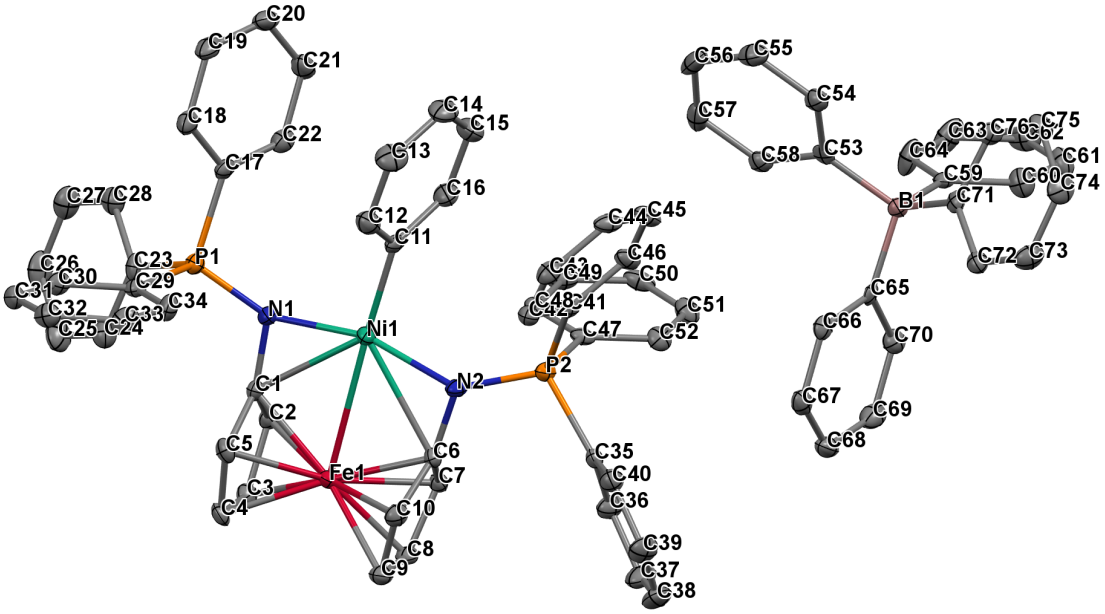

Figure E40. Molecular structure drawing of [fc(NPPh$_3$)$_2$NiPh][BPh$_4$] with thermal ellipsoids at 50% probability; hydrogen atoms were omitted for clarity.

Crystal data for $C_{76}H_{63}BFeN_2NiP_2$; M_r = 1191.59; Triclinic; space group P-1; *a* = 13.6804(12) Å; *b* = 15.2391(13) Å; *c* = 16.5452(14) Å; α = 78.9940(10)°; β = 71.6030(10)°; γ = 78.3080(10)°; V = 3175.0(5) Å^3; Z = 2; T = 100(2) K; λ = 0.71073 Å; μ = 0.620 mm^{-1}; d_{calc} = 1.246 g.cm^{-3}; 25934 reflections collected; 11159 unique (R_{int} = 0.0419); giving R_1 = 0.0346, wR_2 = 0.0735 for 7830 data with [I>2σ(I)] and R_1 = 0.0592, wR_2 = 0.0770 for all 11159 data. Residual electron density (e$^-$.Å^{-3}) max/min: 0.322/-0.404.

[fc(NPPh$_3$)$_2$PdMe][BPh$_4$]

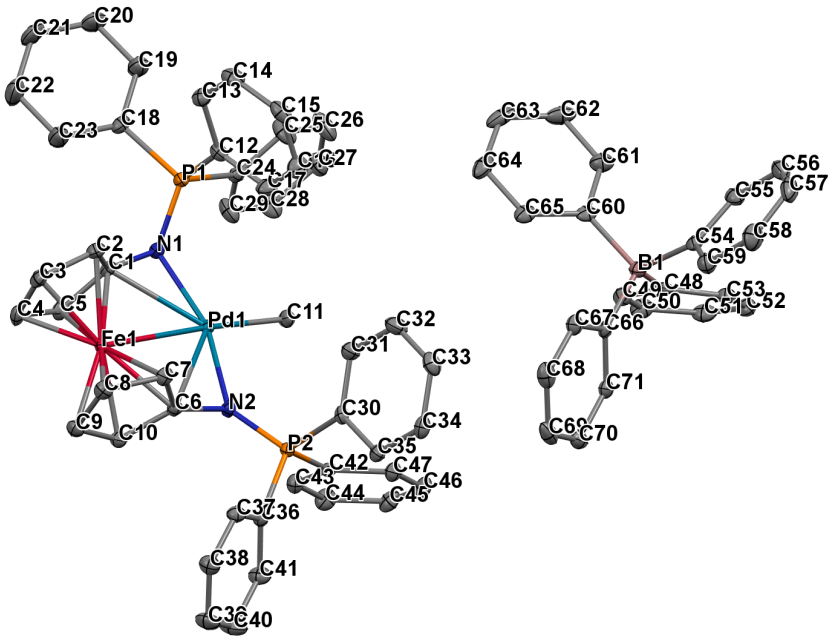

Figure E41. Molecular structure drawing of [fc(NPPh$_3$)$_2$PdMe][BPh$_4$] with thermal ellipsoids at 50% probability; hydrogen atoms were omitted for clarity.

Crystal data for $C_{71}H_{61}BFeN_2P_2Pd$; M_r = 1177.21; Triclinic; space group P-1; *a* = 12.4007(11) Å; *b* = 16.5646(14) Å; *c* = 16.8723(14) Å; α = 61.6650(10)°; β = 82.0190(10)°; γ = 78.0320(10)°; V = 2980.9(4) Å^3; Z = 2; T = 100(2) K; λ = 0.71073 Å; μ = 0.642 mm^{-1}; d_{calc} = 1.312 g.cm^{-3}; 34324 reflections collected; 10478 unique (R_{int} = 0.0188); giving R_1 = 0.0220, wR_2 = 0.0565 for 9596 data with [I>2σ(I)] and R_1 = 0.0251, wR_2 = 0.0575 for all 10478 data. Residual electron density (e$^-$.Å^{-3}) max/min: 0.603/-0.332.

[fc(NPEt$_3$)$_2$PdMe][BPh$_4$]

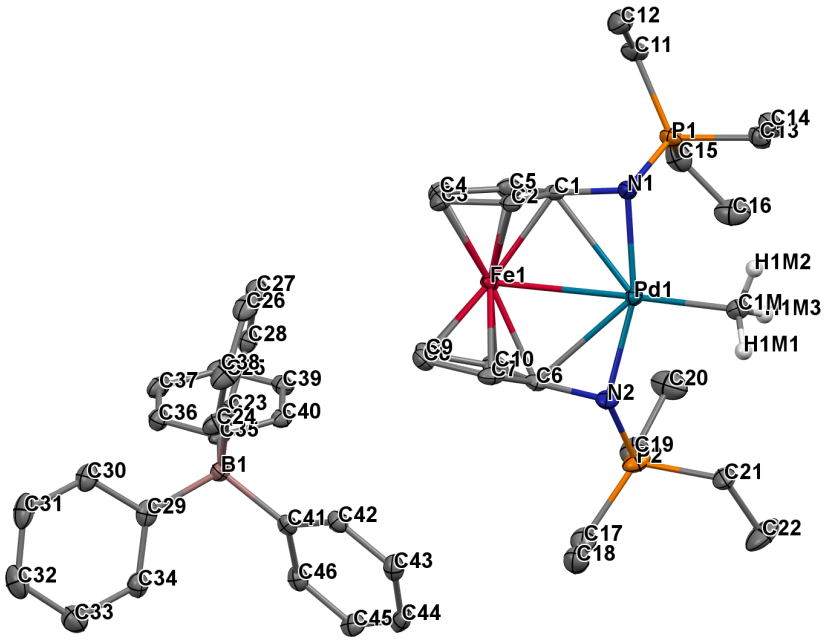

Figure E42. Molecular structure drawing of [fc(NPEt$_3$)$_2$PdMe][BPh$_4$] with thermal ellipsoids at 50% probability; most hydrogen and solvent atoms were omitted for clarity.

Crystal data for $C_{48}H_{63}BCl_2FeN_2P_2Pd$; M_r = 973.90; Monoclinic; space group $P2_1/n$; *a* = 13.7968(10) Å; *b* = 11.2680(8) Å; *c* = 29.080(2) Å; α = 90°; β = 93.2721(12)°; γ = 90°; V = 4513.4(6) Å^3; Z = 4; T = 100(2) K; λ = 0.71073 Å; μ = 0.945 mm^{-1}; d_{calc} = 1.433 g.cm^{-3}; 35644 reflections collected; 7945 unique (R_{int} = 0.0314); giving R_1 = 0.0369, wR_2 = 0.0925 for 6949 data with [I>2σ(I)] and R_1 = 0.0437, wR_2 = 0.0953 for all 7945 data. Residual electron density (e$^-$.Å^{-3}) max/min: 2.636/-1.207.

[fc(NPPh$_3$)$_2$Pd(THF)][BF$_4$]$_2$

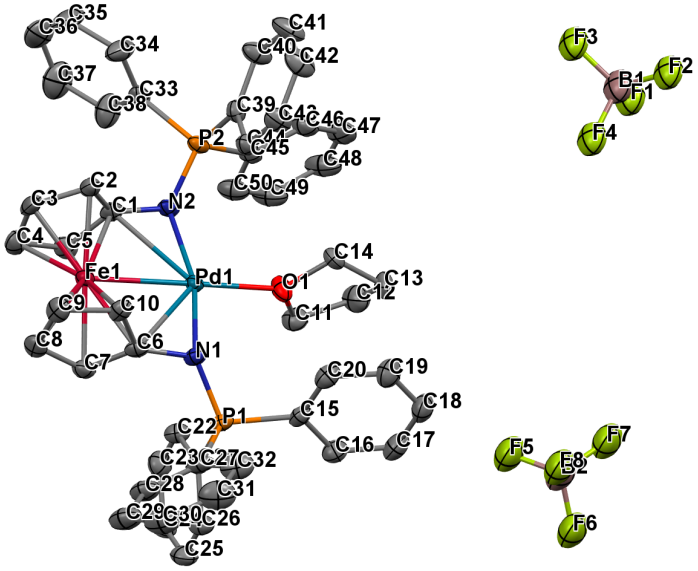

Figure E43. Molecular structure drawing of [fc(NPPh$_3$)$_2$Pd(THF)][BF$_4$]$_2$ with thermal ellipsoids at 50% probability; hydrogen atoms were omitted for clarity.

Crystal data for $C_{50}H_{46}B_2F_8FeN_2OP_2Pd$; M_r = 1088.70; Orthorhombic; space group Pbca; *a* = 20.9759(18) Å; *b* = 16.9627(14) Å; *c* = 31.472(3) Å; α = 90°; β = 90°; γ = 90°; V = 11197.9(16) Å^3; Z = 8; T = 100(2) K; λ = 0.71073 Å; μ = 0.698 mm^{-1}; d_{calc} = 1.292 g.cm^{-3}; 64690 reflections collected; 9856 unique (R_{int} = 0.0251); giving R_1 = 0.0582, wR_2 = 0.1441 for 8766 data with [I>2σ(I)] and R_1 = 0.0653, wR_2 = 0.1482 for all 9856 data. Residual electron density (e$^-$.Å^{-3}) max/min: 1.795/-1.120.

6.6.5 DFT calculations

Table E1. Comparison of geometries from X-ray data and calculations for $[fc(NPPh_3)_2NiPh]^+$, $[fc(NPPh_3)_2PdMe]^+$, and $[fc(NPEt_3)_2PdMe]^+$.

	Ni		**Pd (PPh_3)**		**Pd (PEt_3)**	
Parameter	**Exp.**	**Calculated**	**Exp.**	**Calculated**	**Exp.**	**Calculated**
Fe-M (Å)	2.82	2.81	2.80	2.82	2.78	2.84
M-N(1) (Å)	1.90	1.92	2.03	2.08	2.05	2.09
M-N(2) (Å)	1.90	1.92	2.07	2.09	2.05	2.08
M-C (Å)	1.90	1.89	2.05	2.06	2.06	2.06
N(1)-M-Fe (°)	80.8	81.7	79.5	79.4	80.9	80.1
Fe-M-N(2) (°)	79.5	80.7	81.1	81.1	81.0	79.9
N(1)-M-C (°)	102.7	98.8	97.1	98.1	99.4	100.2
N(2)-M-C (°)	97.0	98.8	102.3	101.8	98.3	99.3

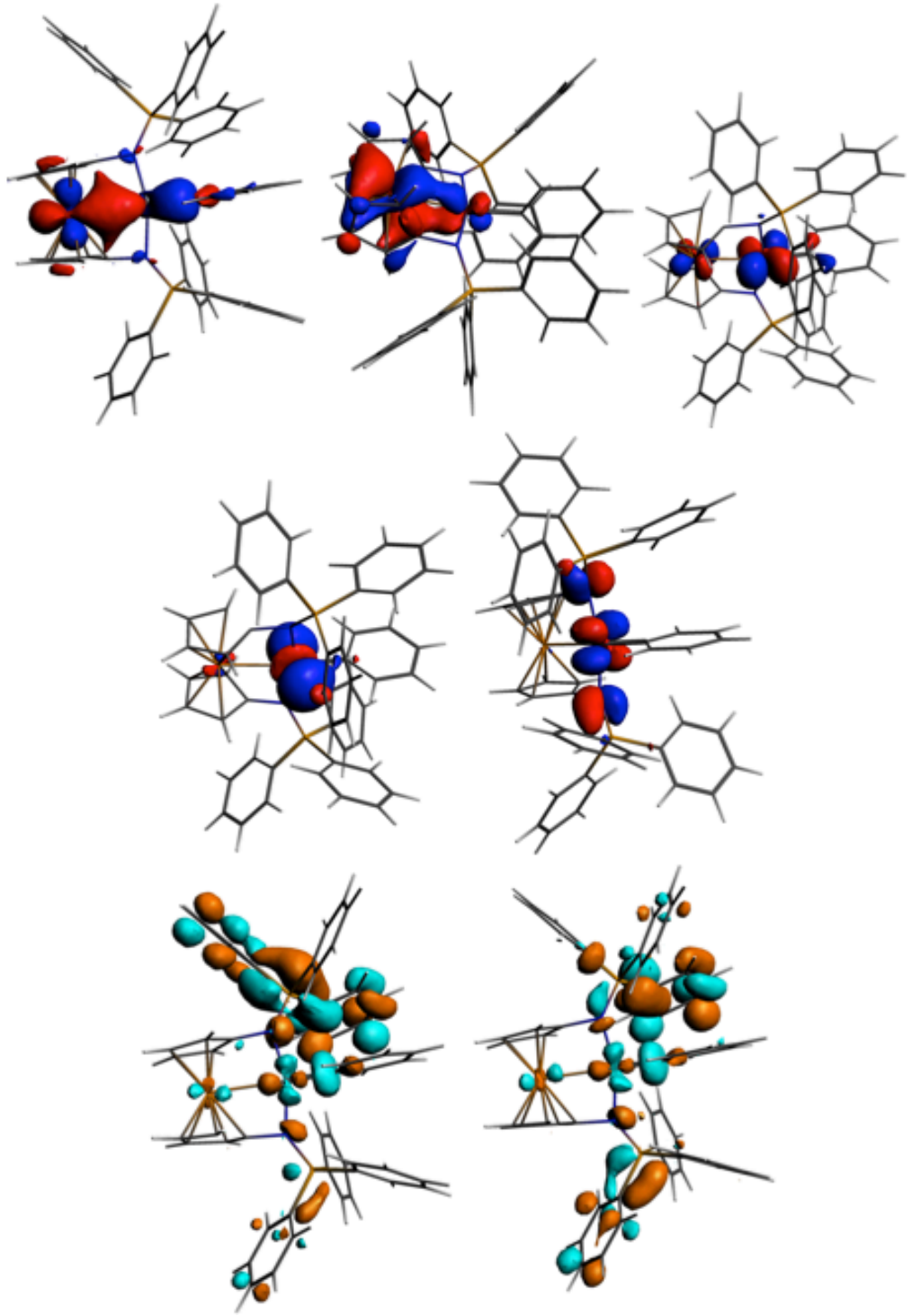

Figure E44. Frontier molecular orbitals for $[fc(NPPh_3)_2NiPh]^+$: HOMO-6 (top left), HOMO-5 (top middle), HOMO-2 (top right), HOMO-1 (middle left), HOMO-1, HOMO (middle right), LUMO (bottom left), LUMO+1 (bottom right); isosurface value = 0.03.

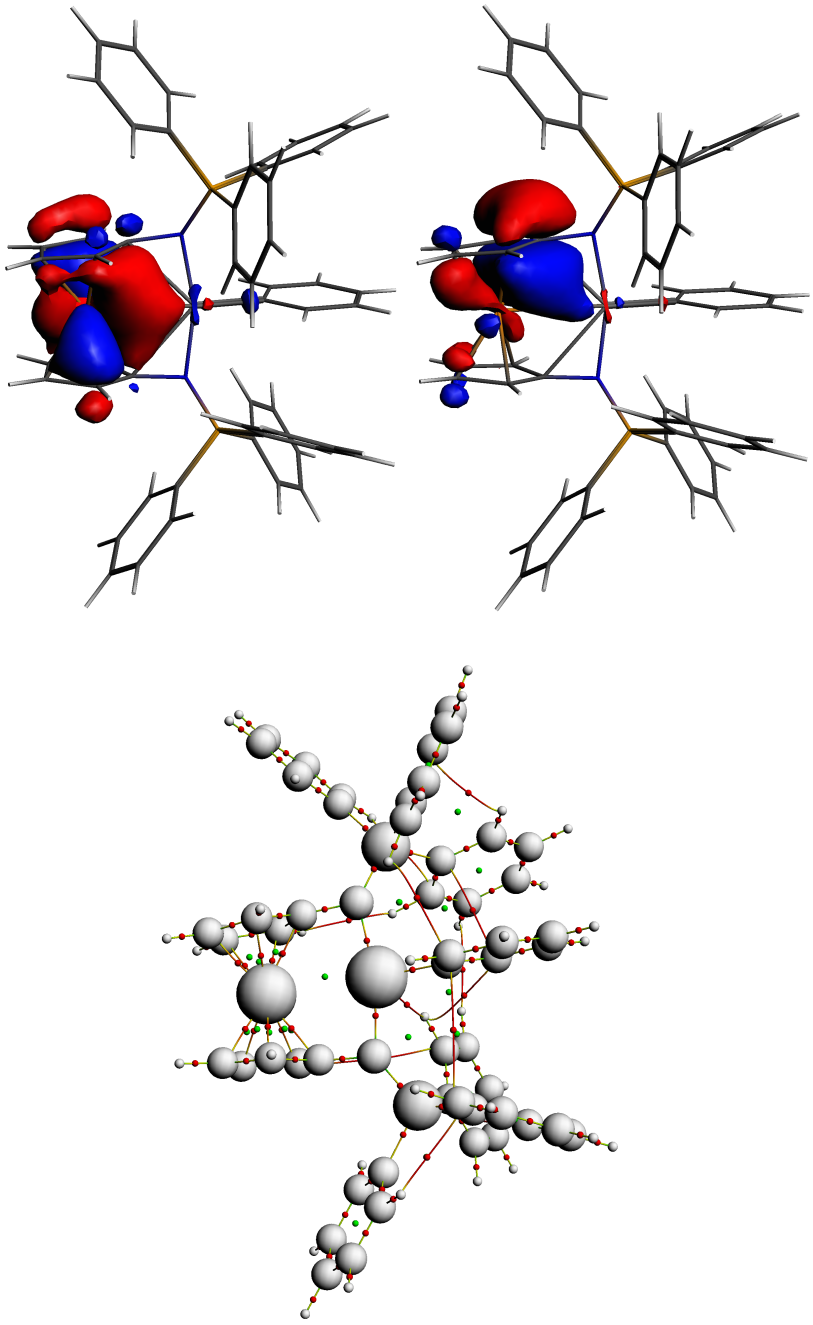

Figure E45. NLMO 89 (top left), NLMO 95 (top right), and Bader bond critical points (bottom) for $[fc(NPPh_3)_2NiPh]^+$.

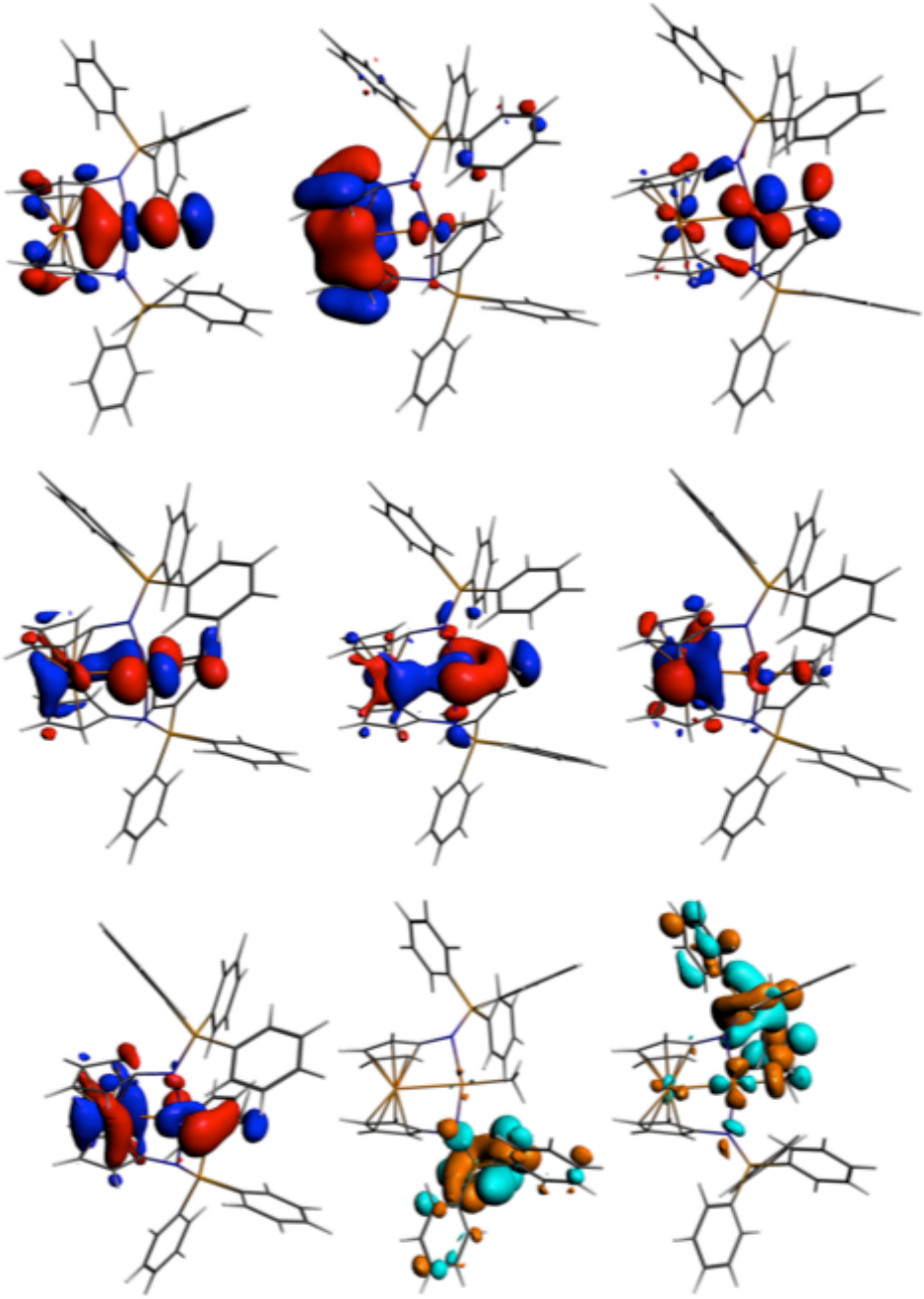

Figure E46. Frontier molecular orbitals for $[fc(NPPh_3)_2PdMe]^+$: HOMO-25 (top left), HOMO-16 (top middle), HOMO-6 (top right), HOMO-5 (middle left), HOMO-2 (middle), HOMO-1 (middle right), HOMO (bottom left), LUMO (bottom middle), LUMO+1 (bottom right); isosurface value = 0.03.

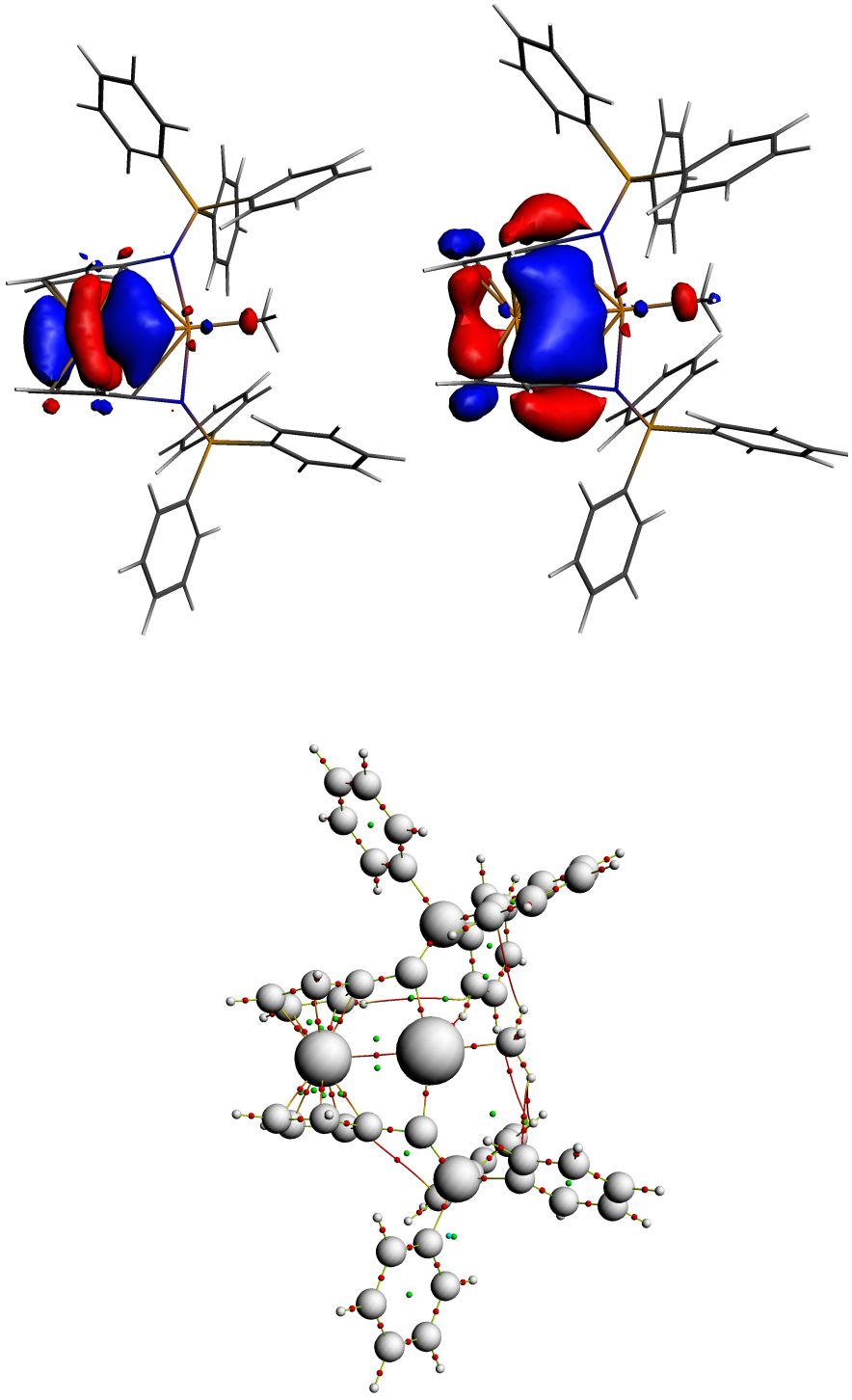

Figure E47. NLMO 93 (top left), NLMO 219 (top right), and Bader bond critical points (bottom) for $[fc(NPPh_3)_2PdMe]^+$.

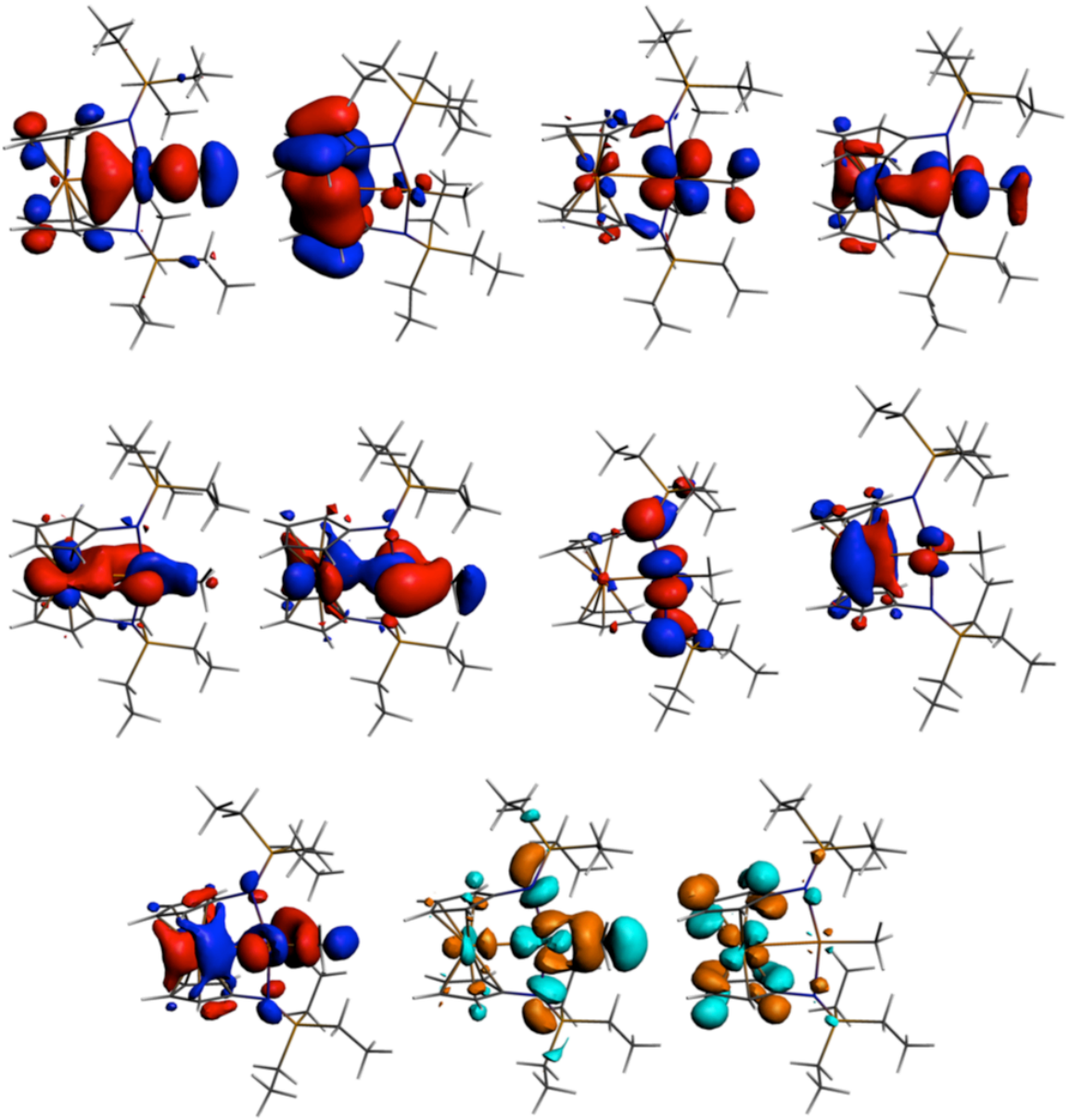

Figure E48. Frontier molecular orbitals for $[fc(NPEt_3)_2PdMe]^+$: HOMO-13 (top left), HOMO-10 (top middle left), HOMO-6 (top middle right), HOMO-5 (top right), HOMO-4 (middle left), HOMO-3 (middle second from left), HOMO-2 (middle second from right), HOMO-1 (middle right), HOMO (bottom left), LUMO (bottom middle), LUMO+1 (bottom right); isosurface value = 0.03.

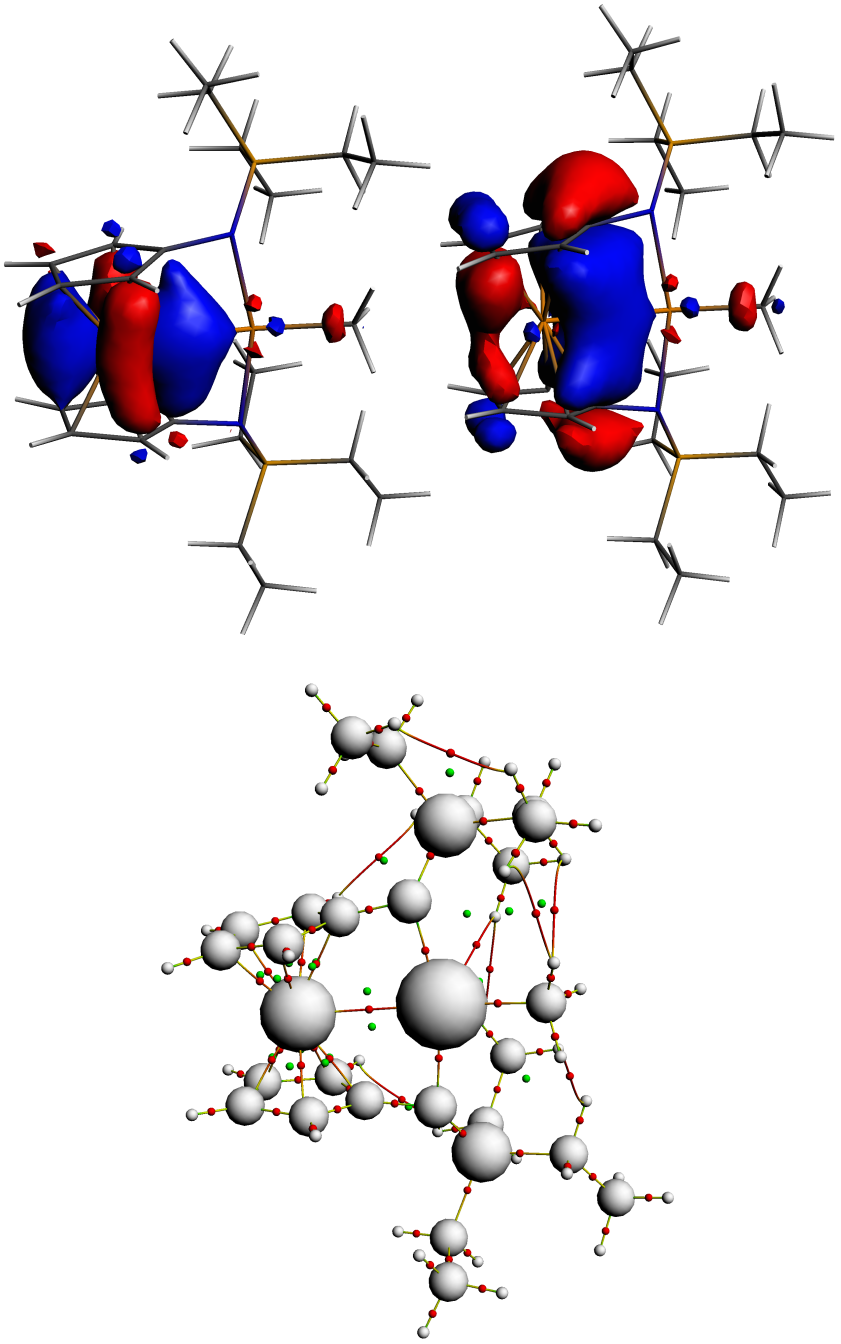

Figure E49. NLMO 69 (top left), NLMO 147 (top right) and Bader bond critical points (bottom) for $[fc(NPEt_3)_2PdMe]^+$.

6.7 References

1. Blanco, V.; Leigh, D. A.; Marcos, V., *Chem. Soc. Rev.* **2015,** *44* (15), 5341-5370.

2. Teator, A. J.; Lastovickova, D. N.; Bielawski, C. W., *Chem. Rev.* **2016,** *116* (4), 1969-1992.

3. Gregson, C. K. A.; Gibson, V. C.; Long, N. J.; Marshall, E. L.; Oxford, P. J.; White, A. J. P., *J. Am. Chem. Soc.* **2006,** *128* (23), 7410-7411.

4. Broderick, E. M.; Guo, N.; Vogel, C. S.; Xu, C.; Sutter, J.; Miller, J. T.; Meyer, K.; Mehrkhodavandi, P.; Diaconescu, P. L., *J. Am. Chem. Soc.* **2011,** *133* (24), 9278–9281.

5. Süßner, M.; Plenio, H., *Angew. Chem. Int. Ed.* **2005,** *44* (42), 6885-6888.

6. Liu, G.; He, H.; Wang, J., *Adv. Synth. Catal.* **2009,** *351* (10), 1610-1620.

7. Ringenberg, M. R.; Kokatam, S. L.; Heiden, Z. M.; Rauchfuss, T. B., *J. Am. Chem. Soc.* **2007,** *130* (3), 788-789.

8. Slone, C. S.; Mirkin, C. A.; Yap, G. P. A.; Guzei, I. A.; Rheingold, A. L., *J. Am. Chem. Soc.* **1997,** *119* (44), 10743-10753.

9. Allgeier, A. M.; Mirkin, C. A., *Angew. Chem. Int. Ed.* **1998,** *37* (7), 894-908.

10. Tennyson, A. G.; Lynch, V. M.; Bielawski, C. W., *J. Am. Chem. Soc.* **2010,** *132* (27), 9420-9429.

11. Ringenberg, M. R.; Nilges, M. J.; Rauchfuss, T. B.; Wilson, S. R., *Organometallics* **2010,** *29* (8), 1956-1965.

12. Lorkovic, I. M.; Duff, R. R.; Wrighton, M. S., *J. Am. Chem. Soc.* **1995,** *117* (12), 3617-3618.

13. Leibfarth, F. A.; Mattson, K. M.; Fors, B. P.; Collins, H. A.; Hawker, C. J., *Angew. Chem. Int. Ed.* **2013,** *52* (1), 199-210.

14. Sud, D.; Norsten, T. B.; Branda, N. R., *Angew. Chem. Int. Ed.* **2005,** *44* (13), 2019-2021.

15. Wang, J.; Feringa, B. L., *Science* **2011,** *331* (6023), 1429-1432.

16. Romanazzi, G.; Degennaro, L.; Mastrorilli, P.; Luisi, R., *ACS Catal.* **2017,** *7* (6), 4100-4114.

17. Quan, S. M.; Wang, X.; Zhang, R.; Diaconescu, P. L., *Macromolecules* **2016,** *49* (18), 6768-6778.

18. Wang, X.; Thevenon, A.; Brosmer, J. L.; Yu, I.; Khan, S. I.; Mehrkhodavandi, P.; Diaconescu, P. L., *J. Am. Chem. Soc.* **2014,** *136* (32), 11264-11267.

19. Biernesser, A. B.; Delle Chiaie, K. R.; Curley, J. B.; Byers, J. A., *Angew. Chem. Int. Ed.* **2016,** *55* (17), 5251–5254.

20. Zhu, Y.; Romain, C.; Williams, C. K., *J. Am. Chem. Soc.* **2015,** *137* (38), 12179-12182.

21. Paul, S.; Romain, C.; Shaw, J.; Williams, C. K., *Macromolecules* **2015,** *48* (17), 6047-6056.

22. Romain, C.; Williams, C. K., *Angew. Chem. Int. Ed.* **2014,** *53* (6), 1607-1610.

23. Liu, B.; Cui, D.; Tang, T., *Angew. Chem. Int. Ed.* **2016,** *55* (39), 11975-11978.

24. Broderick, E. M.; Guo, N.; Wu, T.; Vogel, C. S.; Xu, C.; Sutter, J.; Miller, J. T.; Meyer, K.; Cantat, T.; Diaconescu, P. L., *Chem. Commun.* **2011,** *47*, 9897-9899.

25. Abubekerov, M.; Shepard, S. M.; Diaconescu, P. L., *Eur. J. Inorg. Chem.* **2016,** *2016* (15-16), 2634-2640.

26. Chen, M.; Yang, B.; Chen, C., *Angew. Chem. Int. Ed.* **2015,** *54* (51), 15520-15524.

27. Zou, W.; Pang, W.; Chen, C., *Inorg. Chem. Front.* **2017,** *4*, 795-800.

28. Feyrer, A.; Breher, F., *Inorg. Chem. Front.* **2017,** *4*, 1125-1134.

29. Shepard, S. M.; Diaconescu, P. L., *Organometallics* **2016,** *35* (15), 2446-2453.

30. Klenk, S.; Rupf, S.; Suntrup, L.; van der Meer, M.; Sarkar, B., *Organometallics* **2017,** *36* (10), 2026-2035.

31. Cabrera, K. D.; Rowland, A. T.; Szarko, J. M.; Diaconescu, P. L.; Bezpalko, M. W.; Kassel, W. S.; Nataro, C., *Dalton Trans.* **2017,** *46*, 5702-5710.

32. Blass, B. L.; Hernández Sánchez, R.; Decker, V. A.; Robinson, M. J.; Piro, N. A.; Kassel, W. S.; Diaconescu, P. L.; Nataro, C., *Organometallics* **2016,** *35* (4), 462-470.

33. Ringenberg, M. R.; Wittkamp, F.; Apfel, U.-P.; Kaim, W., *Inorg. Chem.* **2017,** *56* (13), 7501-7511.

34. Warnick, E. P.; Dupuis, R. J.; Piro, N. A.; Scott Kassel, W.; Nataro, C., *Polyhedron* **2016,** *114*, 156-164.

35. Gramigna, K. M.; Oria, J. V.; Mandell, C. L.; Tiedemann, M. A.; Dougherty, W. G.; Piro, N. A.; Kassel, W. S.; Chan, B. C.; Diaconescu, P. L.; Nataro, C., *Organometallics* **2013,** *32* (20 (SI: Ferrocene: Beauty and Function)), 5966–5979.

36. Gusev, O. V.; Kalsin, A. M.; Peterleitner, M. G.; Petrovskii, P. V.; Lyssenko, K. A.; Akhmedov, N. G.; Bianchini, C.; Meli, A.; Oberhauser, W., *Organometallics* **2002,** *21* (17), 3637-3649.

37. Zuideveld, M. A.; Swennenhuis, B. H. G.; Kamer, P. C. J.; van Leeuwen, P. W. N. M., *J. Organomet. Chem.* **2001,** *637-639*, 805-808.

38. Seyferth, D.; Hames, B. W.; Rucker, T. G.; Cowie, M.; Dickson, R. S., *Organometallics* **1983,** *2*, 472-474.

39. Cowie, M.; Dickson, R. S., *J. Organomet. Chem.* **1987,** *326* (2), 269-280.

40. Sato, M.; Suzuki, K.; Asano, H.; Sekino, M.; Kawata, Y.; Habata, Y.; Akabori, S., *J. Organomet. Chem.* **1994,** *470* (1), 263-269.

41. Takemoto, S.; Kuwata, S.; Nishibayashi, Y.; Hidai, M., *Inorg. Chem.* **1998,** *37* (25), 6428-6434.

42. Pick, F. S.; Thompson, J. R.; Savard, D. S.; Leznoff, D. B.; Fryzuk, M. D., *Inorg. Chem.* **2016,** *55* (8), 4059-4067.

43. Metallinos, C.; Tremblay, D.; Barrett, F. B.; Taylor, N. J., *J. Organomet. Chem* **2006,** *691* (9), 2044-2047.

44. Jess, K.; Baabe, D.; Bannenberg, T.; Brandhorst, K.; Freytag, M.; Jones, P. G.; Tamm, M., *Inorg. Chem.* **2015,** *54* (24), 12032-12045.

45. Green, A. G.; Kiesz, M. D.; Oria, J. V.; Elliott, A. G.; Buechler, A. K.; Hohenberger, J.; Meyer, K.; Zink, J. I.; Diaconescu, P. L., *Inorg. Chem.* **2013,** *52* (9), 5603–5610.

46. Duhović, S.; Oria, J. V.; Odoh, S. O.; Schreckenbach, G.; Batista, E. R.; Diaconescu, P. L., *Organometallics* **2013,** *32* (20), 6012–6021.

47. Carver, C. T.; Monreal, M. J.; Diaconescu, P. L., *Organometallics* **2008,** *27*, 363-370.

48. Shafir, A.; Arnold, J., *J. Am. Chem. Soc.* **2001,** *123* (37), 9212-9213.

49. Huang, W.; Khan, S. I.; Diaconescu, P. L., *J. Am. Chem. Soc.* **2011,** *133* (24), 10410-10413.

50. Diaconescu, P. L., *Comments Inorg. Chem.* **2010,** *31* (5-6), 196-241.

51. Diaconescu, P. L., *Acc. Chem. Res.* **2010,** *43* (10), 1352-1363.

52. Monreal, M. J.; Diaconescu, P. L., *Organometallics* **2008,** *27*, 1702-1706.

53. Monreal, M. J.; Carver, C. T.; Diaconescu, P. L., *Inorg. Chem.* **2007,** *46*, 7226-7228.

54. Otón, F.; Ratera, I.; Espinosa, A.; Wurtz, K.; Parella, T.; Tárraga, A.; Veciana, J.; Molina, P., *Chem. Eur. J.* **2010,** *16* (5), 1532-1542.

55. Pangborn, A. B.; Giardello, M. A.; Grubbs, R. H.; Rosen, R. K.; Timmers, F. J., *Organometallics* **1996,** *15* (5), 1518-1520.

56. Zeller, A.; Herdtweck, E.; Strassner, T., *Eur. J. Inorg. Chem.* **2003,** *2003* (9), 1802-1806.

57. Shafir, A.; Power, M. P.; Whitener, G. D.; Arnold, J., *Organometallics* **2000,** *19* (19), 3978-3982.

58. Dhar, D.; Yee, G. M.; Spaeth, A. D.; Boyce, D. W.; Zhang, H.; Dereli, B.; Cramer, C. J.; Tolman, W. B., *J. Am. Chem. Soc.* **2016,** *138* (1), 356-368.

59. ADF2013.01; SCM Scientific Computing & Modeling: Theoretical Chemistry, Vrije Universiteit, Amsterdam, The Netherlands.

60. te Velde, G.; Bickelhaupt, F. M.; Baerends, E. J.; Fonseca Guerra, C.; van Gisbergen, S. J. A.; Snijders, J. G.; Ziegler, T., *J. Comput. Chem.* **2001,** *22* (9), 931-967.

61. Fonseca Guerra, C.; Snijders, J. G.; te Velde, G.; Baerends, E. J., *Theor. Chem. Acc.* **1998,** *99*, 391-403.

62. Perdew, J. P.; Wang, Y., *Phys. Rev. B* **1992,** *45* (23), 13244-13249.

63. Yang, L.; Powell, D. R.; Houser, R. P., *Dalton Trans.* **2007,** (9), 955-964.

64. Sato, M.; Shigeta, H.; Sekino, M.; Akabori, S., *J. Organomet. Chem.* **1993,** *458* (1-2), 199-204.

65. Mayer, I., *Int. J. Quantum Chem.* **1984,** *26* (1), 151-154.

66. Bridgeman, A. J.; Cavigliasso, G.; Ireland, L. R.; Rothery, J., *J. Chem. Soc., Dalton Trans.* **2001,** (14), 2095-2108.

67. Glendening, E. D.; Badenhoop, J. K.; Reed, A. E.; Carpenter, J. E.; Bohmann, J. A.; Morales, C. M.; Landis, C. R.; Weinhold, F. *http://nbo6.chem.wisc.edu:* Theoretical Chemistry Institute, University of Wisconsin, Madison, WI, 2013.

68. Bader, R. F. W., *Atoms in Molecules - A Quantum Theory*. Oxford University Press: Oxford, 1990.

69. Rodríguez, J. I.; Bader, R. F. W.; Ayers, P. W.; Michel, C.; Götz, A. W.; Bo, C., *Chem. Phys. Lett.* **2009,** *472* (1-3), 149-152.

70. Fowe, E. P.; Therrien, B.; Suss-Fink, G.; Daul, C., *Inorg. Chem.* **2007,** *47* (1), 42-48.

71. Makal, A. M.; Plażuk, D.; Zakrzewski, J.; Misterkiewicz, B.; Woźniak, K., *Inorg. Chem.* **2010,** *49* (9), 4046-4059.

CHAPTER 7: CONCLUSIONS AND OUTLOOK

7.1 Conclusions

Our group's investigations into redox switchable systems containing ferrocene-based supporting ligands, prior to the work presented in this dissertation, focused predominantly on early transition and main group metals utilizing symmetrically substituted ferrocenes.[1-6] The work outlined here discusses the advantages and challenges of utilizing late transition metals supported by symmetrically and non-symmetrically substituted ferrocene-based ligands.[7,8]

The development of a ferrocene heteroscorpionate supporting ligand for the use with late transition metals is described in Chapter 2. Although, the supporting ligand was initially designed for nickel-based olefin polymerization, investigations revealed an incompatibility in the redox behaviors of the iron containing ferrocene moiety and nickel, another first row transition metal. Particularly, in the case of the nickel alkyl complex ($fc^{P,B}$)NiMe, the propensity of both metals to undergo one electron redox processes at similar potentials resulted in an irreversible loss of the alkyl ligand, rendering this compound unfit for redox switchable olefin polymerization. On the other hand, the zinc complexes, due to the redox inactive nature of zinc, showed reversible one electron redox processes attributed to the supporting ligand.

Our interest in developing a redox-switchable olefin polymerization system prompted us to reevaluate the choice of secondary metal in combination with the ferrocene heteroscorpionate ligand. Unlike nickel, palladium does not undergo one electron redox processes. As a result, the palladium system explored in Chapter 3 shows a reversible one electron, ligand based redox event. However, due to the saturation of coordination sites in the palladium heteroscorpionate complex ($fc^{P,B}$)PdMe, the reduced state remains inactive towards olefin polymerization and only

upon the addition of one equivalent of oxidant is the polymerization of norbornene observed. At the time of publication, we proposed that the observed polymerization activity is due to increased lability of the phosphine moiety, which leads to the liberation of a coordination site at palladium. Further investigations into the zinc system (Chapter 5) suggest that the oxidation of the ligand does not occur at iron, but instead results in the formation of a phosphine radical. These findings further support the increase in phosphine lability upon oxidation due to the loss of electron density at the phosphorus atom. Future considerations for the appropriate choice of secondary metal should take into account both its redox-active nature and the number of coordination sites available at the metal center.

Due to the reversible nature of the zinc complexes examined in Chapter 2, we looked into the preparation and application of ferrocene heteroscorpionate zinc alkoxide complexes for ring-opening polymerization of cyclic esters and carbonates, as described in Chapters 4 and 5. The reduced form of the zinc benzoxide complex displayed unusual reactivity, which allowed the preparation of multiblock copolymers of L-lactide and trimethylene carbonate (Chapter 4). An extensive investigation into the solution state behavior of the zinc benzoxide complex prior to and during polymerization revealed the retention of its dimeric state. A cooperative effect between the two zinc metal centers could account for the unusual polymerization activity. However, additional studies involving monomeric zinc heteroscorpionate complexes are necessary to support this hypothesis.

Further investigations of the zinc benzoxide complex did not reveal a dependence of monomer selectivity on the oxidation state of the supporting ligand (Chapter 5). Both redox states displayed activity towards the same set of monomers, albeit at slightly different rates. In this case, the loss of monomer selectivity is likely due to the lack of a phosphine-zinc interaction.

As we learned from the palladium example, the electronic and steric effects are imparted through the phosphine moiety upon oxidation of the supporting ligand. Since the phosphine does not interact with the zinc centers in this case, there are no observable differences between the two oxidation states.

Finally, in Chapter 6 we investigated how the interaction between iron in ferrocene and the secondary metal influences redox activity and olefin coordination. For this purpose, several palladium and nickel alkyl complexes containing an iron-nickel or iron-palladium interaction were prepared. Unfortunately, all complexes showed complicated and irreversible redox processes. Furthermore, the metal-metal interactions in all complexes were not labile enough to permit detectable olefin-palladium and olefin-nickel interactions. Based on these results, we concluded that the presence of direct iron-metal interactions in future systems designed for redox-switchable catalysis should be avoided.

7.2 Future directions for the zinc based redox-switchable ring-opening polymerizations

The observed monomer selectivity in the case of the palladium methyl complex ($fc^{P,B}$)PdMe was attributed to the redox-switchable hemilability of the supporting ligand. Based on this hypothesis, we proposed that switching to a more oxophilic metal would result in a more pronounced phosphine hemilability in the reduced state and a lack of phosphine-zinc interaction in the oxidized state. However, this rationale was undermined by the lack of a phosphine-zinc interaction in the case of the zinc benzoxide complex [($fc^{P,B}$)Zn(μ-OCH_2Ph)]$_2$ (Chapter 4) due to the more preferred oxygen-zinc interactions, resulting in an alkoxide-bridged dimer formation. It is likely that due to this lack of a zinc-phosphine interaction, monomer selectivity based on the oxidation state of the supporting ligand was not observed. On the other hand, both the zinc

chloride and the zinc phenoxide complexes display monomeric structures and contain zinc-phosphine interactions. Unfortunately, neither the zinc chloride complex nor the zinc phenoxide complex is capable of initiating ring-opening polymerization. An alternative approach would involve constraining a zinc alkoxide complex into a monomeric structure, and thus retaining the zinc-phosphine interaction. Initial efforts into increasing the steric bulk at the 3-positions of the pyrazoles are currently underway. If successful, the increased steric bulk in close proximity to the alkoxy ligand will discourage dimerization and allow to probe the effects of ligand oxidation on ring-opening polymerizations of cyclic esters and carbonates.

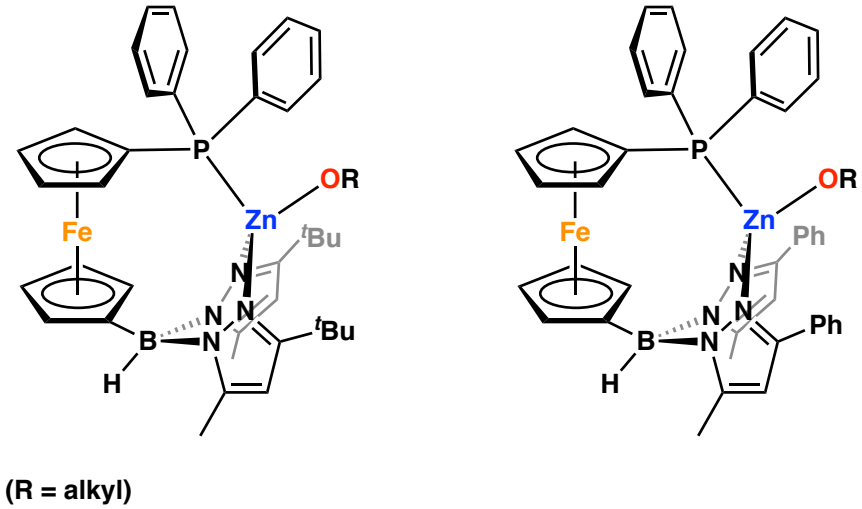

Figure 7-1. Proposed alterations to ferrocene heteroscorpionate zinc alkoxide complexes.

7.3 References

1. Wei, J.; Riffel, M. N.; Diaconescu, P. L. *Macromolecules* **2017**, *50* (5), 1847–1861.

2. Quan, S. M.; Wang, X.; Zhang, R.; Diaconescu, P. L. *Macromolecules* **2016**, *49* (18), 6768–6778.

3. Quan, S. M.; Diaconescu, P. L. *Chem. Commun.* **2015**, *51*, 9643–9646.

4. Wang, X.; Thevenon, A.; Brosmer, J. L.; Yu, I.; Khan, S. I.; Mehrkhodavandi, P.; Diaconescu, P. L. *J. Am. Chem. Soc.* **2014**, *136* (32), 11264–11267.

5. Broderick, E. M.; Guo, N.; Wu, T.; Vogel, C. S.; Xu, C.; Sutter, J.; Miller, J. T.; Meyer, K.; Cantat, T.; Diaconescu, P. L. *Chem. Commun.* **2011**, *47* (35), 9897–3.

6. Broderick, E. M.; Guo, N.; Vogel, C. S.; Xu, C.; Sutter, J.; Miller, J. T.; Meyer, K.; Mehrkhodavandi, P.; Diaconescu, P. L. *J. Am. Chem. Soc.* **2011**, *133* (24), 9278–9281.

7. Abubekerov, M.; Diaconescu, P. L. *Inorg. Chem.* **2015**, *54* (4), 1778–1784.

8. Abubekerov, M.; Shepard, S. M.; Diaconescu, P. L. *Eur. J. Inorg. Chem.* **2016**, *2016* (15-16), 2634–2640.